



12 RESPONSIBLE
CONSUMPTION
AND PRODUCTION



Through waste management programs, recycling initiatives, and sustainable procurement policies, Manipal University Jaipur actively promotes responsible consumption. Workshops and different awareness campaigns cater specifically to the education of the students in the matter of sustainable practices. Alternative production methods research is encouraged towards a change in campus operations and lifestyles of students toward more eco-friendly habits.



Contents

1. Academics
2. Research
3. Events
4. Collaborations



ACADEMICS

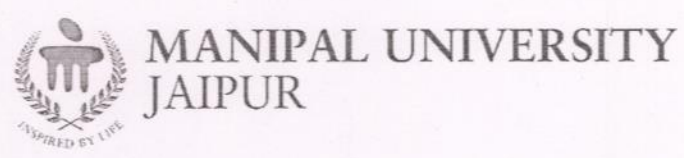
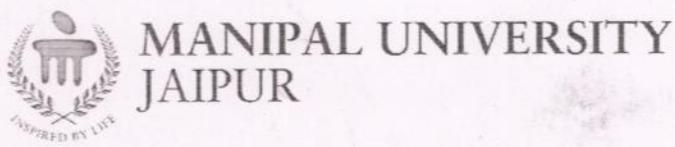


Program/Courses offered in





Sr. No.	Name of Course	Course Code
1	SOLID AND HAZARDOUS WASTE MANAGEMENT	CV6203
2	WASTEWATER TREATMENT SYSTEMS	CV6202
3	ENVIRONMENTAL ECOLOGY	CV6140
4	SANITATION BEHAVIOUR AND ADVOCACY	CV6206
5	EMERGENCY SANITATION	CV6204
6	WATER TREATMENT AND SAFE STORAGE	CY1491
7	GREEN CHEMISTRY	CY1515
8	WATER TECHNOLOGY AND SAFE STORAGE AND APPLICATIONS	CY2281
9	FOOD & BEVERAGE - I	HA1551
10	FOOD & BEVERAGE MANAGEMENT	HA1601
11	ENVIRONMENTAL EDUCATION & MANAGEMENT	HA1802
12	SUPPLY CHAIN MANAGEMENT	MB7553
13	QUALITY MANAGEMENT	MC1591
14	PRODUCTION TECHNOLOGY	MC1656
15	PRODUCTION AND OPERATION MANAGEMENT	MC1761
16	PRINCIPLES OF INDUSTRIAL ENGINEERING	ME1792
17	PRODUCTION PLANNING AND CONTROL	ME1794
18	PRODUCTION AUTOMATION	ME6205
19	ENVIRONMENTAL PSYCHOLOGY	PS1507
20	DEVELOPMENTAL PSYCHOLOGY	PS1508
21	ESTIMATION COSTING & VALUATION	CV1701
22	ETHICS, GOVERNANCE, CSR	HA1502
23	FOOD PRODUCTION FOUNDATION - I	HA1101
24	FOOD & BEVERAGE SERVICE FOUNDATION - I	HA1102
25	FOOD PRODUCTION LAB - I	HA1131
26	FOOD & BEVERAGE SERVICE LAB - I	HA1132
27	HOSPITALITY ORGANIZATIONAL BEHAVIOR	HA1604



FACULTY OF ENGINEERING

SAMM

DEPARTMENT OF MECHATRONICS ENGINEERING

Expert talk on "Advancement in Robotics and Sustainable Application"

Date of Event (07th November 2023)



SUSTAINABLE
DEVELOPMENT
GOALS





Content of Report (index) (Page number may not be required)

1. Introduction of the Event
2. Objective of the Event
3. Beneficiaries of the Event
4. Details of the Guests
5. Brief Description of the event
6. Geotagged Photographs
7. Brochure or creative of the event
8. Schedule of the Event
9. Attendance of the Event
10. Feedback of the event



1. Introduction of the Event

The Department of Mechatronics Engineering, Manipal University Jaipur organized an organising an online Expert talk on “Advancement in Robotics and sustainable application” on 07th November 2023. This workshop will acquaint research scholars, students, of FOE on recent advancement in Robotics application and probable career opportunities in same.

2. Objective of the Event

To create awareness among research scholars, students, on recent advancements in Robotics and its sustainable applications in the Western world. The event also targeted to provide information on opportunities to pursue career and higher study in this field.

3. Beneficiaries of the Event

Students and Research Scholars of MUJ

4. Details of the Guests

The guest speaker, Dr Soumya Kanti Manna, has received his PhD in Medical Robotics and his research interest lies primarily in the areas of designing medical equipment such as wearable exoskeletons for assistance and rehabilitation, sensor deployment for gait analysis, and IoT-based biomedical applications. So far, he has published more than 35 research papers in reputed conferences and journals, working as a guest editor and reviewer in top journals and conferences.

5. Brief Description of the event

Dr Soumya Kanti Manna, provided a very insightful talk on wearable exoskeletons for assistance and rehabilitation, sensor deployment for gait analysis, and IoT-based biomedical applications. It was conducted in online mode in Microsoft Team. The event was started with an introductory note by the organisers, before handing out for the expert talk to the guest. The talk included topics on wearable exoskeletons, most recent and popular research topic on bio-medical robotics and IoT applications on this area. Students from all departments of FOE, MUJ joined the session. The session concluded with valedictory note by HOD, Mechatronics.

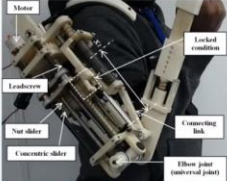



DEPARTMENT OF MECHATRONICS ENGINEERING
INSPIRED BY LIFE
MUJ

6. Photographs

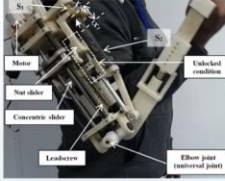
Structural formation of the exoskeleton for different modes of rehabilitation

20 Motor controlled mode



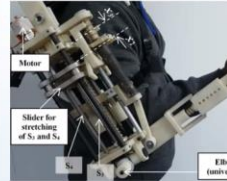
Motor
Lead screw
Nut slider
Connecting link
Concentric slider
Elbow joint (universal joint)
Locked condition

Assistive mode




Motor
Nut slider
Concentric slider
Lead screw
Elbow joint (universal joint)
Unlocked condition

Resistive mode



Motor
Slider for stretching of S₂ and S₃
S₂
Elbow joint (universal joint)

And the rest of the partial force will be by the users. So it is in unlock condition. And I can tell you one thing, there's a mechanism on the top of it. If you see there's the S1 spring



Zoom Meeting with participants: Soumya Manja, RA, Rahul M..., SV, Aaresh R..., SS, Akash T..., LS, Yatin Ko..., DP, Priyansh..., AR, +5



Zoom Meeting grid showing multiple participants in a video conference session.

7. Brochure or creative of the event



**MANIPAL UNIVERSITY
JAIPUR**

EXPERT GUEST LECTURE

Advancement in Robotics and Sustainable Applications

Dr Soumya Manna
School of Engineering, Technology and Design
Canterbury Christ Church University, UK

Organised by:
**Department of Mechatronics,
School of Automobile, Mechanical and Mechatronics (SAAM)**

7th, November 2023 2:00 – 3:00 pm Follow the link to join: [Click here to join the meeting](#)

Conveners: **HOD** **Director**
Dr Shambo Roy Chowdhury Dr Shahbaz Ahmed Siddiqui Prof. Shivaprasad HC
Dr Mrinmoy Misra

8. Schedule of the event

7th November 2023 from 2:00 - 3:30 pm in online mode.

Recording link: https://mujcampus-my.sharepoint.com/:v/g/person/shamboroy_choudhury_jaipur_manipal_edu/ESIQNPI8skRGi8ZxNc9VEoBepKdR_ByzcZV88gmas8sdQ?referrer=Teams.TEAMS-ELECTRON&referrerScenario=MeetingChicletGetLink.view.view

9. Attendance of the Event

Total attendee:- 40

Sl No	Name	Role
1	Shambo Roy Chowdhury [MU - Jaipur]	Organizer
2	Dr. Mrinmoy Misra [MU - Jaipur]	Organizer
3	Dr. Shahbaz Ahmed Siddiqui [MU - Jaipur]	Organizer
4	Soumya Manna	Presenter
5	Divyansh Nagar [Mechatronics - 2022]	Attendee
6	Rahul Marion Anthony [Mechatronics - 2020]	Attendee
7	Surat Rohit Venkat [Mechatronics - 2020]	Attendee

8	Yatin Kohli [Mechatronics - 2020]	Attendee
9	Vanshit Aggarwal [Mechatronics Engineering - 2020]	Attendee
10	Lakshit Sharma [Mechanical - 2020]	Attendee
11	Himanish Bhattacharya [Mechatronics- 2020]	Attendee
12	[BTECH-036-2023-24] HARSHIT JAWA	Attendee
13	Aaresh Rajawat[Mechatronics - 2020]	Attendee
14	[BTECH-031-2023-24] VIBHAV CHANDSI	Attendee
15	[BTECH-005-2023-24] MANUSHREE BARTARIA	Attendee
16	[BTECH-005-2023-24] Harshil Bhardwaj	Attendee
17	Raj Paresh Shah[Mechatronics - 2020]	Attendee
18	[BTECH-007-2023-24] MAYANK GOYAL	Attendee
19	[BTECH-035-2023-24] MEEMANSHA SRIVASTAVA	Attendee
20	[BTECH-006-2023-24] ZIYA PARWEEN	Attendee
21	Harsh Gupta	Attendee
22	Ritik Kumar [Mechatronics - 2021]	Attendee
23	[BTECH-007-2023-24] harshita jain	Attendee
24	Dhruv Desai [Mechatronics - 2020]	Attendee
25	[BTECH-035-2023-24] HEMKANT KUMARRAY	Attendee
26	[BTECH-035-2023-24] MANVIK TALWAR	Attendee
27	Vinayak Kushwah [Mechatronics - 2022]	Attendee
28	Abhay Aaron Apte [MECHATRONICS - 2022]	Attendee
29	[BTECH-031-2023-24] YASH MITTAL	Attendee
30	Akash [Mechatronics - 2022]	Attendee
31	[BTECH-035-2023-24] HARSHIT GOYAL	Attendee
32	Sahil Singh [Automobile - 2020]	Attendee
33	Shashank M K [Mechanical - 2022]	Attendee
34	Priyanshu D. Parikh[Mechatronics - 2020]	Attendee
35	Udit Vohra [MECHATRONICS - 2021]	Attendee
36	Devdutt Patel [MECHATRONICS - 2022]	Attendee
37	Adwaith Ramesh [MECHATRONICS - 2022]	Attendee
38	Moti Kumar Jha [MU - Jaipur]	Attendee
39	Karan Jalwani	Attendee
40	Gunn Verma [MECHATRONICS - 2022]	Attendee



**MANIPAL UNIVERSITY
JAIPUR**



**MANIPAL UNIVERSITY
JAIPUR**

FACULTY OF ENGINEERING

SCHOOL OF COMPUTER AND COMMUNICATION ENGINEERING

**DEPARTMENT OF COMPUTER AND COMMUNICATION
ENGINEERING**

IN ASSOCIATION WITH

IEEE RAJASTHAN SUB SECTION,

**IEEE SENSORS COUNCIL MANIPAL UNIV. JAIPUR STUDENT
BRANCH CHAPTER**

AND

MALAVIYA NATIONAL INSTITUTE OF TECHNOLOGY

IEEE RAJSTHAN SUB SECTION SPONSORED INVITED TALK

ON

**“NANOSHEET-FORKSHEET CO-INTEGRATED N-P TECHNOLOGY
FOR EMERGING TECHNOLOGY”**

Type of Event (INVITED TALK / LECTURE)

Date of Event (9th JUNE 2023)



Content of Report

1. Introduction of the Event
2. Objective of the Event
3. Beneficiaries of the Event
4. Details of the Guests
5. Brief Description of the event
6. Geo-tagged Photographs
7. Brochure or creative of the event
8. Schedule of the Event

1. Introduction of the Event

IEEE Rajasthan Subsection sponsored invited talk on “Nanosheet – Forksheet Co-Integrated N-P Technology for emerging technology was jointly organised by IEEE Rajasthan Subsection in association with Student Branch, IEEE Sensor Council Manipal University Jaipur and Malaviya National Institute of Technology, Jaipur on 9th June 2023 from 4:00 PM onwards at Committee Room, Department of Electronics and Communication Engineering, Malaviya National Institute of Technology. The event was also partly sponsored by Manipal University Jaipur. The keynote speaker is distinguished lecturer of IEEE and had delivered a lecture on the topic “**NANOSHEET-FORKSHEET CO-INTEGRATED N-P TECHNOLOGY FOR EMERGING TECHNOLOGY**” which is an emerging research area in novel nano-electronic devices and sensors design as well as fabrication. Many students and faculty members from Manipal University Jaipur had joined the event in online mode.

2. Objective of the Event

- The primary focus of the event was to shed light on the intricate details of Nanosheet - Fork sheet Co-Integrated N-P Technology and its implications in the rapidly evolving world of emerging technologies.

3. Beneficiaries of the Event:

The beneficiaries of the event would be the students and faculty members doing research in the domain of new emerging nano electronic technologies.

4. Details of the Guests

Prof. Sudeb Dasgupta,
MIEEE, Fellow DAAD, Fellow IUSSTF, Fellow Erasmus Mundus,
Department of Electronics and Communication Engineering,
Indian Institute of Technology, Roorkee
Email: sudeb.dasgupta@ece.iitr.ac.in

5. Brief Description of the event

Inaugural Address: The event began with an inaugural by a distinguished expert in the field. The speaker emphasized the importance of innovative technologies like Nanosheet - Fork sheet Co-Integrated N-P Technology in shaping the future of various industries.

Technical Session: The heart of the event comprised a comprehensive technical session . The session delved into the nuances of Nanosheet - Forksheet Co-Integrated N-P Technology, highlighting its principles, advantages, and potential applications across domains such as electronics, materials science, and energy.

Interactive Discussion: Following the technical session, a lively and engaging discussion took place. Participants had the opportunity to pose questions, share their insights, and engage in thought-provoking discussions with the speaker. This interaction enhanced the overall learning experience and provided valuable insights into the practical aspects of implementing this technology.

The event yielded several positive outcomes, including:

- **Enhanced Knowledge:** Participants gained a deeper understanding of Nanosheet - Forksheet Co-Integrated N-P Technology and its potential applications, contributing to their technical knowledge and awareness.
- **Networking Opportunities:** The event provided a platform for participants to connect with fellow enthusiasts, experts, and professionals in the field, fostering valuable networking relationships.
- **Inspiration:** The event inspired participants to explore innovative technologies and consider their roles in shaping the future of emerging technologies.

6. Photographs



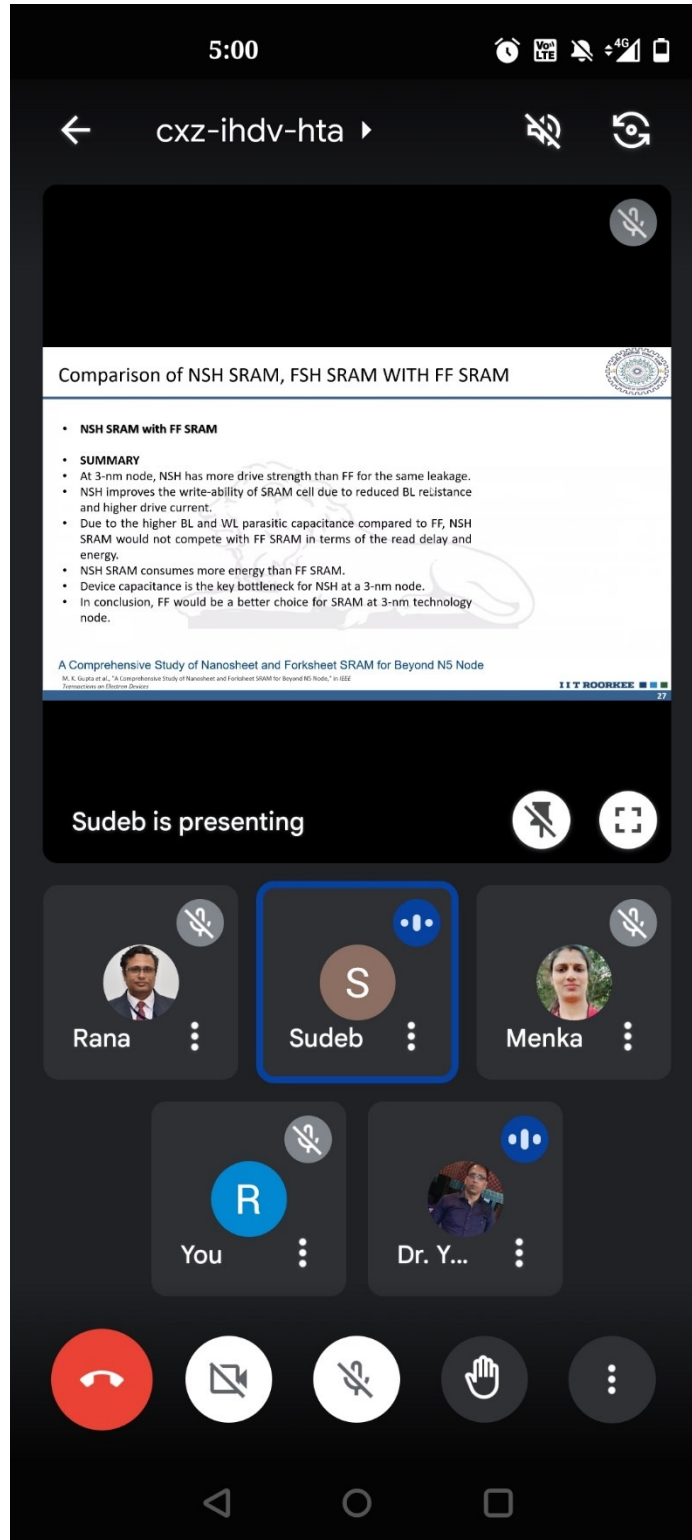
Picture 1: Prof. Sudeb Dasgupta giving the talk



Picture 2: Participants listening to the lecture.



Picture 3: Group Photograph of the Invited Speaker with organizers and participants.



Picture 4: Online lecture screenshot

7. Brochure or creative of the event





IEEE Rajasthan Subsection sponsored Invited Talk On "Nanosheet-Forksheets Co-Integrated N-P Technology for Emerging Technology" will be jointly organized by IEEE Rajasthan Subsection in association with Student Branch, IEEE Sensor Council Manipal University, Jaipur and Malaviya National Institute of Technology Jaipur.

 <p>Organizing Chair</p> <p>Prof. D. Boolchandani, Chairperson, IEEE Rajasthan Subsection, Professor, Department of ECE, Malaviya National Institute of Technology, Jaipur</p>	<p>Resource Person</p> <p>Prof. Sudeb Dasgupta Professor, Department of ECE, Indian Institute of Technology, Roorkee</p> 
-----------------------------------------------------------------------------------------------------------------------------------------------------------------------------------------------------------------------------------------------------------------------------------------------	----------------------------------------------------------------------------------------------------------------------------------------------------------------------------------------------------------------------------------------



June 9, 2023
04:00PM Onwards

Venue:
Committee Room,
Department of Electronics and Communication Engineering,
Malaviya National Institute of Technology, Jaipur

For more Information Contact:

Dr. Menka, Treasurer, IEEE Sensor Council Chapter: Delhi-Rajasthan
Assistant Professor, Department of Electronics and Communication Engineering, Malaviya National Institute of Technology Jaipur, Mobile No. +91-9549650791

Dr. Arun Kishor Johar, Member IEEE Rajasthan SubSection, Executive Committee,
Assistant Professor, Department of Electronics and Communication Engineering, Indian Institute of Information Technology Kota, Mobile No. +91-9549650767

Dr. Renu Kumawat, Faculty Advisor, Student Branch, IEEE Sensor Council, Manipal University Jaipur
Associate Professor, Computer and Communication Engineering Department, Manipal University, Jaipur, Mobile No. +91-9784584471

8. Schedule of the event

Event	Venue / Online Link of Event	Date, Time
Invited Talk	Venue: Committee Room, Dept. of ECE, Malaviya National Institute of Technology, Jaipur Online Link: https://meet.google.com/cxz-ihdv-hta	9 th June 2023, 4:00 PM onwards


 Head
 Department of CCE
 Manipal University Jaipur

Seal and Signature of Head with date



FACULTY OF DESIGN

School of Design & Art

Department of Fashion Design

Interactive Talk

24th Nov 2023

Ashmita



Index

1. Introduction of the Event
2. Objective of the Event
3. Beneficiaries of the Event
4. Details of the Guests
5. Brief Description of the event
6. Photographs
7. Schedule of the Event
8. Attendance of the Event

Adhishita

1. Introduction of the Event

The Department of Fashion Design at Manipal University Jaipur organized a masterclass on "design Process." The lecture was conducted on 3rd Nov 2023, from 2:30 pm to 3:30 pm, via online mode at Manipal University Jaipur. The purpose of the event was to help students and academicians gain a better understanding of the design process.

2. Objective of the Event

The event aimed to provide participants with an in-depth understanding of the circular economy and sustainable practices, leveraging Prof. Charter's extensive experience and expertise. The focus was on how these practices can be implemented across various sectors, with a special emphasis on fashion design. The interactive talk sought to inspire and educate students and researchers on integrating sustainable practices into their work and aligning them with the Sustainable Development Goals (SDGs), particularly focusing on SDG 8: Decent Work and Economic Growth, and SDG 11: Sustainable Cities and Communities. This session was envisioned as an engaging platform for participants to delve into the significance of circular economy principles and their practical application in the realm of fashion design, promoting economic growth through sustainable industrial practices and fostering urban development that respects the limits of natural resources.

3. Beneficiaries of the Event:

Students of Faculty of Design, Manipal University Jaipur

4. Details of the Guest:

Prof. Martin Charter is a renowned sustainability expert with over three decades of experience in director-level roles across multiple industries, including consultancy, leisure, publishing, training, events, and academia. He has a substantial background in strategy, research, marketing, and eco-innovation. His leadership and innovation in sustainable business practices have been widely recognized.

Key Achievements:

Director of The Centre for Sustainable Design: For 28 years, Prof. Charter founded and directed this internationally acclaimed center, focusing on product sustainability and sustainable innovation. Under his leadership, the center generated significant income through research, training, consultancy, and events.

Significant European Commission Involvement: Prof. Charter has actively led and managed numerous EC-funded research and knowledge transfer projects, significantly contributing to sustainability efforts in Europe and Asia.

Global Training Programs: He has conducted worldwide training for large companies and SMEs, covering essential topics like sustainability, business, innovation, design, and marketing.

Expertise in European Manufacturing and Eco-Innovation: As a member of various European Commission expert groups, he has contributed to the development of standards and practices in textiles, metals, and eco-innovation.



Leadership at UCA: His role as Chair of the UCA Environmental & Social Sustainability Working Group highlights his commitment to integrating sustainability into education and academia.

5. Brief Description of the event: -

The interactive talk on "Circular Economy (Sustainable practices)" at Manipal University Jaipur was a comprehensive session that aimed to explore and elucidate the principles of circular economy within the context of fashion design. Led by Prof. Martin Charter, a luminary in sustainability, the event delved into how sustainable practices can be seamlessly integrated into various sectors. It emphasized the alignment of these practices with the Sustainable Development Goals (SDGs), particularly focusing on SDG 8: Decent Work and Economic Growth, and SDG 11: Sustainable Cities and Communities. The talk aimed to foster an understanding among students and research scholars of the critical role circular economy principles play in contemporary design and in promoting sustainable economic and urban development. The session was designed to be engaging, encouraging active participation and discourse, and offering attendees a platform to contribute to and expand their knowledge in sustainable design.

6. Photographs of the event



AN INTERACTIVE TALK ON
**CIRCULAR ECONOMY
(SUSTAINABLE PRACTICES)**

Organized By:
Department of Fashion Design,
SD&A, Faculty of Design

FRIDAY
NOVEMBER, 24th
15:00 - 16:00
(IST)

Speaker
**PROF. MARTIN
CHARTER**

Director of The Centre
for Sustainable Design
(University of Creative
Arts London)

ONLINE
MODE

MANIPAL UNIVERSITY
JAIPUR
University, under Section 2(f) of the UGC Act.

Aspirations



Designing for the Circular Economy

24th November 2023

Manipal University Jaipur, India

Online

Professor Martin Charter

Director, The Centre for Sustainable Design ®

Senior Management Team, Business School for the Creative Industries

University for the Creative Arts (UCA)

UK

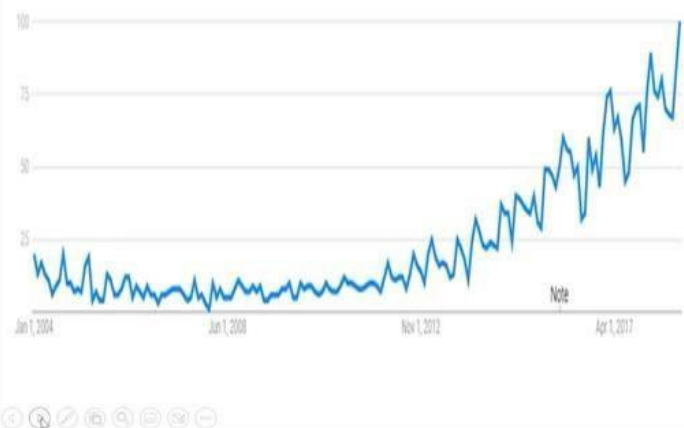


TC323: Six Standards in Development

- **ISO/DIS 59004:** Circular Economy – Terminology, Principles and Guidance for Implementation
- **ISO/DIS 59010:** Circular Economy — Guidance on the transition of business models and value networks
- **ISO/DIS 59020:** Circular economy — Measuring and assessing circularity
- **ISO/CD TR 59031:** Circular economy – Performance-based approach – Analysis of cases studies
- **ISO/CD TR 59032.2:** Circular economy - Review of business model implementation
- **ISO/CD 59040:** Circular Economy — Product Circularity Data Sheet



Google Trends: Circular Economy



Deepshikha

Contact Details

Professor Martin Charter
Director
The Centre for Sustainable Design ®
University for the Creative Arts

Tel: 00 44 (0)1252 892772
Fax: 00 44 (0)1252 892747
Email: mcharter@ucreative.ac.uk
Web: www.cfsd.org.uk



A screenshot of a Zoom meeting interface. It shows four video thumbnails of participants: Dr. Deepshikha Sharma, Mr. Mahboob Anwer, Aanchal Trehan, and Harshwardhan Soni. At the bottom, there is a Zoom control bar with icons for mute, video, chat, and a name tag for 'MC' (Martin Charter).

7. Schedule of the event

The lecture was conducted on 24th Nov 23, from 3:00 pm to 4:00 pm via online mode at Manipal University Jaipur.

8. Total attendee of the Event – 41

S.No.	Full Name
1	Aanchal Trehan [MU - Jaipur]
2	Dr. Deepshikha Sharma [MU - Jaipur]
3	Mr. Mahboob Anwer [MUJ]
4	Indrajeet Kumar [MU - Jaipur]
5	Dr. Sampath Kumar Padmanabha Jinka [MU - Jaipur]
6	Harshwardhan Soni [MU - Jaipur]
7	Prof. Carla Costa Pereira
8	Ms camiile Moco
9	Harshvardhan Singh
10	Vrinda
11	Neha Dagdi
12	Martin Charter
13	Vidisha Bajaj
14	Sakshi Agrawal
15	Simran Parag Patil
16	Drishti Tiwari
17	Rakhi Verma
18	Jagrati Jain
19	Samya Gupta
20	Piyush Raj
21	Tamanna Gracy Singh
22	Navya Gupta
23	Garima Hotwani
24	Khushi Mehta
25	Shruti Verma
26	Krittika
27	Adrija Rathore
28	Shailja

Deepshikha

29	Sneha Sarkar
30	Kovvuru Geetika
31	Camille M.
32	Priya Lodhi
34	Nishtha
35	Khushi Porwal
36	Anu
37	Rajnish Kumar
38	Anushka
39	Harshwardhan Soni
40	Kavya Kalra
41	Shubhi Tambi



Dr. Deepshikha Sharma

Department of Fashion Design

School of Design & Art

Post Event Report



**MANIPAL UNIVERSITY
JAIPUR**

School of Architecture and Design

Expert talk
on

**‘Community Interaction Workshop to Share
knowledge on Community Based Solid Waste
Management Practices’**

Venue: Prithvirajsinghpura, Jaipur, Rajasthan

Time: 11:00 AM onwards

12th May 2023



Index

1. Introduction of the Event	3
2. Objectives of the Event.....	3
3. Beneficiaries of the Event:.....	3
4. Details of the Expert	3
5. Brief Description of the event	3
6. Images.....	4
7. Brochure of the event.....	4
8. Schedule of the event.....	5
9. Attendance of the Event.....	5
10. Weblink.....	6
11. Event Coordinators:.....	6

1. Introduction of the Event:

The School of Architecture & Design at Manipal University Jaipur in association with Mahilla Housing Trust on May 12th, 2023, from 11:00 am onwards, a transformative event unfolded—the "Community Interaction Workshop on Community-Based Solid Waste Management Practices." This gathering served as a platform for knowledge exchange, fostering a collaborative environment where community members shared insights, experiences, and innovative practices in solid waste management. The event aimed to empower participants with practical solutions, strengthening their commitment to sustainable and effective waste management within their communities.

2. Objectives of the Seminar:

- To facilitate the exchange of valuable insights and experiences among community members, promoting a comprehensive understanding of community-based solid waste management practices.
- To provide practical knowledge and tools to empower participants with the skills needed to implement effective and sustainable waste management solutions within their respective communities.
- To foster a collaborative environment to encourage networking and partnership-building among participants, promoting collective efforts towards creating cleaner and healthier communities.

3. Beneficiaries of the Event:

- Common public residing at Prithvirajsinhpora

4. Details of the Expert:

Dr. Madhura is a highly accomplished Architect Planner with 29+ years of experience in Administration, Academics & Research and currently Dean of Faculty of Design at Manipal University Jaipur, and an expert in UPSC, AICTE, CoA and DST Rajasthan & NITI Ayog, Government of India. Her expertise in Sustainable Architecture Design & Planning has been shared through keynotes across universities and governmental bodies. Her scholarly work includes numerous publications and mentoring PhD candidates.

Her research and publications have earned her numerous awards and accolades, including the Indo Pacific Architecture Excellence Award 2021, Education Leadership Award 2019. She is also a UNESCO certified mentor and a member of ICOMOS National Scientific Committee in Working Group of Sustainable Development and in Climate Change and Heritage. She is Fellow Member of various architectural and planning institutes, IGBC etc. contributing to the growth of sustainable and inclusive Design & Planning.

5. Brief Description of the event:

The "Community Interaction Workshop on Community-Based Solid Waste Management Practices" unfolded on May 12th, 2023, from 11:00 am onwards in the rustic setting of Prithvirajsinhpora, a quaint village under the Sanjhariya panchayat in Jaipur, Rajasthan. The event aimed to empower the local community with knowledge and skills for effective waste management. Residents of this rural area actively participated, exchanging insights and experiences. The workshop not only offered practical tools for sustainable waste practices but also facilitated networking and collaboration, fostering a sense of collective responsibility. Amidst the serene surroundings, community members engaged in enriching discussions, contributing to the shared goal of creating a cleaner and healthier environment for Prithvirajsinhpora and its neighboring regions. The event encapsulated a spirit of community collaboration and empowerment, laying the foundation for positive and sustainable changes in solid waste management practices within the rural landscape of Jaipur, Rajasthan.

6. Images



Figure 1: Discussion on Site About Waste Management System



Figure 2: Prof. (Dr.) Madhura Yadav, Delivering about the waste management practice



Figure 3: Prof. (Dr.) Madhura Yadav, Delivering about the waste management practice



Figure 4: Prof. (Dr.) Madhura Yadav, Delivering about the waste management practice

7. Brochure of the Event



Community Interaction/ Workshop to Share Knowledge On Community Based Solid Waste Management Practices

घरेलू अपशिष्ट प्रबंधन

स्वच्छता सरकार की प्राथमिकता

स्वच्छ भारत
एक कदम स्वच्छता की ओर

पहले

जैविक खाद

कोई प्लास्टिक नहीं

सब्जियों के छिलके पशुओं के लिए अच्छे होते हैं

दिनांक:
12 May
2023

विशेषज्ञ:

मधुरा यादव

मिनाली बनर्जी

रचना शर्मा

सामुदायिक-अकादमिक साझेदारी

हम जानते हैं कि समुदायों के पास बहुत ज्ञान होता है, लेकिन हम केवल उन पर भरोसा नहीं कर सकते

कोई यूनिवर्सिटी इसमें कैसे मदद करेगी?

सरकार और विश्वविद्यालय हमारी मदद कर सकती है

स्थानीय लोगों और शिक्षाविदों के बीच ज्ञान के आदान-प्रदान की सुविधा के लिए कोई मंच नहीं

शिक्षाविद: विश्वास बनाने के लिए हमें समुदाय के साथ नियमित रूप से मिलना चाहिए।

हमें वर्तमान सामुदायिक प्रथाओं को समझने के लिए अपशिष्ट संग्रहकों को प्रशिक्षित करना चाहिए।

8. Schedule of the event

11:00 AM onwards

9. Weblink:

10. Event Coordinators:

Prof. (Dr.) Madhura Yadav (Professor & Dean – Faculty of Design, MUJ)

Ms. Rachna Sharma,

Ar. Akshay Gupta (Assistant Professor, SA&D)

Prof. (Dr.) Sunanda Kapoor

Head, Architecture

School of Architecture & Design, Faculty of Design, MUJ



**MANIPAL UNIVERSITY
JAIPUR**

MUJ/Q&C/22/F/1.01



**MANIPAL UNIVERSITY
JAIPUR**

FACULTY OF SCIENCE

SCHOOL OF BASIC SCIENCES

DEPARTMENT OF BIOSCIENCES

**INDUSTRIAL WORKSHOP ON THE OPERATIONS AND HANDLING
OF BIOREACTOR**

Date of Event (11.09.2023-12.09.2023)

1. Introduction of the Event- In this workshop, we get the essential knowledge and practical skills about the bioreactor. A bioreactor is a specialized device used in biotechnology and microbiology to create controlled environments for the growth and cultivation of various biological organisms, primarily microorganisms such as bacteria, yeast, and fungi, as well as cells and tissues. These versatile devices play a pivotal role in various scientific and industrial applications, including pharmaceuticals, biopharmaceuticals, agriculture, environmental remediation, and biofuel production.

2. Objective of the Event

- ***Understanding Bioreactor Principles:*** Fundamental understanding of bioreactor principles, including how they work, their components, and their role in industrial processes.
- ***Bioreactor setup and monitoring:*** Bioreactor setup and monitoring are crucial aspects of bioprocess management, ensuring the controlled cultivation of microorganisms, cells, or tissues for various applications.
- ***Safe Handling and Operation:*** Safe handling of bioreactors, emphasizing the importance of following safety protocols to prevent accidents and ensure the well-being of personnel and the environment.
- ***Process Optimization:*** Optimizing bioprocesses within bioreactors, including parameters like temperature, pH, agitation, and aeration, to maximize productivity and yield.

3. Beneficiaries of the Event: Gain in-depth knowledge and practical skills related to bioreactor setup, operation, and monitoring. This knowledge is beneficial in many food industries. With a better understanding of bioreactor monitoring and control, we can maintain consistent product quality, a crucial factor in industries such as biopharmaceuticals where product safety is paramount.

4. Details of the Guests

Mr. Abhishek Thakur is an engineer at PRS BIO

5. Brief Description of the event:

The "Industrial Workshop on the Operations and Handling of Bioreactor" is a specialized event designed to provide comprehensive knowledge and practical insights into the setup, operation, and management of bioreactors in industrial settings. This workshop

aims to cater to professionals, scientists, researchers, engineers, and individuals across various industries and sectors where bioreactor technology plays a crucial role.

Key elements of this workshop typically include:

In-Depth Learning: The event offers participants a deep dive into the principles, components, and operational aspects of bioreactors. Attendees will gain a thorough understanding of how bioreactors work and their importance in various industries.

Safety and Regulatory Compliance: Safety is a paramount concern when working with bioreactors. The workshop provides guidance on safe handling practices and emphasizes compliance with industry regulations and standards.

Hands-On Experience: The workshop focuses on the opportunity for practical, hands-on experience with bioreactor equipment, allowing them to apply their knowledge in a real-world setting.

Process Optimization: The workshop focuses on strategies and techniques for optimizing bioreactor processes, including monitoring and controlling critical parameters like temperature, pH, agitation, and aeration.

Quality Assurance: Quality control and assurance are essential in industries like pharmaceuticals and biopharmaceuticals. The workshop covers methods for ensuring product quality and consistency.

Industry Insights: The workshop features presentations, case studies, and discussions on current industry trends, innovations, and best practices related to bioreactor technology.

Practical Applications: The knowledge gained from the workshop can be directly applied to various sectors, including pharmaceuticals, biotechnology, environmental science, agriculture, and food production.

Career Development: Individuals attending the workshop can enhance their skills and knowledge, potentially opening up new career opportunities and advancement prospects in their respective fields.

Overall, the "Industrial Workshop on the Operations and Handling of Bioreactor" is a valuable educational and networking event that equips participants with the expertise and confidence to operate bioreactor systems effectively, driving advancements in biotechnology, pharmaceuticals, environmental science, and related fields.

6. Photographs



Dr. Sandeep Srivastava and Dr. Rakesh Kumar Sharma introduced our guest and briefed the workshop.



Our Guest Mr. Abhishek Rathore demonstrated the bioreactor controls

7. Brochure of the event:



**MANIPAL UNIVERSITY
JAIPUR**

DST- FIST supported Department of Biosciences

Industrial Workshop on the Operation and Handling of Bioreactor

September 11-12, 2023





Program Schedule

About the workshop

The Department of Biosciences, Manipal University Jaipur is organizing a workshop on the operation and Handling of Bioreactor. This workshop will provide essential knowledge and practical skills about the bioreactor. The participants will learn about the intricacies of bioreactor setup, monitoring, and sampling, as well as the applications in biotechnology, pharmaceuticals, and more. The industrial expert instructor will guide through hands-on sessions, and interactive discussions, ensuring a comprehensive understanding of bioreactor technology and its real-world applications. This workshop will provide an opportunity to enhance expertise in the dynamic world of bioprocessing.

Date	Timings	Topic
11/09/2023	10:00 A M	Inauguration
	10:30 A M	High Tea
	10:45 A M	Basics of the Bioreactor
	11:30 A M	Reactor Components
	01:00 P M	Lunch Break
	02:30 P M	Reactor Setup
12/09/2023	09:30 A M	Bioreactor run and data acquisition.
	01:00 P M	Lunch Break
	02:30 P M	Q & A Session and Discussions
	03:30 P M	Valedictory Session

About the Department

The Department of Biosciences, Manipal University Jaipur was established in 2012 with a vision of excellence in education and biological sciences and imparting high-quality education and research covering all major areas. The department is now a DST- FIST sponsored department and offers B Sc Biotechnology & Microbiology and M Sc Biotechnology programs. The curriculum is focused to prepare students for higher studies and equip them with knowledge and empower them with skills to become industry-ready candidates. The department routinely involves students as interns in the departmental Start-up and offers them ample opportunities to be part of the innovation and helps to nurture the dreams of entrepreneurship to become the next-gen leaders in Biosciences. The department also involves students in research activities across the interdisciplinary departments and focuses to provide them with training in research institutes and industry.

Advisory Committee

Prof. Lalita Ledwani
(Dean, Faculty of Science)

Dr. Sandeep K Srivastava
(HOD, Biosciences)

Convener

Dr. Rakesh Kumar Sharma
(Department of Biosciences)

Industry Partner

PRS Bio , Chandigarh



8. Schedule of the event

DATE	TIMINGS	TOPIC
11/09/2023	10:00 AM	Inauguration
	10:30 AM	High Tea
	10:45 AM	Basics of Bioreactor
	11:30 AM	Reactor components
	1:00 PM	Lunch Break
	2:30 PM	Reactor setup
12/09/2023	9:30 AM	Bioreactor and data acquisition
	1:30 PM	Lunch Break
	2:30 PM	Q&A Session



MANIPAL UNIVERSITY JAIPUR

Attendance of the Event

Total attendee-71



Department of Biosciences
Manipal University Jaipur

Workshop on the operation and Handling of Bioreactor

Date: 11/09/2023

S. No.	Name	E mail	Signature
1	Abhi Anand	abhiand8576@gmail.com	<i>Abhi Anand</i>
2	Aditi Singh	adit4nic@gmail.com	<i>Aditi Singh</i>
3	Akash Chandra	akashchandra4683@gmail.com	<i>Akash</i>
4	Aman verma	aman.221014005@mu.jaipur.edu	
5	Ankit Choudhary	anunaych2000@gmail.com	
6	Anshi Agarwal	agarwalanshi4@gmail.com	<i>Anshi</i>
7	Anshulika Saxena	anshulika.211002053@mu.jaipur.edu	<i>Anshulika</i>
8	Anushka Singh	anushka2005@gmail.com	<i>Anushka</i>
9	Anvarshu Gopal	anvarshu.211002011@mu.jaipur.edu	<i>Anvarshu</i>
10	Archita Vyas	architavyas09@gmail.com	<i>Archita</i>
11	Arohi Tripathi	arohi7833@gmail.com	<i>Arohi</i>
12	Ayush Rathore	ayush.211003012@mu.jaipur.edu	<i>Ayush Rathore</i>
13	Bhumika Jangir	bhumikajangir041@gmail.com	<i>Bhumika</i>
14	Bonnapati Venkata Sai Sri Sastha Chandra	chandrabns@yahoo.com	<i>Bonnapati</i>
15	DHATVARTHA SINGH BACHELOR	dhabarthasingh@gmail.com	<i>Dhatvart</i>
16	Divya	divya5402@gmail.com	<i>Divya</i>
17	Gaurav Vishwakarma	gaurav.211002033@mu.jaipur.edu	<i>Gaurav</i>
18	Griresh Jaiswal	grireshjaiswal786@gmail.com	<i>Griresh</i>
19	Harshita	Harshita2899@gmail.com	<i>Harshita</i>
20	Ira Dhar	ira.dhar.2004@gmail.com	<i>Ira Dhar</i>
21	Jai Nandwana	jainandwana5@gmail.com	<i>Jai Nandwana</i>
22	Jyotirmayee Paramanya	Paramanyajyotirmayee@gmail.com	<i>Jyotirmayee</i>
23	Madhura Biswas	manoranvas@gmail.com	<i>Madhura</i>
24	Manisha Verma	manishaverma1856@gmail.com	<i>Manisha</i>
25	Mrunal Sunil Mangaje	mrunal.211003007@mu.jaipur.edu	<i>Mrunal</i>
26	Muskan Yadav	muskan.211002040@mu.jaipur.edu	<i>Muskan</i>
27	Nancy Rajgadia	nrajgadia@gmail.com	<i>Nancy</i>
28	Nandini Tungaria	nandini.211003001@mu.jaipur.edu	<i>Nandini</i>
29	Nikki	NKN1526@gmail.com	<i>Nikki</i>

Page 1 of 2

30	Nimisha	nambianimisha3@gmail.com	<i>Nimisha</i>
31	Pratishtha Singh	pratishtha8885@gmail.com	<i>Pratishtha</i>
32	Priti Yadav	py30604@gmail.com	<i>Priti</i>
33	Rahul Shrivastava	rahulshri464@gmail.com	<i>Rahul</i>
34	Rochita Bani	rochita.211002039@mu.jaipur.edu	<i>Rochita</i>
35	Roopal Mishra	roopalnishra98@gmail.com	<i>Roopal</i>
36	Sakshi Nirmal	24.sakshinirmal@gmail.com	<i>Sakshi</i>
37	Sandesh Pralhad Telang	sandeshTelang9@gmail.com	<i>Sandesh</i>
38	Sapna Kumari	Sapna.5.1m.py.123@gmail.com	<i>Sapna</i>
39	Shashwati Kulkarni	Shashwikulkarni7@gmail.com	<i>Shashwati</i>
40	Shaswata Biswas	shaswata.211002017@mu.jaipur.edu	<i>Shaswata</i>
41	Shivani Tiwari	shivantiwari2825@gmail.com	<i>Shivani</i>
42	Sowhit Parvej	shaikh.211002007@mu.jaipur.edu	<i>Sowhit</i>
43	Sriekha Muthumala	srishamuthumala@gmail.com	<i>Sriekha</i>
44	Sylvia Parveen	sylvia.211003009@mu.jaipur.edu	<i>Sylvia</i>
45	Uruvansh Malik	urumalik1@gmail.com	<i>Uruvansh</i>
46	Vanshika Singh Chauhan	vanshika456@gmail.com	<i>Vanshika</i>
47	Vanshita bang	vanshita09.bang@gmail.com	<i>Vanshita</i>
48	Vishnu Priya	vishnuu.pryaaa@gmail.com	<i>Vishnu</i>
49	Bhau - Kuzhwaala	bhanukuzhwaala19@gmail.com	<i>Bhau</i>
50	Jyotsna Rajwade	jyotsnara.97@gmail.com	<i>Jyotsna</i>
51	Vandana Kumari	v88comu@gmail.com	<i>Vandana</i>
52	Tulsi Chauhan	tulsi.chauhan.202@gmail.com	<i>Tulsi</i>
53	Himanshi Sen	himanshi1401198@gmail.com	<i>Himanshi</i>
54	Gourav Jaggi	GOURAVJAGGI.54@gmail.com	<i>Gourav</i>
55	Jana		<i>Jana</i>
56	KSHM P		<i>KSHM P</i>
57	Priyasha Paul	priyashapaul140@gmail.com	<i>Priyasha</i>
58	Debaghya Sankar	debaghya.211002015@mu.jaipur.edu	<i>Debaghya</i>
59	Shikha	shikha.211002020@mu.jaipur.edu	<i>Shikha</i>
60	Jay Bansi	jay.211002046@mu.jaipur.edu	<i>Jay</i>
61	Nisham Sengupta	nisham.221051001@gmail.com	<i>Nisham</i>
62	Bikshita Meja	onejadikshita@gmail.com	<i>Bikshita</i>
63	Rajesh Kumar	rajeshkumar333@gmail.com	<i>Rajesh</i>
64	Rajat Bisi	rajatbisi47@gmail.com	<i>Rajat</i>
65	Runeel Prandhwal	runeel.211051010@mu.jaipur.edu	<i>Runeel</i>

- 65. Manish Raj manish.211003010@mu.jaipur.edu *Manish*
- 66. Samrat Banerjee samrat.211003008@mu.jaipur.edu *Samrat*
- 67. Saboni Singh saboni.211002057@mu.jaipur.edu *Saboni*
- 68. Nareesh Kumar nareesh.211002009@mu.jaipur.edu *Nareesh*
- 69. Harshit Kumar harshit.211002004@mu.jaipur.edu *Harshit*
- 70. Aditya Yadav aditya.211002054@mu.jaipur.edu *Aditya*
- 71. Abhishek Dadhich sabhi5061@gmail.com *Abhishek*

Signature

Seal and Signature of Head with date



DIRECTORATE OF STUDENT'S WELFARE

And

School of Automobile, Mechanical and Mechatronics

Department of Mechatronics

Name of Event- 3D Printing Technology Workshop

Type of Event: Physical

Date of Event: 21 November,2023

content of Report (index)

S.No.	Activity Heads	Page no.
1.	Introduction	1
2.	Objectives	1
3.	Beneficiaries	2
4.	Detailed Description	3
5.	Photographs	4
7.	Schedule of the Event	5
8.	Venue details (for physical events)	6
9.	Brochure of the event	8
10.	Signatures Student Coordinator, Club President, Faculty Coordinator (with Department Name and contact number)	9,10,11

1. Introduction of the Event:

Welcome to the exciting world of 3D printing! This workshop is designed to provide participants with a hands-on experience and a comprehensive understanding of 3D printing technology. Over the next few hours, we will delve into the fundamentals of 3D printing, explore its applications across various industries, and guide you through the process of creating your own 3D-printed objects.

2. Objective of the Event

Objective:

The primary goal of this workshop is to empower participants with a comprehensive understanding of 3D printing technology, fostering hands-on experience and knowledge that can be applied across various disciplines. By the end of the workshop, participants should:

1. **Comprehend 3D Printing Fundamentals:**

Grasp the foundational principles of 3D printing, including the various technologies, processes, and key components involved.

2. **Navigate 3D Printing Software:**

Acquire the skills to use 3D modeling software proficiently for designing objects suitable for 3D printing.

Understand the significance of slicing software in preparing 3D models for the printing process.

3. **Hands-On Design and Printing:**

Gain practical experience by creating a 3D model during the workshop, applying learned skills in a guided, interactive session.

Navigate potential challenges in the 3D printing process and learn problem-solving techniques.

Appreciate Material Science in 3D Printing:

Understand the diverse range of materials used in 3D printing and how material properties impact the final product. Recognize the importance of material selection in achieving desired outcomes.

4. **Explore 3D Printing Applications:**

Explore real-world applications of 3D printing across industries, from healthcare to aerospace, and understand its transformative potential.

5. **Navigate the 3D Printing Landscape:**

Differentiate between various types of 3D printers, understanding their capabilities and applications.

Gain insights into the distinctions between consumer-grade and industrial-grade 3D printers.

6. **Post-Processing Techniques:**

Comprehend post-processing methods to enhance the aesthetics and functionality of 3D-printed objects.

Develop skills in refining and finishing 3D printed models.

7. **Inspire Creativity and Innovation:**

Foster an environment that encourages creativity and innovative thinking in utilizing 3D printing technology.

Encourage participants to envision and explore potential applications in their respective fields.

8. **Promote Future Exploration:**

Provide participants with the knowledge and confidence to further explore 3D printing independently.

Stimulate curiosity about emerging trends and advancements in 3D printing technology.

Through a combination of theoretical insights, hands-on experiences, and practical applications, this workshop aims to equip participants with the skills and inspiration to leverage 3D printing technology as a powerful tool in their professional and creative endeavours.

3. **Beneficiaries of the Event**

The beneficiaries of a 3D printing technology workshop are diverse, spanning across various professional and interest groups. Here are the potential beneficiaries:

Educational Institutions:

Students: Both high school and university students can benefit by gaining practical skills that complement their STEM (Science, Technology, Engineering, and Mathematics) education.

Educators: Teachers and professors can integrate 3D printing into their curricula, enhancing the learning experience and preparing students for future technological advancements.

Professionals and Entrepreneurs:

Engineers and Designers: Acquiring 3D printing skills allows engineers and designers to prototype and iterate designs rapidly, facilitating innovation in product development.

Architects: Understanding 3D printing technology can enhance architectural design and model creation, enabling architects to present their ideas more effectively.

Entrepreneurs: Individuals looking to start their own businesses can explore the potential of 3D printing for prototyping, small-scale manufacturing, and product customization.

Healthcare Professionals:

Medical Researchers: Learn how 3D printing is revolutionizing the healthcare industry, particularly in the fields of anatomical modeling, prosthetics, and personalized medical devices.

Surgeons: Understand how 3D printing is used for surgical planning, creating patient-specific models for better preoperative visualization.

Manufacturing and Industry:

Manufacturing Professionals: Gain insights into how 3D printing is transforming traditional manufacturing processes, including rapid prototyping, tooling, and even end-use part production.

Supply Chain Managers: Explore the potential for on-demand manufacturing and reduced inventory costs through 3D printing technology.

Artists and Designers:

Artists: Incorporate 3D printing into artistic expression, creating sculptures, installations, and designs that were once challenging or impossible to produce through traditional methods.

Fashion Designers: Understand the possibilities of 3D printing in fashion, including customized accessories and avant-garde designs.

4. Details Description:

Workshop Overview:

This comprehensive workshop aims to provide participants with an in-depth understanding of 3D printing technology, covering everything from the fundamentals to practical applications. Participants will engage in hands-on activities, learning to design and print their 3D models while exploring the diverse applications of this cutting-edge technology.

Agenda:

Session 1: Introduction to 3D Printing Technology (1 hour)

Welcome and Icebreaker: Introduction to participants and overview of the day.

Evolution of 3D Printing: A journey through the history and development of 3D printing technology.

Types of 3D Printing Technologies: Detailed exploration of Fused Deposition Modeling (FDM), Stereolithography (SLA), Selective Laser Sintering (SLS), and more.

Key Components of a 3D Printer: Understanding the anatomy of a 3D printer and how each component contributes to the printing process.

Session 2: Materials and Software (1.5 hours)

3D Printing Materials: A comprehensive look at the variety of materials used in 3D printing, including plastics, metals, and bio-compatible materials.

Designing for 3D Printing: Introduction to 3D modeling software (e.g., Tinkercad, Fusion 360) and hands-on exercises to create a simple 3D model.

Slicing Software: Overview of slicing software and its role in converting 3D models into printable instructions.

Session 3: Hands-On Design and Printing (2 hours)

Guided Design Session: Participants design a simple object using 3D modeling software with real-time assistance from instructors.

Troubleshooting Tips: Common issues in 3D printing and how to troubleshoot them.

3D Printing Process: Guided demonstration of the printing process, from loading the filament to post-processing.

5. Photographs

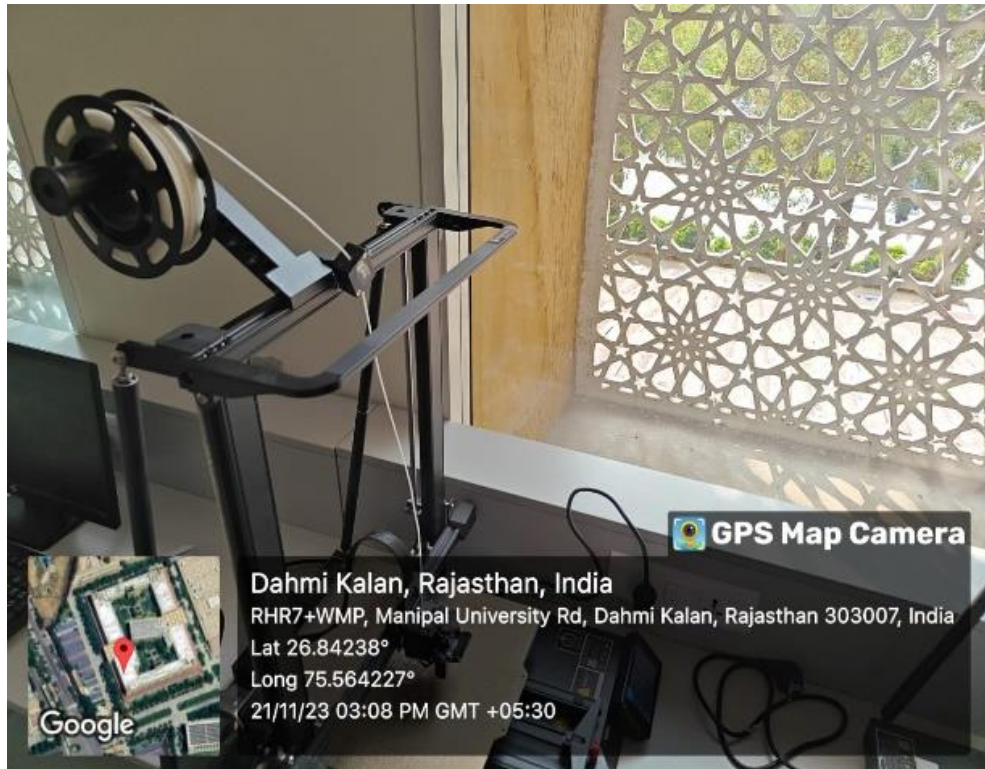


Image 1 : 3D printer



Image 2 : Preparing for the awareness of 3D printing in school



Image 3 : Student Coordinators explaining the 3D printing to the students of school

6. Schedule of the event

Venue: KESAV GLOBAL SCHOOL

Date/Time: 21 November 2023

7. Brochure of the event



MANIPAL UNIVERSITY
JAIPUR
(University under Section 2(f) of the UGC Act)





IEI
MECHATRONICS
STUDENT CHAPTER - MANIPAL UNIVERSITY JAIPUR

3D PRINTING TECHNOLOGY & WORKSHOP

Organized by
IEI Mechatronics Student Chapter
&
Director of Student Welfare



Date : 21-November-2023
Time :- 12pm to 2 Pm

Venue :- Keshav Gobal School,
Araniya Begas Road,
Bagru

Attendance : 47 student and 3 Faculty

S.No.	Reg. No.	Name of The Student	Year
1	229402007	MRIGAKSHI DEV	II
2	229403003	DIVYANSH NAGAR	II
3	229403004	ABHINAV SHARMA	II
4	229403005	M SURAJ SUDHESH	II
5	229403007	PRATEEK JAIN	II
6	229403008	MANEET SINGH BHASIN	II
7	229403011	VIBHOR AGARWAL	II
8	229403012	DEV DUTT PATEL	II



9	229403013	GUNN VERMA	II
10	229403014	CHITRAKSH SAJI PANICKER	II
11	229403015	V SRIKAR	II
12	229403016	ADWAITH RAMESH	II
13	229403020	RAJU KOKATANUR	II
14	229403022	ABHAY AARON APTE	II
15	229403023	AMAN KUMAR KAUSHIK	II
16	229403027	AMOGH AGARWAL	II
17	229403028	VINAYAK KUSHWAH	II
18	229403029	MANAV MANISH MEHTA	II
19	229403030	RISHABH KOTHARI	II
20	229403031	AKASH	II
21	229403032	ADITYA MANOHAR MAIND	II
22	229403033	GAURANG RAJESH JOSHI	II
23	229403034	ADITYA NITIN TUPKARI	II
24	229403035	MECHELEIN ALBERT KENNEDY	II
25	229403036	AKHILESH SHIRKE	II
26	229403037	JOEL JOHNSON	II
27	229403038	DEVANSH HITENDRA SONI	II
28	229408013	DEEVA SACHIN SHUKAL	II
29	219403001	VINITH JAYANANDAN T T	III
30	219403002	ARINDAM MOHAN SINHA	III
31	219403004	DARSHIL DIPESH GALAIYA	III
32	219403005	UDIT VOHRA	III
33	219403008	DHRUMIL KEYUBHAI SHAH	III
34	219403009	YUVAL HITESH SHAH	III
35	219403010	ADITYA SHARMA	III
36	219403018	DHIRAJPRASAD ALMESHPRASAD MAHATO	III
37	219403019	PRATHIT MORESH DESHPANDE	III
38	219403020	MOHAMED RAYAN	III
39	219403022	RITIK KUMAR	III
40	219403023	DIVGYANSHI KUMAR	III
41	219403026	TANAYA RATNADEEP PATEL	III
42	219403028	ALEENA BINU	III
43	219403029	KSHIPA JAISWAL	III
44	219403030	RUPANSH GOYAL	III
45	219403031	ASHWIN PAUL ALDRINE	III
46	219403032	DEVYANI TEWARI	III
47	219403036	RAITHATHA HAPPYN ATULKUMAR	III

Submitted By: 

Ritik Kumar,
3rd year Department of Mechatronics
President of IEI-Mechatronics
Contact Number-7004978674

Mr. Nikhil Vivek Shrivastava
Assistant professor
Department of Mechatronics



Faculty Coordinator
Contact Number - 9579327275

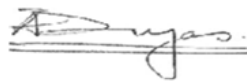
DR. Shahbaz Ahmed Siddiqui
HOD
Department of Mechatronics



Head of Department
Contact Number - 9414253733



Mr. HEMANT KUMAR,
Assistant Director, DSW



(Prof. AD Vyas)
Director, Directorate of Student's Welfare

DIRECTOR STUDENT WELFARE & PROCTOR
MANIPAL UNIVERSITY, JAIPUR



**MANIPAL UNIVERSITY
JAIPUR**

Department of Interior Design

FACULTY OF DESIGN

Make & Take

Kokedama

Hands-on Workshop

22/11/2023



Content of Report

1. Introduction of the Event
2. Objective of the Event
3. Beneficiaries of the Event
4. Details of the Guests
5. Brief Description of the event
6. Photographs
7. Poster of an Event
8. Schedule of the Event
9. Attendance of the Event
10. Link of the event

1. Introduction of the Event

The Department of Interior Design, Faculty of Design at Manipal University Jaipur organized a Kokedama Workshop on 22.11.2023, as a part of the curriculum for 3rd-year B.Des (ID) students. This workshop was conducted under the subject Interior Landscape (ID3105) to provide students with a practical, hands-on experience in the art of preparing Kokedamas. Along with 3rd year B. Des students, this workshop is open for all Manipal University Jaipur students (Diploma, Undergraduate and Postgraduate), Research Scholars, Academicians, Faculty Housing Women, And Industry Professionals with fees of Rs 300/- that included all the materials.

An introduction and demonstration to Kokedama was given by Ms. Geeta Ahluwalia, General Secretary, Kitchen Garden Association, Jaipur. Kitchen Garden Association is an all women lead non-profit organisation in Jaipur. Ar. Sneh Singh (HoD Interior Design) along with Ar. Megha Prabhu K (Asst. Professor, Interior Design) conducted a hands-on 'Make & Take' Kokedama Workshop.

2. Objective of the Event

- Provide 3rd-year B. Des (ID) students with a hands-on experience in the preparation of Kokedamas.
- Enhance the understanding of interior landscaping principles among participants and foster practical skills in crafting Kokedamas, focusing on plant selection, soil composition, and wrapping techniques.
- Facilitate knowledge exchange and collaboration among participants from diverse academic backgrounds, including students, research scholars, academicians, and industry professionals.
- Encourage creativity and innovation in Interior Design through the exploration of Japanese moss ball planters.
- Provide a platform for participants to engage in a Q&A session, allowing for a deeper understanding of the art of Kokedama.
- Create a supportive and inclusive learning environment for all attendees, fostering a sense of community and collaboration within Manipal University Jaipur.

3. Beneficiaries of the Event

The workshop was open to a diverse audience, including 3rd-year B.Des(ID) students, students from other programs (Diploma, Undergraduate, and Postgraduate) at Manipal University Jaipur, research scholars, academicians, Faculty Housing Women, and industry professionals. The inclusive nature of the workshop aimed to foster collaboration and knowledge exchange among participants.

4. Details of the Guests

The honoured guest for the event was Ms. Geeta Ahluwalia, the Secretary of the Kitchen Garden Association Jaipur. Kitchen Garden Association is an all women lead non-profit organisation in Jaipur. Ms. Ahuwalia's expertise in the field brought a valuable perspective to the workshop, and her presence added significant value to the overall learning experience for the participants.

5. Brief Description of the event

The Kokedama workshop provided a unique opportunity for participants to explore the creative and technical aspects of crafting Kokedamas, which are Japanese moss ball planters. The event kicked off with a warm welcome to all attendees, followed by an insightful introduction to the art of Kokedama and its relevance in interior design.

Participants were guided through the step-by-step process of creating their own Kokedamas, emphasizing the selection of suitable plants, soil composition, and wrapping techniques. Ms. Ahuwalia shared her expertise and provided practical tips, enriching the learning experience for everyone involved.

6. Photographs of the Event



Introduction and Demonstration given by Expert, Ms. Geeta Ahluwalia



Demonstration of Kokedama given by Expert, Ms. Geeta Ahluwalia



Participants showcasing their works

7. Poster of the event



MANIPAL UNIVERSITY
JAIPUR

11 SUSTAINABLE CITIES AND COMMUNITIES

15 LIFE ON LAND





DEPARTMENT OF INTERIOR DESIGN,
FACULTY OF DESIGN
IS
ORGANISING A HANDS-ON WORKSHOP ON

Kokedama

Make & Take Interior Landscape

Kokedama, a traditional Japanese art form, transforms plants into living sculptures, encased in moss and twine, suspended like hanging gardens – a harmonious blend of nature and artistry, where plants seem to defy gravity. These captivating green orbs bring an enchanting touch of Zen to any space, inviting serenity and connection with the natural world.

List of Materials provided to you:

- Plants: Ferns and Pothos
- Soil Mix: Peat moss and Clay Soil
- Sheet Moss
- Twine or String
- Scissors
- Plastic Wrap
- Decorative Accent: Miniature figurines

Expert Lecture on:

- How to make Kokedama
- The creative process
- The benefits and aftercare

In collaboration with the Kitchen Garden Association.

It is an all-women-led Non-Profit Organization.

Details of the Workshop:

 Date: 22nd November 2023

 Time: 10:30 am onwards

 Venue: Porch Area, First Floor, Administrative Building

 Registration Fee: Rs. 300
(Inclusive of all materials)

REGISTER YOUR SPOT BY 19.11.2023!
VISIT THE QR CODE FOR GOOGLE FORM



8. Schedule of the event

'Make & Take' Kokedama Workshop 22 November 2023, Wednesday	
Porch Area, 1 st Floor, Administration Building, MUJ	
Time	Event
09:30 am	Registration and Reporting
10:30 am	Welcome address by Ar. Megha Prabhu Karkala Introduction of the Guest Address by Dean, Prof. (Dr.) Madhura Yadav, Dean, FoD
10:45 am	Expert Lecture and Introduction to Kokedama by Ms. Geeta Ahuwalia
11:00 am	Practical Session: Crafting Kokedamas
11:30 am	Making Kokedamas by students
12:45 pm	Completion of Kokedamas and Q&A Session
01:00 pm	Felicitation of Ms. Geeta Ahuwalia and Closing Remarks
01:15 pm	Group Photographs and Exhibition of Students works

9. Attendance of the Event

Sl.No	Participate Name	Participant	Department	Registration No.
1	Kashish Kriplani	Student	B.Des (Interior Design)	210606041
2	Kartik Totla	Student	B.Des (Interior Design)	210606011
3	Aakash Singh	Student	B.Des (Interior Design)	210501007
4	Garima Vijaycharan	Student	B.Des (Interior Design)	210606021
5	Kumari Anjali	Student	B.Des (Interior Design)	210606008
6	Himanshi Sharma	Student	B.Des (Interior Design)	210606028
7	Esha Giri	Student	B.Des (Interior Design)	210606031
8	Anisha Chopra	Student	B.Des (Interior Design)	210606020
9	Rutu Shah	Student	B.Des (Interior Design)	210606007
10	Anushka Rai	Student	B.Des (Interior Design)	210606019
11	Rishika	Student	B.Des (Interior Design)	210606029
12	Paridhi Verma	Student	B.Des (Interior Design)	210606017
13	Naman	Student	B.Des (Interior Design)	210606013
14	Diya Ramchandani	Student	B.Des (Interior Design)	210606039
15	Krishangee Goyal	Student	B.Des (Interior Design)	210606026
16	Avinash Yadav	Student	B.Des (Interior Design)	210606047
17	Himanshi Yadav	Student	B.Des (Interior Design)	210606014
18	Hridyanshi Vyas	Student	B.Des (Interior Design)	210606018
19	Khushi Bhargava	Student	B.Des (Interior Design)	210606010
20	Madhu Tanwar	Student	B.Des (Interior Design)	210606027
21	Riddhi Agarwal	Student	B.Des (Interior Design)	210606038
22	Michelle Earnest	Student	B.Des (Interior Design)	210606043

23	Pooja Jain	Student	B.Des (Interior Design)	23fd10bid00020
24	Shreshtha Gaur	Student	B.Des (Interior Design)	210606012
25	Geetika Gupta	Student	B.Des (Interior Design)	210606037
26	Manya Agarwal	Student	B.Des (Interior Design)	210606015
27	Riya	Student	B.Des (Interior Design)	210606035
28	Ananya Thakan	Student	B.Des (Interior Design)	210606006
29	Devanshi Jain	Student	B.Des (Interior Design)	210606046
30	Drishti Sharma	Student	B.Des (Interior Design)	210606045
31	Sejal Sharma	Student	B.Des (Interior Design)	210606023
32	Samarth Gandhi	Student	B.Des (Interior Design)	210606003
33	Saija Tanya	Student	B.Des (Interior Design)	210606044
34	Garvit Garg	Student	B.Des (Interior Design)	210606001
35	Shruti Dubey	Student	B.Des (Interior Design)	210606022
36	Keshav Katta	Student	B.Des (Interior Design)	210606005
37	Grishma Korjani	Student	B.Des (Interior Design)	210606016
38	Shweta Sharma	Non-Teaching Staff	Non- Teaching Staff	MUJ1134
39	Megha Prabhu Karkala	Assistant Professor	Faculty of Design	MUJ1434
40	Smriti Saraswat	Assistant Professor	Faculty of Design	MUJ1248
41	Dr. Shilpi Gupta	Assistant Professor	Department of Economics	MUJ0403
42	Malini G Prabhu	Faculty Housing Member	Faculty Housing Member	NA
43	Rajendar Kumar	Non-Teaching Staff	GSA	MUJ1300
44	Reetika Choudary	Non-Teaching Staff	Admission Department	MUJ1406
45	Priyanka Samarth	Non-Teaching Staff	Admission Department	MUJ1408
46	Panchami Sharma	Non-Teaching Staff	HR Department	MUJ11002438
47	Kusuma Jinka	Faculty Housing Member	Faculty Housing Member	NA
48	Madan	Non-Teaching Staff	GSA	
49	Gopal	Non-Teaching Staff	GSA	
50	Kush Jee Kamal	Assistant Professor	Faculty of Design	MUJ1714
51	Man Mohan Mehta	Non-Teaching Staff	Admission Department	MUJ0170

Manipal University Jaipur				
Department of Interior Design I FOD				
II Year III Semester - ID3105-Interior Landscape				
KOKEDAMA WORKSHOP - 22.11.2023				
Sl. No.	ROLL No.	NAME	SIGN	
1	210606001	GARVIT GARG		
2	210606003	SAMARTH GANDHI		
3	210606004	VISHVA SAMIRBHAI DAVE	- ABSENT -	
6	210606005	KESHAV KATTA		
5	210606006	ANANYA THAKAN		
6	210606007	RUTU DILIP KUMAR SHAH		
7	210606008	KUMARI ANJALI		
8	210606010	KHUSHI BHARGAVA		
9	210606011	KARTIK TOTLA		
10	210606012	SHRESHTHA GAUR		
11	210606013	NAMAN HODKASIA	- ABSENT -	
12	210606014	HIMANSHI YADAV		
13	210606015	MANYA AGARWAL		
14	210606016	GRISHMA KORJANI		
15	210606017	PARIDHI VERMA		
16	210606018	HRIDYANSHI VIRESH VYAS		
17	210606019	ANUSHKA RAI		
18	210606020	ANISHA CHOPRA		
19	210606021	GARIMA VIJAY CHARAN		
20	210606022	SHRUTI DUBEY		
21	210606023	SEJAL SHARMA		
22	210606026	KRISHANGEE GOYAL		
23	210606027	MADHU TANWAR		
24	210606028	HIMANSHI SHARMA		
25	210606029	RISHIKA		
26	210606031	ESHA GIRI		
27	210606034	KREETI YADAV	- ABSENT -	
28	210606035	RIYA GAUTAM ROY		
29	210606036	HRIDAY SINGH	- ABSENT -	
30	210606037	GEETIKA GUPTA		
31	210606038	RIDDHI AGARWAL		
32	210606039	DIYA RAMCHANDANI		
33	210606041	KASHISH KRIPLANI		
34	210606043	MICHELLE EARNEST		
35	210606044	SAIJA TANYA		
36	210606045	DRISHTI SHARMA		
37	210606046	DEVANSHI JAIN		
38	210606047	AVINASH YADAV		
39	210501007	AKASH		

Manipal University Jaipur				
Department of Interior Design				
Faculty of Design				
KOKEDAMA WORKSHOP - 22.11.2023				
Sl. No.	MUJID/Roll No	NAME	Department	SIGN
1	MUJ1300	Ranjana Kumbh	GT/3/PP	
2	MUJ1406	Reetika Choudhary	Admission	
3	MUJ1408	Rajvardha Semant	Admission	
6				
5	MUJ11002438	Panchami Sharma	HR	
6	FH member	Malini G Prabhu	Faculty Housing	Malini Prabhu
7	FH member	Kusuma Jinka	Faculty Housing	Pooja
8	MUJ403	Dr. Shilpi Gupta	Economics	
9		Nadun	GSA	
10		Copal	GSA	
11	MUJ134	Srishta Sharma	Senior Personal Assistant	
12	MUJ1719	Kyut Dec Kana	IP	
13	MUJ50170	Man Malcom Melin	Admission	Man M
14				

10. Link of MUJ social media page

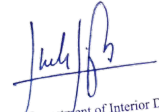
LinkedIn: <https://www.linkedin.com/feed/update/urn:li:activity:7134914090002526208>

Facebook:

- <https://www.facebook.com/share/p/veNm8xBHeCEpUkJh/?mibextid=WC7FNe>
- <https://www.facebook.com/share/p/SESHp8BN95zt4VCP/?mibextid=WC7FNe>

Instagram:

- https://www.instagram.com/p/C0JntI-LnvS/?utm_source=ig_web_copy_link&igshid=MzRIODBiNWFIZA==
- https://www.instagram.com/p/C0Jwf4orIKQ/?utm_source=ig_web_copy_link&igshid=MzRIODBiNWFIZA==


Head, Department of Interior Design
SP&D, Faculty of Design
Manipal University Jaipur



RESEARCH

Summary for Manipal University Jaipur 12



Manipal University Jaipur

2021 to 2023 ▼

Research performance within SDG 12: Responsible Consumption and Production (2023)

Entity: Manipal University Jaipur · Within: All subject areas (ASJC) · Year range: 2021 to 2023 · Data source: Scopus, up to 30 Oct 2024

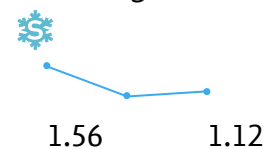
129

Scholarly Output 



1.20

Field-Weighted Citation Impact 



25

International Collaboration 



5,097

Views Count

820

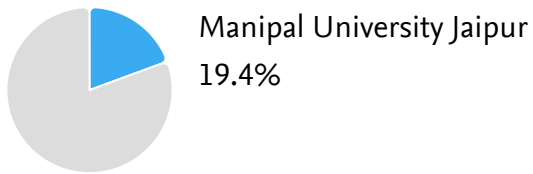
Citation Count 

Collaboration summary within SDG 12: Responsible Consumption and Production (2023)

Entity: Manipal University Jaipur · Within: All
subject areas (ASJC) · Year range: 2021 to 2023 ·
Data source: Scopus, up to 30 Oct 2024

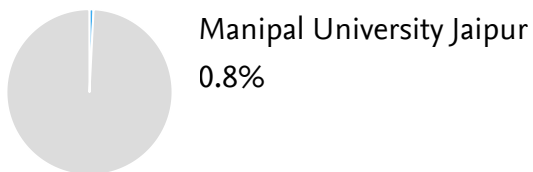
International Collaboration

Publications co-authored with Institutions in other
countries/regions



Academic-Corporate Collaboration

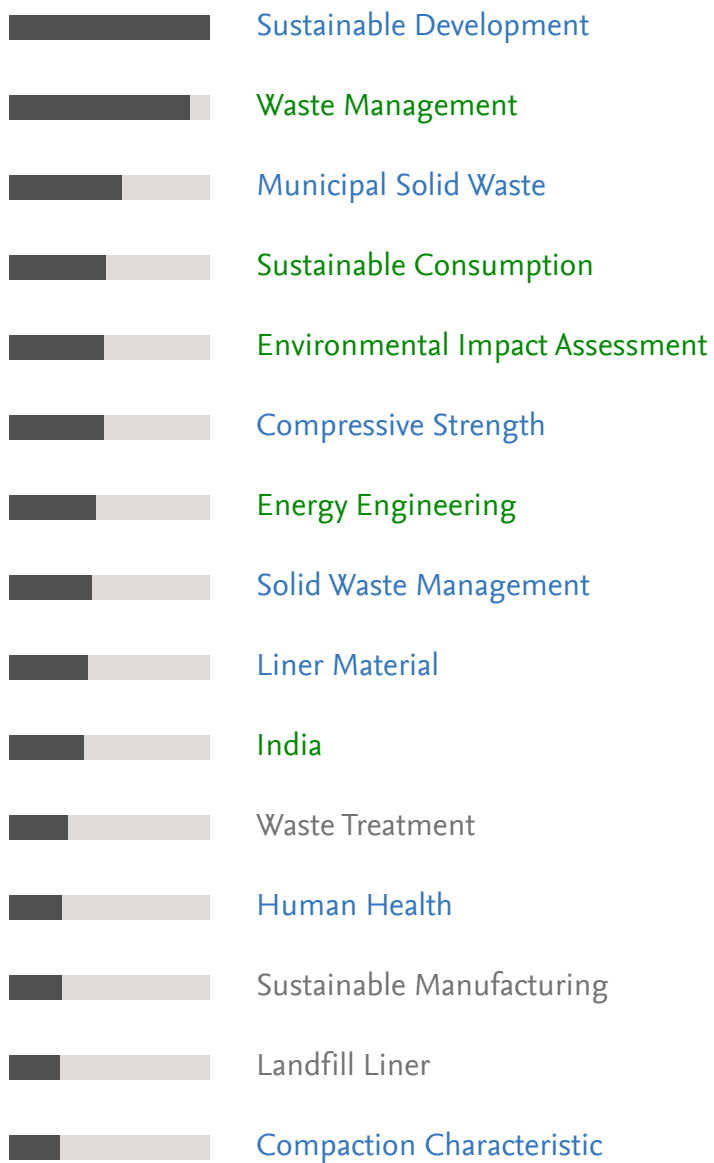
Publications with both academic and corporate
affiliations



Top keyphrases within SDG 12: Responsible Consumption and Production (2023)

Entity: Manipal University Jaipur · Within: All subject areas (ASJC) · Year range: 2021 to 2023 · Data source: Scopus, up to 30 Oct 2024

Top keyphrases by relevance





EVENTS



MANIPAL UNIVERSITY
JAIPUR

FACULTY OF ENGINEERING

**SCHOOL OF ELECTRICAL, ELECTRONICS AND COMMUNICATION
ENGINEERING**

**DEPARTMENT OF ELECTRONICS AND COMMUNICATIONS
ENGINEERING**

***Semiconductor Startups: Market
Scenarios and Prospects***

in collaboration with AIC-MUJ and e-Cell

22nd- 23rd November 2023



Content of Report

1. Introduction of the Event
2. Objective of the Event
3. Beneficiaries of the Event
4. Details of the Guests
5. Brief Description of the event
6. Geo-tagged Photographs
7. Brochure or creative of the event
8. Schedule of the Event
9. Attendance of the Event
10. News Publication
11. Feedback of the Event
12. Link of MUJ website

Prof. S. S. S.

1. Introduction of the Event

Atal Incubation Centre (AIC) in collaboration with department of Electronics & Communication Engineering, Manipal University Jaipur and Directorate of E-Cell, Manipal University Jaipur is planning to organize two days connect event: India Semiconductor Startups: Market Scenario and Prospects tentatively in September 2023. This event will discuss the current Indian scenarios of semiconductor startups government support and schemes for promoting startups, also the current scenarios and prospects will be discussed by the semiconductor industry experts.

The tentative speakers will be from:

einfochips (einfochips, an Arrow Electronics company, is a leading provider of digital transformation and product engineering services. einfochips accelerates time to market for its customers with its expertise in IoT, AI/ML, security, sensors, silicon, wireless, cloud, and power. eInfochips has been recognized as a leader in Engineering R&D services by many top analysts and industry bodies, including Gartner, Zinnov, ISG, IDC, NASSCOM and others).

2. Objective of the Event

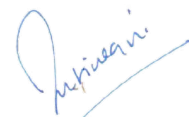
- 1.Opportunity to understand the Indian Semiconductor Market Scenario
- 2.Awareness about the India Semiconductor Mission, Government Initiatives towards the startups in semiconductor area.
- 3.Know about Future Prospects
- 4.Workshop: Ideas for VLSI startups and Research Ideas

3. Beneficiaries of the Event

All MUJ students

4. Details of the Guests

- 1.Mr. Sudhir Naik
Chairman IESA Gujarat, Founder eInfochips
2. Mr. Nilesh Ranpura
Director Engineering
3. Mr. Pranav Joshi
Director Engineering ASIC
4. Mr. Bhavesh Kumar Gopani



ASIC DFT Engineer

5. Mr. Ashish Kumar Patel

Technical Lead

6. Mr. Dipesh Panchal

Physical Design Engineer

5. Brief Description of the event

The event was a whirlwind of knowledge, seamlessly weaving together an ocean of topics that left us enthralled. The experts from elnfochips (An Arrow Company) captivated us with their firsthand experiences. Their passion for the subject matter was infectious, inspired the students to explore the uncharted territories of nanometer technology and pursue careers in this dynamic field.

The event started with the admirable address followed by the insights about the Semiconductor eco-system to brief overview of the insights and role of ASIC in the front-end flow of VLSI. Followed by a great talk on the depths of the startup-ecosystem and the challenges.

During the next day, started with an intriguing and fascinating overview and case study for Design for Test. Followed by an in-depth session on verification in VLSI design. Finally, the seminar was concluded by a show-stopping and marvelous session on Physical Design and Signoff.

6. Photographs



A snippet from the session



Chief Guest addressing the audience

Aspirations

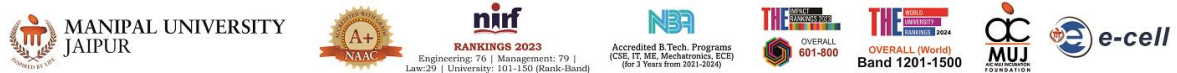


Delegates of the event



Pro-President addressing the audience

7. Brochure or creative of the event:



INDIA SEMICONDUCTOR START-UPS

Market Scenario and Prospects

Manipal University Jaipur

Welcomes
Dignitaries From

Chief Patron
Mr. S. Vaitheeswaran
Chairperson, MUJ

Patron
Dr. G. K. Prabhu
President, MUJ


Co-Patron
Cmde. (Dr.) Jawahar M Jangir
Pro-President, MUJ

Dr. Nitu Bhatnagar
Registrar, MUJ


Dr. Arun Shanbhag
Dean, FoE, MUJ


General Chair
Dr. Amit Soni
Director SEEC, CEO AIC


Dr. Dinesh Kumar Saini
Director, E-Cell



An Arrow Company


Mr. Sudhir Naik
Chairman IESA Gujarat,
Founder- eInfochips


Mr. Nilesh Ranpura
Director Engineering
eInfochips


Mr. Pranav Joshi
Director Engineering ASIC
eInfochips


Mr. Bhavesh Kumar Gopani
Sr.Tech Lead, DFT
eInfochips


Mr. Ashish Kumar Patel
Technical Lead
eInfochips


Mr. Dipesh Panchal
Physical Design Engineer
eInfochips



NOVEMBER
22-23, 2023

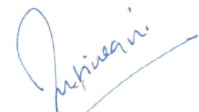
Organized by
Department of Electronics & Communication Engg., School of Electrical, Electronics & Communication Engg.
in collaboration with : AIC-MUJ, E-Cell MUJ & Industry Partner eInfochips

8. Schedule of the event (insert in the report)

Signature

22 November 2023 (Smt.Sharda Pai Auditorium, AB-2)	
9:30 AM - 9:35 AM	Inauguration & Lamp Lighting
9:35 AM - 9:40 AM	Welcome Speech, Prof. Amit Soni, Director SEEC, Manipal University Jaipur
9:40 AM - 9:45 AM	Address by Prof. Arun Shanbag, Dean, FoE, Manipal University Jaipur
9:45 AM - 9:50 AM	Address by Cmde (Dr) Jawarhar M. Jangir, Pro-President, Manipal University Jaipur
9:50 AM - 9:55 AM	Address by Mr. Sudhir Naik, Chairman IESA Gujarat, founder einfochips
9:55 AM - 10:00 AM	Vote of Thanks by Prof. Manish Tiwari, HoD,ECE, Manipal University Jaipur
10:00 AM - 10:30 AM	High Tea
10:30 AM - 11: 45 AM	Overview of Semiconductor eco system/Sand to Silicon-Semiconductor growth and GDP Mr. Sudhir Naik (Chairman IESA Gujarat & Founder einfochips)
11:45 AM - 1:00 PM	ASIC Front end Flow Mr. Pranav Joshi, (Director ASIC, einfochips)
1:00 PM - 2: 00 PM	Lunch
2:00 PM - 4:00 PM	Start-up Eco system, Challenges, and Insights, Mr.Nilesh Ranpura,(Director Engineering,einfochips)
4:00 PM - 5:00 PM	Management Meeting
23 November 2023 (Smt.Sharda Pai Auditorium, AB-2)	
10:00 AM - 11:30 AM	Overview & Case Studies for Design for Test, Mr. Bhavesh Kumar Gopani, (Sr. Tech Lead DFT , einfochips)
11:30 AM - 11:45 AM	Tea Break
11:45 AM - 01:00 PM	Overview & Case Studies for Design for Test, Mr. Akash Kumar Patel,(Technical Lead, einfochips)
1:00 PM - 02:00 PM	Lunch
2:00 PM - 4:00 PM	Physical Design and Signoff, Mr. Dipesh Panchal,(Physical Design Engineer, einfochips)
4:00 PM	Exit Meeting

9. Attendance of the Event (insert in the document only)
Total attendee: 230 (ECE Students) + 10 (other MUJ Students)



Email Address	Name of participant	Affiliation
mujvlsi@gmail.com	s	s
9415020241.vs@gmail.com	Varshanjali Singh	Manipal University Jaipur
utkarsh472001.ut@gmail.com	Utkarsh Raj	Manipal University Jaipur
shahdjay07@gmail.com	Jay Shah	209202204
abhishekdeep48@gmail.com	Abhishek Deep	Manipal University Jaipur
triptibedwal02@gmail.com	Tripti bedwal	Manipal University Jaipur
sagarrao0122@gmail.com	Sagar Yadav	B.Tech ECE / Section - c
shivamdasauni.013@gmail.com	Shivam Dasauni	Manipal University Jaipur
shivang.seth2002@gmail.com	Shivang Seth	Manipal University Jaipur
bhansalivansh29@gmail.com	Vansh Bhansali	Manipal University Jaipur
tourist836@gmail.com	Avneesh Sharma	Manipal University Jaipur
krishnamoorthy774@gmail.com	Krishnamoorthy K	MUJ
nehagarg2629@gmail.com	Neha Garg	ECE
vaishnaviparihar2151@gmail.com	Vaishnavi Parihar	Manipal University Jaipur
adityapareek2105@gmail.com	ADITYA PAREEK	UGC
onerealshreya123@gmail.com	Shreya Sinha	Manipal University Jaipur
yash0404dixit@gmail.com	Sudhanshu Dixit	209202092
msoham70@gmail.com	Soham	Student
gautams106@gmail.com	Gautam Singh	Manipal University Jaipur
kshrey50@gmail.com	Shrey Khandelwal	Manipal University Jaipur
adityashf7@gmail.com	Aditya Sharma	Manipal University Jaipur
aryanpiyush1@gmail.com	Aryan Piyush	Manipal University Jaipur
nihasakiya786@gmail.com	Niha sadiya	3rd year BTech ECE
janves2018@gmail.com	Janve	Faculty of Engineering
sharmasiddhant2063@gmail.com	Siddhant Sharma	Manipal University Jaipur
raiaryan072@gmail.com	Aryan Rai	Manipal University Jaipur
shubhamraj271999@gmail.com	SHUBHAM RAJ	MANIPAL UNIVERSITY JAIPUR
pavankgoli@gmail.com	Goli Pavan Kumar	Faculty of engineering
chinus2606@gmail.com	Sriya Srinath Pillai	Manipal University Jaipur
yuvrajsikarwar708@gmail.com	Yuvraj Singh Sikarwar	Manipal University Jaipur
aadu0413@gmail.com	Aditya gupta	Naac
pratyushtak4@gmail.com	Pratyush Tak	MUJ
vkthakurkhg03@gmail.com	Vikrant Kumar	Manipal University Jaipur



ayushsingrauli@gmail.com	Ayush Gupta	Manipal University Jaipur
garvmishra07980@gmail.com	Garv Mishra	Manipal University jaipur
mraminzaheer1244@gmail.com	Mohd Ramin Zaheer	Manipal University Jaipur
rasikasinha25@gmail.com	Rasika Sinha	Manipal University Jaipur
shannudilli111@gmail.com	Dilli Shanmukha Pranay	Manipal University Jaipur
dev.dd735@gmail.com	Devang Vikram Singh	.
mayankjawla2412@gmail.com	Mayank Jawla	Manipal University Jaipur
abirgautam755@gmail.com	Abir Gautam	Manipal University Jaipur
harshv.adil@gmail.com	Harshvardhan Adil	Manipal University Jaipur
saranjaat096@gmail.com	Dinesh Saran	229202076
bharvipatel1534@gmail.com	Bharvi Patel	Manipal University Jaipur
tanmoypodder839@gmail.com	Tanmoy Podder	Manipal University Jaipur
ayushppanandikar@gmail.com	Ayush Pai Panandikar	Manipal University Jaipur
singhaayush@aol.com	Ayush Kumar Singh	Manipal University (school of electrical, electronics & communication engineering)
jeetjawale392@gmail.com	Jeet jawale	Manipal University jaipur
ujjawalsharma760@gmail.com	Ujjawal Sharma	Engineering
ashishspatil04@gmail.com	Ashish Patil	Manipal University Jaipur
rajuyadav08576@gmail.com	RAJU YADAV	Manipal University Jaipur
skole8864@gmail.com	Siddhant Kole	Btech Ece
poorvakshibargoti@gmail.com	Poorvakshi bargoti	Manipal university Jaipur
sashivbhatnagar15@gmail.com	Sashiv Bhatnagar	Manipal university jaipur
sharaavanthr@gmail.com	Sharaavanthraj	BTech ECE
jangirhimanshu72@gmail.com	Himanshu	MUJ
manastripathi12d@gmail.com	Manas Tripathi	Manipal University
sakshamarora2825@gmail.com	Saksham	.
ballavimisra@gmail.com	Ballavi Misra	Manipal University Jaipur
bidishatalukdar50@gmail.com	Bidisha talukdar	UGC
achra.praveer@gmail.com	Praveer Achra	Manipal university jaipur
kunalgu0322@gmail.com	Kunal Gupta	Manipal University Jaipur
nagpal2002vaibhav@gmail.com	Vaibhav Nagpal	Manipal University Jaipur
pratikmtp@gmail.com	Pratik Patil	Manipal University Jaipur
sgc.karthika.27oct.12sci@gmail.com	Karthika	Manipal University Jaipur

shreyassamar03@gmail.com	Shreyas samar shukla	Manipal University Jaipur
ry7031978@gmail.com	Rishabh	Manipal University Jaipur
abhijeetsachan.088@gmail.com	Abhijeet sachan	Manipal university jaipur
akshat.agarwal0206@gmail.com	Akshat Agarwal	Manipal University Jaipur
goldy4145@gmail.com	Sami verma	Manipal university jaipur
parikhdivy03@gmail.com	Divy Parikh	Manipal University Jaipur
shraddhadayal10@gmail.com	Shraddha Dayal	Manipal University Jaipur
sa8lm10cr7@gmail.com	Aditya Sharma	manipal university jaipur
aditii.tiwari03@gmail.com	Aditi Tiwari	Manipal University Jaipur
soumilhallan2004@gmail.com	Soumil Hallan	Manipal University Jaipur
theanushkasharma28@gmail.com	Anushka sharma	NAAC++
2005.jeevani@gmail.com	G.sai naga jeevani	NAAC++
pateljaideep972@gmail.com	Jaideep Patel	NAAC++
pukhraj.singh2002@gmail.com	Pukhraj Singh	Manipal University Jaipur
nachiket.sailee@gmail.com	Nachiket Gaikwad	MUJ
misslakshmi2411@gmail.com	Lakshmi	Manipal university Jaipur
tanaymalhan@gmail.com	Tanay malhan	Manipal university jaipur
bhavyaverma688@gmail.com	Bhavya Verma	Manipal University Jaipur
quinsegg@gmail.com	Jayant Kumar	NA
vineetpatel5555@gmail.com	Vineet patel	Manipal university jaipur
singhyuvraj8637@gmail.com	Yuvraj Singh	MUJ
kanishkagoyal51@gmail.com	Kanishka goyal	Manipal University Jaipur NAAC A+
harshsakariya28@gmail.com	Sakariya Harsh	Manipal University Jaipur
gargsukrit1605@gmail.com	Sukrit Garg	Muj
akritipradhan987@gmail.com	Akriti Pradhan	Manipal University Jaipur
aadarshpal1907@gmail.com	AADARSH PAL	MUJ
ronakdudani57@gmail.com	Ronak Manoj Dudani	Manipal University Jaipur
gargmohit0605@gmail.com	Mohit Garg	Manipal University Jaipur
pupuli2005@gmail.com	Deepanshu Das	Manipal University jaipur
rohanbhandari2012@gmail.com	Rohan bhandari	Manipal University Jaipur
gbkr7710@gmail.com	GAURAV KUMAR	UGC
sakshiadhikary323@gmail.com	Saksi Adhikari	Studying
glaasya2003@gmail.com	G.V.N.Laasya	Manipal University Jaipur

Rishabh

sam08012001@gmail.com	Samridh Kumar Singh	Student
shobhitmittra2@gmail.com	Shobhit Mittra	Undergraduate Student
samantadev30545@gmail.com	Debanshu Bal Samanta	Manipal University Jaipur
bansaldarsh0@gmail.com	Darsh Bansal	Manipal University Jaipur
abhishubh30@gmail.com	Abhinav Kumar	Manipal University Jaipur
aadarsh.29.ak@gmail.com	Aadarsh kumar	Manipal University jaipur
shmenon005@gmail.com	Shreya Menon	Manipal University Jaipur
jain.kanav1607@gmail.com	KANAV JAIN	Ece
bhatiakanishka930@gmail.com	Kanishka Bhatia	Student 1st year
savir0246@gmail.com	Savir Sharma	Student
rivilight@gmail.com	Riviresh Mishra	Manipal University Jaipur
harshadsharma0001@gmail.com	Harshad Sharma	MUJ NAAC A+
shashwatsingh8639@gmail.com	Shashwat Singh	CSE aiml
nnmalewar@gmail.com	Nikita Malewar	MuJ student
mritunjaythaakur2005@gmail.com	Mritunjay Singh	MUJ
shaihams04@gmail.com	Shaiham Srivastava	NAAC
amitrajpoot2004@gmail.com	Amit Rajpoot	Manipal University Jaipur
chaitanya71agarwal44@gmail.com	Chaitanya Agarwal	CSE (Ai/MI)
manmeetanand2424@gmail.com	Manmeet Kaur Anand	Student
mansiamarnani04@gmail.com	Mansi Amarnani	Manipal University Jaipur
tapariachetna1904@gmail.com	Chetna Taparia	Manipal University Jaipur
mannyaya1203@gmail.com	Mannya Singh	Manipal University Jaipur
garganirudh36@gmail.com	ANIRUDH GARG	MANIPAL UNIVERSITY JAIPUR
shivamgupta074513@gmail.com	Shivam gupta	Student
jatinrawtani@yahoo.com	Jatin Rawtani	Manipal University Jaipur
manthanchawla123@gmail.com	Manthan Chawla	Manipal University Jaipur
navadeeparavasthu1@gmail.com	P.NavaDeep	Manipal University Jaipur
shivam11102005@gmail.com	Shivam Kumar	Manipal university
chinmaybhardwaj711@gmail.com	Chinmay bhardwaj	MUJ
amazingaditya999@gmail.com	ADITYA JHA	Cbse board
123madmaxch@gmail.com	Jhanvi Choukse	IEEE AESS
shifa.sher.khan1@gmail.com	Shifa Khan	Manipal University Jaipur
shivamkhandelwal218@gmail.com	Shivam Khandelwal	Manipal University Jaipur

toshniwalnt@gmail.com	Naman Toshniwal	Manipal University Jaipur
maithilamit193@gmail.com	Amit Sharma	Manipal University Jaipur
rishwkf@gmail.com	Rishav Mitra	Manipal University jaipur
himanshugar2005@gmail.com	Himanshu Garg	B. Tech
waliamanasvi@gmail.com	Manasvi Walia	Manipal university jaipur
anantsharma5553@gmail.com	anant sharma	Manipal University Jaipur
6nupurpalav@gmail.com	Nupur Palav	Manipal
pankhuri.banaras@gmail.com	Pankhuri Prakash	Manipal University
jsinghbasson@gmail.com	Jasanjot Singh	2nd year student
niyati200526@gmail.com	Niyati Gupta	Manipal University Jaipur
piyush.shri448@gmail.com	Piyush Shrivastava	Manipal University Jaipur
hrimansavla@gmail.com	Hriman Savla	Manipal University Jaipur
ikrantyadav0611@gmail.com	IKRANT	MANIPAL UNIVERSITY JAIPUR
yashikapriyadarshi07@gmail.com	Yashika Priyadarshi	Manipal University Jaipur
divyarasuni4340@gmail.com	Divya Rasuni	School of electrical ,electronics and communication engineering in collaboration with enfochips
manandubey25@gmail.com	Manan Dubey	Manipal University Jaipur
housekk07@gmail.com	Kamal Kishor	BTech ECE
sweata1403@gmail.com	Sweata Chakraborty	Manipal University
anshyadavx21@gmail.com	Ansh Yadav	Manipal University Jaipur
amitojsinghoberoi@gmail.com	Amitoj singh Oberoi	Manipal University Jaipur
26sshah@gmail.com	Saumya Shah	Manipal University Jaipur
himanshu.sonu108@gmail.com	Himanshu Kumar	Manipal University Jaipur
arnavdave07@gmail.com	Arnav Dave	Manipal University Jaipur
parthdave1328@gmail.com	Parth dave	Manipal University jaipur
rishi1523raj@gmail.com	Rishi Raj Kuleri	MUJ
yash.shrivastavaaug@gmail.com	Yash Shrivastava	Manipal University Jaipur
kalam.adit@gmail.com	Shaikh Khairul Alam	Manipal
sampathkumar89782@gmail.com	Kuruva Sampath Kumar	Manipal University Jaipur
jayanguptampvm@gmail.com	Jayan gupta	MUJ
princepachauri57@gmail.com	Prince Pachauri	—
parthchopra11@gmail.com	Parth Chopra	Manipal University Jaipur
morekhushi2@gmail.com	khushi more	MANIPAL UNIVERSITY JAIPUR
kartikshrm278@gmail.com	Kartik Sharma	NAAC

brijeetk.medhi@gmail.com	BRIJEET KUMAR MEDHI	MUJ
mansi.aggy@gmail.com	Mansi	Manipal University Jaipur
rupam.irp@gmail.com	Rupam Das	Manipal University Jaipur
pratyushrawat2004@gmail.com	Pratyush Rawat	Student
muskansinghqueens2020@gmail.com	Muskan Singh	Manipal University Jaipur
saubhagyaawasthi99@gmail.com	Saubhagya Awasthi	MUJ
sanjana.rao.0101@gmail.com	Sanjana Rao	Manipal University Jaipur
harkesh977242@gmail.com	Harkesh Singh	Student
roseashish64@gmail.com	Aashish Rose	Manipal University Jaipur
anusingh18784@gmail.com	Anu Singh	Manipal University Jaipur
harshratna1604@gmail.com	Harsh Ratna Upasak	Manipal University Jaipur
pranjalpatel2101@gmail.com	Pranjal Patel	B Tech
praneethmaleedu970@gmail.com	Praneeth Maleedu	Manipal University Jaipur
arinsharma0209@gmail.com	Arin Sharma	Manipal University Jaipur
himanshi.chaddha@gmail.com	Himanshi Chaddha	Manipal University Jaipur
neoza4444@gmail.com	Rugved Panse	-
likithsaivemulapalli@gmail.com	Likith	BTech
pmansihd@gmail.com	Mansi	-
nikhilbagaria3@gmail.com	Nikhil bagaria	Manipal University
nabeelfarooqui07@gmail.com	Nabeel Farooqui	Manipal University Jaipur (UGC)
shruti67003@gmail.com	Shruti Sharma	Manipal University Jaipur
axelblazepers@gmail.com	PIYUSHRAJ SINGH	MANIPAL UNIVERSITY JAIPUR
knitika137@gmail.com	KM NITIKA	Manipal University jaipur
guptapranjal242@gmail.com	Pranjal Gupta	Manipal University Jaipur
chiraggera666@gmail.com	Chirag gera	English
bansalvansh853@gmail.com	Vansh Bansal	MUJ
shuklaaagman@gmail.com	Aagman Shukla	Manipal University Jaipur
shishangthakur@gmail.com	Shishang Thakur	Manipal University Jaipur
mrigangagarwalla04@gmail.com	Mrigang Agarwalla	Manipal University Jaipur
shoborastogi9@gmail.com	Shobhit Rastogi	Manipal University Jaipur
guptashikhar8421@gmail.com	Shikhar Gupta	Manipal University Jaipur
yadav.garv83@gmail.com	Garv Yadav	Manipal University Jaipur
saumyaprasadsinha@gmail.com	SAUMYA PRASAD SINHA	Nil

sparshkr.vaish@gmail.com	Sparsh Kumar Vaish	B. Tech
rudrasankarbishnu@gmail.com	Rudra Sankar Bishnu	Manipal University Jaipur
ayushsaxena2003@gmail.com	Ayush Saxena	Manipal University Jaipur
sheershchandela@gmail.com	Sheersh Chandela	MUJ
kunalkapoor1801@gmail.com	Kunal Kapoor	Manipal University Jaipur
mvyas20304@gmail.com	Manishka Vyas	Manipal University Jaipur
harsh109.adil@gmail.com	Harshvardhan Adil	Manipal University Jaipur
iamraaghavsinghal@gmail.com	Raaghav Singhal	Photonics and Optoelectronics
shubhamdabrework@gmail.com	Shubham dabre	Manipal jaipur
hetdungrani.123@gmail.com	HET KETANKUMAR PATEL	Manipal University Jaipur
soumilaviation@gmail.com	Soumil Hallan	Manipal University Jaipur
rtmystic13@gmail.com	Pranay Agarwal	Student
sarthak.229202059@muj.manipal.edu	Sarthak Jain	Manipal university Jaipur
heyitsdivyanshu@gmail.com	Divyanshu Rai	Student
khetulpatel@gmail.com	Khetul Patel	Manipal jaipur student(Fresher)
jain19harshit@gmail.com	Harshit Tatia	Manipal University Jaipur (Student)
akashraj23042003@gmail.com	Akash Raj	Manipal university jaipur
anonymoushacker8377@gmail.com	Krish Mehta	Manipal University Jaipur
sanskarawate@gmail.com	Sanskar Awate	Manipal University Jaipur
mayaank.bambardekar@gmail.com	Mayaank Bambardekar	Manipal University Jaipur
diwanshupoonia7742@gmail.com	Diwanshu	University
mayankdecpandey@gmail.com	Mayank Pandey	Muj
rishi.bagri1@gmail.com	Rishi Bagri	Engineering
paliwal.shubham4045@gmail.com	Shubham paliwal	Manipal university jaipur
srimankumar0503@gmail.com	Sriman Kumar	Manipal University Jaipur
ankitjha24407@gmail.com	Ankit Kumar Jha	Manipal University Jaipur
aatmajsalunke@gmail.com	Aatmaj Amol Salunke	Manipal University Jaipur
rakeshmeena1164@gmail.com	Rakesh Maiwal	No
shanusharma436833@gmail.com	Shanu sharma	Manipal University Jaipur
ridhi.0504@gmail.com	Ridhi	Muj
a7rajnagarwala@gmail.com	AMAAN Hussain Rajnagarwala	N.A.
yashaaditya5@gmail.com	YASHAADITYA	Manipal University Jaipur

kanishka.chaudhary.kota@gmail.com	Kanishka Chaudhary	Manipal university jaipur
bloggamerz24@gmail.com	Shaurya Jain	Student
shauryasharmaitb@gmail.com	Shaurya Sharma	Btech
singhinderpal274@gmail.com	Inderpal singh	Manipal University jaipur
nandilgovind@gmail.com	Nandil Govind	Muj
shatabdisaha128@gmail.com	Shatabdi Saha	Bachelor of Engineering
namanbhasin2014@gmail.com	Naman Bhasin	Manipal University Jaipur
pradeepdua329@gmail.com	Harshita Dua	Student
jkeshav.soni@gmail.com	Keshav Soni	MUJ
rishirenu13@gmail.com	Rishi Sharma	MUJ
nishant.yadav.3457@gmail.com	OM PATEL	Btech

10. News Publication- News printed in newspaper or online links (if any) for news – insert images)

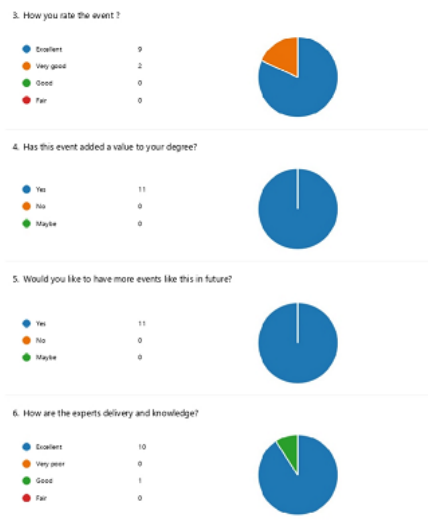
https://www.linkedin.com/posts/aicmuj_semiconductortechonology-semiconductormanufacturing-activity-7133686726132137984-t79M?utm_source=share&utm_medium=member_desktop

https://www.linkedin.com/posts/shilpi-birla-a9a81744_esdm-muj-einfochips-activity-7133504146028019712--Yyh?utm_source=share&utm_medium=member_desktop

11. Feedback report of the Event

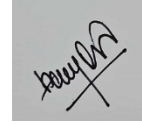
ack form-ISCS 2023

<https://forms.office.com/Pages/DesignPageV2.aspx?prevorigin=Marketing&origin=NeoPortalPage>





12. Link of MUJ website stating the event is uploaded on website



Prof. Amit Soni

Director (SEEC)
Manipal University Jaipur

Seal and Signature of Head with date

Amit Soni



MANIPAL UNIVERSITY
JAIPUR

MUJ/Q&C/021/F/1.01



MANIPAL UNIVERSITY
JAIPUR

DIRECTORATE OF STUDENT'S WELFARE

(SOCIETY CONNECT)

And

Faculty of Management and Commerce

Department of Business Administration

Presents

SWACH BHARAT

OCTOBER 25, 2023

1. Introduction of the Event

School of Business and Commerce in collaboration with Directorate of Student Welfare, Directorate of sports and NCC, NSS organized a “SWACH BHARAT” on October 25, 2023. 52 students participated in the campaign. The event took place in Dehmi Kalan hamlet.

2. Objective of the Event

The aim of the campaign was to raise awareness about Waste Segregation and encourage education on the SWACH BHARAT.

3. Beneficiaries of the Event

Through this initiative, students and villagers had better communication and understanding of the situation.

4. Details of the Guests

The event was laid by the students of BBA, BBA(BA), IMBA

Rotary Club Jaipur Bapu Nagar

Rotary started with the vision of one man — Paul Harris. The Chicago attorney formed the Rotary Club of Chicago on 23 February 1905, so professionals with diverse backgrounds could exchange ideas and form meaningful, lifelong friendships.

Over time, Rotary’s reach and vision gradually extended to humanitarian service. Members have a long track record of addressing challenges in their communities and around the world.

Rotary is a global network of 1.4 million neighbors, friends, leaders, and problem-solvers who see a world where people unite and take action to create lasting change – across the globe, in our communities, and in ourselves. They provide service to others, promote integrity, and advance world understanding, goodwill, and peace through our fellowship of business, professional, and community leaders. We collaborate with community leaders who want to get to work on projects that have a real, lasting impact on people’s lives. We connect passionate people with diverse perspectives to exchange ideas, forge lifelong friendships, and, above all, take action to change the world.

5. Brief Description of the event

The event was initiated to make students aware of their surroundings with respect to Waste and its consequences on the local community. The students went on a rally in groups, holding posters on Wet Waste and Dry Waste. They were chanting slogans “Alag Karo Alag Karo” Gila aur Sukha Kachara Alag Karo, to make the local community aware of the Waste Segregation process.

6. Photographs



Image 1 : Students with faculty



Image 2: Students walking with the Rally through the Village



Image 3: Team of MUJ Students at Village for Rally



Image 4: Team of MUJ Students at Village for Rally

7. Brochure or creative of the event



8. Schedule of the Event

The event took place on October 25, 2023

9. Attendance of the Event

Sr. No	Name of Institution	Registration No	Attendee Name
1	Manipal University Jaipur	23FM10BBA00122	Naresh Choudhary
2	Manipal University Jaipur	23FM10BBA00123	Prem Singhrathore
3	Manipal University Jaipur	23FM10BBA00124	Yash Vardhansingh
4	Manipal University Jaipur	23FM10BBA00125	Krishna Snair
5	Manipal University Jaipur	23FM10BBA00126	Viyom Gupta
6	Manipal University Jaipur	23FM10BBA00127	Aditya Singh shekhawat
7	Manipal University Jaipur	23FM10BBA00128	Sheikh Tabish ahmed
8	Manipal University Jaipur	23FM10BBA00129	Bhavesh Aggarwal
9	Manipal University Jaipur	23FM10BBA00130	Riddhima Gupta
10	Manipal University Jaipur	23FM10BBA00131	Ishita Sharma
11	Manipal University Jaipur	23FM10BBA00132	Akshat Sharma
12	Manipal University Jaipur	23FM10BBA00133	Preksha Sood
13	Manipal University Jaipur	23FM10BBA00134	Tanisha Agarwal
14	Manipal University Jaipur	23FM10BBA00135	Ram Avtarchouhan

15	Manipal University Jaipur	23FM10BBA00136	Sourabh Shekhawat
16	Manipal University Jaipur	23FM10BBA00137	Abhishek Jain
17	Manipal University Jaipur	23FM10BBA00138	Priyanshu Yadav
18	Manipal University Jaipur	23FM10BBA00139	Riddhi Charan
19	Manipal University Jaipur	23FM10BBA00140	Akhil
20	Manipal University Jaipur	23FM10BBA00141	Shaily Kushwaha
21	Manipal University Jaipur	23FM10BBA00142	Deep Mittal
22	Manipal University Jaipur	23FM10BBA00143	Rahul Choudhary
23	Manipal University Jaipur	23FM10BBA00144	Ronil Joshi
24	Manipal University Jaipur	23FM10BBA00145	Arihant Jaisawal
25	Manipal University Jaipur	23FM10BBA00146	Ayush Kumarthakur
26	Manipal University Jaipur	23FM10BBA00147	Angad Yadav
27	Manipal University Jaipur	23FM10BBA00148	Shashank Chaudhary
28	Manipal University Jaipur	23FM10BBA00149	Khushi Gupta
29	Manipal University Jaipur	23FM10BBA00150	Garvita Rathore
30	Manipal University Jaipur	23FM10BBA00151	Anirban Bhattacharyya
31	Manipal University Jaipur	23FM10BBA00152	Keshav Badthuniya
32	Manipal University Jaipur	23FM10BBA00153	Yash Saini
33	Manipal University Jaipur	23FM10BBA00154	Vineet Kumar
34	Manipal University Jaipur	23FM10BBA00155	Bhavuk Parashar
35	Manipal University Jaipur	23FM10BBA00156	Mohit Oshu
36	Manipal University Jaipur	23FM10BBA00157	Honey Chandnani
37	Manipal University Jaipur	23FM10BBA00158	Veer Singh
38	Manipal University Jaipur	23FM10BBA00159	Naman Kriplani
39	Manipal University Jaipur	23FM10BBA00160	Himanshu Yogesh Mittal
40	Manipal University Jaipur	23FM10BBA00161	Amogh Goyal
41	Manipal University Jaipur	23FM10BBA00162	Alina Nadeem
42	Manipal University Jaipur	23FM10BBA00163	Prince Gandhi
43	Manipal University Jaipur	23FM10BBA00164	Devansh Devansh Tiwari
43	Manipal University Jaipur	221016048	Aarohi
44	Manipal University Jaipur	229301387	Soham maskara
45	Manipal University Jaipur	229301650	Karan Kapoor
46	Manipal University Jaipur	229301552	MONIL SHAH
47	Manipal University Jaipur	229311009	Krittika Wadhawan
48	Manipal University Jaipur	229301034	Maulik Mehrotra
49	Manipal University Jaipur	229302340	Shreya Saihgal
50	Manipal University Jaipur	229302257	Yash Dhruv
51	Manipal University Jaipur	229302641	Pankaj Patel
52	Manipal University Jaipur	229310250	Amrit Raj
53	Manipal University Jaipur	220901154	Mehul rawat
54	Manipal University Jaipur	221201002	Palak chawla
55	Manipal University Jaipur	229309070	Pranav Banker
56	Manipal University Jaipur	229303128	Mahi Bhardwaj
57	Manipal University Jaipur	229303305	Karshh Divekar
58	Manipal University Jaipur	229310242	Ashmit

59	Manipal University Jaipur	229301681	Armaan Deep Singh Bedi
60	Manipal University Jaipur	229302281	Shriyam Singh Tiwari
61	Manipal University Jaipur	229301130	Shreyansh Reddy
62	Manipal University Jaipur	220901032	Raj Singh
63	Manipal University Jaipur	211103077	Sanmai Pathak
64	Manipal University Jaipur	211103075	Anvesha Shekhar
65	Manipal University Jaipur	219311129	Shubham Yadav
66	Manipal University Jaipur	221201033	Divanshi Gupta
67	Manipal University Jaipur	229310052	Lakshya Khandelwal
68	Manipal University Jaipur	229303191	Krishang Shukla
69	Manipal University Jaipur	221305050	Baibhav Bhanu Naithani
70	Manipal University Jaipur	229302371	Rishika Bhagawati
71	Manipal University Jaipur	229311168	Rudra Nayyar
72	Manipal University Jaipur	229311024	Shivam Singh
73	Manipal University Jaipur	229311289	puneet more
74	Manipal University Jaipur	229310200	Nainish Mane
75	Manipal University Jaipur	229310153	Diksha M
76	Manipal University Jaipur	221007068	Akshita Pandey
77	Manipal University Jaipur	229309068	Rahul Trivedi
78	Manipal University Jaipur	229309052	Raez Mohammed K P

Dr Narendra Singh Bhati HoD, BBA

(Hemant Kumar)
Assistant Director, Society Connect
Directorate of Student's Welfare

(Prof. AD Vyas)

Director, Directorate of Student's Welfare

DIRECTOR STUDENT WELFARE & PROCTOR
MANIPAL UNIVERSITY, JAIPUR



MUJ/DSW/Student Clubs/2023/Biotech Club MUJ/28th February

DIRECTORATE OF STUDENTS' WELFARE

Nukkad Natak

ON

Solid Waste Management

Department of Biosciences & Biotech Club, Manipal University Jaipur

Date of Event (28th February, 2023)

(Venue: TMA Pai Auditorium)

Index

S.No.	Activity Heads	Page no.
1.	Introduction of the Event	3
2.	Objective of the Event	3
3.	Beneficiaries of the Event	3
4.	Brief Description of the event	3
5.	Photographs	5
6.	Brochure or creative of the event	6
7.	Schedule of the Event	7
8.	Attendance of the Event	7

Introduction of the Event ,

The Department of Biosciences & Biotech Club, Manipal University Jaipur organized a 'Nukkad Natak' on 'Solid Waste Management' on 28th Feb, 23. It was directed by 2nd year students of Department of Biosciences, Divya and Samrat and it was awe-inspiringly performed by the students. This Nukkad Natak was under the guidance of the convenor – Dr. Mousumi Debnath, Faculty Coordinator, Biotech Club.

The performers interacted with the audience and presented an informatic skit on solid waste management and the do's and don'ts of waste disposal.

This skit was a call to action, urging the audience to take responsibility for their waste and make conscious choices in their daily lives. It was an effective way to educate and engage the public on a crucial environmental issue.

Objectives of the Event

- To increase awareness about solid waste management.
- To bring public awareness about the fatality caused by wastes.
- To educate about the waste disposal methods and its do's and don'ts.

Beneficiaries of the Event

- MUJ Students
- Faculty

Brief Description of the event

Conducted under the guidance of the Founder Faculty Coordinator, Biotech Club, Dr. Mousumi Debnath, Faculty of Biosciences, this Nukkad Natak solely aimed in bringing public awareness on solid waste management. It was well directed by students of Department of Biosciences, Divya and Samrat, who commenced from writing the scripts to directing the performers and eventually operated a successful and inspiring Nukkad Natak.

A group of brilliant and motivated performers presented the Nukkad Natak, bringing attention to the problem of solid waste management through a stirring and thought-provoking performance. The show highlighted the negative consequences of littering and the necessity of effective waste management.

The actors portrayed different characters like a litterbug, a garbage collector, and a responsible citizen who showed how the problem of solid waste management can be tackled. The audience was made conscious of the risks that incorrect garbage disposal poses to both the public's health and the environment.

The play also highlighted the role of the government and the civic bodies in managing solid waste.

In conclusion, the Nukkad Natak on Solid Waste Management held on 28th February on the occasion of National Science Day was a highly successful event that effectively highlighted the issue of solid waste management. The play succeeded in spreading awareness about the importance of proper waste management practices and the role of individuals and the government in tackling this issue.

Photographs

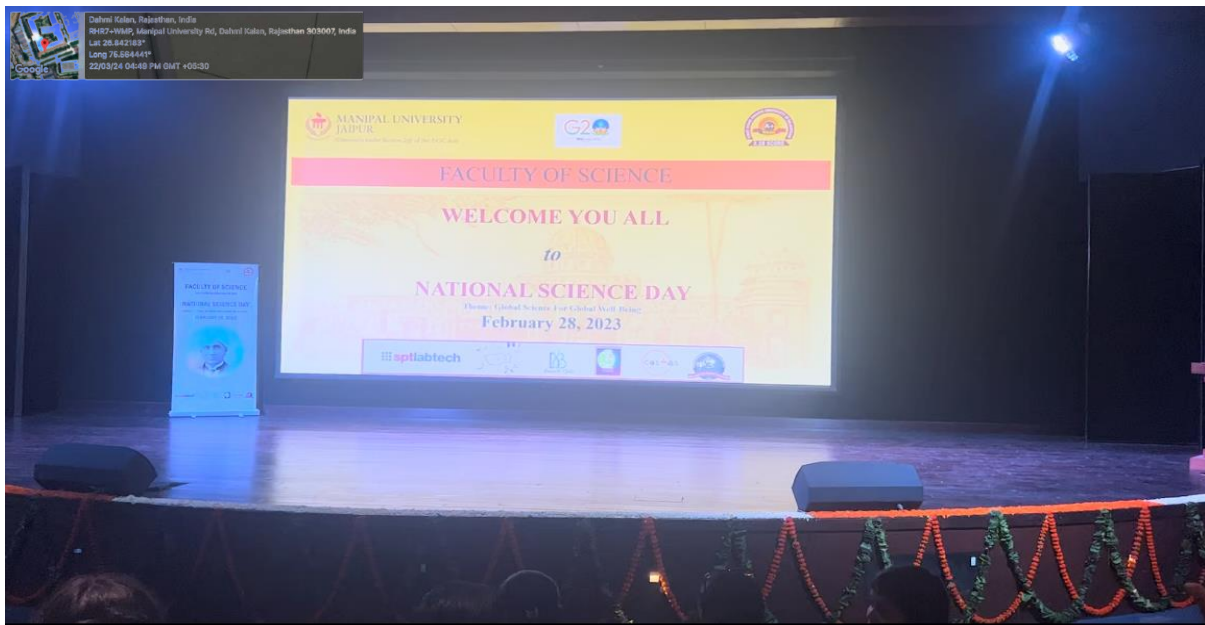


Figure 1 National Science Day; Coordinates: 26.843429; 75.566529; N26°50'36.34" E75°33'59.50"(Manipal University Jaipur)



Figure 2 Nukkad Natak performed by students.; Coordinates: 26.843429; 75.566529; N26°50'36.34" E75°33'59.50"(Manipal University Jaipur)



Figure 3 Nukkad Natak performed by students. Coordinates: 26.843429; 75.566529; N26°50'36.34" E75°33'59.50"(Manipal University Jaipur)



Figure 4 Nukkad Natak performed by students. Coordinates: 26.843429; 75.566529; N26°50'36.34" E75°33'59.50"(Manipal University Jaipur)



Figure 5 Nukkad Natak team and Dr. Mousumi Debnath, Faculty Coordinator, Biotech Club; Coordinates: 26.843429; 75.566529; N26°50'36.34" E75°33'59.50"(Manipal University Jaipur)

Brochure or Creative of the Event



MANIPAL UNIVERSITY
JAIPUR
(University under Section 2(f) of the UGC Act)



BIOTECH CLUB OF MUJ

Presents

NUKKAD NATAK

on

SOLID WASTE MANAGEMENT

DATE AND TIME

28th February, 2PM onwards

VENUE

TMA PAI auditorium, MUJ



Schedule of the event

The event was on the 28th February 2023 from 2:00 PM- 3:00 PM in TMA Pai Auditorium, Academic Block 2.

Attendance of the event: 38

S.No.	Name	Registration No.
1.	Ananya Singh	201002002
2.	Harsh Saxena	201003004
3.	Anvarshu Gopal	211002011
4.	Anshullika Saxena	211002053
5.	Ayushi Gupta	201002029
6.	Divya	211002056
7.	Sylvia Parveen	211003009
8.	Anushka Singh	211002003
9.	Shivani Tiwari	211002002
10.	Aryan Singh	211002038
11.	Muskan Yadav	211002040
12.	Sakshi Nirmal	211002060
13.	Priyasha Paul	211002035
14.	Akash Chandra	211002036
15.	Shashank Goyal	21102043
16.	Nandini	211003001
17.	Mrunal Mangaje	211003007
18.	Sowvhik Parvej	211002007
19.	Aayushi Thakkar	211002061
20.	Manisha Verma	211002009
21.	Rahul Shrivastava	211002050
22.	Debarghya Sarkar	211002015



23.	Samrat Banerjee	211003008
24.	Sneha Srivastava	211002042
25.	Sonali Lalwani	211002041
26.	Suhani Pareek	211002062
27.	Vishnu Priya	211002028
28.	Tarushi Jain	201003001
29.	Dr. Abhijeet Singh	
30.	Dr. Mousumi Debnath	
31.	Dr. Madan Mohan Sharma	
32.	Dr. Rakesh Sharma	
33.	Dr. Nitesh Poddar	
34.	Dr. Monika Sangani	

Ananya Singh

President, Biotech Cub MUJ

Signature of the Student Coordinator

Dr. Mousumi Debnath

School of Basic Science

Signature of the Faculty Coordinator

<p>DIRECTOR STUDENT WELFARE & PROCTOR MANIPAL UNIVERSITY, JAIPUR</p>	 <p>Dr. Arun Kumar Poonia Asst. Director, DSW Clubs</p>
------------------------------------------------------------------------------	-----------------------------------------------------------------------





#UKLO
Annual International
Scientific Conference
2023



International Scientific Journal
horizons
University St. Kliment Ohridski in Bitola

UKLO Annual International Scientific Conference 2023

On the occasion of the *World Science Day for Peace and Development*, the University “St. Kliment Ohridski” - Bitola is announcing a Call for Papers for its *Annual International Scientific Conference 2023* on the following topic:

“MULTIDISCIPLINARY APPROACH TO SUSTAINABLE DEVELOPMENT GOALS”

Bitola, Republic of North Macedonia 17 - 18 November 2023

Mode: Hybrid

World Science Day for Peace and Development emphasizes the importance of science in society and the necessity to involve the broader public in discussions about emerging scientific topics. It highlights the value and applicability of science to our everyday lives.

The 2023 Conference topic is: “Multidisciplinary Approach to Sustainable Development Goals”. Authors are invited to submit papers on any subject related to and within the scope of the Conference topic. Submissions from academics, researchers, and practitioners at any stage of their career, including PhD students, will be accepted.

Short overview:

World Science Day for Peace and Development, celebrated annually on 10 November, emphasizes the importance of science in society and the necessity to involve the broader public in discussions about emerging scientific topics. It highlights the value and applicability of science to our everyday lives. This international scientific conference offers the chance to mobilize the academy and experts from home and abroad around the issue of science for peace and development with a single purpose - *changing the world for the better!* The Conference will open for discussion on the most pressing issues of the UN Agenda 2030: 1. Eliminate Poverty; 2. Erase Hunger; 3. Establish Good Health and Well-Being; 4. Provide Quality Education; 5. Enforce Gender Equality; 6. Improve Clean Water and Sanitation; 7. Grow Affordable and Clean Energy; 8. Create Decent Work and Economic Growth; 9. Increase Industry, Innovation, and Infrastructure; 10. Reduce Inequality; 11. Mobilize Sustainable Cities and Communities; 12. Influence Responsible Consumption and Production; 13. Organize Climate Action; 14. Develop Life Below Water; 15. Life on Land; 16. Guarantee Peace, Justice, and Strong Institutions; 17. Build Partnerships for the Goals.

Important Dates:

- **20 September 2023:** Abstracts submission (up to 300 words in length)
- **17 and 18 November 2023:** Conference dates
- **05 December 2023:** Submission of final papers. Earlier submission of the papers helps us to manage the review process on time. Prepare your final paper following our Guidelines. Papers should be sent as .doc or .docx attachments via the e-mail address: conference@uklo.edu.mk

Submission details:

Interested authors are invited to submit an abstract (up to 300 words in length) and a brief academic CV written narratively by 20 September 2023 via the following link:

https://docs.google.com/forms/d/e/1FAIpQLSfxjz1JoDRQy7GYTCm11mdUffQWeDM_dn2gBh9SowUEKu3cSQ/viewform?vc=0&c=0&w=1&flr=0

Publication:

Submitted articles are subject to initial editorial screening and anonymous peer review by at least two reviewers. Selected papers will be published in a special issue of the *Horizons – International Scientific Journal* (<https://uklo.edu.mk/ojs/index.php/horizons/index>) as a peer-reviewed, interdisciplinary, and international journal published by the University St. Kliment Ohridski in Bitola, indexed in EBSCO, CrossRef, Google Scholar, etc.

Certification:

The papers accepted and presented during the Conference will receive a certification of participation.

Organizing Committee:

Prof. Dr. Sc Igor Nedelkovski, Rector, University “St. Kliment Ohridski” – Bitola

Prof. Dr. Sc Jasmina Bunevska-Talevska, Vice-Rector for Student Affairs, University “St. Kliment Ohridski” - Bitola

Prof. Dr. Sc Jove D. Talevski, Vice-Rector for Finance and Development, University “St. Kliment Ohridski” – Bitola

Prof. Dr. Sc Dragica Odžaklieska, Dean, Faculty of Economics-Prilep, University “St. Kliment Ohridski” – Bitola

Prof. Dr. Sc Mitko Kostov, Dean, Faculty of Technical Sciences-Bitola, University “St. Kliment Ohridski” - Bitola

Prof. Dr Sc Snežana Dičevska, Dean, Faculty of Education-Bitola, University “St. Kliment Ohridski” - Bitola

Prof. Dr. Sc Gordana Dimitrovska, Dean, Faculty of Biotechnical Sciences-Bitola, University “St. Kliment Ohridski” - Bitola

Prof. Dr Sc Danče Sivakova Neškovski, Dean, Faculty of Education-Bitola, University “St. Kliment Ohridski” - Bitola

Prof. Dr. Sc Blagoj Ristevski, Dean, Faculty of Information and Communication Technologies-Bitola, University “St. Kliment Ohridski” - Bitola

Prof. Dr Sc Svetlana Veljanoska, Dean, Faculty of Law-Kičevo, University “St. Kliment Ohridski” - Bitola

Prof. Dr. Sc Nikola Dujovski, Dean, Faculty of Security-Skopje, University “St. Kliment Ohridski” - Bitola

Prof. Dr. Sc Tatjana Kalevska, Dean, Faculty of Technology and Technical Sciences-Veles, University “St. Kliment Ohridski” - Bitola

Assoc. Prof. Dr. Nikola Karabolovski, Dean, Faculty of Veterinary Medicine-Bitola, University “St. Kliment Ohridski” - Bitola

Prof. Dr. Sc Tanja Jovanovska, Director, Higher Medical School-Bitola, University “St. Kliment Ohridski” - Bitola

Prof. Dr. Sc Valentina Pelivanoska, Director, Tobacco Institute-Prilep, University “St. Kliment Ohridski” - Bitola

Conference Secretary:

Elena Kitanovska-Ristoska, PhD, University “St. Kliment Ohridski” - Bitola, North Macedonia

IT Consultant:

Assist. Prof. Dr. Blagoj Nenovski, University “St. Kliment Ohridski” - Bitola, North Macedonia

Short Article Guidelines

Article title: Times New Roman; 14 pt; bold; alignment centered; single-line spacing; All Caps (max. 100 characters with spaces).

Author details: Times New Roman; 12 pt; single-line spacing; alignment centered. Please write the author details in the following order:

John Galt
University “St. Kliment Ohridski” - Bitola, North Macedonia
ORCID iD: <https://orcid.org/0000>
E-mail: galt@uklo.edu.mk

Abstract and keywords: Between 150 and 200 words (5-7 keywords); Times New Roman; 12 pt; single-line spacing; justify. Write your abstract using concise, but complete, sentences. Get to the point quickly and always use the past tense because you are reporting on a study that has been completed. There are four things you need to include: 1) your research problem and objectives, 2) your methods, 3) your key results or arguments, and 4) your conclusion.

Article text: Times New Roman; 12 pt; justify; 1.0 line spacing; margins: Top: 2,5 cm; Bottom: 2,5 cm; Left: 3 cm; Right: 3 cm. The scope of submitted text should not exceed more than 30.000 characters (with spaces) including references. The text should be written in the neuter gender, concisely with correct orthography. Latin phrases should be set in *italics*.

Quotations: If they are brief (3 lines or fewer), quotations should be run on with the text. Longer quotations should be indented, without quotation marks. All indented quotations should be typed single-spaced.

Citation style: The author should follow Chicago Style (author-date system) for referencing, for example: (Dahl 1989, 45); (Geddes 1999, 134-43); (Linz 1975). All references should be given in full at first mention. Subsequent citations can be abbreviated. Footnotes should be kept to a minimum.

Headings and subheadings: Times New Roman; 12 pt; bold.

Tables: Times New Roman; bold; size 10; align heading left; single line spacing. Tables must be created in Word, not Excel. The table heading is situated above the table.

Figures: Times New Roman; bold; size 10; alignment centered; single line spacing. The authors must submit original electronic copies of the figures applied in the article in TIFF, JPG, or PNG format. Figure heading is situated under the figure. Consider aligning tables and figures at the center.

Dates: Dates should be given in the form: 26 December 1981.

Conclusion: The conclusion is intended to help the reader understand why your research should matter to them after they have finished reading the article. A conclusion is where you summarize the article's findings and generalize their importance, discuss ambiguous data, and recommend further research.

These include:

- Presenting the last word on the issues you raised in your article.
- Summarizing your thoughts and conveying the larger implications of your study.
- Demonstrating the importance of your ideas.
- Introducing possible new or expanded ways of thinking about the research problem.

References: The reference list appears at the end of your article, and provides more detailed information about the sources you cited. Each entry in the reference list also begins with the author's last name and the publication date, so that your reader can easily find any source they encounter in the text. For four or more authors, list all of the authors in the reference list; in the text, list only the first author, followed by *et al.* It is alphabetized by the author's last name.

References Examples:

Articles:

Author's surname, Name. year of publication. "Article Title". *Horizons* 8 (1):229-4, DOI: XXX-XXX

Books:

Author's surname, Name. year of publication. *Book Title*. place of publication: publisher.

Contributions in compilations and edited volumes:

Author's surname, Name. year of publication. "Title", In: editor's surname, forename initials (ed./eds.)

Compilation (place of publication: publisher), pages interval, DOI: XXX-XXX

Internet (URL):

When articles, books, or official documents are accessed via the internet, the reference should be formatted as described above; Full URL. where the document is posted should be listed as well as the date when it was accessed.

Author's surname, Name. year of publication. *Book Title*. place of publication: publisher, available at: <http://xxxxxxxxxxxxxxxxxx> (26 December, 2021).

Legislation: Acts and Regulations

The titles of pieces of legislation (Acts, Regulations, rules, and by-laws) should be cited exactly - do not alter spelling or capitalization.

In-Text Citation:

Title of the Act Year

Title of the Act Year (abbreviation of the jurisdiction)

References:

Title of the Act and Date of publication (abbreviation of the jurisdiction)

Note: Legislation is fully included in a list of references, in alphabetical order among other references.

***We suggest utilizing reference management software like Zotero, Mendeley, and similar tools.**

Organizer:

University "St. Kliment Ohridski" - Bitola, Republic of North Macedonia

For more information about the Conference, please contact us:

Contact phone: +389 47 223 788

E-mail: conference@uklo.edu.mk

Web page: www.uklo.edu.mk

We appreciate your interest in our Conference and looking forward to your submission soon. Please forward this information to your colleagues and students.

Kind Regards,

Conference Organizing Team

Fw: CALL for PAPERS: Annual International Scientific Conference UKLO 2023, November 17-18

Prabhpreet Singh [MU - Jaipur] <prabhpreet.singh@jaipur.manipal.edu>

Thu 13/07/2023 17:04

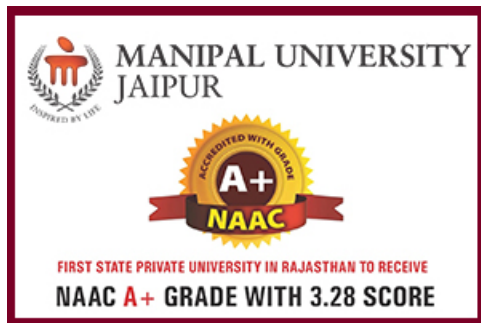
To:goran.ilik@uklo.edu.mk <Goran.ilik@uklo.edu.mk>;nurten.sulejmani@uklo.edu.mk <nurten.sulejmani@uklo.edu.mk>
Cc:Dr. Jayaram E R [MU - Jaipur] <jayaram.er@jaipur.manipal.edu>;Dr. Sonu Agarwal [MU - Jaipur]
<sonu.agarwal@jaipur.manipal.edu>

📎 2 attachments (425 KB)

AISC 2023_Call for Papers.pdf; Manipal Logo.jpeg;

Respected Sir

Manipal University Jaipur logo is attached in the mail. We are thankful for the collaboration.

<https://jaipur.manipal.edu/>

Home | Manipal University Jaipur - 68 years of legacy of Manipal Education

Manipal University in Jaipur is among the list of top universities in Rajasthan offering undergraduate, postgraduate and PHD courses. Know about the campus and other details here.

jaipur.manipal.edu

From: Dr. Sonu Agarwal [MU - Jaipur] <sonu.agarwal@jaipur.manipal.edu>**Sent:** 13 July 2023 17:00**To:** Prabhpreet Singh [MU - Jaipur] <prabhpreet.singh@jaipur.manipal.edu>**Cc:** Dr. Jayaram E R [MU - Jaipur] <jayaram.er@jaipur.manipal.edu>**Subject:** FW: CALL for PAPERS: Annual International Scientific Conference UKLO 2023, November 17-18

Dear Prabhpreet,

Please share the University Logo and Link with the University St. Kliment Ohridski, Bitola for the International Conference.

Regards

From: Prabhpreet Singh [MU - Jaipur] <prabhpreet.singh@jaipur.manipal.edu>**Sent:** Wednesday, July 12, 2023 7:32 PM

To: Dr. Sonu Agarwal [MU - Jaipur] <sonu.agarwal@jaipur.manipal.edu>
Cc: Dr. Jayaram E R [MU - Jaipur] <jayaram.er@jaipur.manipal.edu>; Dr. Santosh Patil [MU - Jaipur] <santosh.patil@jaipur.manipal.edu>; goran.ilik@uklo.edu.mk
Subject: Fwd: CALL for PAPERS: Annual International Scientific Conference UKLO 2023, November 17-18

Respected Madam

St. Kliment Ohridski Bitola are organising International conference. It is hereby requested for logo and link. Trail mail for kind consideration.

Get [Outlook for iOS](#)

From: Nurten Sulejmani <nurten.sulejmani@uklo.edu.mk>
Sent: Wednesday, July 12, 2023 5:49 PM
To: Goran Ilik <goran.ilik@uklo.edu.mk>; REKTOR Korunovski <rector@uklo.edu.mk>
Subject: CALL for PAPERS: Annual International Scientific Conference UKLO 2023, November 17-18

Respected colleagues,

As partner universities with established relations of bilateral cooperation, it is our distinct pleasure to inform you about a major scientific event *Annual International Scientific Conference 2023*, organized by the [University "St Kliment Ohridski" – Bitola](#), Republic of North Macedonia to be held on 17-18 November 2023, on the occasion of celebrating the World Science Day for Peace and Development.

The Conference topic is "Multidisciplinary Approaches to Sustainable Development Goals". Authors are invited to submit papers on any subject related to and within the scope of the Conference topic. Submissions from academics, researchers, and practitioners at any stage of their career, including PhD students, will be accepted. Selected papers will be published in a special issue of the [Horizons - International Scientific Journal](#) as a peer reviewed, interdisciplinary, and international journal published by the University "St. Kliment Ohridski" - Bitola, indexed in EBSCO, CrossRef, Google Scholar etc. The language of the Conference is English.

We now invite abstract submissions for the Conference (by 20 September 2023) at the following link:
https://docs.google.com/forms/d/e/1FAIpQLSfxjz1J0DRQy7GYTCm11mdUffQWeDM_dn2gBh9SowUEKu3cSQ/viewform?vc=0&c=0&w=1&flr=0

To that end, we would be very glad to share it with our friends and invite our partner universities to be presented with the institutional logo and link to their institutional web to act as Conference partners and friends. The main benefit for the Conference partners would be the free publication of accepted papers. So, before we share the detailed information about the Conference – time, venue, and program – we would very much appreciate having your consent accompanied by your institutional logo and a link no later than 31 July 2023 submitted via emails: goran.ilik@uklo.edu.mk and nurten.sulejmani@uklo.edu.mk

After that, we will get back to you with further steps as soon as possible.

Looking forward to hearing from you,

Organizing Team
Ms Nurten Sulejmani
IR Officer

[University "St. Kliment Ohridski" - Bitola](#)

Bulevar 1 Maj bb
7000 Bitola
Republic of N. Macedonia
+ 389 71 217 422

Entrepreneurship Supports a Sustainable Planet

1. Sustainable waste management
2. Discarded plastics → building materials
3. Safe water for rural communities
4. Solar-powered light for off-grid homes
5. Geothermal-powered air conditioning

Logos: Gjenge, MyH2O, ECO STAR, GIBSS, ilumexico

United Nations Environment Programme. Plan young entrepreneurs embracing sustainable business models. Mar 4, 2018. [https://www.unep.org/news-and-stories/story/young-entrepreneurs-embracing-sustainable-business-models](#)

6. SUSTAINABLE WASTE MANAGEMENT
7. DISCARDED PLASTICS → BUILDING MATERIALS
11. SAFE WATER FOR RURAL COMMUNITIES
12. SOLAR-POWERED LIGHT FOR OFF-GRID HOMES
13. GEOTHERMAL-POWERED AIR CONDITIONING

4:33 PM | hbv-xkbp-xdf

Participants: Svetlana Veljanoska, Arianisa Ramadani, Tatjana Gerginova, Anthony Gould, Jehona Murati-Dugolli, Matthew Hull, 15 others, and a participant with a turban.

meet.google.com/hbv-xkbp-xdf

tax laws relevance funny apps Empire NLUMJNC-14 Democracy Web | F... World Report 2013... Cybercrime socie-e... All Bookmarks

Matthew Hull (Presenting)

Entrepreneurship Supports a Sustainable Planet

- 1. Sustainable waste management
- 2. Discarded plastics → building materials
- 3. Safe water for rural communities
- 4. Solar-powered light for off-grid homes
- 5. Geothermal-powered air conditioning

United Nations Environment Programme. Plan young entrepreneurs embracing sustainable business models. Mar 4, 2019. <https://www.unep.org/news-and-stories/en/plan-young-entrepreneurs-embracing-sustainable-business-models>

6	SAFELY WATER FOR SUSTAINABLE
7	ENERGY AFFORDABLE AND CLEAN
11	INDUSTRIES AND INNOVATION
12	RESILIENT INFRASTRUCTURE AND
13	CLIMATE ACTION

Svetlana Veljanoska, Arianisa Ramadani, Tatjana Gerginova, Jehona Murati-Dugolli, Anthony Gould, 15 others, Daniel S. ...

4:34 PM | hbv-xkbp-xdf

Type here to search

30°C 4:34 PM 11/17/2023

The screenshot shows a Google Meet interface. At the top, the browser address bar displays `meet.google.com/hbv-xkbp-xdf`. Below the browser, the Meet header shows the name "Matthew Hull (Presenting)".

The main content area is a presentation slide with the following text and images:
- Logos for "nanu.ath" and "VIRGINIA TECH".
- A group photo of people.
- A photo of a meeting with a sign that says "CHALLENGE".
- A photo of a meeting with a sign that says "VDH".
- The text: "Programs to stimulate sustainable nano-enabled innovation & entrepreneurship".

On the right side, there is a grid of participant video thumbnails. The participants shown are:
- Matthew Hull (top left, speaking)
- An unnamed participant (top middle)
- Anthony Gould (top right)
- Svetlana Vojanoska (middle left, muted)
- Arlanisa Ramadani (middle middle, muted)
- Tatjana Gerginova (middle right, muted)
- Arlinda Muharemi (bottom left, muted)
- 15 others (bottom middle, muted)
- An unnamed participant (bottom right)

At the bottom of the Meet window, there is a control bar with icons for mute, video, chat, reactions, screen share, and end call. The system tray at the very bottom shows the time as 4:50 PM on 11/17/2023, with a temperature of 30°C.

meet.google.com/hbv-xkbp-xdf

Matthew Hull (Presenting)

NanoTechnology Entrepreneurship Challenge (NTEC)

- Promote student-led entrepreneurship across NNCI
- Flexible support to maximize site engagement
 - In-kind instrument time
 - Direct funding (agreement for instrument time, materials)
 - Specialized support for underrepresented groups
 - Voluntary participation in 7-week NTEC Accelerator
- Opportunity to:
 - Explore nano for sustainable solutions
 - Learn "practical" entrepreneurship
 - Transition ideas beyond the lab
 - Fail safely, learn from mistakes
 - Connect NNO sites

NTEC Showcase

4:50 PM | hbv-xkbp-xdf

Matthew Hull, Anthony Gould, Svetlana Vojtanoska, Arlinda Muharemi, Tatjana Gerginova, 15 others

Type here to search

4:50 PM 11/17/2023

meet.google.com/hbv-xkbp-xdf

Innovation & Entrepreneurship

- Reflect society's investment in a sustainable future
- Benefit society in myriad ways aligned with UN SDGs
- Can we better support entrepreneurs?
 - Fragile translational ecosystems facing real threats
 - Nurture more entrepreneurs around physical tech (e.g., nano)
 - Remove barriers to underrepresented groups
 - Emphasize sustainable, responsible innovation

4:56 PM | hbv-xkbp-xdf

Type here to search

30°C

4:56 PM 11/17/2023







meet.google.com/hbv-xkbp-xdf

case laws relevance funny apps Empire NLUIMUNC'14 Democracy Web | F... World Report 2013:... Cybercrime socio-e... All Bookmarks

M Matthew Hull (Presenting)

Entrepreneurship Supports a Sustainable Planet

- 1. Sustainable waste management
- 2. Discarded plastics → building materials
- 3. Safe water for rural communities
- 4. Solar-powered light for off-grid homes
- 5. Geothermal-powered air conditioning

United National Environment Programme. Five young entrepreneurs embracing sustainable business models. Mar 3, 2022. <https://www.unep.org/news-and-stories/story/five-young-entrepreneurs-embracing-sustainable-business-models>

Gjenge MyH2O ECO STAR GIBSS iluméxico

6 CLEAN WATER AND SANITATION
7 AFFORDABLE AND CLEAN ENERGY
11 SUSTAINABLE CITIES AND COMMUNITIES
12 RESPONSIBLE CONSUMPTION AND PRODUCTION
13 CLIMATE ACTION

Svetlana Veljanoska Arianisa Ramadani Tatjana Gerginova

Univerzitet Sv. Klime... Anthony Gould Jehona Murati-Dugolli

Matthew Hull 15 others Prachpreet Singh

4:33 PM | hbv-xkbp-xdf

Type here to search

meet.google.com/hbv-xkbp-xdf

case laws relevance funny apps Empire NLUIMUNC'14 Democracy Web | F... World Report 2013:... Cybercrime socio-e... All Bookmarks

M Matthew Hull (Presenting)

Entrepreneurship Supports a Sustainable Planet

- 1. Sustainable waste management
- 2. Discarded plastics → building materials
- 3. Safe water for rural communities
- 4. Solar-powered light for off-grid homes
- 5. Geothermal-powered air conditioning

United National Environment Programme. Five young entrepreneurs embracing sustainable business models. Mar 3, 2022. <https://www.unep.org/news-and-stories/story/five-young-entrepreneurs-embracing-sustainable-business-models>

Gjenge MyH2O ECO STAR GIBSS iluméxico

6 CLEAN WATER AND SANITATION
7 AFFORDABLE AND CLEAN ENERGY
11 SUSTAINABLE CITIES AND COMMUNITIES
12 RESPONSIBLE CONSUMPTION AND PRODUCTION
13 CLIMATE ACTION

Svetlana Veljanoska Arianisa Ramadani Tatjana Gerginova

Univerzitet Sv. Klime... Anthony Gould Jehona Murati-Dugolli

Matthew Hull 15 others Prachpreet Singh

4:34 PM | hbv-xkbp-xdf

Type here to search

meet.google.com/hbv-xkbp-xdf

case laws relevance funny apps Empire NLUIMUNC'14 Democracy Web | F... World Report 2013... Cybercrime socio-e...

M Matthew Hull (Presenting)

Programs to stimulate sustainable nano-enabled innovation & entrepreneurship

4:50 PM | hbv-xkbp-xdf

Windows taskbar: Type here to search, 30°C, 4:50 PM 11/17/2023

meet.google.com/hbv-xkbp-xdf

case laws relevance funny apps Empire NLUIMUNC'14 Democracy Web | F... World Report 2013... Cybercrime socio-e...

M Matthew Hull (Presenting)

NanoTechnology Entrepreneurship Challenge (NTEC)

- Promote student-led entrepreneurship across NNCI
- Flexible support to maximize site engagement
 - In-kind instrument time
 - Direct funding (\$500/team for instrument time, materials)
 - Diversity Award (support for underrepresented groups)
 - Voluntary participation in 7-week NTEC Accelerator
- Opportunity to:
 - Explore nano for sustainable solutions
 - Learn, "practice" entrepreneurship
 - Transition ideas beyond the lab
 - Fail safely, learn from mistakes
 - Connect NNCI sites

NTEC Showcase

4:50 PM | hbv-xkbp-xdf

Windows taskbar: Type here to search, 30°C, 4:50 PM 11/17/2023

meet.google.com/hbv-xkbp-xdf

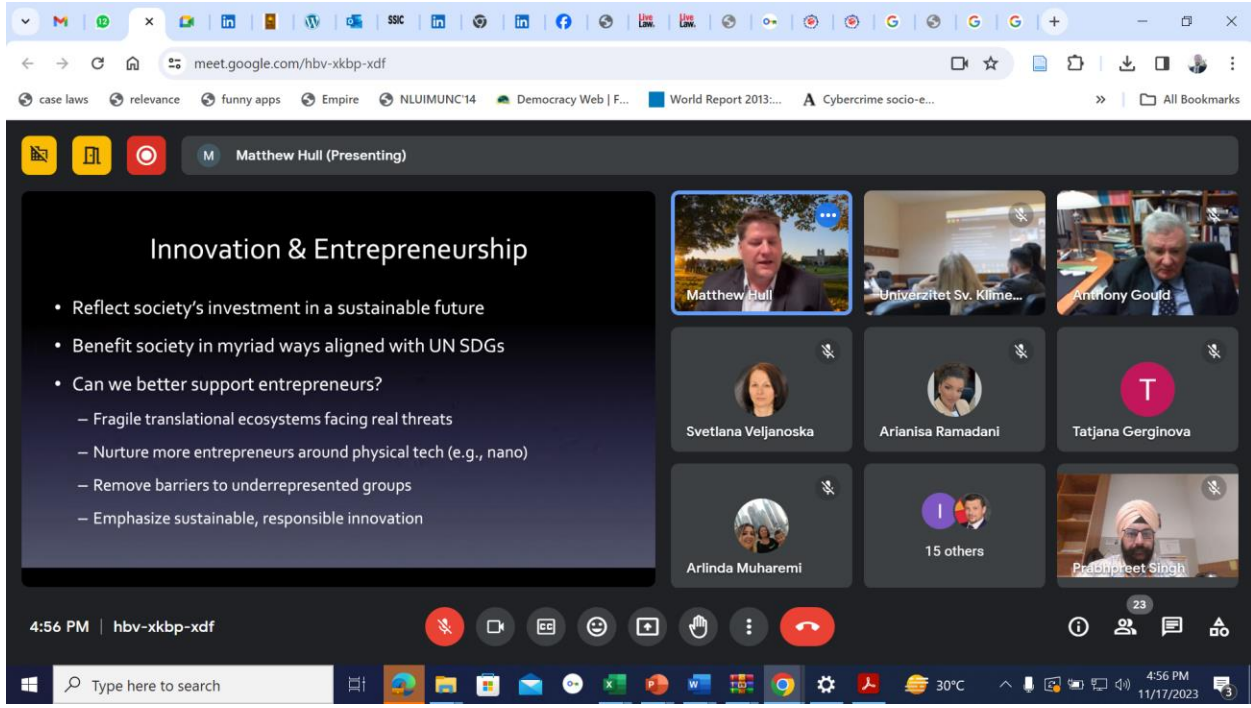
case laws relevance funny apps Empire NLUIMUNC'14 Democracy Web | F... World Report 2013... Cybercrime socio-e... All Bookmarks

M Matthew Hull (Presenting)

Innovation & Entrepreneurship

- Reflect society's investment in a sustainable future
- Benefit society in myriad ways aligned with UN SDGs
- Can we better support entrepreneurs?
 - Fragile translational ecosystems facing real threats
 - Nurture more entrepreneurs around physical tech (e.g., nano)
 - Remove barriers to underrepresented groups
 - Emphasize sustainable, responsible innovation

4:56 PM | hbv-xkbp-xdf



meet.google.com/hbv-xkbp-xdf

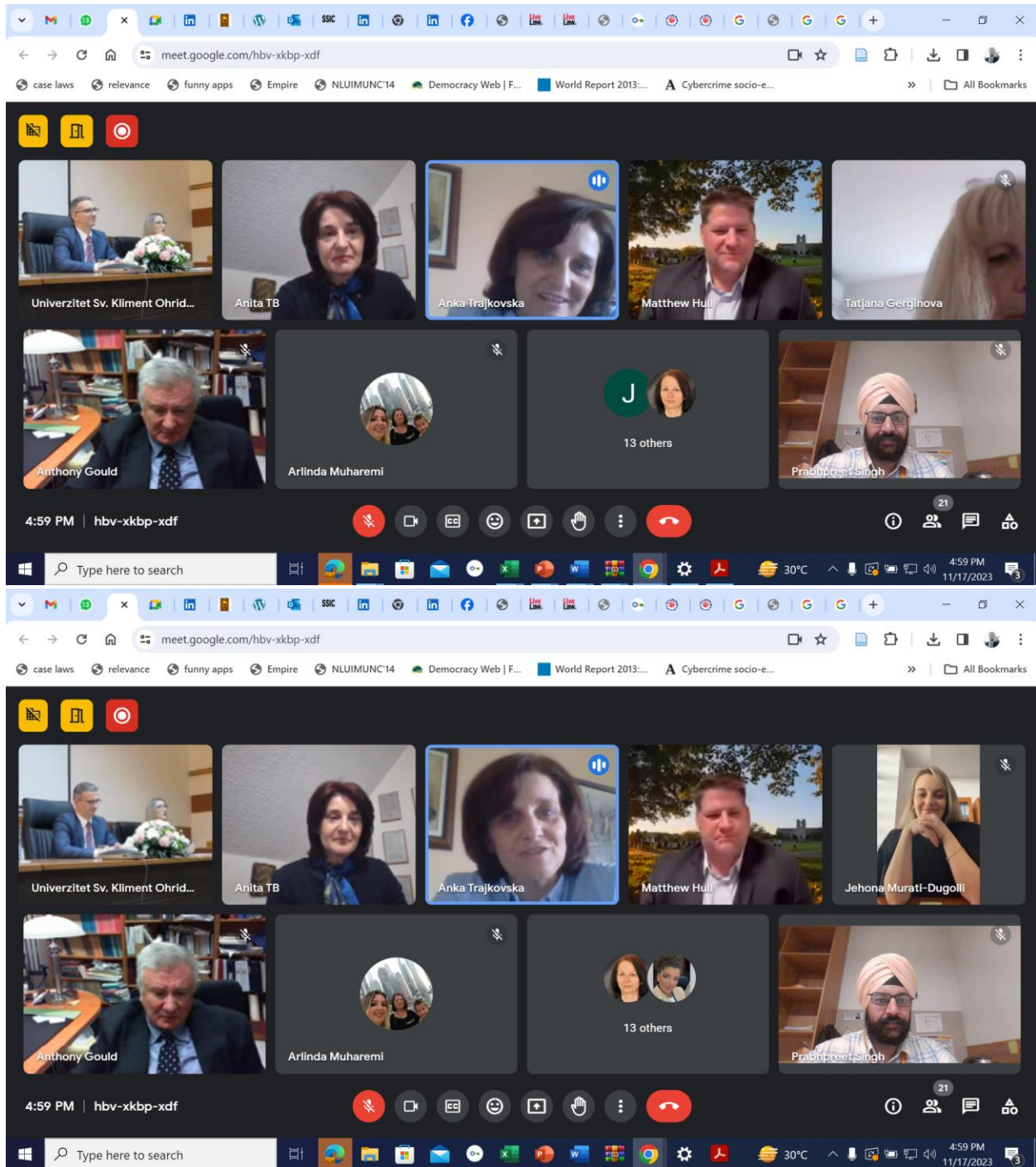
case laws relevance funny apps Empire NLUIMUNC'14 Democracy Web | F... World Report 2013... Cybercrime socio-e... All Bookmarks

Univerzitet Sv. Kliment Ohrid... Anita TB Anka Trajkovska Matthew Hull Tatjana Gerginova

Anthony Gould Arlinda Muharemi 13 other Anka Trajkovska has raised a hand Open queue X

4:58 PM | hbv-xkbp-xdf





Manipal University Jaipur is a partner university in a major scientific event Annual International Scientific Conference 2023, organized by the University “St Kliment Ohridski” – Bitola, Republic of North Macedonia to be held on 17-18 November 2023, on the occasion of celebrating the World Science Day for Peace and Development. The Conference topic is “Multidisciplinary Approaches to Sustainable Development Goals”. I want to thank Professor Goran Ilik for the kind opportunity and Collaboration.

Also, this is the Second International Conference in which both the Universities are Collaborating. University "St Kliment Ohridski" – Bitola, Republic of North Macedonia was a partner university in 4th International Conference on Smart Systems: Innovations in Computing organized by School of Information Technology, Manipal University Jaipur.

https://lnkd.in/du_vb_mT



UKLO Annual International Scientific Conference 2023 (AISC)

World Science Day for Peace and Development, celebrated annually on November 10th, highlights the significance of science in society and the imperative to engage the wider public in discussions regarding emerging scientific subjects. On this occasion, the University “St. Kliment Ohridski” - Bitola is hosting the *Annual International Scientific Conference 2023* on the following topic:

“MULTIDISCIPLINARY APPROACH TO SUSTAINABLE DEVELOPMENT GOALS”

Bitola, Republic of North Macedonia, 17 November 2023

Starting Time: 11:00 CET

Language: English & Macedonian

Place: UKLO Conference Hall (Onsite) & Online

Mode: Hybrid

This AISC offers the chance to mobilize the academy and experts from home and abroad around the issue of science for peace and development with a single purpose - *changing the world for the better!*

The AISC will focus on discussing the key issues outlined in the UN Agenda 2030. These include eliminating poverty, eradicating hunger, improving health and well-being, ensuring quality education, promoting gender equality, enhancing access to clean water and sanitation, advancing affordable and clean energy, fostering decent work and economic growth, encouraging industry, innovation, and infrastructure development, reducing inequality, building sustainable cities and communities, advocating for responsible consumption and production, addressing climate action, protecting life below water and on land, ensuring peace, justice, and strong institutions, and fostering partnerships to achieve these goals.

AISC Partners:





*“Sustainable development requires human ingenuity.
People are the most important resource”.*

- Dr. Dan Shechtman*

** Dr. Shechtman was awarded with a Nobel Prize in Chemistry in 2011. In 2023, Professor Honoris Causa title was given to Dr. Shechtman at the University “St. Kliment Ohridski” – Bitola.*

AISC Partners:





Place: UKLO Conference Hall (Onsite)

10:30 – 11:00 Registration of participants

11:00 – 11:30 Opening ceremony (Onsite & Google Meet Link: <https://meet.google.com/hbv-xkbp-xdf>)

Prof. Dr. sc Igor Nedelkovski, Rector of the University “St. Kliment Ohirdski” - Bitola

Prof. Dr. sc Goran Ilik, Vice-Rector for Science at the University “St. Kliment Ohirdski” - Bitola

Dr. Toni Konjanovski, Mayor of Bitola

Dr. Bisera Kostadinovska – Stojchevska, Minister of Culture of the Republic of North Macedonia

Plenary speakers:

11:35 – 12:00

Anthony M. Gould, PhD, Laval University, Canada

Speech: *“Zero-Sum versus Positive Sum: Sustainable Growth through a Change in Mindset”*

(Google Meet Link: <https://meet.google.com/hbv-xkbp-xdf>)

12:05 – 12:30

Matthew S. Hull, PhD Research Professor/Director, NCFL | Virginia Tech ICTAS, USA

Speech: *“Sustainable Entrepreneurship: A Catalyst for the UN Agenda 2030”*

(Google Meet Link: <https://meet.google.com/hbv-xkbp-xdf>)

12:30 – 12:45 Discussion

12:45-13:00 Coffee break

Moderator: Prof. Dr. Ivona Shushak - Lozanovska

AISC Partners:





PRESENTATION SCHEDULE

17 November 2023

PANEL I

13:00 – 15:15 UKLO Conference Hall (Onsite)

Chair: Prof. dr. sc Ice Ilijevski	
1. Svetlana Nikolovska – EFFICIENCY AND EFFICIENCY OF THE STATE AUTHORITIES AND INSTITUTIONS IN THE SUPPRESSION OF CORRUPTION IN THE REPUBLIC OF NORTH MACEDONIA	13:00-13:15 Onsite
2. Katerina Krstevska - Savovska– PROHIBITION OF TORTURE – MACEDONIAN CRIMINAL LEGISLATION AND COMPARATIVE OVREVIEW	13:15-13:30 Onsite
3. Marina Malish Sazdovska – SUSTAINABLE DEVELOPMENT AS A GLOBAL PHENOMENON	13:30-13:45 Onsite
4. Tatjana Gerginova – GLOBAL SUSTAINABLE DEVELOPMENT	13:45-14:00 Onsite
5. Ice Ilijevski, Ivona Shushak – Lozanovska, Angelina Stanojoska–PROVIDING A “LEGAL IDENTITY” FOR ALL – THE CASE OF THE REPUBLIC OF NORTH MACEDONIA	14:00-14.15 Onsite
6. Gordana Gjorgievska – Nedelkovski, Fatma Bajram, Azemovska – OUR LIBRARY AND SUSTAINABLE DEVELOPMENT GOALS	14:30-14:45 Onsite
7. Liljana Jonoski – A LEVEL OF CONTRIBUTION TO THE AGENDA 2030 THROUGH THE ENFORCEMENT OF GENDER EQUALITY IN NORTH MACEDONIA	14:45-15:00 Onsite
8. Laze Jakimoski – FREEDOM OF AGREEMENT AS A GENERAL PRINCIPLE OF LAW AND ITS LIMITS	14:15-14:30 Onsite
Discussion (Onsite)	15:00-15:15

AISC Partners:



PANEL II

13:00 – 15:15 Online: Google Meet Link: <https://meet.google.com/hbv-xkbp-xdf>

Chair: Prof. dr. sc Aleksandar Ivanov (aleksandar.ivanov@uklo.edu.mk)	
1. Svetlana Veljanovska – ACCESS TO PUBLIC INFORMATION AS A FUNDAMENTAL DEMOCRATIC RIGHT OF CITIZENS	13:00-13:15 Online
2. Agustina Noeli Vasquez – THE DEVELOPMENTAL ETHOS OF PRESIDENTIAL CANDIDATES IN ARGENTINA: A QUALITATIVE ANALYSIS OF THE 2023 ELECTION DEBATE	13:15-13:30 Online
3. Milan Masat- THE SIGNIFICANCE OF THE EVENTS OF THE SHOAH FOR CONTEMPORARY SOCIETY	13:30-13:45 Online
4. Marina Kalashlinska – THE GOVERNMENT PREPAREDNESS TO RESTRICT THE CIVIL LIBERTIES OF MEDIA AS A CRITERION FOR THE PROLIFERATION OF ANTI-DEMOCRATIC TENDENCIES IN UKRAINE	13:45-14:00 Online
5. Branko Leštanin, Željko Nikač – LEGAL AND ORGANIZATIONAL ASPECTS OF FIGHT AGAINST NARCO-CRIMES IN SERBIA: STATE AND DEVELOPMENT	14:00-14:15 Online
6. Marina Kuzmanovska- THE FAMILY AS A FACTOR IN ENCOURAGING OF THE GIFTEDNESS	14:15-14:30 Online
7. Avkash Jadhav – EXAMINING RIGHT TO LIFE AS THE CORE VALUE OF SUSTAINABLE DEVELOPMENT GOALS	14:30-14:45 Online
8. Panche Dameski – CLINICAL EVALUATION OF SURGICAL TREATMENT OF CHERRY EYE WITH MODIFIED MORGAN POCKET TECHNIQUE	14:45-15:00 Online
Discussion (Online)	15:00-15:15

AISC Partners:





15:15-15:30 CLOSING REMARKS (Onsite and Online: Google Meet Link)

Note: Selected papers presented at the AISC will be published in a special issue of “Horizons - International Scientific Journal”, an interdisciplinary, peer-reviewed, and internationally recognized journal published by the University “St. Kliment Ohridski” - Bitola. The journal is indexed in databases such as EBSCO, CrossRef, Google Scholar and more.

Organizer: University “St. Kliment Ohridski” – Bitola, Republic of North Macedonia

Contact phone: +389 47 223 788

E-mail: conference@uklo.edu.mk

Web page: www.uklo.edu.mk

Place: Partizanska 32, Bitola 7000



AISC Partners:





“Sustainable development is the pathway to the future we want for all. It offers a framework to generate economic growth, achieve social justice, exercise environmental stewardship and strengthen governance.”

- Ban Ki-moon

AISC Partners:





Conference Partners:



**MANIPAL UNIVERSITY
JAIPUR**
(University under Section 2(f) of the UGC Act)



AISC Partners:



**MANIPAL UNIVERSITY
JAIPUR**
(University under Section 2(f) of the UGC Act)





MANIPAL UNIVERSITY
JAIPUR



Post Event Report

FACULTY OF DESIGN

5days Executive
Development Program
on

‘Bamboo Renaissance: Modern Design Meets Sustainability’

Venue: Online platform

Time: 9:30 AM-12.00 PM (First day)

2:30 PM-4.00 PM (2nd to 5th day)

18th September- 22nd September 2023





Index

1. Introduction of the Executive development Program	3
2. Objectives of the Executive development Program	3
3. Beneficiaries of the Event:.....	3
4. Details of the Guests.....	3
5. Brief Description of the event	4
6. Images.....	5
7. Brochure of the event.....	6
8. Schedule of the event.....	7
9. Attendance of the Event.....	7
10. Weblink.....	7
11. Event Coordinators:.....	7





1. Introduction of the Executive development Program:

On World Bamboo Day, the Faculty of Design at Manipal University Jaipur organized a 5-day Executive Development Program titled “Bamboo Renaissance: Modern Design Meets Sustainability” in collaboration with their industrial partner, KONBAC, and the Indian Bamboo Forum, in association with the IGBC Student Chapter, MUJ, and MUJ-TEC. The program was conducted in virtual mode from September 18th to September 22nd, 2023.

2. Objectives of the Seminar:

- Understanding the various application of Bamboo in Exterior and interior spaces.
- To create awareness about bamboo in different regions.
- To understand its production and preservation technique techniques.

3. Beneficiaries of the Event:

- UG Students (Architecture, Design and Construction related Fields)
- PG Students (Architecture, Design and Construction related Fields)
- Research Scholars
- Academicians, Practitioners, and Industry Professionals in the fields of Architecture, Design, Civil, and Structural Engineering.

4. Details of the Speakers:

- a) Dr. Jagdish Vengala, Head of EDC & Associate Professor at PVPSIT Vijayawada. Dr. Jagdish Vengala presented various components of bamboo and explained its diverse strength and elastic properties. He also discussed the various IS codes applicable in India for bamboo construction.
- b) Prof. Sankalp, an associate professor from CEPT UNIVERSITY. Prof. Sankalp presented various construction techniques related to Bamboo construction, demonstrating proposals from different parts of the world. He elucidated innovative joinery details pertinent to bamboo construction.
- c) Prof. Charruchandra K. faculty member at CTARA, IIT Mumbai, discussed various species of bamboo and highlighted their unique thermal, bending, tensile, and compressive strength properties. He also showcased the application of innovative joinery details using Bomcrete (HIB) technology in arch construction. In addition, Prof. Charruchandra K. presented models of bamboo structures subjected to different loads, demonstrating their strength and durability.
- d) **Mr. Sanjeev Shashikant Karpe** is a qualified Electrical Engineer has been associated with bamboo Industry for last eighteen years and has pioneered the work in setting up of self-sustainable bamboo-based enterprise in rural India. He is a Founder and Director with Konkan Bamboo & Cane Development Centre (KONBAC), an organization working for sustainable development through use of bamboo as a resource & implementing various bamboo projects successfully for last 17 years. Mr. Sanjeev Karpe explained bamboo construction in India and worldwide.



He stated that bamboo has strong potential to grow in degraded land, requires less water compared to sugarcane, and consumes less embodied energy compared to conventional materials. In the global context, countries such as Colombia and Vietnam have embarked on large-scale bamboo projects, whereas in India, despite being the world's second-largest bamboo producer, its full potential remains largely untapped. In addition, Ar. Sanjeev Karpe presented models of bamboo structures subjected to different loads, demonstrating their strength and durability. Various experiments related to straightening of bamboo and bending it to achieve the required form were also demonstrated.

- e) Mr. Amitava Sil, a Scientist at IWS (Indian Wood Science and Technology), Kolkata, renowned for his extensive knowledge and experience in the preservation treatment of bamboo species. Mr. Amitava Sil provided insights into preservative treatments and fire retardancy in structural bamboo. He elucidated various treatment methods and processes, highlighting their associated benefits. Furthermore, he offered a demonstration of bamboo's structural frame by showcasing its inherent structural properties.

5. Brief Description of the event:

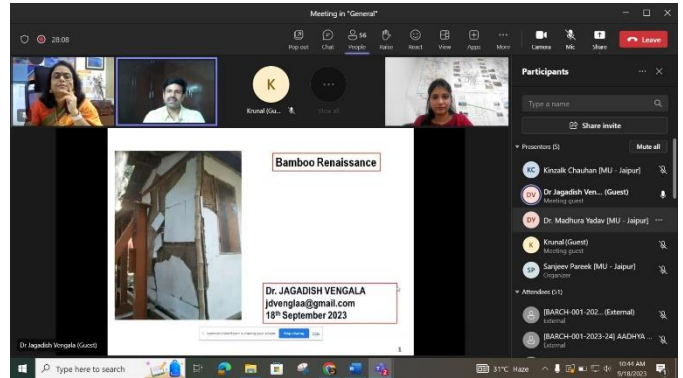
In the context of a Global Environmental crisis, coupled with economic and health challenges, the time has come for radical cultural awareness, politicians, architects, engineers, developers, and construction companies have an enormous responsibility as the construction industry and processes have an enormous negative impact on the environment. Bamboo is a key natural resource and, together with conscious design, draws a new direction for Contemporary Architecture. The Executive Development Program "Bamboo Renaissance: Modern Design Meets Sustainability" is a comprehensive initiative designed to explore the dynamic intersection of modern design principles and sustainable practices within the realm of bamboo. This program is carefully curated to provide Industry Professionals, Academicians, and Researchers with the knowledge and tools needed to harness bamboo's immense potential as an eco-friendly resource in contemporary design and construction. The EDP 2023 will be a great opportunity to facilitate networking with industry experts and peers, enabling participants to exchange ideas, collaborate on projects, and stay updated on emerging trends and innovations in sustainable design.



6. Images



1. Inaugural Address by Prof. (Dr.) Madhura Yadav, Dean, FoD



2. First day expert lecture by Prof. (Dr.) Jagdish Vegala



3. Second day expert lecture by Prof. (Dr.) Sankalp



4. Third day expert lecture by Prof. (Dr.) Charuchandra



5. Fourth day expert lecture by Mr. Sanjeev Karpe



6. Fifth day expert lecture by Mr. Amitava Sil



7. Valedictory session by Mr. Anand Mishra and Mr. Dharendra Madan



7. Brochure of the event:



FACULTY OF DESIGN

in association with
IGBC Student Chapter, MUJ & **MUJ TEC**
 in collaboration with
KONBAC Community First
IBF India Bamboo Forum

EXECUTIVE DEVELOPMENT PROGRAM -2023 (Virtual Mode)

September 18th: 9:30am to 11 am & September 19th to 22nd, 2023 ; 2:30pm to 4:00 pm

BAMBOO RENAISSANCE: Modern Design meets Sustainability



Scan here for Registration



Scan here for Payment

ABOUT MANIPAL UNIVERSITY JAIPUR
 Manipal University Jaipur (MUJ) has redefined academic excellence in the region and inspires students of all disciplines to learn and innovate through hands-on practical experience. The multi-disciplinary university offers career-oriented courses at all levels, i.e., UG, PG, and doctoral across all the streams like Engineering, Architecture, Planning, Fashion Design, Interior Design, Fine Arts, Hospitality, Humanities, Journalism, Basic Sciences, Law, Commerce, Computer Applications, Management, etc. The University has been granted the ATAL Incubation Centre, funded by Niti Aayog, Government of India. Ost.

ABOUT FACULTY OF DESIGN
 The Faculty of Design aims to nurture it as one of its core strengths, with the mission to become the most preferred global destination in design education and research for students, researchers, faculty, collaborators, promoters, investors, and developers. Over time, the Faculty has grown into two Schools: The School of Architecture and Design, & the School of Design & Art & many departments. The Faculty of Design is backed by excellent infrastructure; and intellectual capital within the Faculty. At present Faculty of Design is offering UG, PG, and Doctoral programs in Architecture, Interior Design, Fine Art, Fashion Design and UXID.

IGBC STUDENT CHAPTER
 IGBC Student Chapter Manipal University Jaipur was constituted by the Faculty of Design. IGBC student chapter aims to explore the role of the green building concept in the built and unbuilt environment. The chapter organized various interactive sessions and workshops by experts.

KONBAC BAMBOO PRODUCTS PRIVATE LIMITED
 KONBAC BAMBOO PRODUCTS PRIVATE LIMITED is classified as a non-government company and it is registered and located in MUMBAI. KONBAC provides training, at a national and global level, in Bamboo cultivation, harvesting, and primary and secondary processing. Manufacture of interior & lifestyle accessories. Manufacture of home and office furniture. Construction of cottages, resorts, and buildings.

ABOUT EXECUTIVE DEVELOPMENT PROGRAMME
 In the context of a Global Environmental crisis, coupled with economic and health challenges, the time has come for radical cultural awareness, politicians, architects, engineers, developers, and construction companies have an enormous responsibility as the construction industry and processes have an enormous negative impact on the environment. Bamboo is a key natural resource and, together with conscious design, draws a new direction for Contemporary Architecture.

The Executive Development Program 'Bamboo Renaissance: Modern Design Meets Sustainability' is a comprehensive initiative designed to explore the dynamic intersection of modern design principles and sustainable practices within the realm of bamboo. This program is carefully curated to provide Industry Professionals, Academicians, and Researchers with the knowledge and tools needed to harness bamboo's immense potential as an eco-friendly resource in contemporary design and construction. The EDP 2023 will be a great opportunity to facilitate networking with industry experts and peers, enabling participants to exchange ideas, collaborate on projects, and stay updated on emerging trends and innovations in sustainable design.

WHO CAN PARTICIPATE
 Students, Research Scholars, Academicians, and Practitioners in the field of Architecture, Design, Civil, and Structural Engineering.

REGISTRATION FEE
 INR 500 - For External Participants
 INR 200 - For Research Scholars & Internal Participants

NOTE
 After the successful Completion of EDP, an E-Certificate will be given to all participants

CHIEF GUEST



Mr. SURESH PRABHU
 Former Union Minister, former Member of Parliament and India's Sheriff to the G20, CEO, Chairman, India Bamboo Forum, Founding Chancellor of Globalwood University, Chief, President of London School of Business.

GUEST OF HONOUR



DR PRABHAT KUMAR
 Head, National Bamboo Mission, A Horticulture Commissioner, Department of Agriculture & Fisheries, Welfare, Ministry of Agriculture, Govt. of India, New Delhi.

RESOURCE PERSONS



Mr. SANJEEV KARPE
 Founder Director, KONBAC
 Topic - Modern bamboo construction in India



Prof. SANKALPA
 Associate Prof., FA, CEPT University
 Topic - Cutting-edge Design and Technology



Mr. AMITAVA SIL
 Scientist, IWST, Kolkata
 Topic - Provenance, treatments and fire Retardancy of Structural Bamboo.



Dr. JAGADISH VENGINALA
 Head, EDC & Associate Professor, PVPST, Vijayanagara
 Topic - The Bamboo Renaissance



Prof. CHARRUCHANDRA K.
 Faculty, CTARA, IIT, Mumbai
 Topic - Sustainable Construction Practices



SPECIAL GUEST
Mr. ANAND MISHRA
 Chairman, IGBC Jaipur & Managing Director, Trimurti Builders & Colonizers Pvt. Ltd.

OUR CHAIRS



CHIEF PATRON
MR. S. VAITHEESWARAN
 Chairperson, Manipal University Jaipur



PATRON
Dr. G. K. PRABHU
 President, Manipal University Jaipur



CO-PATRON
Dr. THAMMAIAH CS
 Pro-President, Manipal University Jaipur



CO-PATRON
Dr. NITU BHATNAGAR
 Registrar, Manipal University Jaipur



CONVENER
Dr. MADHURA YADAV
 Dean FOD, Manipal University Jaipur



ORGANISING SECRETARIES
Ar. SANJEEV PAREEK
 Asst. Prof. SA&D



Ar. KINZALK CHAUHAN



FACULTY OF DESIGN

Celebrating World Bamboo Day

By Organizing
EXECUTIVE DEVELOPMENT PROGRAM -2023 (Virtual Mode)

BAMBOO RENAISSANCE: Modern Design meets Sustainability



Scan here for Registration



Scan here for Payment

in association with
MUJ TEC & IGBC STUDENT CHAPTER, MUJ

in collaboration with
KONBAC Community First
IBF India Bamboo Forum

DATE & TIME: (1 hour 30 minutes / Day)
 September 18th: 9:30 am to 11 am & September 19th to 22nd, 2023; 2:30 pm to 4:00 pm

INAUGURAL FUNCTION



CHIEF GUEST
Mr. SURESH PRABHU
 Former Union Minister, former Member of Parliament and India's Sheriff to the G20, CEO, Chairman, India Bamboo Forum, Founding Chancellor of Globalwood University, Chief, President of London School of Business.

GUEST OF HONOUR
DR PRABHAT KUMAR
 Head, National Bamboo Mission, A Horticulture Commissioner, Department of Agriculture & Fisheries, Welfare, Ministry of Agriculture, Govt. of India, New Delhi.

RESOURCE PERSONS



Mr. SANJEEV KARPE
 Founder Director, KONBAC
 Topic - Modern bamboo construction in India

Prof. SANKALPA
 Associate Prof., FA, CEPT University
 Topic - Cutting-edge Design and Technology

Mr. AMITAVA SIL
 Scientist, IWST, Kolkata
 Topic - Provenance, treatments and fire Retardancy of Structural Bamboo.

Dr. JAGADISH VENGINALA
 Head, EDC & Associate Professor, PVPST, Vijayanagara
 Topic - The Bamboo Renaissance

Prof. CHARRUCHANDRA K.
 Faculty, CTARA, IIT, Mumbai
 Topic - Sustainable Construction Practices

VALENCE FUNCTION



CHIEF PATRON
MR. S. VAITHEESWARAN
 Chairperson, Manipal University Jaipur

GUEST OF HONOUR
DR. G. K. PRABHU
 President, Manipal University Jaipur

CO PATRON
DR. THAMMAIAH CS
 Pro-President, Manipal University Jaipur

CO PATRON
DR. NITU BHATNAGAR
 Registrar, Manipal University Jaipur

CONVENER
DR. MADHURA YADAV
 Dean FOD, Manipal University Jaipur

ORGANISING SECRETARIES



Ar. SANJEEV PAREEK
 Asst. Prof. SA&D

Ar. KINZALK CHAUHAN
 Asst. Prof. SA&D

REGISTRATION LINK
https://docs.google.com/forms/d/1EAGC5L8R7h3t0eK1erL8RQ-VLwYV1Hw0n566R1_29x0C08450v0p4m7uac-sq_u_d

PAYMENT LINK
<https://www.payvonov.com/customer/users/payvomer0dpsm11014-F1D47CFC85C870CF8B5299D0898MASIE0219041>

For any queries, please contact : Ar. Sanjeev Pareek - sanjeev.pareek@jaipur.manipal.edu (978600305)



8. Schedule of the event

S.No.	Description	Time
1	Welcome Address by Prof. (Dr.) Madhura Yadav, Director, SA&D, Manipal University Jaipur	9.30 AM
2	Inaugural Address by Hon'ble Mr. Suresh Prabhu, Member of Parliament, India's Sherpa to G7 & G20	9.35 AM
3	Address by Prof. (Dr.) Anuradha Chatterjee, Dean, FoD, Manipal University Jaipur	9.45 AM
4	Address by Mr. Sanjeev Karpe, Director, KONBAC Maharashtra	9.55 AM
5	Presidential Address by Prof. (Dr.) G. K. Prabhu, President, Manipal University Jaipur	10.10 AM
6	Vote of Thanks by Prof. Kinzalk Chauhan, SA&D, Manipal University Jaipur	10.20 AM
7.	Fist day Expert Lecture by Dr. Jagdish Vengela	10.30 AM

9. Attendance of the Event:

5 No	Full Name	Time/Date	59	Guest	22/9/23 9:10:59 pm	118	Guest	22/9/23 4:04:11 pm
1	Sanjeev Pareek (MU -Jaipur)	22/9/23 9:33:32 pm	60	Guest	22/9/23 9:22:56 pm	119	Guest	22/9/23 5:00:51 pm
2	Guest	22/9/23 9:34:07 pm	61	Guest	22/9/23 9:34:03 pm	120	Guest	22/9/23 5:40:56 pm
3	Guest	22/9/23 9:35:33 pm	62	Dr. Sumanika Kapoor (MU -Jaipur)	22/9/23 9:28:44 pm	121	Guest	22/9/23 5:58:09 pm
4	Archish Bahi	22/9/23 9:40:51 pm	63	Dr. Sumanika Kapoor (MU -Jaipur)	22/9/23 9:49:49 pm	122	Pooja (Guest)	22/9/23 5:47:12 pm
5	Archish Bahi	22/9/23 9:40:16 pm	64	Dr. Richa Jagtapraia (MU -Jaipur)	22/9/23 9:25:50 pm	123	Pooja (Guest)	22/9/23 5:37:18 pm
6	Archish Bahi	22/9/23 9:41:51 pm	65	Dr. Richa Jagtapraia (MU -Jaipur)	22/9/23 9:25:35 pm	124	Pooja (Guest)	22/9/23 5:43:22 pm
7	Archish Bahi	22/9/23 9:53:54 pm	66	Dr. Subhash Chandra Devarshi (MU -Jaipur)	22/9/23 9:25:15 pm	125	Kashima Mathur (B-ARCH -2019)	22/9/23 5:47:19 pm
8	Nishikha Nareish Mooli (B Des -10 -2020)	22/9/23 9:50:24 pm	67	Dr. Subhash Chandra Devarshi (MU -Jaipur)	22/9/23 9:36:51 pm	126	Kashima Mathur (B-ARCH -2019)	22/9/23 5:08:32 pm
9	Nishikha Nareish Mooli (B Des -10 -2020)	22/9/23 9:01:23 pm	68	Dr. Subhash Chandra Devarshi (MU -Jaipur)	22/9/23 9:56:45 pm	127	Mansi (B Arch -2020) (Guest)	22/9/23 5:01:26 pm
10	Nishikha Nareish Mooli (B Des -10 -2020)	22/9/23 9:04:46 pm	69	Dr. Subhash Chandra Devarshi (MU -Jaipur)	22/9/23 9:56:54 pm	128	Mansi (B Arch -2020) (Guest)	22/9/23 5:57:49 pm
11	Dr. Adhosh Sami (MU -Jaipur)	22/9/23 9:02:27 pm	70	Guest	22/9/23 9:25:14 pm	129	Guest	22/9/23 6:51:12 pm
12	Guest	22/9/23 9:04:92 pm	71	Guest	22/9/23 9:34:01 pm	130	Guest	22/9/23 5:33:30 pm
13	Guest	22/9/23 9:04:44 pm	72	Nehal Jain (B Arch -2022)	22/9/23 9:26:06 pm	131	Guest	22/9/23 5:33:30 pm
14	Guest	22/9/23 9:05:01 pm	73	Nehal Jain (B Arch -2022)	22/9/23 9:27:18 pm	132	Bhavana Khemka (B ARCH -2021)	22/9/23 5:51:41 pm
15	Guest	22/9/23 9:27:36 pm	74	Raunak Prasad (MU -Jaipur)	22/9/23 9:26:58 pm	133	Karti Gelliot (B ARCH -2021)	22/9/23 6:51:56 pm
16	Guest	22/9/23 9:27:35 pm	75	Raunak Prasad (MU -Jaipur)	22/9/23 9:53:34 pm	134	Vishnavi Shukla (B Arch -2021)	22/9/23 6:52:02 pm
17	Guest	22/9/23 9:53:48 pm	76	Raunak Prasad (MU -Jaipur)	22/9/23 9:13:30 pm	135	Vishnavi Shukla (B Arch -2021)	22/9/23 5:59:09 pm
18	Guest	22/9/23 9:05:19 pm	77	Raunak Prasad (MU -Jaipur)	22/9/23 9:19:37 pm	136	Sahilset yadav (Guest)	22/9/23 6:52:06 pm
19	Guest	22/9/23 9:08:13 pm	78	Arina Iqbal (B Arch -2020)	22/9/23 9:20:55 pm	137	Guest	22/9/23 6:52:06 pm
20	Guest	22/9/23 9:38:16 pm	79	Arina Iqbal (B Arch -2020)	22/9/23 9:30:51 pm	138	Guest	22/9/23 9:43:28 pm
21	Guest	22/9/23 9:01:02 pm	80	Ritu Sharma (PHD -2020)	22/9/23 9:30:51 pm	139	Pransh Kothari (B Arch -2022)	22/9/23 9:52:19 pm
22	Guest	22/9/23 9:02:05 pm	81	Guest	22/9/23 9:33:54 pm	140	Pransh Kothari (B Arch -2022)	22/9/23 9:54:01 pm
23	Guest	22/9/23 9:50:05 pm	82	Guest	22/9/23 9:34:11 pm	141	Pransh Kothari (B Arch -2022)	22/9/23 9:56:02 pm
24	Arjun Adhikari (B ARCH -2021)	22/9/23 9:50:07 pm	83	Guest	22/9/23 9:34:24 pm	142	Pransh Kothari (B Arch -2022)	22/9/23 9:51:13 pm
25	Arjun Adhikari (B ARCH -2021)	22/9/23 9:10:48 pm	84	Guest	22/9/23 9:28:55 pm	143	[BARCH-001-2023-24]TANMAY GUPTA	22/9/23 9:53:30 pm
26	Arjun Adhikari (B ARCH -2021)	22/9/23 9:58:36 pm	85	Guest	22/9/23 9:34:56 pm	144	Guest	22/9/23 9:52:46 pm
27	Arjun Adhikari (B ARCH -2021)	22/9/23 9:41:03 pm	86	Guest	22/9/23 9:53:34 pm	145	Guest	22/9/23 9:06:16 pm
28	Arjun Adhikari (B ARCH -2021)	22/9/23 9:41:07 pm	87	Guest	22/9/23 9:37:54 pm	146	Guest	22/9/23 9:06:16 pm
29	Arjun Adhikari (B ARCH -2021)	22/9/23 9:53:53 pm	88	Guest	22/9/23 9:43:48 pm	147	Vanishika Chandel (B ARCH -2019)	22/9/23 9:35:30 pm
30	Guest	22/9/23 9:53:20 pm	89	Ujjhna Singhal (B-ARCH -2019)	22/9/23 9:38:58 pm	148	Vanishika Chandel (B ARCH -2019)	22/9/23 9:35:23 pm
31	Guest	22/9/23 9:53:48 pm	90	Ujjhna Singhal (B-ARCH -2019)	22/9/23 9:53:54 pm	149	Meha Savena (MU -Jaipur)	22/9/23 9:52:57 pm
32	Guest	22/9/23 9:13:26 pm	91	Pavani Pandey (B-ARCH -2019)	22/9/23 9:36:11 pm	150	Guest	22/9/23 9:53:30 pm
33	Guest	22/9/23 9:35:11 pm	92	Pavani Pandey (B-ARCH -2019)	22/9/23 9:35:54 pm	151	Guest	22/9/23 9:53:30 pm
34	Guest	22/9/23 9:35:23 pm	93	Sneha Singh (MU -Jaipur)	22/9/23 9:39:18 pm	152	Guest	22/9/23 9:54:23 pm
35	Guest	22/9/23 9:24:41 pm	94	Guest	22/9/23 9:54:01 pm	153	Guest	22/9/23 9:54:42 pm
36	Dipanshu Singh Panwar (B Arch -2022)	22/9/23 9:14:24 pm	95	Nandini Rawat (B-ARCH -2019)	22/9/23 9:40:02 pm	154	Sajal Panwar (B Arch -2022)	22/9/23 9:54:10 pm
37	Dipanshu Singh Panwar (B Arch -2022)	22/9/23 9:55:03 pm	96	Nandini Rawat (B-ARCH -2019)	22/9/23 9:55:44 pm	155	Sajal Panwar (B Arch -2022)	22/9/23 9:54:39 pm
38	Ananya Tandon (B ARCH -2022)	22/9/23 9:14:54 pm	97	Nandini Rawat (B-ARCH -2019)	22/9/23 9:56:09 pm	156	Sajal Panwar (B Arch -2022)	22/9/23 9:54:37 pm
39	Ananya Tandon (B Arch -2022)	22/9/23 9:21:25 pm	98	Nandini Rawat (B-ARCH -2019)	22/9/23 9:56:19 pm	157	Sajal Panwar (B Arch -2022)	22/9/23 9:53:19 pm
40	Ananya Tandon (B Arch -2022)	22/9/23 9:21:47 pm	99	Nandini Rawat (B-ARCH -2019)	22/9/23 9:56:45 pm	158	Sajal Panwar (B Arch -2022)	22/9/23 9:53:26 pm
41	Ananya Tandon (B ARCH -2022)	22/9/23 9:31:24 pm	100	Nandini Rawat (B-ARCH -2019)	22/9/23 9:38:17 pm	159	Sajal Panwar (B Arch -2022)	22/9/23 9:53:26 pm
42	Dr. Madhura Yadav (MU -Jaipur)	22/9/23 9:15:04 pm	101	HARSH VARSHAN PATIL (B Arch -2019)	22/9/23 9:41:59 pm	160	Sajal Panwar (B Arch -2022)	22/9/23 9:51:12 pm
43	Dr. Madhura Yadav (MU -Jaipur)	22/9/23 9:53:44 pm	102	HARSH VARSHAN PATIL (B Arch -2019)	22/9/23 9:53:31 pm	161	Sajal Panwar (B Arch -2022)	22/9/23 9:51:42 pm
44	Guest	22/9/23 9:15:56 pm	103	HARSH-001-2023-24 ANANYA	22/9/23 9:42:30 pm	162	Khushi Vaidikumar Chaudhari (B ARCH -2021)	22/9/23 9:55:06 pm
45	Guest	22/9/23 9:53:36 pm	104	HARSH-001-2023-24 ANANYA	22/9/23 9:44:46 pm	163	Khushi Vaidikumar Chaudhari (B ARCH -2021)	22/9/23 9:55:09 pm
46	Vanishika Sharma (B Arch -2022)	22/9/23 9:17:00 pm	105	[BARCH-001-2023-24] ANANYA	22/9/23 9:45:11 pm	164	Ashwanya Singh Rathore (B Arch -2021)	22/9/23 9:55:12 pm
47	Vanishika Sharma (B Arch -2022)	22/9/23 9:31:11 pm	106	[BARCH-001-2023-24] ANANYA	22/9/23 9:46:11 pm	165	Ashmeem Kaur (B ARCH -2021)	22/9/23 9:55:31 pm
48	Vanishika Sharma (B Arch -2022)	22/9/23 9:43:39 pm	107	[BARCH-001-2023-24] CHANDRILYA VERMA	22/9/23 9:42:42 pm	166	Ashmeem Kaur (B ARCH -2021)	22/9/23 9:55:44 pm
49	Vanishika Sharma (B Arch -2021)	22/9/23 9:53:54 pm	108	[BARCH-001-2023-24] CHANDRILYA VERMA	22/9/23 9:43:01 pm	167	Narayan Sharma	22/9/23 9:54:59 pm
50	Guest	22/9/23 9:18:13 pm	109	Arumita Iino (B-ARCH -2018)	22/9/23 9:44:42 pm	168	Guest	22/9/23 9:58:13 pm
51	Guest	22/9/23 9:53:46 pm	110	Arumita Iino (B-ARCH -2018)	22/9/23 9:53:54 pm	169	Guest	22/9/23 9:58:13 pm
52	Kinzalk Chauhan (MU -Jaipur)	22/9/23 9:30:11 pm	111	[BARCH-001-2023-24] ANANYA GUPTA	22/9/23 9:44:45 pm	170	Guest	22/9/23 9:58:09 pm
53	Kinzalk Chauhan (MU -Jaipur)	22/9/23 9:53:49 pm	112	[BARCH-001-2023-24] ANANYA GUPTA	22/9/23 9:45:07 pm	171	Guest	22/9/23 9:58:09 pm
54	Guest	22/9/23 9:21:10 pm	113	Alamara Quazi TM Des (Major Interior Design) -2022)	22/9/23 9:44:58 pm	172	Harsh Shivastav (B Arch -2021)	22/9/23 9:58:09 pm
55	Guest	22/9/23 9:21:13 pm	114	Alamara Quazi TM Des (Major Interior Design) -2022)	22/9/23 9:48:30 pm	173	Harsh Shivastav (B Arch -2021)	22/9/23 9:58:09 pm
56	Guest	22/9/23 9:21:16 pm	115	Rudhraj Bhagwat	22/9/23 9:44:58 pm	174	Alpita B B Bhagwat (B Arch -2021)	22/9/23 9:07:14 pm
57	Guest	22/9/23 9:34:30 pm	116	Guest	22/9/23 9:44:58 pm	175	Kaun Chandrimani (B Arch -2022)	22/9/23 9:08:13 pm
58	Guest	22/9/23 9:34:12 pm	117	Guest	22/9/23 9:43:40 pm	176	Ranya Chandrimani (B Arch -2022)	22/9/23 9:28:01 pm

10. Weblink:

<https://jaipur.manipal.edu/content/dam/manipal/muj/fod/Document/eventlist/EDP%20N%20Bamboo%20-Event%20report.pdf>

11. Event Coordinators:



- Ar. Sanjeev Pareek (Assistant Professor, SA&D)
- Ar. Kinzalk Chauhan (Assistant Professor, SA&D)



EVENT REPORT



**MANIPAL UNIVERSITY
JAIPUR**

FACULTY OF DESIGN

HERITAGE CLUB

School of Architecture and Design

FOOD WALK

Walled City, Jaipur

18th FEBRUARY 2023

Contents

1.	Introduction of the Event	3
2.	Objective of the Event	3
3.	Beneficiaries of the Event	3
4.	Brief Description of the event	3
5.	Brochure of the event	4
6.	Photographs of the Event	5
7.	Attendance of the event	6
8.	Feedback	6
9.	Post Event Link	8
10.	Faculty Coordinator	8

1. Introduction of the Event:

Heritage Club, School of Architecture and Design conducted a Food walk through a well curated route in the walled city of Jaipur for the students of MUJ, where students got to explore the Heritage City of Jaipur through its tasty delicacies while also enjoying the religious vibe in the walled city on the occasion of Mahashivratri.

2. Objective of the Event:

The curated route of Food Walk took the participants to the pink city in order to help them appreciate and admire the following –

- The scrumptious local delicacies along with their specific history.
- The streets featuring continuous small scaled shops and local vendors that thrive upon the city's heart.
- The built heritage of walled city, as the route also covered prominent architectural structures such as Hawa Mahal, Tripolia Gate and Tarkeshwar temple(one of the most prominent shiva temple in Jaipur) etc.

3. Beneficiaries of the Event:

- Students from all faculties of MUJ.
- Faculty members of MUJ

4. Brief Description of the event:

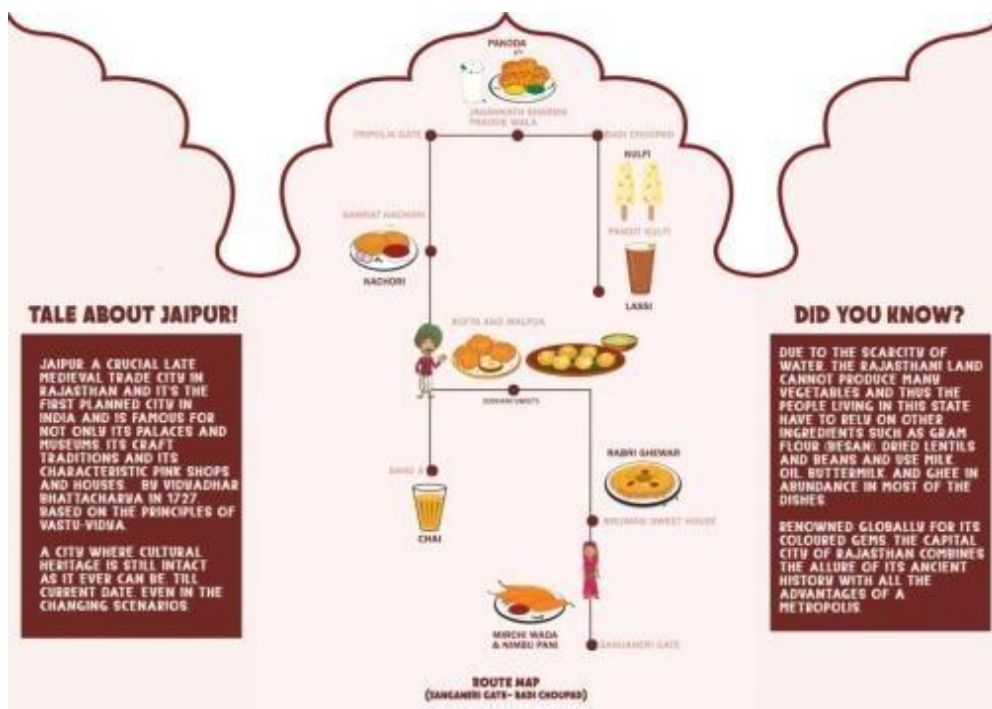
Heritage Club (School of Architecture and Design) conducted a Food Walk in the Walled City of Jaipur to acquaint the student fraternity of MUJ with the food delicacies and heritage beauty of Jaipur, on 18th February 2023. The food walk included several food items which offered different tastes of local Rajasthani cuisines where students could appreciate and admire the taste.

This Food Walk was the third physical event of the Heritage Club, but first of its kind ever. The walk began from Sanganeri Gate and terminated at Zaleb Chowk (route details as per brochure on the following page). Besides briefing about the history of the traditional bazaars, participants were also enlightened about the legacy of diverse cuisines by the enthusiastic food vendors themselves who showed utmost hospitality to the group of students and faculties.

The food menu provided a variety of items ranging from local drinks like nimbu pani to snacks like mirchi bada, kachoris & pakoras to sweets like ghewar and kulfi. The portions of all food items were specially made uniquely after requesting the vendors so that the portions then become easily consumable by a single person. Hence, everyone got an opportunity to taste all items (and the walk made it easy to digest them and create an appetite for the next item 🍷).

The walk ended with a positive feedback and contentment by all the participants. Mementos (key chains) created in-house by the club and school were distributed to everyone as a token of memory and gratitude. E-certificates were also given to all participants and volunteers of the event.

5. Brochure of the event



6. Photographs of the event.



Picture 1- Participants of the Food Walk



Picture 2-Sodhani Sweets (2nd stop)

Food vendors presenting the importance and making of malpua and aloo vada along with the narrative on when the shop was opened.



Picture 3- Sahoo Restaurant (3rd stop)
Participants having a break with Tea.



Picture 4 – Jagannath Pakode Wale (4th stop).



Picture 5- Pandit Kulfi (last stop).

7. Attendance of the Event:

ID	Name2	Registration Number	Course & Branch	h/d	Contact	Signature
1	Divyesh Shankla	210501003	Barch	Day scholar	9894699992	
2	Mansi	200501024	B.arch	Day scholar	7877991098	
3	Ria Rattan Kotwal	210501028	B.Arch	Hosteler	7406524738	
4	Jai	200901001	BBA	Hosteler	969093693	
5	Sonali	211002041	Bio science	Hosteler	8770273605	
6	Sanchoita	200606015	B.ARCH	Hosteler	8408803378	
7	Hrishita Kesarwani	229303266	Cse ai ml	Hosteler	9922490410	
8	Anjali Adhikari	210501025	B Arch	Hosteler	9733182131	
9	Priya Agarwal	211002006	Bsc biotechnology (biosciences)	Hosteler	7061587976	
10	Bhavesh Khemka	210501009	Architecture	Day scholar	9116006663	
11	Ashrav	219301466	Btech cse	Hosteler	9833094011	
12	Shashank Goyal	211002043	Bio science	Hosteler	9024935154	
13	Naman Agrawal	219303093	B.Tech CCE	Hosteler	7013464852	
14	Riddhi Daga	211201064	BJMC	Hosteler	9331214622	
15	Vivek Anand	210901312	Business Administration	Hosteler	8610310054	
16	Yashi Shree	229301030	Btech	Hosteler	9599147349	
17	Dr. Subhash Devrath	-	-	Day scholar	9571188767	
18	Mrs. Suman Devrath	-	-	Day scholar	9571188767	
19	Tejashwini Joshi	210901112	BBA marketing	Hosteler	6309335977	
20	Harshita mandhra	220501018	Architecture	Hosteler	9610814620	
21	Vaishnavi shukla	210501022	Barch	Hosteler	7607694292	
22	Anaya	221151002	1 year phd	Hosteler	7889559667	
23	Abhik	220502004	M.arch	Day scholar	7873726178	
24	Ankita Shrivastava	220501012	B. arch	Day scholar	8839638509	
25	PRACHITA BHWAPURKAR	200501001	B.ARCH	Hosteler	9898711500	
26	Aarshia Chauhan	229302370	BTech IT	Hosteler	9710000136	
27	Vaidehi Agarwal	229302345	Btech IT	Hosteler	9999367467	
28	Arpita garg	229303156	Btech with cce	Hosteler	7983182007	
29	Shriya	220501014	B.arch	Hosteler	9599571767	
30	Kasvi Soni	229311033	Btech cse with iot	Hosteler	9650848355	
31	MOULESH MR	220501005	B arch	Hosteler	9087023888	
32	Rudr Sikaria	220801018	BHM	Hosteler	8638136126	

33	Ahaana Verma	221015001	BCA	Hosteler	9315421451	
34	Mehma Singh	220801003	Bhm management	Hosteler	7267984000	
35	Yash bhargava	221201025	BAJMC	Hosteler	8458922968	
36	Divyansh	229310407	CSE(AI&ML)	Hosteler	7082947781	
37	Anjali choudhary	211002005	Bsc biotechnology	Hosteler	6367051288	
38	Ikshita Bagla	220501021	B.Arch	Hosteler	9336057274	
39	Sajal panwar	220501002	B.arch	Hosteler	9667899121	
40	Mustansir kanchwala	220903021	B.com honours	Hosteler	8871600661	
41	Rijul Chaudhary	220501003	B.arch	Hosteler	8433130649	
42	Aarya Chandiramani	220501010	B.arch	Day scholar	8852953085	
43	Arghya Bhagwat	220501022	B.Arch	Hosteler	8219847663	
44	Pranjal Furi	220606004	B.des interior design	Hosteler	7727031282	
45	Vedika Gupta	221007014	BSc psychology	Hosteler	9310489974	
46	Shinaya Badgujar	221105022	BA Liberal Arts	Day scholar	8209657590	
47	Ayamullah Khan	229309022	B.Tech	hosteler	8530044774	

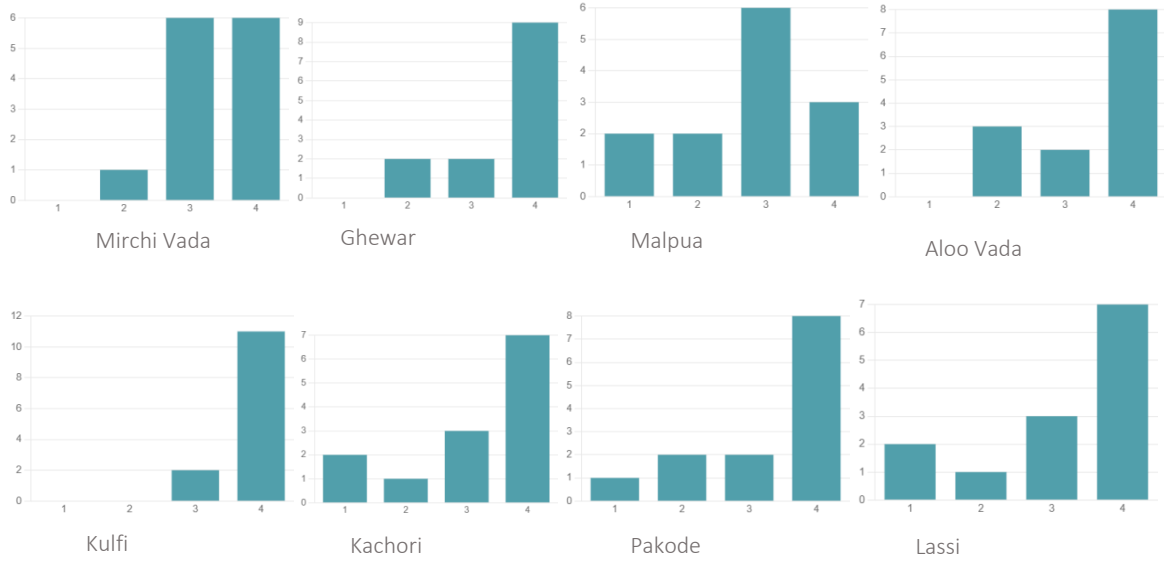
8. Feedback:

Students were amazed by the flavor of cuisines and had a boundless experience while exploring local markets and historical sites through the organized route. They cherished and gave a positive response towards organizing such walks and events in future.

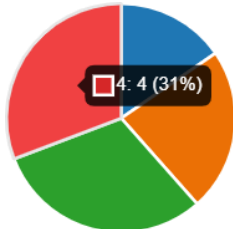
Following is the feedback collected through Google Forms-

Response to each food items by students-

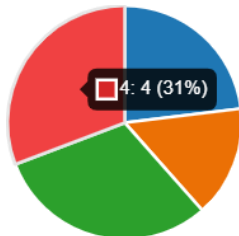
1-Not Bad; 2-Good; 3-Very Good; 4-Delicious



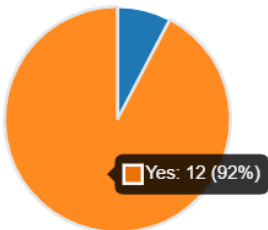
- Route curated for the walk-
1-Very Satisfied; 2-Satisfied; 3-Neutral; 4-Unsatisfied



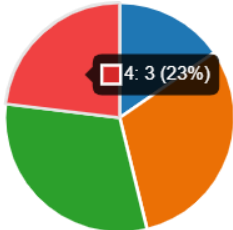
- Walk to be informative-



- Order of the Food Items-



- Overall Experience-



- Feedbacks from Students through forms-

“Walk was well organized”. – Bhavesh Khemka

"Good event... Enjoyed very much". – Rudr Sikaria

"It was a very great experience. Tasting different food items I have never heard of was superb". - Mansi

9. Post event link-

10. Faculty Coordinator:



Signature of Faculty Coordinator
Ar. Ayushi Sharma
Assistant Professor, SA&D
9660311113



Signature of Faculty Coordinator
Ar. Neha Saxena
Associate Professor, SA&D
9950158160



Assistant Director, DSW

**DIRECTOR STUDENT WELFARE & PROCTOR
MANIPAL UNIVERSITY, JAIPUR**



**MANIPAL UNIVERSITY
JAIPUR -**

MUJ/Q&C/22/F/1.01



**MANIPAL UNIVERSITY
JAIPUR**

FACULTY OF ENGINEERING

SCHOOL OF CIVIL AND CHEMICAL ENGINEERING

DEPARTMENT OF BIOTECHNOLOGY AND CHEMICAL ENGINEERING

Industry Visit

To

Central Institute of Plastic Engineering & Technology (CIPET), Jaipur

08/11/2023



Contents of Report

1. Introduction of the Event
2. Objective of the Event
3. Beneficiaries of the Event
4. Details of the Guests
5. Brief Description of the event
6. Geo-tagged Photographs
7. Schedule of the Event
8. Attendance of the Event

1. Introduction of the Event

To showcase the role of Plastics technology and processing in an industrial setting, the Department of Biotechnology and Chemical Engg organized an Industry visit to Central Institute of Plastic Engineering & Technology (CIPET), Jaipur on 8th Nov 2023. B.Tech. Chemical Engineering students (attendance attached) and two faculty (Dr. Harsh Pandey and Dr. Nadana R. Vadivu) accompanied for a half-day activity.

2. Objectives of the Event

- Exposure of students to the Plastics technology domain.
- Develop problem-solving skills in the students.
- Provide useful inputs to industry for developing real systems.
- Facilitate R&D collaboration efforts between the university and the institute.

3. Beneficiaries of the Event

MUJ B.Tech. Chemical Engineering students (attendance attached).

4. Details of the Guest:

At CIPET Jaipur: Dr. Bishnu Panda (Principal, CIPET Jaipur). Correspondence and invitation over email are attached below.

Fw: CIPET Visit- regarding

Dr. Harsh Pandey [MU - Jaipur] <harsh.pandey@jaipur.manipal.edu>

Fri 11/17/2023 1:00 PM

To:Dr. Nadana Raja Vadivu G [MU - Jaipur] <nadana.vadivu@jaipur.manipal.edu>

From: Dr. Anees Ahmed Yunus Khan [MU - Jaipur] <anees.khan@jaipur.manipal.edu>

Sent: Wednesday, November 8, 2023 12:14 PM

To: drbishnupanda@outlook.com <drbishnupanda@outlook.com>; drbishnupanda@gmail.com <drbishnupanda@gmail.com>

Cc: Dr. Harsh Pandey [MU - Jaipur] <harsh.pandey@jaipur.manipal.edu>; Dr. Nadana Raja Vadivu G [MU - Jaipur] <nadana.vadivu@jaipur.manipal.edu>; Dr. Bhavna Tripathi [MU - Jaipur] <bhavna.tripathi@jaipur.manipal.edu>

Subject: CIPET Visit- regarding

Dear Sir,

Based on our telephonic communication, I extend my sincere thanks for providing the opportunity to visit CIPET-Jaipur campus today (8th November 2023) for our students of BTech Chemical Engineering. Dr. Harsh Pandey and Dr. Nadana Raja Vadivu will accompany the students and will reach to your campus by approx. 3 pm today.

Thank you.

5. Brief Description of the event

To showcase the role of Plastics technology and processing in an industrial setting, the Department of Biotechnology and Chemical Engg organized an Industry visit to Central Institute of Plastic Engineering & Technology (CIPET), Jaipur on 8th Nov 2023. B.Tech. Chemical Engineering students (attendance attached) and two faculty (Dr. Harsh Pandey and Dr. Nadana R. Vadivu) accompanied for a half-day activity.

6. Photographs











Sitapura Indl Area, Sitapura, Jaipur RJ 302022

7. Schedule of the event

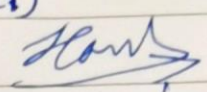
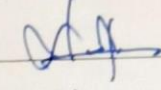
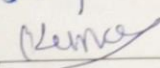
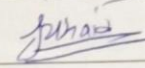
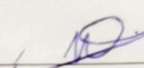
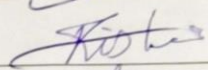
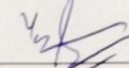
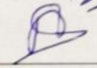
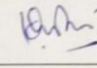
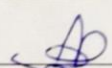
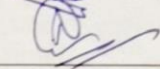
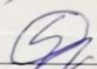
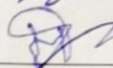

Visit to CIPET, Sitapura, Jaipur on second half, 8th Nov 2023.

8. Attendance of the Event

Total attendee: 14

Attendance

MUJ Dept of Biotech and Chemical Engg
Dept Visit to CIPET Jaipur (8th Nov 2023) Date: 08/11/2023

Dr. Harsh Pandey.	
Dr. Nandana Raja Vadimig	
RUNAL BHAGPATI	
Tusaid Khan	
Mansi Gupta	
Rishan Jain	
YASH SAXENA	
Rugaiya Hila	
Khushi Agarwal	
Amyan Vijay	
NOSHITA NANIKAR	
Shawwat Goyal	
Hardik Sisodia	
Meghank Rastogi	



Seal and Signature of Head with date
Department of Chemical Engg.
Manipal University, Jaipur




**MANIPAL UNIVERSITY
JAIPUR**

FACULTY OF DESIGN

**International Conference on Sustainable Development for
Heritage and Built Environment**

22/06/2023 – 23/06/2023


Head, Department of Interior Design
SD&A, Faculty of Design
Manipal University Jaipur



Content of Report

1. Introduction of the Event
2. Objective of the Event
3. Beneficiaries of the Event
4. Brief Description of the event
5. Photographs
6. Poster of an Event
7. Schedule of the Event
8. Attendance of the Event

1. Introduction of the Event

The conference is inspired from the critical challenge of human, environmental, heritage and built sustainability concerning the present and future generations in a global-scale context. This theme emphasizes the strong foundation that is provided by using research to inform our everyday practices, policies, and analytical approaches. This interdisciplinary forum is for scholars, teachers, and practitioners from the built environment professional discipline who share an interest in—and concern for— sustainability in an holistic perspective, where environmental, cultural, economic and social concerns intersect. It will provide a platform for various individuals to connect the past and present and develop solutions to a more universal and environmentally friendly approach towards built environment.

The conference will include topics such as

- (i) Sustainable approach to design in built environment,
- (ii) Sustainability & built Heritage,
- (iii) Conserving Built Heritage,
- (iv) Sustainable Policies for Environmental and Infrastructure Planning,
- (v) Earth and Environmental Planning & Design

2. Objective of the Event

This conference was a gathering of minds dedicated to addressing the pressing challenges of sustainability that affect our world today and tomorrow. It recognized that sustainability is a multifaceted concept that requires interdisciplinary collaboration and rigorous research. By bringing together scholars, educators, and practitioners, the conference facilitated the exchange of ideas and the development of solutions that promote a more sustainable, resilient, and environmentally friendly built environment.

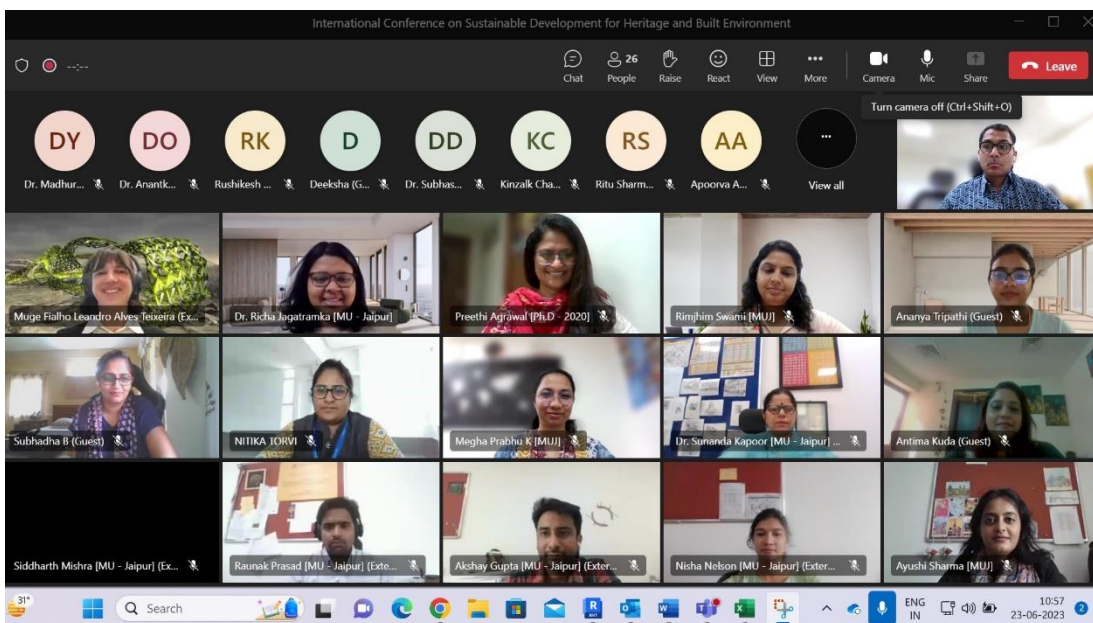
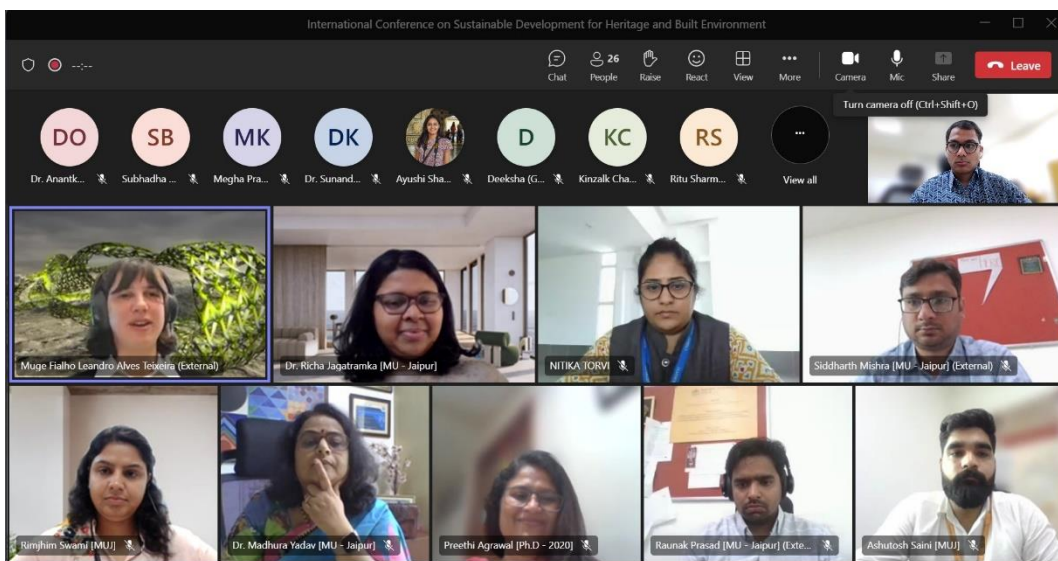
3. Beneficiary of the event

This interdisciplinary forum is for scholars, teachers, and practitioners from the built environment professional discipline who share an interest in—and concern for— sustainability in an holistic perspective, where environmental, cultural, economic and social concerns intersect.

4. Brief Description of the event

The conference was hosted by Department of Interior Design and School of Architecture and Design, Faculty of Design at Manipal University Jaipur. This interactive and engaging event is tailored exclusively for our researchers, as part of our commitment to foster continuous learning, future research opportunities. The presentations focused on sustainability as the prime agenda and paved way for the researchers to present their work at an international level.

5. Photographs of the Event



Snippets of the Conference

6. Poster of the event



**MANIPAL UNIVERSITY
JAIPUR**
(University under Section 2(f) of the UGC Act)

School of Architecture and
Design and Department of
Interior Design

International Conference
on
**“Sustainable
Development for
Heritage and Built
Environment”**

22nd June – 23rd June 2023

Venue:
Manipal University Jaipur/ Hybrid
Mode

About the University
The Manipal Education Group, with its heritage of excellence in higher education for over 60 years, launched Manipal University Jaipur (MUJ) in 2011. MUJ is affiliated by University Grants Commission, Association of Indian Universities, Council of Architecture, Bar Council of India and All India Council of Technical Education. MUJ is the first university in the state of Rajasthan, accredited as A+ (3.28) grade by NAAC. The university offers courses in different disciplines like Architecture, Interior Design, Fashion Design, Applied arts, Engineering, Management, Hospitality, Humanities & Social Sciences, Journalism and Mass communication, Basic Sciences, Law, Business & Commerce.

Organizing Committee
Patron
Dr. G. K. Prabhu (President, MUJ)
Co - Patrons
Dr. Thammaiah Chekkera (Pro-President, MUJ)
Dr. Nitu Bhatnagar (Registrar, MUJ)
Chair:
Dr. Madhura Yadav (Dean, FoD, MUJ)
Dr. J.P. Sampath Kumar (Director, SD&A, MUJ)
Convenors:
Dr. Richa Jagatramka (Assist. Prof., ID-SD&A)
Ar. Raunak Prasad (Assist. Prof., SA&D)
Coordinators:
Ar. Megha Prabhu (Assist. Prof., ID-SD&A)
Ar. Himangshu Kedia (Assist. Prof., ID-SD&A)
Ar. Akshay Gupta (Assist. Prof., SA&D)
Ar. Ashutosh Saini (Assist. Prof., SA&D)

About the Conference
The conference will include topics such as

- (i) Sustainable approach to design in built environment,
- (ii) Sustainability & built Heritage,
- (iii) Conserving Built Heritage,
- (iv) Sustainable Policies for Environmental and Infrastructure Planning,
- (v) Earth and Environmental Planning & Design.

Participants will gain exposure and insight To various sustainable approaches to sustain the heritage as well as define the built environment. It will provide a platform for various individuals to connect the past and present and develop solutions to a more universal and environmentally friendly approach towards built environment.

Submission Deadline:
Call for Papers – 23rd Feb 2023
Abstract Submission – 30th March 2023
Acceptance Notification – 7th April 2023
Full paper Submission – 23rd April 2023

Publication –
Conference proceedings with IOP
Conference Series: Earth and Environmental Science (SCOPUS Indexed)

Notable Speakers
1. Dr Ranjith Dayaranthe , Associate Professor, Asian School of Architecture, Australia
2. Dr Muge Belek Fialho Teixeira, Queensland University of Technology.
3. Dr. Shikha Jain, Director, DRONAH
4. Dr Rajat Gupta, Oxford Brookes, Director, Dept. of sustainable development
5. Ar. Chitra Vishwanath, Biome Bangalore.

Conference Fees :
Students 9500 INR
Academicians & professional 10500 INR

For International Participants
Students - 150 USD
Academicians & professional – 180 USD

For additional information contact –
richa.jagatramka@jaipur.manipal.edu
raunak.prasad@jaipur.manipal.edu

7. Schedule of the event

Time	Event	Speaker
11:00 – 11:30 AM	Opening speech	Dr Richa Jagatramka
11: 30 – 11:35 AM	Welcome address	Dr Madhura Yadav
11: 35 – 11:45 AM	Introduction of international speaker	Ar Himangshu Kedia
11: 45 AM – 12:45 PM	Presentation by Dr Muge	Dr Muge
12: 45 – 01:00 PM	Q & A session	
01:00 – 01:05PM	Vote of Thanks	Ar. Himangshu Kedia

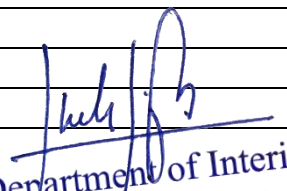
Meeting Link :

https://teams.microsoft.com/l/meetup-join/19%3ameeting_MmRjNjZiN2ltMTc1NS00YmJlLTkwMTItMzBiYTVjNTIOYTRh%40thread.v2/0?context=%7b%22Tid%22%3a%227d0726e8-bf4b-4ac1-99f1-010fb11f1d3f%22%2c%22Oid%22%3a%2216be8839-914f-456c-9836-e6b3ba8fa2f9%22%7d

8. Attendance of the Event

Total attendees – 28 participants from MUJ and outside

Sl.no	Name	Organisation
1	Dr. Richa Jagatramka	FOD
2	Megha Prabhu K	FOD
3	Dr. Sampath Kumar Padmanabha Jinka	FOD
4	Dr. Madhura Yadav	FOD
5	Dr. Anantkumar Dada Ozarkar	FOD
6	Dr. Subhash Chandra Devrath	FOD
7	Nisha Nelson	FOD
8	Preethi Agrawal	Practicing Architect and PhD scholar
9	NITIKA TORVI	Christ University
10	Subhadha B	Christ University
11	Himangshu Kedia	FOD
12	Rushikesh Kolte	MNIT
13	Dr. Sunanda Kapoor	FOD
14	Ananya Tripathi	AKTU - GCA
15	Kinzalk Chauhan	FOD
16	Ritu Sharma	FOS – Phd Scholar
17	Rimjhim Swami	FOD
18	Ayushi Sharma	FOD
19	Apoorva Agarwal	FOD
20	Muge Fialho Leandro Alves Teixeira	QUT Australia
21	Deeksha	MNIT
22	Siddharth Mishra	FOD
23	Akshay Gupta	FOD
24	Ritu Sharma	FOD
25	Neha Saxena	FOD
26	Antima Kuda	MAHE Dubai
27	Raunak Prasad	FOD
28	Ashutosh Saini	FOD


Head, Department of Interior Design
SD&A, Faculty of Design
Manipal University Jaipur



COLLABORATIONS

Rotary International President
Rtn Jennifer Jones

President
PHF Rtn **Radhey Shyam Gupta**
D-13, Indra Puri Colony, Lal Kothi,
Jaipur, Rajasthan 302015 (India)
Mobile: +91-9414779184
eMail: rsgupta9414@gmail.com

Secretary
PHF Rtn **Meeta Mathur**
G-2, Janpath, Shyam Nagar,
Jaipur Rajasthan 302019 (India)
Mobile: +91-9982659532
eMail: alokmeeta@yahoo.com

Treasurer
Rtn **Brajesh Kumar Gupta**
D-28, Indra Puri Colony, Lal Kothi,
Jaipur, Rajasthan 302015 (India)
Mobile: +91-9829072271
eMail: brajeshkgupta24@gmail.com

Club Patron
Maj Donor Rtn Dr **Sudhir Kumar Calla**

President Elect (2024-25)
PHF Rtn CFP **Shalini**

Immediate Past President
MPHF Rtn Er **Narendra Mal Mathur**

Vice Presidents
MPHF Rtn Adv **Ashok Goyal**
PHF Rtn **Desh Deepak Goyal**

Jt. Secretary
Rtn Er **Nand Kishore Maheshwari**

Director – Club Administration
PHF Rtn **Rajendra Tiwari**

Director – Service Projects
Rtn Er **Sudesh Roop Rai**

Director – Environment Service
Rtn **Shyam Sunder Gupta**

Director – Foundation
MPHF Rtn **Vipan Bahl**

Director – Literacy & T.E.A.C.H.
PHF Rtn Dr **Arun Kumar Arya**

Director – Membership
PHF Rtn **Jwala Prasad Sharma**

Director – Public Image & Fellowship
PHF Rtn **Chander Mohan Mahajan**

Director – Publications
PHF Rtn **Basant Jain**

Director – Youth Service
Rtn Prof **Anil Dutt Vyas**

Executive Secretary - I.T.
PHF Rtn Prof **Raj Kishor Pareek**

Club Trainer
MPHF Rtn **Ravi Shanker Sharma**

Sergeant at Arms
PHF Rtn Er **Satish Goyal**

Date: 02/10/23

TO WHOMSOEVER IS CONCERN

Rotaract Club, Directorate of Students' Welfare along with Rotary Club Jaipur, Bapu Nagar conducted a Cleanliness Drive at Dehmi Kalan Village on 2nd October 2023. It was a physical activity which is the Swachhtha Abhiyan involving the students from NSS, DSW and the Rotaract Club MUJ.

We would like to appreciate Rotaract Club, Directorate of Students' Welfare, Manipal University Jaipur for the efforts and express our gratitude towards them.

Regards



Rtn Meeta Mathur
Secretary



**MANIPAL UNIVERSITY
JAIPUR -**

MUJ/Q&C/22/F/1.01



**MANIPAL UNIVERSITY
JAIPUR**

FACULTY OF ENGINEERING

SCHOOL OF CIVIL AND CHEMICAL ENGINEERING

DEPARTMENT OF BIOTECHNOLOGY AND CHEMICAL ENGINEERING

Industry Visit

To

Central Institute of Plastic Engineering & Technology (CIPET), Jaipur

08/11/2023



Contents of Report

1. Introduction of the Event
2. Objective of the Event
3. Beneficiaries of the Event
4. Details of the Guests
5. Brief Description of the event
6. Geo-tagged Photographs
7. Schedule of the Event
8. Attendance of the Event

1. Introduction of the Event

To showcase the role of Plastics technology and processing in an industrial setting, the Department of Biotechnology and Chemical Engg organized an Industry visit to Central Institute of Plastic Engineering & Technology (CIPET), Jaipur on 8th Nov 2023. B.Tech. Chemical Engineering students (attendance attached) and two faculty (Dr. Harsh Pandey and Dr. Nadana R. Vadivu) accompanied for a half-day activity.

2. Objectives of the Event

- Exposure of students to the Plastics technology domain.
- Develop problem-solving skills in the students.
- Provide useful inputs to industry for developing real systems.
- Facilitate R&D collaboration efforts between the university and the institute.

3. Beneficiaries of the Event

MUJ B.Tech. Chemical Engineering students (attendance attached).

4. Details of the Guest:

At CIPET Jaipur: Dr. Bishnu Panda (Principal, CIPET Jaipur). Correspondence and invitation over email are attached below.

Fw: CIPET Visit- regarding

Dr. Harsh Pandey [MU - Jaipur] <harsh.pandey@jaipur.manipal.edu>

Fri 11/17/2023 1:00 PM

To:Dr. Nadana Raja Vadivu G [MU - Jaipur] <nadana.vadivu@jaipur.manipal.edu>

From: Dr. Anees Ahmed Yunus Khan [MU - Jaipur] <anees.khan@jaipur.manipal.edu>

Sent: Wednesday, November 8, 2023 12:14 PM

To: drbishnupanda@outlook.com <drbishnupanda@outlook.com>; drbishnupanda@gmail.com <drbishnupanda@gmail.com>

Cc: Dr. Harsh Pandey [MU - Jaipur] <harsh.pandey@jaipur.manipal.edu>; Dr. Nadana Raja Vadivu G [MU - Jaipur] <nadana.vadivu@jaipur.manipal.edu>; Dr. Bhavna Tripathi [MU - Jaipur] <bhavna.tripathi@jaipur.manipal.edu>

Subject: CIPET Visit- regarding

Dear Sir,

Based on our telephonic communication, I extend my sincere thanks for providing the opportunity to visit CIPET-Jaipur campus today (8th November 2023) for our students of B.Tech Chemical Engineering. Dr. Harsh Pandey and Dr. Nadana Raja Vadivu will accompany the students and will reach to your campus by approx. 3 pm today.

Thank you.

5. Brief Description of the event

To showcase the role of Plastics technology and processing in an industrial setting, the Department of Biotechnology and Chemical Engg organized an Industry visit to Central Institute of Plastic Engineering & Technology (CIPET), Jaipur on 8th Nov 2023. B.Tech. Chemical Engineering students (attendance attached) and two faculty (Dr. Harsh Pandey and Dr. Nadana R. Vadivu) accompanied for a half-day activity.

6. Photographs











Sitapura Indl Area, Sitapura, Jaipur RJ 302022

7. Schedule of the event

Visit to CIPET, Sitapura, Jaipur on second half, 8th Nov 2023.

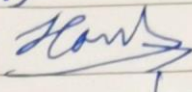
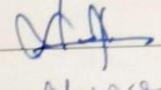
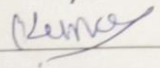
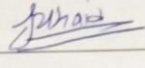
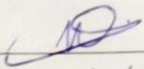
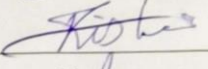
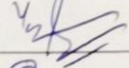
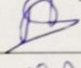
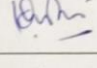
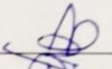
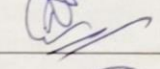
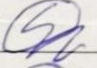
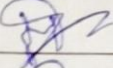
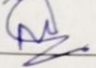
8. Attendance of the Event

Total attendee: 14

Attendance

MUJ Dept of Biotech and Chemical Engg
Dept Visit to CIPET Jaipur (8th Nov 2023)

Date: 08/11/2023

Dr. Harsh Pandey.	
Dr. Nandana Raja Vadimig	
RUNAL BHAGPATI	
Tusaid Khan	
Mansi Gupta	
Rishan Jain	
YASH SAXENA	
Rugaiya Hila	
Khushi Agarwal	
Amyan Vijay	
NOSHITA NANIKAR	
Shawwat Goyal	
Hardik Sisodia	
Meghank Rastogi	



Seal and Signature of Head with date
Department of Chemical Engg.
Manipal University, Jaipur




**MANIPAL UNIVERSITY
JAIPUR**

FACULTY OF DESIGN

**International Conference on Sustainable Development for
Heritage and Built Environment**

22/06/2023 – 23/06/2023


Head, Department of Interior Design
SD&A, Faculty of Design
Manipal University Jaipur



Content of Report

1. Introduction of the Event
2. Objective of the Event
3. Beneficiaries of the Event
4. Brief Description of the event
5. Photographs
6. Poster of an Event
7. Schedule of the Event
8. Attendance of the Event

1. Introduction of the Event

The conference is inspired from the critical challenge of human, environmental, heritage and built sustainability concerning the present and future generations in a global-scale context. This theme emphasizes the strong foundation that is provided by using research to inform our everyday practices, policies, and analytical approaches. This interdisciplinary forum is for scholars, teachers, and practitioners from the built environment professional discipline who share an interest in—and concern for— sustainability in an holistic perspective, where environmental, cultural, economic and social concerns intersect. It will provide a platform for various individuals to connect the past and present and develop solutions to a more universal and environmentally friendly approach towards built environment.

The conference will include topics such as

- (i) Sustainable approach to design in built environment,
- (ii) Sustainability & built Heritage,
- (iii) Conserving Built Heritage,
- (iv) Sustainable Policies for Environmental and Infrastructure Planning,
- (v) Earth and Environmental Planning & Design

2. Objective of the Event

This conference was a gathering of minds dedicated to addressing the pressing challenges of sustainability that affect our world today and tomorrow. It recognized that sustainability is a multifaceted concept that requires interdisciplinary collaboration and rigorous research. By bringing together scholars, educators, and practitioners, the conference facilitated the exchange of ideas and the development of solutions that promote a more sustainable, resilient, and environmentally friendly built environment.

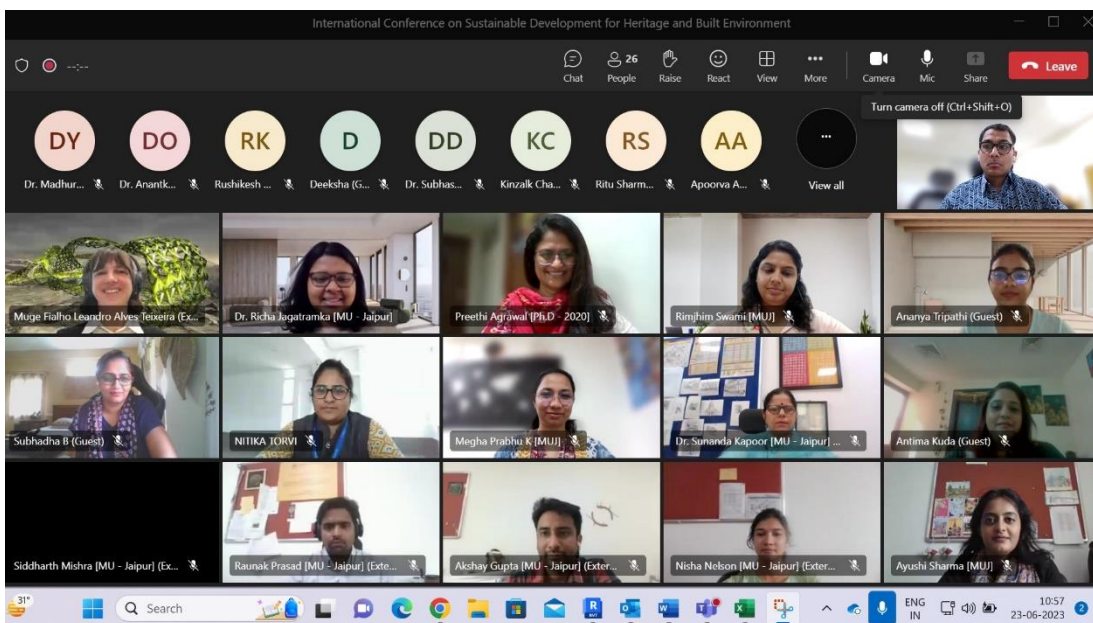
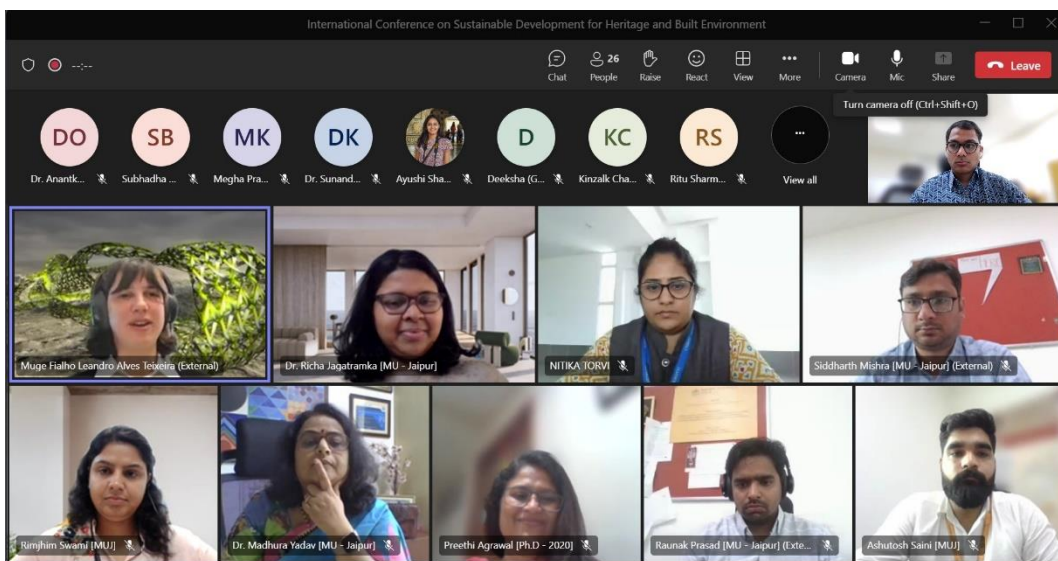
3. Beneficiary of the event

This interdisciplinary forum is for scholars, teachers, and practitioners from the built environment professional discipline who share an interest in—and concern for— sustainability in an holistic perspective, where environmental, cultural, economic and social concerns intersect.

4. Brief Description of the event

The conference was hosted by Department of Interior Design and School of Architecture and Design, Faculty of Design at Manipal University Jaipur. This interactive and engaging event is tailored exclusively for our researchers, as part of our commitment to foster continuous learning, future research opportunities. The presentations focused on sustainability as the prime agenda and paved way for the researchers to present their work at an international level.

5. Photographs of the Event



Snippets of the Conference

6. Poster of the event



**MANIPAL UNIVERSITY
JAIPUR**
(University under Section 2(f) of the UGC Act)

School of Architecture and
Design and Department of
Interior Design

International Conference
on
**“Sustainable
Development for
Heritage and Built
Environment”**

22nd June – 23rd June 2023

Venue:
Manipal University Jaipur/ Hybrid
Mode

About the University
The Manipal Education Group, with its heritage of excellence in higher education for over 60 years, launched Manipal University Jaipur (MUJ) in 2011. MUJ is affiliated by University Grants Commission, Association of Indian Universities, Council of Architecture, Bar Council of India and All India Council of Technical Education. MUJ is the first university in the state of Rajasthan, accredited as A+ (3.28) grade by NAAC. The university offers courses in different disciplines like Architecture, Interior Design, Fashion Design, Applied arts, Engineering, Management, Hospitality, Humanities & Social Sciences, Journalism and Mass communication, Basic Sciences, Law, Business & Commerce.

Organizing Committee
Patron
Dr. G. K. Prabhu (President, MUJ)
Co - Patrons
Dr. Thammaiah Chekkera (Pro-President, MUJ)
Dr. Nitu Bhatnagar (Registrar, MUJ)
Chair:
Dr. Madhura Yadav (Dean, FoD, MUJ)
Dr. J.P. Sampath Kumar (Director, SD&A, MUJ)
Convenors:
Dr. Richa Jagatramka (Assist. Prof., ID-SD&A)
Ar. Raunak Prasad (Assist. Prof., SA&D)
Coordinators:
Ar. Megha Prabhu (Assist. Prof., ID-SD&A)
Ar. Himangshu Kedia (Assist. Prof., ID-SD&A)
Ar. Akshay Gupta (Assist. Prof., SA&D)
Ar. Ashutosh Saini (Assist. Prof., SA&D)

About the Conference
The conference will include topics such as

- (i) Sustainable approach to design in built environment,
- (ii) Sustainability & built Heritage,
- (iii) Conserving Built Heritage,
- (iv) Sustainable Policies for Environmental and Infrastructure Planning,
- (v) Earth and Environmental Planning & Design.

Participants will gain exposure and insight To various sustainable approaches to sustain the heritage as well as define the built environment. It will provide a platform for various individuals to connect the past and present and develop solutions to a more universal and environmentally friendly approach towards built environment.

Submission Deadline:
Call for Papers – 23rd Feb 2023
Abstract Submission – 30th March 2023
Acceptance Notification – 7th April 2023
Full paper Submission – 23rd April 2023

Publication –
Conference proceedings with IOP
Conference Series: Earth and Environmental Science (SCOPUS Indexed)

Notable Speakers

1. Dr Ranjith Dayaranthe , Associate Professor, Asian School of Architecture, Australia
2. Dr Muge Belek Fialho Teixeira, Queensland University of Technology.
3. Dr. Shikha Jain, Director, DRONAH
4. Dr Rajat Gupta, Oxford Brookes, Director, Dept. of sustainable development
5. Ar. Chitra Vishwanath, Biome Bangalore.

Conference Fees :
Students 9500 INR
Academicians & professional 10500 INR

For International Participants
Students - 150 USD
Academicians & professional – 180 USD

For additional information contact –
richa.jagatramka@jaipur.manipal.edu
raunak.prasad@jaipur.manipal.edu

7. Schedule of the event

Time	Event	Speaker
11:00 – 11:30 AM	Opening speech	Dr Richa Jagatramka
11: 30 – 11:35 AM	Welcome address	Dr Madhura Yadav
11: 35 – 11:45 AM	Introduction of international speaker	Ar Himangshu Kedia
11: 45 AM – 12:45 PM	Presentation by Dr Muge	Dr Muge
12: 45 – 01:00 PM	Q & A session	
01:00 – 01:05PM	Vote of Thanks	Ar. Himangshu Kedia

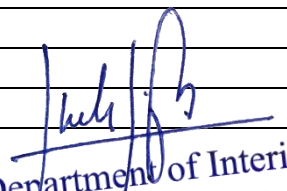
Meeting Link :

https://teams.microsoft.com/l/meetup-join/19%3ameeting_MmRjNjZiN2ltMTc1NS00YmJlLTkwMTItMzBiYTVjNTIOYTRh%40thread.v2/O?context=%7b%22Tid%22%3a%227d0726e8-bf4b-4ac1-99f1-010fb11f1d3f%22%2c%22Oid%22%3a%2216be8839-914f-456c-9836-e6b3ba8fa2f9%22%7d

8. Attendance of the Event

Total attendees – 28 participants from MUJ and outside

Sl.no	Name	Organisation
1	Dr. Richa Jagatramka	FOD
2	Megha Prabhu K	FOD
3	Dr. Sampath Kumar Padmanabha Jinka	FOD
4	Dr. Madhura Yadav	FOD
5	Dr. Anantkumar Dada Ozarkar	FOD
6	Dr. Subhash Chandra Devrath	FOD
7	Nisha Nelson	FOD
8	Preethi Agrawal	Practicing Architect and PhD scholar
9	NITIKA TORVI	Christ University
10	Subhadha B	Christ University
11	Himangshu Kedia	FOD
12	Rushikesh Kolte	MNIT
13	Dr. Sunanda Kapoor	FOD
14	Ananya Tripathi	AKTU - GCA
15	Kinzalk Chauhan	FOD
16	Ritu Sharma	FOS – Phd Scholar
17	Rimjhim Swami	FOD
18	Ayushi Sharma	FOD
19	Apoorva Agarwal	FOD
20	Muge Fialho Leandro Alves Teixeira	QUT Australia
21	Deeksha	MNIT
22	Siddharth Mishra	FOD
23	Akshay Gupta	FOD
24	Ritu Sharma	FOD
25	Neha Saxena	FOD
26	Antima Kuda	MAHE Dubai
27	Raunak Prasad	FOD
28	Ashutosh Saini	FOD


Head, Department of Interior Design
SD&A, Faculty of Design
Manipal University Jaipur



Research papers

Beeswax as a potential replacement of paraffin wax as shape stabilized solar thermal energy storage material: An experimental study

Pushendra Kumar Singh Rathore^a , Krishna Kumar Gupta^b, Bhaskar Patel^b, R.K. Sharma^c, Naveen Kumar Gupta^d

[Show more](#)

Share Cite

<https://doi.org/10.1016/j.est.2023.107714>

[Get rights and content](#)

Highlights

- Beeswax/Bentonite/graphite based SSCPCM for thermal energy storage was prepared.
- SSCPCM shows substantially good thermal energy storage capacity.
- Beeswax based SSCPCM shows excellent heating rate and thermal conductivity.
- SSCPCM was thermally, chemically and physically stable.

Abstract

Thermal Energy Storage (TES) using paraffin wax as Phase Change material (PCM) has been widely used for solar to thermal energy conversion and storage application. Being petroleum by-product, production of paraffin wax have embodied environmental impact and high carbon footprint. Beeswax can replace paraffin's as one of the clean, sustainable, eco-friendly and potential TES PCM. However, TES potential of Beeswax was not investigated thoroughly in previous literatures. Also, limited study has been found which evaluates solar to thermal conversion potential of Beeswax. This study presents a comprehensive analysis of TES performance of Beeswax supported by Bentonite clay and loaded with Graphite was evaluated. Bentonite clay was used as supporting material and Graphite powder is used as additive in varying percentage to form Shape Stabilized Composite Phase Change Material (SSCPCM). SSCPCM was initially investigated for anti-leakage behaviour and was found that Bentonite can hold maximum 40wt% of Beeswax without leakage above phase transition temperature. Thermal energy storage parameters, thermal degradation, solar to thermal conversion performance, chemical stability, surface morphology, and thermal conductivity were evaluated. Bentonite and graphite has shown good morphology to form SSCPCM samples. Also, SSCPCM has proved to be chemically and physically stable thermal energy storage material. Melting enthalpy of 101.79, 100.66, 98.80, 100.43, 96.51, and 105.01 at melting point of 59.43, 58.88, 58.12, 57.98, 57.36, and 57.11 of SSCPCM-0, SSCPCM-1, SSCPCM-3, SSCPCM-5, SSCPCM-7, and SSCPCM-9 was obtained. Adding Graphite has reduced supercooling of SSCPCM samples maximum by 84.13%. Increasing additives in PCM improves heating rate and thermal conductivity of the SSCPCM.

Introduction

Last decade have seen continuous rise in energy demand due to increase in population, globalization, and improvement in living standard. Most of this demand is fulfilled by fossil based fuels such as coal and crude oil. This leads to over-exploitation of limited reserves of fossil fuels causing rapid depletion and excessive greenhouse gas emissions. To mitigate these challenges renewable sources of energy has shown a significant capacity enhancement [1]. Due to abundant availability, low cost, and negligible emissions renewable sources of energy can play a decisive role against climate change. Among various renewable sources, solar energy is one of the major renewable source of energy available to the mankind almost at every location of the planet earth [2]. To harness solar energy various solar technologies such as solar photovoltaic, solar collectors, solar concentrator, solar still, and solar dryers were used for varieties of applications. However, solar energy suffers with serious limitations of limited availability by location, time, and power. These drawbacks leads to poor utilization and low efficiency of solar thermal technologies. To overcome these drawbacks Solar Thermal

Energy Storage (STES) can play a vital role in improving energy efficiency and utilization rate of solar thermal technologies [3].

Thermal Energy Storage (TES) is a technique of storing excessive heat energy in a material and utilizing it as and when it is needed. TES can be classified into two categories (a) Sensible heat storage (b) Latent heat storage [4]. Sensible heat storage is one of the oldest technology of storing thermal energy by rising the temperature of the object whereas in latent heat storage the material undergoes phase transformation to store thermal energy. Phase transformation (solid-liquid and liquid-solid) gives advantage of high energy density at minimum temperature change in comparison to sensible heat storage materials. Latent heat storage using Phase Change Materials (PCM) is the widely used technique for TES for various applications. PCM are the materials which stores thermal energy while undergoing phase transformation (solid-liquid) and releases it by again undergoing phase transformation (liquid-solid) [5]. The storing (charging) and releasing (discharging) of thermal energy in PCM takes place at almost constant temperature or in a narrow temperature range. Additionally, easy availability in large temperature ranges has increased feasibility of latent heat TES technology.

Varieties of PCM are available for TES. However, the most commonly used PCM are paraffin. Paraffin are saturated alkanes having chemical formula as C_nH_{2n+2} . Where n is number of carbon atoms. The melting point of alkanes increases with increase in number of carbon atoms. Paraffin possess various merits such as large melting temperature range, high latent heat, and good storage density with respect to mass [6]. Generally, for building applications the PCM used are having melting temperature range of 20°C to 40°C. However, the melting range of PCM varies depending on climatic temperature of the location [7]. Paraffin suffers with two major drawbacks, first is there low thermal conductivity and second is that they are produced from petroleum products, which is the major producer of harmful emissions. Various attempts were made to overcome the first drawback of low thermal conductivity of paraffin. Loading of Al_2O_3 nanoparticles in paraffin wax was done to improves its thermal conductivity [8]. Result suggest that the thermal conductivity of paraffin wax increases when loaded with Al_2O_3 nanoparticle in liquid state whereas it decreases in liquid state. A study investigates the effect of loading of multi-walled carbon nanotubes, graphene nanoplatelets, and aluminum oxide nanoparticles in PCM [9]. The results shows that after few thermal cycles significant coagulation and deposition of nanoparticles occurs. Also, they suggest that long term stability of paraffin loaded with nanoparticles remains a challenge. Graphene nanoparticles were dispersed in paraffin/water emulsion for enhancing thermal conductivity and photo-thermal performance [10]. Another study shows the effect of loading copper nanoparticles in PCM when subjected to external magnetic field [11]. Some commonly used nanoparticles to improve the thermal energy storage characteristics of the paraffin are graphite [10,12], Al_2O_3 [13], copper nanoparticles [14],

TiO₂ [15], and carbon nanotubes [16]. 1D nanoparticles and 2D nanoparticles are widely used to develop PCM composite with improved thermal, physical, and chemical performance [17]. 1D materials such as Carbon Nanotubes (CNT), Silver nanowires, and Copper nanowires were used as additives in PCM to improve thermal conductivity [18]. Among these 1D materials CNT (SWCNT and MWCNT) is exhaustively analyzed to improve PCM performance. 2D nanomaterials based PCM composites are widely used to improve thermal performance of the PCM [19]. 2D materials have weak van der Waals force and strong covalent bond between in-plane atoms. Widely used 2D materials are Graphene [20], Boron nitride [21], Graphite [22], Nanoclays and MXene [23]. Recently, Mxene based PCM composites are increasingly explored because MXene exhibits high surface area, high thermal conductivity and powerful solar absorption capacity. However, none of these materials were used to evaluate solar to thermal energy storage and conversion of Beeswax. Thus, it can be viewed that there are several methods available which can be considered potential technologies for improving low thermal conductivity of the paraffin. However, none of the articles have discussed the second major drawback i.e. paraffin are the petroleum based products having high carbon footprints. Being petroleum by-product the production and processing of paraffin's is energy intensive and can negatively impact the energy savings measures taken care due to TES using paraffin. A study suggested that the use of PCM based on fossil fuels such as paraffin in buildings is not recommended because of various environmental impact [24]. Environmental risk related to paraffin are also higher especially for the marine environment [25]. Another study suggested to replace traditional fossil based PCM by some ecological friendly PCM in buildings after conducting a life cycle assessment analysis of PCM [26]. A study found that replacing petroleum based paraffin by eco-friendly PCM can reduced 45%–50% greenhouse gas emissions [27]. Thus, it is understood that there is a need to search alternative of petroleum based paraffin wax as thermal energy storage material to reduce the embodied environmental impacts during production and processing [28].

Therefore, the objective of this study is to evaluate the potential of naturally occurring PCM for STES. One of the eco-friendly naturally occurring PCM is Beeswax (BW). Beeswax is produced from bee's hives of honeybees. It is organic non-paraffin PCM. Good thermal energy storage capacity [29,30] has made them a strong contender to replace petroleum based paraffin PCM. This study presents a novel attempt to analyze the solar to thermal energy storage and conversion performance of clean and sustainable PCM called Beeswax. The potential of Beeswax as TES PCM was not evaluated in detail in previous literatures. Also, there is no study available which have analyzed the solar to thermal energy conversion performance of Beeswax. Additionally, in this study chemical and physical stability of Beeswax as Shape Stabilized Composite PCM (SSPCPM) was also investigated.

In this study an eco-friendly and novel Shape Stabilized Composite PCM (SSPCM) was prepared using naturally produced beeswax and naturally occurring Bentonite clay. SSPCM was loaded with graphite at varying wt% to prepare SSCPCM and to investigate its effect on thermo-physical characteristics. Solar to thermal energy conversion performance of the SSCPCM was also investigated.

Access through your organization

Check access to the full text by signing in through your organization.

Access through **Manipal University Jaipur**

Section snippets

Material

Raw Beeswax (BW) was purchased from Madhumakhi Wala located in district Barabanki, India. It has a melting temperature range of 58°C to 62°C, density of 950–961 kg/m³, and have sufficient high latent heat storage capacity as provided by the manufacturer. Bentonite clay was purchased from Sigma-Aldrich in powder form having chemical formula H₂Al₂O₆Si. Graphite powder with average particle size of 44µm and purity of ≥99% was purchased from Aakar Carbons Private Limited, India. Specification ...

Preparation of shape stabilized PCM (SSPCM)

PCM suffers with a major drawback of leakage during phase transition. Therefore, maintaining structural stability during charging and discharging of PCM is important for efficient storage and release of thermal energy. To reduce the chances of leakage of the PCM Shape Stabilized PCM (SSPCM) were prepared. SSPCM was prepared using raw Bentonite clay. Bentonite clay was placed in the furnace at 150°C for 3h to remove water molecules and other unwanted impurities. After 3h, bentonite clay was ...

Characterization

TES parameters such as enthalpy of melting, enthalpy of freezing, melting point, and freezing point are measured using Differential Scanning Calorimetry (DSC). Thermal decomposition of SSCPCM-0, SSCPCM-1, SSCPCM-3, SSCPCM-5, SSCPCM-7, and SSCPCM-9 was measured through Thermogravimetric analysis (TGA). Both DSC and TGA was done using Simultaneous Thermal Analyzer (STA-8000) of Perkin Elmer. STA performs both TGA and DSC analysis in different modes ranging from room temperature to 1600°C. ...

Thermal energy storage characteristics

Thermal energy storage parameters such as melting point, freezing point, melting enthalpy, and freezing enthalpy are the most important characteristic of any PCM to be used as TES material. These characteristics can be investigated through DSC. The DSC curve of pure beeswax and SSCPCM-0, SSCPCM-1, SSCPCM-3, SSCPCM-5, SSCPCM-7, and SSCPCM-9 are shown in Fig. 3(a) and (b) respectively. The heat storage capacity consist of sensible part and latent part. The sensible heating occurs in solid ...

Conclusion

This study investigates the capabilities of Beeswax as potential alternative of paraffin wax for TES as SSCPCM. Various samples of SSCPCM were prepared using Bentonite as supporting material, Beeswax as PCM, and Graphite as additive. Maximum 40wt% of Beeswax was loaded in Bentonite without any leakage during phase transformation. Pure Beeswax shows excellent TES capacity of 206.63J/g (melting) and 203.35J/g (freezing) at melting and freezing temperature of 61.60°C and 54.98°C. Also, about ...

Author statement

We the undersigned declare that this manuscript is original, has not been published before and is not currently being considered for publication elsewhere.

We confirm that the manuscript has been read and approved by all named authors and that there are no other persons who satisfied the criteria for authorship but are not listed. We further confirm that the order of authors listed in the manuscript has been approved by all of us. We understand that the Corresponding Author is the sole contact ...

Declaration of competing interest

The author/authors declare that they have no known competing financial interests or personal relationships that could have appeared to influence the work reported in this paper. ...

[Recommended articles](#)

References (35)

J. Jiang *et al.*

Hybrid generation of renewables increases the energy system's robustness in a changing climate

J. Clean. Prod. (2021)

N. Kannan *et al.*

Solar energy for future world: - a review

Renew. Sust. Energ. Rev. (2016)

J. Xu *et al.*

A review of available technologies for seasonal thermal energy storage

Sol. Energy (2014)

G. Alva *et al.*

An overview of thermal energy storage systems

Energy (2018)

D. Li *et al.*

Incorporation technology of bio-based phase change materials for building envelope: a review

Energy Build. (2022)

A.K. Singh *et al.*

Experimental evaluation of composite concrete incorporated with thermal energy storage material for improved thermal behavior of buildings

Energy (2023)

F. Wang *et al.*

Graphite nanoparticles-dispersed paraffin/water emulsion with enhanced thermal-physical property and photo-thermal performance

Sol. Energy Mater. Sol. Cells (2016)

A. Kumar *et al.*

Study of melting of paraffin dispersed with copper nanoparticles in square cavity subjected to external magnetic field

J. Energy Storage (2022)

A.E. Kabeel *et al.*

Effect of graphite mass concentrations in a mixture of graphite nanoparticles and paraffin wax as hybrid storage materials on performances of solar still

Renew. Energy (2019)

A.N. Keshteli *et al.*

Influence of Al₂O₃ nanoparticle and Y-shaped fins on melting and solidification of paraffin

J. Mol. Liq. (2020)



[View more references](#)

Cited by (34)

Solar to thermal energy storage performance of composite phase change material supported by copper foam loaded with graphite and boron nitride

2024, Solar Energy

[Show abstract](#) 

Advancements in phase change materials for energy-efficient building construction: A comprehensive review

2024, Journal of Energy Storage

[Show abstract](#) 

A review of lignocellulosic biomass-based shape-stable composite phase change materials

2023, Journal of Energy Storage

[Show abstract](#) 

Location optimization of phase change material for thermal energy storage in concrete block for development of energy efficient buildings

2023, Renewable Energy

[Show abstract](#) 

A comprehensive review on solar to thermal energy conversion and storage using phase change materials

2023, Journal of Energy Storage

[Show abstract](#) 

Microencapsulated phase change materials for enhanced thermal energy storage performance in construction materials: A critical review

2023, Construction and Building Materials

[Show abstract](#) 



[View all citing articles on Scopus](#) 

[View full text](#)

© 2023 Elsevier Ltd. All rights reserved.



All content on this site: Copyright © 2024 Elsevier B.V., its licensors, and contributors. All rights are reserved, including those for text and data mining, AI training, and similar technologies. For all open access content, the Creative Commons licensing terms apply.





Bioprospecting of novel ligninolytic bacteria for effective bioremediation of agricultural by-product and synthetic pollutant dyes

Devendra Jain^{a,*}, Jitendra Kumar Navariya^a, Ali Asger Bhojiya^{a,b}, Abhijeet Singh^c, Santosh Ranjan Mohanty^d, Sudhir K. Upadhyay^{e,*}

^a All India Network Project on Soil Biodiversity and Biofertilizers, Department of Molecular Biology and Biotechnology, Rajasthan College of Agriculture, Maharana Pratap University of Agriculture and Technology, Udaipur 313001, India

^b Faculty of Science, US Ostwal Science, Arts and Commerce College, Mangalwad, Chittorgarh, Rajasthan 302024, India

^c Department of Biosciences, Manipal University Jaipur, Jaipur 303007, India

^d All India Network Project on Soil Biodiversity-Biofertilizers, ICAR-Indian Institute of Soil Science, Bhopal 462038, India

^e Department of Environmental Science, V.B.S. Purvanchal University, Jaunpur 222003, India

ARTICLE INFO

Keywords:

Lignin
Methylene blue
Lignin degradation bacteria
Ligninolytic enzymes
16 S rRNA gene sequencing
Biodegradation

ABSTRACT

Lignin is a significant renewable carbon source that needs to be exploited to manufacture bio-ethanol and chemical feedstocks. Lignin mimicking methylene blue (MB) dye is widely used in industries and causes water pollution. Using kraft lignin, methylene blue, and guaiacol as a full carbon source, 27 lignin-degrading bacteria (LDB) were isolated from 12 distinct traditional organic manures for the current investigation. The ligninolytic potential of 27 lignin-degrading bacteria was assessed by qualitative and quantitative assay. In a qualitative plate assay, the LDB-25 strain produced the largest zone, measuring 6.32 ± 0.297 , on MSM-L-kraft lignin plates, while the LDB-23 strain produced the largest zone, measuring 3.44 ± 0.413 , on MSM-L-Guaiacol plates. The LDB-9 strain in MSM-L-kraft lignin broth was able to decolorize lignin to a maximum of $38.327 \pm 0.011\%$ in a quantitative lignin degradation assay, which was later verified by FTIR assay. In contrast, LDB-20 produced the highest decolorization ($49.633 \pm 0.017\%$) in the MSM-L-Methylene blue broth. The highest manganese peroxidase enzyme activity, measuring $6322.314 \pm 0.034 \text{ U L}^{-1}$, was found in the LDB-25 strain, while the highest laccase enzyme activity, measuring $1.5105 \pm 0.017 \text{ U L}^{-1}$, was found in the LDB-23 strain. A preliminary examination into the biodegradation of rice straw using effective LDB was carried out, and efficient lignin-degrading bacteria were identified using 16SrDNA sequencing. SEM investigations also supported lignin degradation. LDB-8 strain had the highest percentage of lignin degradation (52.86%), followed by LDB-25, LDB-20, and LDB-9. These lignin-degrading bacteria have the ability to significantly reduce lignin and lignin-analog environmental contaminants, therefore they can be further researched for effective bio-waste management mediated breakdown.

1. Introduction

Plant biomass naturally decomposes over time and is mostly triggered by enzymatic activity of neighboring bacterial and fungal species (Janusz et al., 2017; da Costa et al., 2018; Jimenez et al., 2018; Lee et al., 2019; Riyadi et al., 2020). Numerous microorganisms, such as bacteria and fungi, have been the focus of the most thorough investigations on lignin alteration and breakdown (Lee et al., 2019; Atiwesh et al., 2022). When lignocellulosic organic wastes are processed for use in the

production of bioethanol and the paper industry, respectively, powerful lignin-degrading microorganisms or their ligninolytic enzymes can be used successfully (Fang et al., 2018; Brink et al., 2019; Li et al., 2022). Plants' rigidity and tensile strength come from lignin, a complex, chemically heterogeneous polymer made up of 4-hydroxyl phenylpropanoid units (Hasanin et al., 2018). Biomass is essentially resistant because lignin acts as a physical barrier to stop cellulose from being hydrolyzed by biological or chemical processes (Wu et al., 2022).

For the production of biofuels, lignocellulosic biomass is highly

* Corresponding authors.

E-mail addresses: devendrajain@mpuat.ac.in, devroshan@gmail.com (D. Jain), sku.env.lko@gmail.com (S.K. Upadhyay).

¹ ORCID: <https://orcid.org/0000-0002-4345-1536>

² ORCID: <https://orcid.org/0000-0002-2228-8063>

desirable as a raw component (Malode et al., 2021). Lignin and cellulose make up the majority of 80% of crop residue/biomass (Chen et al., 2018). Large volumes of lignocellulosic waste are produced by forestry and agricultural activities, paper-pulp companies, wood industries etc. and burning is a common method of decreasing this waste, which otherwise may contribute to pollution (Haile et al., 2021). Therefore, enhancing lignin breakdown has enormous promise to save the environment and build new beneficial products (Gupta et al., 2022). Chemical contaminants like synthetic dyes are significant contributors to water pollution. Methylene blue (MB) dye is one of these and is frequently used in various industries such as dyeing, textile, tannery, and paper, etc. (Bhat et al., 2022; Pham et al., 2022). Using promising microbial isolates, a biological strategy giving a more affordable and sustainable alternative method has been used to remove MB. Microorganisms, which can degrade MB, come from a wide range of taxa, including *Acinetobacter*, *Aspergillus*, *Bacillus*, *Pseudomonas*, *Staphylococcus* etc. (Eslami et al., 2017; Karim et al., 2018; Bharti et al., 2019; Ogunlaja et al., 2020; Kishor et al., 2021b; Haque et al., 2021). To participate in central carbon metabolism, bacteria that degrade lignin and lignin-imitating dyes secrete extracellular enzymes that break down lignin into smaller components (Beckham et al., 2016). A range of extracellular oxidative enzymes, such as laccases, lignin peroxidases (LiPs), manganese peroxidases (MnPs), and multifunctional peroxidases, are released by the lignin-degrading organisms (Kumar and Chandra, 2020).

Several bacteria, in addition to wood-rot fungus, can degrade lignin (Haq et al., 2022). Pretreatments may become economically viable if lignin is removed selectively using lignin-degrading enzymes (Lee et al., 2019; Wu et al., 2022). A biological (or primarily biological) approach to removing lignin could overcome these limitations, enabling the generation of bio-fuel at a cheaper cost and with less impact on the environment. Microorganisms can produce metabolites and enzymes that hasten the breakdown of organic waste and raise the caliber of soil humus (Singh et al., 2017).

The breakdown of rice straw into smaller products so they can be digested by microorganisms occurs through a microbial process (Goodman, 2020). In the past, the majority of these lignin-degrading bacteria were found in soil and the intestines of insects that fed wood (Zhang et al., 2021). This research was focused on identifying and characterizing the microbial inoculants that causes rice straw to break down so quickly. In this study, we identify new lignin-degrading bacteria from a variety of organic sources, characterize them, and assess their potential for lignin degradation.

2. Material and methods

2.1. Isolation and screening of lignin-degrading bacteria

The isolation of LDB was carried out using the method reported by Rahman et al. (2013). The minimal salt media-Luria agar (MSM-L agar) medium supplemented with 1% Kraft lignin (KL) as the primary carbon and energy source was used for the isolation of ligninolytic bacteria from freshly prepared organic manures (Jain et al., 2021) (Table 1). The bacterial strains that showed proper growth were purified on fresh MSM-L agar plates and stored at 4 °C. Screening of LDB was carried out on MSM-L agar plate containing Kraft lignin (0.5%) (Chen et al., 2012b) and guaiacol (10%) (Atalla et al., 2010) and methylene blue indicator dye (50 mg/L) (Bandounas et al., 2011) and incubated at 30 ± 2° C for 4–5 days for the development of the de-colorization zone. After growth, the plates were taken out and flooded with 10 ml of a ferric chloride/potassium ferricyanide solution [1% (w/v)]. After 10 min, the solution was drained off, leaving the agar where the aromatic compounds were present stained blue or green. It was assumed that a yellowish zone where growth had been eradicated was proof of lignin breakdown (McCarthy and Broda, 1984). The degrading of indicator dye is considered a positive test for lignin degradation (Bandounas et al.,

Table 1

Determination of lignolytic activities of lignin degrading bacteria isolated from traditional organic manures.

S. N.	Source	Strain Name	Growth and de-colorization of ligninolytic substrates		
			Kraft Lignin	Guaiacol	Methylene blue
1	JeevaAmrat	SBD-LDB-1	+	+	-
2	BhabhutAmritPani	SBD-LDB-2	+	+	+
3	PanchGavya	SBD-LDB-3	+	+	+
4	MatkaKhad	SBD-LDB-4	+	+	+
5	Vermiwash (Silica enriched)	SBD-LDB-5	+	+	-
6	BeejaAmrat	SBD-LDB-6	+	-	+
7	Vermi Wash	SBD-LDB-7	+	+	+
8	Silica enriched Compost tea	SBD-LDB-8	+	+	+
9	Compost Tea	SBD-LDB-9	+	+	+
10	BD500	SBD-LDB-10	+	+	-
11	BD500	SBD-LDB-11	+	+	+
12	JeevaAmrat	SBD-LDB-12	+	+	-
13	BhabhutAmritPani	SBD-LDB-14	+	+	+
14	PanchGavya	SBD-LDB-15	+	+	-
15	MatkaKhad	SBD-LDB-16	+	+	-
16	Silica enriched vermi wash	SBD-LDB-17	+	+	-
17	BeejaAmrat	SBD-LDB-18	+	-	-
18	Vermi Wash	SBD-LDB-19	+	+	+
19	Compost tea (Silica enriched)	SBD-LDB-20	+	+	+
20	Compost Tea	SBD-LDB-21	+	-	-
21	BD 501	SBD-LDB-22	+	+	+
22	BD 501	SBD-LDB-23	+	+	+
23	PanchGavya	SBD-LDB-24	+	+	+
24	MatkaKhad	SBD-LDB-25	+	+	+
25	Silica enriched vermi wash	SBD-LDB-26	+	+	+
26	BeejaAmrat	SBD-LDB-28	+	+	-
27	Vermi Wash	SBD-LDB-29	+	+	+

2011).

3. Ligninolytic enzyme activity assay

A 50 ml conical flask filled with MSM-L medium was used to inoculate the chosen positive isolates for screening assays. These inoculated flasks were incubated for 6 days per the procedures outlined by Rahman et al. (2013), during which time culture samples were collected for manganese peroxidase (MnP) and laccase activity were assessed using the oxidation of Guaiacol (2-methoxyphenol) and ABTS (2, 2'-azinobis-(3-ethylbenzothiazoline-6-sulphonate) method respectively (Rahman et al., 2013; Bourbonnais et al., 1995).

3.1. Decolorization activity of bacteria on liquid MSM containing MB dye and Kraft lignin

Decolorization of lignin-mimicking dyes i.e. Methylene Blue (MB) was assessed in test tubes as liquid-phase assays. For broth assays, the individual bacterial strains were grown in MSM containing methylene blue indicator dye (50 mg/L) at 30 °C with shaking at 200 rpm. Control without inoculation was also maintained. The samples were centrifuged and dye de-colorization was absorbance was measured at λ_{663} (Saratale et al., 2009).

All the test bacterial cultures were inoculated in 10 ml of MSM-L agar medium containing 0.5% lignin in 25 ml capacity screwed cap tubes with the maintenance of un-inoculated control for comparison. All the tubes were incubated at $30 \pm 2^{\circ}$ C at 120 rpm for 5 days in a shaker incubator and color change was measured by spectrophotometer on the 5th day at 465 nm. The decolorization percentage of 0.5% lignin by respective bacteria was calculated using the formula given by (Sani and Banerjee, 1999).

$$\% \text{ decolorization} = \frac{\text{Initial absorbance} - \text{observed absorbance}}{\text{Initial absorbance}} \times 100$$

Additionally, Fourier transform infrared (FTIR) spectroscopy study was done to verify that the isolates had degraded and depolymerized kraft lignin (Khan et al., 2022).

3.2. In vitro efficacy of ligninolytic bacteria for degradation of agro-waste residues

After being treated with 1% NaOH for 24 h at room temperature, deionized water was used to adjust the pH to 7, and then the rice straw was dried at 80 °C (Yu et al., 2009). The 3 g quantity of pretreated rice straw was immersed in 100 ml flasks in triplicate and steam sterilized and then 5 ml of selected lignin-degrading bacteria were inoculated in each flask incubated for 21 days at ambient temperature (room temperature) and assayed for lignin degradation and the observations of weight reduction and consistency were also monitored (Bakar et al., 2018). After the end of the incubation period, the acid detergent fiber (ADF) and acid detergent lignin (ADL) methods (Thimmaiah, 2009) were used to determine the amount of lignin in rice straw.

4. Effects of bio-pretreatment on the structure of the rice straw

Using a freeze drier, untreated and bio-pretreated rice straw was dehydrated. Using a scanning electron microscope (SEM), the various surface morphologies of the untreated and bio-pretreated rice stover were observed (Dong et al., 2019).

5. Sequencing and Phylogenetic Analysis of 16 S rDNA of Potent LDB Isolates

The five most effective LDB isolates' PCR-amplified 16 S rDNA region was sequenced using an automated DNA sequencer (ABI model 377, Applied Biosystems, USA) in accordance with the normal technique utilizing universal 16 S rDNA primers (27 F and 1492 R; amplicons size \approx 1465 bp). Prior to BLAST, the 16 S rDNA sequences were modified using the Bio Edit software. Utilizing the nucleotide BLASTn programme, the sequences collected during the investigation were compared to previously submitted sequences in the nucleotide database GenBank at the National Center for Biotechnology (NCBI) (Altschul et al., 1990). The online programme CLUSTAL-W was used to align the 16 S rDNA consensus sequences (Thompson et al., 1994). Phylogenetic trees were constructed using this alignment and the greatest likelihood technique using MEGA 6.06 software (Tamura et al., 2013).

6. Statistical analyses

Using SPSS-20, the statistical analysis known as the standard

deviation (SD) was performed on all the observed data. Additionally, correlation functional interaction between all chosen bacterial isolates' production of the enzymes that break down Kraft lignin and Methylene Blue was performed using Past3 software, and correlation heat maps were created using TB tools.

7. Result and discussion

7.1. Isolation and screening of lignin degrading bacteria

The isolation and screening of lignin-degrading bacteria were carried out on the MSM-L agar medium supplemented with Kraft lignin (0.5%), Guaiacol (10%), and Methylene blue (50 mg/L). In the present study, 27 lignin-degrading bacteria were isolated and purified from 12 different organic produces and are summarized in Table 1. All the strains were able to grow on MSM-L containing Kraft lignin (0.5%), whereas 24 strains and 18 strains were able to grow and utilize Guaiacol (10%) and Methylene blue (50 mg/L) respectively. The 16 strains along with the positive culture showed positive growth and de-colorization on all three different ligninolytic substrates. The decolorization zone was measured to determine the lignin degradation index (LDI), and the findings are shown in Table 2. This is the first report that we are aware of lignin-degrading microbial strains being isolated from conventional liquid organic manures.

The various lignin-degrading bacteria were identified in rotting oil palm, empty fruit bunches, rotten wood, textile effluent, and sludge etc. (Faisal et al., 2021; Kishor et al., 2021a). While Harith et al. (2014) isolated 8 strains with lignin degradation ability from agro-industrial waste, Sharifi-Yazdi et al. (2001) isolated 22 LDB strains from decayed plants, Falade et al. (2017) isolated 30 potential strains of ligninolytic bacteria from water and sediment samples, and Couger et al. (2020) isolated lignin-degrading bacteria from the termite gut. Nahrowi et al. (2018) previously reported a correlation between ligninolytic activities of bacterial isolates and the lignin degradation index (LDI), and they

Table 2

Determination of lignolytic activities of lignin degrading bacteria using plate assay by measuring decolourisation zone.

S.NO	Strain Name	Lignin degradation index by measuring decolourisation zone after 72 h	
		Kraft Lignin (0.5%)	Guaiacol (10%)
1	SBD-LDB-1	3.24 ± 0.035	2.86 ± 0.125
2	SBD-LDB-2	2.1 ± 0.10	2.21 ± 0.257
3	SBD-LDB-3	3.6 ± 0.200	2.28 ± 0.145
4	SBD-LDB-4	3.46 ± 0.351	1.31 ± 0.162
5	SBD-LDB-5	1.01 ± 0.11	1.83 ± 0.175
6	SBD-LDB-6	1.04 ± 0.12	ND
7	SBD-LDB-7	3.38 ± 0.325	1.63 ± 0.126
8	SBD-LDB-8	5.23 ± 0.321	3.01 ± 0.225
9	SBD-LDB-9	5.47 ± 0.240	3.21 ± 0.256
10	SBD-LDB-10	3.48 ± 0.141	1.65 ± 0.200
11	SBD-LDB-11	4.53 ± 0.251	3.02 ± 0.087
12	SBD-LDB-12	5.15 ± 0.160	2.21 ± 0.256
13	SBD-LDB-14	2.35 ± 0.100	2.01 ± 0.225
14	SBD-LDB-15	0.94 ± 0.18	1.78 ± 0.257
15	SBD-LDB-16	4.32 ± 0.192	2.26 ± 0.205
16	SBD-LDB-17	5.57 ± 0.222	2.41 ± 0.272
17	SBD-LDB-18	0.98 ± 0.08	ND
18	SBD-LDB-19	1.24 ± 0.250	1.52 ± 0.087
19	SBD-LDB-20	5.17 ± 0.210	3.30 ± 0.174
20	SBD-LDB-21	0.84 ± 0.14	ND
21	SBD-LDB-22	3.34 ± 0.262	2.36 ± 0.127
22	SBD-LDB-23	6.14 ± 0.161	3.44 ± 0.413
23	SBD-LDB-24	6.31 ± 0.298	2.88 ± 0.247
24	SBD-LDB-25	6.32 ± 0.297	3.29 ± 0.187
25	SBD-LDB-26	3.61 ± 0.135	2.09 ± 0.085
26	SBD-LDB-28	1.04 ± 0.13	1.93 ± 0.081
27	SBD-LDB-29	3.42 ± 0.186	2.84 ± 0.177

*ND: Not Detected; Data (Mean of triplicate value ± SD)

demonstrated that lignin-degrading bacterial isolates had LDI values ranging from 2.6 to 1.22, validating the results of the Lignin degradation index by lignin-degrading bacterial strains. Falade et al. (2017) assessed the lignin-degrading activity of bacterial strains using guaiacol decolorization and found that only 5 strains out of 30 displayed decolorization zone, which validates our current findings.

8. Ligninolytic enzyme activity assay

The quantification of ligninolytic enzymes viz. Manganese peroxidase enzyme and Laccase enzyme in the lignin-degrading bacteria were conducted further to understand the mechanism of their ligninolytic activities. The results of the Manganese peroxidase enzyme and Laccase enzyme were summarized in Fig. 1.

Fig. 1 shows the correlation between the percentage of KL and MB elimination and the bacterial enzymes (MnP and laccase). The lines in the graph below indicate the ligninolytic bacteria, while the columns stand in for the enzymes. The level of enzymatic activity was indicated by the colour of the tiles. The bacterial strains SBD-LDB-9, SBD-LDB-8, SBD-LDB-20, SBD-LDB-23, and SBD-LDB-25 that significantly reduce KL and MB were determined to have the highest enzymatic activity, as depicted in Fig. 1.

The highest Manganese peroxidase enzyme activity of $6322.314 \pm 0.034 \text{ U L}^{-1}$ was observed in the strain SBD-LDB-25 whereas the minimum activity of $2630.854 \pm 0.031 \text{ U L}^{-1}$ was observed in SBD-LDB-3 strain. In the case of Laccase enzyme, the maximum degradation activity was observed in SBD-LDB-23 strain of $1.510 \pm 0.017 \text{ U ml}^{-1}$ whereas minimum activity was reported in SBD-LDB-18

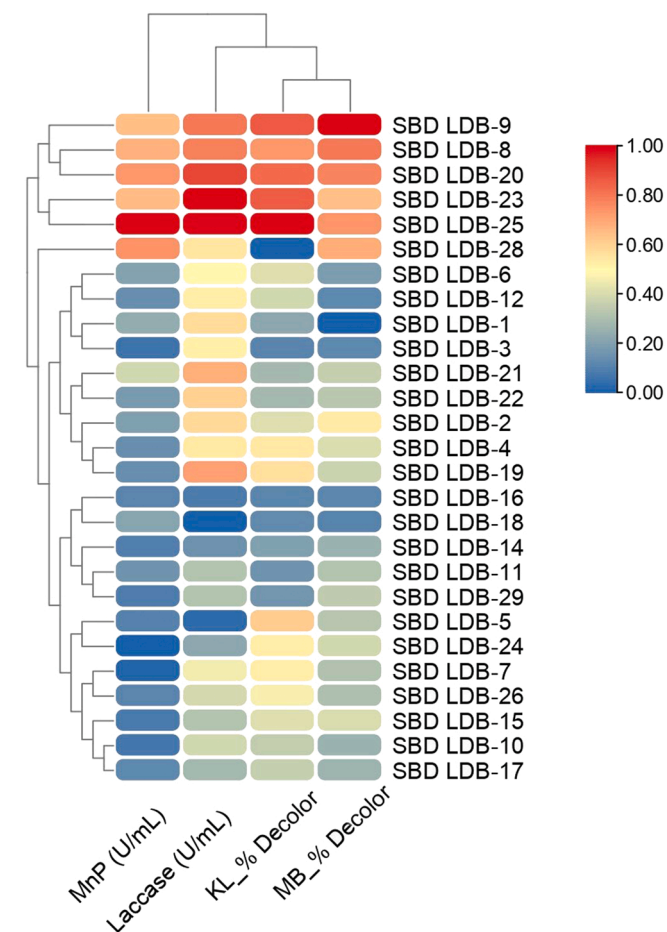


Fig. 1. Heatmap correlation analysis of the percentage of KL (Kraft Lignin) and MB (Methylene Blue) removed by several bacterial isolates producing the enzymes MnP and laccase.

strain of $0.825 \pm 0.026 \text{ U ml}^{-1}$. Shamseldin and Abdelkhalek (2015) studied Manganese peroxidase enzyme activities and reported that MnP activity was found as 1720 U L^{-1} and 1750 U L^{-1} after the third day whereas the Laccase enzymes were found as 810 U L^{-1} and 915 U L^{-1} after six days in two examined LDB strains. The enzyme activities reported by Shamseldin, Abdelkhalek (2015) were lower compared to the results obtained in the present studies. The results observed by Chen et al. (2012a) and Yang et al. (2017) were in close agreement with the result obtained in the present study. Chen et al. (2012b) revealed the maximum Manganese peroxidase activity was 3229.8 U L^{-1} on the 4th day and the highest Laccase activity of 1275 U L^{-1} was recorded at the 5th day of the growth of the bacteria. Yang et al. (2017) reported that the Laccase activity of most LDB increased significantly from 24 to 48 h, with a maximum of 2250 U L^{-1} in the bacterial strain H2 at 60 h incubation. In the case of the Manganese peroxidase enzyme, the highest activity of 1119 U L^{-1} was observed in strain J12 at 24 h.

8.1. Decolorization activity of bacteria on liquid MSM containing MB dye and Kraft lignin

The quantitative determination of the ligninolytic activities of the LDB was identified by measuring of percent decolorization of MSM-L broth medium supplemented with kraft lignin (0.5%) and Methylene blue indicator dye (50 mg/L) after 72hrs of incubation. All the strains showed significant activity and the results of the % degradation of Kraft lignin and methylene blue indicator dye were summarized in Table 3.

The data of the % decolorization is displayed in heat map graph format in Fig. 1. It is a method of condensing information, with the lines denoting the investigated ligninolytic bacteria and the columns denoting Kraft Lignin and Methylene Blue decolorization. The degree of the % decolorization is shown by the colored tiles. Fig. 1 demonstrates that the bacterial strains SBD-LDB-9, SBD-LDB-8, SBD-LDB-20, SBD-LDB-23, and SBD-LDB-25 achieved the highest % decolorization.

The maximum percent decolorization of $38.327 \pm 0.011\%$ was observed by the SBD-LDB-9 strain in MSM-L broth containing Kraft

Table 3
Quantitative determination of Ligninolytic activity of bacteria.

S.N.	Percent decolourisation		
	Strain Name	Kraft lignin (0.25%)	Methylene blue (50 mg/L)
1	SBD-LDB-1	19.566 ± 0.010	17.866 ± 0.013
2	SBD-LDB-2	21.025 ± 0.005	30.250 ± 0.016
3	SBD-LDB-3	23.587 ± 0.025	23.495 ± 0.018
4	SBD-LDB-4	19.771 ± 0.027	21.684 ± 0.012
5	SBD-LDB-5	19.809 ± 0.012	22.222 ± 0.017
6	SBD-LDB-6	24.429 ± 0.021	26.383 ± 0.015
7	SBD-LDB-7	23.419 ± 0.020	28.732 ± 0.012
8	SBD-LDB-8	37.298 ± 0.013	46.256 ± 0.020
9	SBD-LDB-9	38.327 ± 0.011	48.458 ± 0.015
10	SBD-LDB-10	24.317 ± 0.021	29.613 ± 0.007
11	SBD-LDB-11	20.819 ± 0.014	30.886 ± 0.016
12	SBD-LDB-12	30.134 ± 0.028	38.228 ± 0.017
13	SBD-LDB-14	22.409 ± 0.031	29.662 ± 0.019
14	SBD-LDB-15	19.0422 ± 0.012	21.390 ± 0.013
15	SBD-LDB-16	22.858 ± 0.011	23.201 ± 0.014
16	SBD-LDB-17	29.985 ± 0.012	44.542 ± 0.019
17	SBD-LDB-18	17.385 ± 0.015	22.663 ± 0.014
18	SBD-LDB-19	18.387 ± 0.011	30.299 ± 0.012
19	SBD-LDB-20	35.185 ± 0.030	49.633 ± 0.017
20	SBD-LDB-21	23.943 ± 0.016	29.075 ± 0.012
21	SBD-LDB-22	23.228 ± 0.007	32.795 ± 0.006
22	SBD-LDB-23	35.652 ± 0.005	46.941 ± 0.022
23	SBD-LDB-24	22.521 ± 0.019	31.082 ± 0.012
24	SBD-LDB-25	33.558 ± 0.017	47.969 ± 0.007
25	SBD-LDB-26	25.065 ± 0.009	39.452 ± 0.020
26	SBD-LDB-28	16.666 ± 0.009	26.258 ± 0.017
27	SBD-LDB-29	23.251 ± 0.014	30.299 ± 0.010

Data (Mean of triplicate value ± SD)

lignin whereas the minimum activity was observed in the SBD-LDB-28 strain with $16.666 \pm 0.009\%$ decolorization. A similar percent decolorization was observed in MSM-L broth containing Methylene blue dye and after 72 hrs incubation, the maximum percent decolorization ($49.633 \pm 0.017\%$) was observed in the SBD-LDB-20 strain whereas the minimum percent decolorization ($17.866 \pm 0.013\%$) was observed in SBD-LDB-1 strain. It has been speculated that the depolymerization of lignin polymers by bacterial ligninolytic systems, which consists of several enzymes secreted by these bacteria, is what causes the reduction in a color that results from lignin biodegradation. *Bacillus amyloliquefaciens* (SL-7) bacteria produced manganese peroxidase, lignin peroxidase, Laccase activity, and degraded 28.55% of tobacco straw lignin (Mei et al., 2020). Xiong et al. (2013) reported that *Panteoa* spp. strain Sd-1 effectively reduced lignin color (52.4%) after 4 days of incubation. The ligninolytic bacterial strain, *Bacillus velezensis*, was used by Verma et al. (2020) and found that under ideal conditions, this strain had a maximum capacity for KL decolorization and degradation of 56.16% and 40.39%, respectively. These findings were in close agreement with those of the current study.

9. FTIR analysis

The lignin-degrading bacterial isolates were evaluated using FT-IR to determine how they had altered the structural and chemical properties of kraft lignin (Fig. 2). Lignin degradation was evident from the FTIR spectra of untreated and treated kraft lignin using lignin degrading bacteria depicted discrete changes, especially in the FTIR absorbance range from 1350 to 1715 cm^{-1} correlated to the stretching of C=C bonds in the aromatic skeleton of lignin when incubated in the broth for 5 days (Wang et al., 2021). The C=C bonds in the aromatic skeleton of lignin are the primary targets of the ligninolytic enzymes, resulting in lignin structural depolymerization (Zeng et al., 2014). Further, the decrease in absorbance around wave number 3500 – 3000 cm^{-1} corresponds to –OH bonds in alcohol and phenol in lignin in treated samples also indicating lignin degradation (Khan et al., 2022). Kraft lignin's FTIR spectrum underwent significant changes at 3210 cm^{-1} (OH stretching

vibration), 2927 cm^{-1} (stretching vibration of C–H band in CH_2 , CH_3 , and CH_3O groups of the lignin structure), 2860 cm^{-1} (C–H stretching in aromatic methoxyl groups), 1715 cm^{-1} (C=O stretching), 1650 cm^{-1} (Absorbed O–H and conjugated C–O), 1635 cm^{-1} (C=C stretching vibration in benzene ring), 1580 cm^{-1} , 1511 cm^{-1} (attributed to the stretching vibration of aromatic rings), 1420 cm^{-1} (O– CH_3 stretching vibration), 1330 cm^{-1} (–CH stretching vibration), 1042 cm^{-1} (C–O vibrations) and 618 cm^{-1} (stretching vibrations of the C–S bond linked to the aromatic ring) (Kumar et al., 2015; Xu et al., 2018; Ma et al., 2021). The absorbance at 1335 cm^{-1} (S) significantly decreased during biodegradation, but the absorbance at 1275 cm^{-1} (G) barely changed. Significant differences between the FTIR spectra of the treated samples and the control samples showed that the lignin structure was largely destroyed by the different enzymes secreted by LDB used in the present study.

9.1. In vitro screening of lignin-degrading bacteria using rice straw bio-waste as substrate

Furthermore, research was conducted to determine the optimal strain for in vitro degradation of agricultural waste. The consistency of rice straw altered when the lignin content in the straw was broken down by lignin-degrading bacteria, as shown in Fig. 3. The results of the decomposition of rice straw by using lignin degrading bacteria were summarized in Table 4. In rice straw that had been exposed to lignin-degrading bacteria, the amount of lignin was substantially reduced after 20 days after inoculation compared to the control rice straw. Among all LDB strains, the maximum percent lignin degradation were obtained in the SBD-LDB-8 strain (52.86%) followed by SBD-LDB-25 (52.69%), and SBD-LDB-20 (48.01%) and SBD-LDB-9 (45.99%) whereas the minimum percent lignin degradation was observed in SBD-LDB-17 strain (17.98%).

In a comparison of three bacterial isolates for lignin degradation on rice straw, Bakar et al. (2018) found that the rice straw treated with the AMB1 bacterial strain had significantly less lignin, at 4.97% compared to the lignin content of the control which was 8.89 ± 1.0 . Similarly,

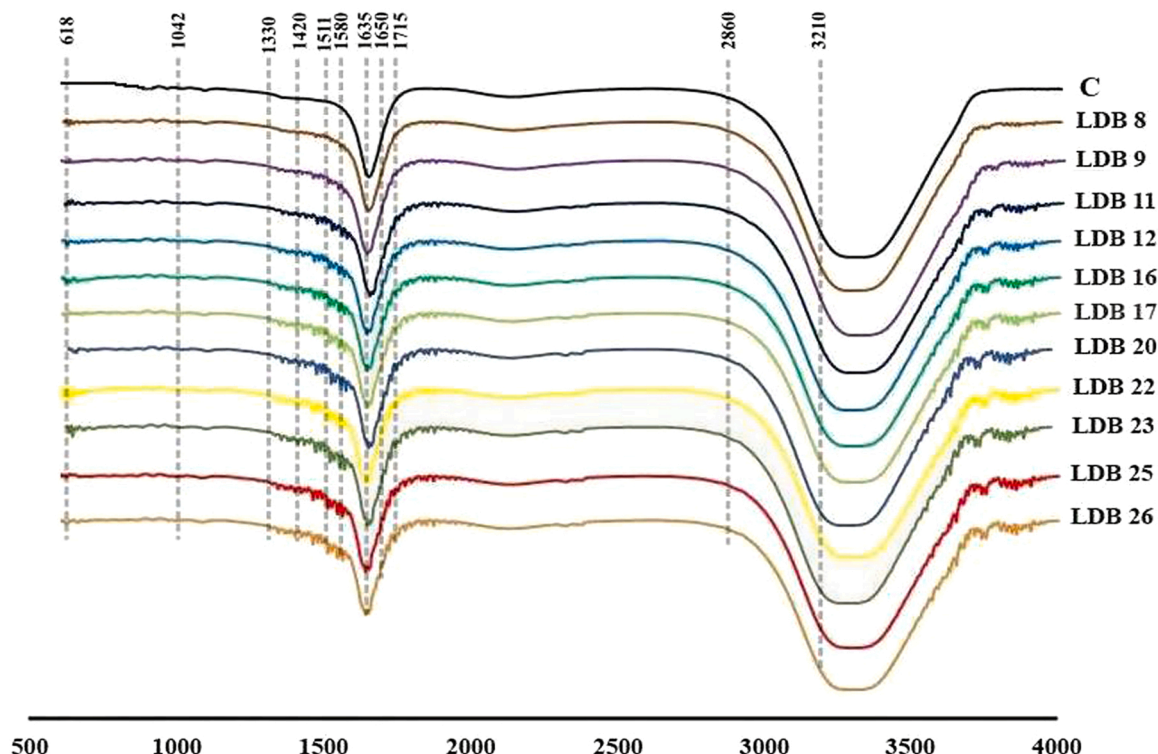


Fig. 2. FTIR spectrum of LDB treated and untreated kraft lignin.



Fig. 3. *In vitro* efficacy evaluation of lignin degrading bacteria for rice-straw degradation.

Table 4

Effect of effective lignin degrading bacteria pretreatment on the composition of rice straw.

Strain Name	ADF %*	ADL %* *	ASH %	Lignin%	% Lignin degradation
CONTROL	88.04	25.35	7	18.35 ± 0.014	100
SBD-LDB-8	68.43	13.98	5.3	8.65 ± 0.018	52.86
SBD-LDB-9	69.55	13.91	4	9.91 ± 0.016	45.99
SBD-LDB-11	76.03	18.73	4.6	14.06 ± 0.044	23.37
SBD-LDB-12	74.06	15.03	4	11.03 ± 0.027	39.89
SBD-LDB-16	75.44	16.55	4.6	11.08 ± 0.045	39.61
SBD-LDB-17	78.14	18.72	3.6	15.05 ± 0.023	17.98
SBD-LDB-20	72.46	13.87	4.3	9.54 ± 0.023	48.01
SBD-LDB-22	77.72	17.73	4.6	13.06 ± 0.015	28.82
SBD-LDB-23	69.42	13.57	3.6	9.91 ± 0.008	45.99
SBD-LDB-25	66.53	12.02	3.3	8.68 ± 0.038	52.69
SBD-LDB-26	76.16	16.78	4	12.78 ± 0.016	30.35

* Acid Detergent Lignin: Lignin+Ash (Data recorded after 21 days pretreatment)

* Acid Detergent Fiber (Cellulose+Hemi-cellulose+Lignin+Mineral);

Ochrobactrum oryzae BMP03 strain-treated rice straw's chemical makeup was investigated by Tsegaye et al. (2018) and reported that the BMP03 treatment degraded and mineralized 53.74% lignin after 14 days of pretreatment. According to Chandra et al. (2007), *Novosphingobium* sp. B-7 bacteria were responsible for 37% of the breakdown of Kraft lignin. Shi et al. (2017) found that after 7 days of pretreatment with the *Cupriavidus basilensis* B-8 bacterial strain, 41.5% of kraft lignin was eliminated, which was quite similar to the findings of the current study.

9.2. Effects of bio-pretreatment on the structure of the rice straw using SEM

The morphological modification of the rice straw that was treated by lignin-degrading bacterial isolates was analysed by scanning electron microscopy. The original rice straw displayed smooth, well-organized, and complete frameworks (Fig. 4). It was noticed that the surface was fairly smooth. It became fragmented and porous after being treated with lignin-degrading bacterial isolates. The rice straw developed some holes. After bacterial treatment, the rice straw's morphology showed that its linkages had been broken, and its lignin contents had been noticeably reduced. Various researchers observed the change in morphology of lignin using SEM which confirm the degradation of lignin visually (Xu et al., 2018; Ma et al., 2021). Dong et al. (2019) analyzes the lignin degradation by SEM technique and they observed that the microbial treated lignin sample became cracked and porous as compared to

ordered and intact structures of untreated lignin samples which further supports the observation in the present study.

9.3. Sequencing and phylogenetic analysis of 16 S rDNA of potent LDB isolates

Based on *in vitro* rice straw degradation efficacy, the comprehensive sequences of the 16 S rDNA genes of the most effective lignin-degrading bacterial strains were sequenced and examined using the nucleotide BLASTn programme. These strains were identified as LDB-8: *Enterobacter ludwigii* (MW264070), LDB-25: *Klebsiella variicola* (MW265009), LDB-20: *Rahnella aquatilis* (MW264333), LDB-9: *Bacillus paramycoides* (MW264994), and LDB-23: *Bacillus paramycoides* (MW423733) as shown in Fig. 5. Table 5 lists the molecular details and NCBI GeneBank accession number associated with these strains. Similar approach was adopted by Upadhyay et al. (2009, 2011) for identification of salt tolerant rhizobacterial isolates. Rahman et al. (2013) characterized lignin-degrading bacteria using 16 SrRNA gene sequencing analysis and identified the bacterial strains as *Bacillus* sp., *Ochrobactrum* sp., and *Leucobactersp.*, with 99% sequence similarity to the strains from NCBI-Gene bank databases. El-Hanafy et al. (2008) isolated two lignin-degrading bacterial strains from Egyptian soils and identified them as *Bacillus* sp. (EU344809) and *Bacillus subtilis* based on the partial 16 S rRNA sequencing (EU344808). From a decomposing empty fruit bunch of an oil palm, Riyadi et al. (2020) isolated and described a lignin-degrading bacterial strain. Based on 16S rDNA sequencing, the isolated strain was identified as *Streptomyces* sp. S6.

10. Conclusion

The current investigation was based on the isolation of 27 lignin-degrading bacteria from 12 conventional manures. These strains were strong in ligninolytic enzymes such laccase and MnP, which can degrade KL and MB. SBD-LDB-8, SBD-LDB-25, SBD-LDB-20, SBD-LDB-9, and SBD-LDB-23 were shown to be the best LDB isolates based on their *in vitro* lignin degradation capacity using rice straw as the substrate. SEM images indicating changes in surface morphological properties linked with lignin breakdown backed up this claim. Despite tremendous progress in the isolation and characterization of lignin-degrading microbes to date, appropriate and effective formulations for waste breakdown and biodegradation of synthetic dyes like MB must be developed. According to these results, the isolated LDB strains from the current study would make a good choice for lignin valorization. Therefore, more thorough research is needed to establish their capacity to degrade waste biomass on the ground and in certain environmental conditions.

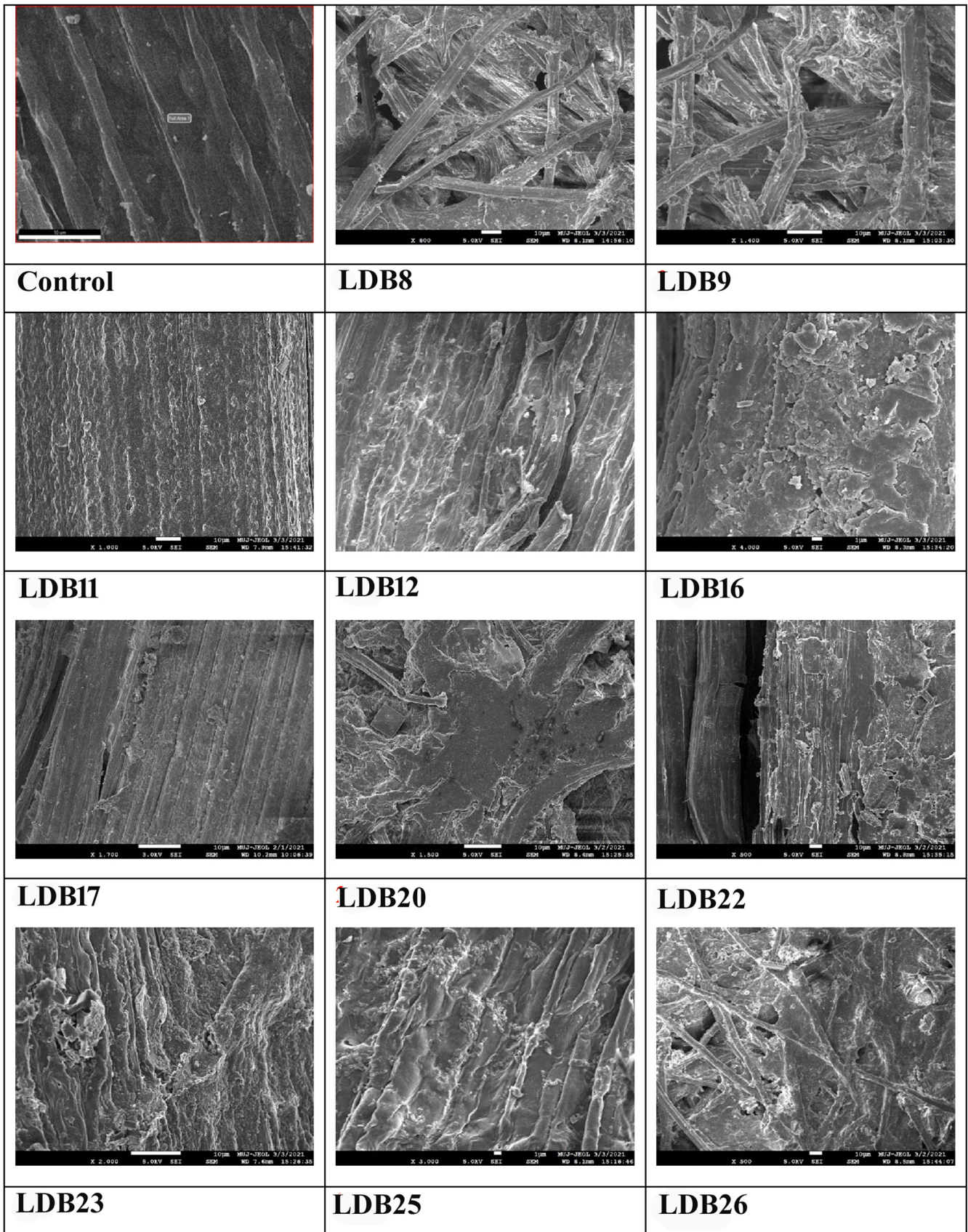


Fig. 4. Scanning electron micrographs of the control and LDB treated rice straw for 21 days.

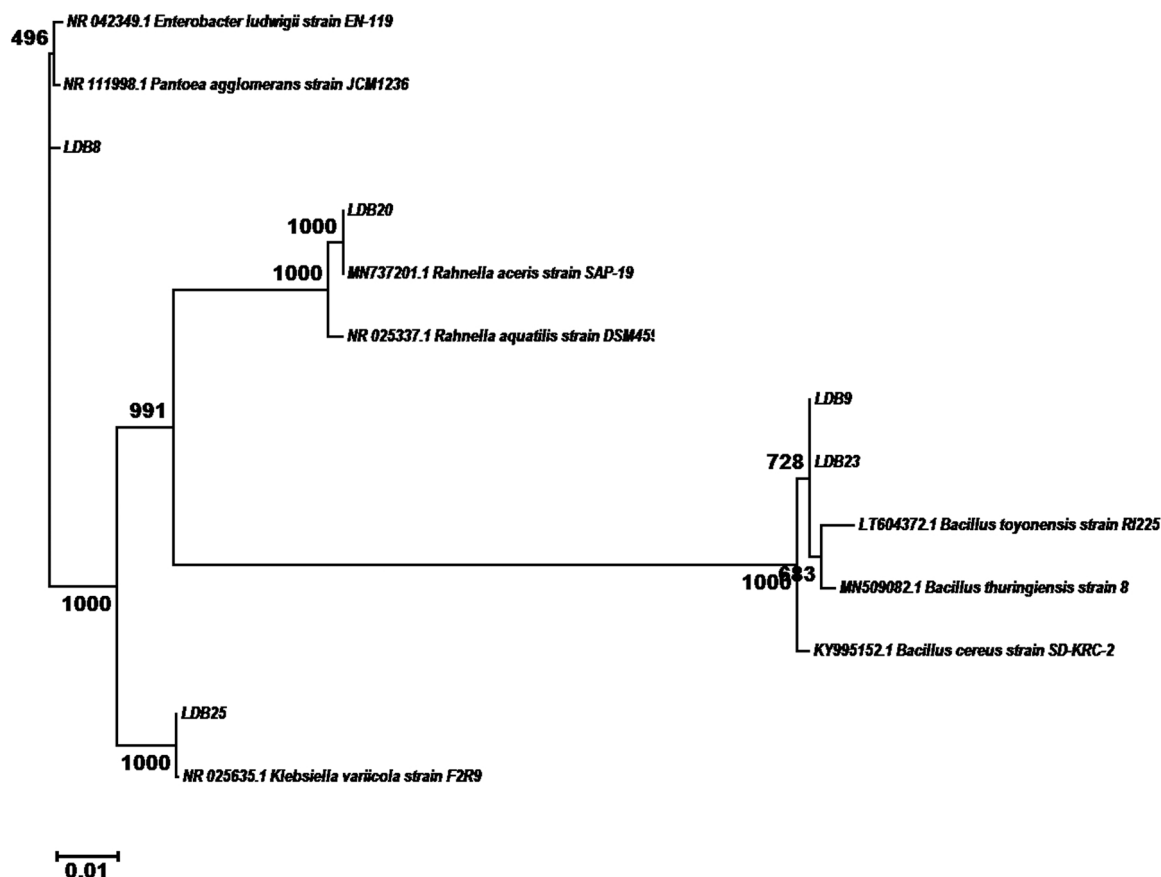


Fig. 5. Phylogenetic analysis of potent lignin degrading bacteria.

Table 5
Molecular identification of potent Lignin Degrading Bacteria.

Strains	Identification/ Accession number	Closest type strain			
		Molecular identity	Strain	Accession number	% Similarity/ Query Coverage
LBD-8	<i>Enterobacter ludwigii</i> / MW264070	<i>Enterobacter ludwigii</i>	EN-119	NR_042349.1	99.71/100
LDB-9	<i>Bacillus paramycooides</i> / MW264994	<i>Bacillus paramycooides</i>	MCCC 1A04098	NR_157734.1	99.00/99.09
LBD-20	<i>Rahnella aquatilis</i> / MW264333	<i>Rahnella aquatilis</i>	DSM 4594	NR_025337.1	99.57/100
LDB-23	<i>Bacillus paramycooides</i> / MW423733	<i>Bacillus paramycooides</i>	MCCC 1A04098	NR_157734.1	99.00/99.09
LBD-25	<i>Klebsiella variicola</i> / MW265009	<i>Klebsiella variicola</i>	F2R9	NR_025635.1	99/100

CRedit authorship contribution statement

DJ conceived and designed the experiments; JKN, AAB performed laboratory experiments; AS performed FTIR and SEM analysis; DJ, AAB, SKU, and SRM wrote the manuscript. All authors read and approved the final manuscript.

Declaration of Competing Interest

The authors declare that they have no known competing financial interests or personal relationships that could have appeared to influence the work reported in this paper.

Data Availability

Data will be made available on request.

Acknowledgments

The financial assistance from the All India Network Project on soil biodiversity and biofertilizers is highly acknowledged.

Disclosure statement

No potential conflict of interest was reported by the authors.

References

- Altschul, S.F., Gish, W., Miller, W., Myers, E.W., Lipman, D.J., 1990. Basic local alignment search tool. *J. Mol. Biol.* 215 (3), 403–410.
- Atalla, M.M., Zeinab, H.K., Eman, R.H., Amani, A.Y., Abeer, A.A.E.A., 2010. Screening of some marine-derived fungal isolates for lignin degrading enzymes (LDEs) production. *Agric. Biol. J. North Am.* 1 (4), 591–599.
- Atiweh, G., Parrish, C.C., Banoub, J., Le, T.T., 2022. Lignin degradation by microorganisms: a review. *Biotechnol. Prog.* 38 (2), e3226 <https://doi.org/10.1002/btpr.3226>.

- Bakar, N.A.A., Rahman, M.H.A., Shakri, N.A., Bakar, S.A., Hamid, A.A., 2018. Preliminary study on rice straw degradation using microbial inoculant under shake flask condition. *Afr. J. Biotechnol.* 17 (49), 1377–1382.
- Bandounas, L., Wierckx, N.J., de Winde, J.H., Ruijsenaars, H.J., 2011. Isolation and characterization of novel bacterial strains exhibiting ligninolytic potential. *BMC Biotechnol.* 11 (1), 94.
- Beckham, G.T., Johnson, C.W., Karp, E.M., Salvachua, D., Vardon, D.R., 2016. Opportunities and challenges in biological lignin valorization. *Curr. Opin. Biotechnol.* 42, 40–53.
- Bharti, V., Vikrant, K., Goswami, M., Tiwari, H., Sonwani, R.K., Lee, J., Tsang, D.C.W., Kim, K.H., Saeed, M., Kumar, S., et al., 2019. Biodegradation of methylene blue dye in a batch and continuous mode using biochar as packing media. *Environ. Res.* 1, 356–364.
- Bourbonnais, R., Paice, M.G., Reid, I.D., Lanthier, P., Yaguchi, M., 1995. Lignin oxidation by laccase isozymes from *Trametes versicolor* and role of the mediator 2,2-azino-bis(3-ethylbenzothiazoline-6-sulfonate) in kraft lignin depolymerization. *Appl. Environ. Microbiol.* 61, 1876–1880.
- Brink, D.P., Ravi, K., Lidén, G., et al., 2019. Mapping the diversity of microbial lignin catabolism: experiences from the eLignin database. *Appl. Microbiol. Biotechnol.* 103, 3979–4002. <https://doi.org/10.1007/s00253-019-09692-4>.
- Chandra, R., Raj, A., Purohit, H.J., Kapley, A., 2007. Characterisation and optimisation of three potential aerobic bacterial strains for kraft lignin degradation from pulp paper waste. *Chemosphere* 67 (4), 839–846.
- Chen, X., Hu, Y., Feng, S., et al., 2018. Lignin and cellulose dynamics with straw incorporation in two contrasting cropping soils. *Sci. Rep.* 8, 1633. <https://doi.org/10.1038/s41598-018-20134-5>.
- Chen, Y.H., Chai, L.Y., Zhu, Y.H., Yang, Z.H., Zheng, Y., Zhang, H., 2012a. Biodegradation of Kraft lignin by a bacterial strain *Comamonas* sp. B-9 isolated from eroded bamboo slips. *J. Appl. Microbiol.* 112 (5), 900–906.
- Chen, Y.H., Chai, L.Y., Tang, C., Yang, Z.H., Zheng, Y., Shi, Y., Zhang, H., 2012b. Kraft lignin biodegradation by *Novosphingobium* sp. B-7 and analysis of the degradation process. *Bioresour. Technol.* 123, 682–685.
- da Costa, R.R., Hu, H., Pilgaard, B., Vreeburg, S.M.E., Schückel, J., Pedersen, K.S.K., Kracún, S.K., Busk, P.K., Harholt, J., Sapountzis, P., Lange, L., Aanen, D.K., Poulsen, M., 2018. Enzyme activities at different stages of plant biomass decomposition in three species of fungus-growing termites. *Appl. Environ. Microbiol.* 84 (5), e01815–e01817. <https://doi.org/10.1128/AEM.01815-17>.
- Couger, M.B., Graham, C., Fathepure, B.Z., 2020. Genome sequence of lignin-degrading *Arthrobacter* sp. Strain RT-1, isolated from termite gut and rumen fluid. *Microbiol. Resour. Announc.* 9, 3.
- Dong, S.-J., Zhang, B.-X., Wang, F.-L., Xin, L., Gao, Y.-F., Ding, W., He, X.-M., Liu, D., Hu, X.-M., 2019. Efficient lignin degradation of corn stalk by *Trametes* with high Laccase activity and Enzymatic stability in salt and ionic liquid. *BioResources* 14 (3), 5339–5354.
- El-Hanafy, A.A., Abd-Elsalam, H.E., Hafez, E.E., 2008. Molecular characterization of two native Egyptian ligninolytic bacterial strains. *J. Appl. Sci. Res.* 4 (10), 1291–1296.
- Eslami, H., Khavidad, S.S., Salehi, F., Khosravi, R., Ali Fallahzadeh, R., Peirovi, R., Sadeghi, S., 2017. Biodegradation of methylene blue from aqueous solution by bacteria isolated from contaminated soil. *J. Adv. Environ. Health Res.* 5, 10–15.
- Faisal, U.H., Sabri, N.S.A., Yusof, N., Tahir, A.A., Said, N.N.M., Riyadi, F.A., Akhir, F.N.M., Othman, N., Hara, H., 2021. Draft genome sequence of lignin-degrading *Agrobacterium* sp. strain S2, isolated from a decaying oil palm empty fruit bunch. *Microbiol. Resour. Announc.* 10, e00259–21. <https://doi.org/10.1128/MRA.00259-21>.
- Falade, A.O., Eyisi, O.A., Mabinya, L.V., Nwodo, U.U., Okoh, A.I., 2017. Peroxidase production and ligninolytic potentials of fresh water bacteria *Raoultella ornithinolytica* and *Ensifer adhaerens*. *Biotechnol. Rep.* 16, 12–17.
- Fang, X., Li, Q., Lin, Y., Lin, X., Dai, Y., Guo, Z., Pan, D., 2018. Screening of a microbial consortium for selective degradation of lignin from tree trimmings. *Bioresour. Technol.* 254, 247–255.
- Goodman, B.A., 2020. Utilization of waste straw and husks from rice production: a review. *J. Bioresour. Bioprod.* 5 (3), 143–162. <https://doi.org/10.1016/j.jobab.2020.07.001>.
- Gupta, J., Kumari, M., Mishra, A., Swati, Akram, M., Thakur, I.S., 2022. Agro-forestry waste management-A review. *Chemosphere* 287 (3), 132321. <https://doi.org/10.1016/j.chemosphere.2021.132321>.
- Haile, A., Gelebo, G.G., Tesfaye, T., Mengie, W., Mebrate, M.A., Abuhay, A., Limeneh, D. Y., 2021. Pulp and paper mill wastes: utilizations and prospects for high value-added biomaterials. *Bioresour. Bioprocess* 8, 35. <https://doi.org/10.1186/s40643-021-00385-3>.
- Haq, I.U., Hillmann, B., Moran, M., et al., 2022. Bacterial communities associated with wood rot fungi that use distinct decomposition mechanisms. *ISME COMMUN* 2, 26. <https://doi.org/10.1038/s43705-022-00108-5>.
- Haque, M.M., Haque, M.A., Mosharaf, M.K., Marcus, P.K., 2021. Decolorization, degradation and detoxification of carcinogenic sulfonated azo dye methyl orange by newly developed biofilm consortia. *Saudi. J. Biol. Sci.* 28, 793–804.
- Harith, Z.T., Ibrahim, N.A., Yusoff, N., 2014. Isolation and identification of locally isolated lignin degrading bacteria. *J. Sustain. Sci. Manag.* 9 (2), 114–118.
- Hasanin, M.S., Mostafa, A.M., Mwafy, E.A., Darwesh, O.M., 2018. Eco-friendly cellulose nano fibers via first reported Egyptian *Humicola fuscoatra* X4: Isolation and characterization. *Environ. Nanotechnol. Monit. Manag.* 10, 409–418.
- Jain, D., Ravina, Bhojiya, A.A., Chauhan, S., Rajpurohit, D., Mohanty, S.R., 2021. Polyphasic characterization of plant growth promoting cellulose degrading bacteria isolated from organic manures. *Curr. Microbiol.* 78, 739–748. <https://doi.org/10.1007/s00284-020-02342-3>.
- Janusz, G., Pawlik, A., Sulej, J., Swiderska-Burek, U., Jarosz-Wilkolazka, A., Paszczynski, A., 2017. Lignin degradation: microorganisms, enzymes involved, genomes analysis and evolution. *FEMS Microbiol. Rev.* 41 (6), 941–962.
- Jimenez, D.J., Chaib, De Mares, M., Salles, J.F., 2018. Temporal expression dynamics of plant biomass-degrading enzymes by a synthetic bacterial consortium growing on sugarcane bagasse. *Front Microbiol.* 9, 299. <https://doi.org/10.3389/fmicb.2018.00299>.
- Karim, M.E., Dhar, K., Hossain, M.T., 2018. Decolorization of textile reactive dyes by bacterial monoculture and consortium screened from textile dyeing effluent. *J. Genet. Eng. Biotechnol.* 16, 375–380.
- Khan, S.I., Zarin, A., Ahmed, S., Hasan, F., Belduz, A.O., Çanakçı, S., Khan, S., Badshah, M., Farman, M., Shah, A.A., 2022. Degradation of lignin by *Bacillus altitudinis* SL7 isolated from pulp and paper mill effluent. *Water Sci. Technol.* 8 (1), 420. <https://doi.org/10.2166/wst.2021.610>.
- Kishor, R., Purchase, D., Saratale, G.D., Saratale, R.G., Ferreira, L.F.R., Bilal, M., Chandra, R., Bharagava, R.N., 2021a. Ecotoxicological and health concerns of persistent coloring pollutants of textile industry wastewater and treatment approaches for environmental safety. *J. Environ. Chem. Eng.* 9, 105012.
- Kishor, R., Saratale, G.D., Saratale, R.G., Ferreira, L.F.R., Bilal, M., Iqbal, H.M.N., Bharagava, R.N., 2021b. Efficient degradation and detoxification of methylene blue dye by a newly isolated ligninolytic enzyme producing bacterium *Bacillus AlbusMW407057*. *Coll. Surf. B Biointerfaces*, 111947. <https://doi.org/10.1016/j.colsurfb.2021.111947>.
- Kumar, A., Chandra, R., 2020. Ligninolytic enzymes and its mechanisms for degradation of lignocellulosic waste in environment. *Heliyon* 6 (2), e03170. <https://doi.org/10.1016/j.heliyon.2020.e03170>.
- Kumar, M., Singh, J., Singh, M.K., Singhal, A., Thakur, I.S., 2015. Investigating the degradation process of kraft lignin by β -proteobacterium, *Pandoraea* sp. ISTRKB. *Environ. Sci. Pollut. Res.* 22, 15690–15702. <https://doi.org/10.1007/s11356-015-4771-5>.
- Lee, S., Kang, M., Bae, J.-H., Sohn, J.-H., Sung, B.H., 2019. Bacterial valorization of lignin: strains, enzymes, conversion pathways, biosensors, and perspectives. *Front. Bioeng. Biotechnol.* 7, 209. <https://doi.org/10.3389/fbioe.2019.00209>.
- Li, X., Shi, Y., Kong, W., Wei, J., Song, W., Wang, S., 2022. Improving enzymatic hydrolysis of lignocellulosic biomass by bio-coordinated physicochemical pretreatment—A review. *Energy Rep.* 8, 696–709. <https://doi.org/10.1016/j.egyr.2021.12.015>.
- Ma, J., Li, Q., Wu, Y., Yue, H., Zhang, Y., Zhang, J., Shi, M., Wang, S., Liu, G.-Q., 2021. Elucidation of ligninolysis mechanism of a newly isolated white-rot basidiomycete *Trametes hirsute* X-13. *Biotechnol. Biofuels* 14, 189. <https://doi.org/10.1186/s13068-021-02040-7>.
- Malode, S.J., Prabhu, K.K., Mascarenhas, R.J., Shetti, N.P., Aminabhavi, T.M., 2021. Recent advances and viability in biofuel production. *Energy Convers. Manag.* X 10, 100070. <https://doi.org/10.1016/j.ecm.2020.100070>.
- McCarthy, A.J., Broda, P., 1984. Screening for lignin-degrading actinomycetes and characterization of their activity against [¹⁴C] lignin-labelled wheat lignocellulose. *Microbiology* 130 (11), 2905–2913.
- Mei, J., Shen, X., Gang, L., Xu, H., Wu, F., Sheng, L., 2020. A novel lignin degradation bacteria-Bacillus amyloliquefaciens SL-7 used to degrade straw lignin efficiently. *Bioresour. Technol.* 310, 123445. <https://doi.org/10.1016/j.biortech.2020.123445>.
- Nahrowi, B., Susilowati, A., Setyaningsih, R., 2018. Screening and identification of lignolytic bacteria from the forest at eastern slope of Lawu Mountain. *AIP Conf. Proc.* 2002 (1), 020–042. <https://doi.org/10.1063/1.5050138>.
- Ogunlaja, A., Nwankwo, I.N., Omaliko, M.E., Oluksani, O.D., 2020. Biodegradation of Methylene Blue as an evidence of synthetic dyes mineralization during textile effluent biotreatment by *Acinetobacter pittii*. *Environ. Process.* 7, 931–947.
- Pham, V.H.T., Kim, J., Chang, S., Chung, W., 2022. Biodegradation of methylene blue using a novel lignin peroxidase enzyme producing bacteria, named *Bacillus* sp. React3, as a promising candidate for dye-contaminated wastewater treatment. *Fermentation* 8, 190. <https://doi.org/10.3390/fermentation8050190>.
- Rahman, N.H.A., Abd Aziz, S., Hassan, M.A., 2013. Production of ligninolytic enzymes by newly isolated bacteria from palm oil plantation soils. *Bio Resour.* 8 (4), 6136–6150.
- Riyadi, F.A., Tahir, A.A., Yusof, N., Sabri, N.S.A., Noor, M.J.M.M., Akhir, F.N.M., Zakaria, Z., Hara, H., 2020. Enzymatic and genetic characterization of lignin depolymerization by *Streptomyces* sp. S6 isolated from a tropical environment. *Sci. Rep.* 10, 7813. <https://doi.org/10.1038/s41598-020-64817-4>.
- Sani, R.K., Banerjee, U.C., 1999. Decolorization of triphenylmethane dyes and textile and dye-stuff effluent by *Kurtzia* sp. *Enzym. Microb. Technol.* 24 (7), 433–437.
- Saratale, R.G., Saratale, G.D., Kalyani, D.C., Chang, J.S., Govindwar, S.P., 2009. Enhanced decolorization and biodegradation of textile azo dye Scarlet R by using developed bacterial consortium-GR. *Bioresour. Technol.* 100 (9), 2493–2500.
- Shamseldin, A., Abdelkhalek, A.A., 2015. Isolation and identification of newly effective bacterial strains exhibiting great ability of lignin and Rice straw biodegradation. *Int. J. Curr. Microbiol. Appl. Sci.* 4 (6), 1039–1049.
- Sharif-Yazdi, M.K., Azimi, C., Khalili, M.B., 2001. Isolation and identification of bacteria present in the activated sludge unit, in the treatment of industrial waste water. *Iran. J. Public Health* 91–94.
- Shi, Y., Yan, X., Li, Q., Wang, X., Xie, S., Chai, L., Yuan, J., 2017. Directed bioconversion of Kraft lignin to polyhydroxy alkanolate by *Cupriavidus basilensis* B-8 without any pretreatment. *Process Biochem.* 52, 238–242.
- Singh, R., Kumar, M., Mittal, A., Mehta, P.K., 2017. Microbial metabolites in nutrition, healthcare and agriculture. *3 Biotech* 7 (1), 15. <https://doi.org/10.1007/s13205-016-0586-4>.
- Tamura, K., Stecher, G., Peterson, D., Filipiński, A., Kumar, S., 2013. MEGA6: molecular evolutionary genetics analysis version 6.0. *Mol. Biol. Evol.* 30 (12), 2725–2729.
- Thimmaiah, S.K., 2009. *Standard Methods Of Biochemical Analysis*. Kalyani Publishers.

- Thompson, J.D., Higgins, D.G., Gibson, J., 1994. CLUSTAL W: improving the sensitivity of progressive multiple sequence alignment through sequence weighting, position-specific gap penalties and weight matrix choice. *Nucleic Acid. Res* 22 (22), 4673–4680.
- Tsegaye, B., Balomajumder, C., Roy, P., 2018. Biodegradation of wheat straw by *Ochrobactrumoryzae* BMP03 and *Bacillus* sp. BMP01 bacteria to enhance biofuel production by increasing total reducing sugars yield. *Environ. Sci. Pollut. Res.* 25 (30), 30585–30596.
- Upadhyay, S.K., Singh, D.P., Saikia, R., 2009. Genetic diversity of plant growth promoting rhizobacteria isolated from rhizospheric soil of wheat under saline condition. *Curr. Micro* 59, 489–496. <https://doi.org/10.1007/s00284-009-9464-1>.
- Upadhyay, S.K., Singh, J.S., Singh, D.P., 2011. Exopolysaccharide-producing plant growth-promoting rhizobacteria under salinity condition. *Pedosphere* 21, 214–222. [https://doi.org/10.1016/S1002-0160\(11\)60120-3](https://doi.org/10.1016/S1002-0160(11)60120-3).
- Verma, M., Ekka, A., Mohapatra, T., Ghosh, P., 2020. Optimization of kraft lignin decolorization and degradation by bacterial strain *Bacillus velezensis* using response surface methodology. *J. Environ. Chem. Eng.* 8 (5), 104–270.
- Wang, M., Dessie, W., Li, H., 2021. Chemically modified lignin: correlation between structure and biodegradability. *J. Renew. Mater.* 9, 2119.
- Wu, Z., Peng, K., Zhang, Y., Wang, M., Yong, C., Chen, L., Qu, P., Huang, H., Sun, E., Pan, M., 2022. Lignocellulose dissociation with biological pretreatment towards the biochemical platform: a review. *Mater. Today Bio* 16, 100445. <https://doi.org/10.1016/j.mtbio.2022.100445>.
- Xiong, X.Q., Liao, H.D., Ma, J.S., Liu, X.M., Zhang, L.Y., Shi, X.W., Yang, X.L., Lu, X.N., Zhu, Y.H., 2013. Isolation of a rice endophytic bacterium, *Pantoea* sp. S d-1, with ligninolytic activity and characterization of its rice straw degradation ability. *Lett. Appl. Microbiol.* 58 (2), 123–129.
- Xu, Z., Qin, L., Cai, M., Hua, W., Jin, M., 2018. Biodegradation of kraft lignin by newly isolated *Klebsiella pneumoniae*, *Pseudomonas putida*, and *Ochrobactrum tritici* strains. *Environ. Sci. Pollut. Res.* 25, 14171–14181. <https://doi.org/10.1007/s11356-018-1633-y>.
- Yang, C.X., Wang, T., Gao, L.N., Yin, H.J., Lu, X., 2017. Isolation, identification and characterization of lignin-degrading bacteria from Qinling, China. *J. Appl. Microbiol.* 123 (6), 1447–1460.
- Yu, G., Wen, X., Li, R., Qian, Y., 2009. In vitro degradation of a reactive azo dye by crude ligninolytic enzymes from non immersed liquid culture of *Phanerochaete chrysosporium*. *Process Biochem.* 41 (9), 1987–1993.
- Zeng, Y., Zhao, S., Yang, S., Ding, S.Y., 2014. Lignin plays a negative role in the biochemical process for producing lignocellulosic biofuels. *Curr. Opin. Biotechnol.* 27, 98–45.
- Zhang, W., Ren, X., Lei, Q., Wang, L., 2021. Screening and comparison of lignin degradation microbial consortia from wooden antiques. *Molecules* 26, 2862 <https://doi.org/10.3390/molecules26102862>.



Comparative evaluation of native *Trichoderma* species from groundnut rhizosphere against stem rot caused by *Sclerotium rolfsii* Sacc.

M. Raja^{1,4} · Rakesh Kumar Sharma¹ · Prashant Prakash Jambhulkar² · R. Thava Prakasa Pandian³ · Pratibha Sharma⁴

Received: 12 November 2022 / Revised: 20 January 2023 / Accepted: 27 February 2023
© Indian Phytopathological Society 2023

Abstract

Sclerotium rolfsii Sacc. is one of the important soil borne pathogen causing stem rot of groundnut prevalent in all growing area worldwide. The present study aimed on the identification of native *Trichoderma* isolates, and its efficacy against the stem rot pathogen in groundnut at field level. Thirty-five isolates of *Trichoderma* spp. isolated from the groundnut rhizosphere were comparatively evaluated for their biocontrol potential against *S. rolfsii* Sacc. and growth promoting traits in groundnut. The morphological studies of the 35 isolates were supported molecularly by amplifying of ITS region and classified into four species namely, *T. asperellum*, *T. citrinoviride*, *T. longibrachiatum* and *T. harzianum* which were further subjected to biocontrol efficacy tests. The highly efficient representative isolates namely, *T. harzianum* Thar23, *T. asperellum* Tasp49, *T. longibrachiatum* Tlongi5 and *T. citrinoviride* Tcitr2 were evaluated to produce lytic enzymes and growth promoting traits. The comparative study of these isolates revealed that, *T. harzianum* Thar23 produced significant ($P < 0.05$) amount of lytic enzymes viz., chitinase (31.36 U/ml), β 1, 3 glucanase (4.1 U/ml) and protease (2.76 U/ml). *T. harzianum* Thar23 promotes plant growth traits namely germination efficacy (31.48%), increase in the shoot length (42%) and root length (42.43%), improved vigor index, and increased relative water content (25.56%). Soil application, seed treatment and drenching with the powder formulation of Thar23 in field for the years 2019 and 2020 significantly ($P < 0.05$) reduced stem rot disease incidence to 59.45% and 53.79% and increased pod yield to 2.85 t/ha and 2.68 t/ha respectively. *T. harzianum* isolate Thar23 will help the groundnut growers for eco-friendly management of stem rot disease and increased yield.

Keywords Groundnut · Lytic enzymes · *S. rolfsii* · Stem rot · *Trichoderma* spp.

Introduction

Groundnut (*Arachis hypogaea* L.) is an important food and oil seed crop due to its high protein and oil content. Several biotic and abiotic factors are responsible for dismal

productivity. Diseases like stem rot, collar rot, root rot, leaf spot, bud necrosis, etc., are critical. Stem rot is also known as sclerotium blight caused by soil borne fungi *S. rolfsii* causes yield loss over 20–25 percent (Annual Report 2015–16). Under warm and high moisture conditions, white mycelium spread over the plant debris, soil and infect the host. The dark brown sclerotia of the pathogen are hard, spherical and 0.5–1.5 mm in size often found in the infected are of host and soil (Aycock 1966). Though fungicides are effective against pathogens, but they cause adverse effect on the environment thus can be replaced by biocontrol agents.

Trichoderma spp. (Teleomorph: *Hypocrea*) is an omnipresent ascomycetous fungus known for its biocontrol and industrial properties. This fungi were named *Trichoderma* in 1794 (Persoon 1794) and years later in 1865, the sexual stage *Hypocrea* species was suggested (Tulasne and Tulasne 1865). Diverse species of *Trichoderma* namely, *T. harzianum*, *T. asperellum*, *T. viride*, *T. virens*, *T. hamatum*

✉ Pratibha Sharma
psharma032003@yahoo.co.in

¹ Department of Biosciences, Manipal University Jaipur, Dehmi Kalan, Jaipur, Rajasthan 303007, India

² Department of Plant Pathology, Rani Lakshmi Bai Central Agricultural University, Jhansi, Uttar Pradesh 284003, India

³ Division of Plant Protection, ICAR-Central Plantation Crops Research Institute, Regional Station, Vittal, Karnataka 574 243, India

⁴ Department of Plant Pathology, Sri Karan Narendra Agriculture University, Jobner, Jaipur, Rajasthan 303328, India

and *T. atroviride* have been reported as biocontrol agents. *T. reesei*, *T. parareesei* and *T. longibrachiatum* are known for industrial enzyme production. *Trichoderma* species are widely present in the soil rhizosphere and documented for symbiotic relationship with the host roots. Due to the importance of the application of *Trichoderma* spp. as biocontrol agent in field condition, it is necessary to explore its biogeography. There are different studies conducted by the researchers to decipher the diversity of the native *Trichoderma* spp. and its application against major plant pathogens at national (Kumar et al. 2012; Agrawal and Kotasthane 2012; Devi et al. 2021; Manzar et al. 2021; Jambhulkar et al. 2022) and global (Li et al. 2016; Boat et al. 2020; Ma et al. 2020; Nofal et al. 2021). However, there is a need to explore the diversity of the native species at groundnut growing area of Jaipur, a semi-arid eastern plain zone of Rajasthan (Agro-climatic Zone- III-A), India.

There are various biocontrol mechanisms viz., mycoparasitism, antibiosis, induced systemic resistance in *Trichoderma* spp. and also known for production of many lytic enzymes viz., chitinases, glucanases, xylanase and proteases etc., as their primary weapons against the fungal pathogens (Sharma et al. 2014) and induce the systemic defence response by activating defence enzymes like peroxidases (PODs), polyphenol oxidases (PPO) and phenylalanine ammonia lyase (PAL) (Malolepsza et al. 2017). Plant growth promotion is crucial component of *Trichoderma* spp. which helps in improvement of plant growth in terms of increased plant biomass, root and shoot length and grain yield. *Trichoderma* colonizes fully on root tissues and triggers various mechanisms which induce plant growth promotion, facilitate nutrient uptake, induce plant defence mechanisms, helps in rhizosphere construction, increase carbohydrate metabolism, induce of phytohormones, root exudates and photosynthesis in host (Sallam et al. 2019). Among the genus of *Trichoderma* spp., *T. harzianum* is the most researched biocontrol species followed by others such as *T. viride*, *T. asperellum*, *T. hamatum*, *T. virens* and *T. koningii* (Keswani et al. 2014). Species like *T. longibrachiatum* and *T. citrinoviride* needs to be studied for its biocontrol and plant growth promoting capabilities. Therefore, the comparative evaluation of biocontrol efficacy and plant growth promoting traits of native isolates of *Trichoderma* spp. will be helpful in the characterization of biocontrol control agents and potential strains can be utilized at field conditions.

In the present study, we have isolated and characterized native isolates of *Trichoderma* from groundnut rhizosphere and potent isolates were comparatively evaluated to assess biocontrol and plant growth promoting potential against groundnut stem rot pathogen *S. rolfsii* under field conditions.

Materials and methods

Collection and isolation of *Trichoderma* isolates

The 60 rhizospheric soil samples were collected from groundnut growing areas of Jaipur (Agro-climatic Zone- III-A), a semi-arid eastern plain zone of Rajasthan, India. The longitude and latitude of collection locations were recorded and are given Table 1. For the isolation of *Trichoderma* spp., the rhizospheric soil samples were serially diluted on *Trichoderma* selective medium (TSM) (Elad et al. 1981) and incubated at $28 \pm 1 \text{ }^\circ\text{C}$ for 4 days. The newly emerging mycelia of fungal colonies were subcultured to fresh potato dextrose agar (PDA) plates and incubated at $28 \pm 1 \text{ }^\circ\text{C}$ for 7 days and maintained in potato dextrose agar (PDA) slants at $4 \text{ }^\circ\text{C}$ for further use in experiment. Culture of *S. rolfsii* was available at Department of Plant Pathology, SKN Agriculture University, Jobner- Jaipur.

Identification of *Trichoderma* isolates

Morphological identification

The purified 35 isolates were identified based on the different morphological characters viz., cultural characters like colour, growth and texture, microscopic features branching of conidiophores, phialides disposition, size and shape of conidia were identified based on the Rifai (1969), Bissett (1984) and Samuels et al. (1999).

Molecular identification

Actively growing *Trichoderma* isolates (5 mm disc) were inoculated into 50 mL potato dextrose broth (PDB) (HIMEDIA Labs, India) and incubated at $28 \pm 2 \text{ }^\circ\text{C}$ for 5–6 days at 180 rpm. The fungal mycelia were harvested using Whatman No. 1 filter paper and washed three times with sterile distilled water. Collected mycelium was grounded finely with liquid nitrogen and stored at $-80 \text{ }^\circ\text{C}$ till further use. Cetyltrimethyl ammonium bromide (CTAB) method was followed for total fungal DNA extraction (Culling 1992). The internal transcribed spacer (ITS) region was amplified by using universal primers ITS1 (5'-TCCGTAGGTGAACCTGCGG-3')/ITS4 (5'-TCCTCCGCTTATTGATATGC3') (White et al. 1990).

PCR reaction mixture was prepared in the final volume of 25 μl containing 2.5 μl of 10X PCR buffer with MgCl_2 , 1 μl of forward and reverse primer each (10 pM), 0.5 μl of 10 mM dNTP's, 0.5 μl of DyNAzyme II DNA Polymerase (2 U/ μl), 2 μl of genomic DNA (50 ng/ μl) and 17.5 μl of Molecular biology grade water and amplified by following

Table 1 List of *Trichoderma* isolates along with NCBI accession numbers and morphological specifications

S. no.	Isolate code	Location	Latitude and longitude	NCBI accession number	<i>Trichoderma</i> spp.	Morphological characteristics
1	Tasp1	Jobner, Jaipur	26° 58' 33.6" N 75° 22' 10.7" E	KT426888	Group I— <i>Trichoderma asperellum</i>	Colony: dark green Conidiophores: regularly branched, with lateral branches and paired Phialides: whorls of 2–4 phialides, straight, slightly wider in middle than base and ampulliform Conidia: globose to subglobose
2	Tasp2	Durgapura, Jaipur	26° 50' 41.0" N 75° 46' 52.5" E	KT426889		
3	Tasp3	Bagru, Jaipur	26° 49' 02.3" N 75° 33' 09.8" E	KT426890		
4	Tasp4	Samod Jaipur	27° 14' 01.5" N 75° 46' 53.1" E	KT426891		
5	Tasp5	Sambhar, Jaipur	27° 00' 12.3" N 75° 11' 24.7" E	KT426892		
6	Tasp6	Chaksu Jaipur	26° 35' 55.6" N 75° 56' 27.1" E	KU170973		
7	Tasp46	Jobner, Jaipur	26° 58' 59.3" N 75° 32' 35.1" E	MT065825		
8	Tasp47	Chaksu Jaipur	26° 36' 14.7" N 75° 55' 33.1" E	MT065826		
9	Tasp48	Durgapura, Jaipur	26° 55' 51.8" N 75° 45' 14.2" E	MT065827		
10	Tasp49	Samod Jaipur	27° 12' 32.6" N 75° 46' 57.5" E	MT065828		
11	Tasp50	Jobner, Jaipur	26° 59' 54.9" N 75° 22' 06.5" E	MT065829		
12	Tasp51	Bagru, Jaipur	26° 50' 08.7" N 75° 33' 19.1" E	MT065830		
13	Thar1	Durgapura, Jaipur	26° 55' 35.0" N 75° 42' 06.1" E	KT426893	Group II— <i>Trichoderma harzianum</i>	Colony: whitish green to pale green Conidiophores: flexuous, branches almost right angled Phialides: whorls of 2–6, ampulliform to laciniform, subulate, short, skittle-shaped, narrower at the base Conidia: globose to subglobose to short obovoid
14	Thar2	Samod Jaipur	27° 11' 08.5" N 75° 46' 59.9" E	KT426894		
15	Thar3	Jobner, Jaipur	26° 57' 56.3" N 75° 22' 35.9" E	KT426895		
16	Thar4	Durgapura, Jaipur	26° 50' 30.0" N 75° 47' 00.2" E	KT426896		
17	Thar5	Jobner, Jaipur	26° 58' 46.2" N 75° 22' 21.1" E	KT426897		
18	Thar20	Samod Jaipur	27° 11' 08.5" N 75° 46' 59.9" E	MT065754		
19	Thar21	Durgapura, Jaipur	26° 50' 46.1" N 75° 46' 46.4" E	MT065755		
20	Thar22	Bagru, Jaipur	26° 50' 08.7" N 75° 33' 19.1" E	MT065756		
21	Thar23	Jobner, Jaipur	26° 58' 33.6" N 75° 22' 10.7" E	MT065757		
22	Thar24	Sambhar, Jaipur	26° 52' 26.2" N 75° 07' 38.4" E	MT065758		
23	Thar25	Chaksu Jaipur	26° 35' 55.6" N 75° 56' 27.1" E	MT065759		

Table 1 (continued)

S. no.	Isolate code	Location	Latitude and longitude	NCBI accession number	<i>Trichoderma</i> spp.	Morphological characteristics
24	Tlongi1	Jobner, Jaipur	26° 93' 21.6" N 75° 37' 73.1" E	KT426898	Group III— <i>Trichoderma longibrachiatum</i>	Colony: dark olive green with yellow tinge Conidiophores: long main branches produce only a few side short branches Phialides: lageniform or bottle shaped Conidia: sub-cylindrical with distinct truncate base
25	Tlongi2	Bagru, Jaipur	26° 49' 02.3" N 75° 33' 09.8" E	KT426899		
26	Tlongi3	Chaksu Jaipur	26° 36' 14.7" N 75° 55' 33.1" E	KT426900		
27	Tlongi4	Samod Jaipur	27° 12' 32.7" N 75° 51' 31.3" E	KT426901		
28	Tlongi5	Sambhar, Jaipur	27° 00' 12.3" N 75° 11' 24.7" E	KT426902		
29	Tlongi25	Durgapura, Jaipur	26° 55' 35.0" N 75° 42' 06.1" E	MT052706	Group IV— <i>Trichoderma citrinoviride</i>	Colony: dusky yellowish green Conidiophores: main branches long and relatively straight Phialides: more elongate, lageniform or narrowly shaped Conidia: less ellipsoidal, apex broadly rounded
30	Tcetri1	Bagru, Jaipur	26° 48' 20.4" N 75° 33' 05.6" E	MT065795		
31	Tcetri2	Chaksu Jaipur	26° 34' 58.2" N 75° 59' 48.2" E	MT065796		
32	Tcetri3	Samod Jaipur	27° 12' 32.7" N 75° 51' 31.3" E	MT065797		
33	Tcetri4	Sambhar, Jaipur	27° 01' 58.6" N 75° 18' 48.0" E	MT065798		
34	Tcetri5	Jobner, Jaipur	26° 59' 40.4" N 75° 20' 49.4" E	MT065799		
35	Tcetri6	Durgapura, Jaipur	26° 50' 24.1" N 75° 46' 51.2" E	MT065800		

protocol: initial denaturation for 1 min at 95 °C, 30 cycles of denaturation for 30 s at 95 °C, primer annealing for 1 min at 60 °C, extension at 72 °C for 1 min and a final extension period for 7 min at 72 °C. The amplified PCR products were electrophoretically separated using 1.2% agarose gel in 1X TAE buffer at 80 V for 1 h. Amplified PCR fragments were visualized in UV light and gel documented. The desired amplified products were gel eluted (GeneJET Gel Extraction Kit, Thermo Scientific™, USA) and sequenced through the Sanger sequencing method (Eurofins Pvt. Ltd). The sequence contig was prepared using CAP3 sequence assembly program and aligned sequence were confirmed with nBLAST (www.ncbi.nlm.nih.gov/BLAST) and submitted to NCBI (<http://www.ncbi.nlm.nih.gov/>).

Phylogenetic analysis

The phylogenetic tree was constructed by aligning the generated sequences using ClustalW multiple sequence alignment program (Thompson et al. 1994) and MEGA7 software program (Kumar et al. 2016). Maximum Composite Likelihood (MCL) method was used to estimate the pairwise distances and bootstrap method was used to study the nodal robustness with a replication of 1000. The Kimura 2-parameter

distance model (Kimura 1980) was used for the construction of maximum-likelihood (ML) tree (Kumar et al. 2016).

Screening for antagonistic activity of *Trichoderma* isolates

Antagonistic activity of different 35 *Trichoderma* isolates against groundnut stem rot pathogen *S. rolfsii* was done by dual culture plate method (Dennis and Webster 1971). Seven days old actively growing mycelial disc (5 mm) of *Trichoderma* isolates and *S. rolfsii* were placed on PDA plates opposite from the periphery and plates without *Trichoderma* served as a control and plates were incubated at 28 ± 2 °C for 5–7 days. The percentage of inhibition was calculated by following formula

$$\text{Percentage of inhibition (PI)} = \frac{C-T}{C} \times 100$$

where 'C' is the radial growth of pathogen in the control PDA plate in cm and 'T' is the radial growth pathogen in test plate in cm.

The antagonism level of these isolates was evaluated according to Bell et al. (1982). *Trichoderma* isolates with significant antagonistic potential against *S. rolfsii* were

evaluated for production of lytic enzymes and plant growth promoting traits in groundnut.

Lytic enzymes assay of selected isolates of four *Trichoderma* spp.

Preparation of cell-free culture filtrate

The cell-free culture filtrate from selected isolates *T. harzianum* Thar23, *T. asperellum* Tasp49, *T. longibrachiatum* Tlongi5 and *T. citrinoviride* Tcitr2 were prepared using freeze-dried mycelia of *S. rolfsii* as a sole carbon source. Actively grown mycelial mat of *S. rolfsii* was harvested from 7 days old PDB broth and homogenized by using liquid nitrogen. The freeze dried pathogen mycelial powder was stored at $-20\text{ }^{\circ}\text{C}$. A 5 mm mycelial disc of actively growing selected *Trichoderma* isolates was inoculated in autoclaved 250 ml of minimal synthetic broth (MSB) containing (g/l) $\text{FeSO}_4\text{-}0.01$, $\text{MnSO}_4\text{-}0.01$, $\text{ZnSO}_4\text{-}0.01$, $\text{KCl}\text{-}0.5$, $\text{MgSO}_4\text{-}0.5$, $\text{K}_2\text{HPO}_4\text{-}1.0$, $\text{NaNO}_3\text{-}3.0$; pH 5.5 amended with 1% freeze dried mycelia of *S. rolfsii* and flasks were kept at $28\pm 2\text{ }^{\circ}\text{C}$ at 180 rpm and filtered through Whatman no. 1 filter paper at different time interval from day 1 to 10.

Estimation of chitinase (EC 3.2.1.14)

Dinitrosalicylic acid (DNSA) method was used to estimate the chitinase production from *Trichoderma* isolates. One millilitre of culture filtrate with 0.5 ml of colloidal chitin and 0.5 ml of 1 M sodium acetate buffer was mixed and incubated at $40\text{ }^{\circ}\text{C}$ for 6 h and centrifuged at 12,000 rpm for 5 min at $4\text{ }^{\circ}\text{C}$. One millilitre of supernatant was mixed with 0.5 ml of DNSA in 1 M NaOH and 0.1 ml of 10 M NaOH and kept at $100\text{ }^{\circ}\text{C}$ for 5 min. The assay mixture was recorded spectrophotometrically at 582 nm and N-acetylglucosamine (GlcNAc) was used as standard. Specific chitinolytic activity was defined as unit of GlcNAc released by 1 ml of enzyme solution under assay conditions.

Estimation of β -1,3-glucanase (EC 3.2.1.39)

β -1,3-Glucanase activity was determined using laminarin as a substrate. The assay mixture contains 0.5 ml of culture filtrate with 1 ml of laminarin in 50 mM acetate buffer (pH 4.8) and was incubated at $50\text{ }^{\circ}\text{C}$ for 10 min. One ml of dinitrosalicylic acid was added to the reaction mixture and kept at $95\text{ }^{\circ}\text{C}$ for 5 min and total amount of reducing sugar was recorded at 540 nm. One unit of β -1,3-glucanase activity was defined as the amount of enzyme required to release one μmol of reducing sugar per minute.

Estimation of protease (EC 3.4.21.4)

Protease activity was determined using 1% casein as substrate in 50 mM phosphate buffer (pH 7.0) was denatured at $100\text{ }^{\circ}\text{C}$ for 15 min in the water bath. The reaction mixture containing 1 ml of casein substrate was added with 3 ml of 10% trichloroacetic acid (TCA) and kept at $4\text{ }^{\circ}\text{C}$ for 1 h. This mixture was centrifuged at 8000 rpm for 15 min at $4\text{ }^{\circ}\text{C}$, and supernatant was recorded at 280 nm. One unit of protease activity was defined as the amount of enzyme solution equivalent to release 1 μmol of tyrosine under assay conditions.

Plant growth promoting traits of selected isolates of four *Trichoderma* spp. in groundnut

The plant growth promoting ability of the selected *Trichoderma* isolates in groundnut (RG-510 Spreading variety) was studied under pot conditions. Groundnut seeds were treated with spore suspensions of each selected *Trichoderma* isolates containing 2×10^8 spores ml^{-1} and were soaked for one hour. Spore suspensions from selected isolates were prepared from PDA plates containing 7 days old cultures of *Trichoderma* by scraping gently on the surface of the plates with sterile distilled water containing 0.01% Tween 20 and filtered through two layers of sterile muslin cloth. The spore concentration was adjusted with the aid of haemocytometer.

Efficacy on seed germination, root, and shoot length and relative water content (RWC)

The germination efficacy of selected *Trichoderma* isolates in groundnut seeds was studied by treating with *Trichoderma* spore suspension (2×10^8 spores ml^{-1}) and transferred to respective pots containing sterile soil along with farm yard manure (FYM) in 10:1 ratio. Seeds treated with sterile water served as control. After 10 days, the number of germinated seedlings in each replication was counted and the germination was calculated and expressed by using the following formula

$$\begin{aligned} &\text{Germination percentage (\%)} \\ &= \frac{\text{Number of germinated seeds}}{\text{Total number of seeds}} \times 100 \end{aligned}$$

Groundnut plants (30 days old) were harvested from each treatment and washed three times with sterile distilled water. The root and shoot length were observed and based on the root and shoot length with germination percentage, the vigour index was calculated by using formula given by Abdul Baki and Anderson (1973).

$$\text{Vigour Index (VI)} = (\text{Mean shoot length} + \text{Mean root length}) \times \text{Germination (\%)}$$

To determine relative water content, the harvested plants were air dried and weighed (fresh weight). For dry weight, the plants were kept in hot air oven at 100 °C for 20 min, and then kept at 80 °C for 24 h at oven then weighed and recorded (Tian et al. 2015). Each control and treatment were repeated three times. The following formula was used to determine RWC of shoots and roots.

$$\text{RWC (\%)} = \frac{\text{FW} - \text{DW}}{\text{FW}} \times 100$$

where, RWC is relative water content, FW: fresh weight, and DW: dry weight.

Groundnut stem rot management by application of selected isolates of four *Trichoderma* spp. under field conditions

The field experiment was conducted in the randomized block design with three replications in the kharif season of 2019 and 2020 at Agronomy Farm, S.K.N. College of Agriculture, Jobner situated 26° 05' N-latitude and 75° 28' E-longitudes and at an altitude of 427 m above mean sea level in Jaipur district of Rajasthan. The region falls in agroclimatic zone III-a (semi-arid eastern plain), and variety RG 510 was used for both experimental years. The seeds were treated with talc-based bioformulation of different *Trichoderma* isolates at 8 g/kg. The spore concentration of the bioformulation was maintained 2×10^8 CFU/g. The treatment schedule is as follows.

T1—Soil application with *T. asperellum* Tasp49 enriched FYM (10: 200) + seed treatment with *T. asperellum* Tasp49 at 8 g/kg seeds + drenching with *T. asperellum* Tasp49 at 8 ml/l at 40 days after sowing.

T2—Soil application with *T. harzianum* Thar23 enriched FYM (10: 200) + seed treatment with *T. harzianum* Thar23 at 8 g/kg seeds + drenching with *T. harzianum* Thar23 at 8 ml/l at 40 days after sowing.

T3—Soil application with *T. longibrachiatum* Tlongi5 enriched FYM (10: 200) + seed treatment with *T. longibrachiatum* Tlongi5 at 8 g/kg seeds + drenching with *T. longibrachiatum* Tlongi5 at 8 ml/l at 40 days after sowing.

T4—Soil application with *T. citrinoviride* Tcetri2 enriched FYM (10: 200) + seed treatment with *T. citrinoviride* Tcetri2 at 8 g/kg seeds + drenching with *T. citrinoviride* Tcetri2 at 8 ml/l at 40 days after sowing.

T5—Untreated control.

Disease incidence was monitored on a weekly basis by observation of symptoms and was calculated by the following formula

$$\text{Disease incidence (DI) (\%)} = \frac{\text{Number of infected plants}}{\text{Total number of plants}} \times 100$$

Shelling of the well dried 100 g pods from each treatment was done and recorded weight of kernels and the shelling percentage was calculated by following formula

$$\text{Shelling percentage} = \frac{\text{Kernel weight}}{\text{Pod weight}} \times 100$$

The pod yield was calculated from each treatment separately after threshing, winnowing, and cleaning the produce was weighed and converted in terms of Tones/ha.

Statistical analysis

The normality of the data was checked and found that data are treatment-wise normally distributed. All the treatments replicated thrice in a completely randomized design and the descriptive statistics of the data are presented as mean value \pm SD. Significance of mycelial growth inhibition, enzyme production and growth promotion were tested by a one-way analysis of variance (ANOVA). The data were analysed by ANOVA using R-programming language and treatment means were compared using Fisher's Protected LSD test at $p=0.05$ (Gomez and Gomez 1984).

Results

Morphological characteristics of *Trichoderma* isolates

Thirty-five isolates of *Trichoderma* spp. were collected from the rhizospheric soil of groundnut growing area of Jaipur District (26.9706° N, 75.3791° E) of Rajasthan, India, which were further morphologically characterized through microscopic studies. Based on morphological features the isolates were classified into four groups I *T. asperellum*, group II *T. harzianum*, group III *T. longibrachiatum* and group IV *T. citrinoviride* (Table 1). The group I consisted of 12 isolates of *T. asperellum* showed dark green and compact colonies on PDA medium with the typically paired and regularly branched conidiophores (Table 1). The conidia were globose to sub-globose in shape with the size of 2.5–3 μ m (Fig. 1). A total of 11 isolates of *T. harzianum* in grouped exhibited whitish green to pale green on PDA surface with short branched and irregular conidiophores at right angle. The shape of conidia was globose to sub-globose to short obovoid with size of 1.5–2 μ m (Fig. 1). The 6 isolates of group III were yellowish green or dark olive green on PDA plates with short, branched conidiophores, lageniform or bottle shaped conidia on long main branches with the size of

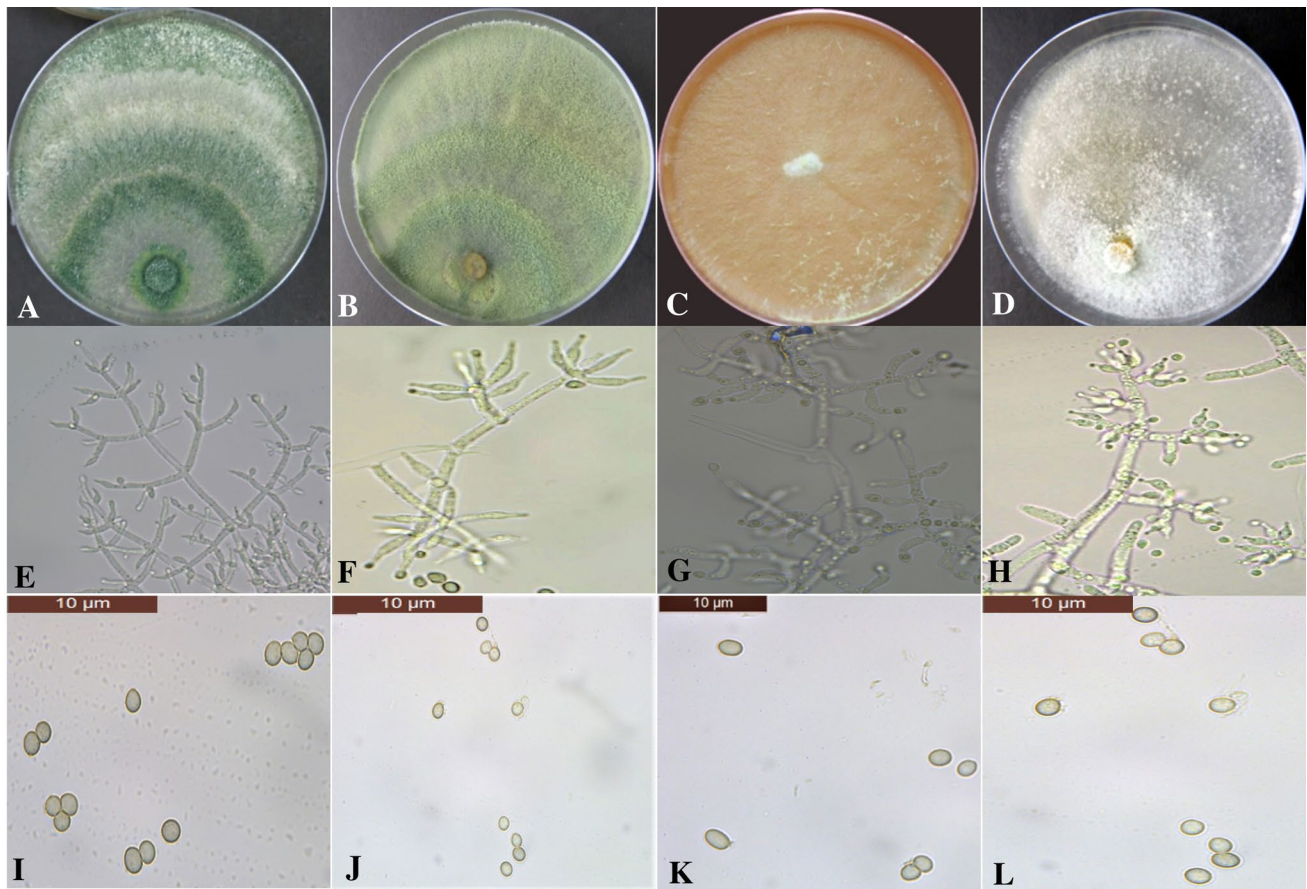


Fig. 1 PDA culture plates showing 7 days old representative isolates of *Trichoderma* spp. **a, e, i** Showing the growth on PDA, branching pattern of phialides and conidia of *T. asperellum* Tasp49. **b, f, j** Showing the growth on PDA, branching pattern of phialides and

conidia of *T. harzianum* Thar23. **c, f, k** Showing growth on PDA, branching pattern of phialides and conidia of *T. longibrachiatum* Tlongi5. **d, h, l** Showing growth on PDA, branching pattern of phialides and conidia of *T. citrinoviride* Tcitr2 (scale bar 10 µm)

2–2.5 µm were classified as *T. longibrachiatum*. The group IV was classified as *T. citrinoviride* consisted of 6 isolates which showed dusky yellowish green colony on PDA with less ellipsoidal, broadly rounded apex conidia with size of 2–2.5 µm, with relatively straight long branched conidiophores, relatively elongate, lageniform or narrowly shaped phialides (Fig. 1).

Molecular characterization of *Trichoderma* isolates and phylogenetic analysis

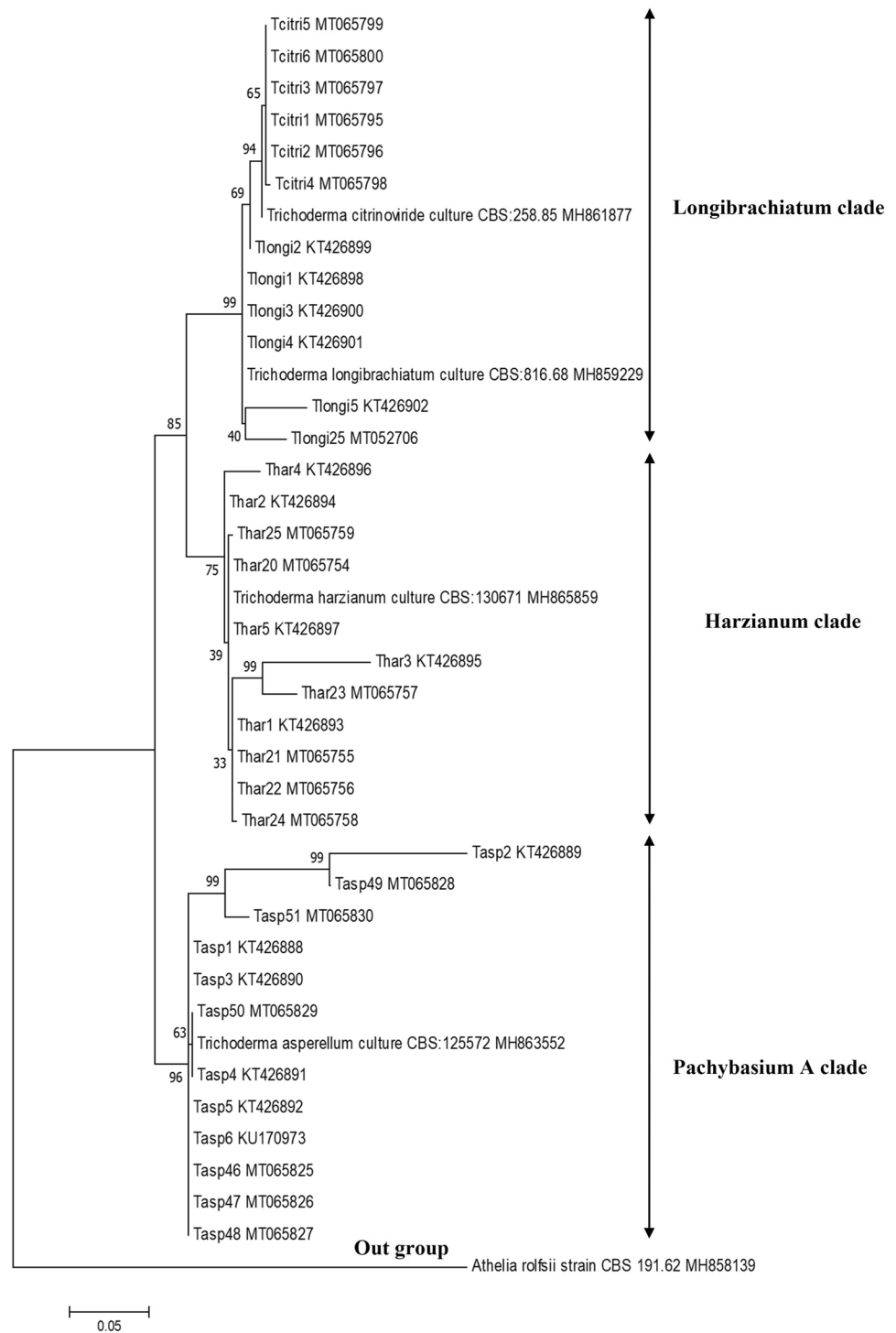
A single amplified product around 550–650 bp of all 35 isolates of *Trichoderma* spp. were sequenced and confirmed with BLAST search tool and submitted to NCBI (Table 1). The BLAST analysis was differentiating at species level with homology percentage of 95–99%, and results obtained from phylogenetic analysis of ITS sequences showed that the 35 *Trichoderma* isolates can be separated into four different species with three distinct clades of *Trichoderma* namely (Fig. 2), the Pachybasium A clade (*T. asperellum*), the

Harzianum clade (*T. harzianum*), and the Longibrachiatum clade (*T. longibrachiatum* and *T. citrinoviride*). The Pachybasium A clade consists of 12 isolates of *T. asperellum* with a bootstrap value of 98%, the clade Harzianum consisting of 11 isolates of *T. harzianum* supported by bootstrap value of 81%. The closely associated species both *T. longibrachiatum* (6 isolates) and *T. citrinoviride* (6 isolates), fall in the section Longibrachiatum clade with 96% bootstrap value indicating the close relationship of both species (Fig. 2).

Antagonistic activity of *Trichoderma* isolates against *S. rolfsii*

The antagonistic activity of 35 isolates of *Trichoderma* spp. against *S. rolfsii* was evaluated by dual culture assay. Two groups of *T. asperellum* and *T. harzianum* exhibited higher antagonistic activity with the range of 62% to 81.7% against *S. rolfsii*. Group III *T. longibrachiatum* and Group IV *T. citrinoviride* recorded moderate or lower mycelial inhibition from 51.43 to 67.5% (Fig. 3). The degree of antagonism was

Fig. 2 Phylogenetic relationships of *Trichoderma* isolates inferred by analysis of ITS region and constructed using two parameter model implemented in the MEGA7 inferred by using the Maximum Likelihood method and Tamura-Nei model. Analysis was conducted in MEGA 7 and the percentage of replicate trees in which the associated taxa clustered together in the bootstrap test



measured by the scale described by Bell et al. (1982). Isolates from *T. asperellum* group namely Tasp1, Tasp3, Tasp6, Tasp46 and Tasp49, from *T. harzianum* group namely, Thar1, Thar3, Thar4, Thar5, Thar20, Thar21, Thar22, Thar23, Thar24 and Thar25 exhibited class 1 level of antagonism, whereas isolates like Tasp2, Tasp4, Tasp5, Tasp47, Tasp48, Tasp50 and Tasp51 from *T. asperellum* group, one

isolate from *T. harzianum* Thar2, some of the isolates from *T. longibrachiatum* group namely Tlongi1, Tlongi2, Tlongi4, Tlongi5 and Tcitr2, Tcitr4 and Tcitr6 from *T. citrinoviride* group expressed the class 2 level of antagonism. Class 3 level of antagonism was observed in Tlongi3 and Tlongi25 from *T. longibrachiatum* and Tcitr1, Tcitr3 and Tcitr5 from *T. citrinoviride* against *S. rolfsii*. Among 35 isolates,

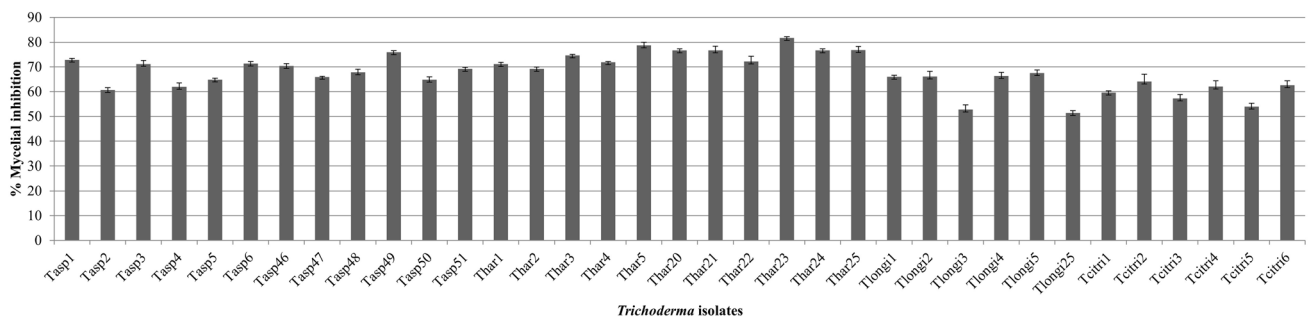


Fig. 3 Per cent mycelial inhibition of *S. rolfii* by different *Trichoderma* isolates in dual culture assay. Treatment means were compared using Fisher's Protected LSD test ($p=0.05$)

the potential isolate from each group namely *T. asperellum* Tasp49 from group I, *T. harzianum* Thar23 from group II, *T. longibrachiatum* Tlongi5 from group III and *T. citrinoviride* Tcetri2 from group IV were selected for the study of lytic enzyme production and plant growth promoting traits in groundnut.

Lytic enzymes assay of selected isolates of four *Trichoderma* spp.

The lytic enzymes like chitinase, β -1,3-glucanase and protease from selected *Trichoderma* isolates were studied by using freeze dried mycelia of *S. rolfii* in MSB as a source of enzyme production. The enzyme activity from the isolates were gradually increased from day 1 to 7 for chitinase and day 1–6 for β -1,3-glucanase and protease and decreased after day 7. Among the selected isolates, *T. harzianum* Thar23 (31.36 U/ml) significantly produced higher amount of chitinase on day 7 followed by *T. asperellum* Tasp49 (25.26 U/ml) (Fig. 4). The other selected isolates *T. longibrachiatum* Tlongi5 (20.1 U/ml) and *T. citrinoviride* Tcetri2 (17.3 U/ml)

exhibited lesser amount of chitinase enzyme activity as compared to other isolates (Fig. 4). Similarly, another lytic enzymes β -1, 3-glucanase and protease are also produced significantly higher 4.1 U/ml and 2.76 U/ml on day 6 by *T. harzianum* Thar23 followed by *T. asperellum* Tasp49 (2.6 U/ml and 2.13 U/ml). The other two selected isolates *T. longibrachiatum* Tlongi5 (1.33 U/ml and 1.16 U/ml) and *T. citrinoviride* Tcetri2 (0.8 U/ml and 0.83 U/ml) showed lesser production of these enzymes compared to other isolates (Fig. 4).

Plant growth promoting traits of selected isolates of four *Trichoderma* spp. in groundnut

The selected isolates were comparatively tested for their growth promoting ability in groundnut under greenhouse conditions. The seeds treated with *T. harzianum* Thar23 and *T. asperellum* Tasp49 significantly increased the germination efficacy to 31.48 and 24.47% and increased the shoot length by 42 and 21.44% and root length by 73.72 and 62.76% compared to control with vigour index of 3598.25 and 3030.65

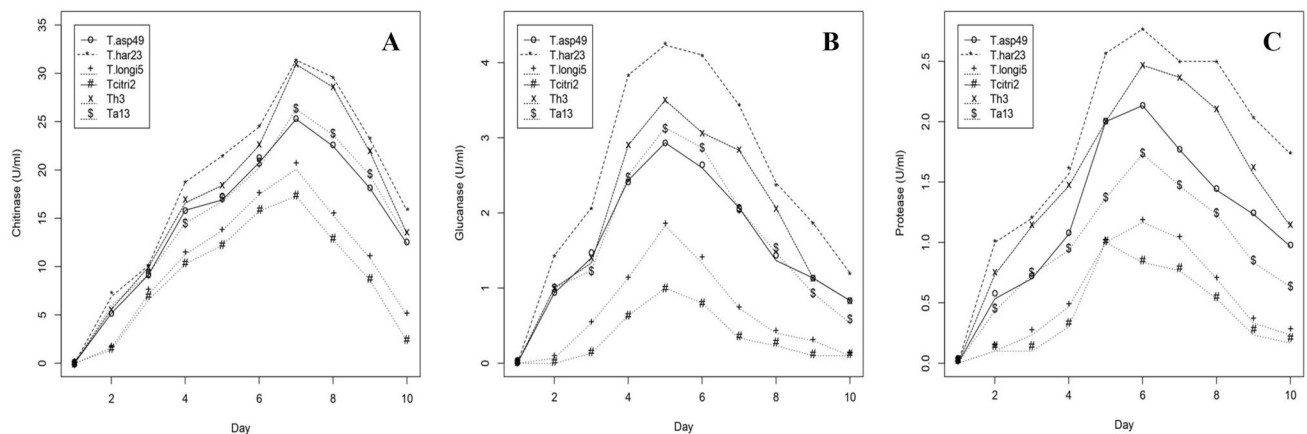


Fig. 4 Lytic enzymes **a** chitinase, **b** β -1,3-glucanase and **c** protease secretion (U/ml) from selected *Trichoderma* isolates at different time intervals

Table 2 Plant growth promoting efficacy of selected *Trichoderma* isolates in groundnut under glasshouse conditions

<i>Trichoderma</i> isolates	Shoot length (in cm)	Root length (in cm)	Germination (%)	Plant vigour index	Relative water content of shoot (%)	Relative water content of root (%)
Tasp49	22.27 ± 1.36 ^c	15.3 ± 0.1 ^c	80.67 ± 0.29 ^d	3030.65 ± 128.31 ^d	75.77 ± 0.02 ^d	77.73 ± 2.38 ^d
Thar23	26.03 ± 0.71 ^d	16.33 ± 0.23 ^d	85.2 ± 0.2 ^e	3598.25 ± 58.05 ^e	78.36 ± 0.27 ^e	81.23 ± 0.59 ^e
Tlongi5	20.36 ± 0.47 ^b	10.8 ± 0.26 ^b	70.33 ± 0.42 ^c	2191.98 ± 35.51 ^c	71.40 ± 0.84 ^c	70.47 ± 0.82 ^c
Tcetri2	19.4 ± 0.46 ^{ab}	9.37 ± 0.15 ^a	68.23 ± 0.25 ^b	1962.78 ± 20.64 ^b	67.55 ± 0.77 ^b	67.25 ± 1.02 ^b
Control	18.33 ± 0.21 ^a	9.4 ± 0.17 ^a	64.8 ± 0.529 ^a	1797.17 ± 26.98 ^a	66.46 ± 0.64 ^a	60.65 ± 2.71 ^a

Values given in the column are the average of three replications followed by standard deviation. The different small letters (a–e) superscripts within the column are significantly difference at $P \leq 0.05$

(Table 2) and increase in plant biomass in terms of the fresh and dry weight of shoot and root. The RWC of shoot and root treated with Thar23 shown higher (81.23%) than control (60.65%) (Table 2). However, the moderate effect on germination efficacy and plant growth promoting traits was observed in seed treatment with *T. citrinoviride* Tcetri2 as compared to other selected isolates (Table 2).

Groundnut stem rot management by application of selected isolates of four *Trichoderma* spp. under field conditions

Field experiments were conducted to evaluate the efficacy of native *Trichoderma* isolates on stem rot disease incidence, shelling percent and pod yield for the year of 2019 and 2020 kharif season. Soil application, seed treatment and drenching with *T. harzianum* Thar23 and *T. asperellum* Tasp49 significantly ($P < 0.05$) reduced stem rot disease incidence up to 59.45%, 52.01% in 2019 and 53.79%, 48.74% for the year of 2020 and increased pod yield in *T. harzianum* Thar23 (2.85 t/ha and 2.68 t/ha) and *T. asperellum* Tasp49 (2.62 t/ha and 2.55 t/ha) treated plots with increased shelling percent (Table 3). However, treatment with *T. longibrachiatum* Tlongi5 and *T. citrinoviride* Tcetri2 shows moderate reduction in disease incidence up to 35.11%, 34.16% in 2019 and 34.16%, 33.21% in 2020 with pod yield of 2.13 t/ha, 2.05 t/ha in 2019 and 2.05 t/ha and 1.95 t/ha in 2020 (Table 3). The results obtained from field experiments that indicate the effect of application of *T. harzianum* Thar23 in improvement of the pod yield up to 51.59% and 38.58% during 2019 and 2020 kharif seasons, respectively.

Discussion

The present study was focused on morphological and molecular characterization, antagonistic ability, and plant growth promoting traits in the potential native *Trichoderma* isolates tested against stem rot pathogen *S. rolfisii* of groundnut. The isolates from rhizosphere soil of groundnut were collected

and characterized based on the morphological characteristics to identify the species level by using the reference of Rifai (1969), Bissett (1984) and Samuels et al. (1999) and classified in to four groups, namely *T. asperellum* (12), *T. harzianum* (11), *T. longibrachiatum* (6) and *T. citrinoviride* (6). Morphological characterization of native *Trichoderma* isolates has earlier been taken up by several researchers (Rifai 1969; Bissett 1984; Pandian et al. 2016; Devi et al. 2021; Jambhulkar et al. 2022). In addition to supporting the reliability of morphological identification, isolates were further characterized molecularly by amplifying ITS region. Kullnig-Gradinger et al. (2002) described the multigene phylogeny approaches for the evolution of *Trichoderma* spp. by using the ITS1 and ITS2, 28S rDNA, mitSSU, *tef* 1 and *ech42* genes. Indian researchers have widely surveyed in different locations of the country and have reported from the different geographical locations like New Delhi (Muthu and Sharma 2011), South Andaman Island (Kumar et al. 2012), Chhattisgarh (Agrawal and Kotasthane 2012), Manipur (Kamala et al. 2015) and Uttarakhand (Manzar et al. 2021), different states of India (Devi et al. 2021). The present study revealed the presence of diverse *Trichoderma* spp. in the rhizosphere of groundnut growing area of Jaipur District of Rajasthan. Mainly *T. asperellum* and *T. harzianum* were found to be dominant species with greater antagonistic potential against a wide range of phytopathogens. Till now, 375 species of *Trichoderma* spp. have been identified and their DNA barcoding information was deposited in the International Subcommittee on Taxonomy of *Trichoderma* (ICTT) (<http://www.trichoderma.info>). The modern *Trichoderma* taxonomy methods help in the precise identification and reorganization of 50 new species of *Trichoderma* per year (Cai and Druzhinina 2021). Similar studies by Manzar et al. (2021) highlighted the phylogenetic relationship among the *Trichoderma* spp. based on the ITS and *tef-1α* sequences. Out of 20 isolates, nineteen isolates belonged to *T. asperellum* as compared to *T. harzianum* (one isolate). With the upcoming trend of development of potential native strains of *Trichoderma* spp. characterization

Table 3 Effect of soil application, seed treatment and drenching with selected *Trichoderma* isolates against *S. rolfisii* in groundnut under field conditions during 2019 and 2020 kharif season

<i>Trichoderma</i> isolates	Per cent disease incidence (PDI)		Reduction over control		Pods per plant		Shelling per cent		Pod yield (t/ha)	
	2019	2020	2019	2020	2019	2020	2019	2020	2019	2020
Tasp49	18.66 ± 0.50 ^c	20.66 ± 0.66 ^c	52.01 ^b	48.74 ^b	25.33 ± 0.57 ^b	29.00 ± 1.00 ^a	61.43 ± 0.37 ^b	58.76 ± 0.51 ^b	2.62 ± 0.03 ^b	2.55 ± 0.04 ^a
Thar23	15.76 ± 0.66 ^d	18.63 ± 0.51 ^d	59.45 ^a	53.79 ^a	31.00 ± 1.00 ^a	22.33 ± 1.15 ^b	66.06 ± 0.15 ^a	62.16 ± 0.25 ^a	2.85 ± 0.04 ^a	2.68 ± 0.02 ^a
Tlongi5	25.23 ± 0.20 ^b	26.46 ± 0.45 ^b	35.11 ^c	34.37 ^c	20.00 ± 1.00 ^c	15.66 ± 0.05 ^c	54.93 ± 0.56 ^c	51.00 ± 0.20 ^c	2.13 ± 0.03 ^c	2.07 ± 0.05 ^b
Tcetri2	25.6 ± 0.43 ^b	26.93 ± 0.47 ^b	34.16 ^c	33.21 ^c	19.33 ± 1.15 ^c	16.00 ± 0.00 ^c	54.66 ± 0.23 ^c	50.50 ± 0.45 ^c	2.05 ± 0.03 ^c	1.95 ± 0.03 ^b
Control	38.9 ± 0.65 ^a	40.33 ± 0.41 ^a	–	–	18.66 ± 0.57 ^c	15.33 ± 0.57 ^c	50.7 ± 0.41 ^d	48.76 ± 0.23 ^d	1.88 ± 0.03 ^d	1.84 ± 0.43 ^c

Values given in the column are the average of three replications followed by standard deviation. The different small letters (a–e) superscripts within the column are significantly difference at $P \leq 0.05$

through molecular and morphological tools have become very important step in research.

To further utilize the native strains for biological control, antagonism tests are required to understand the mechanism under in vitro and in vivo conditions. The antagonistic ability of the *Trichoderma* isolates was tested against *S. rolfisii* showed significant reduction in the mycelial growth of pathogen. Significant variation was observed in the isolates from *T. asperellum* and *T. harzianum* while *T. longibrachiatum* and *T. citrinoviride* exhibited moderate efficacy. The CWDEs are specialized group (glycosyl-hydrolases, oxidoreductases, lyases, and esterases) of enzymes produced by *Trichoderma* spp. which are key component against wide range of phytopathogens. Recently Kaur et al. 2021 reported purified proteins both endochitinase and β -1,3-glucanase from *T. viride* isolate T1#3 degrade the hyphae of *R. solani* causing sheath blight in rice. Several research findings stated that the genus of *Trichoderma* is known to produce CDWs like chitinase, β -1,3-glucanase and protease are playing key role in the suppression of the growth of major soil borne pathogens (Guigon-Lopez et al. 2015; Li et al. 2016; Elamathi et al. 2018; Boat et al. 2020; Macena et al.2020). In recent years, green synthesis of nanoparticles by these species made an impact in the agricultural and food sector due to the secretion of bioactive enzymes, metabolites and accumulation of metals are responsible for reduction of metal ions and helping in the formation nanoparticles. Raja et al. 2021 reported that biologically synthesized nanoparticles by using cell free culture filtrate of *T. harzianum* Th3 inhibits the mycelial growth of groundnut root rot complex pathogens by 60–65%. Production of secondary metabolites during mycoparasitism also a pivotal key of *Trichoderma* spp. in the antagonistic mechanism. For example, secondary metabolites like harzianic acid (HA), 6-pentyl- α -pyrone (6PP), koniginin, harzianopyridone and etc. can be correlated with biocontrol mechanisms (Vinale and Sivasithamparam 2020).

Plant growth promoting fungi (PGPF) are majorly associated with wide range of hosts and helps in transformation of soil nutrients, alter the niche of rhizosphere, elucidate the systemic resistance, and improve the plant growth. *Trichoderma* spp. are one of major beneficial fungal community present in the soil environment which directly create an impact on plants such as increased in number lateral roots and length, cumulative root length and root tips, germination efficacy and seeding growth, improved surface area of roots and leaves, wet and dry weight of plant biomass, and positive effect on flowering. And also responsible for elucidation of plant immunity through increasing jasmonic acid (JA), salicylic acid (SA), ethylene (ET), phytoalexin levels and root exudates in plants, soil nutrients solubilization, and nutrient uptake. Some of the *Trichoderma* spp. are rhizospheric competent in nature that can be able to colonize the plant

roots and enter the epidermis and outer cortex of root system (Harman et al. 2004). Recently Nofal et al. (2021) reported that seedling treatment with 10% cell free culture filtrate of *T. atroviride* from rhizosphere of tomato could improve the plant growth and decreased wilt incidence percentage (8%) caused by *Fusarium oxysporum* f. sp. *lycopersici*. The current study also revealed the impact of seed inoculation with selected native *Trichoderma* isolates which helps in improvement of germination efficacy, root, and shoot length in groundnut. The RWC of the root and shoot in treated plants has been increased which indicates the acceleration in the plant growth. Based on the obtained results, the highly efficient strain *T. harzianum* Thar23 exhibits excellent mycelial growth inhibition of pathogen, lytic enzymes production and improve the plant growth could be used against biotic and abiotic stress at greenhouse and field level in pest management practices.

Performance of microbial antagonistic under field condition is one of the important key factors in commercialization of the product at market level. The present findings were in accordance with several research findings stated that the importance of performance of *Trichoderma* spp. against reduction of different pathogen population at field level (Sharma et al. 2012; Jambhulkar et al. 2022). In this present study, there are differences in performance of *Trichoderma* isolates, however treatment with *T. harzianum* Thar23 enhanced groundnut growth, reduction in *S. rolfisii* disease incidence, significant increase in shelling percentage and pod yield among other isolates.

Conclusion

Based on morpho and molecular characterization 35 native *Trichoderma* isolates were grouped into four different *Trichoderma* spp. namely, *T. asperellum* (12), *T. harzianum* (11), *T. Longibrachiatum* (6) and *T. citrinoviride* (6) from rhizosphere of groundnut and screened based on the antagonistic activity against *S. rolfisii*. The potential isolates from each group viz., *T. harzianum* Thar23, *T. asperellum* Tasp49, *T. longibrachiatum* Tlongi5 and *T. citrinoviride* Tcetri2 were selected for lytic enzyme production and plant growth promoting studies in groundnut. The highly efficient isolate *T. harzianum* Thar23 exhibits excellent mycelial growth inhibition of pathogen, lytic enzymes production and improves the plant growth which could be used in biotic and abiotic stress management in groundnut at both green house and field level.

Acknowledgements The authors are thankful to Head, Department of Plant Pathology, Sri Karan Narendra Agriculture University, Jobner for providing research facilities. This present study is part of first author's Ph.D. programme and thankful to Head, Department of Biosciences,

Manipal University Jaipur for necessary support during the research work.

Funding Funding was provided by Indian Council of Agricultural Research (F. No. Agril. Edn. /9/11/2016/ES/HRD).

Declarations

Conflict of interest The authors declare no competing of interest.

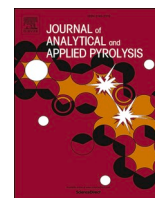
References

- Abdul-Baki AA, Anderson JD (1973) Vigour determination in soybean seed by multiple criteria 1. *Crop Sci* 13(6):630–633
- Agrawal T, Kotasthane AS (2012) Chitinolytic assay of indigenous *Trichoderma* isolates collected from different geographical locations of Chhattisgarh in Central India. *Springerplus* 1(1):1–10
- Annual Report (2015–16) ICAR-directorate of groundnut research, Junagadh-362001, Gujarat, India
- Aycock R (1966) Stem rot and other diseases caused by *Sclerotium rolfisii* or the status of Rolfs' fungus after 70 years. Raleigh (NC): North Carolina Agricultural Experiment Station Bulletin, pp 132–202
- Bell DK, Wells HD, Markham CR (1982) In vitro antagonism of *Trichoderma* spp. against six fungal plant pathogens. *Phytopathology* 72:379–382
- Bissett J (1984) A revision of the genus *Trichoderma* I sect. *Longibrachiatum* sect. nov. *Can J Bot* 2:924–931
- Boat MAB, Sameza ML, Iacomini B, Tchameni SN, Boyom FF (2020) Screening, identification and evaluation of *Trichoderma* spp. for biocontrol potential of common bean damping-off pathogens. *Biocontrol Sci Technol* 30(3):228–242
- Cai F, Druzhinina IS (2021) In honour of John Bissett: authoritative guidelines on molecular identification of *Trichoderma*. *Fungal Divers* 107(1):1–69
- Culling KW (1992) Design and testing of a plant specific PCR primer for ecological evolutionary studies. *Mol Ecol* 1:233–240
- Dennis L, Webster J (1971) Antagonistic properties of some species of *Trichoderma*. III. Hyphal production. *Trans Br Mycol Soc* 57:363–369
- Devi P, Prabhakaran N, Kamil D, Choudhary SP (2021) Polyphasic taxonomy of Indian *Trichoderma* species. *Phytotaxa* 502(1):1–27
- Elad Y, Chet I, Henis Y (1981) A selective medium for improving quantitative isolation of *Trichoderma* spp. from soil. *Phytoparasitica* 9:59–67
- Elamathi E, Malathi P, Viswanathan R, Sundar AR (2018) Expression analysis on mycoparasitism related genes during antagonism of *Trichoderma* with *Colletotrichum falcatum* causing red rot in sugarcane. *J Plant Biochem Biotechnol* 27:351–361
- Gomez KA, Gomez AA (1984) Statistical procedures for agricultural research. Wiley, New York
- Guigon-Lopez C, Vargas-Albores F, Guerrero-Prieto V, Ruocco M, Lorito M (2015) Changes in *Trichoderma asperellum* enzyme expression during parasitism of the cotton root rot pathogen *Phymatotrichopsis omnivora*. *Fungal Biol* 119(4):264–273
- Harman GE, Howell CR, Viterbo A, Chet I, Lorito M (2004) *Trichoderma* species: opportunistic, avirulent plant symbionts. *Nat Rev Microbiol* 2:43–56
- Jambhulkar PP, Raja M, Singh B, Katoch S, Kumar S, Sharma P (2022) Potential native *Trichoderma* strains against *Fusarium verticillioides* causing post flowering stalk rot in winter maize. *Crop Prot* 152:105838

- Kamala T, Devi SI, Sharma KC, Kennedy K (2015) Phylogeny and taxonomical investigation of *Trichoderma* spp. from Indian region of Indo-Burma biodiversity hot spot region with special reference to Manipur. *BioMed Res Int* 1–21
- Kaur R, Kalia A, Lore JS, Kaur A, Yadav I, Sharma P, Sandhu JS (2021) *Trichoderma* sp. endochitinase and β -1,3-glucanase impede *Rhizoctonia solani* growth independently, and their combined use does not enhance impediment. *Plant Pathol* 70:1388–1396
- Keswani C, Mishra S, Sarma BK, Singh SP, Singh HB (2014) Unraveling the efficient applications of secondary metabolites of various *Trichoderma* spp. *Appl Microbiol Biotechnol* 98:533–544
- Kimura MA (1980) Simple method for estimating evolutionary rates of base substitutions through comparative studies of nucleotides sequences. *J Mol Evol* 2:87–90
- Kumar K, Amarasan N, Bhagat S, Madhuri K, Srivastava RC (2012) Isolation and characterization of *Trichoderma* spp. for antagonistic activity against root rot and foliar pathogens. *Indian J Microbiol* 52(2):137–144
- Kullnig-Gradinger CM, Szakacs G, Kubicek CP (2002) Phylogeny and evolution of the fungal genus *Trichoderma*—a multigene approach. *Mycol Res* 106:757–767
- Kumar S, Stecher G, Tamura K (2016) MEGA7: molecular evolutionary genetics analysis version 7.0 for bigger datasets. *Mol Biol Evol* 33:1870–1874
- Li Y, Sun R, Yu J, Saravanakumar K, Chen J (2016) Antagonistic and biocontrol potential of *Trichoderma asperellum* ZJSX5003 against the maize stalk rot pathogen *Fusarium graminearum*. *Indian J Microbiol* 56(3):318–327
- Ma J, Tsegaye E, Li M, Wu B, Jiang X (2020) Biodiversity of *Trichoderma* from grassland and forest ecosystems in Northern Xinjiang, China. *3 Biotech* 10(8):1–13
- Macena AMF, Kobori NN, Mascarin GM, Vida JB, Hartman GL (2020) Antagonism of *Trichoderma*-based biofungicides against Brazilian and North American isolates of *Sclerotinia sclerotiorum* and growth promotion of soybean. *Biocontrol* 65:235–246
- Malolepsza U, Nawrocka J, Szczech M (2017) *Trichoderma virens* 106 inoculation stimulates defense enzyme activities and enhances phenolics levels in tomato plants leading to lowered *Rhizoctonia solani* infection. *Biocontrol Sci Technol* 27(2):180–199
- Manzar N, Singh Y, Kashyap AS, Sahu PK, Rajawat MVS, Bhowmik A, Sharma PK, Saxena AK (2021) Biocontrol potential of native *Trichoderma* spp. against anthracnose of great millet (*Sorghum bicolor* L.) from Tarai and hill regions of India. *Biol Control* 152:104474
- Muthu KA, Sharma P (2011) Molecular and morphological characters: an appurtenance for antagonism in *Trichoderma* spp. *Afr J Biotechnol* 10(22):4532–4543
- Nofal AM, El-Rahman MA, AbdelghanyTM A-M, M, (2021) Mycoparasitic nature of Egyptian *Trichoderma* isolates and their impact on suppression Fusarium wilt of tomato. *Egypt J Biol Pest Control* 31:103
- Pandian RTP, Raja M, Kumar A, Sharma P (2016) Morphological and molecular characterization of *Trichoderma asperellum* strain Ta13. *Indian Phytopathol* 69:297–303
- Persoon CH (1794) *Dispositamethodicafungorum*. *RomersneuesMagazin der Botanik* 1:81–128
- Raja M, Sharma RK, Jambhulkar PP, Sharma KR, Sharma P (2021) Biosynthesis of silver nanoparticles from *Trichoderma harzianum* Th3 and its efficacy against root rot complex pathogen in groundnut. *Mater Today Proc* 43(5):3140–3143
- Rifai MA (1969) A revision of the genus *Trichoderma*. *Mycol Papers* 116:1–56
- Sallam N, Eraky AM, Sallam A (2019) Effect of *Trichoderma* spp. on Fusarium wilt disease of tomato. *Mol Biol Rep* 46(4):4463–4470
- Samuels GJ, Lieckfeldt E, Nirenberg HI (1999) *Trichoderma asperellum*, a new species with warted conidia, and redescription *T. viride*. *Sydowia* 51:71–88
- Schuster A, Schmoll M (2010) Biology and biotechnology of *Trichoderma*. *Appl Microbiol Biotechnol* 87(3):787–799
- Sharma P, Saini MK, Deep S, Kumar V (2012) Biological control of groundnut root rot in farmer's field. *J Agric Sci* 4(8):48–59
- Sharma P, Sharma M, Raja M, Shanmugam V (2014) Status of *Trichoderma* research in India: a review. *Indian Phytopathol* 67(1):1–19
- Thompson JD, Higgins DG, Gibson TJ (1994) CLUSTALW: improving the sensitivity of progressive multiple sequence alignment through sequence weighting, position-specific gap penalties and weight matrix choice. *Nucleic Acids Res* 22:4673–4680
- Tian X, He M, Wang Z, Zhang J, Song Y, He Z, Dong Y (2015) Application of nitric oxide and calcium nitrate enhances tolerance of wheat seedlings to salt stress. *Plant Growth Regul* 77(3):343–356
- Tulasne LR, Tulasne C (1865) *Selecta fungorumcarpologia*. Jussu, Paris
- Vinale F, Sivasithamparam K (2020) Beneficial effects of *Trichoderma* secondary metabolites on crops. *Phytother Res* 34(11):2835–2842
- White TJ, Bruns T, Lee SJWT, Taylor J (1990) Amplification and direct sequencing of fungal ribosomal RNA genes for phylogenetics. In: Innis MA, Gelfand DH, Sninsky JJ, White TJ (eds) *PCR protocols: a guide to methods and applications*. Academic Press, New York, pp 315–322

Publisher's Note Springer Nature remains neutral with regard to jurisdictional claims in published maps and institutional affiliations.

Springer Nature or its licensor (e.g. a society or other partner) holds exclusive rights to this article under a publishing agreement with the author(s) or other rightsholder(s); author self-archiving of the accepted manuscript version of this article is solely governed by the terms of such publishing agreement and applicable law.



Enhancing the pyrolytic conversion of biosolids to value-added products via mild acid pre-treatment

Ibrahim Gbolahan Hakeem^{a,b}, Pobitra Halder^{b,c}, Savankumar Patel^{a,b}, Abhishek Sharma^{b,d}, Rajender Gupta^e, Aravind Surapaneni^{b,f}, Jorge Paz-Ferreiro^a, Kalpit Shah^{a,b,*}

^a Chemical and Environmental Engineering, School of Engineering, RMIT University, Melbourne, VIC 3000, Australia

^b ARC Training Centre for the Transformation of Australia's Biosolids Resources, RMIT University, Bundoora, VIC 3058, Australia

^c School of Engineering, Deakin University, VIC 3216, Australia

^d Department of Chemical Engineering, Manipal University Jaipur, Rajasthan 303007, India

^e Department of Chemical & Materials Engineering, University of Alberta, Edmonton, Canada

^f South East Water Corporation, Frankston, VIC 3199, Australia

ARTICLE INFO

Keywords:

Demineralisation
Metal passivation
Sewage sludge
Pyrolysis
Heavy metals

ABSTRACT

High concentrations of inorganic matter such as silicates, alkali and alkaline earth metals (AAEMs), and heavy metals (HMs) in biosolids limit their pyrolysis conversion to high-value products. Therefore, the reduction or passivation of the deleterious pyrolytic activities of these native inorganics in biosolids can enhance the yield and quality of products obtained during pyrolysis. The pyrolysis of raw and 3% sulfuric acid pre-treated biosolids was carried out in a fluidised bed reactor at 300–700 °C, and the influence of pre-treatment was examined on biochar properties, gas production, and bio-oil composition. At all temperatures, the selective removal of ash-forming elements (demineralisation) in biosolids by pre-treatment improved organic matter devolatilisation yielding higher bio-oil and lower biochar than untreated biosolids. Demineralisation weakened gas production, particularly at higher pyrolysis temperatures. At 700 °C, the in-situ formation of acidic metal sulfate salts in sulfuric acid-infused biosolids facilitated H⁺ release, thereby increasing H₂ yield to a maximum of 15 mol% compared to 8 mol% from untreated biosolids and 4 mol% from demineralised biosolids. Biochar produced from treated biosolids had considerably lower HMs concentration and higher organic matter retention compared to raw biosolids biochar. The effect of pre-treatment on biochar properties was profound at 700 °C pyrolysis temperature. Pre-treatment increased biochar fixed carbon by 57%, calorific value by 37%, fuel ratio by 44%, doubled the specific surface area from 55 to 107 m²/g, and enhanced porous structure formation. At 300 °C, the major chemical compounds in the bio-oil were amides (20%), N-heterocyclics (25%), and ketones (30%), and higher temperatures favoured phenols and aromatic hydrocarbon production. Pre-treatment enhanced the selectivity of furans by 10-fold, anhydrosugars by 2-fold, and aromatic hydrocarbons by 1.5-fold relative to the raw biosolids bio-oil. Acid pre-treatment is a promising strategy for improving biosolids quality as feedstock for pyrolysis to generate high-value products.

1. Introduction

Biosolids (stabilised sewage sludge) are solid residues of the wastewater treatment process. Biosolids are enriched with plant nutrients (N, P, K), facilitating their widespread application on agricultural land. However, the presence of microbial, organic, and inorganic contaminants is reducing the attractiveness of biosolids for direct land application [1]. Therefore, a substantial volume of biosolids may not be safely applied on land due to increasingly stringent regulations on biosolids

management. Non-combustive thermal techniques such as pyrolysis, gasification, and hydrothermal carbonisation/liquefaction have been widely demonstrated for treating biosolids with the potential for contaminant destruction and resource recovery [2,3]. Pyrolysis is the most promising thermal treatment technique for biosolids processing and has been extensively studied under different conditions. At typical pyrolysis conditions (usually 400–700 °C under an inert atmosphere), pathogens and organic contaminants can be effectively degraded, and the waste volume can be reduced by at least 30% while generating solid

* Corresponding author at: Chemical and Environmental Engineering, School of Engineering, RMIT University, Melbourne, VIC 3000, Australia.

E-mail addresses: ibrahim.hakeem@rmit.edu.au (I.G. Hakeem), kalpit.shah@rmit.edu.au (K. Shah).

<https://doi.org/10.1016/j.jaap.2023.106087>

Received 17 May 2023; Received in revised form 13 July 2023; Accepted 15 July 2023

Available online 18 July 2023

0165-2370/© 2023 Elsevier B.V. All rights reserved.

(biochar), liquid (bio-oil), and gaseous (syngas) products [4]. However, despite these promising outcomes, biosolids pyrolysis can be limited by low conversion, poor selectivity, and product contamination [5]. Unlike lignocellulosic biomass, biosolids can have high amounts of inorganic matter (up to 50 wt%), depending on the source and stabilisation method [6]. The high ash content (and low volatile solids) may limit the suitability of biosolids as a pyrolysis feedstock. The inorganic content such as silicates, aluminates, alkali and alkaline earth minerals (AAEMs), and heavy metals (HMs) can inhibit the conversion of organic matter and interferes with the formation pathway of valuable chemical compounds during pyrolysis [7]. After pyrolysis, the inorganic minerals are largely retained in the biosolids-derived biochar at a higher concentration with deleterious influence on the biochar physicochemical properties and application potential [8]. For example, biosolids biochar with higher HMs concentration may not be attractive for land application. Excessively high amounts of ash content and inorganic minerals in biochar can reduce the oxidation resistance of the biochar carbon, lower the ash fusion temperature, and induce slagging and fouling during combustion for energy recovery [9]. Also, higher concentrations of minerals can lower chars' activation potential, reduce microporous structure development, and decrease the specific surface areas [10].

Three improvement strategies, such as i) feed pre-treatment, ii) use of catalysts, and iii) feed co-processing, have been demonstrated to enhance the pyrolytic conversion of biosolids to high-value products [11]. The extensively studied approaches are co-pyrolysis and in-situ catalytic pyrolysis, which involves the wet or dry mixing of biosolids with other biomass feedstock or catalyst additives [12–14]. Besides the opportunity to manage more than one waste stream, the potential advantages of co-processing biosolids with other feedstock in the presence or absence of catalysts include improved process selectivity, faster conversion kinetics, suppression of pollutant release, and enhanced product properties [15,16]. Co-pyrolysis, catalytic pyrolysis, and their combinations have been demonstrated to improve the pyrolytic conversion of biosolids through beneficial synergistic interactions of co-feedstock and catalysts additive. However, there are still some technical issues that require further attention, such as (i) deconvolution of the complex conversion kinetics and synergistic interactions, (ii) poor product homogeneity arising from feedstock variability and feed particle segregation, and (iii) difficulty in catalyst separation and recovery during in-situ operations.

The chemical pre-treatment of biosolids as an initial process step before pyrolysis has not been fully explored. Previous works suggested that mild acid pre-treatment of biosolids can selectively remove inorganic elements and partially hydrolyse recalcitrant organics to produce organic-rich residue suitable for pyrolysis conversion to bio-oil [8, 17–19]. During acid pre-treatment, protons (H^+) from the acid solution replaced free or loosely bound metal ions in biosolids via an ion exchange mechanism, causing the removal of ash-forming elements [11]. Also, deprotonation of carboxylic O–H and hydroxylic O–H functional groups can produce many H^+ and negatively charged polyions that promote the desorption of metal ions in biosolids [20]. Depending on the severity of the acid pre-treatment conditions, disintegration (hydrolysis) of organic matter in biosolids can occur attributed to the disruption of hydroxyl bonds and cleavage of carbonyl groups, as well as the transformation of crystalline compounds to amorphous form, thereby reducing the structural and thermal recalcitrance of the treated residue [21,22]. For example, mild acid (<5% H_2SO_4 at 25 °C and 1 h) pre-treatment of biosolids was reported to remove about 75–95% of inherent HMs and 80–95% AAEMs, which reduced the ash content by 50% without degradation of organic constituents [17]. Then, the pyrolysis of acid-pre-treated biosolids had higher rates of devolatilisation occurring at lower temperatures to produce lower char residues than untreated biosolids [8,17]. Similarly, Liu et al. [18] reported that acid washing using 0.1 M H_2SO_4 at ambient conditions for 12 h reduced biosolids ash content from 32 wt% to 20 wt% and increased carbon content by 26%. Therefore, acid pre-treatment of biosolids before

pyrolysis may be desired for many reasons, such as (i) reduction of HMs concentration and bioavailability in the resultant biochar, (ii) reduction of ash content and increased organic matter retention in biochar, (iii) enhancement of char textural properties and specific surface area, and (iv) improvement of both energy and chemical value of bio-oil through reduction of water and oxygenates content ordinarily catalysed by native AAEMs. Furthermore, there is an extensive demonstration of acid pre-treatment of biosolids for removing HMs and other limiting contaminants, thereby improving the grade of biosolids for unrestricted beneficial land reuse [20,23,24]. Therefore, biosolids pre-treatment may have a two-fold benefit for improving biosolids quality for land application as well as for pyrolysis upcycling.

Existing studies on integrated acid pre-treatment and pyrolysis were centred on understanding the role of inherent metals on biosolids' thermal decomposition behaviour and pyrolysis kinetics [19,25,26]. The analytical pyrolysis of acid-demineralised biosolids or demineralised biosolids spiked with specific metal additive have been used to elucidate the catalytic role of internal or added metals in fostering or inhibiting the release of gaseous nitrogen and sulfur compounds, degradation characteristics of organic matter, volatiles evolution, and pyrolysis activation energy [19,25–27]. There are limited studies on the bench-scale pyrolysis of acid-treated biosolids [18,28]. The role of acid pre-treatment on the distribution of pyrolysis product fractions (oil, char, and gas) and their properties have not been fully documented in the literature. Also, the observed effect of pre-treatment of biosolids in analytical pyrolysis setup may differ in practical reactor systems such as the fluidised bed reactor where gas-solid interactions are faster due to improved mass and heat transfer. Hence, biosolids pre-treatment before pyrolysis demands an extensive investigation in a typical fluid bed reactor under wide conditions of pre-treatment and pyrolysis.

This work studied the pyrolysis of raw and acid-treated biosolids in a fluidised bed reactor at 300–700 °C to understand the role of pre-treatment on biosolids pyrolysis. It was hypothesised that the removal or passivation of inherent metals in biosolids through acid pre-treatment could enhance the biochar quality, influence the formation path of chemical components in the bio-oil, and affect gas production during pyrolysis. Two pre-treatment scenarios were selected to include (i) biosolids acid treatment followed by water washing as a neutralisation step for selective demineralisation and (ii) biosolids acid treatment having residual acid unwashed for metal passivation. The specific objectives of this work were to study the effect of mild acid pre-treatment on (i) biosolids' physicochemical properties and thermal decomposition behaviour, (ii) pyrolysis product distributions, (iii) biochar quality with respect to carbon retention, calorific value, HMs concentration and bioavailability, and surface morphology, (iv) compositions of chemical compounds in the pyrolysis liquid to assess the chemical value of the bio-oil, and (v) compositions and evolution profile of non-condensable pyrolysis gases.

2. Materials and methods

2.1. Biosolids collection and sample preparation

Biosolids used in this study were collected from Mount Martha Water Recycling Plant, South East Water Corporation, Melbourne, Australia. The plant uses a dissolved air flotation process for sludge activation, then anaerobic followed by aerobic digestion for sludge treatment. The digested sludge is then dosed with polymer additives to coalesce the flocs, followed by mechanical dewatering in a centrifuge and drying in solar dryer shed. The biosolids employed in this study are the final solids from the dryer. The as-obtained biosolids were dried in an oven at 105 °C, ground, and sieved to 100–300 μm particle size before further use.

2.2. Biosolids pre-treatment

The pre-treatment procedure was as described in our previous work [17]. The biosolids were pre-treated using a 3% (v/v) sulfuric solution at a solid-to-liquid ratio of 1:10 (g/mL) at 25 °C under continuous stirring at 600 rpm for 1 h. These conditions were obtained from an earlier optimisation study [17]. At the end of the pre-treatment experiment, the slurry was vacuum filtered to separate into aqueous phase (filtrate) and solid residue (treated biosolids). The residue was divided into two portions. The first portion was washed many times with deionised water until the filtrate pH was near neutral to remove residual acid and other water-soluble inorganics. The second portion was used as obtained with no further water washing to study the effects of residual acid on biosolids pyrolysis performance. The raw (untreated) biosolids were denoted as RB, treated biosolids with water washing were denoted as TB, while treated biosolids with no water washing were denoted as TB_{nw}. The generation of large volumes of aqueous waste is a typical limitation of acid pre-treatment; however, our recent work has developed a closed-loop hydrometallurgical process for managing the generated aqueous acidic leachate stream via recycling and metal recovery [23]. The effect of pre-treatment on the pyrolysis behaviour of biosolids was assessed through Thermogravimetry analysis using a high-temperature TG/DSC Discovery series SDT650 equipment (TA instrument).

2.3. Pyrolysis experiments and products yield

Pyrolysis experiments were carried out in a quartz tubular fluidized bed reactor under atmospheric conditions. The details of the pyrolysis rig and reactor specifications can be found in our previous works [15, 29]. The pyrolysis procedure involves weighing 40 g of dry biosolids feed (RB or TB or TB_{nw}) into a clean, dry pre-weighed reactor. The reactor and its content were inserted vertically into a three-zone electrically controlled furnace with an average heating rate of 35 °C/min. The reactor and its content were continuously flushed with a stream of pure nitrogen to create an inert atmosphere before heating the reactor. The experimental setup is shown in Fig S1. Biosolids pyrolysis was conducted at three temperatures: 300, 500, and 700 °C, which were selected to study the effect of pre-treatment on the product distribution and properties over a wide temperature range. During pyrolysis, a continuous stream of nitrogen flow required to achieve a gas velocity equivalent to 2.5 times the minimum fluidisation velocity was maintained using the Ergun correlation described in our previous work [30]. After reaching the desired temperature, the experiment was continued for 60 min, sufficient to complete the pyrolysis process. At the end of each experiment, biochar was collected from the reactor after cooling down to ambient temperature, and bio-oil was collected from the condensers. Non-condensable pyrolysis gas was continuously analysed on-line using micro-GC equipment connected to the pyrolysis gas cleaning units. Nine primary experiments were conducted, 3 samples by 3 temperatures. The pyrolysis product notations are distinguished by sample name-pyrolysis temperature, e.g., RB300 denoted Raw biosolids pyrolysed at 300 °C. At least a single repeat experiment was conducted for all samples, and average data has been reported with error bars representing the standard deviation. Product yields were calculated using Eqs. (1)–(3).

$$\text{Biochar}(\text{wt}\%) = \frac{\text{Weight of biochar}}{\text{Weight of biosolids feed}} \times 100\% \quad (1)$$

$$\text{Bio-oil}(\text{wt}\%) = \frac{W_{CT,after} - W_{CT,before}}{\text{Weight of biosolids feed}} \times 100\% \quad (2)$$

$$\text{Gas}(\text{wt}\%) = 100\% - \text{Biochar}(\text{wt}\%) - \text{Biooil}(\text{wt}\%) \quad (3)$$

Where W_{CT} refers to the weight of the condensers and oil collecting tubes.

2.4. Products characterisation

2.4.1. Biochar

Proximate analysis of biosolids and their biochar were carried out using a TGA 8000 Perkin Elmer equipment, and the ultimate analysis was performed in a CHNS 2400 Series II Perkin Elmer equipment coupled to a thermal conductivity detector. Physicochemical properties such as pH and electrical conductivity (EC) were determined using a pre-calibrated platinum electrode probe. Higher heating value (HHV) was estimated using the correlation of Channiwala and Parikh [31] shown in Eq. (4). Bulk density of the biosolids and biochar samples was determined using the standard measuring cylinder method [30]. FTIR Spectra were captured in absorbance mode over a scanning wavelength of 4000–650 cm^{-1} at 32 scanning times and 4 cm^{-1} resolutions using Frontier FTIR Spectroscopy (Spectrum 100, Perkin Elmer). Scanning electron microscope (SEM) FEI Quanta 200, USA, was used to analyse the surface morphologies of biochar samples after coating with iridium using Leica EM ACE 600 sputter coating instrument. The SEM instrument was operated at 30 kV, and SEM images were captured at the same spot size (5.0) and magnification ($\times 3000$) to compare all samples' surface morphology. Brunauer–Emmett–Teller (BET) Surface Area Analysis was employed to estimate the surface area of the samples using Micromeritics TriStar II instrument.

The concentration of major elements in biosolids and biochar samples was measured using XRF analysis (S4 Pioneer Bruker AXS). Trace elements were measured using ICP-MS analysis following the acid digestion of the biosolids samples in aqua regia following the procedure described in Hakeem et al. [17]. Lastly, the potential soil bioavailable HMs concentration in biochar samples was measured using the diethylenetriamine pentaacetate (DTPA) acid extractable metal procedure [32]. Briefly, the extractant was prepared by weighing 1.97 g of DTPA, 1.47 g of $\text{CaCl}_2 \cdot 2 \text{H}_2\text{O}$, and 14.92 g of triethanolamine and dissolved in deionised water to make up 1 L solution. The pH of the solution was adjusted to 7.3 using concentrated HCl. Then 1 g of biochar sample was added to 10 mL of the pH-adjusted extractant solution, and the mixture was agitated at 250 rpm overnight at room conditions. The metal enrichment factor (MEF_i) and metal retention/recovery (R_i) in the biochar was estimated using Eqs. (5) and (6), respectively [17].

$$\text{HHV} \left(\frac{\text{MJ}}{\text{kg}} \right) = 0.3491C + 1.1783H + 0.1005S - 0.1034O - 0.0151N - 0.0211Ash \quad (4)$$

$$\text{MEF}_i = \frac{\text{Metal}_i \text{ concentration} \left(\frac{\text{mg}}{\text{kg}} \right) \text{ in biochar}}{\text{Metal}_i \text{ concentration} \left(\frac{\text{mg}}{\text{kg}} \right) \text{ in biosolids}} \quad (5)$$

$$R_i(\%) = \text{MEF}_i \times \text{biochar yield (wt}\%) \quad (6)$$

2.4.2. Bio-oil compositions

Pure bio-oil oil samples collected from the condenser during pyrolysis were used for the analysis. Bio-oil samples were dissolved in DCM before analysis in a Gas Chromatography-Mass Spectrometry (GC/MS Agilent Technologies, GC/MSD 5977B, 8860 GC system) instrument. HP-5MS (19091S-433UI) capillary column (30 m length, 0.25 mm I.D. and 0.25 μm film thickness) was used in the GC/MS equipment, and the temperature program of the oven was as follows: isothermal hold at 45 °C for 3 min, ramp to 300 °C at 7 °C/min and isothermal hold at 300 °C for 5 min. Other conditions were 300 °C - injection temperature; 280 °C - MS transfer line; 230 °C - MS ion source; 1 μL - splitless injection volume; 23.0 mL/min - total inlet flow, and helium was used as the carrier gas. The relative composition of chemical compounds in each bio-oil sample was determined by peak area normalisation, denoted as peak area percentage [15]. For further analysis, the identified compounds in each bio-oil sample were categorised into different chemical groups such as oxygenated, nitrogenated, hydrocarbons, phenolics,

anhydrosugars, and sulfur-containing compounds. Acids, alcohols, aldehydes, esters, ethers, furans, and ketones were categorised into oxygenated, while pyrazine, pyridine, pyrrole, azole, amines, amides, and nitriles were categorised into nitrogenated. Phenols and their derivatives are phenolics, while saccharides and sugar alcohols are classified as anhydrosugars. Finally, olefin, paraffin, BTXS (benzene, toluene, xylene, and styrene), and PAHs were classified as hydrocarbons. This classification was used to provide insight into the chemical value of the bio-oil based on dominant platform chemical species and study the effect of pre-treatment on the distribution of the chemical compounds.

2.4.3. Pyrolysis gas compositions

The components and relative compositions (mol%) of the gas stream from each pyrolysis experiment were analysed online using a Micro-GC 490 (Agilent Technologies) instrument connected to the gas scrubbing unit from the pyrolysis reactor. The microGC has been calibrated with standard gases such as CO₂, CO, H₂, N₂, O₂ and C1-C4 hydrocarbon. Pyrolysis gasses were sampled every 4 min until the end of the experiment to identify and quantify the gas components. The gas evolution profile during the pyrolysis was obtained by plotting the relative gas compositions as a function of pyrolysis time.

3. Results and discussions

3.1. Effect of pre-treatment on biosolids physicochemical properties

The effect of H₂SO₄ pre-treatment on the physicochemical properties of biosolids is summarised in Table 1. The mild acid pre-treatment (3% H₂SO₄ at 25 °C for 60 min) of biosolids impacted the proximate compositions of the biosolids without substantial change in the ultimate compositions. Hence demineralisation mechanism dominated the pre-treatment process, which selectively removed inorganic matter. The percentage change in carbon contents was far lower than the percentage change in ash content of biosolids after pre-treatment. Specifically, there was a 40% and 20% decrease in ash content for TB and TB_{nw}, respectively and a 10% increase in the volatile matter for the treated samples. In contrast, the carbon, hydrogen, and nitrogen contents of the treated samples differ by less than 10% relative to the raw biosolids, attributed to the loss of acid-soluble light volatiles. The ash content decreased due to the substantial removal (>60%) of ash-forming elements (such as AAEMs, Fe, Al, and HMs) from the biosolids. Devolatilisation was slightly enhanced by pre-treatment due to the hydrolysis of recalcitrant organics, thereby increasing volatile matter from 57% in raw biosolids to over 63% in treated feeds.

There was also a considerable reduction in HMs concentration, particularly Cu and Zn, which are the major limiting HMs in biosolids for land application. Overall, there was about a 75% reduction in HMs concentration in the TB relative to RB. The intensity of demineralisation and HMs reduction, as well as other physicochemical changes, were lesser in TB_{nw} than in TB due to the subsequent water-washing step performed in the latter, which aided the removal of water-soluble inorganics and organic components. The HMs concentration (except Cu) in TB is within the concentration limit prescribed by Victoria EPA for C1-grade (least contaminant grade) biosolids for unrestricted land application [33]. The bioavailability of the residual HMs in TB is considerably low and can be an attractive material for direct land use in its current form [17]. However, other rapidly emerging contaminants in biosolids, such as per- and polyfluoroalkyl substances (PFAS) and microplastics, might still be present in TB. Our earlier work observed that sulfuric acid pre-treatment could not extract PFAS from biosolids; rather, the process concentrated PFAS in the treated solids due to volume reduction [23]. Therefore, the thermal treatment of TB via pyrolysis might be necessary to completely degrade all potential organic and microbial contaminants and produce quality biochar for land beneficiation and other high-value applications.

Table 1
Effect of pre-treatment on biosolids physicochemical properties.

Properties	Compositions/ Elements	Biosolids samples			C1-grade biosolids*
		RB	TB	TB _{nw}	
Proximate analysis (wt% dry basis)	Moisture	1.9	1.8	0.8	
	Volatile matter	57.5	63.4	63.6	
	Fixed carbon	10.6	16.4	11.3	
	Ash	30.0	18.5	24.3	
Ultimate analysis (wt% dry basis) ^a	Carbon	35.4	36.4	32.9	
	Hydrogen	4.4	5.1	4.5	
	Nitrogen	5.6	5.6	5.5	
	Sulfur	0.9	2.3	7.4	
	Oxygen	23.8	32.1	25.5	
pH		6.8	6.0	2.0	
EC (μS/cm)		1885	2400	9385	
HHV (MJ/kg) ^b		14.4	15.1	14.2	
Bulk density (g/cm ³)		0.78	0.73	0.77	
Solids recovery (%)		-	80	95	
Carbon retention (%) ^c		-	82.3	88.3	
Major elements in ash (wt%)	Al	0.74	0.54	0.56	
	Ca	10.18	5.35	8.54	
	Cl	0.35	0.08	0.08	
	Fe	4.23	4.07	2.25	
	Na	0.12	BDL	BDL ^d	
	K	1.07	0.18	0.35	
	Mg	0.53	0.12	0.12	
	P	1.32	0.54	0.51	
	Si	2.69	3.29	2.91	
	Demineralisation efficiency (%) ^e		-	38.6	19.0
AAEMs removal efficiency (%) ^f		-	77.0	65.2	
Heavy metals (mg/kg)	As	2.5	1.3	1.9	20
	Cd	1.3	0.3	0.5	1
	Co	1.3	0.5	0.9	-
	Cu	690	220	500	100
	Cr	20	13	16	400
	Ni	18	7	12	60
	Mn	210	10	53	-
	Pb	20	18	17	300
	Zn	850	160	560	200
HMs removal efficiency (%)		-	76	35	

^a Obtained by difference Oxygen = (100-C-H-N-S-Ash);

^b Estimated using the correlation of Channiwala and Parikh (Eq. 4)

^c $(\text{Carbon content (wt\% in treated feeds)}) / (\text{Carbon content (wt\%) in raw biosolids}) \times \text{Solids recovery (\%)}$

^d BDL – Below Detection Limit;

^e Based on ash content reduction;

^f Based on average Na, K, Mg, and Ca content reduction

* Biosolids grade for land application as prescribed by EPA Victoria [33].

Notably, there was an increase in sulfur content in TB_{nw} compared to the other two samples indicating the presence of high residual sulfur from H₂SO₄ pre-treatment without any post-treatment water washing. The sulfur from H₂SO₄ could react with organic matter in biosolids to form organosulfur compounds, which might initiate the release of sulfur-containing volatiles during pyrolysis. The FTIR spectra (Fig S2) of the treated biosolids confirmed the formation of organosulfur compounds such as C-S, C=S, S=O, and SO₂NH₂ groups. The water-washing neutralisation steps neutralised residual sulfuric acid and removed the precipitated metal sulfate salts, raising the treated solids' pH to 6.5 (Table 1). However, the water-washing process caused a loss of total solids with a solids recovery of 85% and carbon retention of 82% in TB compared to 95% solids recovery and 88% carbon retention in TB_{nw}. Pre-treatment had a negligible change on the calorific value of the feed materials due to the contrasting effect of ash and oxygen concentration on the HHV correlation (Eq. (4)); however, pre-treatment reduced the bulk density of the biosolids, which was more profound in TB due to the extra water washing step. The overall observation of the acid pre-

treatment process on the changes in the physicochemical properties of biosolids is comparable with the literature [8,18,19]. For instance, in the study of Liu et al. [18], 0.1 M H₂SO₄ pre-treatment of biosolids at ambient temperature for 12 h reduced the ash content by 12 wt% and increased volatile matter and carbon contents by ~10 wt% relative to the untreated biosolids. Tang et al. [19] using 5% HCl, 25 °C and 6 h for biosolids pre-treatment yielded 8 wt% decrease in ash content and ~5 wt% increase in volatile matter and carbon contents while nitrogen and hydrogen contents remained relatively unchanged compared to the raw biosolids. The current work used 3% H₂SO₄, 25 °C and 1 h to achieve 12 wt% reductions in ash content and 6 wt% increments in volatile matter while ultimate compositions were least impacted.

3.2. Effect of pre-treatment on biosolids thermal decomposition behaviour

The influence of pre-treatment on the pyrolysis behaviour of biosolids is illustrated by the various thermographs shown in Fig. 1. The DTG profile (Fig. 1(A)) occurs in three distinct degradation stages, which are: (I) dehydration (50–165 °C), (II) devolatilisation of organic components (150–600 °C), and (III) decomposition of recalcitrant carbonaceous materials and residual char organics (>600 °C). In stage I, the dehydration peak attributed to the loss of moisture and light volatiles occurred at 100 °C with < 4% mass loss. The major mass loss

(>50%) occurred in stage II over three degradation peaks at 250, 350, and 400 °C, corresponding to the thermal decomposition of carbohydrates, lipids and proteins/biopolymers, respectively [34,35]. The last degradation stage III, with < 10% mass loss, peaked at 750 °C and was attributed to the degradation of recalcitrant organics, such as lignin, and a fraction of inorganics, usually carbonates. There were clear differences in the DTG thermograph of RB, TB, and TB_nw with respect to changes in maximum degradation temperatures and rate of weight loss. The maximum degradation temperature shifted to lower values in treated samples compared to the raw sample. In contrast, the raw sample's degradation rate was higher than the treated biosolids. For example, the maximum degradation temperature was 285 °C for RB, and it shifted to 245 °C for TB_nw and 260 °C for TB, and while the rate of weight loss was 5.5%/°C for RB and it slightly decreased to 5.3%/°C for TB and 4.3%/°C for TB_nw. These differences can be attributed to the partial hydrolysis of organic matter and the removal of inorganics by the pre-treatment step, facilitating the thermal devolatilisation reactions at lower degradation temperatures. However, the pre-treatment process also resulted in the slight dissolution of organic matter, which decreased the overall quantity of volatile matter in the treated samples relative to RB, thereby reducing the rate of volatile degradation. The lower rate of TB_nw degradation compared to the other samples confirmed the formation of thermally stable metal sulfate salts, which inhibited organic

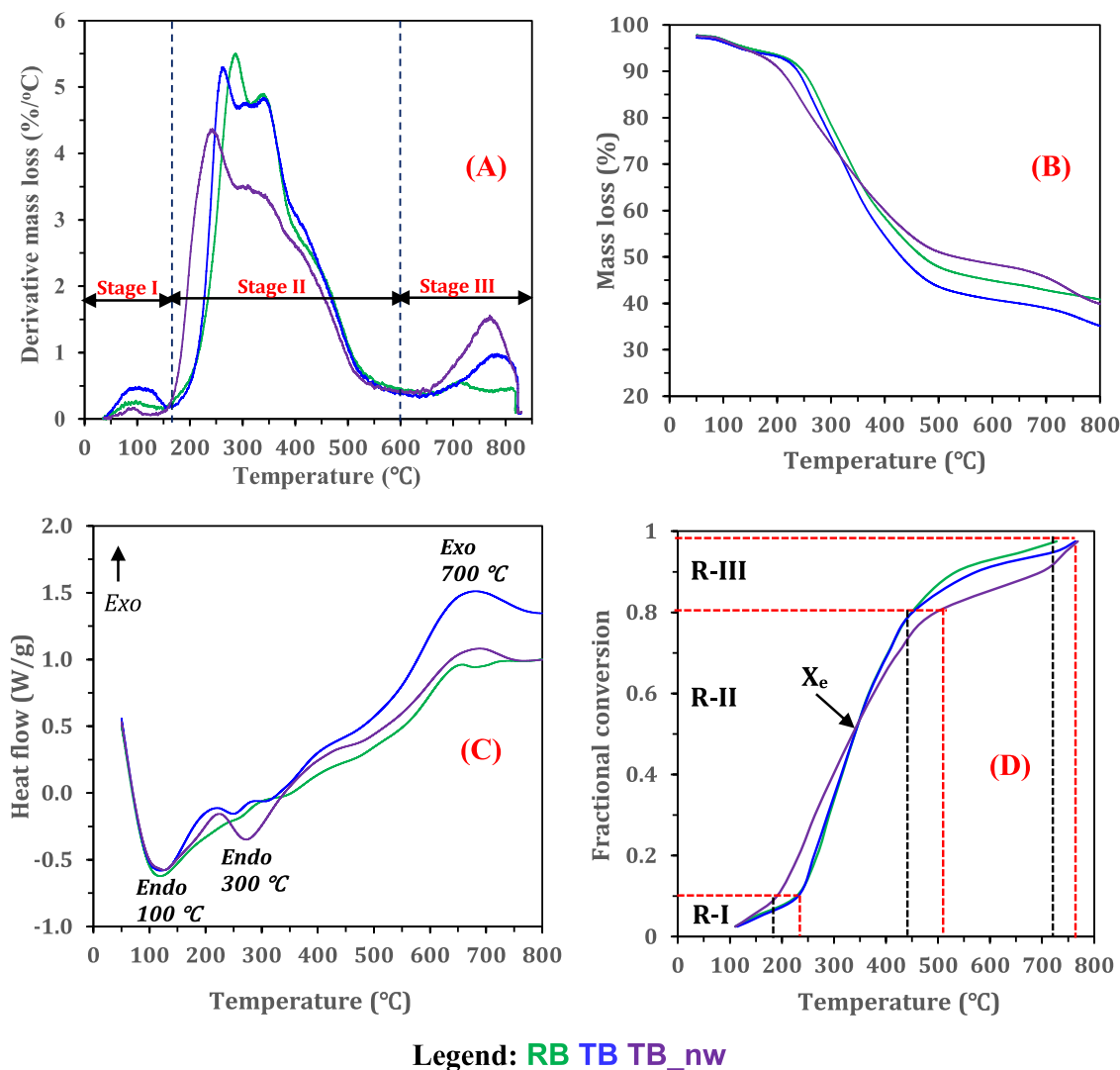


Fig. 1. Effect of pre-treatment on the thermal decomposition behaviour of biosolids (A) DTG thermograph showing decomposition peaks (B) TG mass degradation curve (C) DSC profile showing heat flow (D) plot of fractional conversion as a function of pyrolysis temperature.

matter conversion [36]. The TG curve (Fig. 1(B)) shows that the decomposition profile of TB and RB was closely similar with no overlapping, and at all temperatures, the degradation of TB was always higher than RB. This indicated that both samples have a similar organic matrix, and the lower ash content in TB was largely responsible for the higher mass loss at all temperatures. In contrast, TB_{nw} had a different degradation profile whose mass loss was faster than the other materials up to 320 °C. Beyond this temperature, the mass loss was slower than in the other samples. The residual mass of RB and TB_{nw} was similar (40%), while that of TB was the lowest (35%).

Fig. 1(C) illustrates the DSC curve of the biosolids samples showing the thermal energy flow as a function of pyrolysis temperature. Pyrolysis is an endothermic process where external energy is needed to break chemical bonds and decompose major biochemical components into primary decomposition products. From Fig. 1(C), two distinct endothermic peaks occurred at 100 °C and 300 °C, corresponding to loss of moisture and organic devolatilisation, respectively. After the initial transformation up to 350 °C, the energy needed to heat the feed materials began to decline, and the decrease of heat flow with increasing pyrolysis temperature from 350 to 600 °C was almost linear. During this stage, there are traces of broad endotherms indicating that the decomposition of organic matter at 300–600 °C required minimal thermal energy. However, the non-distinct endotherms made attributing the degradation behaviour to specific organic components difficult. Beyond 600 °C, a small exothermic spike was observed occurring at 650–750 °C attributed to the decomposition of carbon refractories such as aromatic ring, N-alkyl long chain structures, and carbonates with the release of CO₂ [37,38]. The intensity of the endothermic peak at 300 °C in TB_{nw} suggests that the thermal energy required to decompose its organic structure is higher. The infusion of sulfuric acid might have changed the organic structure of TB_{nw} to a thermally recalcitrant matrix through the formation of stable metal sulfate salts, consistent with observations reported in other works [18,39].

The iso-conversional temperature required for the pyrolysis of the three biosolids samples at the same heating rate (20 °C/min) is shown in Fig. 1(D). The figure indicates that the pyrolysis conversion of biosolids occurred over at least three kinetic regimes: i) $\leq 10\%$ conversion occurring at 100–240 °C (R-I), ii) 10–80% conversion occurring at 240–500 °C (R-II), and iii) $\geq 80\%$ conversion at 500–800 °C (R-III). These three kinetic regimes denoted dehydration, primary devolatilisation, and secondary devolatilisation and char cracking stages. However, the temperature required for each conversion stage differs for individual samples. For example, 10% conversion of TB_{nw} occurred at 190 °C and about 230 °C for both RB and TB, suggesting that the dehydration stage occurred faster in TB_{nw} compared to the other two samples. The faster conversion kinetics of TB_{nw} continued into the primary devolatilisation stage up to 50% conversion, after which the rate was slower than RB and TB. Meanwhile, both RB and TB showed similar kinetics, up to 80% conversion, suggesting that the organic structure of both samples is identical. The slightly higher conversion rate of RB beyond 80% can be attributed to the role of native inorganic minerals, which promoted the cracking of recalcitrant organic matter. Notably, the pyrolysis temperature required to achieve 50% conversion was largely similar for all samples (340 °C), as the conversion rate of all samples overlapped at that temperature (indicated by X_c in Fig. 1(D)). Overall, the required pyrolysis temperature was lowest for TB_{nw} at any given conversion $< 50\%$ and was highest at any given conversion $> 50\%$.

3.3. Pyrolysis products distribution: effect of pre-treatment and temperature

The product distribution of raw and treated biosolids at 300–700 °C is shown in Fig. 2. The product yields are expressed in dry feed weight to compare the influence of the temperature and pre-treatment on pyrolysis product distributions (Fig. 2(A)). According to Fig. 2, with

increasing pyrolysis temperature (from 300 to 700 °C), biochar yields decreased while bio-oil and gas products yield increased irrespective of feed material. This trend in product distribution as a function of pyrolysis temperature is consistent with extant literature [29,30,40]. With increasing pyrolysis temperature, mass and heat transfer rates are faster, and several thermolysis decomposition reactions are enhanced with the rapid cleavage of chemical bonds. For all samples, the effect of pyrolysis temperature on biosolids devolatilisation was profound between 300 and 500 °C compared to that between 500 and 700 °C. Nevertheless, bio-oil and gas products yield monotonically increased with temperatures up to 700 °C, indicating that biosolids contain recalcitrant organic fraction requiring higher temperatures to devolatilise. For example, during RB pyrolysis, the conversion was 28.8% at 300 °C; it increased to 49.7% at 500 °C and 58.6% at 700 °C. A similar trend can be observed for TB and TB_{nw}. The DTG profile in Fig. 1(A) showed that most of the organic components in biosolids volatilised at temperatures between 200 and 500 °C. There were only slight improvements in bio-oil and gas yield by raising the temperature to 700 °C.

Pre-treatment had a clear effect on pyrolysis product distribution. From Fig. 2(A), pyrolysis of TB produced lower biochar yield (38.2–65.6 wt%) than that from RB (41.4–71.2 wt%), and the biochar yield from TB_{nw} (43.0–68.7 wt%) was found to be between the yields from RB and TB. In contrast, bio-oil yield from TB (24.7–42.6 wt%) was higher than that from RB (20.6–37.0 wt%) and TB_{nw} (19.6–36.8 wt%). Removal of ash-forming elements from biosolids and partial hydrolysis of the organic matter by H₂SO₄ pre-treatment improved the devolatilisation of TB to produce more bio-oil and less char residues compared to other biosolids samples. It has been indicated that trace levels (< 1 wt%) of certain ash components in biomass have significant catalytic effect during pyrolysis, which can decrease bio-oil yield considerably [41]. From Fig. 1(A), TB_{nw} had the least conversion of all biosolids samples producing the highest biochar yield at 500 and 700 °C. The residual sulfuric acid in TB_{nw} can catalyse crosslinking and polycondensation reactions at higher temperatures to form extra char, thereby increasing biochar yield [42]. The effect of pre-treatment was prominent on the distribution of biochar and bio-oil fractions, suggesting that the removal of inorganics had a remarkable influence on the thermal devolatilisation of organic matter in biosolids. Depending on the metal species and chemical form, mineral components have been shown to play various catalytic roles in releasing pyrolytic volatiles from organic matter [26, 43]. The extent of the interaction of mineral matter on organic matter conversion during biosolids pyrolysis has been elucidated in another work [8]. The gas product yield increased with increasing pyrolysis temperature and was higher for RB and TB_{nw} than for TB. The catalytic effect of the inherent inorganics in RB and residual acid in TB_{nw} facilitated gas production through secondary cracking and dehydration reactions, respectively.

Fig. 2(B) shows the pyrolysis product yield expressed on volatile solids (VS) or dry-ash-free basis to discount the effect of ash matter on product distribution as well as understand the real impact of pre-treatment on the downstream pyrolysis conversion of VS. At all pyrolysis temperatures, RB and TB had a similar yield of bio-oil in the range of 30–53 wt%, and biochar yield (30–59 wt%) was only similar for both samples at 300–500 °C. However, gas and biochar yield varies substantially for RB and TB at 700 °C. This indicates that VS conversion to bio-oil was not negatively impacted by demineralisation as in the case of TB. In contrast, biosolids pre-treatment without the water neutralisation step, as in TB_{nw}, negatively impacted VS conversion to bio-oil during pyrolysis at all temperatures. The higher biochar yield at 500 and 700 °C for treated biosolids compared to the RB clearly indicates the char cracking role of native mineral matter during biosolids pyrolysis. The presence of mineral matter in RB caused a substantial cracking of recalcitrant volatiles at 700 °C to decrease biochar yield and increase gas yield. Consequently, RB conversion was 84% against 75% for treated biosolids. The elevated VS conversion attributed to the internal minerals in RB caused a decrease in fixed carbon and organic matter retention of

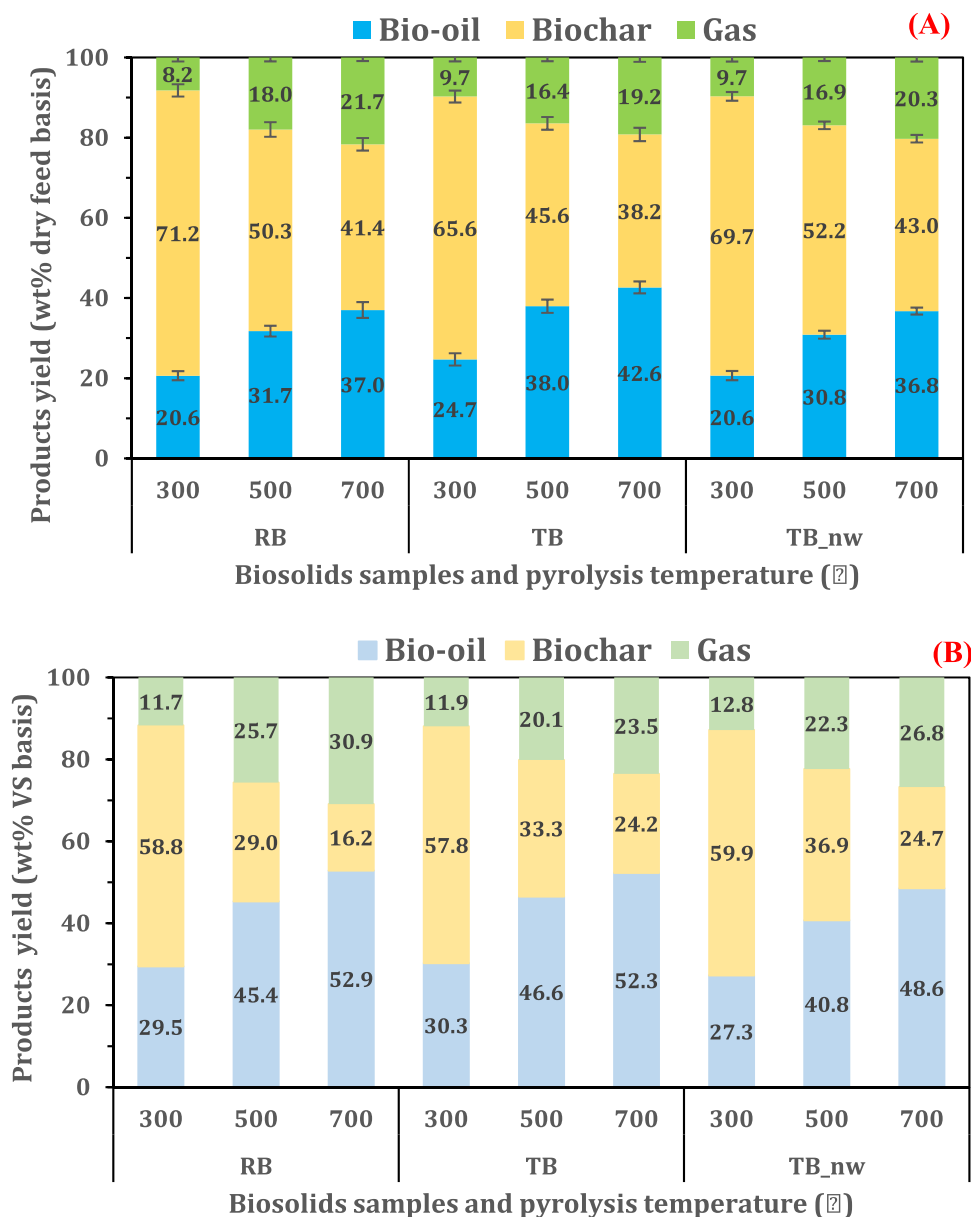


Fig. 2. Effect of pre-treatment and temperature on biosolids pyrolysis product distribution (A) expressed on a dry feed weight basis (B) expressed on volatile solids (dry-ash-free) basis.

the resulting biochar. In contrast, the lower conversion of VS in treated biosolids increased fixed carbon content and organic matter retention in the biochar. The higher biochar yield from the treated samples suggests that the pre-treatment process caused a reduction of thermally labile VS through the dissolution of acid-soluble organics and the loss of total solids during the process. This observation was confirmed by the 80–95% solids recovery and 82–88% carbon retention in treated biosolids relative to RB (Table 1). Besides the loss of total solids and light volatiles during pre-treatment, the residual organic structure might also be impacted by pre-treatment, increasing the stable VS fraction as indicated by the higher fixed carbon contents in treated biosolids. In sum, pre-treatment weakened the pyrolysis conversion of biosolids VS to gas product only at 700 °C.

Under the conditions of this work, there could be more than one mechanism through which acid pre-treatment influenced biosolids organic matter devolatilisation to produce higher bio-oil and lower biochar compared to RB. Perspectives on how biosolids' devolatilisation could be enhanced by acid pre-treatment with water washing step (as in

TB) have been provided.

- i) The substantial reduction of ash content by pre-treatment increased volatile matter concentration in TB. Since the volatile matter content per solid mass is higher in TB than RB, the pyrolysis of equal amounts of TB and RB implies more volatiles per unit TB mass is available for thermal conversion to bio-oil. The lower biochar yield in TB is due to reduced ash content since ash components are largely retained in the biochar. The proximate compositions of the biosolids changed substantially after pre-treatment, with a major opposite shift in the volatile matter and ash matter contents (Table 1).
- ii) During pre-treatment, complex organic components in biosolids can be hydrolysed into simpler components through the disruption of O-H bonds by H⁺ from acid solution and surface deprotonation reaction causing the cleavage of carbonyl groups in protein and carbohydrate structures [20,22]. The partially hydrolysed organic macromolecules in TB are thermally less stable, and their characteristics decomposition temperature occurs in a lower region than untreated biosolids

Table 2
Effect of pre-treatment on biochar physicochemical properties.

Pyrolysis temperature (°C)	300			500			700		
	RB	TB	TB_nw	RB	TB	TB_nw	RB	TB	TB_nw
Proximate analysis (wt% dry basis)									
Moisture	0.37	0.47	0.45	0.80	0.65	0.84	0.84	0.91	0.89
Volatile matter	46.16	52.11	50.69	29.28	30.67	35.67	20.07	21.70	16.71
Fixed carbon	14.66	18.45	13.28	17.62	27.66	17.15	19.99	31.32	27.26
Ash	38.82	28.97	35.57	52.31	41.02	46.35	59.10	46.06	55.15
Ultimate analysis (wt% dry basis)									
Carbon	39.35	45.08	40.07	32.82	41.67	35.34	30.41	37.27	30.21
Hydrogen	3.18	3.57	2.80	1.01	1.50	1.08	0.29	0.83	0.48
Nitrogen	6.55	7.35	6.39	5.47	5.63	5.21	3.25	4.83	4.01
Sulfur	0.89	2.58	6.13	0.58	3.12	6.06	0.65	3.14	7.32
Oxygen ^a	11.22	12.45	9.04	7.81	7.07	5.97	6.30	7.87	2.84
Other properties									
O/C	0.21	0.21	0.17	0.18	0.13	0.13	0.16	0.16	0.07
H/C	0.97	0.95	0.84	0.37	0.43	0.37	0.11	0.27	0.19
pH	5.8	5.5	4.1	7.8	6.8	6.3	9.8	9.4	9.6
EC ($\mu\text{S}/\text{cm}$)	722	1042	2614	305	1500	1868	2160	3218	2902
Bulk density (g/cm^3)	0.79	0.74	0.69	0.80	0.78	0.67	0.83	0.70	0.65
HHV (MJ/kg) ^b	15.49	18.19	16.13	10.71	14.95	12.54	9.07	12.44	10.33
Fuel ratio (FC/VM) ^c	0.32	0.35	0.26	0.60	0.90	0.48	1.00	1.44	1.63
Organic matter retention (%VS) ^d	58.8	57.8	58.6	29.0	33.3	36.8	16.3	24.2	24.7

^a Obtained by difference, i.e. $\text{O} = 100 - (\text{C} + \text{H} + \text{N} + \text{S} + \text{Ash})$;

^b Estimated by the correlation of Channiwala and Parikh [31] (Eq. 4);

^c Fuel ratio was estimated by dividing the fixed carbon content (wt%) by the volatile matter content (wt%) in each sample;

^d Calculated by dividing the volatile solids (VS) in biochar (Biochar yield (wt%)–ash content (wt%)) by the corresponding VS in the respective feedstock (100 (wt%)–ash content (wt%)).

(The TGA/DTG curve confirmed the shift to lower degradation temperature) (Fig. 1(A)).

The results of this work provide insight into the impact of acid pre-treatment on biosolids pyrolysis product distribution under a wide range of temperatures. However, the findings cannot sufficiently identify the specific organic chemical bonds and components being transformed during pyrolysis, aided or inhibited by pre-treatment. Further studies are needed to comprehensively understand the pre-treatment process and the exact mechanisms through which organic matter devolatilisation occurs to increase bio-oil yield.

3.4. Effect of pre-treatment on biochar quality

3.4.1. Physicochemical properties

The physicochemical properties such as proximate and ultimate analyses, caloric value, pH, carbon retention and bulk densities of the resultant biochar obtained from the three biosolids feed samples at 300–700 °C are summarised in Table 2. Generally, volatile matter (VM) decreased, while fixed carbon (FC) and ash content increased in all biochar samples with increasing pyrolysis temperature. However, the increase in FC was negatively influenced by higher ash contents in biochar as the metal oxides in the ash can further oxidise FC, particularly at higher temperatures. During pyrolysis, thermally labile organic matter in the biosolids is removed, leading to substantial volume reduction. As a result, recalcitrant organic matter and inorganic matter are concentrated in the biochar. Increasing pyrolysis temperature increased the intensity of organic matter degradation and inorganic matter retention. The reduction of VM with increasing temperature had a consequential decrease in the ultimate compositions (C, H, N, O) of the biochar through dehydration, deoxygenation, decarboxylation, and denitrogenation reactions. Pre-treatment had clear effects on the proximate and ultimate compositions of the biochar samples. At all pyrolysis temperatures, biochar obtained from treated feeds had lower ash contents and higher FC than RB-biochar due to the prior removal of the ash-forming elements via the pre-treatment demineralisation process. TB-derived biochar had the highest VM and FC increase, and the lowest ash contents decrease compared to corresponding biochar obtained from

other biosolids feeds, albeit at the cost of biochar yield. Pre-treatment with water neutralisation steps retained higher organic matter in the biochar (24–58%), supported by the higher carbon contents and calorific value in the TB-derived biochar relative to RB and TB_nw biochar (Table 2). Also, the fuel ratio of TB biochar was higher than RB-biochar, particularly at 700 °C; the fuel ratio of treated biosolids biochar was higher by 44–63% than RB-biochar. It is then suggested that removing minerals before pyrolysis can be a promising approach for strengthening biochar carbon-sequestration and energy-recovery potential. Also, the lower ash contents in the TB-derived biochar can enhance the biochar-carbon resistance to thermal and chemical oxidation, thereby increasing the carbon stability, as demonstrated in previous work [8]. However, the increase in sulfur contents in the biochar may be an undesired outcome of the pre-treatment process, particularly when the sulfuric acid pre-treatment is not followed by the water-washing neutralisation step, as in TB_nw. Nevertheless, sulfur is an essential plant micronutrient in biochar for land application, and the pre-treatment can enrich the derived biochar of sulfur contents compared to RB-biochar.

The elemental H/C and O/C ratio is typically used to measure biochar aromaticity and biochemical stability and can be correlated to pyrolysis temperature [44]. The decrease in the H/C ratio indicated higher biochar aromaticity due to the strong degree of carbonisation with increasing pyrolysis temperature [40]. Biochar produced at higher temperatures and from pre-treated biosolids had aromatic and hydrophobic structures through the loss of oxygen-containing functional groups (such as hydroxyl and carboxyl). Nan et al. [8] also observed that removing inherent minerals from sewage sludge via acid pre-treatment facilitated the disappearance of oxygen-containing functional groups such as C=O, O=C–O, and C–O, while promoting C–C/C=C bonds, indicating higher aromatisation of biochar. Pyrolysis temperature plays an important role in shaping biochar's surface chemistry and organic structure. At lower temperatures (<500 °C), the hydrogen-bonding network in the organic compounds is eliminated, and hydroxyl groups are oxidised to carboxyls. At higher temperatures, methylene groups are heavily dehydrogenated to aromatic structures [45]. The bulk (or apparent) densities of the biochar obtained at 300–700 °C from the three biosolids feed samples were found to vary substantially. Generally, there was a monotonic increase in bulk density with increasing pyrolysis

Table 3
Effect of pre-treatment and pyrolysis temperature on metal concentration in biochar.

Temp. (°C)	300			500			700		
	RB	TB	TB_nw	RB	TB	TB_nw	RB	TB	TB_nw
Major metal oxides (wt%)									
Al ₂ O ₃	2.1	1.7	1.7	3.0	2.5	2.0	3.4	2.8	2.7
CaO	14.3	8.7	12.9	17.3	10.8	14.2	18.8	11.7	15.9
Fe ₂ O ₃	6.6	4.6	4.0	8.0	6.0	4.7	8.2	6.4	5.0
K ₂ O	1.5	0.3	0.5	1.8	0.4	0.6	1.9	0.4	0.6
MgO	1.1	0.3	0.3	1.6	0.5	0.4	1.8	0.5	0.5
Na ₂ O	0.5	BDL ^a	BDL	0.7	BDL	BDL	0.7	BDL	BDL
P ₂ O ₅	3.4	1.5	1.3	4.4	1.9	1.4	4.8	2.1	1.7
SiO ₂	7.7	10.6	8.6	10.6	14.9	8.9	11.9	16.0	11.4
Heavy metals (mg/kg)									
As	3.0	2.0	2.5	3.5	2.4	3.0	2.1	1.7	1.9
Cd	1.8	0.5	0.7	2.5	0.7	1	1.8	0.8	0.8
Cr	30	15	23	47	28	32	35	30	22
Cu	890	1100	1600	950	1200	1800	1200	1400	1900
Ni	26	10	17	38	13	24	29	16	16
Pb	29	25	21	37	40	34	40	40	36
Zn	1300	400	770	1500	580	970	1600	530	930

^a BDL – Below detection limit

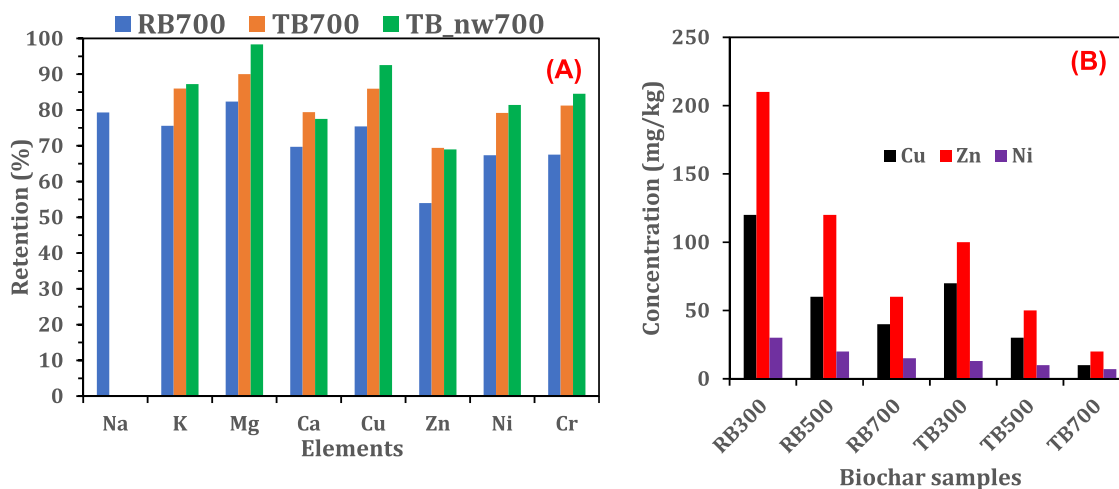


Fig. 3. Effect of pre-treatment on (A) metal retention in biosolids biochar at 700 °C (B) bioavailable HMs concentration in biosolids biochar.

temperature reflected by the extent of volume reduction caused by pyrolysis. The bulk density of the RB-biochar was the highest, followed by TB_nw and TB-biochar, which is reflective of the lower ash content in treated biosolids relative to raw biosolids at a given pyrolysis temperature. Lastly, the pH of the biochar was observed to generally increase with increasing temperature largely due to the destruction of acidic functional groups and the increase in the concentration of basic functional groups such as char-N as well as metal oxides in the ash contents. Biochar produced from TB_nw at 300 °C was more acidic (pH 4) than biochar from other biosolids samples (pH 5.5–5.8) due to residual sulfuric acid in TB_nw. However, the pH of all biochar samples was similar at 700 °C suggesting the inherent acid in TB_nw has no influence on the resultant biochar pH, possibly because acidic metal sulfate salts have been cracked into normal metal sulfate or oxides form.

3.4.2. Metals concentration, retention, and bioavailability

The effect of pre-treatment on the concentration of inorganic elements in biochar was assessed. The compositions and concentration of metal oxides and HMs in the raw and treated biosolids-derived biochar produced at 300–700 °C are summarised in Table 3. The major ash-forming elements enriched in the biochar are oxides of Ca, Si, Fe, P, Al, K, Mg, and Na in decreasing order. Expectedly, the metal concentration increased with increasing pyrolysis temperature (decreasing biochar yield). The metal concentrations were highest for the RB biochar

samples containing the full spectrum of metal components. The prior removal of inorganic elements during pre-treatment substantially reduced the final concentration in the treated biosolids biochar. Notably, Na removal in biosolids via pre-treatment was almost 100%; consequently, Na₂O was only detected in RB biochar and was below the detection limit in all treated biosolids biochar samples. According to Fig. 3(A), the metal contents in the respective biosolids feed were largely retained in their derived biochar with a retention rate of > 90%, confirming the thermal stability of the metal species at the pyrolysis conditions. However, at the highest pyrolysis temperature (700 °C), there appears to be some volatilisation of AAEMs, particularly Ca and K, attributed to the decomposition of Ca-containing minerals such as CaCO₃ in the case of RB and CaSO₄ hydrates in the case of treated biosolids. In addition, the sublimation of KCl at high temperatures may cause K loss from the biochar [29]. Moreover, recalcitrant organics bonded to mineral matter may decompose at high temperatures leading to the release of metal species to the gas phase, lowering their recovery in the biochar [46].

Heavy metals are limiting contaminants in biosolids and their derived char, particularly for land application purposes. The HMs concentration in the biochar obtained from the three biosolids samples at 300–700 °C is shown in Table 3. The concentration generally increases with temperature with an enrichment factor of at least 1.2 times the concentration in the parent biosolids at 300 °C and up to 2.5 times at

700 °C. Up to 500 °C, there was an upward trend in the increase in the HMs concentration. However, at 700 °C, there was a decline in the concentration of the metals attributed to the rise in the thermal volatilities of certain elements. Specifically, at 700 °C, less than 50% of As and Cd were retained in the biochar, and Zn retention was less than 70%. Zhang et al. [47] reported similar observations during sewage sludge pyrolysis, with Hg being completely partitioned in the oil and gas product fractions as low as 300 °C while Cd and As had less than 10% recovery in the biochar at 650 °C. At 700 °C, the thermal volatilities of HMs can be ranked as Cu < Cr < Ni < Pb < Zn < As = Cd, suggesting that Cu, Cr, and Ni were least involved in migration during biosolids pyrolysis. This observation was similar to that reported in previous works [29,47]. Cu had the highest retention in biochar due to the high affinity of Cu to organic matter [17]. The higher organic matter retention in TB/TB_nw biochar also explains the higher Cu concentration in treated biosolids biochar compared to RB biochar. The poor removal of Pb with sulfuric acid resulted in the inconsequential effect of pre-treatment on Pb concentration in the biochar obtained from all samples. The concentration of all other HMs was lower in treated

biosolids biochar compared to RB biochar, with the lowest for TB biochar. However, the enrichment factor for a given HM was higher in TB biochar than in RB biochar. The low ash content in TB weakens the dilution effect resulting in higher MEF. For instance, in biochar obtained at 500 °C, Cd concentration increases by 1.9 times for RB and 2.3 times for TB; similarly, Zn enrichment was 1.8 for TB and 3.6 for TB. Besides the reduction of metal concentration by pre-treatment, there was an increase in the stability of the metal as their recovery in the biochar was higher for treated samples than the RB (Fig. 3(A)). The removal of acid-exchangeable (ionisable) and reducible metal (bound to carbonates and Fe-Mn oxides) fractions during pre-treatment facilitated the transformation and stabilisation of the remaining HMs in the treated samples to oxidisable (bound to organic matter) and residual fractions (bound to silicates) [48]. Therefore, stabilising HMs in the TB and TB_nw biochar compared to RB biochar can reduce the undesired migration of HMs into oil and gas product fraction during biosolids pyrolysis.

The reduction of HMs concentration and the increased metal stability in the biochar facilitated by pre-treatment may not be enough indication of the potential toxicity of the residual HMs. Therefore, DTPA-plant

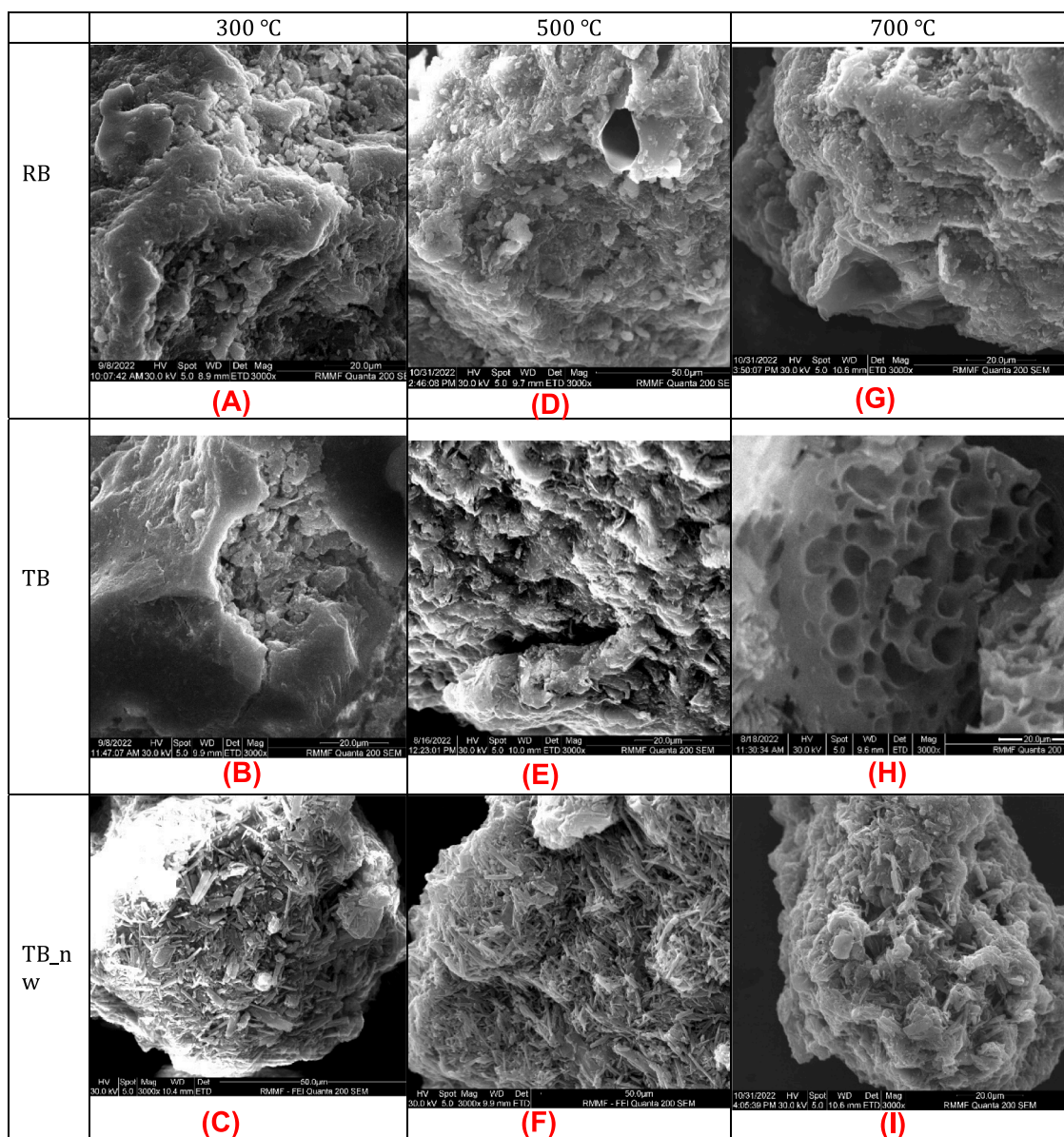


Fig. 4. Effect of pre-treatment and temperature on the surface morphology of biosolids biochar (A) RB300 (B) TB300 (C)TB_nw300 (D) RB500 (E) TB500 (F) TB_nw500 (G) RB700 (H) TB700 (I) TB_nw700.

available HMs concentration was assessed, and the result showed that pre-treatment drastically reduces the bioavailable metal concentration in the biochar (Fig. 3(B)). Specifically, at 500 °C, the DTPA-extractable Cu concentration from RB biochar was 60 mg/kg, while it was 20 mg/kg for TB biochar. Similarly, Zn bioavailable concentration in TB biochar was reduced by at least 50% compared to RB biochar at the same pyrolysis temperature. The effect of pre-treatment follows a similar trend for Ni bioavailable concentration reaching about 7 mg/kg in TB700 compared to 15 mg/kg in RB700. The higher organic matter retention and surface functional groups in TB biochar could promote organometallic complexation reaction, thereby enhancing HMs immobilisation in the char matrix and decreasing the extractable metal concentrations [49].

3.4.3. Morphological properties

The SEM imaging of the biochar obtained from raw and treated biosolids samples at 300–700 °C is shown in Fig. 4. There was a clear distinction in the image of the samples, highlighting the effect of pre-treatment and pyrolysis temperatures on biochar surface morphology. The image of the biochar obtained at 300 °C (Fig. 4(A-C)) showed a bulky structure with particle shrinkage resulting from the dehydration and decarboxylation of organic matter. The char sample from RB and TB appeared similar (Fig. 4(A&B)), and the biochar sample from TB_nw (Fig. 4(C)) had a flaky structure with a surface covering arising from the acidic metal sulfate salts. At 500 °C, the image of the char samples (Fig. 4(D-F)) showed a matured organic conversion with the compact structure becoming disintegrated into small fragments; however, the pore structure is not well developed with traces of pore openings. The char from TB_nw still showed the thermally stable metal sulfate salts coverings, limiting the full development of the pores (Fig. 4(F)). At 700 °C (Fig. 4(G-I)), organic compounds have been completely degraded, and the char cracking reaction removed residual volatiles, opening up pores within the char matrix and exposing the char surface. TB biochar has a strong pore development (Fig. 4(H)) due to enhanced devolatilisation and lower ash residues. The RB700 (Fig. 4(G)), due to its high ash content, had poor pore structure development attributed to the creation of stable organometallic compounds within the aromatic structures, which are recalcitrant to thermal volatilisation at 700 °C [29]. It has been suggested that high levels of ash-forming minerals in biosolids would require higher pyrolysis temperatures for their biochar pore structure to be fully developed compared to low-ash-containing biomass biochar [6]. Hence, reducing the ash minerals in biosolids by mild sulfuric acid pre-treatment was beneficial in producing biochar with a porous structure, albeit the effect was profound only at 700 °C. However, the presence of residual acid and acidic metal sulfate salts inhibited volatile removal and caused pore blockage, as observed in the SEM images of TB_nw.

The BET-specific surface areas and average pore volume of the biochar samples are summarised in Table 4. At 300 °C, the surface area (15–25 m²/g) of the biochar from all feed samples was largely similar;

however, the pore volume of TB (0.024 cm³/g) was almost double of the RB (0.012 cm³/g) supporting the elevated rate of inorganic removal by pre-treatment and organic matter removal from the bulk of TB sample during pyrolysis. Increasing the pyrolysis temperature to 500 °C increased the biochar surface area by at least 40%, reaching 27 m²/g for RB and 40 m²/g for TB, and a further increase in temperature to 700 °C increased the surface area to 55 m²/g for RB and 107 m²/g to TB. The 2-fold higher surface area of TB-biochar compared to RB-biochar was supported by the improved pore structure development of TB biochar, as shown in Fig. 4(H). Higher surface area and pore volume are indicative of the stability of the char structure, which can enhance their application in catalysis and adsorption [6]. The pore size distribution indicates that the biochar materials are largely mesoporous with pore width in the 2–50 nm range. However, the relatively lowest pore width in the case of TB_nw indicates possible pore blockage by the poorly soluble metal sulfate salt, particularly CaSO₄ hydrates that covers the surface as observed under the SEM imaging.

3.5. Effect of pre-treatment on bio-oil compositions

The chemical compositions identified through the GC/MS analysis of the bio-oil obtained from the pyrolysis of raw and treated biosolids are summarised in Table 5. The results showed that the bio-oil is a complex mixture of various chemical compounds grouped into oxygenates, nitrogenated compounds, sulfur-containing, and hydrocarbons. Temperature and pre-treatment considerably affect the evolution of volatile organic compounds in the bio-oil. Generally, for all biosolids samples, the yield of nitrogenated and oxygenated compounds decreased with increasing pyrolysis temperature, while hydrocarbons and phenol yield increased with temperature. The effects of pre-treatment on the distribution of chemical components in the bio-oil varied with pyrolysis temperature. For instance, pre-treatment enhanced hydrocarbon production from 20% in RB to 30–35% in treated biosolids at ≥ 500 °C, whereas anhydrosugars yield was increased from 2.1% in RB to 4.5% in TB only at 300 °C, while phenolics yield was similar for all bio-oils at all temperatures.

The bio-oil obtained at 300 °C consists mainly of high molecular weight nitrogenated and oxygenated compounds, with major chemical species being *N*-heterocyclics and ketones. Nitrogenated compounds in bio-oil originated from the thermal devolatilisation of proteins, while ketonic compounds are from the primary decomposition of carbohydrates. *N*-heterocyclics could be formed by dehydrogenation of the amino group present in proteins and nucleic acids in biosolids and through the addition of HCN and/or NH₃ to benzene/toluene aromatic ring during pyrolysis [50]. Dehydration and decarboxylation of organic matter are prominent thermolysis reactions at lower temperatures resulting in the formation of high-molecular-weight reactive oxygenate fragments such as R-CHO, R-C-O-R, R-CO-OH, and R-O-R [51]. Pyrolysis at 300 °C was selective for producing a few kinds of *N*-heterocyclics, amides/amines, and ketones, irrespective of the biosolids feed

Table 4
Surface properties of biochar samples.

Pyrolysis temperature (°C)	Feed samples	Surface properties		
		BET specific surface area (m ² /g)	BJH average pore volume (cm ³ /g)	BJH average pore width (nm)
300	RB	15.2	0.012	7.94
	TB	25.2	0.024	8.00
	TB_nw	20.5	0.015	7.84
500	RB	26.9	0.021	8.67
	TB	43.7	0.030	8.81
	TB_nw	32.9	0.017	8.22
700	RB	55.3	0.039	7.65
	TB	106.9	0.061	8.54
	TB_nw	72.5	0.043	7.03

Table 5
GC/MS analysis showing the chemical composition of the bio-oil samples.

Bio-oil compositions									
Pyrolysis temperature (°C)	300			500			700		
Biosolids samples	RB	TB	TB_nw	RB	TB	TB_nw	RB	TB	TB_nw
Compounds	Peak Area (%)								
Pyrazine	14.1	2.9	16.3	-	-	2.3	4.5	-	-
Pyridine	8.3	6.4	8.5	3.0	1.5	2.3	1.7	1.0	8.5
Pyrrrole	3.4	0.4	-	8.2	1.4	0.4	1.6	5.7	0.5
Azole	0.3	0.2	-	0.9	6.3	0.9	9.0	8.0	0.5
Amines	5.3	5.8	16.9	3.4	2.0	0.6	1.3	0.4	4.6
Amides	19.3	17.6	8.5	7.4	4.8	2.1	4.2	2.3	1.6
Nitriles	1.8	1.1	3.2	4.5	7.1	7.2	3.8	5.9	6.5
Total Nitrogenated	52.5	34.4	53.4	27.3	23.0	15.8	26.2	23.7	22.2
Esters	1.2	2.9	3.5	8.3	15.0	18.8	14.4	10.9	13.0
Ethers	-	-	-	2.5	-	-	2.5	-	-
Ketones	30.5	37.7	16.7	20.9	11.5	8.8	10.6	8.6	6.1
Aldehydes	-	1.0	-	-	0.8	-	-	0.9	1.0
Acids	2.1	4.5	7.8	4.4	0.9	3.8	3.6	3.3	6.9
Alcohols	2.1	0.5	-	0.8	1.5	9.3	1.5	3.0	6.6
Furans	1.0	10.6	10.4	-	-	-	-	-	0.5
Total Oxygenated	37.0	57.2	38.4	36.9	29.7	40.6	32.6	26.7	34.0
1,4:3,6-Dianhydro- α -D-glucopyranose	1.2	1.9	-	-	-	-	-	-	-
2,3,4-Trimethyllevoglucosan	0.5	0.4	-	-	-	-	-	-	-
Maltol	-	0.7	0.7	-	-	-	-	-	-
Others	0.4	1.5	-	-	-	-	-	-	-
Total Anhydrosugars	2.1	4.5	0.7	-	-	-	-	-	-
Phenols	8.6	1.0	2.7	11.3	9.3	4.7	8.9	10.2	6.0
<i>p</i> -Cresol	-	-	-	4.1	5.3	1.4	4.8	6.2	4.2
Total Phenolics	8.6	1.0	2.7	15.4	14.6	6.1	13.7	16.4	10.2
Olefin	-	0.3	1.0	1.9	2.1	2.1	2.9	2.3	1.8
Paraffin	-	1.2	0.8	6.2	7.7	8.1	11.6	10.4	5.2
BTXS ^a	-	0.6	1.2	12.4	20.6	25.0	13.1	18.6	20.9
Polyaromatic	-	-	-	-	0.4	0.3	-	0.8	2.8
Total Hydrocarbons	-	2.1	3.0	20.5	30.8	35.5	27.6	32.1	30.7
Total S-containing compounds	-	1.0	1.5	-	2.0	2.7	-	0.9	3.0

^a BTXS- Benzene, Toluene, Xylene, and Styrene

samples. However, inherent minerals in RB and residual acid in TB_nw facilitated denitrogenation reactions to generate more volatile-N compounds than TB. For instance, at 300 °C, total N-compounds were 53% for RB and TB_nw and 34% for TB. Significant thermal cracking of heavy N-heterocyclic compounds to simple aromatic/aliphatic N-compounds occurred at higher pyrolysis temperatures (500–700 °C), reducing total nitrogenated compounds in the bio-oil to \approx 23% for all samples. The effect of pre-treatment on the evolution of N-compounds was less intense at 500 and 700 °C. It has been observed that the interaction between mineral matter and N-containing compounds in biosolids was strongly limited by pyrolysis temperature [52].

Notably, anhydrosugars (including sugar alcohols) production was sensitive to pyrolysis temperatures. It was detected only at 300 °C, and the yield was improved by more than 50% following the removal of AAEMs in TB. At 500–700 °C, pre-treatment had no impact on the production of anhydrosugars as they are highly susceptible to secondary degradation facilitated by metal and acid catalysts as well as higher pyrolysis temperatures [53]. However, biosolids pre-treatment favoured the production of sugar dehydration products such as maltol and furans (10%), mainly comprising 3-HMF, furfural, and 5-methyl furfural. The acid catalysis of sugars is a popular route to enhance the formation of furfural compounds [54]. The passivation of AAEMs by acid infusion selectively enhanced sugar dehydration products, such as levoglucosone and furfural, whose yield was observed to be related to the quantity of acid added [55]. Phenols and their derivatives may originate from biosolids pyrolysis through the secondary decomposition of polysaccharides and proteins and are generally enhanced at higher temperatures from aromatisation reactions [56]. At 300 °C, the total phenolics yield was less than 10%, mostly detected in RB bio-oil. At higher temperatures, phenolics yield increased to \approx 15% for both RB and TB, whereas it was no more than 10% for TB_nw. Mineral removal by pre-treatment had no significant effect on phenol production; however,

residual acid in TB_nw suppressed phenol formation relative to RB. Other works [36,57] have also suggested that phenol precursor such as lignin is relatively inert to AAEMs. While AAEMs are largely inert in catalysing the cleavage of the ester group in lignin to produce guaiacols (vinyl-phenols), it has been found effective in promoting the cleavage of β -O-4 aryl ether bonds to produce simple phenolic monomers such as cresols [55]. This could explain the higher yield of *p*-cresol with acid-pre-treated biosolids compared to RB.

Hydrocarbon production increased monotonically with temperature, and it grew from 0% to 3% at 300 °C to 20–35% at 500 °C for all samples, with RB having the lowest yield. Raising the temperature to 700 °C increased hydrocarbon yield to 28% for RB, slightly decreasing the yield to about 32% for treated biosolids. Monoaromatic hydrocarbons, mainly benzene, toluene, xylene, and styrene (BTXS), are the major compounds in the bio-oil at higher temperatures \geq 500 °C. In contrast, aliphatic hydrocarbons, mainly paraffin and olefin, were detected in bio-oil from untreated biosolids at $<$ 500 °C. Acid pre-treatment enhanced aromatisation reactions, which increased the yields of monoaromatic hydrocarbons due to the suppression of AAEMs-catalysed ring opening and fragmentation reactions that would otherwise convert -CH to light oxygenates, COx gases, and char [36,58]. In a previous study [36], acid washing and infusion enhanced the formation of aromatic hydrocarbons by \sim 30%; however, both pre-treatment did not significantly change the yield of olefins, similar to the observation in the current work. The weaker effect of inherent AAEMs caused by acid pre-treatment increased the formation of undesired stable polycyclic aromatic hydrocarbons (PAHs) in bio-oil from TB and TB_nw; however, PAHs were not detected in RB bio-oil at all temperatures. AAEMs and their minerals can enhance the cracking of heavy PAHs into monoaromatics, particularly at higher temperatures [59]. Lastly, aromatic sulfur compounds such as benzothiazole, thiazolidine, thiophene, and aliphatic S-compounds, mainly methyl sulfides, were detected in the bio-oil obtained from treated

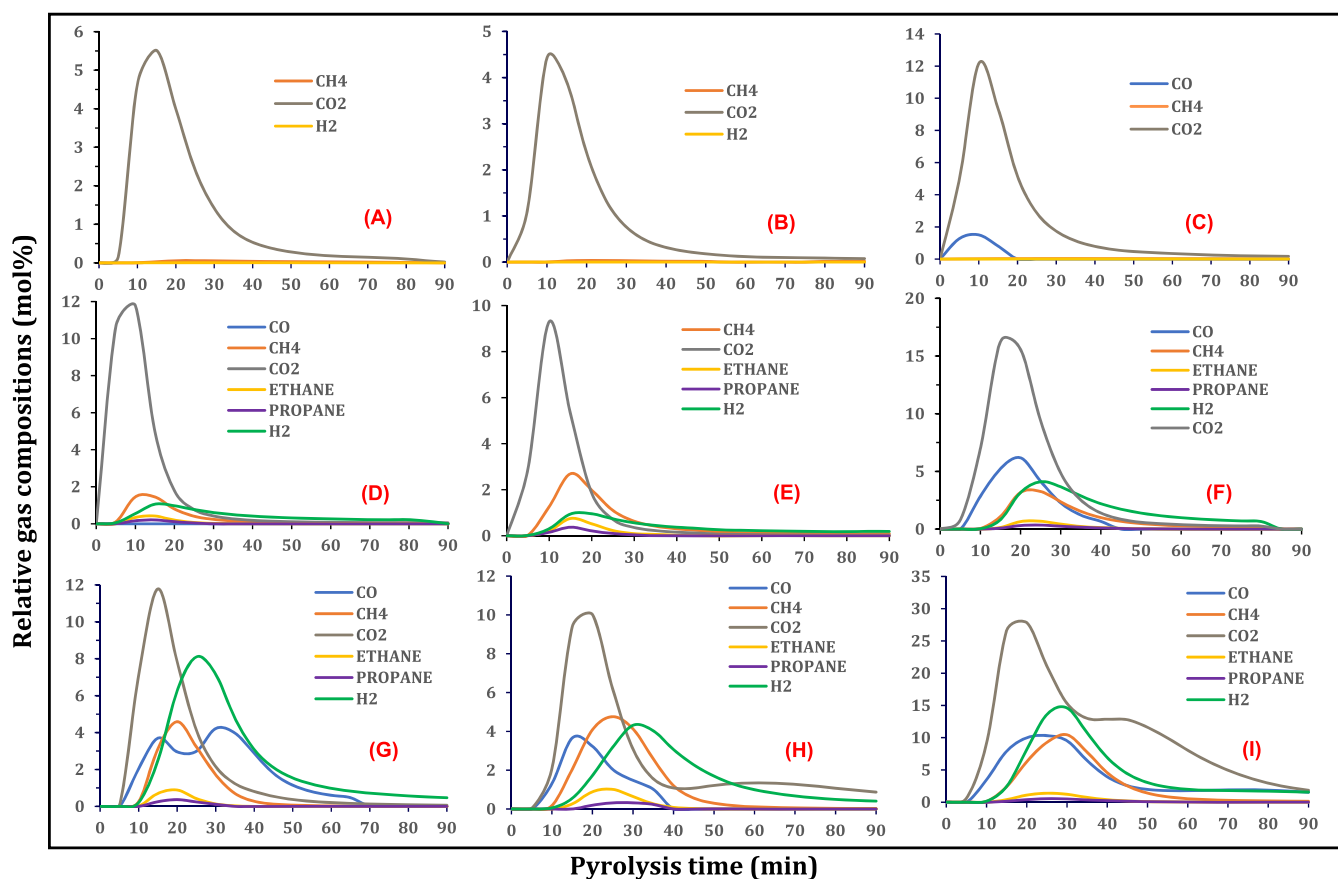


Fig. 5. Effect of pre-treatment and temperature on pyrolysis gas compositions (A) RB300 (B) TB300 (C)TB_nw300 (D) RB500 (E) TB500 (F) TB_nw500 (G) RB700 (H) TB700 (I) TB_nw700.

biosolids. The evolution of these S-compounds was stronger at ≥ 500 °C and for TB_nw (up to 3%). Therefore, the acid treatment should be accompanied by a neutralisation step, as in TB, to mitigate the release of volatile S-compounds.

Due to the generally high nitrogen and oxygen contents, the bio-oil may not be suitable as fuel for energy recovery. However, the chemical value of the bio-oil obtained at 300 °C can be explored for the selective recovery of N-containing compounds, and the ketone-rich fraction can be subjected to catalytic hydrodeoxygenation to produce olefins [60]. Therefore, biosolids pyrolysis at 300 °C may be considered a thermal pre-treatment step for the reduction of nitrogen and oxygen contents and improve hydrocarbon yield during subsequent pyrolysis at higher temperatures [61]. The addition of acid pre-treatment can further enhance the chemical value of the bio-oil by increasing sugars, furans, and aromatic hydrocarbon, as observed in the current work. Fonts et al. [62] reported that ammonia, α -olefins, n-paraffins, aromatic hydrocarbons, nitriles, phenols, fatty acids, short carboxylic acids and indole were the most attractive chemical compounds in biosolids bio-oil.

3.6. Effect of pre-treatment on pyrolysis gas compositions

The evolution profile of non-condensable gases from the pyrolysis of raw and treated biosolids at 300–700 °C is shown in Fig. 5. The identified gas components are carbon oxides (CO and CO₂), H₂, and C₁–C₃ saturated hydrocarbon gases (methane, ethane, and propane). The concentration of the gases was low at the start of pyrolysis as the feed was gradually heated to the desired temperature. The gas concentration steadily increased between 10 and 30 min; after that, the concentration gradually decreased, reaching zero at 60–90 min. The most abundant

gas components were H₂, CO, CO₂ and CH₄, while only traces of ethane and propane were detected at higher pyrolysis temperatures > 500 °C. Generally, gas production increased with increasing pyrolysis temperature due to the profound thermal cracking of primary decomposition products and secondary reactions. At 300 °C (Fig. 5(A–C)), CO₂ was the dominant gas component, with traces of CH₄ and H₂ in the pyrolysis gas stream largely from the decarboxylation of organic matter. At higher pyrolysis temperatures, gasification reactions matured, and more gas components were formed at higher concentrations stemming from the thermal cracking of heavy molecular weight volatiles to lighter ones accompanied by the release of C₁–C₃ hydrocarbons (Fig. 5(D–I)). At 700 °C (Fig. 5(G–I)), the gas evolution was stronger, and the concentrations were highest attributed to the profound secondary cracking reactions heightened by char-volatile interactions [63].

The removal or passivation of inherent metals in biosolids via pre-treatment affected the gas evolution and concentration during pyrolysis, especially at higher pyrolysis temperatures. The pyrolysis of TB produced less CO₂, CO, and H₂ but slightly more C₁–C₃ hydrocarbons than RB, suggesting that pre-treatment inhibited gas production due to the inferior catalytic cracking effect of ash elements. For example, at 700 °C, the highest CO and H₂ concentration was 4.2 mol% and 8 mol%, respectively, for RB (Fig. 5(G)), and it was 3.6 mol% and 4.3 mol%, respectively, for TB (Fig. 5(H)). Secondary cracking was prominent and catalysed by the native metal in RB, leading to higher concentrations of CO and H₂. The second CO peak in RB at 700 °C (Fig. 5(G)) after 30 min pyrolysis time can be attributed to Boudouard char gasification reactions where CO₂ is reacted with carbon to give CO [30]. Notably, the highest gas concentrations were observed during the pyrolysis of TB_nw at all temperatures. The XRD pattern of TB_nw identified Ca(HSO₄)₂ and

Fe(HSO₄)₃ as the major acidic sulfate salts, which facilitated H₂ production via the release of H⁺ through thermal hydrolysis reactions to form normal sulfate salts (CaSO₄ and Fe₂(SO₄)₃) [64]. The presence of residual acid in TB_{nw} had a remarkable catalytic effect on gas production, with CO₂, CO, CH₄, and H₂ yield reaching a maximum concentration of 28 mol%, 10 mol%, 10.5 mol%, and 15 mol%, respectively (Fig. 5(I)). Whereas, with the full spectrum of metals in RB, the maximum gas concentration at 700 °C was 12 mol% CO₂, 4 mol% CO, 4.5 mol% CH₄, and 8 mol% H₂ (Fig. 5(G)). The improved gas production in TB_{nw} despite lean mineral matter compared to RB was attributed to the dehydration reactions catalysed by residual H₂SO₄, favouring water-gas reactions [42]. Biosolids acid pre-treatment for demineralisation (as in TB) can be helpful to weaken gas production and CO₂ release, while pre-treatment as in TB_{nw} strengthened gas production, and CO₂ yield was more than 2-fold higher than that from RB.

4. Conclusions

The quality of biosolids as feedstock for pyrolysis can be improved by acid pre-treatment to selectively remove the ash-forming elements and HMs without degrading the organic matter. Mild acid pre-treatment process (using 3% v/v H₂SO₄ at 25 °C for 60 min) followed by a water washing step achieved about 40% reduction of ash content and a 10% increase in volatile matter with carbon retention of 80%. In contrast, the acid treatment without the water washing step achieved lower demineralisation efficiency (28%) with higher carbon retention (88%). At all operating temperatures, the pyrolysis of neutralised acid-treated biosolids produced higher bio-oil and lower biochar yield due to improved organic matter devolatilisation and inorganic content reduction. The presence of residual acid in treated biosolids inhibited organic matter conversion to bio-oil; however, it enhanced gas production attributed to dehydration reactions and hydrolysis of acidic metal sulfate salts to normal metal sulfate salts. Biochar obtained from treated biosolids had higher organic matter retention, calorific value, fuel ratio, and fixed carbon due to the weakened catalytic cracking of organics, particularly at higher pyrolysis temperatures. Biosolids pre-treatment increased the stability and reduced the concentration and bioavailability of HMs in the derived biochar. The bio-oil composition was impacted by pre-treatment, and at 300 °C, anhydrosugars yield doubled in treated biosolids' bio-oil compared to raw biosolids' bio-oil. While pre-treatment did not have much effect on phenol production, monoaromatic hydrocarbon yield was remarkably improved. However, the evolution of PAHs and sulfur-containing compounds was stronger during the pyrolysis of treated biosolids than raw biosolids. Biosolids acid pre-treatment with the water washing step is preferred to increase bio-oil yield and enhance biochar quality.

CRedit authorship contribution statement

Ibrahim Gbolahan Hakeem: Conceptualization, Methodology, Formal analysis, Investigation, Writing - original draft, Writing - review & editing. **Pobitra Halder:** Validation, Writing - review & editing. **Savankumar Patel:** Writing - review & editing. **Abhishek Sharma:** Writing - review & editing. **Rajender Gupta:** Writing - review & editing. **Aravind Surapaneni:** Resources, Supervision. **Jorge Paz-Ferreiro:** Supervision, Writing - review & editing. **Kalpita Shah:** Conceptualization, Methodology, Validation, Supervision, Project administration.

Declaration of Competing Interest

The authors declare that they have no known competing financial interests or personal relationships that could have appeared to influence the work reported in this paper.

Data availability

Data will be made available on request.

Acknowledgements

This work is supported through Top-Up Scholarships provided by the School of Engineering, RMIT University and the ARC Training Centre for the Transformation of Australia's Biosolids Resource at RMIT University, Australia. The use of the Scanning Electron Microscope instrument in the RMIT Microanalysis and Microscopy Facility is acknowledged. The BET equipment in the Advanced Porous Materials Lab at RMIT University was used in this study. Finally, the first author acknowledged the PhD research stipend scholarship received from RMIT University, Australia.

Appendix A. Supporting information

Supplementary data associated with this article can be found in the online version at [doi:10.1016/j.jaap.2023.106087](https://doi.org/10.1016/j.jaap.2023.106087).

References

- [1] A. Gianico, C.M. Braguglia, A. Gallipoli, D. Montecchio, G. Mininni, Land application of biosolids in Europe: possibilities, con-strains and future perspectives, *Water* 13 (2021) 103, <https://doi.org/10.3390/W13010103>.
- [2] N. Gao, K. Kamran, C. Quan, P.T. Williams, Thermochemical conversion of sewage sludge: A critical review, *Prog. Energy Combust. Sci.* 79 (2020), 100843, <https://doi.org/10.1016/j.pecs.2020.100843>.
- [3] W. Zhang, Y. Liang, Effects of hydrothermal treatments on destruction of per- and polyfluoroalkyl substances in sewage sludge, *Environ. Pollut.* 285 (2021), 117276, <https://doi.org/10.1016/J.ENVPOL.2021.117276>.
- [4] J.J. Ross, D.H. Zitomer, T.R. Miller, C.A. Weirich, P.J. Mcnamara, Emerging investigators series: pyrolysis removes common microconstituents triclocarban, triclosan, and nonylphenol from biosolids, *Environ. Sci. Water Res. Technol.* 2 (2016) 282–289, <https://doi.org/10.1039/C5EW00229J>.
- [5] O.S. Djangja, Z.C. Wang, F. Wang, Y.P. Xu, P.G. Duan, Pyrolysis of municipal sewage sludge for biofuel production: A review, *Ind. Eng. Chem. Res.* 59 (2020) 16939–16956, <https://doi.org/10.1021/acs.iecr.0c01546>.
- [6] S. Patel, S. Kundu, P. Halder, N. Ratnmayake, M.H. Marzbali, S. Aktar, E. Selezneva, J. Paz-Ferreiro, A. Surapaneni, C.C. de Figueiredo, A. Sharma, M. Megharaj, K. Shah, A critical literature review on biosolids to biochar: an alternative biosolids management option, *Rev. Environ. Sci. Biotechnol.* 19 (2020) 807–841, <https://doi.org/10.1007/s11157-020-09553-x>.
- [7] P. Giudicianni, V. Gargiulo, C.M. Grottola, M. Alfè, A.I. Ferreiro, M.A.A. Mendes, M. Fagnano, R. Ragucci, Inherent metal elements in biomass pyrolysis: a review, *Energy Fuels* 35 (2021) 5407–5478, <https://doi.org/10.1021/ACS.ENERGYFUELS.0C04046>.
- [8] H. Nan, F. Yang, L. Zhao, O. Mašek, X. Cao, Z. Xiao, Interaction of inherent minerals with carbon during biomass pyrolysis weakens biochar carbon sequestration potential, *ACS Sustain. Chem. Eng.* 7 (2018) 1591–1599, <https://doi.org/10.1021/ACSSUSCHEMENG.8B05364>.
- [9] Y. Niu, H. Tan, S. Hui, Ash-related issues during biomass combustion: Alkali-induced slagging, silicate melt-induced slagging (ash fusion), agglomeration, corrosion, ash utilization, and related countermeasures, *Prog. Energy Combust. Sci.* 52 (2016) 1–61, <https://doi.org/10.1016/j.pecs.2015.09.003>.
- [10] M.J. Bentley, J.P. Kearns, B.M. Murphy, R.S. Summers, Pre-pyrolysis metal and base addition catalyzes pore development and improves organic micropollutant adsorption to pine biochar, *Chemosphere* 286 (2022), 131949, <https://doi.org/10.1016/J.CHEMOSPHERE.2021.131949>.
- [11] I.G. Hakeem, P. Halder, C.C. Dike, K. Chiang, A. Sharma, J. Paz-Ferreiro, K. Shah, Advances in biosolids pyrolysis: Roles of pre-treatments, catalysts, and co-feeding on products distribution and high-value chemical production, *J. Anal. Appl. Pyrolysis* 166 (2022), 105608, <https://doi.org/10.1016/J.JAAP.2022.105608>.
- [12] R. Patel, P. Zaveri, N.S. Munshi, Microbial fuel cell, the Indian scenario: developments and scopes, *Biofuels* 10 (2019) 101–108, <https://doi.org/10.1080/17597269.2017.1398953>.
- [13] N.A. Haji Morni, C.M. Yeung, H. Tian, Y. Yang, N. Phusunti, M.S. Abu Bakar, A. K. Azad, Catalytic fast Co-Pyrolysis of sewage sludge—sawdust using mixed metal oxides modified with ZSM-5 catalysts on dual-catalysts for product upgrading, *J. Energy Inst.* 94 (2021) 387–397, <https://doi.org/10.1016/J.JOEL.2020.10.005>.
- [14] Z. Qiu, Y. Zhai, S. Li, X. Liu, X. Liu, B. Wang, Y. Liu, C. Li, Y. Hu, Catalytic co-pyrolysis of sewage sludge and rice husk over biochar catalyst: Bio-oil upgrading and catalytic mechanism, *Waste Manag* 114 (2020) 225–233, <https://doi.org/10.1016/J.WASMAN.2020.07.013>.
- [15] N. Rathnayake, S. Patel, I.G. Hakeem, J. Pazferreiro, A. Sharma, R. Gupta, C. Rees, D. Bergmann, J. Blackbeard, A. Surapaneni, K. Shah, Co-pyrolysis of biosolids with lignocellulosic biomass: Effect of feedstock on product yield and composition, *Process Saf. Environ. Prot.* (2023), <https://doi.org/10.1016/J.PSEP.2023.02.087>.

- [16] X. Wang, S. Deng, H. Tan, A. Adeosun, M. Vujanović, F. Yang, N. Duić, Synergetic effect of sewage sludge and biomass co-pyrolysis: A combined study in thermogravimetric analyzer and a fixed bed reactor, *Energy Convers. Manag* 118 (2016) 399–405, <https://doi.org/10.1016/j.enconman.2016.04.014>.
- [17] I.G. Hakeem, P. Halder, M.H. Marzbali, S. Patel, N. Rathnayake, A. Surapaneni, G. Short, J. Paz-Ferreiro, K. Shah, Mild sulphuric acid pre-treatment for metals removal from biosolids and the fate of metals in the treated biosolids derived biochar, *J. Environ. Chem. Eng.* 10 (2022), 107378, <https://doi.org/10.1016/J.JECE.2022.107378>.
- [18] G. Liu, M.M. Wright, Q. Zhao, R.C. Brown, Hydrocarbon and ammonia production from catalytic pyrolysis of sewage sludge with acid pretreatment, *ACS Sustain. Chem. Eng.* 4 (2016) 1819–1826, <https://doi.org/10.1021/acssuschemeng.6b00016>.
- [19] S. Tang, C. Zheng, Z. Zhang, Effect of inherent minerals on sewage sludge pyrolysis: Product characteristics, kinetics and thermodynamics, *Waste Manag* 80 (2018) 175–185, <https://doi.org/10.1016/j.wasman.2018.09.012>.
- [20] Z. Yang, D. Wang, G. Wang, S. Zhang, Z. Cheng, J. Xian, Y. Pu, T. Li, Y. Jia, Y. Li, W. Zhou, X. Xu, Removal of Pb, Zn, Ni and Cr from industrial sludge by biodegradable washing agents: Caboxyethylthiosuccinic acid and itaconic-acrylic acid, *J. Environ. Chem. Eng.* 9 (2021), 105846, <https://doi.org/10.1016/J.JECE.2021.105846>.
- [21] R. Kumar, V. Strezov, H. Weldekidan, J. He, S. Singh, T. Kan, B. Dastjerdi, Lignocellulose biomass pyrolysis for bio-oil production: A review of biomass pre-treatment methods for production of drop-in fuels, *Renew. Sustain. Energy Rev.* 123 (2020), 109763, <https://doi.org/10.1016/J.RSER.2020.109763>.
- [22] V.T. Pham, C.Y. Guan, P.C. Han, B.M. Matsagar, K.C.W. Wu, T. Ahamad, C. Y. Chang, C.P. Yu, Acid-catalyzed hydrothermal treatment of sewage sludge: effects of reaction temperature and acid concentration on the production of hydrolysis by-products, *Biomass - Convers. Biorefinery.* 13 (2021) 7533–7546, <https://doi.org/10.1007/S13399-021-01495-W/FIGURES/5>.
- [23] I.G. Hakeem, P. Halder, S. Aktar, M.H. Marzbali, A. Sharma, A. Surapaneni, G. Short, J. Paz-Ferreiro, K. Shah, Investigations into the closed-loop hydrometallurgical process for heavy metals removal and recovery from biosolids via mild acid pre-treatment, *Hydrometallurgy* 218 (2023), 106044, <https://doi.org/10.1016/J.HYDROMET.2023.106044>.
- [24] I. Beauchesne, R. Ben Cheikh, G. Mercier, J.F. Blais, T. Ourada, Chemical treatment of sludge: In-depth study on toxic metal removal efficiency, dewatering ability and fertilizing property preservation, *Water Res* 41 (2007) 2028–2038, <https://doi.org/10.1016/J.WATRES.2007.01.051>.
- [25] J. Shao, R. Yan, H. Chen, H. Yang, D.H. Lee, Catalytic effect of metal oxides on pyrolysis of sewage sludge, *Fuel Process. Technol.* 91 (2010) 1113–1118, <https://doi.org/10.1016/j.fuproc.2010.03.023>.
- [26] S. Tang, C. Zheng, F. Yan, N. Shao, Y. Tang, Z. Zhang, Product characteristics and kinetics of sewage sludge pyrolysis driven by alkaline earth metals, *Energy* 153 (2018) 921–932, <https://doi.org/10.1016/j.energy.2018.04.108>.
- [27] S. Tang, S. Tian, C. Zheng, Z. Zhang, Effect of Calcium Hydroxide on the Pyrolysis Behavior of Sewage Sludge: Reaction Characteristics and Kinetics, *Energy Fuels* 31 (2017) 5079–5087, <https://doi.org/10.1021/acs.energyfuels.6b03256>.
- [28] Y. Kim, W. Parker, A technical and economic evaluation of the pyrolysis of sewage sludge for the production of bio-oil, *Bioresour. Technol.* 99 (2008) 1409–1416, <https://doi.org/10.1016/j.biortech.2007.01.056>.
- [29] N. Rathnayake, S. Patel, P. Halder, S. Aktar, J. Pazferreiro, A. Sharma, A. Surapaneni, K. Shah, Co-pyrolysis of biosolids with alum sludge: Effect of temperature and mixing ratio on product properties, *J. Anal. Appl. Pyrolysis* 163 (2022), 105488, <https://doi.org/10.1016/J.JAAP.2022.105488>.
- [30] S. Patel, S. Kundu, P. Halder, G. Veluswamy, B. Pramanik, Slow pyrolysis of biosolids in a bubbling fluidised bed reactor using biochar, activated char and lime, *J. Anal. Appl. Pyrolysis* 144 (2019) 1–11, <https://doi.org/10.1016/j.jaap.2019.104697>.
- [31] S.A. Channiwala, P.P. Parikh, A unified correlation for estimating HHV of solid, liquid and gaseous fuels, *Fuel* 81 (2002) 1051–1063, [https://doi.org/10.1016/S0016-2361\(01\)00131-4](https://doi.org/10.1016/S0016-2361(01)00131-4).
- [32] W.L. Lindsay, W.A. Norvell, Development of a DTPA Soil Test for Zinc, Iron, Manganese, and Copper, *Soil Sci. Soc. Am. J.* 42 (1978) 421–428, <https://doi.org/10.2136/SSSAJ1978.03615995004200030009X>.
- [33] E.P.A. Victoria, Guidelines for Environmental Management: Biosolids Land Application, Southbank, Victoria 3006, Australia, 2004.
- [34] X. Wang, L. Sheng, X. Yang, Pyrolysis characteristics and pathways of protein, lipid and carbohydrate isolated from microalgae *Nannochloropsis* sp, *Bioresour. Technol.* 229 (2017) 119–125, <https://doi.org/10.1016/J.BIORTECH.2017.01.018>.
- [35] S.R. Patel, S.K. Kundu, P.K. Halder, A. Setiawan, J. Paz-Ferreiro, A. Surapaneni, K. V. Shah, A Hybrid Kinetic Analysis of the Biosolids Pyrolysis using Thermogravimetric Analyser, *ChemistrySelect* 3 (2018) 13400–13407, <https://doi.org/10.1002/slct.201802957>.
- [36] K. Wang, J. Zhang, B.H. Shanks, R.C. Brown, The deleterious effect of inorganic salts on hydrocarbon yields from catalytic pyrolysis of lignocellulosic biomass and its mitigation, *Appl. Energy* 148 (2015) 115–120, <https://doi.org/10.1016/j.apenergy.2015.03.034>.
- [37] X. Zhu, L. Zhao, F. Fu, Z. Yang, F. Li, W. Yuan, M. Zhou, W. Fang, G. Zhen, X. Lu, X. Zhang, Pyrolysis of pre-dried dewatered sewage sludge under different heating rates: Characteristics and kinetics study, *Fuel* 255 (2019), 115591, <https://doi.org/10.1016/J.FUEL.2019.05.174>.
- [38] N. Gao, J. Li, B. Qi, A. Li, Y. Duan, Z. Wang, Thermal analysis and products distribution of dried sewage sludge pyrolysis, *J. Anal. Appl. Pyrolysis* 105 (2014) 43–48, <https://doi.org/10.1016/J.JAAP.2013.10.002>.
- [39] S. Zhou, Z. Wang, S. Liaw, C. Li, M. Garcia-perez, Effect of sulfuric acid on the pyrolysis of Douglas fir and hybrid poplar wood: Py-GC / MS and TG studies, *J. Anal. Appl. Pyrolysis* 104 (2013) 117–130, <https://doi.org/10.1016/j.jaap.2013.08.013>.
- [40] S. Aktar, M.A. Hossain, N. Rathnayake, S. Patel, G. Gasco, A. Mendez, C. de Figueiredo, A. Surapaneni, K. Shah, J. Paz-Ferreiro, Effects of temperature and carrier gas on physico-chemical properties of biochar derived from biosolids, *J. Anal. Appl. Pyrolysis* 164 (2022), 105542, <https://doi.org/10.1016/J.JAAP.2022.105542>.
- [41] D. Carpenter, T.L. Westover, S. Czernik, W. Jablonski, Biomass feedstocks for renewable fuel production: a review of the impacts of feedstock and pretreatment on the yield and product distribution of fast pyrolysis bio-oils and vapors, *Green. Chem.* 16 (2014) 384–406, <https://doi.org/10.1039/C3GC41631C>.
- [42] S. Zhou, D. Mourant, C. Lievens, Y. Wang, C. Li, M. Garcia-perez, Effect of sulfuric acid concentration on the yield and properties of the bio-oils obtained from the auger and fast pyrolysis of Douglas Fir, *Fuel* 104 (2013) 536–546, <https://doi.org/10.1016/j.fuel.2012.06.010>.
- [43] Y. Zhang, P. Lv, J. Wang, J. Wei, P. Cao, N. Bie, Y. Bai, G. Yu, Product characteristics of rice straw pyrolysis at different temperature: Role of inherent alkali and alkaline earth metals with different occurrence forms, *J. Energy Inst.* 101 (2022) 201–208, <https://doi.org/10.1016/J.JOEI.2022.01.016>.
- [44] X. Sun, R. Shan, X. Li, J. Pan, X. Liu, R. Deng, J. Song, Characterization of 60 types of Chinese biomass waste and resultant biochars in terms of their candidacy for soil application, *GCB Bioenergy* 9 (2017) 1423–1435, <https://doi.org/10.1111/GCBB.12435>.
- [45] X. Xiao, Z. Chen, B. Chen, H/C atomic ratio as a smart linkage between pyrolytic temperatures, aromatic clusters and sorption properties of biochars derived from diverse precursory materials, *Sci. Rep.* 6 (2016), <https://doi.org/10.1038/srep22644>.
- [46] M. Praspaliauskas, N. Pedišius, N. Striugas, Elemental Migration and Transformation from Sewage Sludge to Residual Products during the Pyrolysis Process, *Energy Fuels* 32 (2018) 5199–5208, https://doi.org/10.1021/ACS.ENERGYFUELS.8B00196/ASSET/IMAGES/LARGE/EF-2018-001968_0006.JPEG.
- [47] Z. Zhang, R. Ju, H. Zhou, H. Chen, Migration characteristics of heavy metals during sludge pyrolysis, *Waste Manag* 120 (2021) 25–32, <https://doi.org/10.1016/j.wasman.2020.11.018>.
- [48] D. del Mundo Dacera, S. Babel, Use of citric acid for heavy metals extraction from contaminated sewage sludge for land application, *Water Sci. Technol.* 54 (2006) 129–135, <https://doi.org/10.2166/wst.2006.764>.
- [49] Z. Cui, G. Xu, B. Ormeci, H. Liu, Z. Zhang, Transformation and stabilization of heavy metals during pyrolysis of organic and inorganic-dominated sewage sludges and their mechanisms, *Waste Manag* 150 (2022) 57–65, <https://doi.org/10.1016/J.WASMAN.2022.06.023>.
- [50] A. Fullana, J.A. Conesa, R. Font, I. Martin-Gullon, Pyrolysis of sewage sludge: nitrogenated compounds and pretreatment effects, *J. Anal. Appl. Pyrolysis* 69 (2003) 561–575, [https://doi.org/10.1016/S0165-2370\(03\)00052-4](https://doi.org/10.1016/S0165-2370(03)00052-4).
- [51] X. Yang, B. Wang, Y. Guo, F. Yang, F. Cheng, Co-hydrothermal carbonization of sewage sludge and coal slime for clean solid fuel production: a comprehensive assessment of hydrochar fuel characteristics and combustion behavior, *Biomass - Convers. Biorefinery* (2022), <https://doi.org/10.1007/s13399-022-03601-y>.
- [52] L.H. Wei, L.N. Wen, M.J. Liu, T.H. Yang, Interaction Characteristics of Mineral Matter and Nitrogen during Sewage Sludge Pyrolysis, *Energy Fuels* 30 (2016) 10505–10510, <https://doi.org/10.1021/acs.energyfuels.6b02146>.
- [53] I.G. Hakeem, P. Halder, M.H. Marzbali, S. Patel, S. Kundu, J. Paz-Ferreiro, A. Surapaneni, K. Shah, Research progress on levoglucosan production via pyrolysis of lignocellulosic biomass and its effective recovery from bio-oil, *J. Environ. Chem. Eng.* 9 (2021), 105614, <https://doi.org/10.1016/j.jece.2021.105614>.
- [54] S.R.G. Oudenhoven, R.J.M. Westerhof, N. Aldenkamp, D.W.F. Brilman, S.R.A. Kersten, Demineralization of wood using wood-derived acid: Towards a selective pyrolysis process for fuel and chemicals production, *J. Anal. Appl. Pyrolysis* 103 (2013) 112–118, <https://doi.org/10.1016/j.jaap.2012.10.002>.
- [55] S. Zhou, Y. Xue, J. Cai, C. Cui, Z. Ni, Z. Zhou, An understanding for improved biomass pyrolysis: Toward a systematic comparison of different acid pretreatments, *Chem. Eng. J.* 411 (2021), 128513, <https://doi.org/10.1016/J.CEJ.2021.128513>.
- [56] X. Huang, J.P. Cao, P. Shi, X.Y. Zhao, X.B. Feng, Y.P. Zhao, X. Fan, X.Y. Wei, T. Takarada, Influences of pyrolysis conditions in the production and chemical composition of the bio-oils from fast pyrolysis of sewage sludge, *J. Anal. Appl. Pyrolysis* 110 (2014) 353–362, <https://doi.org/10.1016/J.JAAP.2014.10.003>.
- [57] P.R. Patwardhan, R.C. Brown, B.H. Shanks, Understanding the Fast Pyrolysis of Lignin, *ChemSusChem* 4 (2011) 1629–1636, <https://doi.org/10.1002/CSSC.201100133>.
- [58] D.L. Dalluge, T. Daugaard, P. Johnston, N. Kuzhiyil, M.M. Wright, R.C. Brown, Continuous production of sugars from pyrolysis of acid-infused lignocellulosic biomass, *Green. Chem.* 16 (2014) 4144–4155, <https://doi.org/10.1039/c4gc00602j>.
- [59] S. Hu, L. Jiang, Y. Wang, S. Su, L. Sun, B. Xu, L. He, J. Xiang, Effects of inherent alkali and alkaline earth metallic species on biomass pyrolysis at different temperatures, *Bioresour. Technol.* 192 (2015) 23–30, <https://doi.org/10.1016/j.biortech.2015.05.042>.
- [60] A. Witsuthammakul, T. Sooknoi, Selective hydrodeoxygenation of bio-oil derived products: ketones to olefins, *Catal. Sci. Technol.* 5 (2015) 3639–3648, <https://doi.org/10.1039/C5CY00367A>.
- [61] Y. Liu, Y. Zhai, S. Li, X. Liu, X. Liu, B. Wang, Z. Qiu, C. Li, Production of bio-oil with low oxygen and nitrogen contents by combined hydrothermal pretreatment and

- pyrolysis of sewage sludge, *energy* 203 (2020), 117829, <https://doi.org/10.1016/J.ENERGY.2020.117829>.
- [62] I. Fonts, A. Navarro-Puyuelo, N. Ruiz-Gómez, M. Atienza-Martínez, A. Wisniewski, G. Gea, Assessment of the production of value-added chemical compounds from sewage sludge pyrolysis liquids, *Energy Technol.* 5 (2017) 151–171, <https://doi.org/10.1002/ente.201600183>.
- [63] Q. Guo, Z. Cheng, G. Chen, B. Yan, J. Li, L. Hou, F. Ronsse, Assessment of biomass demineralization on gasification: From experimental investigation, mechanism to potential application, *Sci. Total Environ.* 726 (2020), 138634, <https://doi.org/10.1016/J.SCITOTENV.2020.138634>.
- [64] N. Kuzhiyil, D. Dalluge, X. Bai, H. Kim, Pyrolytic sugars from cellulosic biomass, *ChemSusChem* 0 (2012) 1–10, <https://doi.org/10.1002/cssc.201200341>.

[Journals \(/about/journals\)](/about/journals)[Topics \(/topics\)](/topics)[Information \(/authors\)](/authors)[Author Services](#) [\(/authors/english\)](/authors/english)[Initiatives \(/about/initiatives\)](/about/initiatives)[About \(/about\)](/about)[Sign In / Sign Up \(/user/login\)](/user/login)[Submit \(https://susy.mdpi.com/user/manuscripts/upload?journal=symmetry\)](https://susy.mdpi.com/user/manuscripts/upload?journal=symmetry)

Search for Articles:



Advanced Search

[Journals \(/about/journals\)](/about/journals) / [Symmetry \(/journal/symmetry\)](/journal/symmetry) / [Volume 15 \(/2073-8994/15\)](/2073-8994/15) / [Issue 3 \(/2073-8994/15/3\)](/2073-8994/15/3) / [10.3390/sym15030725](https://doi.org/10.3390/sym15030725) /



[\(/journal/symmetry\)](/journal/symmetry)

Submit to this Journal
(https://susy.mdpi.com/user/manuscripts/upload?form%5Bjournal_id%5D%3D44)


Review for this Journal
(<https://susy.mdpi.com/volunteer/journals/review>)

Propose a Special Issue
(</journalproposal/sendproposalspecialissue/symmetry>)

► Article Menu

Article Menu



 **Ranjit Kumar Upadhyay** (https://sciprofiles.com/profile/2603009?utm_source=mdpi.com&utm_medium=website&utm_campaign=avatar_name) 🔍 ☰

[Subscribe SciFeed \(/2073-8994/15/3/725/scifeed_display\)](#)

[Recommended Articles](#)

[Related Info Link](#) ▾

[More by Authors Links](#) ▾

Article Views 1489

Citations 7

[Table of Contents](#) ^

- [Abstract](#)
- [Introduction](#)
- [Flow Analysis](#)
- [Solution Process](#)
- [Correlation Analysis](#)
- [Computational Results and Discussion](#)
- [Conclusions](#)
- [Author Contributions](#)
- [Funding](#)
- [Data Availability Statement](#)
- [Acknowledgments](#)
- [Conflicts of Interest](#)
- [Nomenclature](#)
- [References](#)

⏪

[Order Article Reprints \(/2073-8994/15/3/725/reprints\)](#)

Open Access Article

1 [\(https://v](#)
[domain=www.mc](#)
Altmetric

Heat and Mass Transport in Casson Nanofluid Flow over a 3-D Riga Plate with Cattaneo-Christov Double Flux: A Computational Modeling through Analytical Method

Share



by Karuppusamy Loganathan ¹  (<https://orcid.org/0000-0002-6435-2916>),
S. Eswaramoorthi ²  (<mailto:eswaran.bharathiar@gmail.com>)  (<https://orcid.org/0000-0003-0528-3591>),
P. Chinnasamy ^{3,*}  (<mailto:chinnasamyponnusamy@gmail.com>)  (<https://orcid.org/0000-0002-3202-4299>),
Reema Jain ^{1,*}  (<mailto:reemajain197@gmail.com>)  (<https://orcid.org/0000-0001-9989-247X>),
Ramkumar Sivasakthivel ⁴  (<https://orcid.org/0000-0002-6224-6167>), Rifaqat Ali ⁵ and
N. Nithya Devi ⁶

Help



Discuss in

groups

([https://s](https://groups/utm_sou)



- ¹ Department of Mathematics and Statistics, Manipal University Jaipur, Jaipur 303007, Rajasthan, India
 - ² Department of Mathematics, Dr. N.G.P. Arts and Science College, Coimbatore 641035, Tamil Nadu, India
 - ³ Department of Computer Science and Engineering, MLR Institute of Technology, Hyderabad 500043, Telangana, India
 - ⁴ Department of Computer Science, School of Sciences, CHRIST (Deemed to be University), Bengaluru 560029, Karnataka, India
 - ⁵ Department of Mathematics, College of Science and Arts, King Khalid University, Muhayil 61413, Saudi Arabia
 - ⁶ Department of Science and Humanities, Faculty of Engineering, Karpagam Academy of Higher Education, Coimbatore 641021, Tamil Nadu, India
- * Authors to whom correspondence should be addressed.

Symmetry **2023**, *15*(3), 725; <https://doi.org/10.3390/sym15030725>
(<https://doi.org/10.3390/sym15030725>)

Submission received: 2 February 2023 / Revised: 1 March 2023 / Accepted: 7 March 2023 / Published: 14 March 2023

(This article belongs to the Special Issue **Symmetry in System Theory, Control and Computing (/journal/symmetry/special_issues/I3QT160A8I)**)

Download 

Browse Figures

([https://pub.mdpi-res.com/symmetry/symmetry-](https://pub.mdpi-res.com/symmetry/symmetry-15-00725/article_deploy/html/images/symmetry-15-00725-g001.png?1678790346)

[15-00725/article_deploy/html/images/symmetry-15-00725-g001.png?1678790346](https://pub.mdpi-res.com/symmetry/symmetry-15-00725/article_deploy/html/images/symmetry-15-00725-g001.png?1678790346))

([https://pub.mdpi-res.com/symmetry/symmetry-15-](https://pub.mdpi-res.com/symmetry/symmetry-15-00725/article_deploy/html/images/symmetry-15-00725-g002.png?1678790344)

[00725/article_deploy/html/images/symmetry-15-00725-g002.png?1678790344](https://pub.mdpi-res.com/symmetry/symmetry-15-00725/article_deploy/html/images/symmetry-15-00725-g002.png?1678790344))

([https://pub.mdpi-res.com/symmetry/symmetry-15-](https://pub.mdpi-res.com/symmetry/symmetry-15-00725/article_deploy/html/images/symmetry-15-00725-g003.png?1678790335)

[00725/article_deploy/html/images/symmetry-15-00725-g003.png?1678790335](https://pub.mdpi-res.com/symmetry/symmetry-15-00725/article_deploy/html/images/symmetry-15-00725-g003.png?1678790335))

 (https://pub.mdpi-res.com/symmetry/symmetry-15-00725/article_deploy/html/images/symmetry-15-00725-g004.png?1678790334)
(https://pub.mdpi-res.com/symmetry/symmetry-15-00725/article_deploy/html/images/symmetry-15-00725-g005a.png?1678790343)
(https://pub.mdpi-res.com/symmetry/symmetry-15-00725/article_deploy/html/images/symmetry-15-00725-g005b.png?1678790336)
(https://pub.mdpi-res.com/symmetry/symmetry-15-00725/article_deploy/html/images/symmetry-15-00725-g006.png?1678790340)
(https://pub.mdpi-res.com/symmetry/symmetry-15-00725/article_deploy/html/images/symmetry-15-00725-g007.png?1678790342)
(https://pub.mdpi-res.com/symmetry/symmetry-15-00725/article_deploy/html/images/symmetry-15-00725-g008.png?1678790332)
(https://pub.mdpi-res.com/symmetry/symmetry-15-00725/article_deploy/html/images/symmetry-15-00725-g009.png?1678790338)



[Versions Notes \(/2073-8994/15/3/725/notes\)](/2073-8994/15/3/725/notes)

Abstract

This work examines the non-Newtonian Cassonnanofluid's three-dimensional flow and heat and mass transmission properties over a Riga plate. The Buongiorno nanofluid model, which is included in the present model, includes thermo-migration and random movement of nanoparticles. It also took into account the Cattaneo–Christov double flux processes in the mass and heat equations. The non-Newtonian Casson fluid model and the boundary layer approximation are included in the modeling of nonlinear partial differential systems. The homotopy technique was used to analytically solve the system's governing equations. To examine the impact of dimensionless parameters on velocities, concentrations, temperatures, local Nusselt number, skin friction, and local Sherwood number, a parametric analysis was carried out. The velocity profile is augmented in this study as the size of the modified Hartmann number increases. The greater thermal radiative enhances the heat transport rate. When the mass relaxation parameter is used, the mass flux values start to decrease.

Keywords: 3-D flow (</search?q=3-D+flow>); Casson nanofluid (</search?q=Casson+nanofluid>); Riga plate (</search?q=Riga+plate>); Cattaneo–Christov model (</search?q=Cattaneo%E2%80%93Christov+model>); HAM (</search?q=HAM>)

A new fluid with better performance is valuable for accomplishing in industrial technologies. Choi and Eastman [1] were the first who coined the word nanofluid and showed that the dispersion of nanosized particles increased the thermal physical properties of an ordinary fluid. Recently, various applications have been used in cooling transformers, heat change, food processing, and many others. "In the presence of partial slip, nanofluid past a stretching surface with boundary layer flow was explored by Das [2] and it is realized that the thermophoretic force escalates the heat transfer rate. Kuznetsov and Nield [3] investigated the nanofluid model with Brownian motion and thermophoresis and the heat transfer rate diminished due to these effects. Hamad et al. [4] acquired the results of MHD nanofluid flow on a flat plate. The two nanoparticles namely *Cu* and *Ag* have a greater cooling concert, according to the researchers. The impact of non-Newtonian nanofluid flow on a stretching sheet (SS) was investigated by Nadeem and co-workers [5], who discovered that the nanoparticle volume fraction (NPVF) reinforced the greater amount of the thermophoresis variable. Khan and Pop [6] studied the 2D flow of a nanoliquid owing to an SS using a numerical approach and identified that the presence of the BM parameter controls the heat. Sajid et al. [7] probed the cross non-Newtonian hybrid nanofluid flow with heat sink/source and thermal radiation. They investigated the novel tetra hybrid Tiwari and Das nanofluid model on blood flow arteries. The influence of Reiner–Philippoff hybrid nanofluid flow over a non-linear heat source/sink and mathematical Fourier heat law was delved by Sajid et al. [8]. They solved the problem numerically by employing the Galerkin method of finite elements. Hassan et al. [9] analytically proposed the boundary layer problem due to a SS.

Flows of fluid due to a permeable space are significant in various chemical, manufacturing, biological and industrial systems, such as crude oil purification, water development in reservoirs, grain stockpiling, and blood flow. A relevant analysis of Darcy–Forchheimer fluid flow can be carried out by attempts ([10,11,12,13,14,15]). These analyses incorporate the Darcy law to consider the permeable medium. However, the stability of this law for smaller velocity is inappropriate in plenty of practical conditions where the permeable medium has weak porosity separation near the wall area and a significant flow rate. The viscous and inertial forces have been given by the Darcy–Forchheimer (DF) model. Consequently, this model accurately described the fluid flow and heat transport as the permeable medium. Zubair et al. [16] deliberated the prominent features of Darcy–Forchheimer time flow of nanomaterials using Cattaneo–Christov heat diffusion (CCHD) theory and the speed of liquid increases when elevating the inertia coefficient. The second law analysis with DF model for MHD nanoliquid flow past a SS was conducted by Abbas et al. [17]. Ahmad et al. [18] presented the 3D couple stress MHD flow nanoliquid for DF model due to an exponentially SS. Their outcome explores that the speed of fluid upsurges with enhancing the inertia parameter.

A survey of non-Newtonian fluids in the modern era has paid particular attention to the current engineers and researchers owing various prominent features in the industrial area. The complexity of non-Newtonian fluid has made it difficult to explain all relations in one constitutive expression. So, the non-Newtonian fluid is prominent from viscous material. It is lesser than the order of differential system in the non-Newtonian fluid. A lot of models have been presented with

their different properties. One of the non-Newtonian models is known as CF. This model explained as human blood flow at a low shear rate and explained viscoelastic fluid with prominent features. Thamaraikannan et al. [19] investigated the MHD Casson fluid flow past a porous channel with the effect of body acceleration. Chemically reactive CF induced by exponentially inclined permeability was carried out by Reddy [20]. Hayat et al. [21] explored the chemically reactive flow of CNF over a heated SS with a heat sink/source. They discovered that when mass Biot number is present, the fluid concentration and its associated BL thickness rise. Casson nanofluid was assessed by Aboehashari et al. [22] using heat and mass transport characteristics owing to a stretched surface.

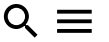
The Riga plate (RP) is a well-known actuator made out of magnets and electrodes that stay there and alternately generate Lorentz's force, which quickly decreases with distance. Zubaidi et al. [23] explored the nanofluid flow over a RP. Chemical reaction and viscosity dissipation in a nanofluid's mixed convective flow on a Riga plate was delved by Vaidya et al. [24]. They noticed that when the modified Hartmann number increased, the velocity profile grew and the temperature profile shrinks. Rafique et al. [25] numerically investigated the micropolar nanofluid flow over a Riga plate. They found that the fluid speed was bolstered as the modified Hartmann number improved. Riga plate with convective boundary conditions on a nanofluid under radial SS was scrutinized by Prasad et al. [26]. They noted that the modified Hartmann number improves the speed profile and slumps the temperature distribution. Darvesh et al. [27] probed the infinite shear rate of the Cross-fluid viscosity model, which is then coupled with the Riga plate and they used the Keller Box method. Recently, the Riga plate model of a nanofluid with a non-Fourier heat flux was numerically inspected by Divya et al. [28]. They found that a rise in the modified Hartmann number leads to weaken the skin friction coefficient.

Influenced by the above-mentioned investigations and applications recently, many researchers are attributing attention to revealing the thermal effect of nanoliquid flow with Cattaneo–Christov flux due to a Darcy–Forchheimer porous medium. However, the investigations over this flow over a Riga plate have not yet begun. To fill this gap the authors examined the Casson nanofluid flow over a 3-D Riga plate with a Cattaneo–Christov flux Darcy–Forchheimer porous medium. The results of this study are helpful in different engineering applications such as glass blowing, the spinning of fibers and the continuous casting of metals.

2. Flow Analysis

We consider the Cattaneo–Christov theory in a 3D Casson nano-liquid flow past a permeable Riga surface. The surface was considered with x and y directions with velocities $u(x) = ax$ and $v(y) = by$, respectively. Let T_w and C_w are represented by the surface of temperature and concentration which are always larger than the ambient temperature and concentration represented by T_∞ and C_∞ . The nanofluid formulation was the physical properties of thermophoresis and Brownian movement parameters. Porous medium was tackled through the Darcy–Forchheimer model. The lower plate was considered as heated with hotter fluid T_f and creates a heat transport coefficient h_c . The known fluid behaves as heat-generating or absorbing. The flow geometry is given in **Figure 1** and the governing equations are taken from [29,30]:

$$\frac{\partial u}{\partial x} + \frac{\partial v}{\partial y} + \frac{\partial w}{\partial z} = 0 \tag{1}$$



$$\left[u \frac{\partial u}{\partial x} + v \frac{\partial u}{\partial y} + w \frac{\partial u}{\partial z} \right] = v \left[\left(\frac{\beta + 1}{\beta} \right) \frac{\partial^2 u}{\partial z^2} \right] - \left[\frac{v}{k_1} u \right] - [Fu^2] + \frac{\pi j_0 M_0 \exp\left(-\frac{\pi}{\epsilon} z\right)}{8\rho} \tag{2}$$

$$\left[u \frac{\partial v}{\partial x} + v \frac{\partial v}{\partial y} + w \frac{\partial v}{\partial z} \right] = v \left[\left(\frac{\beta + 1}{\beta} \right) \frac{\partial^2 v}{\partial z^2} \right] - \left[\frac{v}{k_1} v \right] - [Fv^2] \tag{3}$$

$$\begin{aligned} \rho c_p \left[u \frac{\partial T}{\partial x} + v \frac{\partial T}{\partial y} + w \frac{\partial T}{\partial z} \right] &= K \frac{\partial^2 T}{\partial z^2} + \tau \left[D_B \frac{\partial C}{\partial z} \frac{\partial T}{\partial z} + \frac{D_T}{T_\infty} \left(\frac{\partial T}{\partial z} \right)^2 \right] \\ &- \lambda_E \left[\frac{\partial^2 T}{\partial x^2} u^2 + \frac{\partial^2 T}{\partial y^2} v^2 + \frac{\partial^2 T}{\partial z^2} w^2 + \frac{\partial^2 T}{\partial x \partial y} 2uv + \frac{\partial^2 T}{\partial y \partial z} 2vw + \frac{\partial^2 T}{\partial x \partial z} 2uw + \right. \\ &\left. + \frac{\partial u}{\partial z} \frac{\partial T}{\partial z} w + \frac{\partial v}{\partial x} \frac{\partial T}{\partial x} u + \frac{\partial v}{\partial y} \frac{\partial T}{\partial x} v + \frac{\partial v}{\partial z} \frac{\partial T}{\partial z} w + \frac{\partial w}{\partial x} \frac{\partial T}{\partial x} u + \frac{\partial w}{\partial y} \frac{\partial T}{\partial x} v + \frac{\partial w}{\partial z} \frac{\partial T}{\partial z} w \right] \end{aligned} \tag{4}$$

$$\begin{aligned} u \frac{\partial C}{\partial x} + v \frac{\partial C}{\partial y} + w \frac{\partial C}{\partial z} &= D_B \frac{\partial^2 C}{\partial z^2} + \frac{D_T}{T_\infty} \frac{\partial^2 T}{\partial z^2} - \lambda_c \left[\frac{\partial^2 C}{\partial x^2} u^2 + \frac{\partial^2 C}{\partial y^2} v^2 + \frac{\partial^2 C}{\partial z^2} w^2 + \frac{\partial^2 C}{\partial x \partial y} 2uv + \right. \\ &\left. \frac{\partial u}{\partial x} \frac{\partial C}{\partial x} u + \frac{\partial u}{\partial y} \frac{\partial C}{\partial x} v + \frac{\partial u}{\partial z} \frac{\partial C}{\partial z} w + \frac{\partial v}{\partial x} \frac{\partial C}{\partial x} u + \frac{\partial v}{\partial y} \frac{\partial C}{\partial x} v + \frac{\partial v}{\partial z} \frac{\partial C}{\partial z} w + \frac{\partial w}{\partial x} \frac{\partial C}{\partial x} u + \frac{\partial w}{\partial y} \frac{\partial C}{\partial x} v + \right. \\ &\left. \frac{\partial w}{\partial z} \frac{\partial C}{\partial z} w \right] \end{aligned} \tag{5}$$

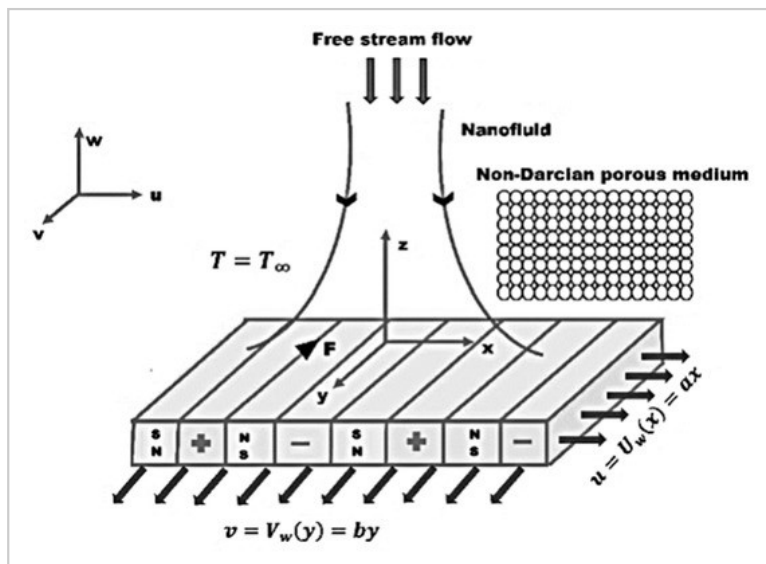
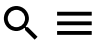


Figure 1. Physical geometry.

The boundary points are

$$\left\{ \begin{aligned} u(x, y, 0) &= ax, v(x, y, 0) = by, w(x, y, 0) = 0, -k \frac{\partial T}{\partial z}(x, y, 0) = h_f [T_f(x, y, 0) - T_\infty] \\ u(x, y, \infty) &\rightarrow 0, v(x, y, \infty) \rightarrow 0, \frac{\partial u}{\partial z}(x, y, \infty) \rightarrow 0, \frac{\partial v}{\partial z}(x, y, \infty) \rightarrow 0, T(x, y, \infty) = T_\infty \end{aligned} \right. \quad (6)$$



Now, we state the symmetry transformations [31]:

$$u = axf'(\eta), \eta = \left(\frac{a}{v}\right)^{0.5}z, v = ayg'(\eta), w = -\sqrt{av} [f(\eta) + g(\eta)], \theta(\eta) = \frac{T - T_\infty}{T_f - T_\infty} \quad (7)$$

$$\phi(\eta) = \frac{C - C_\infty}{C_w - C_\infty}$$

With the help of Equation (7), Equations (2)–(5) will be reduced to the following form

$$\left(1 + \frac{1}{\beta}\right) f'''' - f'^2 + [f + g]f'' - \lambda f' - Frf'^2 + Ha e^{-d_1 \eta} = 0 \quad (8)$$

$$\left(1 + \frac{1}{\beta}\right) g'''' - g'^2 + [f + g]g'' - \lambda g' - Frg'^2 = 0 \quad (9)$$

$$\frac{1}{Pr} \theta'' + [f + g] \theta' - \Gamma [f + g]^2 \theta'' + [f + g] [f' + g'] \theta' + Nb \theta' \phi' + Nt \theta'^2 + Hg \theta = 0 \quad (10)$$

$$\phi'' + Le [f + g] \phi' - Le \Gamma_C [f + g]^2 \phi'' + Le [f + g] [f' + g'] \phi' + \frac{Nt}{Nb} \theta'' = 0 \quad (11)$$

The boundary conditions are,

$$\begin{aligned} f(0) &= 0, g(0) = 0, \\ f'(0) &= 1, g'(0) = \epsilon, f'(\infty) = 0, g'(\infty) = 0, f''(\infty) = 0, g''(\infty) = 0 \\ &= -Bi(1 - \theta(0)), \theta(\infty) = 0, \phi(0) = 1, \phi(\infty) = 0 \end{aligned} \quad (12)$$

Here, the non-dimensional variables are defined as

$$\lambda = \frac{\nu}{k_1 a}, Fr = \frac{C_b}{\sqrt{k_1}}, Ha = \frac{\pi j_0 M_0}{8 a^3 x \rho}, d_1 = -\frac{\pi}{b} \sqrt{\frac{\nu}{a}}, Pr = \frac{\nu}{\alpha_m}, \Gamma = \lambda_E a, Nb = \frac{\tau_{DB}}{\nu} (C_w - C_\infty)$$

$$Hg = \frac{Q_0}{\rho c_{pa}}, \Gamma_C = \lambda_C a, \text{ and } Le = \frac{\alpha_m}{D_B}$$

The engineering concerns “skin friction”, “local Nusselt number (LNN)”, and “local Sherwood number (LSN)” are defined below:

$$\text{MDPI} \left| \begin{array}{l} \text{Re}^{0.5} C f_x = \left(1 + \frac{1}{\beta} \right) f''(0) = \text{skin friction in } x - \text{direction} \end{array} \right.$$



$$\text{Re}^{0.5} C f_y = \left(1 + \frac{1}{\beta} \right) g''(0) = \text{skin friction in } y - \text{direction}$$

$$\text{Re}^{-0.5} Nu_x = -\theta'(0) = \text{local Nusselt number}$$

$$\text{Re}^{-0.5} Sh_x = -\phi'(0) = \text{local Sherwood number}$$

3. Solution Process

The transformed nonlinear ODE Equations (8)–(11) with the boundary conditions in Equation (12) are solved using HAM technique. This techniques used solve highly non-linear problems. The advantage of this method is to freely fix initial approximations and linear operators. The flow chart of this method is illustrated in **Figure 2**.

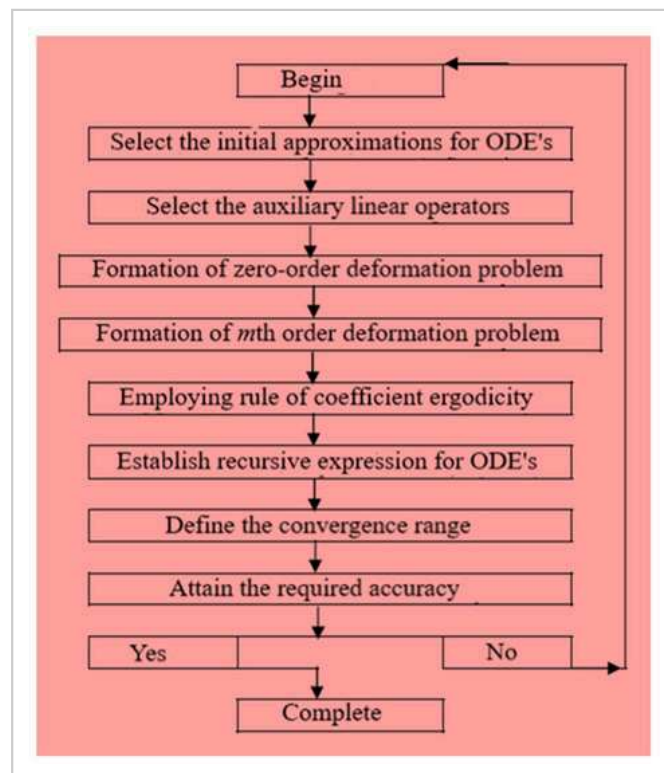


Figure 2. Flow chart of HAM.

The convergences values are of h_f , h_g , h_θ and h_ϕ are plotted in **Figure 3**. The range of convergence is $-1.4 \leq h_f, h_g \leq 0.0$, and $-1.75 \leq h_\theta, h_\phi \leq 0.1$. **Table 1** observes the order of $f''(0)$, $g''(0)$, $\theta'(0)$, and $\phi'(0)$ are 15 th order.

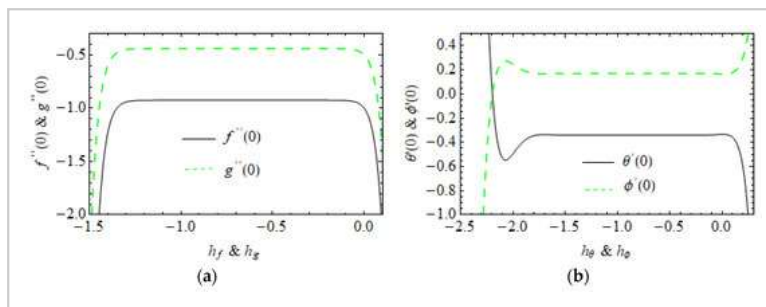


Figure 3. The h - curves of (a) $f''(0)$, $g''(0)$ and (b) $\theta'(0)$, $\phi'(0)$.

Table 1. HAM order.

HAM order			

4. Correlation Analysis

For analyzing the concert of a thermal system design, the system of equations is required. The acquired numerical data are utilized to generate the system of equations using linear regression analysis. The skin friction, heat and mass relationship equations:

$$Re^{0.5}Cf_x = -1.840454 + 0.428572 * Ha - 0.525588 * \lambda + 0.262804 * \beta - 0.340727 * Fr$$

$$Re^{0.5}Cf_y = -0.765295 - 0.014398 * Ha - 0.307248 * \lambda + 0.099039 * \beta - 0.093480 * Fr$$

$$\frac{Nu}{\sqrt{Re}} = 0.343840 + 0.002102 * Ha - 0.004278 * \lambda - 0.001629 * \beta - 0.001564 * Fr$$

$$\frac{Sh}{\sqrt{Re}} = -0.171920 - 0.001051 * Ha + 0.002139 * \lambda + 0.000814 * \beta + 0.000782 * Fr$$

For $Ha = [0.0, 0.3]$, $\lambda = [0.0, 0.2]$, $\beta = [1, 2]$ and $Fr \in [0, 1]$ with maximum error is 0.028.

5. Computational Results and Discussion

In this section, the investigation is taken to scrutinize an essential description of the different dimensional factors on velocity along x and y directions, temperature, and concentration of nanoparticles. **Table 2** elucidates the comparison analysis of Nu_x for numerous parameters from

Muhammad et al. [31]. This table ensures the accuracy of obtained results and the precision of numerical computation utilized in this analysis. It is noted that there is an outstanding achievement with the earlier publication. **Table 3** provides the characteristics of $\Gamma, \Gamma_c, Nb, Nt, Bi$ and Hg on Nu_x and Sh_x for CNF and VNF. It is realized that the HTG grows when mounting the size of Γ, Γ_c and Bi and it decays when improving the size of Nt and Hg for both fluids. Furthermore, the LNN remains fixed when changing the Nb values, see Muhammad et al. [31]. The LSN decays when varying the size of Γ, Γ_c, Nt and Bi and it rise when changing the values of Nb and Hg for both fluids.

Table 2. Comparison of local Nusselt number with Muhammad et al. [31].

Table 3. The LNN and LSN for different combinations of $\Gamma, \Gamma_c, Nb, Nt, Bi$ and Hg for both fluids.

Figure 4a,b display the velocity $f'(\eta)$ and $g'(\eta)$ against the various value of Casson fluid parameter β on $\lambda = 0.2$ and $\lambda = 0$. It is noted that the augmentation of β produces a reduction in velocity profile and boundary layer thickness. The influence of Ha on $f'(\eta)$ and $g'(\eta)$ is employed in **Figure 4c,d** on $\lambda = 0.2$ and $\lambda = 0$. The larger value of Ha increases the velocity profile in both directions. The existence of a modified Hartman number enhanced the motion of Casson fluid. Also, the larger fluid velocity attains when $\lambda = 0.0$ than the $\lambda = 0.2$ when varying β and Ha values in both directions. Moreover, the Riga plate is an electromagnetic device that pushes the movement of the flow in a specific direction. **Figure 5a,b** illustrates the intensification of the temperature with the rising value of Biot number Bi on RP, SP, porous RP and non-porous RP. The Biot number is the leading function of temperature distribution in the case of $Ha = (0.0, 0.3)$ and $\lambda = (0.0, 0.2)$. Physically, enhancing the value of Bi obtained stronger heat convection at the wall of the surface. The impact of Hg on the temperature field on heated RP and SP is exposed in **Figure 5c**. The temperature field enlarges for greater values of Hg . Additionally, heat has been induced due to a greater value of Hg , which is the reason the temperature profile is enlarged in the sense of heating RP and SP. In contrast, an opposite trend is observed in **Figure 5d** for cooling RP and SP. The impact of Nt on $\theta(\eta)$ for fluid heat generating and absorbing on a RP is examined in **Figure 5e** and seen that the $\theta(\eta)$ develops when raising the Nt values. Thermophoresis attained through a temperature difference produces

a faster flow that moves away from the stretching sheet. The temperature inside the surface increases due to faster flow, resulting in an amelioration of the temperature profile. **Figure 5f** elucidates the thermal relaxation time Γ on temperature distribution on heated and cooled RP. It is detected that the temperature field and corresponding thermal layer thickness depreciated by the enhancing value of Γ on heated RP. A larger value of Γ results in particles of materials needing extra time to transport heat near its particles which is responsible for the lessening of the thermal layer. The opposite behavior getting for cooled RP.

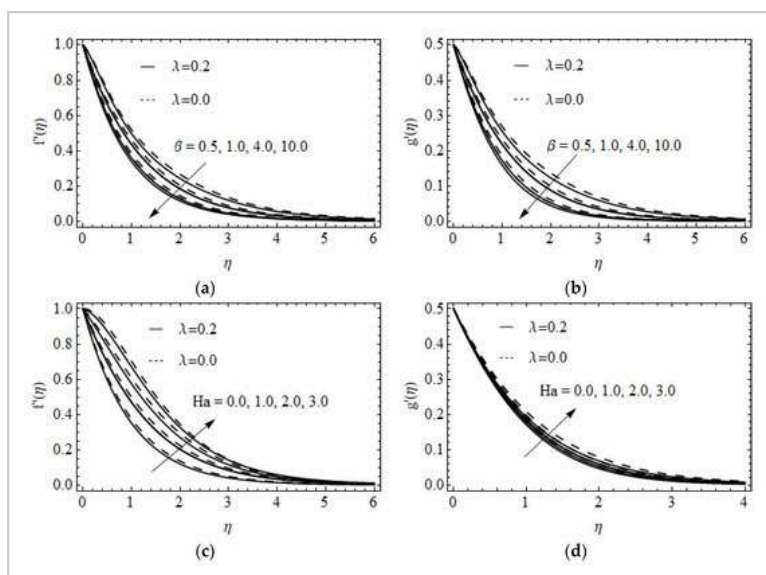


Figure 4. The x -direction (a,c) and y -direction (b,d) velocity for various values of β and Ha for porous and non-porous RP.

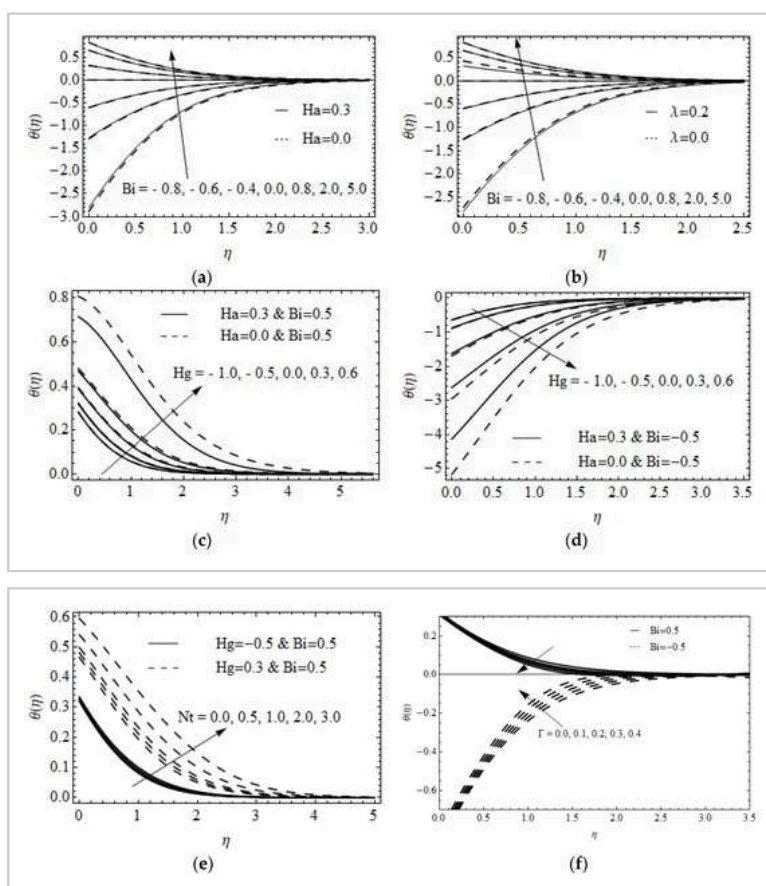




Figure 5. The variations of $\theta(\eta)$ for various values of Bi (a,b) over RP and SP (a), porous and non-porous RP (b), Hg (c,d) for convective heating (c) and cooling (d) RP and SP, Nt (e) for heat generating and absorption and Γ (f) for convective heating and cooling RP.

Figure 6a,b reveals the influence of Biot number Bi on $\phi(\eta)$ for the case of ($Ha = 0.0, Ha = 0.3$) and ($\lambda = 0.0, \lambda = 0.2$), it is clear from the figure that the concentration of nanoparticles and its corresponding layer thickness are accelerated due to the larger value of Bi for all cases. The variation of Hg on $\phi(\eta)$ for heated and cooled RP and SP was displayed in **Figure 6c,d**. Increasing the value of Hg leads to accelerate in $\phi(\eta)$ due to heated RP and a reduction cooled RP. The effect of Nb on $\phi(\eta)$ on fluid heat generating and absorbing on heated and cooled RP is shown in **Figure 6e,f**. It is seen that $\phi(\eta)$ decays when strengthening the Nb in headed RP and the opposite trend attains in cooled RP for both fluid heat generating and absorbing cases. The variation of Ha and λ for CNF and VNF on the drag friction coefficient in the x , and y directions were presented in **Figure 7a,b**. In **Figure 7a** shows that the Cf_x climbs with an enhancement in Ha and it is suppresses for a higher size of λ and Cf_y diminishes with an improvement in Ha and λ for both fluids, see **Figure 7b**. **Figure 8a** displays the LNN Nu_x for Ha and λ . The growth of Ha escalates the LNN and it decays for larger quantity of λ . On the contrary, **Figure 8b** presents that the LNN Nu_x and Nu_x is a lessening function of Hg and Nt . The contour plot of LNN for Pr and λ for CNF and VNF was illustrated in **Figure 8c,d**. The LSN for various values of λ & Ha and Nt & Hg for both fluids were displayed in **Figure 9a,b**. It is seen that the LSN improves when enhancing the values of λ and Hg . The opposite nature attains for Ha and Nt . The impact of Nb and Nt on LSN for heated and cooled RP was displayed in **Figure 9c,d**. The quite opposite nature occurs in heating and cooling cases. The contour plot of LSN for various values of Γ_c and Le for both fluids was addressed in **Figure 9e,f**.

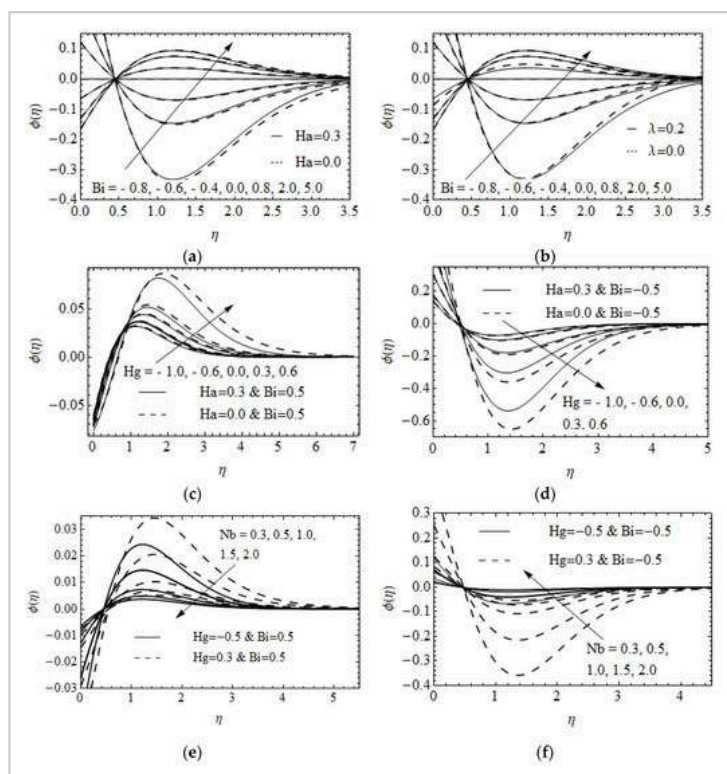




Figure 6. The variations of $\phi(\eta)$ for different values of Bi (a,b) for SP and RP(a), porous and non-porous RP (b), Hg (c,d) for convective heating RP and SP (c) and convective cooling RP and SP (d), Nb (e,f) for convective heating with heat generation and absorption (e) and convective cooling with heat generation and absorption (f).

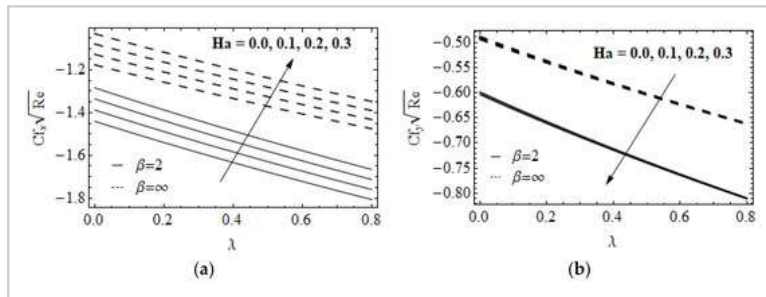


Figure 7. The Skin friction in x -direction (a) and y -direction (b) with different values of Ha and λ for both fluids.

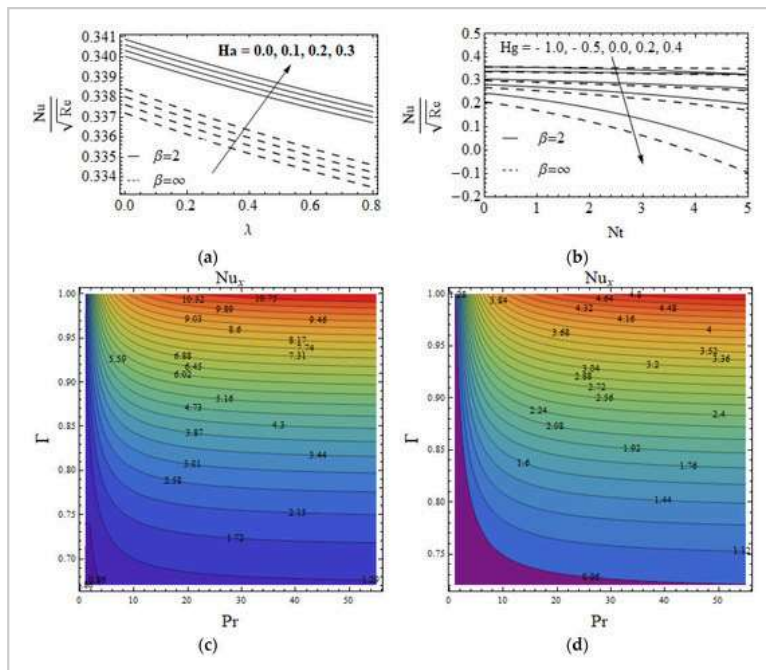


Figure 8. The Nu_x variations Ha & λ (a), Hg & Nt (b) for both fluids and Pr & Γ (c, d) for Casson nanofluid (c) and viscous nanofluid (d).

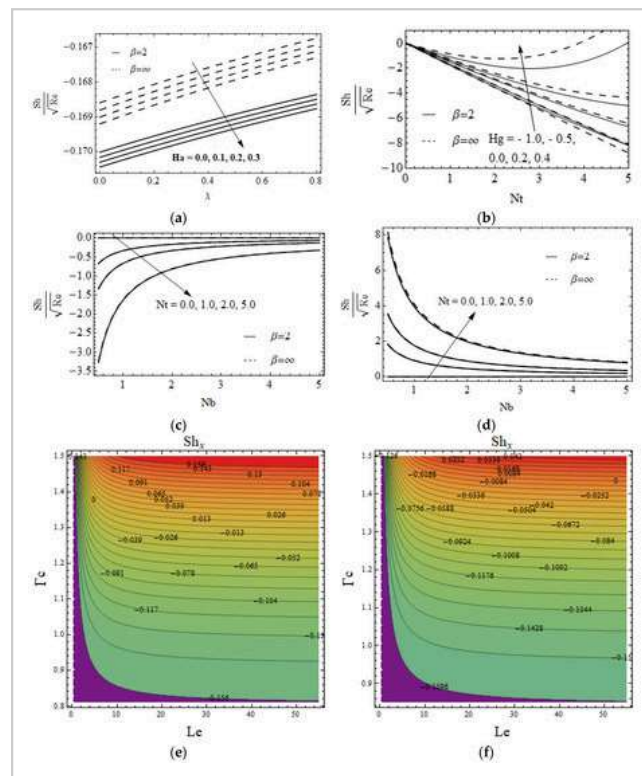


Figure 9. The Sh_x for λ & Ha (a) and Nt & Hg (b) for both fluids and Nb & Nt with $Bi = 0.5$ (c) and $Bi = -0.5$ (d), Le & Γ_C for Casson nanofluid (e) and viscous nanofluid (f).

6. Conclusions

The Darcy–Forchheimer flow of the 3-D Casson nanofluid owing to the Riga plate was investigated using the Cattaneo–Christov dual diffusion theory. In addition, the homotopy technique was used for the solution process. The most important finding is highlighted below.

- The skin friction rate in x – direction enhances and in y – direction decays when enhancing the modified Hartman number.
- The larger skin friction rate occurs in viscous nanofluid than the Casson nanofluid.
- Thermal layer thickness amplifies with an augmented value of Bi .
- A larger value of Hg upsurges in the thermal layer in the case of $Bi = 0.5$ while the thermal layer reduces with a larger value of Hg for $Bi = -0.5$.
- The thermal relaxation parameter improves the local Nusselt number for both fluids.
- In the future, we will extend this work with the Tiwari and Das model with a hybrid nanofluid case.

Author Contributions

Conceptualization, S.E. and K.L.; Methodology, K.L.; Software, K.L.; Validation, P.C. and N.N.D.; Formal analysis, R.S.; Investigation, R.J. and P.C.; Writing—original draft, K.L.; Writing—review & editing, K.L. and R.A.; Project administration, K.L.; Funding acquisition, K.L. All authors have read and agreed to the published version of the manuscript.

Deanship of Scientific Research at King Khalid University for funding the work through a small group project under grant number R.G.P 1/169/43.



Data Availability Statement

Not applicable.

Acknowledgments

The authors extend their appreciation to the Deanship of Scientific Research at King Khalid University for funding the work through a small group project under grant number R.G.P 1/169/43.

Conflicts of Interest

The authors declare no conflict of interest.

Nomenclature

a, b	Constants (–)
Bi	Biot number (–)
C	Concentration (kg m^{-3})
C_∞	Ambient concentration (kg m^{-3})
C_w	Surface concentration of nanoparticles (kg m^{-3})
C_p	Specific heat ($\text{J kg}^{-1}\text{K}^{-1}$)
C_{fx}	Skin friction in x -direction (–)
C_{fy}	Skin friction in y -direction (–)
D_B	Brownian diffusion coefficient ($\text{m}^2 \text{s}^{-1}$)
D_T	Thermophoretic diffusion coefficient ($\text{m}^2 \text{s}^{-1}$)
$f(\eta)$	Velocity similarity function in x – direction (–)
$g(\eta)$	Velocity similarity function in y – direction (–)
Hg	Heat generation/absorption parameter (–)
k	Thermal conductivity ($\text{m kgs}^{-3}\text{K}^{-1}$)
k_1	Permeability of the porous medium
Le	Lewis number (–)
Nb	Brownian motion parameter (–)
Nt	Thermophoresis parameter (–)
Nu_x	Local Nusselt number (–)
Pr	Prandtl number (–)
Re	Reynolds number (–)

- Q_0 Heat generation/absorption coefficient (–)
- Sh_x Local Sherwood number (–)
- T Temperature (K)
- T_W Surface temperature of nanoparticles
- T_∞ Ambient temperature (K)
- u_w Velocity of the sheet (m s^{-1})
- u, v, w Velocity components (m s^{-1})
- x, y, z Cartesian coordinates (m)

Greeks

- β Casson fluid parameter (–)
- γ Viscoelastic parameter (–)
- $\phi(\eta)$ Concentration similarity function (–)
- ϵ Stretching ratio (–)
- η Similarity parameter (–)
- λ Porous parameter (–)
- Γ Heat thermal relaxation time parameter (–)
- Γ_c Mass thermal relaxation time parameter (–)
- ν Kinematic viscosity ($\text{m}^2 \text{s}^{-1}$)
- τ Ratio of the effective heat capacity (–)
- $\theta(\eta)$ Temperature similarity function (–)
- ρ Density (kg m^{-3})
- σ Electrical conductivity ($\text{S}^3 \text{m}^2 \text{kg}^{-1}$)
- BM Brownian movement
- CNF Casson nanofluid
- VNF Viscous nanofluid
- RP Riga Plate
- LLN Local Nusselt number
- LSN Local Sherwood Number
- SP Stationary Plate
- DF Darcy-Forchheimer
- CCHF Cattaneo-Christov heat flux
- NPVF Nanoparticle volume fraction
- SS Stretching sheet
- CCHD Cattaneo-Christov heat diffusion



1. Choi, S.U.; Eastman, J.A. Enhancing thermal conductivity of fluids with nanoparticles. *ASME Fluids Eng. Div.* **1995**, *231*, 99–105. [Google Scholar (https://scholar.google.com/scholar_lookup?title=Enhancing+thermal+conductivity+of+fluids+with+nanoparticles&author=Choi,+S.U.&author=Eastman,+J.A.&publication_year=1995&journal=ASME+Fluids+Eng.+Div.&volume=231&pages=99%E2%80%93105)]
2. Das, K. Nanofluid flow over a non-linear permeable stretching sheet with partial slip. *J. Egypt. Math. Soc.* **2015**, *23*, 451–456. [Google Scholar (https://scholar.google.com/scholar_lookup?title=Nanofluid+flow+over+a+non-linear+permeable+stretching+sheet+with+partial+slip&author=Das,+K.&publication_year=2015&journal=J.+Egypt.+Math.+Soc.&volume=23&pages=451%E2%80%93456&doi=10.1016/j.joems.2014.06.014)] [CrossRef (<https://doi.org/10.1016/j.joems.2014.06.014>)] [Green Version (<https://core.ac.uk/download/pdf/82087844.pdf>)]
3. Kuznetsov, A.V.; Nield, D.A. Natural convective boundary layer flow of a nanofluid past a vertical plate. *Int. J. Therm. Sci.* **2010**, *49*, 243–247. [Google Scholar (https://scholar.google.com/scholar_lookup?title=Natural+convective+boundary+layer+flow+of+a+nanofluid+past+a+vertical+plate&author=Kuznetsov,+A.V.&author=Nield,+D.A.&publication_year=2010&journal=Int.+J.+Therm.+Sci.&volume=49&pages=243%E2%80%93247&doi=10.1016/j.ijthermalsci.2009.07.015)] [CrossRef (<https://doi.org/10.1016/j.ijthermalsci.2009.07.015>)]
4. Hamad, M.A.A.; Pop, I.; Ismail, A.M. Magnetic field effects on free convection flow of a nanofluid past a vertical semi-infinite at plate. *Nonlinear Anal. Real World Appl.* **2011**, *12*, 13381346. [Google Scholar (https://scholar.google.com/scholar_lookup?title=Magnetic+field+effects+on+free+convection+flow+of+a+nanofluid+past+a+vertical+semi-infinite+at+plate&author=Hamad,+M.A.A.&author=Pop,+I.&author=Ismail,+A.M.&publication_year=2011&journal=Nonlinear+Anal.+Real+World+Appl.&volume=12&pages=13381346&doi=10.1016/j.nonrwa.2010.09.014)] [CrossRef (<https://doi.org/10.1016/j.nonrwa.2010.09.014>)]
5. Nadeem, S.; Haq, R.U.; Khan, Z.H. Numerical solution of non-Newtonian nanofluid flow over a stretching sheet. *Appl. Nanosci.* **2014**, *4*, 625631. [Google Scholar (https://scholar.google.com/scholar_lookup?title=Numerical+solution+of+non-Newtonian+nanofluid+flow+over+a+stretching+sheet&author=Nadeem,+S.&author=Haq,+R.U.&author=Khan,+Z.H.&publication_year=2014&journal=Appl.+Nanosci.&volume=4&pages=625631&doi=10.1007/s13204-013-0235-8)] [CrossRef (<https://doi.org/10.1007/s13204-013-0235-8>)] [Green Version (<https://core.ac.uk/download/pdf/81846490.pdf>)]

(https://scholar.google.com/scholar_lookup?title=Boundary-layer+flow+of+a+nanofluid+past+a+stretching+sheet&author=Khan,+W.A.&author=Pop,+I.&publication_year=2010&journal=Int.+Heat+Mass+Transf.&volume=53&pages=2477%E2%80%932483&doi=10.1016/j.ijheatmasstransfer.2010.01.032) [CrossRef (<https://doi.org/10.1016/j.ijheatmasstransfer.2010.01.032>)]

7. Sajid, T.; Jamshed, W.; Eid, M.R.; Altamirano, G.C.; Aslam, F.; Alanzi, A.M.; Abd-Elmonem, A. Magnetized Cross tetra hybrid nanofluid passed a stenosed artery with nonuniform heat source (sink) and thermal radiation: Novel tetra hybrid Tiwari and Das nanofluid model. *J. Magn. Magn. Mater.* **2023**, *569*, 170443. [Google Scholar ([https://scholar.google.com/scholar_lookup?title=Magnetized+Cross+tetra+hybrid+nanofluid+passed+a+stenosed+artery+with+nonuniform+heat+source+\(sink\)+and+thermal+radiation:+Novel+tetra+hybrid+Tiwari+and+Das+nanofluid+model&author=Sajid,+T.&author=Jamshed,+W.&author=Eid,+M.R.&author=Altamirano,+G.C.&author=Aslam,+F.&author=Alanzi,+A.M.&author=Abd-Elmonem,+A.&publication_year=2023&journal=J.+Magn.+Magn.+Mater.&volume=569&pages=170443&doi=10.1016/j.jmmm.2023.170443](https://scholar.google.com/scholar_lookup?title=Magnetized+Cross+tetra+hybrid+nanofluid+passed+a+stenosed+artery+with+nonuniform+heat+source+(sink)+and+thermal+radiation:+Novel+tetra+hybrid+Tiwari+and+Das+nanofluid+model&author=Sajid,+T.&author=Jamshed,+W.&author=Eid,+M.R.&author=Altamirano,+G.C.&author=Aslam,+F.&author=Alanzi,+A.M.&author=Abd-Elmonem,+A.&publication_year=2023&journal=J.+Magn.+Magn.+Mater.&volume=569&pages=170443&doi=10.1016/j.jmmm.2023.170443))] [CrossRef (<https://doi.org/10.1016/j.jmmm.2023.170443>)]
8. Sajid, T.; Jamshed, W.; Ibrahim, R.W.; Eid, M.R.; Abd-Elmonem, A.; Arshad, M. Quadratic regression analysis for nonlinear heat source/sink and mathematical Fourier heat law influences on Reiner-Philippoff hybrid nanofluid flow applying Galerkin finite element method. *J. Magn. Magn. Mater.* **2023**, *568*, 170383. [Google Scholar (https://scholar.google.com/scholar_lookup?title=Quadratic+regression+analysis+for+nonlinear+heat+source/sink+and+mathematical+Fourier+heat+law+influences+on+Reiner-Philippoff+hybrid+nanofluid+flow+applying+Galerkin+finite+element+method&author=Sajid,+T.&author=Jamshed,+W.&author=Ibrahim,+R.W.&author=Eid,+M.R.&author=Abd-Elmonem,+A.&author=Arshad,+M.&publication_year=2023&journal=J.+Magn.+Magn.+Mater.&volume=568&pages=170383&doi=10.1016/j.jmmm.2023.170383)] [CrossRef (<https://doi.org/10.1016/j.jmmm.2023.170383>)]

- Hassani, M.; Tabar, M.M.; Nemati, H.; Domairry, G.; Noori, F. An analytical solution for the boundary layer flow of a nanofluid past a stretching sheet. *Int. J. Therm. Sci.* **2011**, *50*, 2256–2263. [Google Scholar (https://scholar.google.com/scholar_lookup?title=An+analytical+solution+for+boundary+layer+flow+of+a+nanofluid+past+a+stretching+sheet&author=Hassani,+M.&author=Tabar,+M.M.&author=Nemati,+H.&author=Domairry,+G.&author=Noori,+F.&publication_year=2011&journal=Int.+J.+Therm.+Sci.&volume=50&pages=2256%E2%80%932263&doi=10.1016/j.ijthermalsci.2011.05.015)] [CrossRef (<https://doi.org/10.1016/j.ijthermalsci.2011.05.015>)]
10. Sriramalu, A.; Kishan, N.; Anand, R.J. Steady Flow and heat transfer of a viscous incompressible fluid flow through porous medium over a stretching sheet. *J. Energy Heat Mass Transf.* **2001**, *23*, 483495. [Google Scholar (https://scholar.google.com/scholar_lookup?title=Steady+Flow+and+heat+transfer+of+a+viscous+incompressible+fluid+flow+through+porous+medium+over+a+stretching+sheet&author=Sriramalu,+A.&author=Kishan,+N.&author=Anand,+R.J.&publication_year=2001&journal=J.+Energy+Heat+Mass+Transf.&volume=23&pages=483495)]
11. Liu, I.C. Flow and heat transfer of viscous fluid saturated in porous media over a permeable non-isothermal stretching sheet. *Transp. Porous Media* **2006**, *64*, 375–392. [Google Scholar (https://scholar.google.com/scholar_lookup?title=Flow+and+heat+transfer+of+viscous+fluid+saturated+in+porous+media+over+a+permeable+non-isothermal+stretching+sheet&author=Liu,+I.C.&publication_year=2006&journal=Transp.+Porous+Media&volume=64&pages=375%E2%80%93392&doi=10.1007/s11242-005-5235-z)] [CrossRef (<https://doi.org/10.1007/s11242-005-5235-z>)]
12. Nadeem, S.; Haq, R.U.; Akbar, N.S.; Khan, Z.H. MHD three-dimensional Casson fluid flow past a porous linearly stretching sheet. *Alex. Eng. J.* **2013**, *52*, 577682. [Google Scholar (https://scholar.google.com/scholar_lookup?title=MHD+three-dimensional+Casson+fluid+flow+past+a+porous+linearly+stretching+sheet&author=Nadeem,+S.&author=Haq,+R.U.&author=Akbar,+N.S.&author=Khan,+Z.H.&publication_year=2013&journal=Alex.+Eng.+J.&volume=52&pages=577682&doi=10.1016/j.aej.2013.08.005)] [CrossRef (<https://doi.org/10.1016/j.aej.2013.08.005>)]
13. Pramanik, S. Casson fluid flow and heat transfer past an exponentially porous stretching surface in presence of thermal radiation. *Ain Shams Eng. J.* **2014**, *5*, 205–212. [Google Scholar (https://scholar.google.com/scholar_lookup?title=Casson+fluid+flow+and+heat+transfer+past+an+exponentially+porous+stretching+surface+in+presence+of+thermal+radiation&author=Pramanik,+S.&publication_year=2014&journal=Ain+Shams+Eng.+J.&volume=5&pages=205%E2%80%93212&doi=10.1016/j.asej.2013.05.003)] [CrossRef (<https://doi.org/10.1016/j.asej.2013.05.003>)] [Green Version (<https://core.ac.uk/download/pdf/82180541.pdf>)]



- Mahanta, G.; Shaw, S. Three-dimensional Casson fluid flow past a porous linear stretching sheet with convective boundary conditions. *Alex. Eng. J.* **2015**, *54*, 653–6599. [Google Scholar (https://scholar.google.com/scholar_lookup?title=Three-dimensional+Casson+fluid+flow+past+a+porous+linearly+stretching+sheet+with+convective+boundary+conditions&author=Mahanta,+G.&author=Shaw,+S.&publication_year=2015&journal=Alex.+Eng.+J.&volume=54&pages=653%E2%80%936599&doi=10.1016/j.aej.2015.04.014)] [CrossRef (<https://doi.org/10.1016/j.aej.2015.04.014>)]
15. Abbas, T.; Bhatti, M.M.; Ayub, M. Aiding and opposing of mixed convection Casson nanofluid flow with chemical reactions through a porous Riga plate. *Proc. Inst. Mech. Eng. Part E J. Process Mech. Eng.* **2017**, *232*, 519–527. [Google Scholar (https://scholar.google.com/scholar_lookup?title=Aiding+and+opposing+of+mixed+convection+Casson+nano fluid+flow+with+chemical+reactions+through+a+porous+Riga+plate&author=Abbas,+T.&author=Bhatti,+M.M.&author=Ayub,+M.&publication_year=2017&journal=Proc.+Inst.+Mech.+Eng.+Part+E+J.+Process+Mech.+Eng.&volume=232&pages=519%E2%80%93527&doi=10.1177/0954408917719791)] [CrossRef (<https://doi.org/10.1177/0954408917719791>)]
16. Zubair, M.; Shah, Z.; Islam, S.; Khan, W.; Dawar, A. Study of three dimensional Darcy Forchheimer squeezing nanofluid flow with Cattaneo-Christov heat flux based on four different types of nanoparticles through entropy generation analysis. *Adv. Mech. Eng.* **2019**, *11*, 117. [Google Scholar (https://scholar.google.com/scholar_lookup?title=Study+of+three+dimensional+Darcy+Forchheimer+squeezing+nano fluid+flow+with+Cattaneo-Christov+heat+flux+based+on+four+different+types+of+nanoparticles+through+entropy+generation+analysis&author=Zubair,+M.&author=Shah,+Z.&author=Islam,+S.&author=Khan,+W.&author=Dawar,+A.&publication_year=2019&journal=Adv.+Mech.+Eng.&volume=11&pages=117&doi=10.1177/1687814019851308)] [CrossRef (<https://doi.org/10.1177/1687814019851308>)] [Green Version (<https://journals.sagepub.com/doi/pdf/10.1177/1687814019851308>)]
17. Abbas, S.Z.; Khan, W.A.; Kadry, S.; Ijaz, M.; Khan Waqas, M.; Khan, M.I. Entropy optimized Darcy Forchheimernanoid (Silicon dioxide, Molybdenum disulfide) subject to temperature dependent viscosity. *Comput. Methods Programs Biomed.* **2020**, *190*, 105363. [Google Scholar ([https://scholar.google.com/scholar_lookup?title=Entropy+optimized+Darcy+Forchheimernanoid+\(Silicon+dioxide,+Molybdenum+disulfide\)+subject+to+temperature+dependent+viscosity&author=Abbas,+S.Z.&author=Khan,+W.A.&author=Kadry,+S.&author=Ijaz,+M.&author=Khan+Waqas,+M.&author=Khan,+M.I.&publication_year=2020&journal=Comput.+Methods+Programs+Biomed.&volume=190&pages=105363&doi=10.1016/j.cmpb.2020.105363](https://scholar.google.com/scholar_lookup?title=Entropy+optimized+Darcy+Forchheimernanoid+(Silicon+dioxide,+Molybdenum+disulfide)+subject+to+temperature+dependent+viscosity&author=Abbas,+S.Z.&author=Khan,+W.A.&author=Kadry,+S.&author=Ijaz,+M.&author=Khan+Waqas,+M.&author=Khan,+M.I.&publication_year=2020&journal=Comput.+Methods+Programs+Biomed.&volume=190&pages=105363&doi=10.1016/j.cmpb.2020.105363))] [CrossRef (<https://doi.org/10.1016/j.cmpb.2020.105363>)]

Thounthong, P. Darcy Forchheimer MHD couple stress 3D nanofluid over an exponentially stretching sheet through Cattaneo-Christov convective heat flux with zero nanoparticles mass flux conditions. *Entropy* **2019**, *21*, 867. [Google Scholar

(https://scholar.google.com/scholar_lookup?

title=Darcy+Forchheimer+MHD+couple+stress+3D+nanofluid+over+an+exponentiall y+stretching+sheet+through+Cattaneo-Christov+convective+heat+flux+with+zero+nanoparticles+mass+flux+conditions&a uthor=Ahmad,+M.W.&author=Kumam,+P.&author=Shah,+Z.&author=Farooq,+A.A.&a uthor=Nawaz,+R.&author=Dawar,+A.&author=Islam,+S.&author=Thounthong,+P.&pu blication_year=2019&journal=Entropy&volume=21&pages=867&doi=10.3390/e21090 867)] [CrossRef (<https://doi.org/10.3390/e21090867>)] [Green Version (<https://www.md pi.com/1099-4300/21/9/867/pdf>)]

19. ThamaraiKannan, N.; Karthikeyan, S.; Chaudhary, D.K.; Kayikci, S. Analytical investigation of magnetohydrodynamic non-Newtonian type Casson nanofluid flow past a porous channel with periodic body acceleration. *Complexity* **2021**, *2021*, 7792422. [Google Scholar (https://scholar.google.com/scholar_lookup? **title=Analytical+investigation+of+magnetohydrodynamic+non-Newtonian+type+Casson+nanofluid+flow+past+a+porous+channel+with+periodic+b ody+acceleration&author=ThamaraiKannan,+N.&author=Karthikeyan,+S.&author=C haudhary,+D.K.&author=Kayikci,+S.&publication_year=2021&journal=Complexity&v olume=2021&pages=7792422&doi=10.1155/2021/7792422)] [CrossRef (<https://doi.org/10.1155/2021/7792422>)]**
20. Reddy, P.B.A. Magnetohydrodynamic flow of a Casson fluid over an exponentially inclined permeable stretching surface with thermal radiation and chemical reaction. *Mech. Eng.* **2017**, *232*, 519–527. [Google Scholar (https://scholar.google.com/scholar_lookup? **title=Magnetohydrodynamic+flow+of+a+Casson+fluid+over+an+exponentially+incl i ned+permeable+stretching+surface+with+thermal+radiation+and+chemical+reactio n&author=Reddy,+P.B.A.&publication_year=2017&journal=Mech.+Eng.&volume=232 &pages=519%E2%80%93527&doi=10.1016/j.asej.2015.12.010)] [CrossRef (<https://doi.org/10.1016/j.asej.2015.12.010>)] [Green Version ([https://core.ac.uk/downl oad/pdf/81164444.pdf](https://core.ac.uk/download/pdf/81164444.pdf))]**
21. Hayat, T.; Bilal Ashraf, M.; Shehzad, S.A.; Alsaedi, A. Mixed convection ow of Casson nanofluid over a stretching sheet with convectively heated chemical reaction and heat source/sink. *J. Appl. Fluid Mech.* **2015**, *8*, 803–813. [Google Scholar (https://scholar.google.com/scholar_lookup? **title=Mixed+convection+ow+of+Casson+nanofluid+over+a+stretching+sheet+with+c onvectively+heated+chemical+reaction+and+heat+source/sink&author=Hayat,+T.&a uthor=Bilal+Ashraf,+M.&author=Shehzad,+S.A.&author=Alsaedi,+A.&publication_ye ar=2015&journal=J.+Appl.+Fluid+Mech.&volume=8&pages=803%E2%80%93813)**]

- Abolbashari, M.H.; Freidoonimehr, N.; Nazari, F.; Rashidi, M.M. Analytical modeling of entropy generation for Casson nano-fluid flow induced by a stretching surface. *Adv. Powder Technol.* **2015**, *26*, 542–552. [Google Scholar (https://scholar.google.com/scholar_lookup?title=Analytical+modeling+of+entropy+generation+for+Casson+nano-fluid+flow+induced+by+a+stretching+surface&author=Abolbashari,+M.H.&author=Freidoonimehr,+N.&author=Nazari,+F.&author=Rashidi,+M.M.&publication_year=2015&journal=Adv.+Powder+Technol.&volume=26&pages=542%E2%80%93552&doi=10.1016/j.apt.2015.01.003)] [CrossRef (<https://doi.org/10.1016/j.apt.2015.01.003>)]
23. Al-Zubaidi, A.; Nazeer, M.; Saleem, S.; Hussain, F.; Ahmad, F. Flow of nanofluid towards a Riga surface with heat and mass transfer under the effects of activation energy and thermal radiation. *Int. J. Mod. Phys. B* **2021**, *35*, 2150266. [Google Scholar (https://scholar.google.com/scholar_lookup?title=Flow+of+nano-fluid+towards+a+Riga+surface+with+heat+and+mass+transfer+under+the+effects+of+activation+energy+and+thermal+radiation&author=Al-Zubaidi,+A.&author=Nazeer,+M.&author=Saleem,+S.&author=Hussain,+F.&author=Ahmad,+F.&publication_year=2021&journal=Int.+J.+Mod.+Phys.+B&volume=35&pages=2150266&doi=10.1142/S0217979221502660)] [CrossRef (<https://doi.org/10.1142/S0217979221502660>)]
24. Vaidya, H.; Prasad, K.V.; Tlili, I.; Makinde, O.D.; Rajashekhar, C.; Khan, S.U.; Kumar, R.; Mahendra, D.L. Mixed convective nanofluid flow over a non-linearly stretched Riga plate. *Case Stud. Therm. Eng.* **2021**, *24*, 100828. [Google Scholar (https://scholar.google.com/scholar_lookup?title=Mixed+convective+nano-fluid+flow+over+a+non-linearly+stretched+Riga+plate&author=Vaidya,+H.&author=Prasad,+K.V.&author=Tlili,+I.&author=Makinde,+O.D.&author=Rajashekhar,+C.&author=Khan,+S.U.&author=Kumar,+R.&author=Mahendra,+D.L.&publication_year=2021&journal=Case+Stud.+Therm.+Eng.&volume=24&pages=100828&doi=10.1016/j.csite.2020.100828)] [CrossRef (<https://doi.org/10.1016/j.csite.2020.100828>)]
25. Rafique, K.; Alotaibi, H.; Ibrar, N.; Khan, I. Stratified flow of micropolar nanofluid over Riga plate: Numerical analysis. *Energies* **2022**, *15*, 316. [Google Scholar (https://scholar.google.com/scholar_lookup?title=Stratified+flow+of+micropolar+nano-fluid+over+Riga+plate:+Numerical+analysis&author=Rafique,+K.&author=Alotaibi,+H.&author=Ibrar,+N.&author=Khan,+I.&publication_year=2022&journal=Energies&volume=15&pages=316&doi=10.3390/en15010316)] [CrossRef (<https://doi.org/10.3390/en15010316>)]

- Prasad, K.V.; Vaidya, H.; Mebarek-Oudina, F.; Choudhari, R.; Nisar, K.S.; Jamsheer, W. Impact of surface temperature and convective boundary conditions on a nanofluid flow over a radially stretched Riga plate. *Proc. Inst. Mech. Eng. Part E J. Process Mech. Eng.* **2022**, *236*, 942–952. [Google Scholar (https://scholar.google.com/scholar_lookup?title=Impact+of+surface+temperature+and+convective+boundary+conditions+on+a+nanofluid+flow+over+a+radially+stretched+Riga+plate&author=Prasad,+K.V.&author=Vaidya,+H.&author=Mebarek-Oudina,+F.&author=Choudhari,+R.&author=Nisar,+K.S.&author=Jamshed,+W.&publication_year=2022&journal=Proc.+Inst.+Mech.+Eng.+Part+E+J.+Process+Mech.+Eng.&volume=236&pages=942%E2%80%93952&doi=10.1177/09544089211054407)] [CrossRef (<https://doi.org/10.1177/09544089211054407>)]
27. Darvesh, A.; Wahab, H.A.; Sarakorn, W.; Sánchez-Chero, M.; Apaza, O.A.; Villarreyes, S.S.C.; Palacios, A.Z. Infinite shear rate viscosity of cross model over Riga plate with entropy generation and melting process: A numerical Keller box approach. *Results Eng.* **2023**, *17*, 100942. [Google Scholar (https://scholar.google.com/scholar_lookup?title=Infinite+shear+rate+viscosity+of+cross+model+over+Riga+plate+with+entropy+generation+and+melt+ing+process:+A+numerical+Keller+box+approach&author=Darvesh,+A.&author=Wahab,+H.A.&author=Sarakorn,+W.&author=S%C3%A1nchez-Chero,+M.&author=Apaza,+O.A.&author=Villarreyes,+S.S.C.&author=Palacios,+A.Z.&publication_year=2023&journal=Results+Eng.&volume=17&pages=100942&doi=10.1016/j.rineng.2023.100942)] [CrossRef (<https://doi.org/10.1016/j.rineng.2023.100942>)]
28. Divya, S.; Eswaramoorthi, S.; Loganathan, K. Numerical computation of Ag/Al₂O₃ nanofluid over a Riga plate with heat sink/source and non-Fourier heat flux model. *Math. Comput. Appl.* **2023**, *28*, 20. [Google Scholar (https://scholar.google.com/scholar_lookup?title=Numerical+computation+of+Ag/Al2O3+nanofluid+over+a+Riga+plate+with+heat+sink/source+and+non-Fourier+heat+flux+model&author=Divya,+S.&author=Eswaramoorthi,+S.&author=Loganathan,+K.&publication_year=2023&journal=Math.+Comput.+Appl.&volume=28&pages=20&doi=10.3390/mca28010020)] [CrossRef (<https://doi.org/10.3390/mca28010020>)]
29. Ahmad, A.; Asghar, S.; Afzal, S. Flow of nanofluid past a Riga plate. *J. Magn. Magn. Mater.* **2016**, *402*, 44–48. [Google Scholar (https://scholar.google.com/scholar_lookup?title=Flow+of+nanofluid+past+a+Riga+plate&author=Ahmad,+A.&author=Asghar,+S.&author=Afzal,+S.&publication_year=2016&journal=J.+Magn.+Magn.+Mater.&volume=402&pages=44%E2%80%9348&doi=10.1016/j.jmmm.2015.11.043)] [CrossRef (<https://doi.org/10.1016/j.jmmm.2015.11.043>)]

30 Al-Kouz, W.; Owhaib, W. Numerical analysis of Casson nanofluid three-dimensional flow over a rotating frame exposed to a prescribed heat flux with viscous heating. *Sci. Rep.* **2022**, *12*, 4256. [Google Scholar (https://scholar.google.com/scholar_lookup?title=Numerical+analysis+of+Casson+nanofluid+three-dimensional+flow+over+a+rotating+frame+exposed+to+a+prescribed+heat+flux+with+h+viscous+heating&author=Al-Kouz,+W.&author=Owhaib,+W.&publication_year=2022&journal=Sci.+Rep.&volume=12&pages=4256&doi=10.1038/s41598-022-08211-2)] [CrossRef (<https://doi.org/10.1038/s41598-022-08211-2>)]

31. Muhammad, T.; Alsaedi, A.; Hayat, T.; Shehzad, S.A. A revised model for Darcy-Forchheimer three-dimensional flow of nanofluid subject to convective boundary condition. *Results Phys.* **2017**, *7*, 2791–2797. [Google Scholar (https://scholar.google.com/scholar_lookup?title=A+revised+model+for+Darcy-Forchheimer+three-dimensional+flow+of+nanofluid+subject+to+convective+boundary+condition&author=Muhammad,+T.&author=Alsaedi,+A.&author=Hayat,+T.&author=Shehzad,+S.A.&publication_year=2017&journal=Results+Phys.&volume=7&pages=2791%E2%80%9932797&doi=10.1016/j.rinp.2017.07.052)] [CrossRef (<https://doi.org/10.1016/j.rinp.2017.07.052>)]

Disclaimer/Publisher’s Note: The statements, opinions and data contained in all publications are solely those of the individual author(s) and contributor(s) and not of MDPI and/or the editor(s). MDPI and/or the editor(s) disclaim responsibility for any injury to people or property resulting from any ideas, methods, instructions or products referred to in the content.

© 2023 by the authors. Licensee MDPI, Basel, Switzerland. This article is an open access article distributed under the terms and conditions of the Creative Commons Attribution (CC BY) license (<https://creativecommons.org/licenses/by/4.0/> (<https://creativecommons.org/licenses/by/4.0/>)).

Share and Cite



(mailto:?)

&subject=From%20MDPI%3A%20%22Heat%20and%20Mass%20Transport%20in%20Casson%20Nanofluid%20Flow%20over%20a%203-D%20Riga%20Plate%20with%20Cattaneo-Christov%20Double%20Flux%3A%20A%20Computational%20Modeling%20through%20Analytical%20Method"&body=https://www.mdpi.com/2193842%3A%0A%0AHeat%20and%20Mass%20Transport%20in%20Casson%20Nanofluid%20Flow%20over%20a%203-D%20Riga%20Plate%20with%20Cattaneo-Christov%20Double%20Flux%3A%20A%20Computational%20Modeling%20through%20Analytical%20Method%0A%0AAbstract%3A%20This%20work%20examines%20the%20non-

Newtonian%20Cassonnanofluid%26rsquo%3Bs%20three-dimensional%20flow%20and%20heat%20and%20mass%20transmission%20properties%20over%20a%20Riga%20plate.%20The%20Buongiorno%20nanofluid%20model%2C%20which%20is%20included%20in%20the%20present%20model%2C%20includes%20thermo-migration%20and%20random%20movement%20of%20nanoparticles.%20It%20also%20took%20into%20account%20the%20Cattaneo%26ndash%3BChristov%20double%20flux%20processes%20in%20the%20mass%20and%20heat%20equations.%20The%20non-Newtonian%20Casson%20fluid%20model%20and%20the%20boundary%20layer%20approximation%20are%20included%20in%20the%20modeling%20of%20nonlinear%20partial%20differential%20systems.%20The%20homotopy%20technique%20was%20used%20to%20analytically%20solve%20the%20system%26rsquo%3Bs%20governing%20equations.%20To%20examine%20the%20impact%20of%20dimensionless%20parameters%20on%20velocities%2C%20concentrations%2C%20temperatures%2C%20local%20Nusselt%20number%2C%20skin%20friction%2C%20and%20local%20Sherwood%20number%2C%20a%20parametric%20analysis%20was%20carried%20out.%20The%20velocity%20profile%20is%20augmented%20in%20this%20study%20as%20the%20size%20of%20the%20modified%20Hartmann%20number%20increases.%20The%20greater%20thermal%20radiative%20enhances%20the%20heat%20transport%20rate.%20When%20the%20mass%20relaxation%20parameter%20is%20used%2C%20the%20mass%20flux%20values%20start%20to%20decrease.)

([https://twitter.com/intent/tweet?](https://twitter.com/intent/tweet?text=Heat+and+Mass+Transport+in+Casson+Nanofluid+Flow+over+a+3-D+Riga+Plate+with+Cattaneo-Christov+Double+Flux%3A+A+Computational+Modeling+through+Analytical+Method&hashtags=mdpisymmetry&url=https%3A%2F%2Fwww.mdpi.com%2F2193842&via=Symmetry_MDPI)

[text=Heat+and+Mass+Transport+in+Casson+Nanofluid+Flow+over+a+3-D+Riga+Plate+with+Cattaneo-Christov+Double+Flux%3A+A+Computational+Modeling+through+Analytical+Method&hashtags=mdpisymmetry&url=https%3A%2F%2Fwww.mdpi.com%2F2193842&via=Symmetry_](https://www.mdpi.com/2193842)

[MDPI\) !\[\]\(c3d993ca47bfe2a953c700506ce31fa0_img.jpg\) \(\[http://www.linkedin.com/shareArticle?\]\(http://www.linkedin.com/shareArticle?mini=true&url=https%3A%2F%2Fwww.mdpi.com%2F2193842&title=Heat%20and%20Mass%20Transport%20in%20Casson%20Nanofluid%20Flow%20over%20a%203-D%20Riga%20Plate%20with%20Cattaneo-Christov%20Double%20Flux%3A%20A%20Computational%20Modeling%20through%20Analytical%20Method%26source%3Dhttps%3A%2F%2Fwww.mdpi.com%26summary%3DThis%20work%20examines%20the%20non-Newtonian%20Cassonnanofluid%26rsquo%3Bs%20three-dimensional%20flow%20and%20heat%20and%20mass%20transmission%20properties%20over%20a%20Riga%20plate.%20The%20Buongiorno%20nanofluid%20model%2C%20which%20is%20included%20in%20the%20present%20model%2C%20includes%20thermo-migration%20and%20random%20movement%20of%20nanoparticles.%20It%20also%20took%20into%20account%20the%20Cattaneo%26ndash%3BChristov%20double%20flux%20processes%20in%20the%20mass%20and%20heat%20equations.%20The%20non-Newtonian%20Casson%20fluid%20model%20and%20the%20boundary%20layer%20approximation%20are%20included%20in%20the%20modeling%20of%20nonlinear%20partial%20differential%20systems.%20The%20homotopy%20technique%20was%20used%20to%20analytically%20solve%20the%20system%26rsquo%3Bs%20governing%20equations.%20To%20examine%20the%20impact%20of%20dimensionless%20parameters%20on%20velocities%2C%20concentrations%2C%20temperatures%2C%20local%20Nusselt%20number%2C%20skin%20friction%2C%20and%20local%20Sherwood%20number%2C%20a%20parametric%20analysis%20was%20carried%20out.%20The%20velocity%20profile%20is%20augmented%20in%20this%20study%20as%20the%20size%20of%20the%20modified%20Hartmann%20number%20increases.%20The%20greater%20thermal%20radiative%20enhances%20the%20heat%20transport%20rate.%20When%20the%20mass%20relaxation%20parameter%20is%20used%2C%20the%20mass%20flux%20values%20start%20to%20decrease.\)\)](http://www.linkedin.com/shareArticle?mini=true&url=https%3A%2F%2Fwww.mdpi.com%2F2193842&title=Heat%20and%20Mass%20Transport%20in%20Casson%20Nanofluid%20Flow%20over%20a%203-D%20Riga%20Plate%20with%20Cattaneo-Christov%20Double%20Flux%3A%20A%20Computational%20Modeling%20through%20Analytical%20Method%26source%3Dhttps%3A%2F%2Fwww.mdpi.com%26summary%3DThis%20work%20examines%20the%20non-Newtonian%20Cassonnanofluid%26rsquo%3Bs%20three-dimensional%20flow%20and%20heat%20and%20mass%20transmission%20properties%20over%20a%20Riga%20plate.%20The%20Buongiorno%20nanofluid%20model%2C%20which%20is%20included%20in%20the%20present%20model%2C%20includes%20thermo-migration%20and%20random%20movement%20of%20nanoparticles.%20It%20also%20took%20into%20account%20the%20Cattaneo%26ndash%3BChristov%20double%20flux%20processes%20in%20the%20mass%20and%20heat%20equations.%20The%20non-Newtonian%20Casson%20fluid%20model%20and%20the%20boundary%20layer%20approximation%20are%20included%20in%20the%20modeling%20of%20nonlinear%20partial%20differential%20systems.%20The%20homotopy%20technique%20was%20used%20to%20analytically%20solve%20the%20system%26rsquo%3Bs%20governing%20equations.%20To%20examine%20the%20impact%20of%20dimensionless%20parameters%20on%20velocities%2C%20concentrations%2C%20temperatures%2C%20local%20Nusselt%20number%2C%20skin%20friction%2C%20and%20local%20Sherwood%20number%2C%20a%20parametric%20analysis%20was%20carried%20out.%20The%20velocity%20profile%20is%20augmented%20in%20this%20study%20as%20the%20size%20of%20the%20modified%20Hartmann%20number%20increases.%20The%20greater%20thermal%20radiative%20enhances%20the%20heat%20transport%20rate.%20When%20the%20mass%20relaxation%20parameter%20is%20used%2C%20the%20mass%20flux%20values%20start%20to%20decrease.))

[mini=true&url=https%3A%2F%2Fwww.mdpi.com%2F2193842&title=Heat%20and%20Mass%20Transport%20in%20Casson%20Nanofluid%20Flow%20over%20a%203-D%20Riga%20Plate%20with%20Cattaneo-Christov%20Double%20Flux%3A%20A%20Computational%20Modeling%20through%20Analytical%20Method%26source%3Dhttps%3A%2F%2Fwww.mdpi.com%26summary%3DThis%20work%20examines%20the%20non-Newtonian%20Cassonnanofluid%26rsquo%3Bs%20three-dimensional%20flow%20and%20heat%20and%20mass%20transmission%20properties%20over%20a%20Riga%20plate.%20The%20Buongiorno%20nanofluid%20model%2C%20which%20is%20included%20in%20the%20present%20model%2C%20includes%20thermo-migration%20and%20random%20movement%20of%20nanoparticles.%20It%20also%20took%20into%20account%20the%20Cattaneo%26ndash%3BChristov%20double%20flux%20processes%20in%20the%20mass%20and%20heat%20equations.%20The%20non-Newtonian%20Casson%20fluid%20model%20and%20the%20boundary%20layer%20approximation%20are%20included%20in%20the%20modeling%20of%20nonlinear%20partial%20differential%20systems.%20The%20homotopy%20technique%20was%20used%20to%20analytically%20solve%20the%20system%26rsquo%3Bs%20governing%20equations.%20To%20examine%20the%20impact%20of%20dimensionless%20parameters%20on%20velocities%2C%20concentrations%2C%20temperatures%2C%20local%20Nusselt%20number%2C%20skin%20friction%2C%20and%20local%20Sherwood%20number%2C%20a%20parametric%20analysis%20was%20carried%20out.%20The%20velocity%20profile%20is%20augmented%20in%20this%20study%20as%20the%20size%20of%20the%20modified%20Hartmann%20number%20increases.%20The%20greater%20thermal%20radiative%20enhances%20the%20heat%20transport%20rate.%20When%20the%20mass%20relaxation%20parameter%20is%20used%2C%20the%20mass%20flux%20values%20start%20to%20decrease.\)](https://www.mdpi.com/2193842)  ([https://www.facebook.com/sharer.php?](https://www.facebook.com/sharer.php?url=https://www.mdpi.com/2193842)

[u=https://www.mdpi.com/2193842](https://www.mdpi.com/2193842)  ([http://www.reddit.com/submit?](http://www.reddit.com/submit?url=https://www.mdpi.com/2193842)

[url=https://www.mdpi.com/2193842](https://www.mdpi.com/2193842) ([http://www.mendeley.com/import/?](http://www.mendeley.com/import/?url=https://www.mdpi.com/2193842)

[url=https://www.mdpi.com/2193842](https://www.mdpi.com/2193842))

MDPI and ACS Style

Loganathan, K.; Eswaramoorthi, S.; Chinnasamy, P.; Jain, R.; Sivasakthivel, R.; Ali, R.; Devi, N.N. Heat and Mass Transport in Casson Nanofluid Flow over a 3-D Riga Plate with Cattaneo-Christov Double Flux: A Computational Modeling through Analytical Method. *Symmetry* **2023**, *15*, 725. <https://doi.org/10.3390/sym15030725>

AMA Style

Loganathan K, Eswaramoorthi S, Chinnasamy P, Jain R, Sivasakthivel R, Ali R, Devi NN. Heat and Mass Transport in Casson Nanofluid Flow over a 3-D Riga Plate with Cattaneo-Christov Double Flux: A Computational Modeling through Analytical Method. *Symmetry*. 2023; 15(3):725. <https://doi.org/10.3390/sym15030725>

Chicago/Turabian Style

Loganathan, Karuppusamy, S. Eswaramoorthi, P. Chinnasamy, Reema Jain, Ramkumar Sivasakthivel, Rifaqat Ali, and N. Nithya Devi. 2023. "Heat and Mass Transport in Casson Nanofluid Flow over a 3-D Riga Plate with Cattaneo-Christov Double Flux: A Computational Modeling through Analytical Method" *Symmetry* 15, no. 3: 725. <https://doi.org/10.3390/sym15030725>

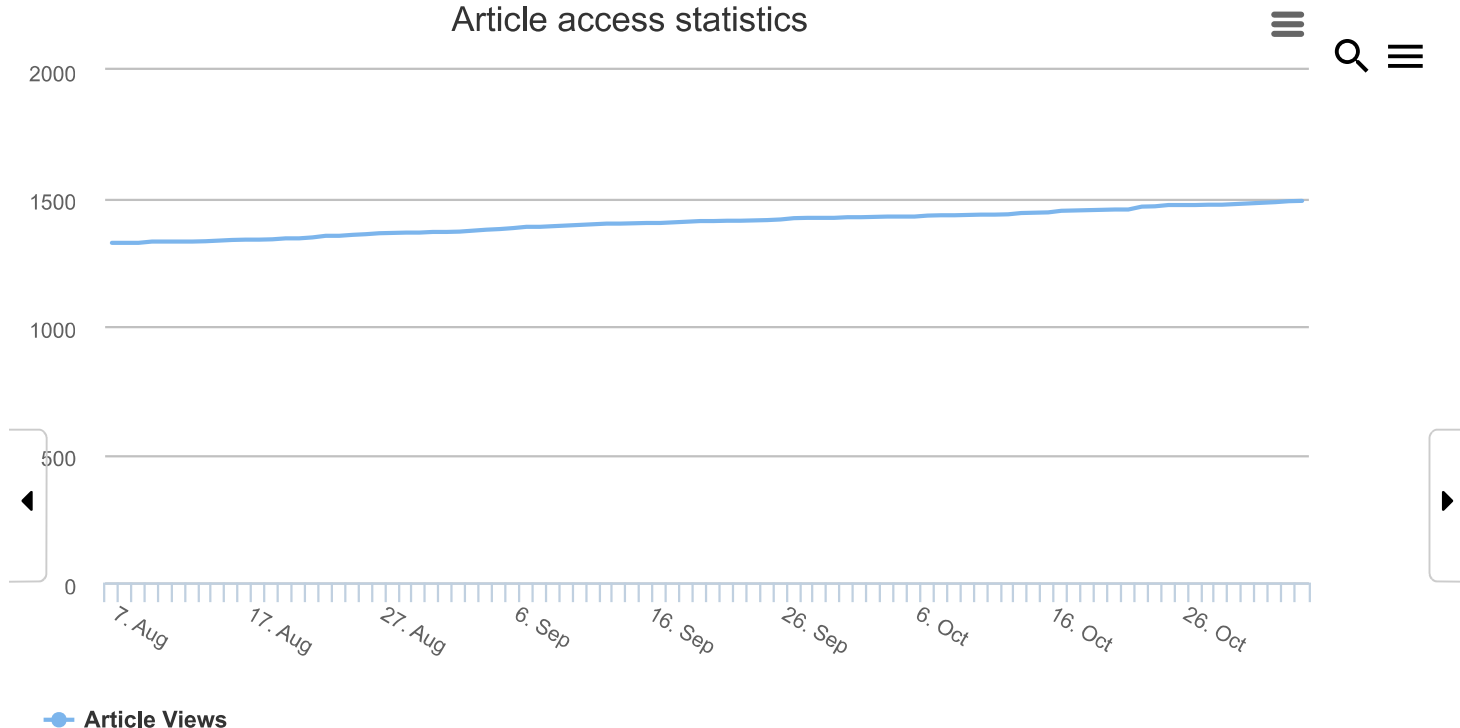
ⓘ Note that from the first issue of 2016, this journal uses article numbers instead of page numbers. See further details **here** (<https://www.mdpi.com/about/announcements/784>).

Article Metrics

Citations

Web of Science	Scopus	Crossref	ads	Google Scholar
	7 (https://partnerID=HzO:GWVersion=2&	6	(https://ui.adsat	Christov+Doubl

Article access statistics



For more information on the journal statistics, click [here \(/journal/symmetry/stats\)](/journal/symmetry/stats).

ⓘ Multiple requests from the same IP address are counted as one view.

[Symmetry \(/journal/symmetry\)](/journal/symmetry), EISSN 2073-8994, Published by MDPI

[RSS \(/rss/journal/symmetry\)](/rss/journal/symmetry) **[Content Alert \(/journal/symmetry/toc-alert\)](/journal/symmetry/toc-alert)**

Further Information

[Article Processing Charges \(/apc\)](/apc)

[Pay an Invoice \(/about/payment\)](/about/payment)

[Open Access Policy \(/openaccess\)](/openaccess)

[Contact MDPI \(/about/contact\)](/about/contact)

[Jobs at MDPI \(https://careers.mdpi.com\)](https://careers.mdpi.com)

Guidelines

[For Authors \(/authors\)](/authors)

[For Reviewers \(/reviewers\)](/reviewers)

[For Editors \(/editors\)](/editors)

[For Librarians \(/librarians\)](/librarians)

[For Publishers \(/publishing_services\)](/publishing_services)

[For Societies \(/societies\)](/societies)

[For Conference Organizers \(/conference_organizers\)](#)
MDPI Initiatives

[Sciforum \(https://sciforum.net\)](https://sciforum.net)

[MDPI Books \(https://www.mdpi.com/books\)](https://www.mdpi.com/books)

[Preprints.org \(https://www.preprints.org\)](https://www.preprints.org)

[Scilit \(https://www.scilit.net\)](https://www.scilit.net)

[SciProfiles \(https://sciprofiles.com?utm_source=mdpi.com&utm_medium=bottom_menu&utm_campaign=initiative\)](https://sciprofiles.com?utm_source=mdpi.com&utm_medium=bottom_menu&utm_campaign=initiative)

[Encyclopedia \(https://encyclopedia.pub\)](https://encyclopedia.pub)

[JAMS \(https://jams.pub\)](https://jams.pub)

[Proceedings Series \(/about/proceedings\)](#)

Follow MDPI

[LinkedIn \(https://www.linkedin.com/company/mdpi\)](https://www.linkedin.com/company/mdpi)

[Facebook \(https://www.facebook.com/MDPIOpenAccessPublishing\)](https://www.facebook.com/MDPIOpenAccessPublishing)

[Twitter \(https://twitter.com/MDPIOpenAccess\)](https://twitter.com/MDPIOpenAccess)

Subscribe to receive issue release notifications and newsletters from MDPI journals

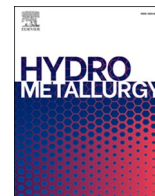
Select options

Enter your email address...

Subscribe

© 1996-2024 MDPI (Basel, Switzerland) unless otherwise stated

[Disclaimer](#) [Terms and Conditions \(/about/terms-and-conditions\)](#)
[Privacy Policy \(/about/privacy\)](#)



Investigations into the closed-loop hydrometallurgical process for heavy metals removal and recovery from biosolids via mild acid pre-treatment

Ibrahim Gbolahan Hakeem^{a,b}, Pobitra Halder^{b,c}, Shefali Aktar^a, Mojtaba Hedayati Marzbali^{a,b}, Abhishek Sharma^{b,d}, Aravind Surapaneni^{b,e}, Graeme Short^e, Jorge Paz-Ferreiro^a, Kalpit Shah^{a,b,*}

^a Chemical and Environmental Engineering, School of Engineering, RMIT University, Melbourne, VIC 3000, Australia

^b ARC Training Centre for the Transformation of Australia's Biosolids Resource, RMIT University, Bundoora, VIC 3082, Australia

^c School of Engineering, Deakin University, VIC 3216, Australia

^d Department of Chemical Engineering, Manipal University, Jaipur, Rajasthan 303007, India

^e South East Water Corporation, Frankston, VIC 3199, Australia

ARTICLE INFO

Keywords:

Leachate recycling
Biosolids treatment
Heavy metals
Metal recovery
Metal extraction

ABSTRACT

Biosolids contain heavy metals (HMs), restricting their beneficial reuse in agricultural land. However, these metals can be a valuable resource in many applications if recovered efficiently. Therefore, the removal and recovery of HMs and other limiting contaminants in biosolids without degrading the organic nutrients of the resulting treated biosolids demands holistic investigations. A closed-loop hydrometallurgical treatment process for metal removal and recovery from biosolids was developed in this study. Firstly, mild acid treatment using 3% v/v H₂SO₄ at 25 °C, 600 rpm for 30 min was performed in a 1 L continuous stirred tank reactor to extract common HMs (such as As, Cd, Co, Cr, Cu, Ni, Pb, and Zn) from biosolids into the aqueous phase. The effects of solids concentration and acid types on the HMs extraction efficiency were studied. Then, the primary acid leachate stream was continuously recycled for metal extraction from biosolids until the dissolved metals in the solution reached saturation concentration. After that, the dissolved metals were recovered in staged NaOH precipitation and adsorption. Low solids contents (<5% w/v) using mineral acids having pH <2 and oxidation-reduction potential (ORP) ~500 mV (versus SHE) favoured HMs solubilisation from biosolids with an average extraction efficiency of 70%. The dissolution of ferric iron (Fe³⁺) by H₂SO₄ and subsequent in-situ formation of ferric sulfate enhanced the metal extraction strength of the spent leachate stream during recycling. However, the solids loading in each leaching process must be kept low to prevent ferric concentration build-up and precipitation as the leachate pH steadily increases above 2 during recycling. Amongst the metal recovery methods investigated, H₂O₂ oxidation prior to 2-stage NaOH precipitation had the highest efficiency with 75–95% HMs recovery. The clarified stream was used to neutralise the acidic treated biosolids to close the process loop. The complete process flowsheet was developed with mass balances, and the fate of nutrients (mainly C, N, and P) and major *per-* and polyfluoro alkyl substances (PFAS) were overviewed.

1. Introduction

Biosolids, also known as stabilised sewage sludge, are the by-product of the wastewater treatment process. Biosolids contain valuable organic and inorganic components (mainly N, P, and K) that constitute important plant nutrients. These nutrients facilitate the application of a substantial volume of biosolids in agricultural soils in many countries, including Australia (Paz-ferreiro et al., 2018). However, heavy metals

(HMs) and other contaminants such as pesticides, microbial pathogens, microplastics, and surfactants are limiting the attractiveness of biosolids for direct land application with increasingly stringent regulations (EPA Victoria, 2004; LeBlanc et al., 2009). Thermochemical treatment of sub-grade biosolids via pyrolysis, gasification, hydrothermal carbonisation/liquefaction or incineration process can effectively degrade the organic and microbial contaminants (Kundu et al., 2021; Ross et al., 2016). However, HMs remain a persistent pollutant in biosolids and their

* Corresponding author at: Chemical and Environmental Engineering, School of Engineering, RMIT University, Melbourne, VIC 3000, Australia.
E-mail address: kalpit.shah@rmit.edu.au (K. Shah).

thermally-derived products due to the low thermal degradation as well as the formidable bioaccumulation and high environmental toxicity of HMs (Feng et al., 2018).

The pre-treatment of biosolids is considered an effective process for removing the HMs before land application or thermal processing. Several pre-treatment methods, including chemical leaching with acids (Gaber et al., 2011; Stylianou et al., 2007), chelating agents (Gheju et al., 2011; Leštan et al., 2008), ferric salts (Bayat and Sari, 2010; Ito et al., 2000), ionic liquids (Abouelela et al., 2022; Yao et al., 2021), surfactants (Guan et al., 2017; Tang et al., 2017), and microbial agents (Pathak et al., 2009; Xiang et al., 2000) have been investigated for this purpose. Amongst all, leaching with acids is the most common, efficient with short operation times, and cost-effective with high industrial maturity (Babel and del Mundo Dacera, 2006; Gunarathne et al., 2020; Hakeem et al., 2022a). The high oxidising potential, as well as the low pH of acids, are favourable for metal dissolution (Ma et al., 2020). In addition, most metal cations are basic and readily ion-exchangeable with protons from acids (Persson et al., 2017). Therefore, acid leaching plays a leading role in hydrometallurgical processes for metals recovery from different materials, including biosolids (Gunarathne et al., 2020; Montenegro et al., 2016). In a typical acid leaching process, a high liquid-to-solid ratio is desired to achieve high HMs dissolution by overcoming thermodynamic equilibrium, which occurs when the solid dissociates to such an extent that the metal species are fully saturated in the solution (Lee et al., 2006). Hence, acid leaching is usually accompanied by a large volume of aqueous waste stream with dilute metal concentrations. Metal recovery from this dilute stream is unattractive and improper disposal poses environmental threats.

One of the potential ways to manage the resulting leachate stream from biosolids pre-treatment is to reuse and recycle the stream for another leaching process until the leachate stream gets saturated with HMs. The heavily concentrated leachate stream can be a precursor for recovering valuable metals. Recycling the aqueous acidic leachate stream can be attractive for metal extraction due to its low pH, high oxidation-reduction potential (ORP), and presence of surrogate leaching components such as dissolved ferric sulfates or chlorides (Beauchesne et al., 2007; Ito et al., 2000; Strasser et al., 1995). In addition, recycling the acidic waste stream can reduce the overall acid solution requirements during the metal extraction process, with the potential to favour the techno-economics of the process. The effect of process variables such as temperature, acid concentration, solids contents, agitation speeds, and contact time on HMs removal efficiency has been elucidated in previous studies (del Mundo Dacera and Babel, 2006; Gaber et al., 2011; Hakeem et al., 2022b; Yang et al., 2021). However, there is a limited investigation on the recyclability of the acidic leachate stream as a solvent for metal extraction from raw biosolids (Shim, 2023). Particularly, the effects of solids loading on the recycling performance of the leachate stream have not been reported in extant literature.

The overall hydrometallurgical process can be grouped into three sequential stages: metal extraction, leachate concentration and purification, and metal recovery (Gunarathne et al., 2020). The growing interest in resource recovery has increased the prospect of critical element extraction and recovery from biosolids via hydrometallurgical operations (Tyagi and Lo, 2013). However, metal recovery from biosolids has not been fully explored in the literature beyond the acid leaching stage, which removes the metals from biosolids to the liquid phase, as described earlier. Therefore, developing a comprehensive hydrometallurgical process chain to understand the feasibility of metal recovery from biosolids through the production of less contaminated biosolids is desired. While the metal extraction stage is the most critical in the overall hydrometallurgical process, leachate purification and metal recovery are the most challenging because acidic solvents have poor selectivity during metal solubilisation. Moreover, biosolids have many metal and non-metal components that elute simultaneously into solution during acid leaching. For example, the co-solubilisation of iron, aluminium, and alkali and alkaline earth metals (AAEMs) alongside HMs

usually complicates the selective recovery of valuable metals from the leachate stream (Lee et al., 2002). In some cases, elements such as carbon (C), nitrogen (N), and phosphorous (P) are dissolved in the acidic stream, interfering with the purification and recovery of desired metals.

The main techniques for metal recovery from aqueous streams are chemical precipitation (Liang et al., 2019; Marchioretto et al., 2005), electrodeposition (Yao et al., 2021), adsorption (Singh et al., 2020), ion exchange (Yoshizaki and Tomida, 2000), and solvent extraction (Montenegro et al., 2016). Chemical precipitation using caustic soda (NaOH) or slaked lime (Ca(OH)₂) and adsorption are the most common, less laborious, and suitable for multi-components metal streams typical of biosolids leachate (Li et al., 2021; Marchioretto et al., 2005). However, the efficacy of alkali precipitation of HMs is challenged by the amphoteric nature of some metal ions having different optimum hydroxides solubility as well as interferences from other metal species, particularly iron (de Fátima da Silva et al., 2020). Given the number of metal in a biosolids leachate stream, identifying suitable metal recovery methods will depend on the final composition, metal concentration, and pH (Sethurajan et al., 2017). Studies involving the chemical precipitation of multiple metal from real biosolids leach solutions are limited in the literature (Marchioretto et al., 2005). Chemical precipitation and adsorption have only been extensively applied on metal ores leachate or simulated wastewater containing single or dual metal components (Ait Ahsaine et al., 2017; Ni et al., 2019; Xu et al., 2009).

In summary, the full spectrum of chemical treatment of biosolids for HMs removal involving metal extraction, separation of solids from the leach liquor, leachate concentration and purification, and metal recovery is missing in the literature. Hence, this study explored a comprehensive mild acid treatment of biosolids for HMs extraction and the subsequent recovery of the metal from the concentrated leachate stream. The specific objectives of the work were to (i) study the effect of acid solution and solids concentration on the extraction efficiency of metals from biosolids, (ii) investigate the reusability and extraction performance of the primary leachate stream through partial and complete recycling at optimum solids concentrations, (iii) examine the efficacy of staged NaOH co-precipitation, H₂O₂ oxidation followed by NaOH co-precipitation, and biochar adsorption for the purification and recovery of HMs from the concentrated leachate stream, (iv) understand the fate of dissolved nutrients (mainly C, N, K, and P) and *per*- and poly-fluoro alkyl substance (PFAS) compounds in the process streams, and (v) develop and propose optimum process flow diagrams with mass balances for biosolids metal removal and recovery. This detailed investigation will help to understand the feasibility of developing an in-situ or ex-situ hydrometallurgical process for biosolids HMs decontamination with potential for nutrient and critical metal recovery within the existing wastewater treatment facilities.

2. Materials and methods

2.1. Biosolids preparation and analyses

Biosolids used in this study were obtained from Mount Martha Water Recycling Plant, South East Water Corporation, Victoria, Australia. The biosolids production process was described in our previous study (Hakeem et al., 2022b). Before use in the pre-treatment experiments, biosolids were dried overnight in an oven at 105 °C and sieved to 100–300 µm particle size. The elemental composition was determined by X-ray Fluorescence (XRF, S4 AXS Bruker), ultimate analysis was performed using a CHNS Series II Perkin Elmer instrument, and the metal concentration was measured using Inductive Coupled Plasma-Mass Spectrometry (ICP-MS 2200 series, Agilent Technologies). The chemicals used in this work were of analytical grades. They include 98% H₂SO₄ (Chem-Supply Pty Ltd), 65% HNO₃ (Univar Pty Ltd), 35% HCl (Emplura Pty Ltd), 99% glacial acetic acid (Sigma Aldrich), 99.5% citric acid (Sigma Aldrich), 21–23% ferric sulfate pentahydrate (Chem-Supply) and 30% hydrogen peroxide (Rowe Scientific Pty Ltd). Milli-Q

water with a resistivity of 18.2 MΩ cm was used throughout this study. Table 1 shows the composition of the biosolids. The concentration of some of the HMs, such as Cu, Zn, and Cd, is higher than that prescribed for the least contaminant grade (C1) for unrestricted beneficial reuse of biosolids according to Victoria EPA biosolids guidelines (EPA Victoria, 2004).

2.2. Heavy metals fractionation in the biosolids

The efficacy of acid leaching for metal extraction depends on the chemical fractionation of the metal in the biosolids matrix (Geng et al., 2020). Therefore, according to previous literature, a modified three-step Community Bureau of Reference (BCR) sequential extraction technique was used to determine the distribution of metal in the biosolids (Liu et al., 2021, 2018; Wang et al., 2019). This method allows the chemical classification of HMs species in biosolids, soils, and sediments into four major fractions: exchangeable (F-1), reducible (F-2), oxidisable (F-3), and residual (F-4) based on the ease of extraction with standard reagents (Zhao et al., 2018). The F-1 refers to acid-ionisable metals, F-2 are metals bound to carbonates and Fe—Mn oxides, F-3 are metals bound to organic matter and sulfides, and F-4 are bound to silicates and recalcitrant organics. Depending on the severity of the acid leaching conditions, such as acid concentration (or pH), temperature, and time, F-1, F-2, and F-3 metals can be removed at various rates in decreasing order, while F-4 metals are hardly removed via chemical leaching. The result of this analysis is presented in Fig. S1. From Fig. S1, the potential mobility of the metals in the biosolids can be estimated by adding F-1 and F-2 metal percentages (Geng et al., 2020), and this can be ranked as Mn > Zn > Cd ≈ Ni ≈ Co > Cr > As > Pb > Cu ≈ Fe. Copper has the highest F-3 percentage due to the higher affinity of Cu to organic matter (Beauchesne et al., 2007), while Fe and Pb have the highest F-4 percentages. Copper is the most challenging HM to remove in biosolids via acid leaching; this observation has been widely reported in other works (Beauchesne et al., 2007; Blais et al., 2005; Mercier et al., 2002). Therefore, the extraction of Cu under mild acid leaching conditions may be limited.

2.3. Biosolids metals extraction

The batch pre-treatment procedure was as described previously (Hakeem et al., 2022b). All leaching experiments were conducted at room temperature (25 ± 2 °C) using 3% (v/v) acid concentration under continuous stirring at 600 rpm for 30 ± 2 min in a 1 L continuous stirred tank reactor. These are the optimised conditions from our previous investigation (Hakeem et al., 2022b). The effect of acid types was studied by using three mineral acids (H₂SO₄, HCl, HNO₃) and two organic acids (acetic and citric) to extract HMs (such as As, Cd, Co, Cr, Cu, Ni, Pb, and Zn) from biosolids at 5% (w/v) solids loading using 3% (v/v) acid solution. Similarly, the effect of solids concentration was studied by leaching biosolids at 1, 3, 5, 10, 15 and 20% (w/v) solids using 3% (v/v) H₂SO₄ solution. At the end of each metal extraction experiment, the slurry was transferred into Eppendorf tubes and centrifuged at 4000 rpm for 30 min. The leachate stream was carefully decanted into sample vials, and the residue (treated biosolids) was dried and stored for further analysis. The pH and ORP of the leachate stream

were measured, and 1 mL aliquot of the well-mixed leachate was filtered, diluted, and quantified for metals by ICP-MS. All leaching experiments were performed in triplicates, and average results were reported with errors expressed as the standard deviation of the measurements. A schematic illustration of the metal extraction process including the downstream separation and metal recovery processes is shown in Fig. 1.

2.4. Concentration of the leachate stream

2.4.1. Total recycling of the leachate

The recovered aqueous stream from the parent (primary) pre-treatment was reused fully for another extraction process at 5% and 10% (w/v) fresh biosolids loading; all other conditions remain unchanged. The process was repeated for five leaching cycles (after the parent leaching) using 100% spent leachate stream and fresh biosolids in each cycle. The volume of the leachate stream and mass of the fresh biosolids were adjusted to achieve 5% or 10% solids loading in each cycle. It is assumed that the metals dissolved in the leachate will remain in the solution all the time unless the pH ≥ 2.5 , where ferric precipitation will be initiated. During the recycling, precipitate from poorly soluble metals such as Ca and Pb is partitioned in the treated solids. The parent (primary) leachate stream and leachate stream after each successive recycle are denoted by R0 and Rn, where $n = 1, 2, 3$ etc., denotes the number of cycles.

2.4.2. Partial recycling of the leachate

A constant volume pre-treatment experiment was performed with biosolids to liquid (g/mL) ratio of 1:10 (10% solids) and 1:20 (5% solids) using the recovered leachate. A fixed mass of biosolids (10 g or 5 g) and a solution volume of 100 mL were maintained for this experiment. The recycled stream was topped with fresh 3% (v/v) H₂SO₄ to maintain the solution volume at 100 mL for each leaching experiment. The added fresh lixiviant (FL) volume replaced the lost solution volume during each leaching cycle, including aliquots taken for analysis. Thus, the make-up ratio (volume of FL to volume of spent leachate) was ~15 vol% and ~20 vol% at 5% and 10% solids, respectively. The number of effective leaching cycles (n) was determined by continuously reusing the spent stream with make-up solution until the solution became saturated with dissolved metals. At the end of each leaching cycle, the recovered leachate stream was filtered to reduce suspended solids carryover before reusing it in another leaching cycle. All pre-treatment experiment with leachate recycling was repeated at least two times, and average data was reported.

2.5. Metals recovery

Most HMs precipitate out of solution at a pH range of 7–12 (Fu and Wang, 2011); however, the concentrated leachate stream obtained from the partial leachate recycling experiment was in the acidic pH (2.45). Therefore, an alkaline solution is required to adjust the solution pH to the metal precipitation region. Since each metal has different optimal precipitation pH depending on the metal ion concentration in the solution (Sethurajan et al., 2017), a typical pH of 9 was chosen for the precipitation experiment. A concentrated NaOH (6 M, pH 14) solution

Table 1
Metals composition of biosolids.

Metal type	Source	Metals composition (mg/kg)								
		Ca	Mg	Na	K	Al	Fe	Mn	Mo	Ba
Major and trace metals	This study	35,600	3630	2790	3530	5180	13,440	210	6	185
		Cr	Ni	Pb	Cd	As	Co	Cu	Zn	
Heavy metals	This study	22	14	17	1.3	2	3	825	815	
	C1 grade*	400	60	300	1	20	–	100	200	
	C2 grade*	3000	270	500	10	60	–	2000	2500	

* Biosolids contaminant grade as prescribed by Victoria EPA biosolids guidelines (EPA Victoria, 2004).

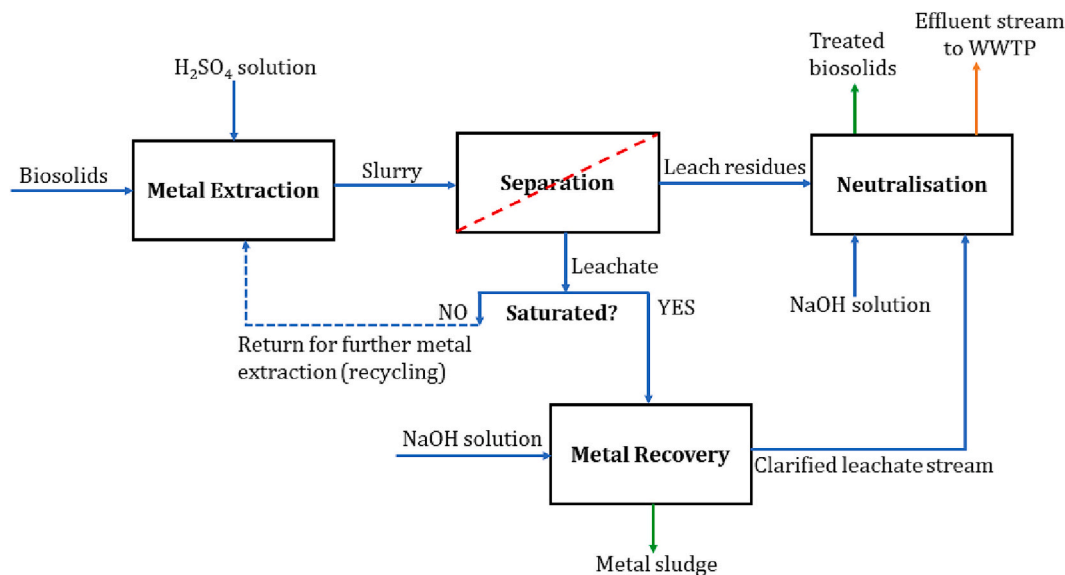


Fig. 1. Schematic of biosolids hydrometallurgical process for metal removal and recovery.

was used for the precipitation of metal ions to reduce the dilution effect on the concentration of the metals. The metal ion precipitation experiment was designed in the following ways to maximise the recovery of the HMs from other metal and non-metal contaminants.

- 1) Two-step NaOH precipitation when Fe/Al precipitation was considered: 20 mL of well-mixed and filtered leachate stream was measured in a conical flask, and 6 M NaOH was added in drops under continuous stirring until the solution pH was 4.5 ± 0.2 . The pH of the solution was monitored via a well-calibrated pH meter, and the amount of NaOH added was noted. The sample was left to stay still for 2 h and centrifuged at 4000 rpm for 30 min to recover the precipitates. Then, 5 mL of the clarified stream was treated in the second step with NaOH in drops until the solution pH was 9.0 ± 0.5 ; the solution was left to settle for 2 h and centrifuged to recover the precipitates. The concentration of metal in the treated liquid after each step was measured by ICP-MS.
- 2) Single-step NaOH precipitation when Fe/Al precipitation was not considered: 10 mL of the leachate stream was treated with NaOH until the final pH was 9.0 ± 0.5 . The presence of Fe and Al in the stream may help in the co-precipitation reaction with HMs since Fe^{3+} and Al^{3+} salts are common coagulants used in the wastewater treatment process.
- 3) Fenton reaction by adding H_2O_2 when oxidation of Fe and dissolved organics were considered: Ferric iron is known to precipitate at low pH <4 , whereas ferrous has a high precipitation pH >8.5 , so H_2O_2 can oxidise ferrous to ferric for recovery at stage 1 (pH 4.5). Moreover, dissolved organics in the form of COD (chemical oxygen demand) can limit HMs recovery, so the oxidation of dissolved organic by H_2O_2 was considered before NaOH precipitation. Briefly, a few drops of 30% v/v H_2O_2 (<0.5 mL) were added to 10 mL of well-filtered leachate stream. Then, the pH of the stream was adjusted to 4.5 with the addition of NaOH in drops to recover Fe/Al. The clarified stream was treated in a second stage to co-precipitate all other metals at pH 9.0 by adding NaOH.
- 4) Adsorption: An attempt to use biochar for adsorption when the leachate stream was at acidic pH (2.45) caused the leaching of metals from the biochar to the liquid, so adjustment of the leachate pH is necessary. Ten mL of clarified leachate (pH 4.5) obtained after the first step of Fe/Al precipitation was used for the adsorption experiment. Biochar produced from raw biosolids at 500 °C for 3 h residence time in a muffle furnace was used as the adsorbent and

charged at a dose of 0.05 g per mL leachate (0.048 g/g leachate). The adsorption was carried out at room temperature overnight under a constant agitation speed of 250 rpm. The mixture was filtered to separate the biochar and the aqueous stream, which was analysed for metal contents by ICP-MS. It should be noted that the presence of HMs in biosolids-biochar is a major concern only for land application of biochar. Metal-loaded biochar can have many valuable applications in catalysis and energy storage (Shen and Chen, 2022; Wang et al., 2017). Besides, biochar adsorption could be an effective and cheaper alternative than alkali precipitation for recovering dissolved metals from the acidic leachate stream.

2.6. Process configurations and the fate of nutrients and PFAS

The process flow diagram was developed to capture the entire hydrometallurgical treatment chain from metal extraction via acid leaching to metal recovery via alkali precipitation and, finally, the neutralisation of treated solids. Material balances were performed assuming a steady-state operation. The flow of C, N, and P in the process streams from the biosolids feed to the leachate stream and treated biosolids was overviewed. Similarly, twenty-eight compounds of PFAS (per- and polyfluoroalkyl substances) were measured in the raw biosolids, neutralised treated biosolids, the acidic leachate, and the final liquid effluent. The change in pH of both solid and liquid streams along the treatment chain might influence the leachability and the final fate of PFAS compounds (Kabiri et al., 2022). The C and N content in the raw and treated biosolids was determined using a CHN Series II Perkin Elmer instrument, while P content was measured by XRF analysis. Total organic carbon dissolved in the leachate stream was measured using TOC-L (Shimadzu Corporation). Total N representing the sum of total Kjeldahl nitrogen (TKN) and NO_x and total P analysis, as well as PFAS analysis, were performed externally at ALS Water Resource Group, Melbourne, Australia.

3. Results and discussions

3.1. Effect of acid types

The efficiency of three mineral acids (sulfuric, nitric and hydrochloric) and two organic (acetic and citric) acids at the same volume concentration of 3% (v/v) and 5% (w/v) solids were studied on HMs extraction (Fig. 2). Mineral acids outperformed organic acids, and

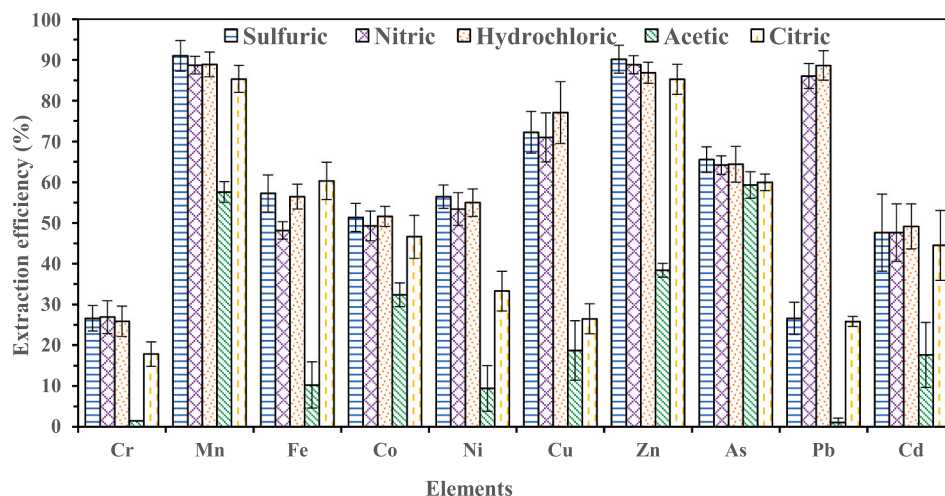


Fig. 2. Effect of mineral and organic acid solutions on the metal extraction efficiency from biosolids (conditions: 5% (w/v) solids, 3% (v/v) acid concentration, 25 °C, 30 min, and 600 rpm).

except for Pb, all mineral acids perform similarly in the metal extraction process. The high ionising power and extremely low pH of the mineral acids (~1.7) compared to the organic acids (~2.7) favoured the solubilisation of HMs (Gaber et al., 2011). Most sulfate, nitrate, and chloride salts are highly soluble in water and dilute acids, which may explain the similar metal extraction efficiencies of the three mineral acids. Sulfuric acid performed poorly in removing Pb owing to the low solubility (0.038 g/L) of PbSO_4 in water ($K_{sp@298\text{ K}} 1.6 \times 10^{-8}$). Generally, organic acids are considered weak acids ($\text{pK}_a > 1$) as the ionised hydrogen concentration is typically lower than strong acids ($\text{pK}_a < 0$) at the same molar concentration. For instance, the ionised hydrogen concentration of nitric acid is 100% of the acid concentration, whereas the ionised hydrogen concentration of citric acid is equivalent to 1.3–2.1% of nitric acid concentration (Lee et al., 2005). Therefore, it is expected that both organic acids have weaker ionic strength to desorb HMs ions in the biosolids, especially at low acid concentrations. However, of the two organic acids, citric acid was competitive with mineral acids despite having a similar pH to acetic acid in the metal extraction process. Citric acid is a natural chelating agent, and citrate ions form soluble complexes with cations of metals (Ma et al., 2020). Moreover, acetic acid is dicarboxylic while citric acid is tricarboxylic; the presence of an extra carboxylic group in citric acid also favours the number of available chelating sites for metal extraction (Gheju et al., 2011). Therefore, the chelating mechanism of citric acid was responsible for the high metal extraction rather than the acidolysis (reaction with H^+) mechanism for the mineral acid-based leaching. Studies have demonstrated that the oxidation-reduction potential (ORP) of the leaching solvents can affect their metal extraction ability since metal solubilisation usually involves an ion-exchange reaction with protons from acid (Babel and del Mundo Dacera, 2006; Bayat and Sari, 2010; Blais et al., 2005; Pathak et al., 2009). In this work, 3% nitric acid had the highest ORP of 611 mV, followed by sulfuric acid (590 mV) and hydrochloric acid (473 mV). This ORP value can be related to the amount of dissolved oxygen each solvent can donate to participate in redox reactions involving metal ions and H^+ . However, there is no obvious difference in the removal efficiency of the three mineral acids for all metal ions (except Pb), irrespective of the ORP of the slurry/solution. Hence, the metal leaching process observed in this study can be stated to be largely controlled by the solution pH. This observation is contrary to a few studies reporting that both the leaching solution pH and ORP influence HMs solubilisation in biosolids (Beauchesne et al., 2007; Blais et al., 2005; Mercier et al., 2002). In particular, Cu dissolution was found to be driven by the redoxolysis mechanism rather than acidolysis due to the higher affinity of Cu to organic matter in sludge (Blais et al., 2005; Strasser et al., 1995). Based on this, the

leaching of biosolids was further tested with strong oxidising solutions such as 3% acidified ferric sulfate (670 mV) and ferric sulfate added hydrogen peroxide (603 mV). However, no significant improvement in metal extraction was observed, particularly for Cu and Cr, compared to mineral acids (data not shown). A previous study has reported that there was an optimum pH at which ORP of slurry becomes influential on HMs extraction efficiency (Beauchesne et al., 2007). Also, different washing agents may have various degrees of affinity and selectivity for different HMs. The removal efficiencies of multiple HMs in biosolids can be greatly improved by composite or sequential treatment (Shi et al., 2020). From these results, sulfuric acid was selected for subsequent experiments due to the relatively low cost of H_2SO_4 , industrial maturity, and lesser toxicity of sulfates of HMs than their corresponding nitrates or chlorides salts at the same molar concentration (Erichsen Jones, 1934; Nie et al., 2015).

3.2. Effect of solids concentration

The effect of solids concentration on the metal extraction from biosolids using 3% v/v H_2SO_4 at 25 °C, 600 rpm for 30 min was investigated, and the results are presented in Fig. 3. The solids concentration significantly influenced the extraction of the metals ($p < 0.05$). The extraction of all metals (except Pb and Cr) at lower solids contents (1–3%) achieved ~60–95% removal compared to 30–80% removal at higher solids content (5–15%). This behaviour is expected from the stoichiometry of the leaching/desorption reaction. Notably, Mn and Zn had the least variation in extraction efficiency with the change in solids concentration because they have the highest proportion (75–90%) of acid-leachable metal fractions (F-1 + F-2) in the biosolids used in this study (Fig. S1). The change in solids concentration was largely inconsequential on Cr and Pb extraction. The consistent low solubilisation of Cr in biosolids can be attributed to the poor mobility of Cr; the trivalent metal ions such as Fe and Cr are more difficult to extract than the divalent ions such as Zn, Ni, and Cd due to the competitive uptake of protons by the more reactive species. Lead has the highest residual (inert) fraction (F-4) of all metals in the biosolids (Fig. S1); therefore, its extraction is usually limited by common acids (Gheju et al., 2011; Xiao et al., 2015). Moreover, H_2SO_4 is not a suitable lixiviant for Pb extraction due to the low solubility of PbSO_4 in water (see Fig. 2). The removal efficiencies of all other metals increased with decreasing solid/liquid ratio, and the maximum extraction efficiency for all metals was observed at the lowest solids content (1%). The result agrees with previous literature on the effect of solids concentration on metal extraction (Bayat and Sari, 2010; Kuan et al., 2010; Wu et al., 2009). Low solids content is

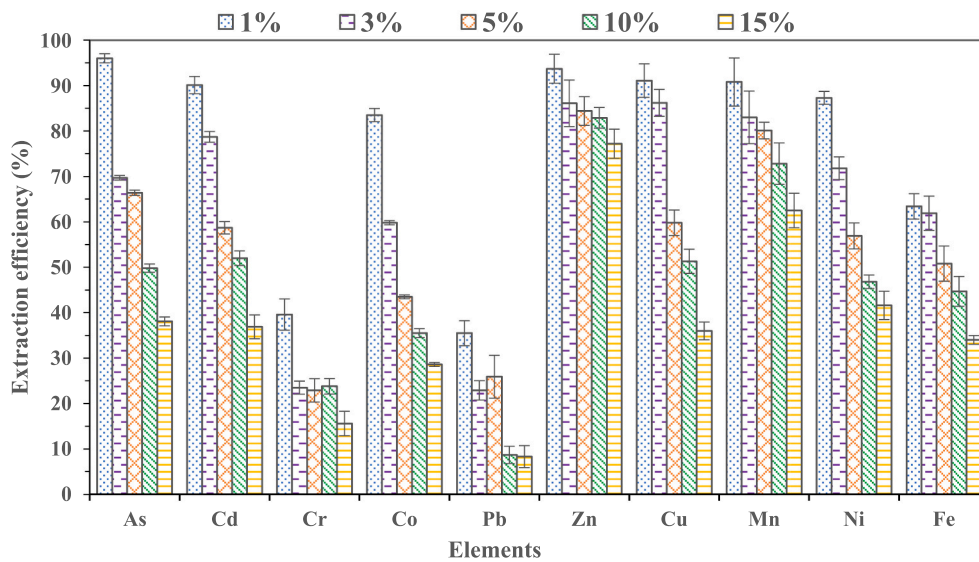


Fig. 3. Effect of solids concentration (w/v) on metal extraction efficiency from biosolids (conditions: 3% (v/v) H₂SO₄, 25 °C, 30 min, and 600 rpm).

associated with a higher volume of lixiviant and higher proton (H⁺) concentration, benefiting the dissolution of acid-exchangeable HMs fraction (F-1) in the biosolids. Since there are more H⁺ than available surface chelating sites on the biosolids, the excess H₂SO₄ can penetrate the biosolids pores and react with more metal ions, particularly the reducible (F-2) and oxidisable (F-3) HMs fractions, leading to overall higher extraction efficiency (Yang et al., 2021).

Table S1 shows the dissolved metal ion concentration in the leachate at different solids loading. The dissolved metal ion concentration in mg/

L liquid increased with increasing solids contents, while the metal ion concentration in mg/kg solids decreased with increasing solids contents (Table S1). Treatment using 1% (w/v) solids concentration produced cleaner biosolids, while the 15% (w/v) solids produced a highly concentrated metal-laden leachate stream which can make the recovery of metals more attractive. On the other hand, lower solid loading produced a dilute liquor stream. Moreover, 1% solids concentration appears unrealistic in practical scenarios in wastewater treatment plants (WWTPs). Besides, lower solids concentration is associated with higher

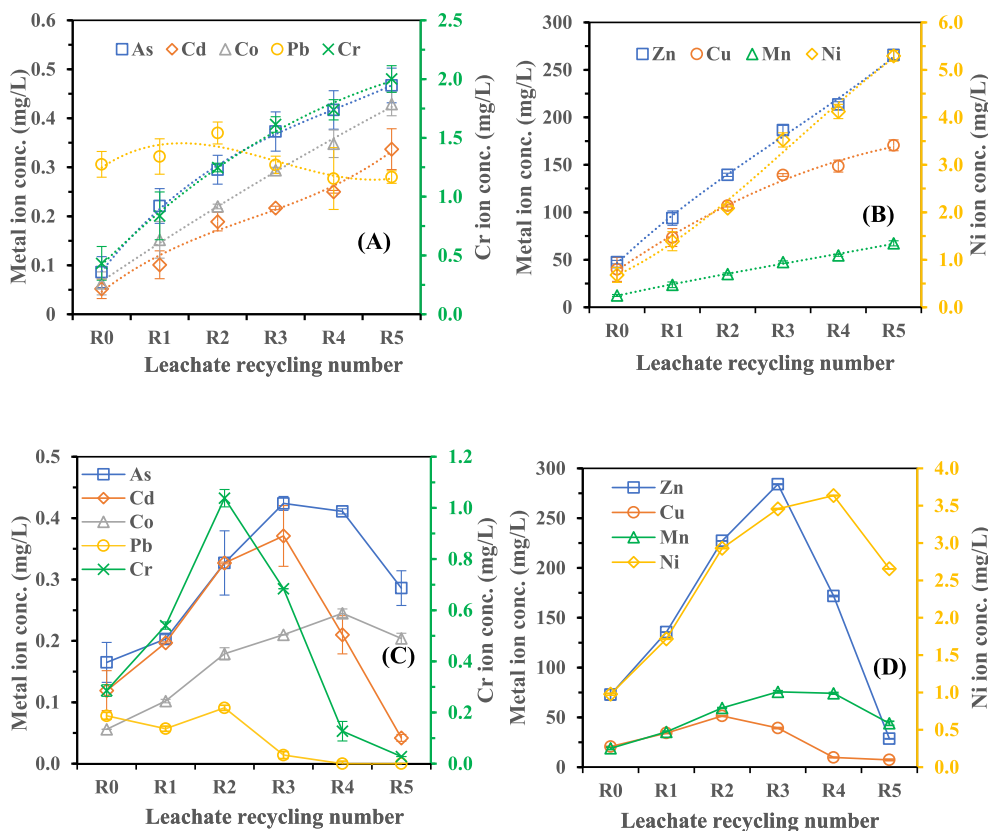


Fig. 4. Effect of fresh biosolids concentration on 100% recycling of the leachate stream (A) & (B) 5% solids (C) & (D) 10% solids (conditions: 3% (v/v) H₂SO₄, 25 °C, 30 min, and 600 rpm).

lixiviant consumption, and dewaterability can be challenging (Vesilind and Hsu, 1997). Similarly, at 15% solids, the mass transfer limitation was significant, negatively impacting mixing and liquid recovery, and the overall metal ion removal efficiency was the lowest. In fact, at 20% solids, mixing and separation became difficult, and the leaching process was not successful (data not reported). Hence, a moderate 5–10% solids loading may be a good balance and are the typical value in most biosolids leaching operations (Gheju et al., 2011; Wang et al., 2015; Wu et al., 2009).

3.3. Recyclability of the leachate stream

3.3.1. Metal saturation concentration and the leachate recycling efficiency

The cumulative metal concentration in the leachate stream after five successive leaching cycles at 5% and 10% solids using 3% v/v H₂SO₄ solution, 25 °C, 30 min, and 600 rpm is presented in Fig. 4(A–D). It is obvious that the primary leachate stream (R0) from the parent leaching experiment has not reached its maximum extraction capacity as more metals were extracted from fresh biosolids using the R0 stream five times. At 5% solids, the R0 stream had higher extraction strength than that at 10% because of the higher liquid-to-solid ratio and the dilute concentration of the dissolved metal. A higher liquid-to-solid ratio slowed the attainment of thermodynamic equilibrium between the dissolved metal species and the acidic solution (Lee et al., 2006). The leachate streams obtained at 10% solids were saturated faster compared to 5% solids. The primary leachate at 5% solids was recycled up to five times without reaching saturation point (Fig. 4(A&B)), while the leachate at 10% solids can only be reused up to three times, beyond which a rapid decline in cumulative concentration was observed (Fig. 4(C&D)). There was at least a 3-fold increase in the concentration of all metals (except Pb) by completely reusing the primary leachate stream from R0 to R5 (Fig. 4(A&B)). At 5% solids, the percentage increase in metal ion concentration in the leachate from R0 to R3 can be ranked as Cu(II) (249) < Cr(III) (273) < Mn(II) (284) < Zn(II) (293) < Cd(II) (317) < As(III) (334) < Co(II) (367) < Ni(II) (419). However, at 10% solids (Fig. 4(C&D)), there was a lesser increase in the cumulative concentration from R0 to R3, and the percentage increase was Cu(II) (90) < Cr(III) (139) < As(III) (157) < Cd(II) (212) < Ni(II) (254) < Co(II) (275) < Zn(II) (290) < Mn(II) (300). The percentage increase in cumulative concentration for Mn and Zn was similar at 5% and 10% solids, whereas there was a substantial decrease in the accumulation of other metals at 10% solids compared to 5% solids. Expectedly, higher solids loading limited the efficiency of metal accumulation during leachate recycling at the same extraction cycle with 5% solids. In particular, the cumulative Cu loading during recycling was severely impacted at 10% solids, possibly due to the dominant redox reaction between soluble Cu(II) and iron(II) sulfate, the mechanism which has been elucidated in previous literature (Matocha et al., 2005). The 100% recycling of the leachate stream at 10% solids performed competitively with 5% solids only in removing easily leachable metal fractions (F-1 and F-2) such as Zn and Mn, while the removal of other metal species dominant in F-3 was largely difficult. The removal of metal ions in F-3 fractions will require abundant protons from fresh H₂SO₄ solution as well as harsh oxidising conditions to break the organometallic bond (Beauchesne et al., 2007). The monotonic decline in the extraction efficiency after the third recycling at 10% solids (Fig. 4(C&D)) was due to Al/Fe-induced co-precipitation of metal from the leachate to the solid phase as the solution pH approaches 3, which is conducive for ferric precipitation (Marchiorretto et al., 2005). The pH of the R5 stream at 10% solids was 4.5, while it was 2.4 at 5% solids.

Furthermore, it was observed that all metal extraction profiles followed closely that of Fe, and the improved extraction of HMs using the spent leachate stream can be attributed to the role of ferric sulfate hydrates in the metal desorption process. The iron source in the biosolids is the ferric salt coagulant used during the wastewater treatment process. Sulfuric acid solution can partly dissolve ferric-containing salts (such as

FeCl₃ or FeOOH), and then dissolved ferric ion can form ferric sulfate through ion exchange reaction with SO₄²⁻ or HSO₄⁻ from H₂SO₄ (Demol et al., 2022). Ferric sulfate is a well-known leaching agent which acidifies by hydrolysis (Fe³⁺ + H₂O = FeOH²⁺ + H⁺) and increases the elution efficiency of HMs from soils and biosolids (Bayat and Sari, 2010; Ito et al., 2000; Shi et al., 2020; Strasser et al., 1995). X-ray photoelectron spectra of the metal precipitates confirmed the presence of ferric sulfate (Fig. S2). The effective extraction of HMs by dissolved Fe³⁺ is due to its ability to oxidise metal sulfides to soluble metallic ions and the release of more protons through the hydrolysis of ferric hydrates (Pathak et al., 2009). The dissolution of inherent ferric-containing components in biosolids and the subsequent formation of ferric sulfates extended the overall extraction strength of the leachate stream during recycling. The presence of native ferric salts was beneficial for the reuse of the leachate stream; however, there is a critical Fe³⁺ concentration beyond which it counteracts the HMs extraction as Fe³⁺ precipitates at a low pH value (<4). It was observed that the higher the concentration of Fe in the stream, the better the extraction efficiency of other metals up to a certain Fe concentration (~1400 mg/L). This is consistent with the study of Ito et al. (2000), who observed that the higher the amount of ferric iron added, the lower the pH of the lixiviant and the higher the extraction efficiency of HMs (~80%) from digested biosolids at low solids concentration (2% w/w). In other studies, leaching at pH 2 with acidified ferric iron outperformed H₂SO₄ in extracting common HMs from biosolids (Bayat and Sari, 2010; Ito et al., 2000). The combination of ferric sulfate and acid solutions at different dosage had positive synergistic interactions for the solubilisation of multiple HMs from biosolids and soils (Beauchesne et al., 2007; Shi et al., 2020).

3.3.2. Effect of make-up solution on the leachate recyclability

The cumulative metal ion concentration in the leachate stream after ten successive cycles with the addition of make-up lixiviant between each cycle is shown in Fig. 5. A constant feed rate of 5 g or 10 g of dry biosolids per 100 mL liquid for a 30 min leaching cycle was maintained. Contrary to the observation at 100% leachate recycling, without adding make up lixiviant (Fig. 4), the continuous addition of 3% H₂SO₄ as FL prolonged the extraction strength of the spent leachate until R8 stage (Fig. 5). At 5% solids (Fig. 5), there was a substantial increase (at least 250%) in the cumulative metal ion concentration (except for Pb) from R0 to R10. For instance, Ni(II) was concentrated from 0.5 to 3.5 mg/L, Zn(II) from 38.9 to 277 mg/L, Cu(II) from 11.5 to 100 mg/L, As(III) from 0.14 to 0.51 mg/L, Cd(II) from 0.04 to 0.34 mg/L, Cr(III) from 0.12 to 1.2 mg/L, Co(II) from 0.04 to 0.22 mg/L, and Mn(II) from 10.3 to 71.5 mg/L. There was a steady increase in the cumulative metal ion concentration from R0 to R4 due to the low make-up ratio of the FL in the total leachate stream (<25%). The addition of FL to the leachate stream possibly aided the dilution of the metal ion concentration and hence enhanced the extraction strength (and capacity) of the stream. Up to R7, the increase in the metal ion concentration far outweighed the dilution effect of the added fresh solution. Nevertheless, adding FL was not beneficial beyond R6 as the leachate had been fully saturated with the metal ions. This observation was due to the similar extent of metal ions dilution and extraction efficiency in the stream by the added FL beyond R6. At R6, increasing the make-up ratio above 15 vol% would likely enhance the metal extraction strength of the stream further. The overall extraction trend of the HMs was largely governed by Fe, which reached saturation at R6. Contrary to the observation for 100% leachate recycling without adding make up lixiviant (Fig. 4), the continuous addition of the FL and the acidifying effect of Fe³⁺ kept the pH of the leachate stream at <2 throughout the process, limiting ferric precipitation.

The addition of make-up acid lixiviant was less beneficial in enhancing the recyclability of the leachate stream at 10% solids compared to 5% solids (Fig. S3). There was no monotonic increase in the concentration of metal ions, and the irregular increase and decrease in the cumulative concentration across the ten leaching cycles can be

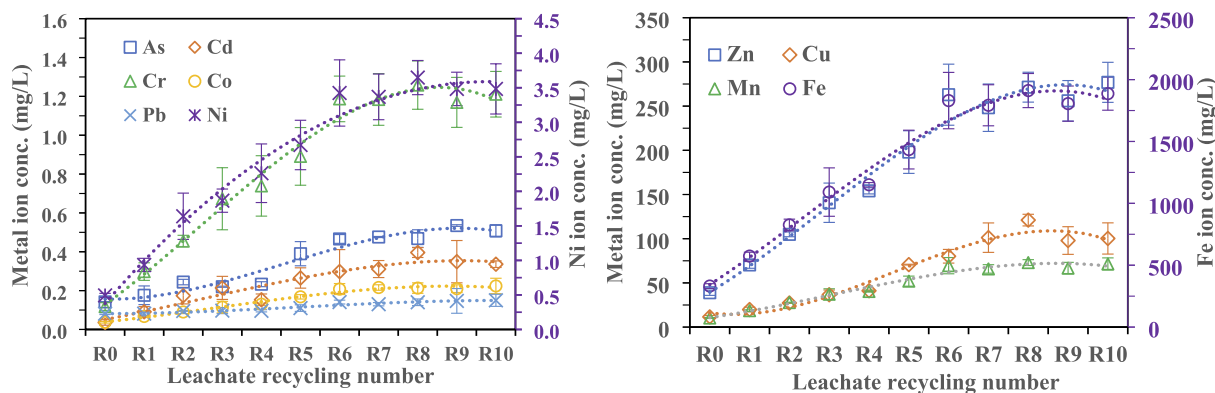


Fig. 5. Effect of make-up lixiviant on the recyclability strength of the leachate stream at 5% fresh biosolids concentration (conditions: 3% (v/v) H₂SO₄, 25 °C, 30 min, and 600 rpm).

attributed to Fe(III) precipitation. The leachate at 10% solids saturated faster than at 5% solids, and pH increased rapidly, thus facilitating Fe (III) precipitation much earlier. Iron(III) co-precipitated other metals in the stream. Contrary to the observation at 5% solids, adding FL between successive leaching could not suppress Fe precipitation (Fig. S3) at 10% solids. The dilution and acidifying effect of the FL on the metal ion concentration in the leachate stream were minimal at higher solids loading. The sharp rise in solution pH rather than the increase in Fe concentration stimulated Fe co-precipitation reaction at 10% solids. For instance, at 10% solids, Fe precipitation began at a maximum concentration of ~1400 mg/L (pH 2.45), whereas, at 5%, no Fe precipitation occurred even at the maximum concentration of 1830 mg/L (pH 1.85). At low pulp density (5% solids), the overall extraction efficiency of the spent stream was competitive with the FL, and the performance improved with increasing Fe concentration in the stream. Acidified ferric salt leaching is optimally performed at low solids concentration (<5% w/v) to avoid a rapid increase in pH and minimise ferric precipitation, which is counterproductive for HMs solubilisation (Bayat and Sari, 2010; Ito et al., 2000).

Leachate recycling could bring significant cost savings for H₂SO₄ lixiviant besides environmental benefits. The 100% recycling of the spent leachate at 5% solids loading for five leaching cycles (Fig. 4) could save 4.5 times the required H₂SO₄ volume at 90% liquid recovery per leaching cycle. Similarly, for the partial recycling of the leachate with 15% make-up lixiviant at 5% solids for six leaching cycles (Fig. 5), there

could be ~5 times reduction in the volume of H₂SO₄. Assuming a linear relationship between H₂SO₄ volume and cost, around 400% cost savings can be achieved with leachate recycling with make-up lixiviant, which may substantially lower the cost of acid leaching.

3.4. Metal recovery from the concentrated leachate stream

A single-step or two-step NaOH co-precipitation and biochar adsorption were investigated for recovering HMs from the saturated leachate stream. Metals like Cr, Cu, Pb, and Zn do not form hydroxide precipitates at pH <6, allowing the separation from ferric iron and aluminium, which precipitate at pH <5 (Marchioretto et al., 2005). Table S2 shows the metal ion composition of the leachate stream used for the metal recovery experiments. It was observed that the concentration of Zn, Mn, and Cu in the leachate was up to 100 mg/L. Concentrations of all other HMs were < 5 mg/L, while Fe, Al, and alkali and alkaline earth metals (AAEMs: Na, K, Mg, and Ca) were highly concentrated in the stream (>500 mg/L). The metal recovery at each precipitation stage is shown in Table 2, while the overall metal recovery from the different methods is shown in Fig. 6.

The single-stage NaOH precipitation at pH 9 recovered about 9–99% of the HMs. The recovery efficiency of the metals can be ranked as Zn (99%) ≈ Cd (99%) > Cr (97%) > Pb (79%) > Co (33%) > Ni (31%) > As (11%) > Cu (9%). The precipitation of these HMs was accompanied by the precipitation of >90% for Fe, Al, Ca, Mg, and Mn. The precipitation

Table 2
Metals recovery from the leachate stream under different methods.

Description	Metals	NaOH consumption, pH, and metal removal efficiency in different methods					
		Single-stage co-precipitation	2-stage co-precipitation		H ₂ O ₂ pre-2-stage co-precipitation	Biochar sorption	
Stages	–	One stage	1st	2nd	1st	2nd	One stage
NaOH (g/mL) ^a	–	0.11	0.04	0.08	0.05	0.06	0.04
pH range	–	2.5–9.0	2.5–4.5	4.5–9.0	2.5–4.5	4.5–9.0	2.5–4.5
Heavy metals (%) ^b	As	11.4	20.4	8.4	13.0	60.6	19.0
	Cd	98.9	32.7	94.3	35.5	97.2	46.8
	Co	32.9	3.2	32.3	13.4	51.5	32.1
	Cr	97.4	72.7	85.5	82.6	57.3	47.1
	Cu	9.30	15.1	31.3	24.5	49.0	56.0
	Ni	30.7	3.50	33.2	33.2	73.8	70.5
	Pb	78.7	34.0	78.7	80.9	26.6	3.80
	Zn	99.3	35.5	96.3	50.0	99.0	56.8
Other metals (%) ^b	Al	97.4	91.4	77.9	95.4	96.6	95.8
	Ca	91.0	2.30	88.9	23.8	76.9	20.9
	Fe	98.5	99.0	59.5	99.1	96.1	46.6
	K	18.7	16.8	22.3	24.7	46.2	22.6
	Mg	98.0	3.40	99.0	13.3	92.2	29.6
	Mn	99.3	11.4	99.2	22.1	94.4	35.6

^a 6 M NaOH consumed (g/mL leachate).

^b The metal removal efficiency in the second stage refers to the percentage removal of the remaining metal in solution after the first stage.

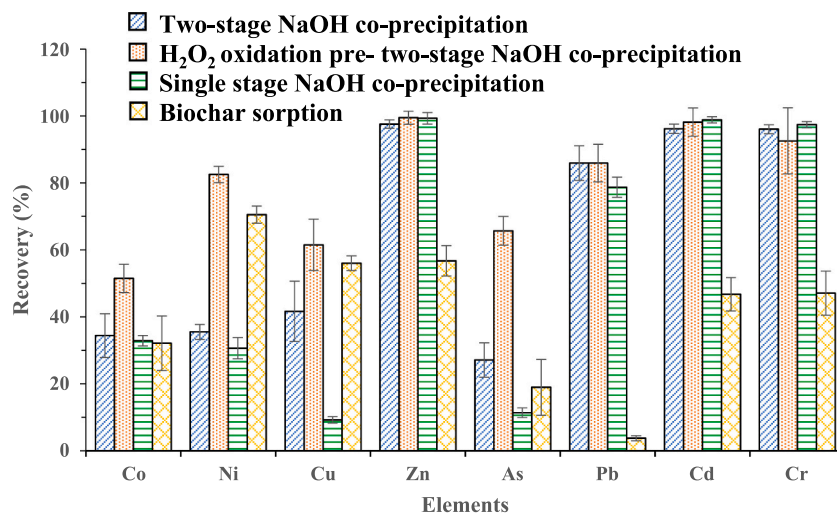


Fig. 6. Overall removal efficiency of HMs under different recovery techniques.

of Co, Ni, As, and Cu was low under this condition due to the high solubility of their respective metal hydroxide at pH 9 (see Fig. S4). It was hypothesised that the presence of Fe and Al would facilitate the precipitation of HMs in the stream. However, the presence of both metal salts did not improve HMs recovery at the basic pH 9 relative to the observation at acidic pH 4.5. The co-precipitating effect of Fe and Al on the other metals cannot be observed under the single-stage recovery, and only the solubility of the various metal hydroxides at pH 9 can be assessed. The single-stage precipitation resulted in a low recovery efficiency of some HMs and, at the same time, produced a highly contaminated HMs sludge stream. This may reduce the attractiveness of the recovered metal sludge for downstream separation and subsequent applications in catalysis or smelting.

The staged recovery of the metals at pH 4.5 (stage 1) and pH 9.0 (stage 2) effectively precipitated Fe and Al from the leachate stream in the first stage, while most of the HMs were recovered in the second stage (Table 2). About 99% Fe and 91% Al were recovered in the first stage (pH 4.5); however, 3–73% of some HMs were co-precipitated. For example, 73% Cr, 36% Zn, 34% Pb, 33% Cd, 20% As, 15% Cu, 4% Ni and 3% Co were co-precipitated with Fe/Al at pH 4.5. The removal of these HMs at pH 4.5 was due to the sorption capacity and co-precipitating ability of Fe and Al hydroxides (Lee et al., 2002). No precipitation of these metals was observed at pH 4.5 in the absence of Fe and Al when the solution of their pure salts was treated with NaOH (data not shown). Only Cd and Zn had the highest removal efficiency of >94% in the second stage. In comparison, other HMs' removal efficiency was 8–79%, similar to the single-stage precipitation from solutions of same pH value of 9 (Table 2). The recovery of As was minimal in the staged NaOH co-precipitation; the highest recovery of 20% occurred at pH 4.5, which could be attributed to the formation of ferric arsenate (Hao et al., 2018). The major benefit of the dual-stage precipitation, aside from the selective recovery of Al, Fe and Cr, was the improvement in Cu recovery from 9% in the single-stage to 31% in the two-stage at pH 9. The mechanism involving the precipitation of ferric iron and the associated Cu loss from solution has been elucidated elsewhere (Javed and Asselin, 2020). The chosen pH 9 is a compromise for the recovery of all the HMs; further optimisation studies are required to identify the optimum recovery pH for each metal species in the solution. From the theoretical solubility curve for metal hydroxides (Fig. S4), Cu has the lowest solubility (<0.1 mg/L) at pH 9 relative to other HMs. However, this theoretical solubility behaviour contradicts the low recovery of Cu (<50%) at pH 9 with a solubility concentration of 36 mg/L. Probable explanations for this include the affinity of Cu(II) to dissolved organic ligands making complexes and the crystal growth vs (super)saturation level of the various metals in the solution (Weng et al., 2002). Moreover, the leachate

stream contains many metal and non-metal species, which may cause significant deviation from the theoretical solubility behaviour of pure metal in aqueous systems.

Adding H₂O₂ prior to NaOH precipitation improved the recovery of some HMs from the leachate. For example, without adding H₂O₂, the overall recovery of As was 27%; however, it increased to 66% when H₂O₂ was added. Similarly, Cu recovery increased by 47%, Co recovery improved by 53%, and Ni recovery increased by 130%. In fact, increasing the amount of H₂O₂ added by a unit volume before the staged NaOH precipitation further increased the recovery of As, Co, Cu, and Ni by 48%, 22%, 18%, and 68%, respectively (Fig. S5). The addition of H₂O₂ had no improvement on the recovery of Zn, Pb, Cd, and Cr compared to the sole 2-stage NaOH co-precipitation. The oxidation of dissolved organics by H₂O₂ enhanced the desorption of metal species. The biosolids used in this study contain organically bonded HMs (F-3 fraction; Fig. S1), where the bonding strength can be ranked as Cu > As > Co > Ni. The complexation of HMs with dissolved organic matter in aqueous solutions has been reported to influence the solubility and mobility of metals (Weng et al., 2002).

The removal efficiency of the HMs via biochar adsorption was poor compared to the alkali precipitation and did not follow any specific trend. Only a modest 3–70% uptake was achieved, with the highest for Ni and the lowest for Pb. The performance of biochar adsorption for HMs uptake from aqueous solutions is influenced by many factors, including the adsorbent properties, pH, adsorbate concentration, temperature, and solution chemistry of the metal species (Ni et al., 2019). Most of these factors have not been optimised in this study and may contribute to the relatively poor removal efficiency of the biochar sorption process. The FTIR spectra of the biochar before and after the sorption (Fig. S6) confirmed the non-depletion of the surface functional group of the biochar, suggesting the dominance of physisorption. Chemisorption usually involves the chemical reaction between the charged surface functional group of the biochar adsorbent and the metal ions via electrostatic precipitation, organo-metallic complexation, and deprotonation phenomena (Yang et al., 2021).

3.5. Process configurations and mass balances

The various unit operations were put together in a process flow diagram (Fig. 7) to provide an insight into the materials requirement of the treatment process demonstrated in this work. Based on our findings, leachate recycling is only attractive at 5% solids which can considerably lower acid and alkali consumption. However, processing 10% solids with no leachate recycling may be favourable commercially. Fig. 7(A) shows the mass balance for processing 10% solids with no leachate

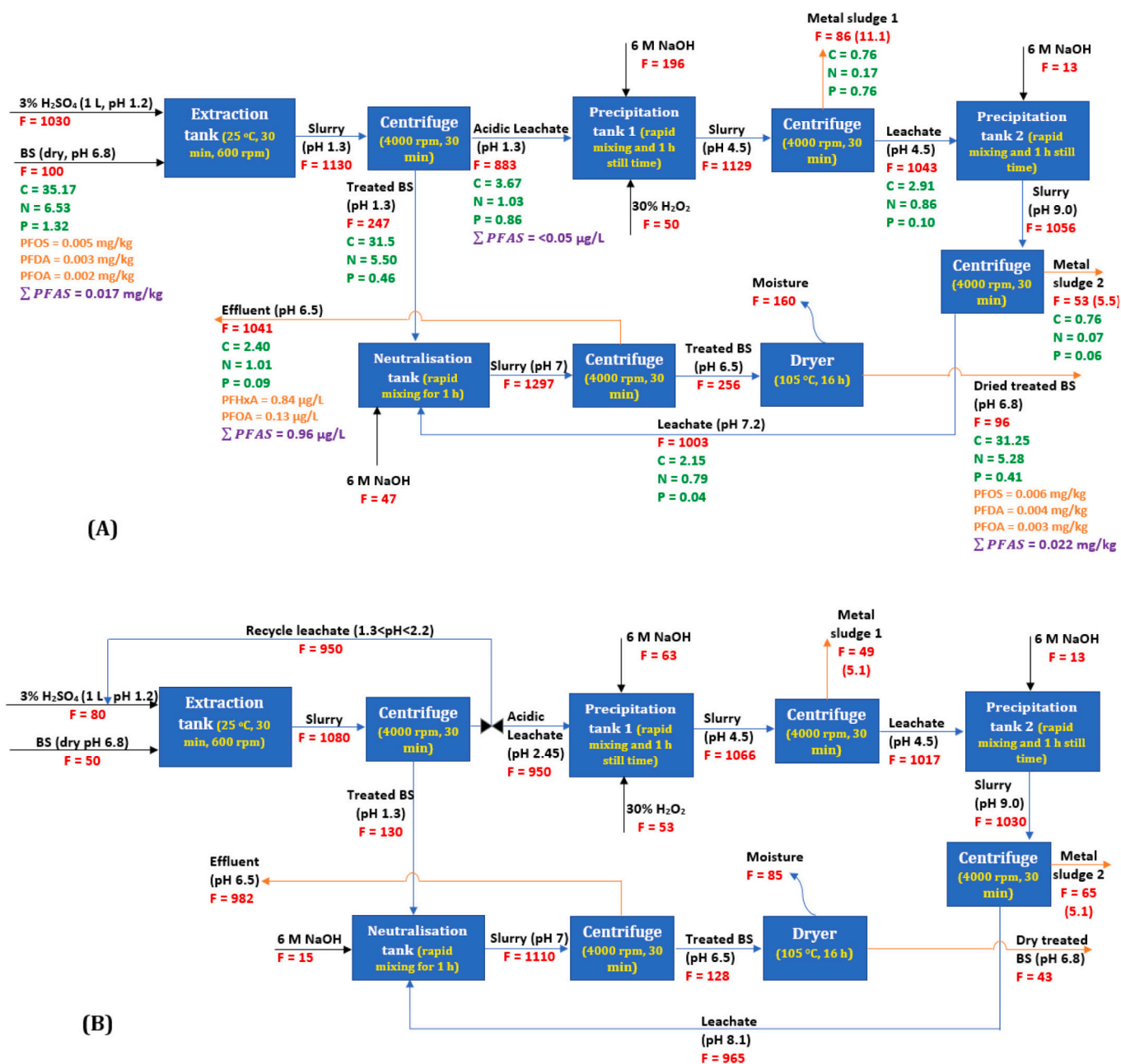


Fig. 7. Process block flow diagram for HMs removal and recovery from biosolids. (A) for processing 10% solids with no leachate recycling (B) for processing 5% solids with leachate recycling (with top-up lixiviant). Red font (F) denotes mass flow in grams; the flowrate in parenthesis corresponds to the dry weight of the metal sludge; green font (C, N, and P) denotes carbon, nitrogen, and phosphorous mass flows in grams, while the purple font denotes total PFAS concentration in the major streams. (For interpretation of the references to colour in this figure legend, the reader is referred to the web version of this article).

recycling, while Fig. 7(B) shows the balance for processing 5% solids with leachate recycling with make-up lixiviant. The separation of solids from the leachate produced acidic treated biosolids (pH 1.3), which cannot be used directly for land application or thermal processing without prior neutralisation or conditioning. A considerable volume of water is required to wash off residual acid in the treated biosolids and raise the pH to near neutral values. It is proposed that the clarified alkali stream be used to neutralise the acidic treated biosolids in an attempt to close the process loop and reduce the volume of aqueous waste generated. In Fig. 7, the total mass flow of streams (grams) in and out of each unit operation is denoted as F, and carbon, nitrogen and phosphorous mass flows (in grams) are denoted as C, N, and P, respectively. For a 1:10 w/v (biosolids to H₂SO₄ solution ratio) feed rate (Fig. 7(A)), the

overall liquid recovery was 77%, while overall solids recovery was 96% (dry biosolids basis). When the feed ratio was changed to 1:20 w/v (5% solids) with leachate recycling, the mass balance is shown in Fig. 7(B). Overall liquid and solids recovery was 84% and 86%, respectively. Notably, the leachate recycling yielded about a 92% and 43% decrease in H₂SO₄ and NaOH consumption, respectively. The lixiviant consumption changes remarkably when processing 5% solids with no leachate recycling (Fig. S7). The total H₂SO₄ consumption (g/g biosolids) doubled, and total NaOH consumption increased by 25% relative to processing 10% solids. The overall results with respect to solids and liquid recovery, metal sludge recovery as well as H₂SO₄ and NaOH consumption at different process configurations are summarised in Table 3. At 10% solids processing, the major composition (wt%) of

Table 3
Summary of process performance at different configurations.

Indicators	Unit	Process configurations		
		10% solids with no leachate recycling	5% solids with no leachate recycling	5% solids with leachate recycling with make-up lixiviant
Overall solids recovery	wt% dry basis	96	87.6	85.8
Overall liquid recovery	wt%	76.7	80.3	82.4
Total metal sludge recovery	g/g dry biosolids	0.17	0.19	0.21
H ₂ SO ₄ consumption ^a	g/g dry biosolids	0.57	1.14	0.09
NaOH consumption ^b	g/g dry biosolids	0.50	0.63	0.36

^a H₂SO₄ stock solution (98% Assay, SG = 1.84).

^b NaOH (Analytical reagent grade pellets, SG = 2.13).

recovered metal sludge 1 is 10.7% Fe, 8.8% Na, 8.2% S, 7.9% P, and 5.5% Al while that of metal sludge 2 is 13.1% Na, 12.5% S, 12.4% Ca, 6.0% P, and 3.3% Mg. The detailed composition is provided in Table S3, and the thermal stability profile of the recovered metal sludge is shown in Fig. S8. The recovered metal can be employed in a number of potential applications in catalysis, smelting, and materials production, such as metal-based adsorbents/nanomaterials depending on the required purity and properties (Tawalbeh et al., 2021; Yu et al., 2022).

3.6. Fate of nutrients and PFAS

Considering the processing of 10% solids with no leachate recycling, the balance around organic nutrients (C, N, and P) is presented in Fig. 7 (A). The overall process modestly preserved the organic matter in the biosolids as the reduction in C, N, and P contents from raw biosolids to treated biosolids was 11%, 19%, and 65% (w/w), respectively. This observation on nutrient dissolution is comparable to other studies. For example, Mercier et al. (2002) reported about 19% decrease in dissolved organic carbon in treated sludge compared to raw sludge. Similarly, Beauchesne et al. (2007) and Shiba and Ntuli (2017) observed about 77% P and 82% P solubilisation, respectively, from biosolids treatment using H₂SO₄ (pH <2). The excessive dissolution of P in biosolids is a typical limitation of mineral acid leaching. The joint use of ferric salts and/or H₂O₂ with H₂SO₄ has been reported to enhance P retention in biosolids as ferric phosphate (Beauchesne et al., 2007). However, unlike C and N, which largely remain in the dissolved form in the liquid streams, >90% of the total dissolved P was recovered at the metal precipitation stages. Phosphorous has a high affinity for metal ions (particularly Fe) in aqueous media which can be recovered as metal phosphate precipitates (Vardanyan et al., 2018). The dissolution and recovery of P is more sensitive to pH compared to C and N. In the neutralisation stage, where the acid-leached biosolids are treated with NaOH, about 1% C, 4% N and 11% P were further lost from the solids to the liquid phase. The final effluent stream contains about 0.23% C, 0.10% N and 0.009% P (w/w). The guideline for the disposal of this effluent stream as trade wastewater was assessed with respect to the organic and metal concentration load (Table S4). All the metals and organic nutrient concentrations (except for N) are within the acceptable criteria set by South East Water Recycling Corporation, Melbourne, Australia. The excess nitrogen can be removed from the effluent stream by adsorption, and the final liquid can be safely discharged.

Per- and poly-fluoroalkyl substances (PFAS) are rapidly becoming a limiting contaminant for biosolids reuse in agricultural land. Therefore, there is interest in understanding the fate of the plethora of PFAS compounds during the hydrometallurgical treatment process. Twenty-eight common PFAS compounds, the major ones being PFOA (C₈HF₁₅O₂), PFOS (C₈HF₁₇O₃S), PFDA (C₁₀HF₁₉O₂), PFBS (C₄HF₉O₃S), and PFHxA (C₆HF₁₁O₂), were measured in the raw biosolids, treated biosolids (with leachate neutralisation), acidic leachate, and the final effluent stream. The representative PFAS compounds detected in the

selected process streams and the total sum of PFAS are shown in Fig. 7 (A). The overall PFAS result is presented in Table S5. The acid extraction (at pH <2) did not leach out the PFAS compounds in the raw biosolids (0.0165 mg/kg), as the concentration of the PFAS in the acidic leachate stream was <0.05 µg/L. However, there appears to be an increase in the leachability of PFAS compounds with a carboxylic head group (particularly PFHxA and PFOA) at the neutralisation stage at pH > 7. The leaching of these PFAS compounds from the acidic treated biosolids (pH 1.3) slightly increased the concentration of the PFAS compounds in the final effluent to 0.96 µg/L. Nevertheless, the PFAS compounds reaching the liquid stream are substantially negligible (<1 µg/L), and the PFAS are largely retained in the treated biosolids (0.0221 mg/kg). Further investigations into the mechanisms controlling the mobility and the final fate of the diverse PFAS compounds during biosolids acid pre-treatment are needed.

Lastly, the viability of the developed closed-loop process with respect to residual nutrients and HMs concentration in the treated biosolids was briefly assessed. The concentration of nutrients and HMs in the treated biosolids with leachate neutralisation was compared with treated biosolids obtained under two different neutralisation washing scenarios at the same pre-treatment conditions. The neutralisation washing scenarios were (i) treated biosolids with leachate neutralisation, (ii) treated biosolids with no neutralisation, and (iii) treated biosolids with deionised water neutralisation. The concentration of the residual nutrients, HMs, and PFAS in the three treated biosolids streams are presented in Table 4. The concentrations are further benchmarked with EPA Victoria prescribed concentration for contaminant-grade biosolids (C1-grade and C2-grade) (EPA Victoria, 2004). The C1-grade refers to the least contaminant grade biosolids with respect to HMs concentration which can be applied to land unrestrictedly. Except for Cu in all scenarios, all other HMs concentrations met the requirements of C1-grade biosolids, with the lowest concentration obtained in treated biosolids with water neutralisation step. Most metal sulfates are soluble in water; therefore, water neutralisation washing helped in the dissolution of metal sulfate salts as well as the removal of H₂SO₄-insoluble metal species. Hence it is proposed that the treated biosolids obtained with the leachate neutralisation step be neutralised in a second step with deionised water to reduce the residual metal concentration load further, particularly for Cu. There is largely an inconsequential difference in residual nutrient concentration in the treated biosolids with respect to neutralisation washing scenarios.

4. Conclusions

This work provided a detailed investigation into the hydrometallurgical process for extracting and recovering HMs from biosolids. The extraction performance of mineral acids (H₂SO₄, HNO₃ and HCl) was similar and only citric acid performed competitively with mineral acids in achieving ~70% extraction of HMs at 5% solids loading. Low solids content (1–5% w/v) favoured HMs extraction and produced a leachate

Table 4

Concentration of residual nutrients, metals, and PFAS in biosolids streams obtained under different neutralisation washing scenarios by processing 10% solids.

Content	Elements/ abbreviations	Streams, pH, and concentration					
		Raw biosolids	Treated biosolids (no washing) ^a	Treated biosolids (leachate washing) ^b	Treated biosolids (water washing) ^c	C1-grade biosolids ^d	C2-grade biosolids ^d
	pH	6.8	2.0	6.5	7.0	7.0	7.0
Nutrients (% w/w dry feed basis)	C	35.4	32.9	35.2	36.4	–	–
	N	5.6	5.5	6.2	5.6	–	–
	K	1.1	0.4	0.3	0.2	–	–
	P	1.3	0.5	0.4	0.5	–	–
Major metals (% w/w dry feed basis)	Na	0.1	BDL ^e	1.5	BDL	–	–
	Mg	0.5	0.1	0.1	0.1	–	–
	Al	0.7	0.6	0.4	0.5	–	–
	Ca	10.2	8.5	6.8	5.4	–	–
	Fe	4.2	2.3	2.9	4.1	–	–
Trace metals (mg/kg dry feed basis)	As	<5	<5	<5	<5	20	60
	Cd	1.3	0.5	0.4	0.3	1	10
	Co	<5	<5	<5	<5	–	–
	Cu	690	380	420	220	100	2000
	Cr	20	16	14	14	400	3000
	Hg	0.7	0.9	0.9	0.9	1	5
	Mn	210	53	39	17	–	–
	Mo	8	8	8	9	–	–
	Ni	18	12	14	8	60	270
	Pb	20	17	18	18	300	500
	Se	5	4	4	3	3	50
	Zn	850	160	160	48	200	2500
Major PFAS ^f (mg/kg dry feed basis)	PFBS	0.0005	–	0.0003	–	–	–
	PFDA	0.0028	–	0.0040	–	–	–
	PFHxA	0.0014	–	0.0014	–	–	–
	PFOS	0.0048	–	0.0060	–	–	–
	PFOA	0.0019	–	0.0029	–	–	–
	∑PFAS	0.0165	–	0.0221	–	–	–

^a Refers to the as-obtained acidic treated biosolids.^b Refers to the treated biosolids obtained from the closed-loop process developed in this study (see Fig. 7(A)).^c Refers to treated biosolids obtained from deionised water washing post the acid treatment step until neutral pH.^d Refers to contaminant-grade biosolids as prescribed in Victoria EPA biosolids management guidelines (EPA Victoria, 2004).^e BDL- Below detection limit.^f Abbreviations and chemical formulae–PFBS: Perfluorobutanesulfonic acid, C₄HF₉O₃S.PFDA: Perfluorodecanoic acid, C₁₀HF₁₉O₂.PFHxA: Perfluorohexanoic acid, C₆HF₁₁O₂.PFOS: Perfluorooctanesulfonic acid, C₈HF₁₇O₃S.PFOA: Perfluorooctanoic acid, C₈HF₁₅O₂.

stream with dilute metal concentration suitable for recycling, whereas high solids content >5% w/v produced a highly concentrated leachate stream attractive for metal recovery. The leachate stream produced at 5 and 10% solids can be completely recycled at least two times to reach saturation levels of metal ion concentration. However, the recycling of the leachate stream was only attractive at 5% solids; the rapid build-up of ferric iron concentration and increase in solution pH limit the recycling performance of the leachate stream at 10% solids loading. The continuous addition of fresh H₂SO₄ solution as a make-up lixiviant during the partial recycling (85%) of the spent leachate stream enhanced the dilution of the metal ion concentration and suppressed the precipitation of ferric from the solution at 5% solids. The oxidation of dissolved organics by H₂O₂ before the 2-stage NaOH precipitation achieved the optimum metal recovery of ~75% from the concentrated leachate stream. The developed process modestly preserved the organic nutrient to a larger extent in the treated biosolids with about 11% loss of carbon and 19% loss of nitrogen. The leaching of PFAS from biosolids into the aqueous phase was limited under the investigated conditions. The findings of this work provide a framework for developing a hydrometallurgical process for biosolids treatment which may be implemented within the existing wastewater treatment facilities.

CRediT authorship contribution statement

Ibrahim Gbolahan Hakeem: Conceptualization, Methodology,

Formal analysis, Investigation, Software, Writing – original draft. **Pobitra Halder:** Validation, Visualization, Data curation, Writing – review & editing. **Shefali Aktar:** Formal analysis. **Mojtaba Hedayati Marzbali:** Validation, Writing – review & editing. **Abhishek Sharma:** Writing – review & editing. **Aravind Surapaneni:** Resources, Supervision, Writing – review & editing. **Graeme Short:** Methodology, Supervision. **Jorge Paz-Ferreiro:** Supervision, Writing – review & editing. **Kalpiti Shah:** Conceptualization, Validation, Supervision, Project administration.

Declaration of Competing Interest

The authors declare that they have no known competing financial interests or personal relationships that could have appeared to influence the work reported in this paper.

Acknowledgements

This work is supported through Top-up scholarships from the School of Engineering, RMIT University and the ARC Training Centre for the Transformation of Australia's Biosolids Resources at RMIT University, Australia. The first author acknowledges the postgraduate scholarship received from RMIT University, Australia.

Appendix A. Supplementary data

Supplementary data to this article can be found online at <https://doi.org/10.1016/j.hydromet.2023.106044>.

References

- Abouelela, A.R., Mussa, A.A., Talhami, M., Das, P., Hawari, A.H., 2022. Industrial sludge valorization and decontamination via lipid extraction and heavy metals removal using low-cost protic ionic liquid. *Sci. Total Environ.* 835, 155451 <https://doi.org/10.1016/j.scitotenv.2022.155451>.
- Ait Ahsaine, H., Zbair, M., El Haouti, R., 2017. Mesoporous treated sewage sludge as outstanding low-cost adsorbent for cadmium removal. *Desalin. Water Treat.* 85, 330–338. <https://doi.org/10.5004/dwt.2017.21310>.
- Babel, S., del Mundo Dacera, D., 2006. Heavy metal removal from contaminated sludge for land application: a review. *Waste Manag.* 26, 988–1004. <https://doi.org/10.1016/j.wasman.2005.09.017>.
- Bayat, B., Sari, B., 2010. Comparative evaluation of microbial and chemical leaching processes for heavy metal removal from dewatered metal plating sludge. *J. Hazard. Mater.* 174, 763–769. <https://doi.org/10.1016/j.jhazmat.2009.09.117>.
- Beauchesne, I., Cheikh, R. Ben, Mercier, G., Blais, J.F., Ouarda, T., 2007. Chemical treatment of sludge: in-depth study on toxic metal removal efficiency, dewatering ability and fertilizing property preservation. *Water Res.* 41, 2028–2038. <https://doi.org/10.1016/j.watres.2007.01.051>.
- Blais, J.-F., Meunier, N., Sasseville, J.-L., Tyagi, R.D., Mercier, G., Hammy, F., 2005. Hybrid chemical and biological process for decontaminating sludge from municipal sewage. *US 6,855,256 B2*.
- de Fátima da Silva, M., de Sousa Oliveira, M.R., dos Santos, I.D., Radino-Rouse, P., Mansur, M.B., 2020. Iron precipitation strategies from nickel laterite ore sulfuric acid leach liquor. *Miner. Process. Extr. Metall. Rev.* 1–12 <https://doi.org/10.1080/08827508.2020.1809392>.
- del Mundo Dacera, D., Babel, S., 2006. Use of citric acid for heavy metals extraction from contaminated sewage sludge for land application. *Water Sci. Technol.* 54, 129–135. <https://doi.org/10.2166/wst.2006.764>.
- Demol, J., Ho, E., Soldenhoff, K., Karatchevseva, I., Senanayake, G., 2022. Beneficial effect of iron oxide/hydroxide minerals on sulfuric acid baking and leaching of monazite. *Hydrometallurgy* 211, 105864. <https://doi.org/10.1016/j.hydromet.2022.105864>.
- EPA Victoria, 2004. *Guidelines for Environmental Management: Biosolids Land Application*. Southbank, Victoria 3006, Australia.
- Erichsen Jones, J., 1934. *The Toxic Action of Heavy Metal Salts on the Three-Spined Stickleback (Gasterosteus Aculeatus)*. Aberystwyth, Wales.
- Feng, J.J., Jia, L., Liu, Q.Z., Chen, X.L., Cheng, J.P., 2018. Source identification of heavy metals in sewage sludge and the effect of influent characteristics: a case study from China. *Urban Water J.* 15, 381–387. https://doi.org/10.1080/1573062X.2018.1483525/SUPPL_FILE/NURW_A_1483525_SM7700.PDF.
- Fu, F., Wang, Q., 2011. Removal of heavy metal ions from wastewaters: a review. *J. Environ. Manag.* 92, 407–418. <https://doi.org/10.1016/j.jenvman.2010.11.011>.
- Gaber, S., Rizk, M., Yehia, M., 2011. Extraction of certain heavy metals from sewage sludge using different types of acids. *Biokemistri* 23, 41–48. <https://doi.org/10.4314/biokem.v23i1>.
- Geng, H., Xu, Y., Zheng, L., Gong, H., Dai, L., Dai, X., 2020. An overview of removing heavy metals from sewage sludge: achievements and perspectives. *Environ. Pollut.* 266, 115375 <https://doi.org/10.1016/j.envpol.2020.115375>.
- Gheju, M., Pode, R., Manea, F., 2011. Comparative heavy metal chemical extraction from anaerobically digested biosolids. *Hydrometallurgy* 108, 115–121. <https://doi.org/10.1016/j.hydromet.2011.03.006>.
- Guan, R., Yuan, X., Wu, Z., Wang, H., Jiang, L., Li, Y., Zeng, G., 2017. Functionality of surfactants in waste-activated sludge treatment: a review. *Sci. Total Environ.* 609, 1433–1442. <https://doi.org/10.1016/j.scitotenv.2017.07.189>.
- Gunarathne, V., Rajapaksha, A.U., Vithanage, M., Alessi, D.S., Selvasembian, R., Naushad, M., You, S., Oleszczuk, P., Ok, Y.S., 2020. Hydrometallurgical processes for heavy metals recovery from industrial sludges. *Crit. Rev. Environ. Sci. Technol.* 1–42 <https://doi.org/10.1080/10643389.2020.1847949>.
- Hakeem, I.G., Halder, P., Dike, C.C., Chiang, K., Sharma, A., Paz-Ferreiro, J., Shah, K., 2022a. Advances in biosolids pyrolysis: roles of pre-treatments, catalysts, and co-feeding on products distribution and high-value chemical production. *J. Anal. Appl. Pyrolysis* 166, 105608. <https://doi.org/10.1016/j.jaap.2022.105608>.
- Hakeem, I.G., Halder, P., Marzbali, M.H., Patel, S., Rathnayake, N., Surapaneni, A., Short, G., Paz-Ferreiro, J., Shah, K., 2022b. Mild sulphuric acid pre-treatment for metals removal from biosolids and the fate of metals in the treated biosolids derived biochar. *J. Environ. Chem. Eng.* 10, 107378 <https://doi.org/10.1016/j.jece.2022.107378>.
- Hao, L., Liu, M., Wang, N., Li, G., 2018. A critical review on arsenic removal from water using iron-based adsorbents. *RSC Adv.* 8, 39545–39560. <https://doi.org/10.1039/C8RA08512A>.
- Ito, A., Umata, T., Aizawa, J., Takachi, T., Morinaga, K., 2000. Removal of heavy metals from anaerobically digested sewage sludge by a new chemical method using ferric sulfate. *Water Res.* 34, 751–758. [https://doi.org/10.1016/S0043-1354\(99\)00215-8](https://doi.org/10.1016/S0043-1354(99)00215-8).
- Javed, T., Asselin, E., 2020. Fe(III) precipitation and copper loss from sulphate-chloride solutions at 150 °C: a statistical approach. *Metals (Basel)* 10, 669. <https://doi.org/10.3390/MET10050669>.
- Kabiri, S., Tucker, W., Navarro, D.A., Bräunig, J., Thompson, K., Knight, E.R., Nguyen, T. M.H., Grimison, C., Barnes, C.M., Higgins, C.P., Mueller, J.F., Kookana, R.S., McLaughlin, M.J., 2022. Comparing the leaching behavior of per- and polyfluoroalkyl substances from contaminated soils using static and column leaching tests. *Environ. Sci. Technol.* 56, 368–378. https://doi.org/10.1021/ACS.EST.1C06604/ASSET/IMAGES/LARGE/ESI06604_0005.JPEG.
- Kuan, Y.C., Lee, I.H., Chern, J.M., 2010. Heavy metal extraction from PCB wastewater treatment sludge by sulfuric acid. *J. Hazard. Mater.* 177, 881–886. <https://doi.org/10.1016/j.jhazmat.2009.12.115>.
- Kundu, S., Patel, S., Halder, P., Patel, T., Hedayati Marzbali, M., Pramanik, B.K., Paz-Ferreiro, J., De Figueiredo, C.C., Bergmann, D., Surapaneni, A., Megharaj, M., Shah, K., 2021. Removal of PFASs from biosolids using a semi-pilot scale pyrolysis reactor and the application of biosolids derived biochar for the removal of PFASs from contaminated water. *Environ. Sci. Water Res. Technol.* 7, 638–649. <https://doi.org/10.1039/d0ew00763c>.
- LeBlanc, R.J., Matthews, P., Richard, R.P., 2009. *Global atlas of excreta, wastewater sludge, and biosolids management: Moving forward the sustainable and welcome uses of a global resource*. United Nations Human Settlements Programme, UN-HABITAT, P.O. Box 30030, Nairobi 00100, Kenya.
- Lee, G., Bigham, J.M., Faure, G., 2002. Removal of trace metals by coprecipitation with Fe, Al and Mn from natural waters contaminated with acid mine drainage in the Ducktown Mining District, Tennessee. *Appl. Geochem.* 17, 569–581. [https://doi.org/10.1016/S0883-2927\(01\)00125-1](https://doi.org/10.1016/S0883-2927(01)00125-1).
- Lee, I.H., Wang, Y.J., Chern, J.M., 2005. Extraction kinetics of heavy metal-containing sludge. *J. Hazard. Mater.* 123, 112–119. <https://doi.org/10.1016/J.JHAZMAT.2005.03.035>.
- Lee, I.H., Kuan, Y.C., Chern, J.M., 2006. Factorial experimental design for recovering heavy metals from sludge with ion-exchange resin. *J. Hazard. Mater.* 138, 549–559. <https://doi.org/10.1016/J.JHAZMAT.2006.05.090>.
- Leštan, D., Luo, C., Ling, Li, X., Dong, 2008. The use of chelating agents in the remediation of metal-contaminated soils: a review. *Environ. Pollut.* 153, 3–13. <https://doi.org/10.1016/j.envpol.2007.11.015>.
- Li, Y., Yu, Han, Liu, L., Yu, Hongbing, 2021. Application of co-pyrolysis biochar for the adsorption and immobilization of heavy metals in contaminated environmental substrates. *J. Hazard. Mater.* 420, 126655 <https://doi.org/10.1016/J.JHAZMAT.2021.126655>.
- Liang, S., Chen, H., Zeng, X., Li, Z., Yu, W., Xiao, K., Hu, J., Hou, H., Liu, B., Tao, S., Yang, J., 2019. A comparison between sulfuric acid and oxalic acid leaching with subsequent purification and precipitation for phosphorus recovery from sewage sludge incineration ash. *Water Res.* 159, 242–251. <https://doi.org/10.1016/J.WATRES.2019.05.022>.
- Liu, T., Liu, Z., Zheng, Q., Lang, Q., Xia, Y., Peng, N., Gai, C., 2018. Effect of hydrothermal carbonization on migration and environmental risk of heavy metals in sewage sludge during pyrolysis. *Bioresour. Technol.* 247, 282–290. <https://doi.org/10.1016/J.BIORTECH.2017.09.090>.
- Liu, L., Huang, L., Huang, R., Lin, H., Wang, D., 2021. Immobilization of heavy metals in biochar derived from co-pyrolysis of sewage sludge and calcium sulfate. *J. Hazard. Mater.* 403, 123648 <https://doi.org/10.1016/J.JHAZMAT.2020.123648>.
- Ma, D., Su, M., Qian, J., Wang, Q., Meng, F., Ge, X., Ye, Y., Song, C., 2020. Heavy metal removal from sewage sludge under citric acid and electroosmotic leaching processes. *Sep. Purif. Technol.* 242, 116822 <https://doi.org/10.1016/j.seppur.2020.116822>.
- Marchioretto, M.M., Bruning, H., Rulkens, W., 2005. Heavy metals precipitation in sewage sludge. *Sep. Sci. Technol.* 40, 3393–3405. <https://doi.org/10.1080/01496390500423748>.
- Matocha, C.J., Karathanasis, A.D., Rakshit, S., Wagner, K.M., 2005. Reduction of copper (II) by iron(II). *J. Environ. Qual.* 34, 1539–1546. <https://doi.org/10.2134/jeq2005.0002>.
- Mercier, G., Blais, J.F., Hammy, F., Lounès, M., Sasseville, J.L., 2002. A decontamination process to remove metals and stabilise Montreal sewage sludge. *Sci. World J.* 2, 1121–1126. <https://doi.org/10.1100/tsw.2002.201>.
- Montenegro, V., Agatzini-Leonardou, S., Oustadakis, P., Tsakiridis, P., 2016. Hydrometallurgical treatment of EAF dust by direct sulphuric acid leaching at atmospheric pressure. *Waste Biomass Valorization* 76 (7), 1531–1548. <https://doi.org/10.1007/S12649-016-9543-Z>.
- Ni, B.J., Huang, Q.S., Wang, C., Ni, T.Y., Sun, J., Wei, W., 2019. Competitive adsorption of heavy metals in aqueous solution onto biochar derived from anaerobically digested sludge. *Chemosphere* 219, 351–357. <https://doi.org/10.1016/J.CHEMOSPHERE.2018.12.053>.
- Nie, J., Pan, Y., Shi, J., Guo, Y., Yan, Z., Duan, X., Xu, M., 2015. A comparative study on the uptake and toxicity of nickel added in the form of different salts to maize seedlings. *Int. J. Environ. Res. Public Health* 12, 15075–15087. <https://doi.org/10.3390/IJERPH121214972>.
- Pathak, A., Dastidar, M.G., Sreekrishnan, T.R., 2009. Bioleaching of heavy metals from sewage sludge: a review. *J. Environ. Manag.* <https://doi.org/10.1016/j.jenvman.2008.11.005>.
- Paz-Ferreiro, J., Nieto, A., Méndez, A., Askeland, M.P.J., Gasco, G., 2018. Biochar from biosolids pyrolysis: a review. *Int. J. Environ. Res. Public Health* 15, 1–16. <https://doi.org/10.3390/ijerph15050956>.
- Persson, H., Kantarelis, E., Evangelopoulos, P., Yang, W., 2017. Wood-derived acid leaching of biomass for enhanced production of sugars and sugar derivatives during pyrolysis: in fl uence of acidity and treatment time. *J. Anal. Appl. Pyrolysis* 127, 329–334. <https://doi.org/10.1016/j.jaap.2017.07.018>.
- Ross, J.J., Zitomer, D.H., Miller, T.R., Weirich, C.A., Mcnamara, P.J., 2016. Emerging investigators series: pyrolysis removes common microconstituents trichloroan, triclosan, and nonylphenol from biosolids. *Environ. Sci. Water Res. Technol.* 2, 282–289. <https://doi.org/10.1039/C5EW00229J>.

- Sethurajan, M., Lens, P.N.L., Horn, H.A., Figueiredo, L.H.A., van Hullebusch, E.D., 2017. Leaching and recovery of metals. In: Rene, E.R. (Ed.), *Sustainable Heavy Metal Remediation*. Springer International Publishing AG, pp. 161–206. https://doi.org/10.1007/978-3-319-61146-4_6.
- Shen, Y., Chen, L., 2022. Catalytic pyrolysis of cellulose with biochar modified by Ni–Co–Mn cathode material recovered from spent lithium-ion battery. *Chemosphere* 305, 135430. <https://doi.org/10.1016/J.CHEMOSPHERE.2022.135430>.
- Shi, J., Pang, J., Liu, Q., Luo, Y., Ye, J., Xu, Q., Long, B., Ye, B., Yuan, X., 2020. Simultaneous removal of multiple heavy metals from soil by washing with citric acid and ferric chloride. *RSC Adv.* 10, 7432–7442. <https://doi.org/10.1039/C9RA09999A>.
- Shiba, N.C., Ntuli, F., 2017. Extraction and precipitation of phosphorus from sewage sludge. *Waste Manag.* 60, 191–200. <https://doi.org/10.1016/J.WASMAN.2016.07.031>.
- Shim, M.J., 2023. Recycling of washing agents for heavy metal removal from digested sewage sludge. *Int. J. Environ. Sci. Technol.* 1–12 <https://doi.org/10.1007/S13762-023-04757-4/FIGURES/9>.
- Singh, S., Kumar, V., Dhanjal, D.S., Datta, S., Bhatia, D., Dhiman, J., Samuel, J., Prasad, R., Singh, J., 2020. A sustainable paradigm of sewage sludge biochar: valorization, opportunities, challenges and future prospects. *J. Clean. Prod.* 269, 122259 <https://doi.org/10.1016/J.JCLEPRO.2020.122259>.
- Strasser, H., Brunner, H., Schinner, F., 1995. Leaching of iron and toxic heavy metals from anaerobically-digested sewage sludge. *J. Ind. Microbiol.* 14, 281–287. <https://doi.org/10.1007/BF01569940>.
- Stylianou, M.A., Kollia, D., Haralambous, K.J., Inglezakis, V.J., Moustakas, K.G., Loizidou, M.D., 2007. Effect of acid treatment on the removal of heavy metals from sewage sludge. *Desalination* 215, 73–81. <https://doi.org/10.1016/j.desal.2006.11.015>.
- Tang, J., He, J., Liu, T., Xin, X., 2017. Removal of heavy metals with sequential sludge washing techniques using saponin: optimization conditions, kinetics, removal effectiveness, binding intensity, mobility and mechanism. *RSC Adv.* 7, 33385–33401. <https://doi.org/10.1039/C7RA04284A>.
- Tawalbeh, M., Al-Othman, A., Salamah, T., Alkasrawi, M., Martis, R., El-Rub, Z.A., 2021. A critical review on metal-based catalysts used in the pyrolysis of lignocellulosic biomass materials. *J. Environ. Manag.* 299, 113597 <https://doi.org/10.1016/J.JENVMAN.2021.113597>.
- Tyagi, V.K., Lo, S.L., 2013. Sludge: a waste or renewable source for energy and resources recovery? *Renew. Sust. Energ. Rev.* <https://doi.org/10.1016/j.rser.2013.05.029>.
- Vardanyan, A., Kafa, N., Konstantinidis, V., Shin, S.G., Vyrides, I., 2018. Phosphorus dissolution from dewatered anaerobic sludge: effect of pHs, microorganisms, and sequential extraction. *Bioresour. Technol.* 249, 464–472. <https://doi.org/10.1016/J.BIORTECH.2017.09.188>.
- Vesilind, P.A., Hsu, C.C., 1997. Limits of sludge dewaterability. *Water Sci. Technol.* 36, 87–91. [https://doi.org/10.1016/S0273-1223\(97\)00673-2](https://doi.org/10.1016/S0273-1223(97)00673-2).
- Wang, Xuejiang, Chen, J., Yan, X., Wang, Xin, Zhang, J., Huang, J., Zhao, J., 2015. Heavy metal chemical extraction from industrial and municipal mixed sludge by ultrasound-assisted citric acid. *J. Ind. Eng. Chem.* 27, 368–372. <https://doi.org/10.1016/J.JIEC.2015.01.016>.
- Wang, Y., Zhang, Y., Pei, L., Ying, D., Xu, X., Zhao, L., Jia, J., Cao, X., 2017. Converting Ni-loaded biochars into supercapacitors: implication on the reuse of exhausted carbonaceous sorbents. *Sci. Report.* 71 (7), 1–8. <https://doi.org/10.1038/srep41523>.
- Wang, X., Chi, Q., Liu, X., Wang, Y., 2019. Influence of pyrolysis temperature on characteristics and environmental risk of heavy metals in pyrolyzed biochar made from hydrothermally treated sewage sludge. *Chemosphere* 216, 698–706. <https://doi.org/10.1016/J.CHEMOSPHERE.2018.10.189>.
- Weng, L., Temminghoff, E.J.M., Lofts, S., Tipping, E., Van Riemsdijk, W.H., 2002. Complexation with dissolved organic matter and solubility control of heavy metals in a sandy soil. *Environ. Sci. Technol.* 36, 4804–4810. https://doi.org/10.1021/ES0200084/SUPPL_FILE/ES0200084_S.PDF.
- Wu, C.H., Kuo, C.Y., Lo, S.L., 2009. Recovery of heavy metals from industrial sludge using various acid extraction approaches. *Water Sci. Technol.* 59, 289–293. <https://doi.org/10.2166/wst.2009.859>.
- Xiang, L., Chan, L.C., Wong, J.W.C., 2000. Removal of heavy metals from anaerobically digested sewage sludge by isolated indigenous iron-oxidizing bacteria. *Chemosphere* 41, 283–287. [https://doi.org/10.1016/S0045-6535\(99\)00422-1](https://doi.org/10.1016/S0045-6535(99)00422-1).
- Xiao, Z., Yuan, X., Li, H., Jiang, L., Leng, L., Chen, X., Zeng, G., Li, F., Cao, L., 2015. Chemical speciation, mobility and phyto-accessibility of heavy metals in fly ash and slag from combustion of pelletized municipal sewage sludge. *Sci. Total Environ.* 536, 774–783. <https://doi.org/10.1016/J.SCITOTENV.2015.07.126>.
- Xu, Y., Xie, Y., Liu, J., Yan, L., Yang, R., 2009. Enrichment of valuable metals from the sulfuric acid leach liquors of nickeliferous oxide ores. *Hydrometallurgy* 95, 28–32. <https://doi.org/10.1016/J.HYDROMET.2008.04.003>.
- Yang, Z., Wang, D., Wang, G., Zhang, S., Cheng, Z., Xian, J., Pu, Y., Li, T., Jia, Y., Li, Y., Zhou, W., Xu, X., 2021. Removal of Pb, Zn, Ni and Cr from industrial sludge by biodegradable washing agents: Caboxyethylthiosuccinic acid and itaconic-acrylic acid. *J. Environ. Chem. Eng.* 9, 105846 <https://doi.org/10.1016/J.JECE.2021.105846>.
- Yao, J.G., Tan, S.Y., Metcalfe, P.I., Fennell, P.S., Kelsall, G.H., Hallett, J.P., 2021. Demetallization of sewage sludge using low-cost ionic liquids. *Environ. Sci. Technol.* 55, 5291–5300. <https://doi.org/10.1021/acs.est.0c03724>.
- Yoshizaki, S., Tomida, T., 2000. Principle and process of heavy metal removal from sewage sludge. *Environ. Sci. Technol.* 34, 1572–1575. <https://doi.org/10.1021/es990979s>.
- Yu, H., Naidu, G., Zhang, C., Wang, C., Razmjou, A., Han, D.S., He, T., Shon, H., 2022. Metal-based adsorbents for lithium recovery from aqueous resources. *Desalination* 539, 115951. <https://doi.org/10.1016/J.DESAL.2022.115951>.
- Zhao, B., Xu, X., Zeng, F., Li, H., Chen, X., 2018. The hierarchical porous structure biochar assessments produced by co-pyrolysis of municipal sewage sludge and hazelnut shell and Cu(II) adsorption kinetics. *Environ. Sci. Pollut. Res.* 25, 19423–19435. <https://doi.org/10.1007/S11356-018-2079-Y>.

Positive temperature coefficient of resistance of Mg-GeO₂ nanowire array film

Cite as: J. Appl. Phys. **133**, 045302 (2023); doi: 10.1063/5.0130729

Submitted: 14 October 2022 · Accepted: 31 December 2022 ·

Published Online: 24 January 2023



View Online



Export Citation



CrossMark

Ankita Choudhury,¹ Arka Dey,¹  Chiranjib Ghosh,¹  Avijit Dalal,¹  Rajat Mahapatra,²  Saikat Biswas,² 
Nilanjan Halder,³  and Aniruddha Mondal^{1,a)} 

AFFILIATIONS

¹Department of Physics, National Institute of Technology Durgapur, Durgapur 713209, India

²Department of Electronics and Communication Engineering, National Institute of Technology Durgapur, Durgapur 713209, India

³Department of Physics, Manipal University Jaipur, Jaipur 303007, Rajasthan, India

^{a)}Author to whom correspondence should be addressed: aniruddhamo@gmail.com

ABSTRACT

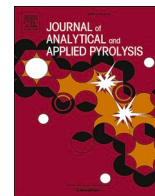
Here, glancing angle deposition is employed to synthesize the undoped GeO₂ and Mg-doped (0.4 and 0.8 at. %) GeO₂ nanowires (NWs) on a Si substrate. The microscopic images show the formation of the NW-like morphology of the grown materials. The gradual decrease in the average ratio of length to diameter depicts the worsening of the formation of NWs with the incorporation of Mg into the GeO₂ host lattice. This also affects the crystallinity characteristics of the materials, which have been demonstrated from the selected area electron diffraction (SAED) pattern of the materials. The polycrystallinity nature of undoped GeO₂ NWs changes to amorphous due to the introduction of Mg, which has been confirmed from both the obtained SAED and x-ray diffraction patterns of the samples. The presence of Mg was confirmed from the obtained broad bands at 473 and 437 cm⁻¹ in the Fourier transmission spectrum of the doped samples. The increasing conductance with the temperature of Au/undoped GeO₂ devices can be explained by the thermionic emission process, whereas the Mg-GeO₂ device shows an overall decrease in conductance with increasing temperature. We have ascribed the origin of this abnormal conductance as the positive temperature coefficient of resistance, which is one of the first reports, due to the generation of random grain boundaries and enormous electron trapping at the Au/Mg-GeO₂ NW junction. Furthermore, the undoped GeO₂ NW device shows good temperature-dependent conductivity as well as stability compared to the doped one.

Published under an exclusive license by AIP Publishing. <https://doi.org/10.1063/5.0130729>

I. INTRODUCTION

Ultra-wide bandgap (UWBG) semiconductors are receiving significant attention from the research community for their usability in the field of scientific and technological applications due to their excellent properties coupled with exceptional thermal and chemical stabilities.^{1–3} These UWBG semiconductors hold promise to meet the emerging needs and demands of current and future technologies.⁴ Germanium dioxide (GeO₂) is one of the widely used UWBG oxide semiconductors. Due to its versatile properties, it achieved unwavering attention in the field of high-power electronics, deep-UV optoelectronics/photronics, and energy storage applications.⁵ GeO₂ is treated as one of the capable materials for optical waveguides and nano-connections in optoelectronic communications due to its attractive optical and electronic properties

and high thermal stability.^{6,7} One-dimensional nanostructures including nanowires, nanotubes, and nanorods have attracted rapidly growing interest due to their fascinating properties and unique applications in areas ranging from physics, chemistry, life sciences, to materials science.⁸ These nanostructures are treated as building blocks in a wide variety of nanoscale electronic and photonic devices. An emerging area of research is the characterization of nanowire networks and their application in macroelectronics and energy harvesting. Metal oxide nanowire networks are an attractive alternative due to the ease of growth of nanowires while still providing appealing electrical properties. Nanowires emerge as one of the most interesting ones as they combine low dimensionality due to their small diameters with high aspect ratios, which makes them a good approximation to one-dimensional structures. Other advantages of these nanowires include access to a large range



Pyrolytic conversion of agricultural residue using continuous auger reactor for resource recovery

Sivasankar Kakku^a, Sowkhya Naidu^a, Mukesh Bhatt^a, Anand G. Chakinala^a,
Jyeshtharaj Joshi^{b,c}, Shina Gautam^d, Kaustubha Mohanty^e, Gaurav Kataria^a,
Abhishek Sharma^{a,f,*}

^a Waste to Resources Laboratory, Department of Chemical Engineering, Manipal University Jaipur, Rajasthan 303007, India

^b Department of Chemical Engineering, Institute of Chemical Technology Mumbai, Maharashtra 400019, India

^c Marathi Vidyan Parishad, Mumbai, Maharashtra 400022, India

^d Department of Chemical Engineering, Shroff Rotary Institute of Chemical Technology, Gujarat 393135, India

^e Department of Chemical Engineering, Indian Institute of Technology Guwahati, Guwahati 781039, India

^f Chemical & Environmental Engineering, School of Engineering, RMIT University, Melbourne, Victoria 3000, Australia

ARTICLE INFO

Keywords:

Biomass pyrolysis
Auger reactor
Chemical value
Bio-oil
Biochar

ABSTRACT

In this research work, agricultural residue was pyrolytically converted in a continuous semi pilot auger reactor. Studies have been carried out with variation in operating conditions such as temperature, and its effect on product yield and quality has been analyzed comprehensively. It was found that with increase in temperature from 400 to 500 °C, the oil yield increased; however, reduced on further increasing the temperature. The char yield decreased from 50 to 20 wt% and gas yield increased with rising temperature. For cotton stalk pyrolysis, maximum biochar yield of 51% was obtained at 400 °C, whereas maximum bio-oil yield of 46.5% was obtained at 500 °C. Maximum gas yield of 55% was obtained with mustard husk feedstock at 700 °C temperature. Water content of the cotton stalk bio-oil (35%) was found to be lower than mustard husk bio-oil (79%). The water content in bio-oil was found to enhance with increase in temperature. GC-MS analysis confirmed that different chemical value compounds are present in the bio-oils obtained from both cotton stalk and mustard husk. In addition, the chars obtained had a calorific value of 24.15 MJ/kg for cotton stalk and 24.57 MJ/kg for mustard husk. At 500 °C, biochar showed good thermal stability in TGA analysis and major weight loss occurred in the temperature range of 500–600 °C. It was also observed that biochar contains high amount of micronutrients and can be used for improving crop productivity by partially replacing synthetic fertilizers.

1. Introduction

With a phenomenal increase in the world population, it is expected that there will be a crunch in the fuel inventory by 2050 [1]. In addition, with the usage of fossil fuels and rapid industrialization, increased carbon emissions are leading to global warming across the globe causing catastrophic events. Therefore, to meet the energy demands and to reduce the environmental impact, renewable energy resources are being studied extensively which can potentially replace the fossil fuels. This led to enhanced interest in the utilization of biomass-based feedstocks which increased the share of bioenergy up to 13.5% in 2018 and ranked 4th among all the types of energy resources [2]. Biomass has shown a greater impact on controlling the atmospheric concentrations of

greenhouse gases, leading to low carbon economy [3–7]. Countries around the globe are striving to achieve carbon-neutral environment as the carbon emissions from burning of fossil fuels have negative impact on the atmosphere [8]. Agro waste is the residue after harvesting of crops and includes stems, leaves, and stalks [9], that mainly consists of hemicellulose, cellulose, and lignin [10]. Agricultural residues has the potential to contribute significantly towards the production of renewable fuels using energy efficient conversion processes [11,12].

The leading producers of mustard are the Canada, Russia, China, and India, with a total annual production of 85 MT where ~14% of the world's total production comes from India in the year 2022 [13]. Cotton is produced in ~32 million hectares with an approximate yield of 786 kg/hectare worldwide having a production of 115 Million bales for the

* Corresponding author at: Waste to Resources Laboratory, Department of Chemical Engineering, Manipal University Jaipur, Rajasthan 303007, India.

E-mail address: abhishek.sharma@jaipur.manipal.edu (A. Sharma).

<https://doi.org/10.1016/j.jaap.2023.105951>

Received 21 November 2022; Received in revised form 6 March 2023; Accepted 12 March 2023

Available online 15 March 2023

0165-2370/© 2023 Elsevier B.V. All rights reserved.

year 2022 as reported by the United States Department of Agriculture (USDA) [14].

Cotton stalk and mustard husk pyrolysis in different type of reactors is reported by many researchers. Al Afif et al. [15] studied the pyrolysis of cotton stalk biomass in a lab scale batch reactor by varying the temperature from 300 °C to 800 °C. Considerable biochar yield of 46.5% was obtained at 400 °C and oil yield up to 33% at 800 °C. Temperature was found to have a major influence on the process in terms of its mass and energy yield. Slow pyrolysis of cotton stalk by Chouhan et al. [16] obtained 17% bio-oil yield with 38% bio-char. The bio-oil was found to have a lower water content of 9.7% with a calorific value of 18.36 MJkg⁻¹. Ayse and Putun [17] also used a similar fixed tubular reactor to quickly pyrolyze cotton stalk and straw at 400–700 °C. They obtained highest oil yield of 39.51% at 550 °C with a sweeping gas flow of 200 cm³min⁻¹. Pyrolysis of cotton stalk carried out by Yingquan et al. [18] in a fixed bed reactor reported an optimum temperature range between 550 °C and 750 °C with the charcoal produced having a higher calorific value of 28 MJkg⁻¹ and a larger surface area of > 200 m².g⁻¹ and the calorific value of the gas ranging between 8 and 9 MJm⁻³. The bio-oil yields of 0.05 kg/kg of cotton stalk pyrolysis in a batch reactor was reported at 850 °C by Chen et al. [19]. Putun et al. [20] investigated the catalytic pyrolysis of cotton stalk in a Heinze-type reactor fixed bed to see the influence on liquid and solid products yields and composition. With a particle size range of 0.85 < D_p < 1.85 mm, pyrolysis of cotton stalk at a final temperature of 550 °C produced an oil yield of 23.82%. The oil production attained a maximum of 24.77% in a sweep gas environment (100 cm³/min of N₂ flow rate) of particle size and nitrogen flow rate. Chen et al. [21] have studied the changes in the CaO/biomass (Ca/B) mass ratios and pyrolysis temperatures in which they suggested that CaO might operate as a reactant, absorbent, and catalyst at Ca/B ratios of <0.2, > 0.2, and > 0.4, respectively. Maximum oil yield up to 50% were reported at 600 °C and in the presence of CaO. Fast pyrolysis of cotton stalk was reported by Zheng Ji-lu et al. [22] at 480–530 °C in a fluidized bed reactor where maximum bio-oil yields of ~55 wt% were obtained at 510 °C and it is claimed that the obtained bio-oil can be directly used as a fuel oil in a boiler. Similar studies of cotton stalk pyrolysis in a fluidized bed reactor were reported by Sui et al. [23] in the range of 400–600 °C with four condensers at different temperatures. The condenser with 0 °C collected almost 90% of tiny molecular compounds such as acetic acid, ketones, aldehydes, and water, whereas the 100 °C condenser collected organics with mid-boiling points (Phenols).

Since most of the studies reported are carried out in batch reactor, these results may not be useful for continuous operations and for process scale up. Studies with auger reactor were reported by Somsak et al. [24] for the pyrolysis of cassava rhizome that resulted in highest oil output of 50 wt%, and heating value of 28.5 MJ.kg⁻¹, were attained at 550 °C. Sand was used as the heat carrier during the pyrolysis process, and 2 kg. h⁻¹ of feed was added throughout the process. The operating parameters used for these studies resulted in the bio-oil having a lower water content but a greater solid particle content. Barley straw and wood pellets pyrolyzed in a twin co-axial auger by Yang et al. [25] produced 28% char, 18% gas, and 54% oil. Both the reactor and the hot gases filter were progressively heated to 450 °C throughout the experimental campaign and maintained at that temperature for 30 min. Pyrolysis of hardwood, softwood, wheat straw, and wheat bran in a twin-auger by Henrich et al. [26] have shown that when compared to other feeds, soft and hard woods generated oil in higher proportions of 69.1 wt% and 66.5 wt%, respectively.

Although, majority of the research till date was reported using lab and batch scale reactors [27–29], in this study biomass pyrolysis was carried out extensively in a semi-continuous pilot scale auger reactor [30]. Two different biomass feeds obtained from discrete locations was studied at distinct temperatures and analyzed in terms of their product yield and composition. Change in composition of the oil with respect to temperature have been examined with focus of this research being the chemical value of oil rather than its fuel value. Characterization of

bio-oil, the functional groups and other biochar properties was studied. These results help in evaluating the feasibility of the pilot scale demonstrations and addressing the issues pertaining to such large scale systems.

2. Experimental section

2.1. Materials and methods

Cotton stalk and mustard husk used in this study were obtained locally and converted into pellets. The average length and diameter of the pellet was ~4.6 ± 1 cm and ~0.6 ± 0.2 cm, respectively.

2.2. Experimental set-up

2.2.1. Auger reactor

The customized reactor has a processing capacity of 1–10 kg.h⁻¹ of biomass. It is fitted with three electrical heating zones that may be operated individually, enabling to adjust the reactor's internal temperature. Using a variable frequency drive, the screw rotation speed may be changed during operation from 5 rpm to 15 rpm, which maintains the feedstocks residence time inside the reactor. The reactor outlet is attached with two condensers in which the first condenser was maintained at 25 ± 5 °C with tap water circulation and the second condenser was maintained at 10 ± 5 °C with ice-cold water circulation.

2.2.2. Experimental procedure

Schematic diagram of the continuous flow auger reactor used in this study is shown in Fig. 1 which consisted of three heating zone, each having a 7.5 KW capacity. In the first series of trials, temperatures were increased by 100 °C steps between 400 °C and 700 °C in an oxygen-deficient environment. Tests were run for 90 min with a reactor screw speed of 5 rpm until no more substantial gas release would occur which is noticed with a gas flow meter attached to the reactor. Oil fractions were collected separately from the two condenser vessels (V₁ and V₂) that are analyzed for its composition and water content. The aqueous and oil phases of the liquid product were separated and weighed, whereas char was extracted from the collection chamber. The amounts of oil and char obtained was measured and the gas yields was calculated by difference.

2.3. Characterization techniques

Bio-oil fractions were analyzed using a Gas chromatograph Mass Spectrometry (GC-MS) analyzer (Shimadzu, Model: QP2020) to quantify their chemical contents. This was equipped with a column (Rxi-5 MS) having dimensions (30 m × 0.25 mm ID and 0.25 μm film thickness) and the method used for analysis was as follows: The GC column was maintained at an oven temperature of 50 °C and an injection temperature of 250 °C. Helium as a carrier gas was maintained at 1.18 mL/min with split ratio of 15. The column oven temperature was initially held at 50 °C for 2 min and then increased at a rate of 6 °C/min to 90 °C, followed by another 6 °C/min increase to 120 °C. The temperature was then increased at a rate of 8 °C/min to 250 °C and finally at a rate of 10 °C/min to 280 °C. The MS ion source temperature was set to 230 °C, while the interface temperature was maintained at 250 °C. Prior to the analysis, the oil samples were pre-processed in which 200 mg of pyrolysis oil was dissolved in 10 mL of solvent (acetone/hexane). Samples were diluted with solvent and dehydrated using 4 g of anhydrous sodium sulphate before being filtered through a 0.22 μm syringe mesh filter [31]. The water content was determined using the Karl Fischer Titrator (1760 by ESICO).

Thermo Gravimetric Analysis (TGA) of feed and biochar was carried out through Shimadzu T60 with 20°C/min in nitrogen atmosphere. The carbonaceous residue was measured in accordance with ASTM D 524-Ramsbottom [32,33].

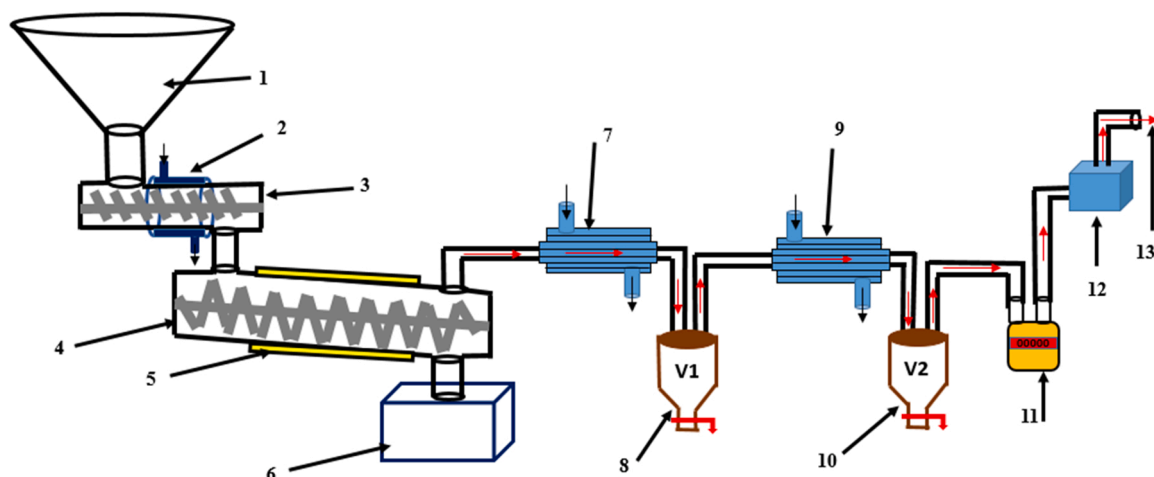


Fig. 1. Schematic of continuous auger pyrolysis reactor used in this study. 1. Hoper, 2. Cooling Jacket, 3. Feeder, 4. Reactor, 5. Heatingzone, 6. Char collector chamber 7. Condenser 1, 8. Oil collector vessel V1, 9. Condenser 2, 10. Oil collector vessel V2, 11. Gas flow meter, 12. Scrubber, 13. Vent gases.

The elemental analysis was performed using an LECO-Truspec CHNS analyzer. ASTM D7582 and ASTM D3176 standards were followed in determining the proximate and ultimate analysis. For in-depth analysis and characterization of the feed and product samples, a variety of instrumentation techniques are used such as scanning electron microscopy (SEM; JEOL make JSM-7610 F-Plus), and Fourier transform infrared spectroscopy (FTIR; Bruker alpha). FTIR analysis was done in transmittance mode to identify the functional groups in char and oil. SEM/EDX was carried out to determine the surface morphology of the char samples and to qualitatively determine the presence of different components in the char samples.

3. Results and discussion

3.1. Feed analysis

Ultimate and proximate properties of cotton stalk and mustard husk show that the cotton stalk having high ash content and low fixed carbon compared to mustard husk and with no changes in other properties.

Thermogravimetric analysis (TGA) is used to examine the thermal degradation behaviour of the feedstocks by varying the temperature from 400° to 700°C. Initial weight loss occurred up to 120 °C due to the removal of bound and unbound moisture present in the feed material as shown in Fig. 2 and around ~10% moisture removal was noticed for both the feedstocks. Decomposition of hemicellulose and cellulose starts at around 280 °C and 340 °C and within this temperature range, some extent of lignin also decomposes. With both the feeds, the residue obtained was similar having ~18% after 800 °C and the Differential thermogravimetric (DTG) curves for both the feeds also showed identical thermal decomposition ranging from 400° to 600°C.

Table 1

Proximate and ultimate analysis of biomass feed.

Parameters	Cotton stalk	Mustard husk
Loss on drying @ 110 °C (%)	4.50	6.40
Ash @ 800 °C (%)	4.73	3.68
Volatile Matter (%)	71.10	69.30
Fix Carbon (%)	19.67	20.62
Carbon (%)	44.94	44.47
Hydrogen (%)	7.32	6.03
Oxygen (%)	46.85	48.09
Nitrogen (%)	0.69	0.54
Sulphur (%)	0.20	0.87

3.2. Product yield distribution

The current study mainly focusses on the pyrolysis of cotton stalk and mustard husk biomass in an auger reactor. Biomass pyrolysis was carried out in the temperature range of 400 °C – 700 °C for both the feedstocks.

In case of cotton stalk, the oil yield was 34.5% at 400 °C which further increased up to 46.5% at 500 °C as shown in Fig. 3(a). With further increase in the temperature, no significant change in oil yield was obtained and thus, the optimum temperature was considered as 500 °C. Maximum char yield of 51.1% was obtained at 400 °C, which decreased with increase in temperature and lowest char yield of 17% was obtained at 700 °C. The gas yield gradually increased with increase in temperature and maximum gas yield of 51.7% was observed at 700 °C. This is due to the vapour phase thermal cracking of volatiles as well as the decomposition of char at higher temperatures. Similar observations of product trends were seen with the mustard husk where maximum oil yield of 46% was obtained at 500 °C as shown in Fig. 3(b). The optimum temperature was found to be similar to that of cotton stalk. Char yield was observed to be low as compared with cotton stalk. 47% char was observed at 400 °C and it decreased to 19.5% at 700 °C. The gas yields with mustard husk were found to be higher when compared with cotton stalk. No significant changes in the gas yield were observed at 400 °C and 500 °C, and it raised from 18% to 55% with increase in temperature from 500 °C to 700 °C.

The oil yields from different condenser fractions at different temperatures for both the feeds are shown in Fig. 4 It is evident from the figure that maximum oil was collected in V₁ condenser compared to V₂ condenser which is relatively operated even at lower temperature. Mainly because most of the volatiles were condensed with normal water at room condition and rest were condensed at lower temperature in condenser 2. For both the feeds, the yield trend recorded in both condensers revealed that oil yield rose with increasing temperature up to 500 °C, but then decreased in condenser V₁ above this temperature. While, with increasing temperature the oil fraction in the second condenser V₂ increased steadily with temperature up to 700 °C.

In Fig. 5, a comparative study of cotton stalk pyrolysis carried out in different reactors (fixed bed and fluidized bed) are summarized with respect to the obtained oil yields. In literature, no studies were found using continuous auger reactors for both cotton stalk and mustard husk. Most of the studies used lab scale fixed bed reactors, followed by few pilot scale operations with fluidized bed reactors. In a fixed bed reactor, cotton stalk was employed as granular powder with a particle size of < 1 mm, and a maximum oil yield of 50% was reported. However, a maximum oil yield from cotton stalk pyrolysis of 55% was produced in a fluidized bed reactor with 0.20 – 0.42 mm size of cotton stalk [34]. In

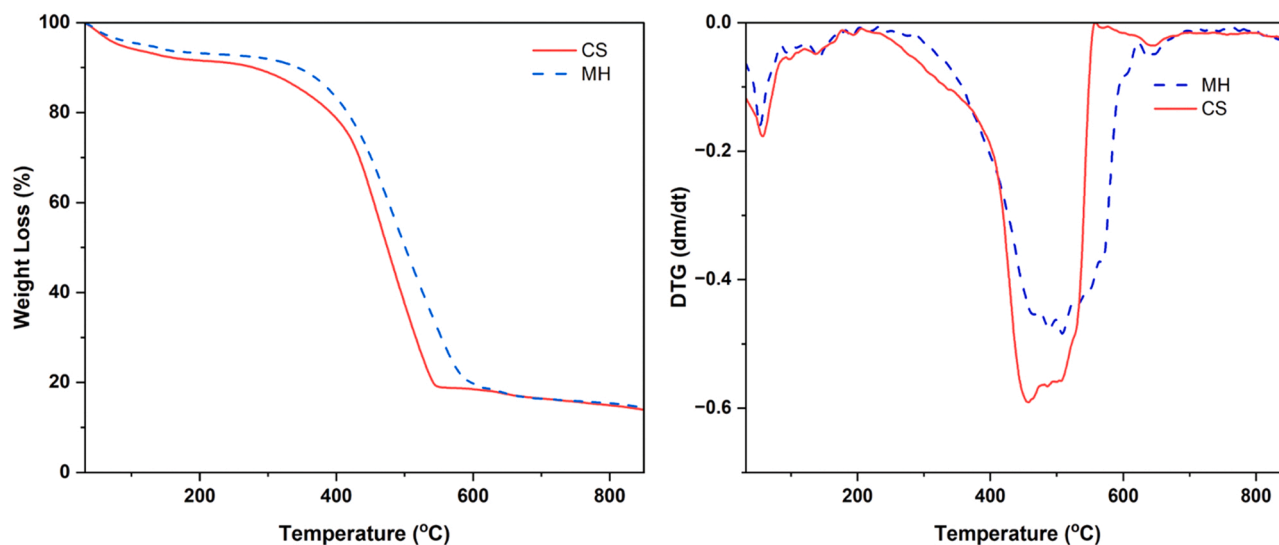


Fig. 2. (a) TGA and (b) DTG of Cotton stalk and Mustard husk feedstock.

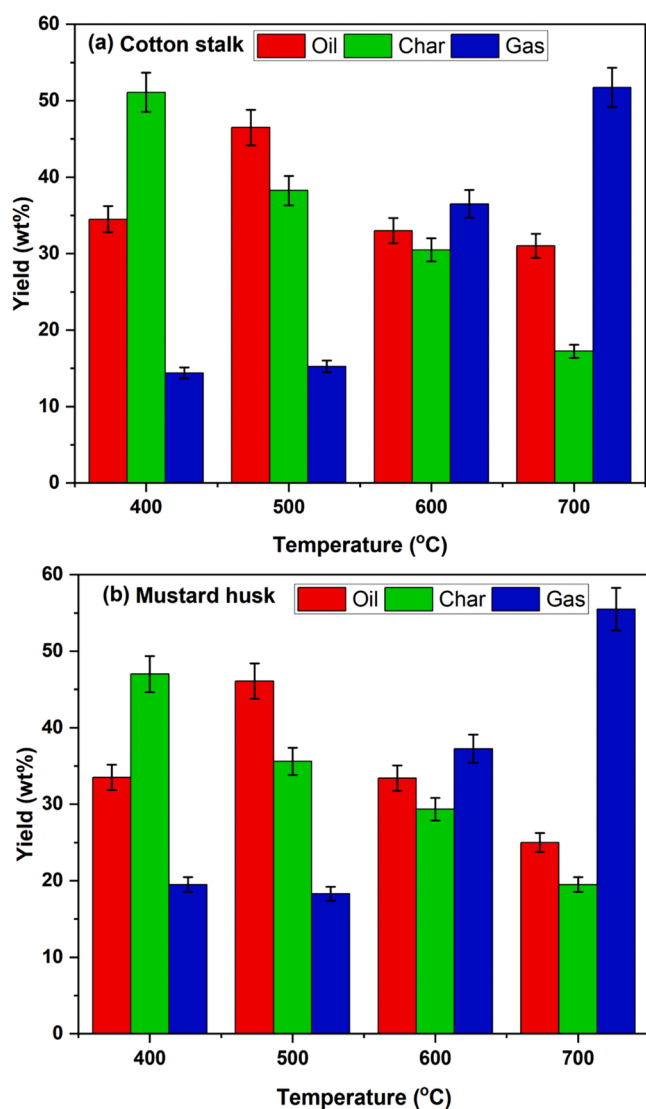


Fig. 3. Pyrolysis product yields of a) cotton stalk and b) mustard husk pyrolysis at different temperatures [Total feed input – ~3 kg; Screw rpm – 5].

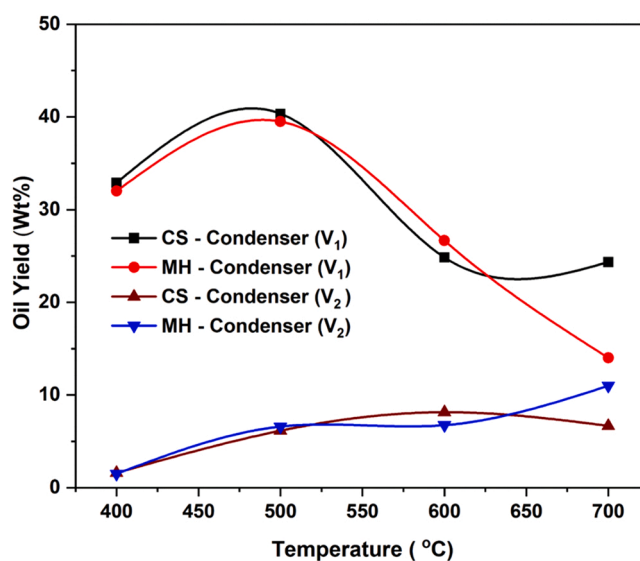


Fig. 4. Bio-oil yield distribution of cotton stalk and mustard husk at different temperatures obtained in different condenser fractions (V₁ & V₂).

the current study, the maximum bio-oil recovered, from the continuous auger reactor using the cotton stalk pellets with the size of 30 – 40 mm was ~ 46.5 wt%. In contrast to the studies mentioned above, where particles sizes of < 1 mm are used, in this study larger pellets were used with a size of > 30 mm, which favors secondary cracking reactions, a particle size of 2 mm is usually the upper limit because any further growth will accelerate the secondary pyrolysis reaction and lower the production of bio-oil. [35].

3.3. Oil analysis

The oil fractions obtained were analyzed using acetone (polar) and hexane (non-polar) for composition. As shown in Fig. 6, the chemical composition of the oil was classified into aliphatic, ketone, phenolic, nitrogenous, acid, alcohols, furan and others. It is evident from the figure that the composition of oils was relatively different with different solvents owing to its solubility. With acetone as a solvent, it was observed that oil produced from cotton stalk mainly consisted of high amounts of aliphatic such as 4,5-dihydro-2,4,4-trimethyl-, 3-

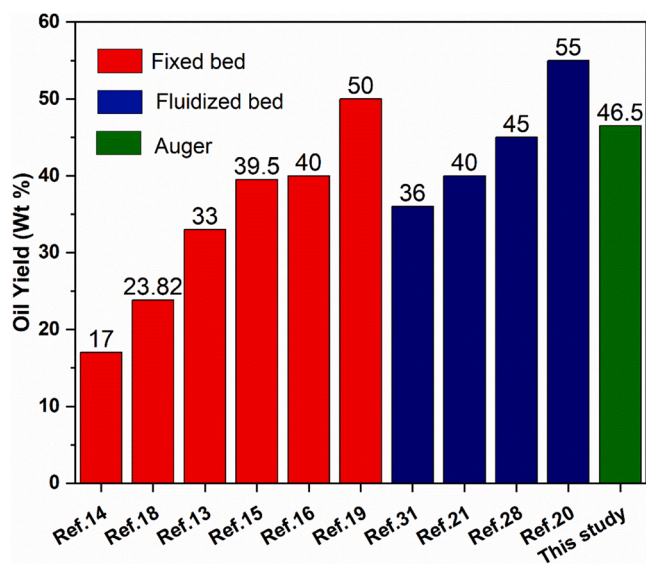


Fig. 5. Cotton stalk Pyrolysis oil yields comparison with literature.

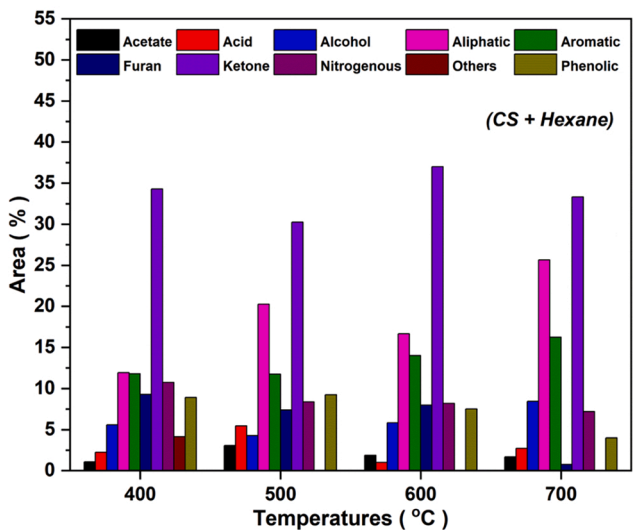
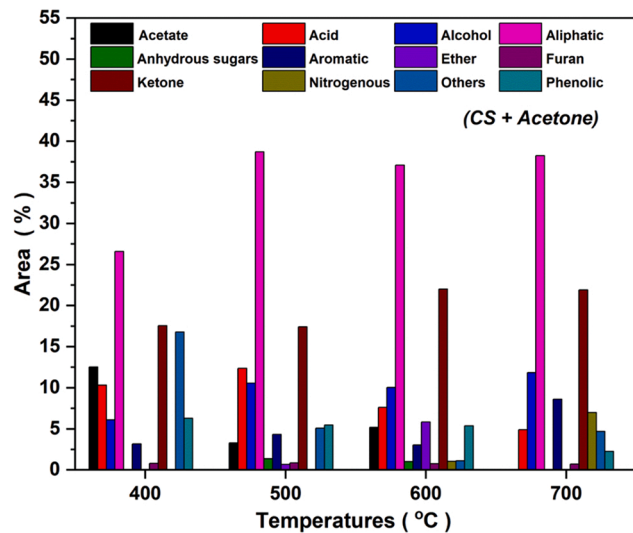


Fig. 6. Cotton stalk bio-oil composition analysis using polar (acetone) and non-polar (hexane) solvents.

Cyclopentene-1,2-diol, cis-, Hexadecane, and 1-Tetracosene. With increase in temperature from 400 °C to 500 °C, the amount of aliphatic increased from 26% to 39%. On further increasing the temperature, there was no significant change in the yield of aliphatics. Ketones were the second highest compounds present in the bio-oil and the amount of ketones were increased with increase in temperature. Ketones mainly contain 3-Penten-2-one, 4-methyl-, 1, 2-Cyclopentanedione, 3-methyl-, and Cyclohexanone, 4-acetyl- etc. Acetates were also present in good amount at 400 °C, which decreased with increase in temperature. The amount of phenolic compounds remained constant for the entire temperature range. Alcohols were gradually increased with temperature from 400 °C to 700 °C. Higher amount of acids were present at 500 °C, which reduced with further increase in temperature.

Hexane as a solvent mainly dissolved the non-polar compounds present in the oil. Higher amount of ketones were present, followed by the aliphatics and acids, in the bio-oil as shown in Fig. 5. In case of hexane, it contained Cyclopentane, 1-acetyl-1,2-epoxy-, 2-Hexanone, 3,4-dimethyl-, entanal, 2,2-dimethyl-, Bicyclo[3.1.1, heptan-2-one, 3, 4-Dihydroxy-5-methyl-dihydrofuran-2-one, 2-Cyclopenten-1-one, Cyclopentane, 1-acetyl-1, 2-epoxy-, 1, 2- Cyclopentanedione, 3-methyl. Aromatic compounds were found to be increased with increase in temperature when compared, the CS bio-oil had high amounts of aromatic compounds (e.g., Toluene, 2 H-Imidazole, 2,2,4,5-tetramethyl-, Pyrazine, 2,6-dimethyl-, Styrene, Ethylbenzene, Benzene, 1,2,4-trimethyl-, Oxazole). Most of the nitrogenous compound and furan present in the bio-oil were dissolved in Hexane solvent. These compounds typically consisted of Pyridine, 2-methyl-, N, N-Dimethylacetamide, alpha-Methyl-alpha-propylsuccinimide, Pyrazine, methyl-) and (2-Furanmethanol, tetrahydro-, 2-Furanone, 2, 5-dihydro-3, 5-dimethyl. Other than these compounds, acetates, acids and alcohols were also present in the CS bio-oil.

Acetone extracted bio-oil obtained from mustard husk showed high amounts of aliphatics (~47%) with increase in temperature. The aliphatics content reduced while the ketone content increased at higher pyrolysis operating temperatures. As shown in Fig. 7, mustard husk bio-oil had a good amount of anhydrous sugars which were almost absent in the oil produced from cotton stalk. Bio-oil contained a good amount of alcohols and phenolic compounds. Bio-oil obtained at high temperature had large amounts of mixed and unidentified compounds which may possibly be due to the interaction of different compounds. Major compounds identified in the bio-oil were Propanoic acid, 1-methylethyl ester, 1-Tridecene, Hexadecane, D-Allose, 1-Nonadecene, 1-Pentadecene, 1,2-Cyclopentanedione, 3-methyl-, 2-Furanmethanol, Oxazole, 4,5-dihydro-2,4,4-trimethyl.

Hexane extraction of bio-oil mainly consisted of ketones that was present in higher amount (40%) at 500 °C. The yield of aromatic compounds which includes Toluene, Phenol, p-Xylene were increased with temperature. In case of mustard husk, aliphatics content increased with temperature with maximum yields achieved at 600 °C as shown in Fig. 7. At lower temperatures, the yields of acidic components was found to be maximum which decreased significantly with increase in temperature. Overall, aliphatic, ketone, phenolic and acid compounds were present large amounts in the bio-oil for both cotton stalk and mustard husk. The trend of graphs for acetone and hexane were almost similar. With both extraction solvents (hexane and acetone), the aliphatic and ketones were majorly extracted followed by phenolic compounds. Majority of the hydrophenolics, carbohydrates, and sugars in their aqueous states came from lignocellulosic biomass. Furan is produced because of the hemicellulose and phenolic bonds that were cleaved during the breakdown of the β -O-4 link in the lignin [36].

Fourier Transform Infrared Spectroscopy (FTIR) analysis of bio-oil at different temperatures ranging from 400 °C to 700 °C was done to identify accompanying functional groups in the products. Spectral output for pyrolysis oil was shown in Fig. 8. The large absorbance peak of O-H stretching vibration of 3305 cm^{-1} confirms the alcohol and phenol groups in the pyrolysis liquid. The H_2O release can also be the

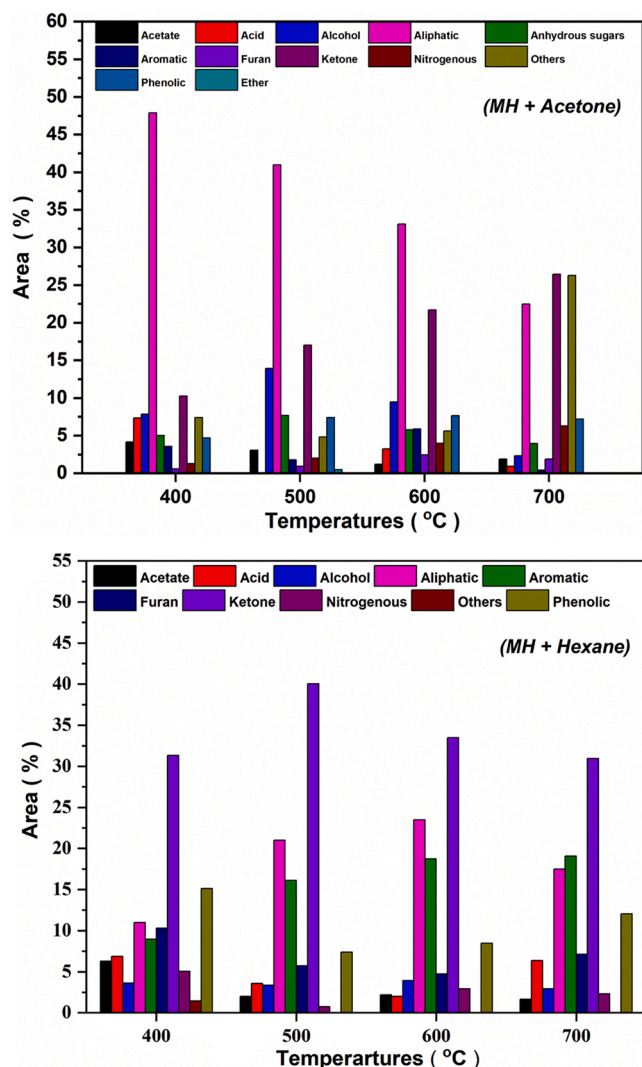


Fig. 7. Mustard husk bio-oil composition analysis using polar (acetone) and non-polar (hexane) solvents.

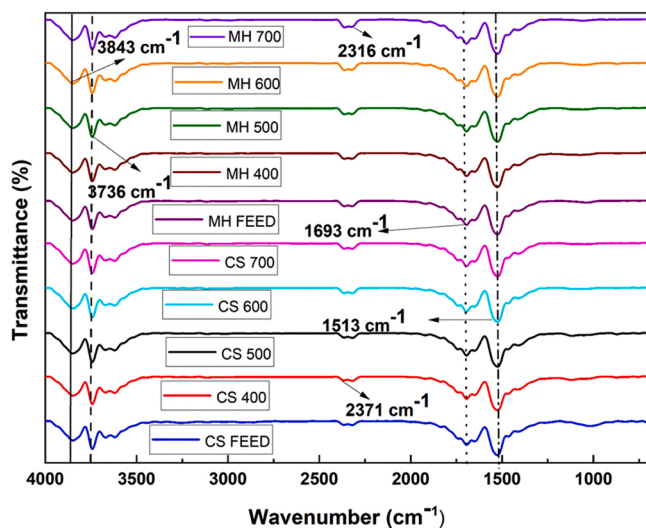


Fig. 8. FTIR spectra of bio-oil fractions at different conditions.

reason for it. The presence of ketones and aldehydes is connoted by the presence of C=O absorbance peak at 1645 cm^{-1} . The medium narrow absorbance peak of C-C bond vibration of 1449 cm^{-1} , indicates the methyl group [37]. Alcohols, carboxylic acids, ethers, and esters were represented by the potential absorbance peak of C-O bond of wave number $1112\text{--}1374\text{ cm}^{-1}$.

The amount of water present in the bio-oil obtained from both feedstocks at various temperatures is shown in Fig. 9. Cotton stalk bio-oil was found to have a lower water content than mustard husk bio-oil. Cotton stalk oil was found to have a minimum water content of 35 wt % of water and a maximum of 72 wt%, whereas mustard husks had a minimum of 79% and a maximum of 90%. These findings demonstrated that oil's water content increased when temperature was raised which may be attributed to the possible dehydration reactions that are favoured at $500\text{ }^{\circ}\text{C}$. In this work, cotton stalk oil was found to be superior compared to mustard husk oil.

The obtained oil samples from different feeds were also analysed in terms of the carbon residue and it was found that the carbon residue dropped from 26 wt% to 12 wt% with increase in temperature from $400\text{ }^{\circ}\text{C}$ to $600\text{ }^{\circ}\text{C}$ for the oils obtained from CS and MH. Based on these results, reforming these oils could result in the formation of coke, leading to a potential loss of up to 12 wt% of carbon in the form of coke. Low temperature oils tend to have a more coking tendency compared to high temperature oils.(Table 1).

3.4. Char analysis

The operating conditions of the reactor was found to be crucial for the creation of organic biochar in this experimental work, having its effects apparent not only in biochar yield but also in terms of its physicochemical properties, as indicated in Table 2. When cotton stalk and mustard husk were heated to temperatures between $400\text{ }^{\circ}\text{C}$ and $700\text{ }^{\circ}\text{C}$, the total organic carbon (TOC) content in the biochar increased from 56.80 wt% to 63.10 wt% and 61.10–64.10 wt%, respectively, while the total hydrogen and nitrogen content decreased in both the biochar. Imam et al. [38] also provided a description of a comparable investigation. According to the scientists, deprivation of hydrogen occurs as a result of the cleaving of biochar's weaker structural connections, which results in a carbon-rich substance. According to the current research, the highest carbon content was 64.10 wt% for mustard husk and 63.10 wt% for cotton stalk. This enhanced carbon to a nitrogen ratio (C/N) of around 37.88 and 47.46 in biochar produced from cotton stalk and

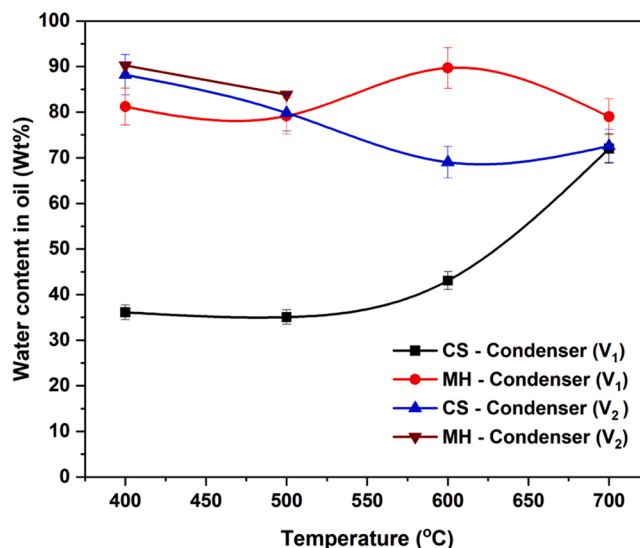


Fig. 9. Bio-oil water content of cotton stalk and mustard husk obtained from different condensers (V_1 and V_2).

Table 2
Proximate and ultimate analysis of biochar at different temperatures.

Parameters	Cotton stalk				Mustard husk			
	400 °C	500 °C	600 °C	700 °C	400 °C	500 °C	600 °C	700 °C
Loss on drying @ 110 °C (%)	5.89	5.30	6.62	6.67	5.42	6.12	5.69	7.59
Volatile Matter (%)	40.21	38.62	28.01	36.64	43.08	59.74	42.63	43.37
Fix Carbon (%)	30.48	36.85	25.6	35.31	25.68	15.47	13.92	19.67
Ash @ 800 °C (%)	23.42	19.23	39.77	21.38	25.82	18.67	37.76	29.37
Carbon (%)	56.80	63.10	62.30	61.60	61.10	61.80	64.10	62.60
Hydrogen (%)	3.18	2.07	1.48	1.02	3.03	2.65	1.17	0.87
Nitrogen (%)	1.86	1.80	1.74	1.63	1.72	1.49	1.45	1.32
Sulphur (%)	0.36	0.38	0.40	0.23	0.58	0.29	0.38	0.24
Oxygen (%)	37.8	32.65	34.08	35.52	33.57	33.77	32.9	34.97
H/C	0.06	0.03	0.02	0.02	0.05	0.04	0.02	0.01
O/C	0.67	0.52	0.55	0.58	0.55	0.55	0.51	0.56
C/N	30.55	35.15	35.86	37.88	35.5	41.56	44.32	47.46
(N + O)/C	0.70	0.55	0.58	0.60	0.58	0.57	0.54	0.58
Calorific Value (MJ/kg)	21.84	24.12	24.15	23.85	26.64	23.01	24.57	23.54
pH	8.74	8.61	8.03	7.99	8.21	8.5	8.44	8.11

mustard husk, respectively. In both situations, the amount of volatile substances dropped as the temperature rose and the amount of fixed carbon increased.

Since plants immediately absorb inorganic nitrogen via their root systems, nitrogen (N) is one of the most important nutrients to impact plant development and productivity [39,40]. Total nitrogen content is influenced by pyrolysis temperature; for both feeds, it first increases at low temperatures and further reduces at higher temperatures. The biochar's strength is influenced by the feedstock biomass utilised and the manufacturing circumstances. In this investigation, we found that cotton stalk and mustard husk biochar both contained 1.86 wt% and 1.72 wt% nitrogen, respectively.

Furthermore, Spokas' research [41] on the stability of biochar in soil revealed that a lower oxygen-to-carbon (O/C) ratio produced biochar that was more stable. The study concluded that biochar would probably have a half-life of less than 100 years when the oxygen-to-carbon molar ratio (O/C) is larger than 0.6. If it falls between 0.2 and 0.6, the half-life will be between 100 and 1000 years. The half-life is larger than 1000 years if the oxygen to carbon molar ratio is less than 0.2. The oxygen-to-carbon ratio in the present experimental investigation was 0.67 for cotton stalk and 0.56 for mustard husk; as a result, the biochar that was formed is expected to be more stable in the soil with a half-life of between 100 and 1000 years [41]. Biochar formed at 400 °C just for cotton stalks has an O/C ratio of 0.67, indicating a half-life of less than 100 years. Similar to this, the H/C ratio is a reliable predictor of the carbon structure and soil stability of biochar. The degree of

aromatization in the biochar generated is indicated by the lowest hydrogen-to-carbon molar ratio (H/C), which was found in biochar made from cotton stalk and mustard husk to be 0.02 and 0.01. At least 70% of the organic carbon in biochar is anticipated to persist in soil for at least 100 years with 95% confidence when the H/C molar ratio is less than or equal to 0.4 [42]. In this investigation, it was discovered that the biochar generated used less or the same amounts of H/C and O/C molar ratios as biochar produced in a batch-type reactor utilising a variety of agricultural wastes, animal dung, grasses, and wood [43–45]. The hydrogen and oxygen concentration of char decreases as the temperature rises. H/C ratio drops from 0.06 at 400 °C to 0.02 at 700 °C for cotton stalk and from 0.05 at 400 °C to 0.01 at 700 °C for mustard husk, showing an increase in the aromaticity and carbon-rich nature of char. Also, the drop in the ((O+N)/C) ratio, also known as the polarity index, suggests a decrease in the surface polar functional groups of biochar produced from cotton stalk at elevated pyrolysis temperatures [46]. Both cotton stalk and mustard husk exhibited high calorific values of up to 24.15 MJ kg⁻¹ and 24.57 MJ kg⁻¹ at varying temperatures of operation. All pH values of biochar examined in this work were in the alkaline range and were not substantially affected by an increase in temperature.

In Fig. 10, the surface morphology of char samples made from agricultural residues that were examined using a scanning electron microscope (SEM) at various temperatures is demonstrated. It was observed that the char surface contains high amount of pores which can reduce soil bulk density and can increase its porosity, and thus enhances

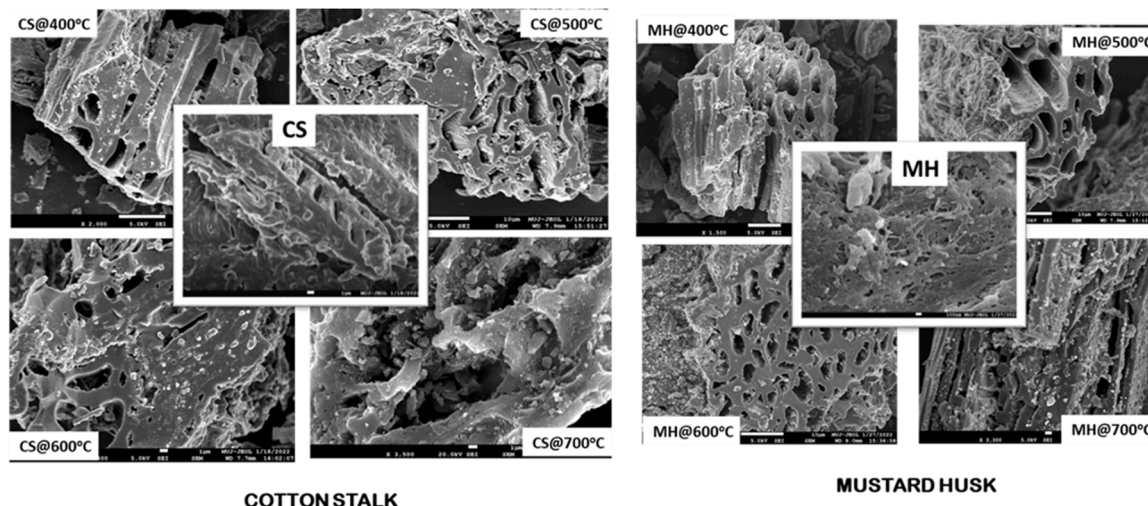


Fig. 10. FESEM analysis of cotton stalk and mustard husk biochar.

Table 3
Elemental analysis of biochar at different temperatures.

Elements	Cotton stalk (wt%)					Mustard husk (wt%)				
	Feed	400 °C	500 °C	600 °C	700 °C	Feed	400 °C	500 °C	600 °C	700 °C
C	48.7	55	70.9	74.8	75.2	36.4	55.8	78.6	81.4	80.3
O	40.4	26.6	13.3	16.3	16.4	55.7	18.6	10	13.3	10.2
Mg	0.6	0.8	1	0.9	1	1.1	1.3	0.5	0.8	0.5
Si	1.5	1	0.5	0.9	0.3	0.2	0.7	0.4	0.5	0.4
P	0.7	0.7	0.9	0.4	0.5	0.3	0.7	0.8	0.6	0.6
S	1.2	0.7	0.9	0.7	0.5	1.2	1.3	1.1	0.3	1.2
K	4.2	0.8	5.3	4.4	5	2.3	9.6	6	2.5	4.0
Ca	2.7	14.4	7.2	1.7	1.1	2.9	11.9	2	0.6	2.4

the soil properties for harvesting. It also increases the water retention capacity. The pyrolysis reaction conditions, and the composition of biomass influences the surface morphology and the quality of the biochar. Biochar showed different pore sizes which were mainly in the size range of 0.5–5 μm .

Energy Dispersive X-Ray analysis showed that carbon content of the biochar produced from cotton stalk and mustard husk increased with increase in temperature as shown in Table 3. High carbon content in the biochar at higher temperature was mainly due to the fixed carbon

present in the feed materials. Biochar contains good amount of micro-nutrients which includes P, K, Mg, Ca and S. Mustard husk contains high amount of potassium (K) compared with cotton stalk. Elemental oxygen decreased from 26.6 wt% to 13.3 wt% for cotton stalk and 18.6–10 wt% for mustard husk. Overall, with increases in temperature, the carbon density increased in the biochar. The oxygenated compounds were decomposed at higher temperature.

Functional groups in the char was analysed using Fourier Transform Infrared Spectroscopy (FTIR) at various temperatures ranging from 400 °C to 700 °C. Fig. 11 display the spectral result for the char produced during pyrolysis. Presence of aromatic C–H group was observed at 2371 cm^{-1} and 2316 cm^{-1} and it confirms the occurrence of N–H functional group [47]. The peak at 1693 cm^{-1} represents the stretching of carbonyl bonds (C=O) of the carboxylic groups or conjugated ketone. Corresponding weak R–OH band was also found in the band 3900–3700 cm^{-1} representing a monomeric alcohol, phenol and carboxylic groups.

3.4.1. Thermal decomposition behaviour

Thermal stability of biochar samples obtained at different conditions was analysed through TGA studies as shown in Fig. 12 where it can be observed that with increasing pyrolysis conditions the moisture content of the char from cotton stalk increased from 5% to 10%. No significant weight loss (< 5%) with respect to moisture content in the mustard husk was noticed with increasing pyrolysis temperature. It is noteworthy that the biochar of mustard husk obtained at lower pyrolysis temperatures decomposed rapidly at 500 °C while mustard husk biochar obtained at 600 °C and 700 °C were relatively stable enough and degraded very slowly. Similar behaviour of biochar decomposition was noticed with cotton stalk derived biochar. The final residues or mineral matter of different biochar derived from cotton stalk and mustard husk at different

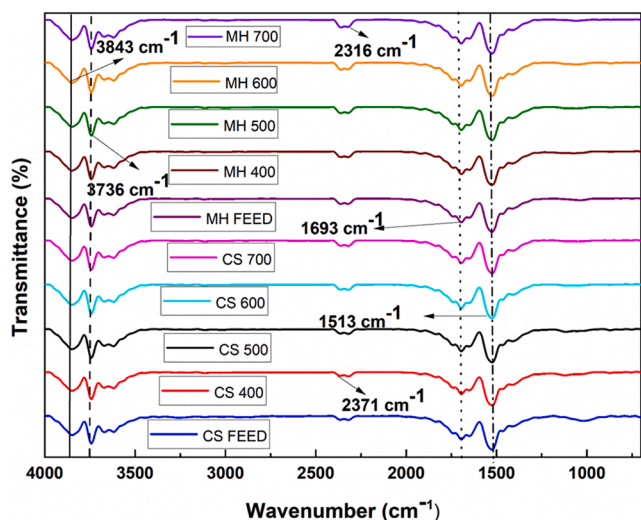


Fig. 11. FTIR spectra of biochar at different conditions. > .

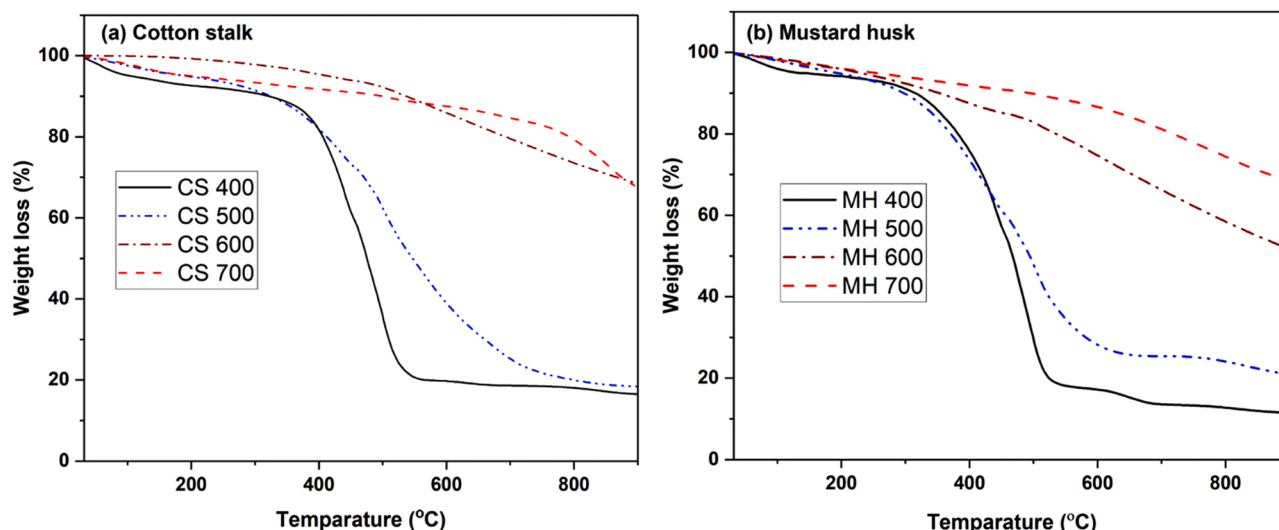


Fig. 12. Thermal decomposition behaviour of the obtained biochar (a) Cotton stalk and (b) Mustard husk at different conditions.

conditions is in the range 10–25%.

4. Conclusions

In this study, continuous slow pyrolysis of cotton stalk and mustard husk in auger reactor at different temperatures ranging from 400° to 700°C is reported. Results showed that with increase in temperature, the oil yield increased up to 500 °C and reduced beyond this temperature. The char yield decreased, and gas yield increased with increasing temperature. The product yield with mustard husk is quite similar to that of cotton stalk feed. However, the water content in cotton stalk bio-oil was found to be lower than mustard husk bio-oil, and the water content was found to be increasing with temperature. Oil analysis indicated presence of aliphatic, ketonic, phenolic and acidic compounds in bio-oils obtained from both the feedstock. Additionally, the chars obtained have high calorific and nutrient value, and can be used for various agricultural and non-agricultural applications. The results of these studies are highly promising and will lay the foundation for process scale up and product upgradation using such agricultural residue material.

Funding sources

The authors wish to express their gratitude to Department of Science and Technology, Delhi, India (Grant: DST/TDT/WM/2019/62(G)) and Bharuch Enviro Infrastructure Ltd. Ankleshwar, Gujarat, India (Grant: BEIL/ANK/2020/ MOU-MUJ).

CRedit authorship contribution statement

Sivasankar Kakku: Conceptualization, Investigation, Methodology, Validation, Writing – original draft. **Sowkhya Naidu:** Investigation, Methodology, Validation, Writing – review & editing. **Mukesh Bhatt:** Investigation, Methodology, Writing – review & editing. **Anand G. Chakinala:** Validation, Supervision, Writing – review & editing. **Jyeshtharaj Joshi:** Writing – review & editing. **Shina Gautam:** Writing – review & editing. **Kaustubha Mohanty:** Writing – review & editing. **Gaurav Kataria:** Writing – review & editing. **Abhishek Sharma:** Conceptualization, Validation, Supervision, Writing – review & editing.

Declaration of Competing Interest

The authors declare that they have no known competing financial interests or personal relationships that could have appeared to influence the work reported in this paper.

Data Availability

No data was used for the research described in the article.

Acknowledgement

The corresponding author would like to thank Department of Science and Technology, Government of India, and Bharuch Enviro Infrastructure Limited, India, for their financial support and Central Analytical Facility (CAF), Sophisticated Analytical Instrument Facility (SAIF) and Waste to Resources laboratory, Manipal University Jaipur for providing analytical and experimental facilities for this research work.

References

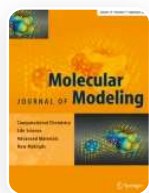
- B.G. Desai, CO₂ emissions - drivers across time and countries, *Curr. Sci.* 115 (2018), <https://doi.org/10.18520/cs/v115/i3/386-387>.
- International Energy Agency, *Renewables Information - Overview (2020 Edition)*, IEA Stat. (2020).
- M. Svazas, V. Navickas, E. Krajnakova, J. Nakonieczny, Sustainable supply chain of the biomass cluster as a factor for preservation and enhancement of forests, *J. Int. Stud.* 12 (2019), <https://doi.org/10.14254/2071-8330.2019/12-2/20>.
- V. Daioglou, J.C. Doelman, B. Wicke, A. Faaij, D.P. van Vuuren, Integrated assessment of biomass supply and demand in climate change mitigation scenarios, *Glob. Environ. Change* 54 (2019), <https://doi.org/10.1016/j.gloenvcha.2018.11.012>.
- F. Creutzig, N.H. Ravindranath, G. Berndes, S. Bolwig, R. Bright, F. Cherubini, H. Chum, E. Corbera, M. Delucchi, A. Faaij, J. Fargione, H. Haberl, G. Heath, O. Luccon, R. Plevin, A. Popp, C. Robledo-Abad, S. Rose, P. Smith, A. Stromman, S. Suh, O. Maser, *Bioenergy and climate change mitigation: an assessment*, *GCB Bioenergy* 7 (2015), <https://doi.org/10.1111/gcbb.12205>.
- P. Stegmann, M. Londo, M. Junginger, The circular bioeconomy: Its elements and role in European bioeconomy clusters, *Resour. Conserv. Recycl.* X 6 (2020), <https://doi.org/10.1016/j.rccr.2019.100029>.
- Y. Kang, Q. Yang, P. Bartocci, H. Wei, S.S. Liu, Z. Wu, H. Zhou, H. Yang, F. Fantozzi, H. Chen, *Bioenergy in China: evaluation of domestic biomass resources and the associated greenhouse gas mitigation potentials*, *Renew. Sustain. Energy Rev.* 127 (2020), <https://doi.org/10.1016/j.rser.2020.109842>.
- J. Dach, P. Boniecki, J. Przybył, D. Janczak, A. Lewicki, W. Czekala, K. Witaszek, P. C. Rodríguez Carmona, M. Ciešlik, *Energetic efficiency analysis of the agricultural biogas plant in 250kWe experimental installation*, *Energy* 69 (2014), <https://doi.org/10.1016/j.energy.2014.02.013>.
- P. Rao, V. Rathod, *Valorization of food and agricultural waste: a step towards greener future*, *Chem. Rec.* 19 (2019), <https://doi.org/10.1002/tcr.201800094>.
- D. Vamvuka, E. Kakaras, E. Kastanaki, P. Grammelis, *Pyrolysis characteristics and kinetics of biomass residuals mixtures with lignite*, *Fuel* (2003), [https://doi.org/10.1016/S0016-2361\(03\)00153-4](https://doi.org/10.1016/S0016-2361(03)00153-4).
- A. Demirbas, *Biofuels sources, biofuel policy, biofuel economy and global biofuel projections*, *Energy Convers. Manag.* 49 (2008), <https://doi.org/10.1016/j.enconman.2008.02.020>.
- B. Biswas, N. Pandey, Y. Bisht, R. Singh, J. Kumar, T. Bhaskar, *Pyrolysis of agricultural biomass residues: Comparative study of corn cob, wheat straw, rice straw and rice husk*, *Bioresour. Technol.* 237 (2017), <https://doi.org/10.1016/j.biortech.2017.02.046>.
- International Production Assessment Division: *Rapeseed 2022 world production*, (n.d.).
- Cotton: *World Markets and Trade*, 2023.
- R. Al Afif, S.S. Anayah, C. Pfeifer, *Batch pyrolysis of cotton stalks for evaluation of biochar energy potential*, in: *E.3S. Web Conf.*, 2019. <https://doi.org/10.1051/e3sconf/201911600001>.
- Ashish Pratap Singh Chouhan, A. Slow Pyrolysis of Cotton Stalk (Gossypium arboreum) Waste for Bio-Oil Production, *J. Pharm. Chem. Biol. Sci.* 3 (n.d.) 143–149.
- A.E. Pütün, *Biomass to bio-oil via fast pyrolysis of cotton straw and stalk*, *Energy Sources* 24 (2002), <https://doi.org/10.1080/009083102317243656>.
- Y. Chen, H. Yang, X. Wang, S. Zhang, H. Chen, *Biomass-based pyrolytic polygeneration system on cotton stalk pyrolysis: influence of temperature*, *Bioresour. Technol.* 107 (2012), <https://doi.org/10.1016/j.biortech.2011.10.074>.
- G. Chen, J. Andries, H. Spliethoff, D.Y.C. Leung, *Experimental investigation of biomass waste (rice straw, cotton stalk, and pine sawdust) pyrolysis characteristics*, *Energy Sources* 25 (2003), <https://doi.org/10.1080/00908310390142361>.
- A.E. Pütün, N. Özbay, E.P. Önal, E. Pütün, *Fixed-bed pyrolysis of cotton stalk for liquid and solid products*, *Fuel Process. Technol.* 86 (2005), <https://doi.org/10.1016/j.fuproc.2004.12.006>.
- X. Chen, Y. Chen, H. Yang, W. Chen, X. Wang, H. Chen, *Fast pyrolysis of cotton stalk biomass using calcium oxide*, *Bioresour. Technol.* 233 (2017), <https://doi.org/10.1016/j.biortech.2017.02.070>.
- J. lu Zheng, W. ming Yi, N. na Wang, *Bio-oil production from cotton stalk*, *Energy Convers. Manag.* 49 (2008), <https://doi.org/10.1016/j.enconman.2007.11.005>.
- H. Sui, H. Yang, J. Shao, X. Wang, Y. Li, H. Chen, *Fractional condensation of multicomponent vapors from pyrolysis of cotton stalk*, *Energy Fuels* 28 (2014), <https://doi.org/10.1021/ef5006012>.
- S. Sirijanorn, K. Sriprateep, A. Pattiya, *Pyrolysis of cassava rhizome in a counter-rotating twin screw reactor unit*, *Bioresour. Technol.* 139 (2013), <https://doi.org/10.1016/j.biortech.2013.04.024>.
- Y. Yang, J.G. Brammer, A.S.N. Mahmood, A. Hornung, *Intermediate pyrolysis of biomass energy pellets for producing sustainable liquid, gaseous and solid fuels*, *Bioresour. Technol.* 169 (2014), <https://doi.org/10.1016/j.biortech.2014.07.044>.
- E. Henrich, N. Dahmen, F. Weirich, R. Reimert, C. Kornmayer, *Fast pyrolysis of lignocellulosics in a twin screw mixer reactor*, *Fuel Process. Technol.* 143 (2016), <https://doi.org/10.1016/j.fuproc.2015.11.003>.
- P. Li, X. Shi, X. Wang, J. Song, S. Fang, J. Bai, G. Zhang, C. Chang, S. Pang, *Bio-oil from biomass fast pyrolysis: yields, related properties and energy consumption analysis of the pyrolysis system*, *J. Clean. Prod.* 328 (2021), <https://doi.org/10.1016/j.jclepro.2021.129613>.
- A.K. Mishra, R.K. Misra, M. Mohanty, *Value-added biocarbon production through slow pyrolysis of mixed bio-oil wastes: studies on their physicochemical characteristics and structure–property–processing co-relation*, *Biomass Convers. Biorefin.* (2022), <https://doi.org/10.1007/s13399-022-02906-2>.
- R. Landrat, M. Abawalo, M.T. Piko ñ, K. Turczyn, *Bio-oil derived from teff husk via slow pyrolysis process in fixed bed reactor and its characterization*, *Energies* (2022) <https://doi.org/https://doi.org/10.3390/en15249605>.
- F. Rego, H. Xiang, Y. Yang, J.L. Ordoñas, K. Chong, J. Wang, A. Bridgwater, *Investigation of the role of feedstock properties and process conditions on the slow pyrolysis of biomass in a continuous auger reactor*, *J. Anal. Appl. Pyrolysis* 161 (2022), <https://doi.org/10.1016/j.jaap.2021.105378>.

- [31] N. Ali, P. Ubhrani, M. Tagotra, M. Ahire, A step towards environmental waste management and sustainable biofuel (ethanol) production from waste banana peelings, *Am. J. Eng. Res.* 3 (2014).
- [32] J.G. Speight, *Handbook of Petroleum Product Analysis*, John Wiley & Sons, 2015.
- [33] J.G. Speight, The chemistry and technology of petroleum, *Chem. Technol. Pet.* (2014), <https://doi.org/10.1201/b16559>.
- [34] M.C. Stokes Hughes, L. Mcfall, M. Christiansen, N. Zepernick, Comparison of fuel yield of biomaterials between fast pyrolysis and gasification, *PAM Rev. Energy Sci. Technol.* 4 (2017), <https://doi.org/10.5130/pamr.v4i0.1448>.
- [35] K.M. Qureshi, A.N. Kay Lup, S. Khan, F. Abnisa, W.M.A. Wan Daud, Optimization of palm shell pyrolysis parameters in helical screw fluidized bed reactor: Effect of particle size, pyrolysis time and vapor residence time, *Clean. Eng. Technol.* 4 (2021), <https://doi.org/10.1016/j.clet.2021.100174>.
- [36] J.N. Murwanashyaka, H. Pakdel, C. Roy, Step-wise and one-step vacuum pyrolysis of birch-derived biomass to monitor the evolution of phenols, *J. Anal. Appl. Pyrolysis* 60 (2001), [https://doi.org/10.1016/S0165-2370\(00\)00206-0](https://doi.org/10.1016/S0165-2370(00)00206-0).
- [37] N. Ali, M. Saleem, K. Shahzad, A. Chughtai, Bio-oil production from fast pyrolysis of cotton stalk in fluidized bed reactor, *Arab. J. Sci. Eng.* 40 (2015), <https://doi.org/10.1007/s13369-015-1801-z>.
- [38] T. Imam, S. Capareda, Characterization of bio-oil, syn-gas and bio-char from switchgrass pyrolysis at various temperatures, *J. Anal. Appl. Pyrolysis* 93 (2012), <https://doi.org/10.1016/j.jaap.2011.11.010>.
- [39] J. Lynch, Root architecture and plant productivity, *Plant Physiol.* 109 (1995), <https://doi.org/10.1104/pp.109.1.7>.
- [40] C.J. Atkinson, J.D. Fitzgerald, N.A. Hipps, Potential mechanisms for achieving agricultural benefits from biochar application to temperate soils: a review, *Plant Soil* 337 (2010), <https://doi.org/10.1007/s11104-010-0464-5>.
- [41] K.A. Spokas, Review of the stability of biochar in soils: Predictability of O:C molar ratios, *Carbon Manag.* 1 (2010), <https://doi.org/10.4155/cmt.10.32>.
- [42] A. Budai, A.R. Zimmerman, A.L. Cowie, J.B.W. Webber, B.P. Singh, B. Glaser, C.A. Masiello, D. Andersson, F. Shields, J. Lehmann, M. Camps Arbestain, M. Williams, S. Sohi, S. Joseph, Biochar Carbon Stability Test Method: An assessment of methods to determine biochar carbon stability, *Int. Biochar Initiat.* (2013).
- [43] L. Wang, A. Shahbazi, M.A. Hanna, Characterization of corn stover, distiller grains and cattle manure for thermochemical conversion, *Biomass Bioenergy* 35 (2011), <https://doi.org/10.1016/j.biombioe.2010.08.018>.
- [44] K.B. Cantrell, P.G. Hunt, M. Uchimiya, J.M. Novak, K.S. Ro, Impact of pyrolysis temperature and manure source on physicochemical characteristics of biochar, *Bioresour. Technol.* 107 (2012), <https://doi.org/10.1016/j.biortech.2011.11.084>.
- [45] X. He, Z. Liu, W. Niu, L. Yang, T. Zhou, D. Qin, Z. Niu, Q. Yuan, Effects of pyrolysis temperature on the physicochemical properties of gas and biochar obtained from pyrolysis of crop residues, *Energy* 143 (2018), <https://doi.org/10.1016/j.energy.2017.11.062>.
- [46] X. Xiao, Z. Chen, B. Chen, H/C atomic ratio as a smart linkage between pyrolytic temperatures, aromatic clusters and sorption properties of biochars derived from diverse precursory materials, *Sci. Rep.* 6 (2016), <https://doi.org/10.1038/srep22644>.
- [47] J.A. Rodriguez, J.F. Lustosa Filho, L.C.A. Melo, I.R. de Assis, T.S. de Oliveira, Influence of pyrolysis temperature and feedstock on the properties of biochars produced from agricultural and industrial wastes, *J. Anal. Appl. Pyrolysis* 149 (2020), <https://doi.org/10.1016/j.jaap.2020.104839>.

Tailoring epoxy coating with acetoxime derivative of zinc for advanced anticorrosive performance on mild steel: experimental and computational insights

Original Paper Published: 30 August 2023

Volume 29, article number 300, (2023) Cite this article



Journal of Molecular Modeling

[Aims and scope](#)

[Submit manuscript](#)

[Ishita Chopra](#), [Saraswati Kumari Ola](#), [S. Gopalakrishnan](#) & [Veena Dhayal](#)

135 Accesses [Explore all metrics](#) →

Abstract



Context

In this work, the corrosion inhibitive effect of acetoxime derivative of zinc chloride, ($\text{ZnCl}_2 \cdot 2\text{HON}=\text{C}(\text{CH}_3)_2$) (ZA), was investigated on mild steel in epoxy/polyamide coating. ZA was used to modify diglycidyl ether of bisphenol A (DGEBA) to yield novel anticorrosive coating (epoxy-ZA) with excellent barrier characteristic. The dispersal of ZA may lead to the formation of Zn–O–C and O–Zn–O linkages in the polymer framework which act as inorganic fillers producing a dense structure of hybrid coating. In electrochemical findings, electrochemical impedance spectroscopy (EIS) and Tafel polarization (TP) indicate higher protection efficiency for epoxy-ZA coatings (99.99 and

99.93 % for EIS and TP, respectively) as compared to others. Using surface analysis and electrochemical data, it was concluded that an inhibition synergy was developed when ZA was taken instead of acetoxime or zinc chloride (ZC) alone in the coating formulation.

Methods

Fourier transform infrared (FT-IR) was used to investigate epoxy interaction with zinc compounds and scanning electron microscopy (SEM) was used to investigate morphology of the samples. To reinforce the experimental results, reactivity of crosslinked epoxy and epoxy-ZA coatings with metallic surface was also explored using density functional theory (DFT) with basis set B3LYP/6-311G(d,p) and molecular dynamics (MD) methods by using Forcite module. Modification of epoxy with ZA enhances its interaction with steel surface in dry as well as in wet conditions as indicated by the adhesion energy calculated by MD simulations.

 This is a preview of subscription content, [log in via an institution](#)  to check access.

Access this article

[Log in via an institution](#)

Buy article PDF 39,95 €

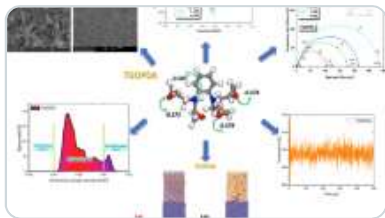
Price includes VAT (India)

Instant access to the full article PDF.

Rent this article via [DeepDyve](#) 

[Institutional subscriptions](#) →

Similar content being viewed by others



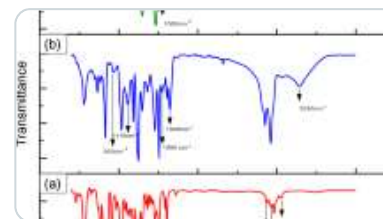
Synthesis and Characterization of New Macromolecular Epoxy Resin as an Effective...

Article | 13 February 2024



Robust corrosion guard, mechanical and UV aging properties of metal complex/epoxy...

Article | Open access
21 July 2022



Synergistic anticorrosive properties of titanium tetra-acetoximate modified...

Article | 25 August 2023

Data availability

The authors confirm that the data supporting the findings of this study are available within the article (and/or) its supplementary materials.

References

1. Chigondo M, Chigondo F (2016) Recent natural corrosion inhibitors for mild steel: an overview. *J Chem* 2016. <https://doi.org/10.1155/2016/6208937>
2. Tabatabaei Majd M, Bahlakeh G, Dehghani A et al (2019) Combined molecular simulation, DFT computation and electrochemical studies of the mild steel corrosion protection against NaCl solution using aqueous Eucalyptus leaves extract molecules linked with zinc ions. *J Mol Liq* 294:111550. <https://doi.org/10.1016/J.MOLLIQ.2019.111550>
3. Dagdag O, el Harfi A, Essamri A et al (2018) Phosphorous-based epoxy resin composition as an effective anticorrosive coating for steel. *Int J Ind Chem* 9:231–240. <https://doi.org/10.1007/S40090-018-0152-5/FIGURES/13>

[Article](#) [CAS](#) [Google Scholar](#)

4. Kumari Ola S, Priyanka SS et al (2021) A review: graphene modified polymer coatings for corrosion protection. IOP Conf Ser Earth Environ Sci 796:012027.

<https://doi.org/10.1088/1755-1315/796/1/012027>

[Article](#) [Google Scholar](#)

5. Dagdag O, Hsissou R, el Harfi A et al (2020) Epoxy resins and their zinc composites as novel anti-corrosive materials for copper in 3% sodium chloride solution: experimental and computational studies. J Mol Liq 315:113757.

<https://doi.org/10.1016/J.MOLLIQ.2020.113757>

[Article](#) [CAS](#) [Google Scholar](#)

6. Palimi MJ, Alibakhshi E, Ramezanzadeh B et al (2018) Screening the anti-corrosion effect of a hybrid pigment based on zinc acetyl acetonate on the corrosion protection performance of an epoxy-ester polymeric coating. J Taiwan Inst Chem Eng 82:261–272. <https://doi.org/10.1016/J.JTICE.2017.10.014>

[Article](#) [CAS](#) [Google Scholar](#)

7. Aboorvakani R, Kennady Vethanathan SJ, Madhu KU (2020) Influence of Zn concentration on zinc oxide nanoparticles and their anti-corrosion property. J Alloys Compd 834:155078. <https://doi.org/10.1016/J.JALLCOM.2020.155078>

[Article](#) [CAS](#) [Google Scholar](#)

8. Wan S, Chen H, Ma X et al (2021) Anticorrosive reinforcement of waterborne epoxy coating on Q235 steel using NZ/BNNS nanocomposites. Prog Org Coat 159:106410.

<https://doi.org/10.1016/J.PORGCOAT.2021.106410>

[Article](#) [CAS](#) [Google Scholar](#)

9. Joz Majidi H, Mirzaee A, Jafari SM et al (2020) Fabrication and characterization of graphene oxide-chitosan-zinc oxide ternary nano-hybrids for the corrosion inhibition of mild steel. *Int J Biol Macromol* 148:1190–1200.

<https://doi.org/10.1016/J.IJBIOMAC.2019.11.060>

[Article](#) [CAS](#) [PubMed](#) [Google Scholar](#)

10. Asaldoust S, Ramezanzadeh B (2020) Synthesis and characterization of a high-quality nanocontainer based on benzimidazole-zinc phosphate (ZP-BIM) tailored graphene oxides; a facile approach to fabricating a smart self-healing anti-corrosion system. *J Colloid Interface Sci* 564:230–244.

<https://doi.org/10.1016/J.JCIS.2019.12.122>

[Article](#) [CAS](#) [PubMed](#) [Google Scholar](#)

11. Chopra I, Ola SK, Priyanka et al (2022) Recent advances in epoxy coatings for corrosion protection of steel: experimental and modelling approach-A review. *Mater Today Proc.* <https://doi.org/10.1016/J.MATPR.2022.04.659>

12. Ibrahim M, Kannan K, Parangusan H et al (2020) Enhanced corrosion protection of epoxy/ZnO-NiO nanocomposite coatings on steel. *Coatings* 10(10):783.

<https://doi.org/10.3390/COATINGS10080783>

[Article](#) [CAS](#) [Google Scholar](#)

13. Kirtay S (2014) Characterization of SiO₂-TiO₂ Hybrid corrosion protective coatings on mild steel. *J Mater Eng Perform* 12(23):4309–4315.

<https://doi.org/10.1007/S11665-014-1218-Y>

[Article](#) [Google Scholar](#)

14. Hasnidawan JN, Azlina HN, Norita H et al (2017) ZnO Nanoparticles for anti-corrosion nanocoating of carbon steel. *Mater Sci Forum* 894:76–80.

<https://doi.org/10.4028/WWW.SCIENTIFIC.NET/MSF.894.76>

15. Ghaffari MS, Naderi R, Sayehbani M (2015) The effect of mixture of mercaptobenzimidazole and zinc phosphate on the corrosion protection of epoxy/polyamide coating. *Prog Org Coat* 86:117–124.
<https://doi.org/10.1016/J.PORGCOAT.2015.04.020>

[Article](#) [CAS](#) [Google Scholar](#)

16. Alinejad S, Naderi R, Mahdavian M (2017) Effect of inhibition synergism of zinc chloride and 2-mercaptobenzoxazole on protective performance of an ecofriendly silane coating on mild steel. *J Ind Eng Chem* 48:88–98.
<https://doi.org/10.1016/J.JIEC.2016.12.024>

[Article](#) [CAS](#) [Google Scholar](#)

17. Al-Masoud MA, Khalaf MM, Mohamed IMA et al (2022) Computational, kinetic, and electrochemical studies of polyaniline functionalized ZnO and ZnO-SiO₂ nanoparticles as corrosion protection films on carbon steel in acidic sodium chloride solutions. *J Ind Eng Chem* 112:398–422. <https://doi.org/10.1016/J.JIEC.2022.05.037>

[Article](#) [CAS](#) [Google Scholar](#)

18. Naderi R, Mahdavian M, Attar MM (2009) Electrochemical behavior of organic and inorganic complexes of Zn(II) as corrosion inhibitors for mild steel: solution phase study. *Electrochim Acta* 54:6892–6895.
<https://doi.org/10.1016/J.ELECTACTA.2009.06.073>

[Article](#) [CAS](#) [Google Scholar](#)

19. Mahdavian M, Naderi R (2011) Corrosion inhibition of mild steel in sodium chloride solution by some zinc complexes. *Corros Sci* 53:1194–1200.
<https://doi.org/10.1016/J.CORSCI.2010.12.013>

20. Askari F, Ghasemi E, Ramezanzadeh B, Mahdavian M (2014) Mechanistic approach for evaluation of the corrosion inhibition of potassium zinc phosphate pigment on the steel surface: application of surface analysis and electrochemical techniques. *Dyes Pigments* 109:189–199. <https://doi.org/10.1016/J.DYEPIG.2014.05.024>

[Article](#) [CAS](#) [Google Scholar](#)

21. Alibakhshi E, Ghasemi E, Mahdavian M (2014) Sodium zinc phosphate as a corrosion inhibitive pigment. *Prog Org Coat* 77:1155–1162. <https://doi.org/10.1016/J.PORGOAT.2014.03.027>

[Article](#) [CAS](#) [Google Scholar](#)

22. Mahdavian MA, Attar MM (2005) Investigation on zinc phosphate effectiveness at different pigment volume concentrations via electrochemical impedance spectroscopy. *Electrochim Acta* 50:4645–4648. <https://doi.org/10.1016/J.ELECTACTA.2005.02.015>

[Article](#) [Google Scholar](#)

23. Poshtiban F, Bahlakeh G, Ramezanzadeh B (2019) A detailed computational exploration and experimental surface/electrochemical analyses of mild steel functionalized by zinc-aminotris methylene phosphonic acid complex film. *Appl Surf Sci* 495:143582. <https://doi.org/10.1016/J.APSUSC.2019.143582>

[Article](#) [CAS](#) [Google Scholar](#)

24. Rezaee N, Attar MM, Ramezanzadeh B (2013) Studying corrosion performance, microstructure and adhesion properties of a room temperature zinc phosphate conversion coating containing Mn²⁺ on mild steel. *Surf Coat Technol* 236:361–367. <https://doi.org/10.1016/J.SURFCOAT.2013.10.014>

25. Ola SK, Chopra I, Choudhary P et al (2022) A review of nanoparticle coating with galvanized steel and industrially significant zinc corrosion inhibitors. *NanoWorld J* 8:185–193. <https://doi.org/10.17756/nwj.2022-s1-029>

[Article](#) [CAS](#) [Google Scholar](#)

26. Atal MK, Sharma R, Saini A et al (2016) Synthesis and characterization of organotin(IV) semicarbazones: potential precursors for nanosized tin oxide. *J Solgel Sci Technol* 79:114–121. <https://doi.org/10.1007/S10971-016-4013-4/METRICS>

[Article](#) [CAS](#) [Google Scholar](#)

27. Li X, Deng S, Xie X (2014) Experimental and theoretical study on corrosion inhibition of oxime compounds for aluminium in HCl solution. *Corros Sci* 81:162–175. <https://doi.org/10.1016/J.CORSCI.2013.12.021>

[Article](#) [CAS](#) [Google Scholar](#)

28. Saini A, Laxmi Sharma J, Sharma RK et al (2019) Zinc oxide derived from zinc(II)/acetoxime system: formation pathway and solar-driven photocatalytic and antimicrobial applications. *J Sol-Gel Sci Technol* 91:644–653. <https://doi.org/10.1007/S10971-019-05061-9>

[Article](#) [CAS](#) [Google Scholar](#)

29. Williams DBG, Lawton M (2010) Drying of organic solvents: quantitative evaluation of the efficiency of several desiccants. *J Org Chem* 75:8351–8354. https://doi.org/10.1021/JO101589H/ASSET/IMAGES/MEDIUM/JO-2010-01589H_0003.GIF

[Article](#) [CAS](#) [PubMed](#) [Google Scholar](#)

30. Li X, Deng S, Fu H, Mu G (2008) Synergistic inhibition effect of rare earth cerium(IV) ion and anionic surfactant on the corrosion of cold rolled steel in H₂SO₄ solution. *Corros Sci* 50:2635–2645. <https://doi.org/10.1016/J.CORSCI.2008.06.026>
[Article](#) [CAS](#) [Google Scholar](#)
31. Li X, Deng S, Fu H, Li T (2009) Adsorption and inhibition effect of 6-benzylaminopurine on cold rolled steel in 1.0 M HCl. *Electrochim Acta* 54:4089–4098. <https://doi.org/10.1016/J.ELECTACTA.2009.02.084>
[Article](#) [CAS](#) [Google Scholar](#)
32. Hsissou R, Benhiba F, Echihi S et al (2021) Performance of curing epoxy resin as potential anticorrosive coating for carbon steel in 3.5% NaCl medium: combining experimental and computational approaches. *Chem Phys Lett* 783:139081. <https://doi.org/10.1016/J.CPLETT.2021.139081>
[Article](#) [CAS](#) [Google Scholar](#)
33. Hsissou R, Benhiba F, El Aboubi M et al (2022) Synthesis and performance of two ecofriendly epoxy resins as a highly efficient corrosion inhibition for carbon steel in 1 cM HCl solution: DFT, RDF, FFV and MD approaches. *Chem Phys Lett* 806:139995. <https://doi.org/10.1016/J.CPLETT.2022.139995>
[Article](#) [CAS](#) [Google Scholar](#)
34. Choudhary S, Garg A, Mondal K (2016) Relation between open circuit potential and polarization resistance with rust and corrosion monitoring of mild steel. *J Mater Eng Perform* 25(7):2969–2976. <https://doi.org/10.1007/S11665-016-2112-6>
[Article](#) [CAS](#) [Google Scholar](#)
35. Lu BT, Luo JL, Norton PR, Ma HY (2009) Effects of dissolved hydrogen and elastic and plastic deformation on active dissolution of pipeline steel in anaerobic

groundwater of near-neutral pH. *Acta Mater* 57:41–49.

<https://doi.org/10.1016/J.ACTAMAT.2008.08.035>

[Article](#) [CAS](#) [Google Scholar](#)

36. de Lara LR, Jagdheesh R, Ocaña JL (2016) Corrosion resistance of laser patterned ultrahydrophobic aluminium surface. *Mater Lett* 184:100–103.

<https://doi.org/10.1016/J.MATLET.2016.08.022>

[Article](#) [Google Scholar](#)

37. Berrani A, Meryem Z, Benassaoui H et al (2018) Evaluation of inhibitory effect of the methanolic extract of the two parts from *Anabasis aretioides* plant against the corrosion of E 24 steel in a neutral solution NaCl 3. 5%. *Anal Bioanal Electrochem* 10:1299–1316

[CAS](#) [Google Scholar](#)

38. Kelnar I, Kaprálková L, Krejčíková S et al (2021) Formation of graphene oxide-based ordered structures in epoxy: effect of grafted polymer chains. *Polym-Plast Technol Mater* 60:1084–1097. <https://doi.org/10.1080/25740881.2021.1876882>

[Article](#) [CAS](#) [Google Scholar](#)

39. Li FZ, Lu ZL, Yang ZH, Qi K (2015) Surface interaction energy simulation of ceramic materials with epoxy resin. *Polimery* 60:468–471.

<https://doi.org/10.14314/POLIMERY.2015.468>

[Article](#) [Google Scholar](#)

40. Bahlakeh G, Ghaffari M, Saeb MR et al (2016) A close-up of the effect of iron oxide type on the interfacial interaction between epoxy and carbon steel: combined molecular dynamics simulations and quantum mechanics. *J Phys Chem C* 120:11014–11026.

https://doi.org/10.1021/ACS.JPCC.6B03133/ASSET/IMAGES/MEDIUM/JP-2016-03133Y_0015.GIF

[Article](#) [CAS](#) [Google Scholar](#)

41. Verma C, Olasunkanmi LO, Ebenso EE et al (2016) Adsorption behavior of glucosamine-based, pyrimidine-fused heterocycles as green corrosion inhibitors for mild steel: experimental and theoretical studies. *J Phys Chem C* 120:11598–11611. https://doi.org/10.1021/ACS.JPCC.6B04429/SUPPL_FILE/JP6B04429_SI_001.PDF

[Article](#) [CAS](#) [Google Scholar](#)

42. Ghosal A, Ahmad S (2017) High performance anti-corrosive epoxy–titania hybrid nanocomposite coatings. *New J Chem* 41:4599–4610. <https://doi.org/10.1039/C6NJ03906E>

[Article](#) [CAS](#) [Google Scholar](#)

43. Sowri Babu K, Ramachandra Reddy A, Sujatha C et al (2013) Synthesis and optical characterization of porous ZnO. *J Adv Ceram* 2:260–265. <https://doi.org/10.1007/S40145-013-0069-6/METRICS>

[Article](#) [CAS](#) [Google Scholar](#)

44. Singh D, Saini A, Dhayal V, Agarwal DC (2019) Oxime-modified aluminum(III) Isopropoxide: a promising sol–gel precursor for corrosion resistive nano-alumina coating on an aluminum alloy. *Prot Met Phys Chem Surf* 55:682–688. <https://doi.org/10.1134/S2070205119040245>

[Article](#) [CAS](#) [Google Scholar](#)

45. Bahlakeh G, Ramezanzadeh B (2017) A detailed molecular dynamics simulation and experimental investigation on the interfacial bonding mechanism of an epoxy adhesive on carbon steel sheets decorated with a novel cerium-lanthanum

nanofilm. ACS Appl Mater Interfaces 9:17536–17551.

https://doi.org/10.1021/ACSAMI.7B00644/SUPPL_FILE/AM7B00644_SI_001.PDF

[Article](#) [CAS](#) [PubMed](#) [Google Scholar](#)

46. Dagdag O, Guo L, Safi Z et al (2020) Epoxy resin and TiO₂ composite as anticorrosive material for carbon steel in 3% NaCl medium: experimental and computational studies. J Mol Liq 317:114249.

<https://doi.org/10.1016/J.MOLLIQ.2020.114249>

[Article](#) [CAS](#) [Google Scholar](#)

Acknowledgements

Veena Dhayal is grateful to Department of Automobile Engineering, IISc Bangalore, as the computational work was done there. VD is also thankful to Science and Engineering Research Board, New Delhi for funding this work (TAR/2020/000233). We are also thankful to CAF and SAIF labs, Manipal University Jaipur for carrying out all the analysis.

Funding

Veena Dhayal is thankful to Science and Engineering Research Board, New Delhi for funding this work (TAR/2020/000233).

Author information

Ishita Chopra and Saraswati Kumari Ola have equal contribution to this work.

Authors and Affiliations

Department of Chemistry, Manipal University Jaipur, Jaipur, 303007, India

Ishita Chopra, Saraswati Kumari Ola & Veena Dhayal

Department of Aerospace Engineering, Indian Institute of Science, Bangalore, 560012, India

S. Gopalakrishnan

Contributions

Ishita Chopra: rough draft of computational work was done by her.

Saraswati Kumari Ola: rough draft of experimental work was done by her.

S. Gopalakrishnan: review of computational work.

Veena Dhayal: review and editing of draft.

Corresponding author

Correspondence to [Veena Dhayal](#).

Ethics declarations

Competing interests

The authors declare no competing interests.

Additional information

Publisher's note

Springer Nature remains neutral with regard to jurisdictional claims in published maps and institutional affiliations.

Supplementary information

[ESM 1](#)

(DOCX 1296 kb)

Rights and permissions

Springer Nature or its licensor (e.g. a society or other partner) holds exclusive rights to this article under a publishing agreement with the author(s) or other rightsholder(s); author self-archiving of the accepted manuscript version of this article is solely governed by the terms of such publishing agreement and applicable law.

[Reprints and permissions](#)

About this article

Cite this article

Chopra, I., Ola, S.K., Gopalakrishnan, S. *et al.* Tailoring epoxy coating with acetoxime derivative of zinc for advanced anticorrosive performance on mild steel: experimental and computational insights. *J Mol Model* 29, 300 (2023). <https://doi.org/10.1007/s00894-023-05705-2>

Received

19 May 2023

Accepted

21 August 2023

Published

30 August 2023

DOI

<https://doi.org/10.1007/s00894-023-05705-2>

Keywords

[Corrosion inhibition](#)

[Diglycidyl ether of bisphenol A](#)

[Acetoxime derivative of ZnCl₂](#)

[Electrochemical test](#)

[DFT](#)

[MD](#)



OPEN ACCESS

EDITED BY

Sirikanjana Thongmee,
Kasetsart University, Thailand

REVIEWED BY

Ramzan Ahmed,
University of Science and Technology,
Meghalaya, India
Mithun Kumar Ghosh,
Govt College Hatta, India

*CORRESPONDENCE

Devendra Jain,
✉ devroshan@gmail.com,
✉ devendrajain@mpuat.ac.in

SPECIALTY SECTION

This article was submitted to
Nanoscience,
a section of the journal
Frontiers in Chemistry

RECEIVED 30 January 2023

ACCEPTED 23 March 2023

PUBLISHED 07 April 2023

CITATION

Singh D, Jain D, Rajpurohit D, Jat G,
Kushwaha HS, Singh A, Mohanty SR,
Al-Sadoon MK, Zaman W and
Upadhyay SK (2023), Bacteria assisted
green synthesis of copper oxide
nanoparticles and their potential
applications as antimicrobial agents and
plant growth stimulants.
Front. Chem. 11:1154128.
doi: 10.3389/fchem.2023.1154128

COPYRIGHT

© 2023 Singh, Jain, Rajpurohit, Jat,
Kushwaha, Singh, Mohanty, Al-Sadoon,
Zaman and Upadhyay. This is an open-
access article distributed under the terms
of the [Creative Commons Attribution
License \(CC BY\)](https://creativecommons.org/licenses/by/4.0/). The use, distribution or
reproduction in other forums is
permitted, provided the original author(s)
and the copyright owner(s) are credited
and that the original publication in this
journal is cited, in accordance with
accepted academic practice. No use,
distribution or reproduction is permitted
which does not comply with these terms.

Bacteria assisted green synthesis of copper oxide nanoparticles and their potential applications as antimicrobial agents and plant growth stimulants

Deepak Singh¹, Devendra Jain^{1*}, Deepak Rajpurohit¹,
Gajanand Jat², Himmat Singh Kushwaha³, Abhijeet Singh⁴,
Santosh Ranjan Mohanty⁵, Mohammad Khalid Al-Sadoon⁶,
Wajid Zaman⁷ and Sudhir K. Upadhyay⁸

¹Department of Molecular Biology and Biotechnology, Maharana Pratap University of Agriculture and Technology, Udaipur, India, ²Department of Soil Science and Agricultural Chemistry, Maharana Pratap University of Agriculture and Technology, Udaipur, India, ³Material Research Centre, Malviya National Institute of Technology, Jaipur, India, ⁴Department of Biosciences, Manipal University Jaipur, Jaipur, India, ⁵All India Network Project on Soil Biodiversity-Biofertilizers, ICAR-Indian Institute of Soil Science, Bhopal, India, ⁶Department of Zoology, College of Science, King Saud University, Riyadh, Saudi Arabia, ⁷Department of Life Sciences, Yeungnam University, Gyeongsan, Republic of Korea, ⁸Department of Environmental Science, V. B. S. Purvanchal University, Jaunpur, India

Copper oxide nanoparticles (CuO-NPs) have piqued the interest of agricultural researchers due to their potential application as fungicides, insecticides, and fertilizers. The *Serratia* sp. ZTB29 strain, which has the NCBI accession number MK773873, was a novel isolate used in this investigation that produced CuO-NPs. This strain can survive concentrations of copper as high as 22.5 mM and can also remove copper by synthesizing pure CuO-NPs. UV-VIS spectroscopy, DLS, Zeta potential, FTIR, TEM, and XRD techniques were used to investigate the pure form of CuO-NPs. The synthesized CuO-NPs were crystalline in nature (average size of 22 nm) with a monoclinic phase according to the XRD pattern. CuO-NPs were found to be polydisperse, spherical, and agglomeration-free. According to TEM and DLS inspection, they ranged in size from 20 to 40 nm, with a typical particle size of 28 nm. CuO-NPs were extremely stable, as demonstrated by their zeta potential of -15.4 mV. The ester (C=O), carboxyl (C=O), amine (NH), thiol (S-H), hydroxyl (OH), alkyne (C-H), and aromatic amine (C-N) groups from bacterial secretion were primarily responsible for reduction and stabilization of CuO-NPs revealed in an FTIR analysis. CuO-NPs at concentrations of 50 $\mu\text{g mL}^{-1}$ and 200 $\mu\text{g mL}^{-1}$ displayed antibacterial and antifungal activity against the plant pathogenic bacteria *Xanthomonas* sp. and pathogenic fungus *Alternaria* sp., respectively. The results of this investigation support the claims that CuO-NPs can be used as an efficient antimicrobial agent and nano-fertilizer, since, compared to the control and higher concentrations of CuO-NPs (100 mg L^{-1}) considerably improved the growth characteristics of maize plants.

KEYWORDS

novel bacterial isolate, 16s-rDNA sequencing, CuO-NPs-green synthesis, confirmatory tests, antimicrobial and plant growth-promoting activity

1 Introduction

Nanotechnology research is the most active research region in contemporary materials science (Singh et al., 2018; Rajput et al., 2021a; Bhavyasree and Xavier, 2022). Nanomaterials synthesis through conventional physical and chemical methods has several adverse features *viz.*, critically high pressure and temperature conditions, utilization of expensive and hazardous chemicals, a longer reaction time and absorbance of toxic by-products on nanomaterial surface (Buazar et al., 2019; Sukumar et al., 2020). Properties of NPs determined by their size, shape, composition, crystalline, and structure (Sharma et al., 2020; Hidangmayum et al., 2022; Rajput et al., 2022). Recent years have seen a significant increase in the significance of green synthesis techniques for nanomaterials, making it one of the very popular methods in modern material sciences (Sukhwal et al., 2017; Mahboub et al., 2022).

Green synthesis has become one of the most preferred methods to overcome the adverse effects physical and chemical synthesis such as critical conditions of temperature and pressure, expensive and toxic chemicals, long reflux time of reaction, toxic by-products *etc.* (Sukhwal et al., 2017; Jain et al., 2020). Metal-tolerant bacteria are important nano-factories that not only accumulates and also detoxify heavy metals due to the various mechanism, *i.e.*, reductase enzymes, EPS, *etc.*, to reduce metal salts to nanomaterials (Jain et al., 2012; Jain et al., 2020; Garg et al., 2022). The nanomaterial synthesis using plant extracts may be easier than microbial synthesis however the microbial synthesis is more cost-effective and freer from any seasonal and plant growth stage variation.

Inorganic metal oxide NPs, *viz.*, CuO, ZnO, MgO, TiO₂, SiO₂, *etc.*, with significant antimicrobial features as well as their selective toxicity, point to potential applications of these materials in medical devices and diagnostics, therapeutics, and nanomedicine against human pathogens (Mohsen and Zahra, 2008; Sobha et al., 2010; Jain D. et al., 2022). These inorganic oxide NPs are beneficial as antibacterial agents because they are more effective against resistant pathogens. According to Makhluaf et al. (2005), crystalline structure and particle shape of nanomaterials have relatively little effect on antibacterial behavior, but a high concentration of smaller-size nanoparticles with a higher surface area does.

The simplest copper compound in the family is copper oxide, which has a variety of possibly practical physical characteristics (Buazar et al., 2019). Copper oxide (CuO) has drawn more interest than other nanomaterials because of its distinctive qualities, which include stability, conductivity, catalytic activity, and anticancer and antibacterial activities. Copper oxide nanoparticles (CuO-NPs) are receiving more attention owing to their availability and lower cost when compared to more costly and noble metals like gold and silver, as well as their effective potential for application as microbial agents (Sankar et al., 2014). Among them, CuO-NPs has drawn a lot of attention in research areas including solar cells, biodiesel, photocatalysis, water pollutant removal, supercapacitors, and electrocatalysis owing to their desired qualities, such as cheap cost, non-toxicity, and ease of manufacturing (Grigore et al., 2016).

By preventing the growth of bacteria, fungi, viruses, and algae, CuO-NPs have important antimicrobial qualities (Amin et al., 2021; Bukhari et al., 2021). Furthermore, compared to other organic antimicrobials like silver and gold, nanoscale copper oxide has a

longer shelf life. According to Keabadile et al. (2020) green synthesis of CuO-NPs with acceptable physio-chemical characteristics has previously been performed with several microbial precursors as reductants. However, very little study has been done on the synthesis of CuO-NPs employing bacteria that are copper-resistant. Hence, the current investigation was conducted to tackle this issue and build a bacteria-assisted synthesis of CuO-NPs and assessment of their antimicrobial and plant growth stimulating activities.

2 Materials and methods

2.1 Source, minimum inhibitory concentration, and molecular identification of copper-tolerant bacteria

The maximum copper tolerance concentration (MTC) was determined on LB agar medium (in triplicate) having an increased concentration of CuSO₄ (2.5–25 mM), and the MTCs were noted from the concentration of CuSO₄ at which the isolate failed to demonstrate growth. The different bacterial isolates were utilized in this study taken from our lab, which were isolated from Zn-Pb ore mine tailings areas of Zawar mines in Udaipur, Rajasthan, India (Jain et al., 2020). According to a previously illustrated method, the 16S rDNA region was amplified and sequenced to perform molecular characterization of copper-tolerant bacteria (Janda and Abbott, 2007).

2.2 Bacterial-assisted synthesis of copper oxide nanoparticles

The synthesis of CuO-NPs was borne out by using copper (Cu) tolerant bacterial isolate (ZTB29) with little modification technique of earlier published (John et al., 2021). The bacterial strain that showed the highest tolerance against copper ion, was inoculated in LB medium (100 mL) and incubated at 28°C with 150 rpm. After 24 h, 5 mM CuSO₄·5H₂O was dropped into the bacterial culture and incubated for 48 h at 28°C until the solution color changed from blue to green. This combination was then centrifuged at 4,000 rpm for 20 min at 4°C to separate the bacterial cell pellet, and the CuO-NPs were produced by centrifuging the residual supernatant at 14,000 rpm for 15 min at 4°C. The obtained CuO-NP pellet was washed twice with deionized water, dried at 80°C in an oven and used for further characterization. A control experiment without copper-tolerant bacteria was also done and upon inclusion of 5 mM CuSO₄·5H₂O, the color change was not seen which states no nanoparticles formation.

2.3 Characterization of CuO-NPs

CuO-NPs were primarily characterized using UV-Vis absorption scanning at 200–1,000 nm using a nanophotometer (Make: Implen, Germany) as the method outlined by Davaeifar et al. (2019). Dynamic Light Scattering (DLS) and Zeta potential were performed by the earlier described method (Rajput et al., 2021b) by using Malvern zeta-sizer nanoseries (United Kingdom). The FTIR spectroscopy (Perkin Elmer)

was performed for CuO-NPs (in KBr pellets) in the 4,100–400 cm^{-1} range (Garg et al., 2022). Around 10 μL of CuO-NPs dispersed in milli Q water were placed onto carbon-coated copper TEM grid for transmission electron microscopy (Tecnai G220 (FEI) S-Twin 200kv) (Sukhwal et al., 2017). The dried powder of CuO-NPs was further characterized by XRD (X'Pert Pro X-ray diffractometer, PAN analytical BV) with Cu K α radiation set with 40 kV and 30 mA (Sukhwal et al., 2017).

2.4 Antimicrobial activities of CuO nanoparticles

Antibacterial activities of bacterial-assisted CuO-NPs were studied by both disc diffusion method and well diffusion using LB agar medium against plant pathogenic bacteria *Xanthomonas* sp. Briefly, 1 mL bacterial suspension ($>10^7$ CFU mL^{-1}) was spread by spreader on LB agar Petri-plates, and in disc diffusion method, the sterile filter paper disk, dipped in a known concentration of CuO-NPs was placed on LB agar plates whereas, in well diffusion method, 5 mm wells (prepared by sterile cork-borer on LB agar Petri-plates) were loaded with CuO-NPs and incubated for inhibition zone development (Jain et al., 2020). The antifungal activities of CuO-NPs were investigated by using the poisoned food technique and spore germination test. The radial mycelia growth of test fungi *Alternaria* sp. was recorded on PDA containing different concentrations of CuO-NPs (50, 75, 100, 150, and 200 $\mu\text{g mL}^{-1}$). PDA plates without CuO-NPs were used as a control. These plates were kept for incubation at 25°C until full radical growth was observed in the control. The different concentration of CuO-NPs was used as per the CRD design in triplicate and the significant difference among treatment were determined by Turkey–Kramer HSD test at $p = 0.05$.

2.5 In vitro studies of CuO-NPs on the growth of maize

The experimental pot was filled with agricultural soil supplemented with sterile planting mixture, seeded with maize seed (PRATAP-3), and placed inside the plant growth chamber (humidity: 60%, light intensity: 750 $\mu\text{mol/m}^2\text{s}$ with 15 h light and 9 h dark conditions at 25°C–20°C). Seven days old maize seedlings were treated with CuO-NPs concentrations viz. 0, 25, 50, 75, 100, 200, and 300 mg L^{-1} (in Hoagland solution) as foliar spray. The shoot length (cm), root length (cm), chlorophyll content (SPAD-502 + Chlorophyll Meter, Spectrum Technologies, India), Copper content [atomic absorption spectroscopy (AAS), Make: Electronics co. India Ltd. Modal no. AAS4141] was studied in 21 days old seedlings (Garg et al., 2022).

3 Result

3.1 Source, screening of MTC against copper and molecular identification of potent copper-tolerant bacteria

The bacterial isolates ZTB15, ZTB24, ZTB28, and ZTB29 were tested for their maximum copper (CuSO_4) tolerance levels in

nutritional broth and observed Minimum inhibitory concentration (MIC). The bacterial isolate ZTB29 had a very maximum MIC of 22.5 mM copper in the medium and was able to withstand high doses of copper in the current experiment (Supplementary Table S1). A further selection of the ZTB29 strain was made for the bacterially aided synthesis of copper oxide CuO-NPs. The ZTB-29 isolate's 16S rRNA gene was sequenced in its entirety and put into nucleotide-nucleotide BLAST analysis. The strains' similarity and matches to previously published bacterial rDNA sequences allowed scientists to identify them as *Serratia* sp. (Figure 1). The ZTB29 nucleotide sequence was deposited to NCBI with the accession MK773873. The detailed biochemical, plant growth promoting and other physiological attributes of the ZTB29 strain were summarized in (Supplementary Table S2) which enables the ZTB29 strain to not only bioremediate excess copper but also to promote plant growth.

3.2 ZTB29 assisted copper oxide nanoparticles synthesis and its confirmatory examination

The easily observed synthetic bacterial growth in the bottom of the flask demonstrated the reaction between the bacterium and copper sulfate, the precursor salt. The starting solution's color changed from light blue to green when 5 mM copper sulfate was added drop by drop to the bacterial suspension, indicating the production of CuO-NPs. The greatest absorbance of 285 nm by using UV-visible spectroscopy was observed, indicating that copper sulfate (which does not produce any absorbance at 285 nm: Supplementary Figure S1), the starting material, was converted to CuO-NPs, as shown in (Figure 2).

The surface charge, size distribution, and potential stability of the nanoparticles contained in a liquid were characterized using dynamic light scattering (DLS) and zeta potential, respectively. Particles in the solution ranged in size from 15 nm to 30 nm and were homogeneous in size. The average CuO-NPs particle size was 21 ± 5.4 nm which was created with a homogenous dispersion (Figure 3A). The TEM investigations provided strong support for the DLS findings. The presence of bacterial cell artifacts or the agglomeration of nanoparticles may be responsible for the second large-size distribution peak at about 1,000 nm. The zeta potential's magnitude (–30 mV to +30 mV) determines the stability and primarily depends upon the surface charge of the generated nanomaterials. The produced nanoparticles have a Zeta potential of –15.4 mV, which demonstrates that they were quite stable at ambient temperature (Figure 3B). The similar zeta potential value was observed even after 1 year of synthesis with CuO-NPs suggesting CuO-NPs were stable for 1 year or more. Zeta potential with a negative value indicates a strong repelling force between the particles, which inhibits agglomeration.

Fourier transform infrared spectroscopy (FTIR) technique was utilized to recognize the occurrence of different functional groups found in a sample. Depending on the infrared absorption range 600–4,000 cm^{-1} in FTIR analysis, the absorbance range 3,200–3,550 cm^{-1} is indicated for O-H stretching, 2,371 cm^{-1} observance for O=C=O stretching, 1,624 cm^{-1} observance for C=C stretching, 1,058 cm^{-1} observance for C-OH stretching,

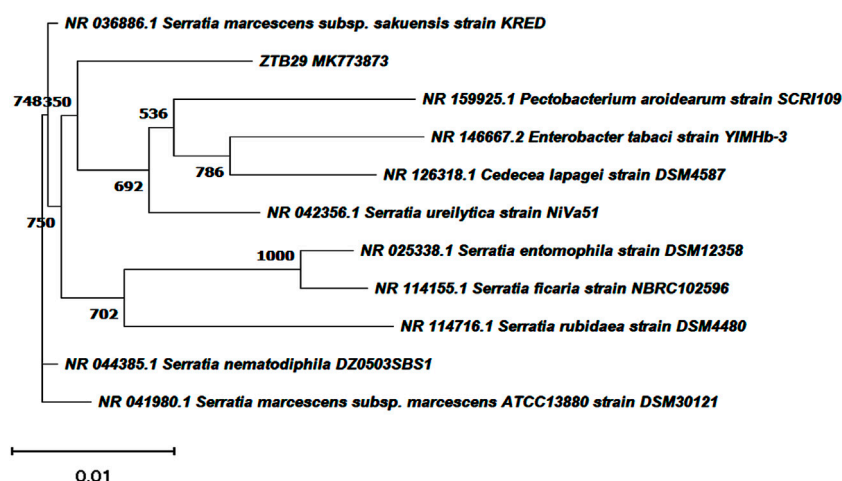


FIGURE 1

Neighbourhood joining tree showing the polygenetic relationship of copper tolerant bacterial strain ZTB29 *Serratia* sp. (NCBI Accession: MK773873).

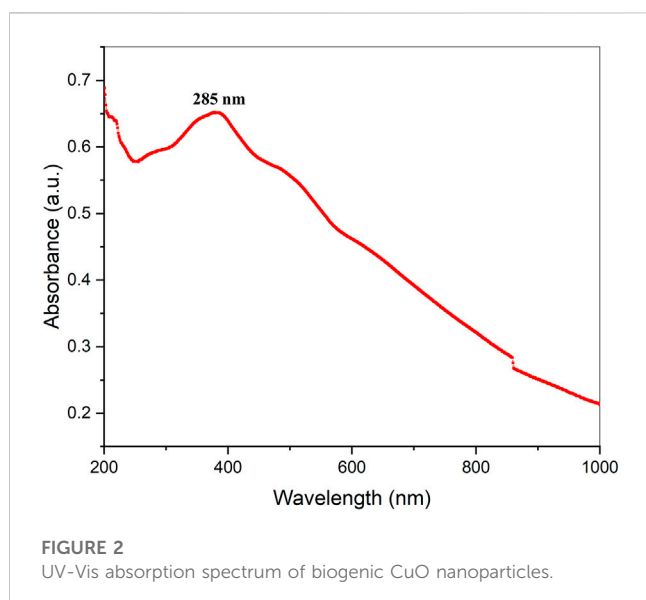


FIGURE 2

UV-Vis absorption spectrum of biogenic CuO nanoparticles.

1,377 cm^{-1} observance for the existence of CO_2 when compared with the standard database. The 608 cm^{-1} vibration attributed to CuO formation confirms the synthesis of pure CuO nanostructures. FTIR study revealed that the carboxyl (C=O), hydroxyl (OH), amine (NH), alkyne (C-H), thiol (S-H), ester (C=O) and aromatic amine (C-N) groups from the bacterial secretion are responsible for the copper reduction and CuO-NPs stabilization (Figure 4). The details of the different FTIR peaks observed in bacteria assisted CuO-NPs and the bacterial extract used for CuO-NPs synthesis were described in the Supplementary Table S3 and Supplementary Figure S2. The CuO-NP's size and shape were studied using TEM. TEM analysis revealed the formation of different shapes of copper oxide nanostructures (Figure 5). It was evident from TEM studies that CuO-NPs were polydisperse and spherical which were free from agglomeration. The particles were in the size range of 20–40 nm with 28 nm average particles size.

X-ray diffraction (XRD) was performed to study the phase (structure) and purity (composition) of the biosynthesized CuO-NPs using copper-tolerant bacteria. The XRD pattern (Figure 6) depicted the creation of pure and crystalline CuO-NPs. The peaks at $2\theta = 32.548, 35.466,$ and 38.769 were assigned to the (110) (002) and (111) reflection lines of monoclinic CuO-NPs compared to JCPDS file No. 01-080-1268. The average crystallite size calculated based on the Scherrer technique for synthesized CuO-NP was 22 nm.

3.3 Antimicrobial activities of CuO-NPs

The CuO-NPs ($50 \mu\text{g mL}^{-1}$) showed significant antibacterial activity by generating an inhibition zone in well diffusion assay (Figure 7A). The disc contacting $50 \mu\text{g mL}^{-1}$ CuO-NPs demonstrated antibacterial activity against *Xanthomonas* sp. as it showed a clear inhibition zone (Figure 7B), which was higher compare to Neomycin ($30 \mu\text{g mL}^{-1}$) and lower compare to Rifampicin ($5 \mu\text{g mL}^{-1}$). The highest inhibition of 91% in fungal mycelia and 88% spore germination was detected at the $200 \mu\text{g mL}^{-1}$ CuO-NPs concentration (Table 1). The rate of mycelia inhibition and spore germination was proportional to CuO-NPs concentration (Figure 8). The results observed in the present study revealed CuO-NP can be used as an efficient nano fungicide against soil-born fungus.

3.4 Influence of CuO-NPs on maize seedling

The shoot and root length, plant biomass, total chlorophyll and copper content were considerably high in the maize plantlet (21 days old) compared to the untreated control plantlet (Table 2). The maximum shoot and root length, biomass and chlorophyll content were observed in 100 mg L^{-1} CuO-NPs application and contributed to plant growth significantly as efficient nano-fertilizers. The CuO-NPs ($<100 \text{ mg L}^{-1}$) caused significant toxicity to maize seedlings and resulted in decreased growth parameters.

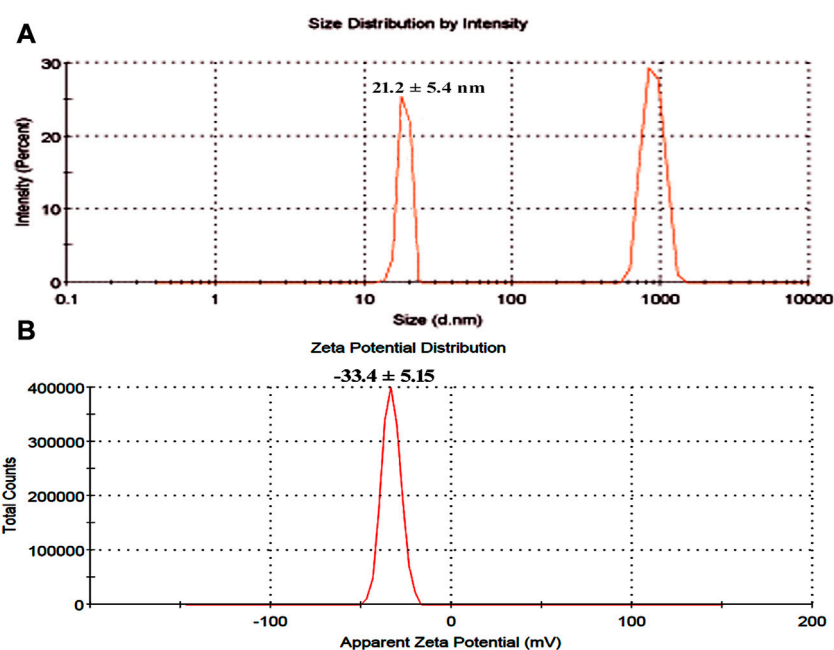


FIGURE 3

(A) Particle size determination using dynamic light scattering (B) Zeta potential analysis of bacterial assisted CuO nanoparticles.

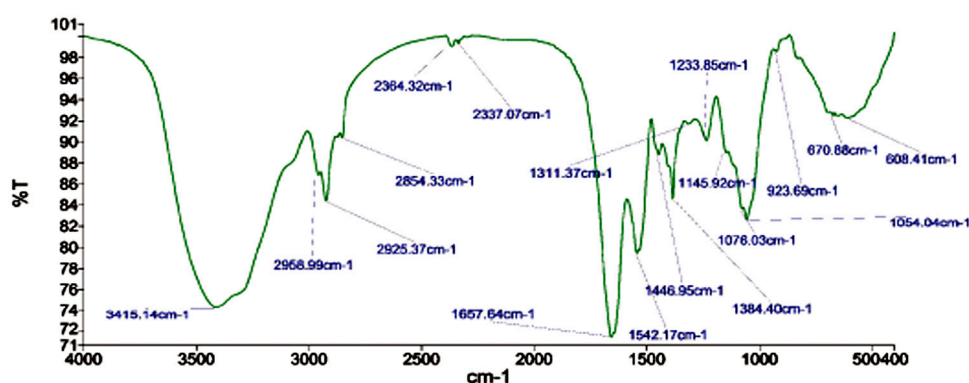


FIGURE 4

FTIR analysis of biogenic CuO nanoparticles.

4 Discussions

The new study could pave the way for bioprospecting for metal-tolerant microorganisms for the quick and easy synthesis of nanoparticles with a variety of applications (Jain et al., 2012; Jain et al., 2020). John et al. (2021) investigated bacterial strain copper tolerance at various CuSO₄ concentrations, and the bacterial strain *Marinomonas*, which tolerated 5 mM CuSO₄, was employed to produce copper and CuO-NPs. Similar findings were found in the current investigation. Tiwari et al. (2016) synthesized CuO-NPs from a copper-resistant *Bacillus cereus* isolate that tolerated >10 mM of copper. The *B. cereus* isolate was able to and was identified as *B. cereus* using 16S rDNA amplification and sequencing. The change of color depends on the surface plasmon vibration of the

nanoparticles (Abdulhameed et al., 2019). Shantkriti and Rani (2014) observed that the color of the reaction changed from blue to dark green when CuSO₄ was added to the *Pseudomonas fluorescens* solution, which corroborated the findings. The bacteria-assisted green synthesis of metal and metal oxide nanoparticles is dependent on the bacteria's ability to remediate harmful metal concentrations by reducing metal ions to nanoparticles (Jain et al., 2020). As a result, copper-tolerant bacteria produce copper and copper oxide nanomaterials by mimicking the natural biomineralization processes that these microbes have adapted to under dangerous copper concentrations (John et al., 2021).

UV-visible absorption spectroscopy can be used to characterize metallic nanoparticles based on surface plasmon resonance (SPR) (Upadhyay et al., 2023). UV-visible spectroscopy (wavelength scan

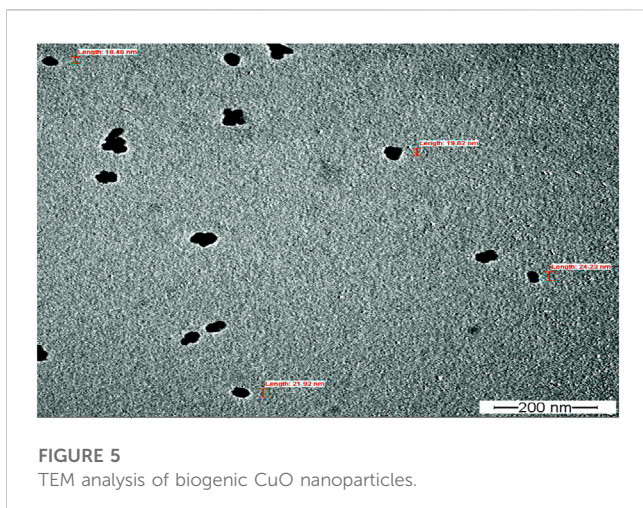


FIGURE 5
TEM analysis of biogenic CuO nanoparticles.

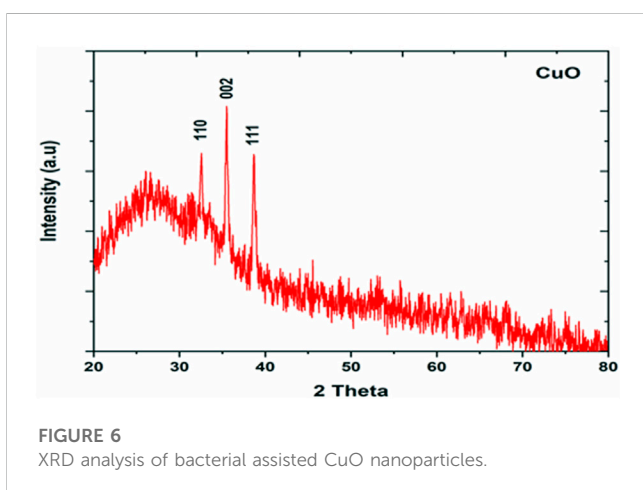


FIGURE 6
XRD analysis of bacterial assisted CuO nanoparticles.

between 200 and 1,000 nm) was used to observe the solution resulting from the bluish-to-greenish color alterations of copper-tolerant bacteria (Zhao et al., 2022). The spectra of CuO-NPs generated employing copper-tolerant bacteria showed pronounced absorption at 285 nm wavelength, confirming the conversion of the starting material (copper sulfate) to the final product (CuO nanoparticles) as shown in Figure 3. Tshireletso et al. (2021) revealed that the UV-VIS absorption spectra of green-produced CuO-NPs from citrus peel extracts resulted in a notable absorbance at 290 nm. Due to surface plasmon resonance, Sankar et al. (2014) found that the UV-Vis spectra of papaya leaf extract medicated CuO-NPs spanned between 250–300 nm. In contrast, the different experiments revealed distinct absorption peaks and spectrums, which could be attributable to different forms of copper and copper oxide nanomaterials and the technology employed for nanomaterial fabrication.

DLS confirmed that the produced CuO-NPs had a homogeneous particle size distribution (15 nm–30 nm) and an average particle size of 21 ± 5.4 nm (Figure 4A), which TEM investigations also validated. The CuO-NPs' -15.4 mV zeta value clearly demonstrated their fairly stable character, as illustrated in Figure 4B. Nardella et al. (2022) conducted DLS investigations of biosynthesized CuO-NPs and reported a 24.4 nm Z-average diameter, while the zeta potential value, which frequently analyses the stability of nanoparticles, was found to be -16.1 mV, confirming the nanoparticles' stability. Nagaraj et al. (2019) reported

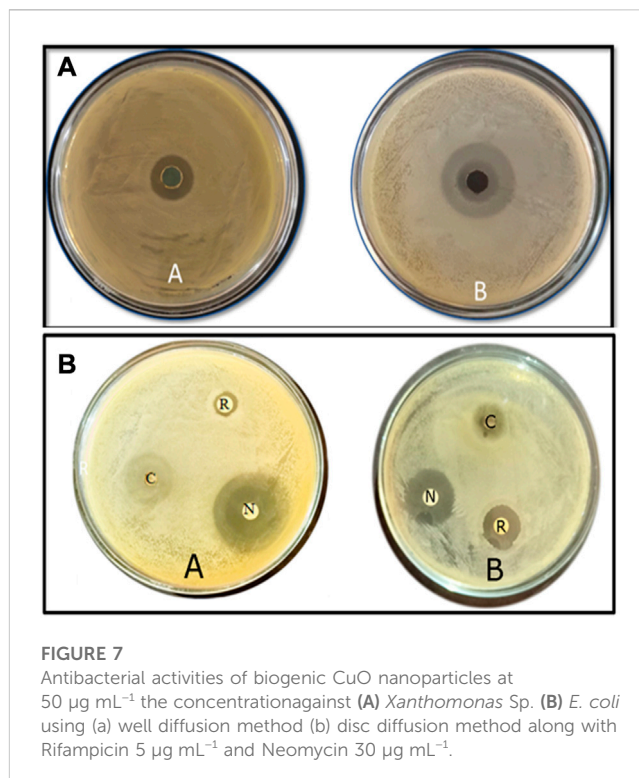


FIGURE 7
Antibacterial activities of biogenic CuO nanoparticles at $50 \mu\text{g mL}^{-1}$ the concentration against (A) *Xanthomonas* Sp. (B) *E. coli* using (a) well diffusion method (b) disc diffusion method along with Rifampicin $5 \mu\text{g mL}^{-1}$ and Neomycin $30 \mu\text{g mL}^{-1}$.

the *Pterolobium hexapetalum* leaf extract-mediated synthesized CuO-NPs and the synthesized nanoparticles were extensively distributed and highly dispersed in the 10–76 nm size range, however, the associated zeta potential was -27.6 mV attributed to moderate stability of nanoparticles.

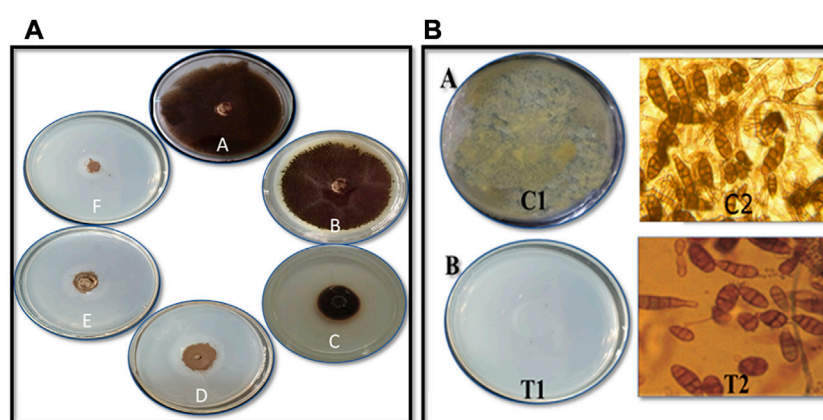
FTIR study indicated the presence of different compounds from the bacterial secretion involved in the reduction and stabilization of CuO-NPs. Amin et al. (2021) observed the FTIR peaks at 518.4 and 600.1 cm^{-1} (formation of CuO nanostructure and Cu–O stretching), $1,021.14$ and 800.58 cm^{-1} (assigned to C–O and C–H bending) and $1,412.3$ and $1,636.4 \text{ cm}^{-1}$ (O–H bending and C=C stretching). John et al. (2021) studied FTIR spectroscopy of CuO-NPs synthesized from marine bacteria indicating the presence of $-\text{C}=\text{O}$, $-\text{OH}$, $-\text{NH}$, $-\text{CH}_2$ scissor vibrations of aliphatic compounds and C=C bonds inside the biomolecules suggesting the interaction of these biomolecules with CuO-NPs also observed in the present study.

TEM analysis revealed the formation of polydisperse and roughly spherical CuO-NPs which were free from agglomeration with the 20–40 nm size range (average particle size is 28 nm). The CuO-NPs as water suspension are slightly agglomerated due to their interaction with water and due to such inter-particle interactions viz. van der Waals, electrostatic and magnetic forces, etc. Previously, similar results of biogenic CuO-NPs were reported by several studies (Ida et al., 2010; Cheng and Walker, 2010; Chandra et al., 2014; Sagadevan and Koteswari, 2015; Kimber et al., 2020; Singh et al., 2019) as observed in TEM. John et al. (2021) reported the TEM micrographs of CuO-NPs from marine bacteria and reported the synthesis of monodispersed, spherical/ovoidal NPs of 10 nm–70 nm size with ~ 40 nm average size. The irregular shape can be attributed to bacterial metabolites on the surface of nanoparticles as stabilizing and reducing agents. Bukhari et al. (2021) reported the *Streptomyces* sp. mediated Cu-NPs synthesis of uniform and spherical nanoparticles (1.72–13.49 nm) in the TEM

TABLE 1 Effect of varying concentrations of CuO nanoparticles on *in vitro* mycelial growth and spore germination of phytopathogenic fungi *Alternaria* sp.

Treatment (CuO nanoparticles)	Percent inhibition mycelia growth	Percent inhibition spore germination
Control	0.0 ± 0.0 _A	5.33 ± 1.52 _A
50 µg mL ⁻¹	15.0 ± 1.53 _B	15.0 ± 2.0 _B
75 µg mL ⁻¹	70.0 ± 1.53 _C	55.0 ± 2.0 _C
100 µg mL ⁻¹	77.0 ± 5.7 _{CD}	64.3 ± 2.51 _D
150 µg mL ⁻¹	81.0 ± 2.0 _D	74.0 ± 1.0 _E
200 µg mL ⁻¹	91.0 ± 1.52 _E	88.0 ± 2.0 _F

*Each value is mean of 3 replicates from 2 experiments. Mean ± SE, followed by same letter in column of each treatment is not significant difference at $p = 0.05$ by Tukey–Kramer HSD, test, % inhibition rate was calculated compared to the germination of the control (0%).

**FIGURE 8**

Antifungal activity of CuO nanoparticles against *Alternaria* sp. on (A) mycelial growth inhibition by poisoned food technique (A) Control (B) 50 µg mL⁻¹ (C) 75 µg mL⁻¹ (D) 100 µg mL⁻¹ (E) 150 µg mL⁻¹ and (F) 200 µg mL⁻¹ CuO nanoparticles (B) Spore germination inhibition by (A) Pour plate technique C1 - Crude spore suspension and T1 - 200 µg mL⁻¹ CuO nanoparticles (B) Microscopic studies C2: Control, T2: 200 µg mL⁻¹ CuO nanoparticles.

TABLE 2 *In vitro* studies on the effect of CuO-NPs on growth of maize seedling (Data are means of three replicates ±SD. Data are recorded after 21 days of germination).

Treatment	Average shoot length (cm)	Shoot dry weight (g)	Average root length (cm)	Chlorophyll index (SPAD)	Copper content in maize seedling (ppm)
Control	18.4 ± 1.7	4.4 ± 1.1	12.8 ± 2.1	10.03 ± 2.11	0.041 ± 0.02
T 1	24.5 ± 2.4	7.8 ± 2.3	14.8 ± 3.2	12.33 ± 2.65	0.055 ± 0.08
T 2	28.8 ± 2.8	8.3 ± 1.6	21.6 ± 2.4	13.63 ± 2.49	0.088 ± 0.06
T 3	32.4 ± 2.2	8.4 ± 2.1	24.1 ± 1.9	14.14 ± 2.43	0.092 ± 0.08
T 4	34.2 ± 3.1	10.6 ± 1.8	24.8 ± 2.3	16.86 ± 4.5	0.098 ± 0.09
T 5	29.4 ± 2.3	9.1 ± 1.5	22.7 ± 2.1	13.93 ± 2.8	0.012 ± 0.05
T 6	21.1 ± 1.9	7.5 ± 1.2	15.1 ± 1.7	11.26 ± 2.3	0.015 ± 0.05

images. Krishna et al. (2020) synthesized CuO nanoparticles from *Cinnamomum malabatum* aqueous leaf extract and the TEM revealed spherically shaped CuO-NPs with 11 nm–24 nm size range which was also in close agreement with the present study.

The XRD pattern revealed the pure CuO-NPs were crystalline in nature. Ali et al. (2021) performed XRD of CuO-NPs and the detected peaks in their study confirmed the monoclinic phase of CuO compared to JCPDS card 000021040 which was also seen in the present study. Further, the characteristic crystallite size measured

using the Scherrer equation was found to be 24.7 nm also supports the finding of the present study. Buazaret al. (2019) reported that clear and sharp peaks in XRD can be ascribed to the highly crystalline structure of nanomaterials. Similar results of the crystallite size of CuO-NPs in the range of 9–23 nm were solely dependent on the precursor conditions (Tavakoli et al., 2019).

The CuO-NPs exhibited superior antimicrobial activities and have a significant potential to control phytopathogens. Krishna et al. (2020) reported significant antibacterial activities of CuO-NPs against human pathogenic bacteria viz., *Escherichia coli*, *Staphylococcus aureus*, *Pseudomonas aeruginosa* and *Proteus mirabilis* using well diffusion method and similar results were also observed against plant pathogenic bacteria in the present study. Abboud et al. (2014) reported significant antimicrobial activities of CuO-NPs synthesized from the alga extract against *Enterobacter aerogenes* and *S. aureus* and the observed radial diameter of the inhibition zone was 14 and 16 mm, respectively. Bhavyasree and Xavier (2022) extensively reviewed the copper and CuO nanomaterial and their antimicrobial properties and demonstrated the mechanism of antibacterial action which includes mechanical damage, gene toxicity, and oxidative stress injury. The bio-molecules absorbed on the surface may also help in the antimicrobial activities of CuO-NPs.

The CuO-NPs (200 g mL⁻¹ concentration) exhibited superior antifungal activities. Qamar et al. (2020) showed reasonable results for the antifungal activity of CuO-NPs against *Trichophyton rubrum*. Rabiee et al. (2020) synthesized *Achillea millefolium* extract-mediated CuO-NPs and reported significant *in vitro* antifungal activities against four different fungi. The biosynthesized CuO-NPs showed effective antifungal activities owing to the entering of CuO-NPs on fungal membranes and negatively effect the cell divisions *via* strong interaction on the respiratory chains.

The use of CuO-NPs (100 mg L⁻¹) resulted in the improvement of plant growth attributes as copper-based nano-fertilizer. The specific doses of CuO-NPs can play a remarkable role in plant growth promotion are advocated by several researchers (Singh et al., 2018; Rajput et al., 2022) due to the increase bio-availability of Cu²⁺ which led to accelerating the mobilization of food reserves during germination, greater activation of copper enzymes such as cytochrome C oxidase, etc. CuO-NPs in the optimum dose can significantly influence the plant growth and act as efficient nano-fertilizers.

5 Conclusion

In conclusion, we present a straightforward, quick, and environmentally friendly method for producing CuO-NPs with exceptional antibacterial properties. Different approaches have been applied to clarify the size, shape, composition, and stability, and the findings demonstrate that the synthesized nanoparticles are very stable and monoclinic, with the largest particles falling within the size range of 28 nm in diameter. The CuO-NPs may function as a potent bactericide and fungicide that may be employed to combat plant infections as a result of the positive results. With the right toxicological information, the greenly produced CuO-NPs have a large potential and may be used for a variety of tasks, including food processing and control, biomedical forms, product packaging, and more. According to the observations of this study, CuO-NPs are a novel class of antimicrobial agents that may be developed and applied in sustainable agriculture.

Data availability statement

The datasets presented in this study can be found in online repositories. The names of the repository/repositories and accession number(s) can be found below: <https://www.ncbi.nlm.nih.gov/>-, MK773873.

Author contributions

DJ designed the research. DS, DR, GJ performed the experiments. SM, SU interpreted the data. HK and AS performed TEM, DLS, Zeta, FTIR and XRD. DJ and SU wrote manuscript. MS and WZ revised and proofread manuscript. All authors reviewed the manuscript.

Funding

Gratefully acknowledge the support by Researchers Supporting Project Number (RSP2023R410), King Saud University, Riyadh, Saudi Arabia. The financial assistance from All India Network Project on soil biodiversity and Bio-fertilizer project and MPUAT, India.

Acknowledgments

The authors would like to extend their sincere appreciation to the Researchers Supporting Project Number (RSP2023R410), King Saud University, Riyadh, Saudi Arabia. The financial assistance from All India Network Project on soil biodiversity & Bio-fertilizer project and the equipment support from IDP, NAHEP project are gratefully acknowledged.

Conflict of interest

The authors declare that the research was conducted in the absence of any commercial or financial relationships that could be construed as a potential conflict of interest.

Publisher's note

All claims expressed in this article are solely those of the authors and do not necessarily represent those of their affiliated organizations, or those of the publisher, the editors and the reviewers. Any product that may be evaluated in this article, or claim that may be made by its manufacturer, is not guaranteed or endorsed by the publisher.

Supplementary material

The Supplementary Material for this article can be found online at: <https://www.frontiersin.org/articles/10.3389/fchem.2023.1154128/full#supplementary-material>

References

- Abdoud, Y., Saffaj, T., Chagraoui, A., Bouari, A. El., Brouzi, K., and Tanane, O. (2014). Biosynthesis, characterization and antimicrobial activity of copper oxide nanoparticles (CONPs) produced using Brown alga extract (*Bifurcariabifurcata*). *Appl. Nanosci.* 4, 571–576. doi:10.1007/s13204-013-0233-x
- Abdulhameed, A. S., Jawad, A. H., and Mohammad, A. K. T. (2019). Synthesis of chitosan-ethylene glycol diglycidyl ether/TiO₂ nanoparticles for adsorption of reactive orange 16 dye using a response surface methodology approach. *Bioresour. Technol.* 293, 122071. doi:10.1016/j.biortech.2019.122071
- Ali, M., Ijaz, M., Ikram, M., Ul-Hamid, A., Avais, M., and Anjum, A. A. (2021). Biogenic synthesis, characterization and antibacterial potential evaluation of copper oxide nanoparticles against *Escherichia coli*. *Nanoscale Res. Lett.* 16, 148. doi:10.1186/s11671-021-03605-z
- Amin, F., Khattak, B., Alotaibi, A., Qasim, M., Ahmad, I., Ullah, R., et al. (2021). Green synthesis of copper oxide nanoparticles using *Aerjavanica* leaf extract and their characterization and investigation of *in vitro* antimicrobial potential and cytotoxic activities. *Evidence-Based Complement. Altern. Med.* 5589703, 1–12. doi:10.1155/2021/5589703
- Bhavyasree, P. G., and Xavier, T. S. (2022). Green synthesised copper and copper oxide-based nanomaterials using plant extracts and their application in antimicrobial activity: Review. *Curr. Res. Green Sustain. Chem.* 5, 100249. doi:10.1016/j.crgsc.2021.100249
- Buazar, F., Sweidi, S., Badri, M., and Kroushawi, F. (2019). Biofabrication of highly pure copper oxide nanoparticles using wheat seed extract and their catalytic activity: A mechanistic approach. *Green Process. Synthesis* 8, 691–702. doi:10.1515/gps-2019-0040
- Bukhari, S. I., Hamed, M. M., Al-Agamy, M. H., Gazwi, H. S. S., Radwan, H. H., and Youssif, A. M. (2021). Biosynthesis of copper oxide nanoparticles using *Streptomyces* MHM38 and its biological applications. *Hindawi J. Nanomater.* 6693302, 1–16. doi:10.1155/2021/6693302
- Chandra, S., Kumar, A., and Kumar, T. (2014). Synthesis and characterization of copper nanoparticles by reducing agent. *J. Saudi Chem. Soc.* 18 (2), 149–153. doi:10.1016/j.jscs.2011.06.009
- Cheng, G., and Walker, A. R. H. (2010). Transmission electron microscopy characterization of colloidal copper nanoparticles and their chemical reactivity. *Anal. Bioanal. Chem.* 396, 1057–1069. doi:10.1007/s00216-009-3203-0
- Davaeifar, S., Modarresi, M. H., Mohammadi, M., Hashemi, E., Shafiei, M., Maleki, H., et al. (2019). Synthesizing, characterizing, and toxicity evaluating of phycocyanin-ZnO nanorod composites: A back to nature approaches. *Colloids Surfaces B Biointerfaces* 175, 221–230. doi:10.1016/j.colsurfb.2018.12.002
- Garg, K. K., Jain, D., Rajpurohit, D., Kushwaha, H. S., Daima, H. K., Stephen, B. J., et al. (2022). Agricultural significance of silica nanoparticles synthesized from a silica Solubilizing Bacteria. *Comments Inorg. Chem.* 42 (4), 209–225. doi:10.1080/02603594.2021.1999234
- Grigore, M. E., Biscu, E. R., Holban, A. M., Gestal, M. C., and Grumezescu, A. M. (2016). Methods of synthesis, properties and biomedical applications of CuO nanoparticles. *Pharm. (Basel)* 9 (4), 75. doi:10.3390/ph9040075
- Hidangmayum, A., Debnath, A., Guru, A., Singh, B. N., Upadhyay, S. K., and Dwivedi, P. (2022). Mechanistic and recent updates in nano-bioremediation for developing green technology to alleviate agricultural contaminants. *Int. J. Environ. Sci. Technol.*, 1–26. doi:10.1007/s13762-022-04560-7
- Ida, K., Sugiyama, Y., YukiChujyo, Y., Tomonari, M., Tomoharu Tokunaga, T., Sasaki, K., et al. (2010). *In-situ* TEM studies of the sintering behavior of copper nanoparticles covered by biopolymer nanoskin. *J. Electron Microsc.* 59, 75–80. doi:10.1093/jmicro/dfq055
- Jain, N., Bhargava, A., Tarafdar, J. C., Singh, S. K., and Panwar, J. (2012). A biomimetic approach towards synthesis of zinc oxide nanoparticles. *Appl. Microbiol. Biotechnol.* 97 (2), 859–869. doi:10.1007/s00253-012-3934-2
- Jain, D., Kour, R., Bhojiya, A. A., Meena, R. H., Singh, A., Mohanty, S. R., et al. (2020). Zinc tolerant plant growth promoting bacteria alleviates phytotoxic effects of zinc on maize through zinc immobilization. *Sci. Rep.* 10, 13865. doi:10.1038/s41598-020-70846-w
- Jain, D., Kushwaha, H. S., Rathore, K. S., Stephen, B. J., Daima, H. K., Jain, R., et al. (2022). Fabrication of iron oxide nanoparticles from ammonia vapor and their importance in plant growth and dye degradation. *Part. Sci. Technol.* 40, 97–103. doi:10.1080/02726351.2021.1929601
- Jain, R., Bohra, N., Singh, R. K., Upadhyay, S. K., Srivastava, A. K., and Rajput, V. D. (2022). “Nanomaterials for plants: From ecophysiology to signaling mechanisms and nutrient uptake,” in *The role of nanoparticles in plant nutrition under soil pollution. Sustainable plant nutrition in a changing world*. Editors V. D. Rajput, K. K. Verma, N. Sharma, and T. Minkina (Cham: Springer). doi:10.1007/978-3-030-97389-6_8
- Janda, J. M., and Abbott, S. L. (2007). 16S rRNA gene sequencing for bacterial identification in the diagnostic laboratory: Pluses, perils, and pitfalls. *J. Clin. Microbiol.* 45 (9), 2761–2764. doi:10.1128/JCM.01228-07
- John, M. S., Nagothi, J. A., Zannotti, M., Giovannetti, R., Mancini, A., Ramasamy, K., P., et al. (2021). Biogenic synthesis of copper nanoparticles using bacterial strains isolated from an antarctic consortium associated to a psychrophilic marine ciliate: Characterization and potential application as antimicrobial agents. *Mar. Drugs* 19 (5), 263. doi:10.3390/md19050263
- Keabadile, O. P., Aremu, A. O., Elugoke, S. E., and Fayemi, O. E. (2020). Green and traditional synthesis of copper oxide nanoparticles-comparative study. *Nanomater. (Basel)* 10 (12), 2502. doi:10.3390/nano10122502
- Kimber, R. L., Bagshaw, H., Smith, K., Buchanan, D. M., Coker, V. S., Cavet, J. S., et al. (2020). Biomineralization of Cu 2S nanoparticles by geobactersulfurreducens. *Appl. Environ. Microbiol.* 86, 009677–e1020. doi:10.1128/AEM.00967-20
- Krishna, B. A., Kumar, P. N., and Prema, P. (2020). Green synthesis of copper oxide nanoparticles using *Cinnamomum malabratrum* leaf extract and its antibacterial activity. *Indian J. Chem. Technol.* 27, 525–530.
- Mahboub, H. H., Rashidian, G., Hoseinifar, S. H., Kamel, S., Zare, M., Ghafarifarsani, H., et al. (2022). Protective effects of *Allium hirtifolium* extract against foodborne toxicity of Zinc oxide nanoparticles in Common carp (*Cyprinus carpio*). *Comp. Biochem. Physiol. Part C Toxicol. Pharmacol.* 257, 109345. doi:10.1016/j.cbpc.2022.109345
- Makhluף, S., Dror, R., Nitzan, Y., Abramovich, R. J., and Gedanken, A. (2005). Microwave-assisted synthesis of nanocrystalline MgO and its use as a bactericide. *Adv. Funct. Mater.* 15, 1708–1715. doi:10.1002/adfm.200500029
- Mohsen, J., and Zahra, B. (2008). Protein nanoparticle: A unique system as drug delivery vehicles. *Afr. J. Biotechnol.* 7, 4926.
- Nagaraj, E., Karuppanan, K., Shanmugam, P., and Venugopal, S. (2019). Exploration of biosynthesized copper oxide nanoparticles using *pterolobiumhexapetalum* leaf extract by photocatalytic activity and biological evaluations. *J. Clust. Sci.* 30, 1157–1168. doi:10.1007/s10876-019-01579-8
- Nardella, M. I., Fortino, M., Barbanente, A., Natile, G., Pietropaolo, A., and Arnesano, F. (2022). Multinuclear metal-binding ability of the N-terminal region of human copper transporter Ctr1: Dependence upon pH and metal oxidation state. *Front. Mol. Biosci.* 9, 897621. doi:10.3389/fmolb.2022.897621
- Qamar, H., Rehman, S., Chauhan, D. K., Tiwari, A. K., and Upmanyu, V. (2020). Green synthesis, characterization and antimicrobial activity of copper oxide nanomaterial derived from *momordica charantia*. *Int. J. Nanomed.* 15, 2541–2553. doi:10.2147/IJN.S240232
- Rabiee, N., Bagherzadeh, M., Kiani, M., Ghadiri, A. M., Etesamifar, F., Jaberzadeh, A. H., et al. (2020). Biosynthesis of copper oxide nanoparticles with potential biomedical applications. *Int. J. Nanomed.* 15, 3983–3999. doi:10.2147/IJN.S255398
- Rajput, V. D., Minkina, T., Fedorenko, A., Chernikova, N., Hassan, T., Mandzhieva, S., et al. (2021a). Effects of zinc oxide nanoparticles on physiological and anatomical indices in spring barley tissues. *Nanomaterials* 11, 1722. doi:10.3390/nano11071722
- Rajput, V. D., Singh, A., Minkina, T., Rawat, S., Mandzhieva, S., Sushkova, S., et al. (2021b). Nano-enabled products: challenges and opportunities for sustainable agriculture. *Plants* 10, 2727. doi:10.3390/plants10122727
- Rajput, V. D., Minkina, T., Upadhyay, S. K., Kumari, A., Ranjan, A., Mandzhieva, S., et al. (2022). Nanotechnology in the restoration of polluted soil. *Nanomaterials* 12, 769. doi:10.3390/nano12050769
- Sagadevan, S., and Koteeswari, P. (2015). Analysis of structure, surface morphology, optical and electrical properties of copper nanoparticles. *J. Nanomed. Res.* 2 (5), 133–136. doi:10.15406/jnmr.2015.02.00040
- Sankar, R., Manikandan, P., Malarvizhi, V., Fathima, T., and ShivashangariRavikumar, K. S.V. (2014). Green synthesis of colloidal copper oxide nanoparticles using *Carica papaya* and its application in photocatalytic dye degradation. *Spectrochim. Acta Part A Mol. Biomol. Spectrosc.* 121, 746–750. doi:10.1016/j.saa.2013.12.020
- Shantkriti, S., and Rani, P. (2014). Biological synthesis of Copper nanoparticles using *Pseudomonas fluorescens*. *Int. J. Curr. Microbiol. Appl. Sci.* 3 (9), 374–383.
- Sharma, M., Sharma, A., and Majumder, S. (2020). Synthesis, microbial susceptibility and anti-cancerous properties of copper oxide nanoparticles-review. *Nano Express* 1 (1), 012003. doi:10.1088/2632-959x/ab9241
- Singh, J., Dutta, T., Kim, K. H., Rawat, M., Samddar, P., and Kumar, P. (2018). ‘Green’ synthesis of metals and their oxide nanoparticles: Applications for environmental remediation. *J. Nanobiotechnol.* 16 (1), 84. doi:10.1186/s12951-018-0408-4
- Singh, J., Kumar, V., Kim, K. H., and Rawat, M. (2019). Biogenic synthesis of copper oxide nanoparticles using plant extract and its prodigious potential for photocatalytic degradation of dyes. *Environ. Res.* 177, 108569. doi:10.1016/j.envres.2019.108569
- Sobha, K., Surendranath, K., Meena, V. K., Jwala, T., Swetha, N., and Latha, K. S. M. (2010). Emerging trends in nanobiotechnology. *J. Biotechnol. Mol. Rev.* 5, 01–12.
- Sukhwai, A., Jain, D., Joshi, A., Rawal, P., and Kushwaha, H. S. (2017). Biosynthesized silver nanoparticles using aqueous leaf extract of *Tagetespatula* L. and evaluation of their antifungal activity against phytopathogenic fungi. *IET Nanobiotechnol.* 11, 531–537. doi:10.1049/iet-nbt.2016.0175
- Sukumar, S., Rudrasenan, A., and PadmanabhanNambiar, D. (2020). Green-Synthesized rice-shaped copper oxide nanoparticles using *Caesalpinia bonducella*

seed extract and their applications. *ACS-Omega* 5 (2), 1040–1051. doi:10.1021/acsomega.9b02857

Tavakoli, S., Kharaziha, M., and Ahmadi, S. (2019). Green synthesis and morphology dependent antibacterial activity of copper oxide nanoparticles. *J. Nanostruct.* 9 (1), 163–171. doi:10.22052/JNS.2019.01.018

Tiwari, M., Jain, P., Hariharapura, R., Kashinathan, N., Bhat, B., Nayanabhirama, U., et al. (2016). Biosynthesis of copper nanoparticles using copper-resistant *Bacillus cereus*, a soil isolate. *Process Biochem.* 51, 1348–1356. doi:10.1016/j.procbio.2016.08.008

Tshireletso, P., Ateba, C. N., and Fayemi, O. E. (2021). Spectroscopic and antibacterial properties of CuONPs from orange, lemon and tangerine peel

extracts: Potential for combating bacterial resistance. *Molecules* 26, 586. doi:10.3390/molecules26030586

Upadhyay, S. K., Devi, P., Kumar, V., Pathak, H. K., Kumar, P., Rajput, V. D., et al. (2023). Efficient removal of total arsenic ($As^{3+}/5+$) from contaminated water by novel strategies mediated iron and plant extract activated waste flowers of marigold. *Chemosphere* 313, 137551. doi:10.1016/j.chemosphere.2022.137551

Zhao, H., Maruthupandy, M., Al-mekhlafi, F. A., Chackaravathi, G., Ramachandran, G., and Chelliah, C. K. (2022). Biological synthesis of copper oxide nanoparticles using marine endophytic actinomycetes and evaluation of biofilm producing bacteria and A549 lung cancer cells. *J. King Saud Univ. - Sci.* 34 (3), 101866. doi:10.1016/j.jksus.2022.101866

RESEARCH ARTICLE | MAY 31 2023

Characterization of AgNPs biosynthesized from stem and leaf extracts of *Cissus quadrangularis* and *C. rotundifolia* ✓

Smita Purohit; Divya Pancholi; Niranjan Kunwar; ... et. al

 Check for updates

AIP Conference Proceedings 2752, 030003 (2023)

<https://doi.org/10.1063/5.0136566>


View
Online


Export
Citation

CrossMark

Articles You May Be Interested In

Determination of fruit maturation and ripening potential on postharvest quality of *Passiflora quadrangularis* L.

AIP Conference Proceedings (July 2021)

Phenetic analysis of *Passiflora* in Probolinggo-East Java based on generative characteristic

AIP Conference Proceedings (May 2021)

Effects of High Intensity Sound upon *Micrococcus pyogenes*, var. *aureus*

J Acoust Soc Am (June 2005)

Downloaded from http://pubs.aip.org/aip/acp/article-pdf/doi/10.1063/5.0136566/17910206030003_1_5.0136566.pdf

AIP Advances

Why Publish With Us?

-  **25 DAYS**
average time to 1st decision
-  **740+ DOWNLOADS**
average per article
-  **INCLUSIVE**
scope

[Learn More](#)

 AIP
Publishing

Characterization of AgNPs Biosynthesized from Stem and Leaf Extracts of *Cissus quadrangularis* and *C. rotundifolia*

Smita Purohit¹, Divya Pancholi¹, Niranjana Kunwar¹, Rajpal Choudhary² and Rohit Jain^{2, a)}

Author Affiliations

¹Department of Botany, The IIS University, Jaipur, Rajasthan, India, 302020

²Department of Biosciences, Manipal University Jaipur, Rajasthan, India, 303007

Author Emails

^{a)} Corresponding author: rohit.jain@jaipur.manipal.edu

Abstract. Antimicrobial activity of silver nanoparticles biosynthesized from leaf and stem extracts of *Cissus quadrangularis* and *C. rotundifolia* was assessed against two pathogenic microbes (*Micrococcus*, *Proteus vulgaris*). Methanolic extracts of both stem and leaves of *C. quadrangularis* and *C. rotundifolia* were prepared using soxhlet method. Qualitative profiling of secondary metabolites confirmed the presence of saponins in *C. quadrangularis* extracts, while tannins and flavonoids were present in extracts of both the plants. AgNPs biosynthesized from both leaf and stem extracts were characterized using SEM and FTIR. Antimicrobial assays of all the four crude extracts and NPs derived from leaf and stem extract revealed that none of the crude extracts of *C. quadrangularis* showed antimicrobial activity against either *P. vulgaris* or *Micrococcus*, while nanoparticles derived from stem extracts exhibited higher (~2.5 times) activity against *P. vulgaris* than that against *Micrococcus*. In contrast, both the extracts of *C. rotundifolia* and AgNPs derived from stem extract showed similar inhibitory effect on growth of both tested microorganisms. Nanoparticles biosynthesized from leaf extract of *C. rotundifolia* showed higher activity (~1.6 times) against *P. vulgaris* than that against *Micrococcus*. AgNPs derived from *C. quadrangularis* stem extract exhibited ~1.5 times higher activity than that of *C. rotundifolia* derived AgNPs against *P. vulgaris*. This study therefore indicates that the rich phytochemical profile and antimicrobial potential of *Cissus* sp. can further be used to develop non-toxic herbal formulations with multiple medicinal properties.

INTRODUCTION

Fast evolving nature of microbial pathogens and increasing toll of nosocomial infections has been one of the frontline challenges in development of efficient antimicrobial drugs [1]. Moreover, emergence of multidrug resistant variants due to excessive use of antibiotics has further made the need for identification of novel antimicrobial agents of paramount importance [2, 3].

Nanotechnology has emerged as a powerful tool in past few decades due to their vast applications in clinical imaging & detection, targeted drug delivery, biomedicines and cancer treatment therapies [4]. Various metal nanoparticles have effectively been used against various microbial pathogens due to their small size, higher surface area to volume ratio, which enables their close interaction with the microbial membranes [5]. Further, the pathogens are unlikely to develop resistance against these metals, as metal nanoparticles attack the microbes by targeting multiple regions, thus for developing resistance, the pathogens would have to mutate all the targeted sites [6].

Silver and its salts have been used as antimicrobial agents for ages, infact it has been one of the popular treatment/remedy for microbial infections since ancient times. Applications of silver-containing or silver-coated materials as antimicrobial agents has been well established over decades and has been used as an excellent anti-bacterial growth control agent in prostheses, catheters, burn wounds, dental materials and vascular grafts [7]. In recent decade, silver nanoparticles (AgNPs) have emerged as efficient nanomedicine against infectious agents due to

their unique chemical, optical, electromagnetic, and mechanical properties [8]. Among all known antibacterial metal nanoparticles, AgNPs have been reported to have highest bactericidal activity & biocompatibility and has been reported to be highly effective not only against bacteria, but also against fungal and viral pathogens [6, 9]. AgNPs also exhibit other therapeutic activities including anti-cancer, anti-inflammatory, anti-angiogenesis and many more [9].

Synthesis of AgNPs using conventional physico-chemical methods such as electrochemical reduction, thermal evaporation, beam electron irradiation and vapor condensation has declined in recent past due to use of toxic chemicals, time consuming & difficult to scale up process, complicated downstream processing, which also makes the process cost expensive [9, 10]. Biological synthesis of nanoparticles using microorganisms, enzymes and plants enables fast, high yields and cost-effective downstream processing, and thus have been widely used for synthesis of AgNPs based nanomedicines. Synthesis of silver nanoparticles using plant extracts have gained lot of impetus in past few decades due to faster synthesis rate, higher stability, more diversity in size and shape, lower synthesis cost, and environment friendly approach [11]. Some of the common plants that have been used for green synthesis of silver nanoparticles include *Moringa oleifera*, *Azadirachta indica*, *Xanthium strumarium*, *Tinospora cordifolia*, *Brassica rapa* and Red onion [12-18].

Cissus, member of grape family Vitaceae is known as natural reservoir of an important medicinal compound, resveratrol. This compound has been well reported to exhibit wide range of pharmaceutical properties including cardioprotection, chemoprotection, and many more (Bertelli and Das 2009; Das et al. 2011).

C. quadrangularis L. and *C. rotundifolia* (Forsk.) Vahl are two important medicinal plants of the grape family known for their diverse medicinal applications in Indian medicinal system. These are known as natural bone healing plants and have been used for the purpose since ancient times [19]. Different plant parts of both the plants have been reported to exhibit therapeutic properties against various disorders including asthma, syphilis, tumors, haemorrhoids, menorrhagia, leucorrhoea, scurvy, obesity and gout [20-24]. Apart from being used as nutritional supplement, *Cissus* sp. also exhibit pharmaceutical properties including antioxidant, anti-inflammatory, analgesic, anti-diabetic, anti-neurodegenerative, analgesic, gastroprotective and antimicrobial [25-27]. Till date, there are no significant reports on antimicrobial activity of *C. rotundifolia* and even that for *C. quadrangularis* are scarce.

Proteus vulgaris and *Micrococcus luteus* are amongst the most opportunistic bacterial pathogens and are major among causative agents of hospital borne infections. Despite of various antibacterial agents available, the fast-evolving nature and increasing fatality of nosocomial infections it has become imperative to develop more efficient drugs against these pathogens.

Therefore, in the present study, antimicrobial potential of AgNPs biosynthesized from methanolic leaf and stem extracts of *C. quadrangularis* and *C. rotundifolia* against *P. vulgaris* and *Micrococcus* has been reported for the first time. This study provides new insights into some important medicinal properties and phytochemical composition of these two invaluable medicinal plants.

MATERIALS & METHODS

Plant sample collection & preparation

Plant samples (leaf & stem) of *C. quadrangularis* (CQ) and *C. rotundifolia* (CR) were collected from Smriti Kulish Van Biodiversity Park, Jaipur, Rajasthan, India, thoroughly washed under running tap water, air dried, pulverised into fine powder and stored at 4°C till further use.

Metabolite extraction & qualitative profiling

Leaf & stem powder were subjected to Soxhlet extraction method [22]. Briefly, dried powder (20 g) was extracted with 500 ml methanol (HiMedia, India) using Soxhlet apparatus (Borosil, India) for 24h. The resulting extracts were filtered using Whatmann filter paper No. 1, concentrated upto 1 ml volume in rotary evaporator (Sigma, India) and stored at 4°C till further use. All the four extracts (CRS, CRL, CQS, CQL) were analysed for the presence of alkaloids, flavonoids, saponins, tannins and phenols using Hager's test, lead acetate solution test, foam test and ferric chloride test, respectively.

AgNPs synthesis and characterization

5 ml of extract was mixed with equal volume of 0.1 M AgNO₃ solution (HiMedia, India) and the mixture was incubated at RT for 20 min or until the color of the mixture changed from green to dark brown. The nanoparticles were extracted from the mix by centrifugation at 8000 rpm for 30 min. The pellet was resuspended in double distilled water and stored at 4°C till further use. The chemical composition and shape of the synthesized AgNPs was determined using FTIR (Bruker, USA) and SEM (Jeol, USA), respectively as per method reported by [28].

Antimicrobial activity

Standard strains of *Micrococcus luteus* (MTCC 106) and *Proteus vulgaris* (MTCC 426) were procured from MTCC, Institute of Microbial Technology, Chandigarh, India. Antimicrobial activity of all the crude extracts and biosynthesized AgNPs was performed using disc diffusion method. Briefly, sterilized filter paper discs of 6 mm diameter were dipped in different extracts and AgNP solution and were transferred onto sterilised nutrient agar petri plates pre-inoculated with 24 h old broth culture of *M. luteus* and *P. vulgaris*. Methanol was used as control, and the strains were inoculated using spread plate technique. The plates were then incubated at 37°C for 24 h and the zone of inhibition was recorded.

RESULTS & DISCUSSION

Extract yield & composition

Yield of *C. rotundifolia* stem (CRS) and *C. quadrangularis* leaf (CQL) extracts was maximum, producing ~1.53 g and 1.08 g extract per 20 g sample, respectively. CRL and CQS extracts yielded about 0.67 g and 0.87 g extract per 20 g sample, respectively. The difference in the extract yields could be attributed to the different phytochemical composition and their differential solubility in methanol. The higher yield indicates presence of more methanol soluble compounds, or in other words more polar compounds. It can be assumed that CQL and CRS are richer in polar metabolites as compared to their stem and leaf counterparts, respectively. Murthy [22] reported higher CQ stem extract yield in polar solvents with maximum in water followed by methanol. Higher solubility of CQ extracts in polar solvents has also been confirmed by [29]

Phytochemical composition of both plants was similar, such that presence of flavonoids & tannins was confirmed in leaf extracts of both plants, while that of flavonoids, tannins and saponins was confirmed in both stem extracts (CQS & CRS). Alkaloids were not detected in either of the four extracts. Further, in a similar study presence of polyphenols and ascorbic acid has been reported in methanolic stem extract of CQ [22].

Characterization of AgNPs

Change in color of solution from green to brown after addition of AgNO₃ solution was observed. Change in color of the extract has been reported as visible indicator of reduction of silver ions, excitation of surface plasmon resonance and formation of small nano-sized particles [30, 31]. AgNPs synthesised from all the four extracts were spherical and ~100 - 200 nm in size (Figure 1). The nanoparticles formed aggregates and were present in the form of large agglomerates. However, these aggregates when mixed in appropriate solvent, formed a uniform suspension. The AgNPs biosynthesised with plant extracts often round in shape and form aggregates [30].

The FTIR spectrum of the biosynthesized AgNPs from different extracts were almost similar. The peaks at 1624 cm⁻¹ and 1521 cm⁻¹ represents C=O (carbonyl group) and C-N groups, respectively. Presence of peak at 1748 cm⁻¹ confirms presence of medium stretch from C=O bond due to dimer formation. Wavenumber 2851 cm⁻¹ corresponds to weak carbonyl (C=O) vibrations, wherein 1458 cm⁻¹ & 2851 cm⁻¹ corresponds to C=C vibrations. Further, presence of peak at 1248 cm⁻¹ and 791 cm⁻¹ confirmed presence of N-H bond. The C-N bond stretching represented by peak at 1035 cm⁻¹ is probably due to aliphatic amines. A downward shift in the FTIR spectra of AgNPs indicates binding functional groups at their surface. Such downward shift was recorded in C=O and C-N peaks and an upward shift was recorded in O-H peak.

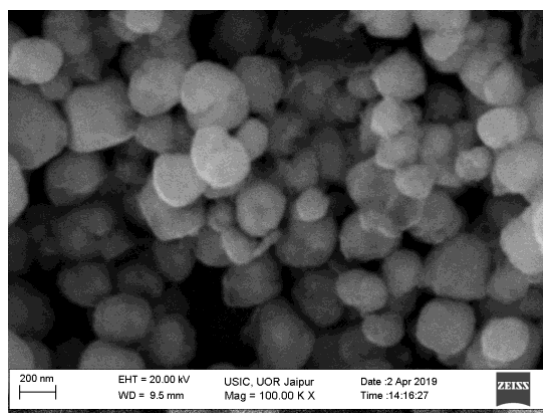


FIGURE 1. Scanning electron microscopic image of AgNPs synthesized using *Cissus* extracts

Antibacterial activity of AgNPs

Crude extracts of CQ did not showed any inhibitory effect against either of the tested pathogens, while the nanoparticles synthesised from these extracts showed significant activity. Absence of activity from CQ stem and leaf crude extracts indicates that the antimicrobial activity exhibited by its nanoparticles is most likely due to the silver, which is a well known bactericidal agent. In contrast, both extracts of CR showed good inhibitory activity against both pathogens. Moreover, the nanoparticles derived from CR extracts showed enhanced inhibitory effect, and igher inhibition was recorded for CRL extracts. All the nanoparticles showed greater inhibitory activity against *P. vulgaris*, which could be attributed to the greater biocompatibility for *P. vulgaris*. Though AgNPs synthesised from both CQ & CR extracts showed enhanced antibacterial activity, yet higher activity was shown by CQS AgNPs, which however was not considered as a good candidate for formulation of antibacterial nanomedicine, as its crude extracts did nt showed any inhibition, thus the inhibition was most likely only due to the silver. CQ stem stem extracts have been reported to be effective against gram positive bacteria (*Bacillus subtilis*, *B. cereus*, *Staphylococcus aureus*) than gram negative bacteria (*Pseudomonas aeruginosa*, *E. coli*), and thus have been rendered relatively resistant to the CQ stem extracts [22]. Inactivity or lower activity of crude CQ extracts has also been reported against *K. penumoniae*, *E. faecalis*, *V. cholerae* and *S. typhi* [31]. Ethnol & aqueous extracts of CQ have been reported to show significant inhibitory effect against *P. mirabilis* [32].

CONCLUSION

The present study was aimed to explore the potential of *C. quadrangularis* and *C. rotundifolia* as bioactive ingredient in antibacterial nanomedicinal formulations. Phytochemical profiling of the extracts confirmed the presence of flavonoids and tannins in all the extracts. Antimicrobial assays of all the crude extracts of CQ and NPs derived from leaf and stem extract revealed that none of the crude extracts showed antimicrobial activity, whereas nanoparticles derived from stem extracts showed significant antimicrobial potential, with higher (~2.5 times) activity against *P. vulgaris* than that against *M. luteus*. On the contrary, all extracts of *C. rotundifolia* exhibited antimicrobial activity against both pathogens. Nanoparticles biosynthesized from leaf and stem extracts of *C. rotundifolia* exhibited higher activity than the crude extracts against *P. vulgaris*, while it was similar to the crude extracts against Micrococcus. This study therefore indicates that the rich phytochemical profile and antimicrobial potential of *C. rotundifolia* extracts can further be used to develop efficient and non-toxic herbal drugs formulations against various pathogenic microbes.

ACKNOWLEDGEMENT

Authors would like to acknowledge the Department of Botany, IIS University for providing all the laboratory facilities that were required to conduct the experiments related to this work.

REFERENCES

1. H. Charkhian, A. Bodaqlouie, E. Soleimannezhadbari, L. Lotfollahi, N. Shaykh-Baygloo, R. Hosseinzadeh, N. Yousefi and M. Khodayar, *Curr. Microbiol.* **77**, 2674-2684 (2020).
2. A. Singh, J. Kumar, V. Sharma, D. Singh, P. Kumari, J. Nishad, V. Gautam and R. Kharwar, *S. Afr. J. Bot.* **140**, 87-94 (2021).
3. B. Al-Sum and A. Al-Arfaj, *Sci. J. Clin. Med.* **2**, 110-113 (2013).
4. H. Zulfiqar, A. Zafar, M. Rasheed, Z. Ali, K. Mehmood, A. Mazher, M. Hasan and N. Mahmood, *Nanoscale Adv.* **1**, 1707-1713 (2019).
5. J. J. Ramyadevi, K. A. Marikani, G. Rajakumar and A. Rahuman, *Mat. Letters* **71**, 114-116 (2012).
6. B. Chudasama, A. Vala, N. Andhariya, R. Mehta and R. Upadhyay, *J. Nanoparticle Res.* **12**, 1677-1685 (2010).
7. K. Szczepanowicz, J. Stefanska, R. Socha and P. Warszynski, *Physicochem. Prob. Min. Process.* **45**, 85-98 (2010).
8. D. Suárez, J. Colón, W. García-Mercado, D. Piñero-Cruz and S. Bailón-Ruiz, *MRS Adv.* **5**, 975-984 (2020).
9. R. Hamouda, M. Abd El-Mongy and K. Eid International, *J. Pharm.* **14**, 359-368 (2018).
10. G. Marslin, R. Selvakesavan, G. Franklin, B. Sarmento and A. Dias, *Int. Journal of Nanomedicine* **10**, 5955 (2015).
11. S. Iravani, *Green Chem* **13**, 2638-2650 (2011).
12. J. Mittal, A. Batra, A. Singh and M. M. Sharma, *Adv. Nat. Sci. Nanosci. Nanotech.* **5**, 043002 (2014).
13. J. Mittal, R. Jain and M. M. Sharma, *Adv. Nat. Sci. Nanosci. Nanotech.* **8**, 025011 (2017).
14. J. Mittal, U. Pal, L. Sharma, A. Verma, M. Ghosh and M. Sharma, *IET Nanobiotech.* **14**, 230-238 (2020).
15. H. Mehewish, M. Rajoka, Y. Xiong, H. Cai, R. Aadil, Q. Mahmood, Z. He and Q. Zhu, *J. Environ. Chem. Eng.* **9**, 105290 (2021).
16. H. Abdullah, S. Asseri, W. Mohamad, S. Kan, A. Azmi, F. Julius and P. Chia, *Environ. Pollut.* **271**, 116295 (2021).
17. S. Ahmed, Saifullah, M. Ahmad, B. Swami and S. Ikram, *J Rad. Res. App. Sci.* **9**, 1-7 (2016).
18. K. B. Narayanan and H. H. Park, *Eur. J. Plant Path.* **140**, 185-192 (2014).
19. S. Stohs and S. Ray, *Phytother. Res.* **27**, 1107-1114 (2013).
20. M. Sen and B. Dash, *Int. J. Green Pharm.* **6**, 169-173 (2012).
21. S. Chanda, Y. Baravalia and K. Nagani, *J. Pharmacogn. Phytochem.* **2**, (2013).
22. K. Murthy, A. Vanitha, M. Swamy and G. Ravishankar, *J. Med. Food* **6**, 99-105 (2003).
23. G. Mishra, S. Srivastava and B. Nagori, *Int. J. Pharmtech. Res.* **2**, 1298-1310 (2010).
24. S. Kumar, A. Anandan and M. Jegadeesan, *Arch. Appl. Sci. Res.* **4**, 1782-1787 (2012).
25. M. Jainu and C. Devi, *Chem.-Biol. Interact.* **161**, 262-270 (2006).
26. G. Mate, N. Naikwade, C. Magdum, A. Chowki and S. Patil, *Int. J. Green Pharm.* **2**, 118-121 (2008).
27. G. Vijayalakshmi, O. Aysha and S. Valli, *World J. Pharm. Pharm. Sci.* **4**, 1702-1713 (2015).
28. S. Gupta, S. Kachhwaha, S. Kothari, M. Bohra and R. Jain, *ACS Omega* **5**, 29189-29198 (2020).
29. S. Srivastava, I. Seethalakshmi and L. Rebecca, *J. Chem. Pharmaceut. Res.* **5**, 131-134 (2013).
30. P. Agarwal, V. Bairwa, S. Kachhwaha and S. Kothari, *Int. J. Nanotech. App.* **4**, 1-8 (2014).
31. K. Renugadevi, D. Inbakandan, M. Bavaniatha and V. Poornima, *Int. J. Pharma Bio Sci.* **3**, 437-445 (2012).
32. A. Raj, A. Selvaraj, V. Gopalakrishnan and S. Dorairaj, *J. Herb. Med. Toxicol.* **4**, 177-180 (2010).

A review on co-pyrolysis of agriculture biomass and disposable medical face mask waste for green fuel production: recent advances and thermo-kinetic models

Melvin X. J. Wee¹, Bridgid L. F. Chin (✉)^{1,2}, Agus Saptoro¹, Chung L. Yiin^{3,4}, Jiuan J. Chew⁵, Jaka Sunarso⁵, Suzana Yusup⁶, Abhishek Sharma^{7,8}

¹ Department of Chemical and Energy Engineering, Faculty of Engineering and Science, Curtin University Malaysia, CDT 250, Miri 98009, Malaysia

² Energy and Environment Research Cluster, Faculty of Engineering and Science, Curtin University Malaysia, CDT 250, Miri 98009, Malaysia

³ Department of Chemical Engineering and Energy Sustainability, Faculty of Engineering, Universiti Malaysia Sarawak (UNIMAS), Kota Samarahan 94300, Malaysia

⁴ Institute of Sustainable and Renewable Energy (ISuRE), Universiti Malaysia Sarawak (UNIMAS), Kota Samarahan 94300, Malaysia

⁵ Research Centre for Sustainable Technologies, Faculty of Engineering, Computing and Science, Swinburne University of Technology, Kuching 93350, Malaysia

⁶ Generation Unit (Fuel Technology & Combustion), Tenaga Nasional Berhad (TNB) Research Sdn Bhd, Kajang 43000, Malaysia

⁷ Department of Chemical Engineering, Manipal University Jaipur, Jaipur 303007, India

⁸ Chemical & Environmental Engineering, School of Engineering, RMIT University, Melbourne, Victoria 3000, Australia

© Higher Education Press 2023

Abstract The Association of Southeast Asian Nations is blessed with agricultural resources, and with the growing population, it will continue to prosper, which follows the abundance of agricultural biomass. Lignocellulosic biomass attracted researchers' interest in extracting bio-oil from these wastes. However, the resulting bio-oil has low heating values and undesirable physical properties. Hence, co-pyrolysis with plastic or polymer wastes is adopted to improve the yield and quality of the bio-oil. Furthermore, with the spread of the novel coronavirus, the surge of single-use plastic waste such as disposable medical face mask, can potentially set back the previous plastic waste reduction measures. Therefore, studies of existing technologies and techniques are referred in exploring the potential of disposable medical face mask waste as a candidate for co-pyrolysis with biomass. Process parameters, utilisation of catalysts and technologies are key factors in improving and optimising the process to achieve commercial standard of liquid fuel. Catalytic co-pyrolysis involves a series of complex mechanisms, which cannot be explained using simple iso-conversional models. Hence, advanced conversional models are introduced, followed by the evolutionary models and predictive models, which can solve the non-linear catalytic co-pyrolysis reaction kinetics. The outlook and challenges for

the topic are discussed in detail.

Keywords biomass, COVID-19 waste, catalyst, pyrolysis, kinetics

1 Background

1.1 Bioenergy from biomass as a crucial renewable energy source

Association of Southeast Asian Nation (ASEAN) projected its population to grow by 100 million from 2014 to 2025, with an annual growth of 5%, and 4% in energy demand per year. Hence, the association has set the goal to increase its renewable energy share from 9.4% to 23% of the primary energy supply in the ASEAN region [1]. In order to meet the target, member countries has strategise several policies, laws, and regulations [2], as summarised in Table 1, which includes ASEAN member countries and their strategies [3].

Following this, ASEAN countries are known as the top agriculture producers. Hence, there are significant prospects for bioenergy as a strategy to help realise the ASEAN renewable energy generation and consumption goals. For example, Indonesia and Malaysia are the major players in the oil palm industry, followed by Thailand as

Table 1 ASEAN member countries renewable energy policies

Country	Policies/strategies	Ref.
Cambodia	<p>Energy Sector Development Policy and Rural Electrification Policy, 2007 Rural electrification fund subsidy and investment incentives are provided as support to the policy</p> <ul style="list-style-type: none"> • Providing reliable, affordable quality supply of electricity to the consumers • Promoting private-owned facilities in the renewable energy sector to instigate competition between the companies • Providing electricity to 70% of the rural households by the year 2030 	[4]
India	<p>The Electricity Act, 2003</p> <ul style="list-style-type: none"> • To encourage the co-generation of electricity with renewable sources <p>• Specify the terms and conditions for the determination of tariff, which forms the National Electricity Policy and the Tariff policy</p> <p>Tariff Policy, 2006</p> <ul style="list-style-type: none"> • States that renewable energy shall be distributed with a preferential tariff determined by the appropriate commission <ul style="list-style-type: none"> • Bidding process within suppliers offering renewable energy from the same source <p>National Rural Electrification Policies, 2006</p> <ul style="list-style-type: none"> • Provision of access of electricity to all households by the year 2009 <ul style="list-style-type: none"> • Quality and reliable power supply at affordable rates <ul style="list-style-type: none"> • Providing off grid solutions for rural areas <p>Integrated Energy Policy Report (Planning Commission), 2006 Recommends a solution to meet the energy demand of India in an integrated process up to 2031–2032</p>	[5]
Indonesia	<p>Government Rule No. 3 on Supply of Electricity, 2005 To ease the private-own power producers to set up renewable energy plants</p> <p>Blueprint of National Energy Implementation Program 2005–2025</p> <ul style="list-style-type: none"> • To outline plans for energy supply security <p>• To provide guidelines for various sectors involving renewable and non-renewable energies</p> <ul style="list-style-type: none"> • To provide subsidies to enhance energy efficiency <p>Presidential Regulation No. 5 on National Energy Policy, 2006</p> <ul style="list-style-type: none"> • To set goals to promote diversification of energy sources • To reduce energy consumption by 1% per year as target <p>Presidential Decree No. 1 on Supply and Use of Biofuels, 2006 Setting targets and guidelines for biofuels utilisation and development</p> <p>Ministerial Regulation No. 2 on Medium Scale Power Generation from Renewable Energy Sources, 2006 To set pricing guidelines for projects ranging from 1 to 10 MW</p> <p>Energy Law, 2007 Providing renewable energy developers with investment incentives</p> <p>Electricity Law, 2010 To encourage private companies to participate in energy supply To provide priority in the utilisation of renewable energy To promote small scaled distributed power generation from renewable sources</p> <p>Ministerial Regulation No. 4/2012, 2012 To set the Feed-in-Tariff for electricity generated from biomass</p> <p>Ministerial Regulation No. 27/2014, 2014</p> <ul style="list-style-type: none"> • To set goals to increase the renewable energy portion to 23% by the year 2025, and 31% by 2050 <ul style="list-style-type: none"> • Feed-in-tariffs for renewable energy • To encourage the government and private sectors to utilise biofuels for power generation 	[6]
Malaysia	<p>Five-Fuel Diversification Policy, 2001 To include renewable energy in the energy supply mix of power generation</p> <p>National Biofuel Policy, 2006</p> <ul style="list-style-type: none"> • To reduce dependency on fossil fuels <p>• Providing subsidies to promote the demand for alternate sources of energy</p> <p>National Renewable Energy Policy and Action Plan, 2010</p> <ul style="list-style-type: none"> • Increase the renewable energy contribution in the energy supply mix <ul style="list-style-type: none"> • Promote growth of the renewable energy sector <ul style="list-style-type: none"> • Maintaining the renewable energy at an affordable price • Instigate awareness to the community on renewable energy 	[7]
Thailand	<p>Committee on Biofuel Development and Promotion (CBDP), 2008 Government subsidies from the State Oil Fund biodiesel price reduction</p> <p>Second Alternative Energy Development Plan (2008–2022), 2008</p> <ul style="list-style-type: none"> • To increase the proportion of alternative energy to 20% of the national total energy consumption by 2022 <ul style="list-style-type: none"> • To utilise renewable energy as a substitute for imported oil <ul style="list-style-type: none"> • To increase energy security of Thailand • Promote integrated green energy utilisation in communities • Enhance the development of alternative energy industry • Research and development of efficient technology to harvest renewable energy 	[8]
Vietnam	<p>Renewable Energy Action Plan, 2001 Government intervention to promote renewable energy</p> <p>The Law of Electric, 2004 Support electricity generation from renewable sources by providing investment incentives, preferential electricity prices and taxes</p> <p>Decision 1855/QĐ-TTg: 27 Dec 2007</p> <ul style="list-style-type: none"> • National Energy Development Strategy up to 2020 with outlook to 2050 <p>• To encourage the development of new and renewable energies, bioenergy to meet the socioeconomic requirements</p> <ul style="list-style-type: none"> • To meet the target of 5% of primary commercial energy by 2020 and 11% by 2050 <p>Decision No. 177/QĐ-TTg: 20 Nov 2007</p> <ul style="list-style-type: none"> • To develop biofuel, as an alternative for fossil fuels • To build a legal framework for biofuel development <ul style="list-style-type: none"> • To develop materials for biofuel production <ul style="list-style-type: none"> • To enhance biofuel extraction <p>National Program for Biofuels Development, 2011</p> <ul style="list-style-type: none"> • Develop biofuel to partly replace fossil fuels • Create the legal framework for biofuel development • Develop relevant materials for biofuel production <ul style="list-style-type: none"> • Develop biofuel extraction technologies 	[9]

(Continued)

Country	Policies/strategies	Ref.
Myanmar	<p>Myanmar Energy Master Plan, 2015</p> <ul style="list-style-type: none"> • To study the energy demand development from 2014 to 2035 • To set a goal to achieve 15%–20% share of renewable energy in 2020 <ul style="list-style-type: none"> • To improve the rural renewable energy usage • To achieve 57% hydropower, 5% solar and wind by 2030 	[10]
Laos	<p>The Electric Law, 1997</p> <p>Setting standards for the administration, production, distribution, transmission and the import and export of electricity</p> <p>The Power Sector Policy Statement, 2001</p> <ul style="list-style-type: none"> • To increase the electricity supply rate to 90% by 2020 • Promotes the public and private partnerships in hydropower development (500 kV grid) <p>The 8th National Socio-economic Development Plan (NSEDP), 2016–2020</p> <p>Promotes sustainability and diversification of renewable energy sources</p> <p>The Renewable Energy Development Strategy</p> <p>To increase the renewable energy share to 30% and substitute 10% of the transport fuel with biofuels by 2025</p>	[11]
Philippines	<p>R. A. No. 9367: The Biofuels Act, 2006</p> <p>Encourage the utilisation of biofuel-blended transport fuels by providing fiscal incentives</p> <p>R. A. No. 9513: The Renewable Energy Act, 2008</p> <ul style="list-style-type: none"> • Enhance the renewable energy development by providing fiscal and non-fiscal incentives <ul style="list-style-type: none"> • To reduce the country's reliance of fossil fuels <p>• Adopts renewable portfolio standards, feed-in-tariffs, net-metering, and Green Energy Option policy instruments</p>	[12]

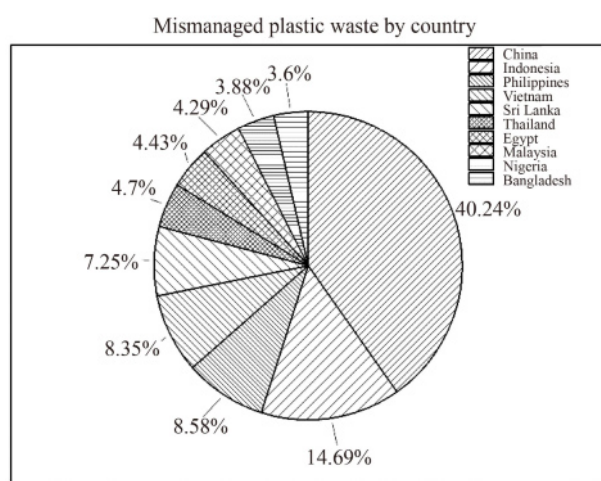


Fig. 1 Mismanaged plastic waste generated by countries. Reprinted with permission from Ref. [24], copyright 2015, American Association for the Advancement of Science.

shown in Fig. 1. In Indonesia, the production volume reached 45.86 million tonnes in 2019 [13]. Meanwhile, Malaysia produced 18.5 million tonnes in the same year [14]. However, the palm oil produced only represents 10% by weight of the total harvest; and the remainder contributed to the oil palm biomass, i.e., oil palm empty fruit bunch (EFB), palm kernel shell (PKS), palm pressed fibres (PPF), and oil palm frond [15]. To accommodate the rising population, food demand such as rice and wheat production in India has grown dramatically. In 1960, rice and wheat production was 34.6 and 11 million tonnes, respectively, and had risen to 118.9 and 107.6 million tonnes respectively in 2019 [16]. The rapid generation of biomass poses sustainability issues and waste management complications. Fortunately, this agriculture biomass is made up of lignocellulosic constituents, which include cellulose (23.3–44.9 wt %), hemicellulose (17.3–34.0 wt %),

and lignin (12–53.5 wt %) [17]. Cellulose is a complex polymer of glucose held by β -1,4-glycosidic bonds, intramolecular and intermolecular H-bonds. Hemicellulose is a heterogeneous polysaccharide, consisting of hexoses (i.e., glucose, mannose, galactose, xylose, arabinopyranose, arabinofuranose, and glucuronic acid). Lignin is made up of guaiacyl propane, syringyl propane and *p*-hydrophenyl propane [17,18]. These constituents serve as the basic precursors for the conversion into fuel, fibres, and aromatics [19]. Other properties from the proximate and ultimate analysis are depicted in Table 2, which shows that the biomass contains 50 to 70 wt % of volatile matter. In comparison, the carbon and hydrogen contents are 36–53 and 5.0–7.3 wt %, respectively.

Besides that, plastic or polymer waste generation has increased over the years. According to Geyer et al. [23], the study reports that cumulative plastic waste generation of primary and secondary plastic has reached 6300 million tonnes from 1980 to 2015. Only 12% of these plastic wastes were incinerated, while 9% were recycled. Furthermore, according to Jambeck et al. [24], ASEAN member countries such as Indonesia, Philippines, Vietnam, Thailand, and Malaysia contributed approximately 41% of the mismanaged plastic waste as illustrated in Fig. 1. Moreover, according to Abnisa and Alaba [25], the global composition of plastic wastes comprises of 26.67% low density polyethylene (LDPE), 25.33% polypropylene (PP), 18.67% high density polyethylene (HDPE), 14.67% polyethylene terephthalate (PET), 8% polystyrene (PS), and 6.67% polyvinyl chloride (PVC). Furthermore, with the rapid rise of confirmed cases of the novel coronavirus disease (COVID-19), the need for personal protective equipment (PPE) is high, resulting in the rapid generation of COVID-19 related wastes, exacerbating the current plastic waste management issue. According to Liang et al. [26], there are two categories of COVID-19 related wastes which are (1) wastes generated

Table 2 Proximate and ultimate analysis of different agriculture biomasses [20–22]

Sample	PKS	PPF	EFB	Rice husk	Rice straw (RS)	Bagasse
Proximate analysis/(wt %)						
Moisture	5.73	6.56	8.75	4.50	–	–
Ash	2.21	5.33	3.02	12.40	13.60	6.50
Volatile matter	73.74	75.99	79.67	58.60	70.10	72.70
Fixed carbon	18.37	12.39	8.65	24.40	16.30	20.80
Ultimate analysis/(wt %)						
C	53.78	50.27	48.79	43.20	37.10	36.30
H	7.20	7.07	7.33	5.00	5.20	5.80
S	0.51	0.63	0.68	0.00	0.10	0.00
N	0.00	0.42	0.00	0.30	0.50	0.30
O	36.3	36.28	40.18	51.4	43.5	51.10

from within hospitals or healthcare facilities, which are considered medical wastes and are collected and disposed of with appropriate measures (i.e., identification, collection, separation, storage, transportation, treatment, and disposal) [26], and (2) the wastes generated outside those facilities, which include disposable medical face masks (DMFM) and gloves. These wastes do not have proper waste management and are often treated as municipal solid, and plastics wastes. Besides that, according to the World Health Organisation (WHO) [27], the demand for these PPE, i.e., DMFM, and gloves, is expected to rise 20% by the year 2025. If these wastes are not managed properly, it will lead to major environmental complications. In some parts of the ASEAN region (i.e., Cambodia, Philippines, India, and Indonesia), poor waste management issues such as landfills and illegal dumping were present even before COVID-19. These uncontrollable landfills would escalate into space limitations and release toxic pollutants to the environment [28]. Moreover, the random disposal of these wastes could also lead to microplastic pollution, accumulating in the food chain, especially in aquatic life [29].

1.2 Biomass and polymer waste conversion pathways: pyrolysis

Therefore, strategies to recover energy from these wastes are keys to minimize the waste accumulation and their impacts to the environment. To convert these high-energy feedstocks into valuable fuel, there are two main pathways to convert the lignocellulosic biomass and plastic wastes into biofuels or green fuels, i.e., bio-chemical conversion and thermochemical conversion. In bio-chemical conversion, the larger and complex compounds are broken down into simpler molecules, with bacteria and enzymes. However, this method has limited feedstock options, and is not suitable to convert synthetic polymers like plastic wastes [30]. Besides that, thermochemical conversion includes low-temperature carbonisation, intermediate-temperature pyrolysis, and high-temperature gasification. Among these thermochemical

processes, pyrolysis represents a promising technology in terms of high fuel-to-feed ratios [31]. In addition, the pyrolysis process is favoured as the process that can be carried out at atmospheric pressure and faster conversion rates (<1 s) [32]. Moreover, the pyrolysis process is compatible with a wide variety of feedstocks aside from lignocellulosic biomass, i.e., plastics, and waste tires [33–36]. The pyrolysis process involves production of biofuel in the form of bio-oil, as well as producing valuable bio-chemicals such as alcohols, aldehydes, ketones, acids, furans, anhydrosugars, and phenols from biomass [37]. Fast pyrolysis yields the highest amount of bio-oil (65–75 wt %), while slow pyrolysis produces less bio-oil (20–50 wt %), with a larger proportion of bio-gas (20–50 wt %) and biochar (25–35 wt %) [38]. A detailed information on the different pyrolysis modes can be found in these references [38–43].

This paper focuses on the issues of the growing generation of biomass in ASEAN region, as well as the single-use plastics (i.e., DMFM) generated due to the COVID-19 pandemic. Following this, this review outlines the potential of co-pyrolysis of the biomass with plastic wastes as a technique to produce value-added bio-oil. Besides that, this review also looks into the technologies, (i.e., catalyst selection) and technical aspects (i.e., pyrolysis parameters) of the co-pyrolysis process. In addition, the kinetic models, and the advancements to describe the catalytic co-pyrolysis of biomass and plastic wastes are also outlined. Finally, the outlook detailing the significance and the limitations of the co-pyrolysis technique is discussed.

2 Bibliometric analysis

Bibliometric analysis is defined as the analysis of scientific publications using statistical methods to provide an outline of the research area [44]. Several publications have adopted this method in research areas of bio-diesels [45], municipal solid waste management [44], invest-

ments [46], and even COVID-19 [47]. This method of analysis provides a systematic way to sort and analyse a great number of publications, in terms of citations, co-citations, author keywords, and countries.

In this project, the bibliometric analysis of the field of pyrolysis of biomass was conducted in VOSviewer1.6.11. The utilisation of the software has been widely employed in this study, providing a visualisation of the relationships between publications in a research area or topic. The online publication database platform, Scopus, was utilised in the collection of the database for this study. The search phrase and Boolean Operators for this study were “pyrolysis AND biomass AND plastic AND bio-oil OR oil palm OR catalyst”, the publication year was limited from 2019 to 2023, and limited to journal articles only. A

total of 1448 publications were fitted into VOSviewer to analyse the co-occurrence of author keywords more than 20 times and are visualised in Fig. 2. The top-ranked link strength keywords, excluding the search phrases, include catalytic pyrolysis, co-pyrolysis, biochar, oxygen reduction reaction, and hydrogen. Based on this study, the current research trend involves around catalytic pyrolysis or co-pyrolysis, and focuses on the oxygen reduction, hydrogen and biochar formation from the process. Furthermore, another analysis of the bibliographic coupling of countries was carried out and the results were visualised in Fig. 3. The result suggests that China, United States, South Korea, Malaysia, and Australia are the active countries involved in this research area.

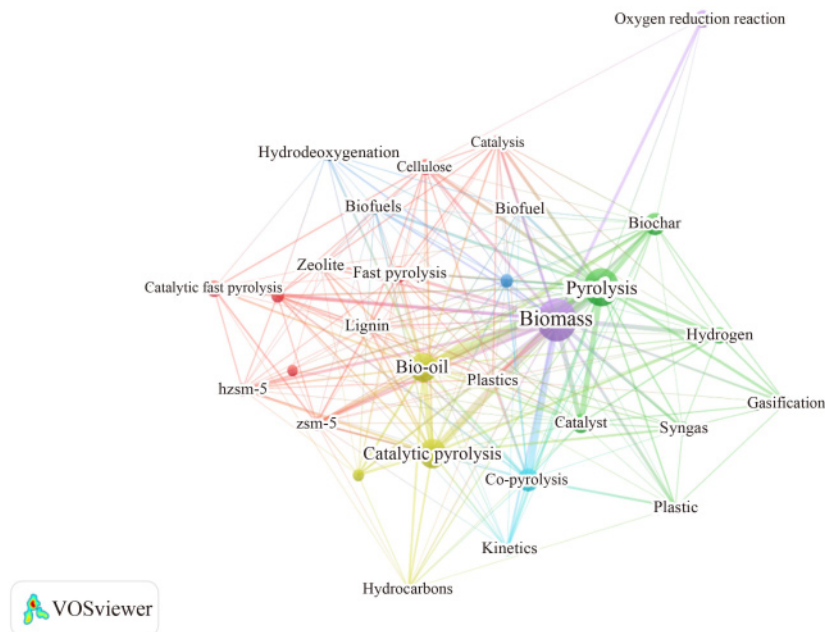


Fig. 2 Co-occurrence of author's keywords > 20 times by publication year.

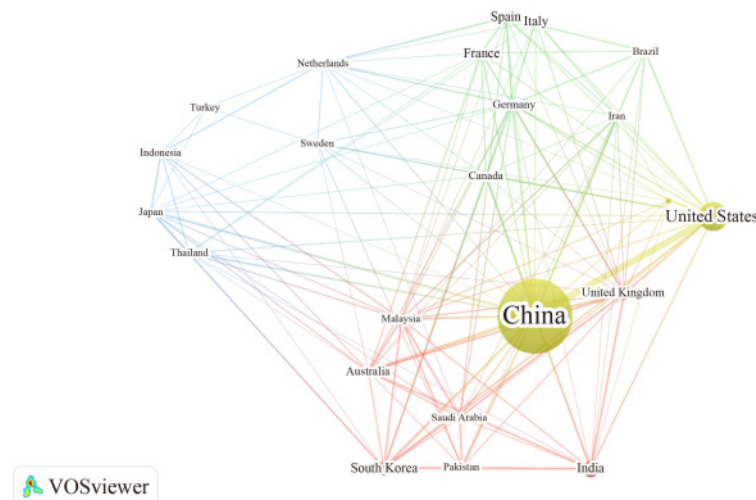


Fig. 3 Bibliographic coupling of countries by year.

3 Pyrolysis technologies/techniques for bio-oil production

Initially, most of the research studies focus on mono-component such as biomass [20,48–54] or plastic waste [55–60] in the pyrolysis process for bio-oil production. However, the pyrolysis of lignocellulosic biomass produces low quality bio-oil and yield [61]. Biomass-derived pyrolysis oil is high in oxygen content, corrosive in nature, and thermally unstable. Bio-oil generally requires upgradation using a hydrogen source and a catalyst, which makes the process complicated and expensive [37]. For plastic pyrolysis, the volatile products contain harmful compounds, i.e., polycyclic aromatic hydrocarbons (PAHs) [62–64]. PAH is a macromolecular aromatic compound with carcinogenic and mutagenic characteristics that pose health concerns upon exposure [65]. Hence, there is a growing interest in improving the pyrolysis process to produce bio-oil with enhanced properties, i.e., co-pyrolysis of two or more feedstock, and the utilisation of catalysts for product upgrading.

3.1 Mechanisms of co-pyrolysis with polymers

Hence, it is crucial to understand the reaction mechanism of co-pyrolysis of biomass and plastic wastes. Several studies have explored the co-pyrolysis of biomass with polymer wastes, i.e., RS and sugarcane bagasse with PP, and PS [34]; corn stover, ipil, and narra, with HDPE, LDPE and PP [35]; RS with waste tires [36]; sawdust with LDPE [66]. These studies show that the co-pyrolysis technique is promising in improving the bio-oil quality and calorific value, reducing energy costs by lowering the activation energy. According to Lin et al. [67], the widely accepted mechanism of co-pyrolysis of biomass with plastics can be summarised in a two-step mechanism: (1) the free radicals generated from the pyrolysis of biomass initiate the β -scission of the polymers, inhibiting the intermolecular and intramolecular H transfer, producing aliphatic hydrocarbons and reduced alkadienes; (2) the H transfers from the polymers reacting with the biomass-derived radicals to form stable compounds. This mechanism allows an increase in the decomposition rate of the biomass, greatly reducing the char yield as reported by Onal et al. [68]. The addition of a hydrogen-rich plastic waste to biomass influenced the energy recovery efficiency of bio-oil by affecting the real-time power output, reaction time, and changes in the bio-oil composition [69]. Besides that, the biomass decomposes first at a lower temperature forming free radicals, i.e., OH radicals. These radicals react with the pyrolysis products of plastic, larger molecular weight organics (C_{12}) were formed with the co-pyrolysis of biomass and LDPE [70]. According to Navarro et al. [34], this mechanism reduces the selectivity for the secondary reaction to occur,

reducing the char yield (i.e., 8.6 and 10 wt % reduction of char with the co-pyrolysis of B and PS, B and PP, respectively). Besides that, according to a study by Ojha et al. [71], the formation of C_8 – C_{20} alcohols was observed, which was explained by the reaction of hydrocarbon free radicals from PP, with water from the dehydration reaction from cellulose. According to Uzoejinwa et al. [72], synthetic polymers are derived from petroleum products with high carbon and hydrogen contents, low oxygen content, and contains high calorific values. Hence, making it suitable potential as a co-feedstock for the biomass pyrolysis. Furthermore, these polymer wastes also showed similar properties of high volatile matter, higher heating value (HHV) and lower heating value (LHV) than biomass, as observed in Table 3.

3.2 Pyrolysis reaction parameters that influence the bio-oil yield

During pyrolysis, multiple factors affect the outcome of the process, which are, reactor temperature, heating rate, feedstock particle size, and residence time. Studies on these parameters are crucial to improve the pyrolysis process in terms of bio-oil product yield and quality. Generally, the operating parameters are adjusted, to impede the secondary tar cracking reactions, which reduces the bio-oil yield.

3.2.1 Pyrolysis temperature

The role of temperature is to provide sufficient thermal energy for the decomposition of the biomass. It is important to note that for the main constituents of biomass, cellulose, hemicellulose, and lignin, their temperature degradation ranges are 225–325, 325–375, and 250–500 °C, respectively. Hence, an optimal temperature of 500 °C is sufficient to encompass these temperature ranges. Nevertheless, the optimal temperature differs with the compositions of varying feedstock [74]. Furthermore, according to Dai et al. [75], bio-oil yield peaks at the

Table 3 Proximate and ultimate analysis of polymers [22,34,60,73]

Sample	PP	PS	LDPE	HDPE	Waste tires
Proximate analysis/(wt %)					
Moisture	0.20	–	–	0.00	1.10
Ash	0.10	0.00	–	0.00	8.10
Volatile matter	99.80	99.50	99.98	100.00	62.50
Fixed carbon	0.00	0.50	0.02	0.00	28.20
Ultimate analysis/(wt %)					
C	85.40	89.50	85.47	85.34	84.60
H	14.50	8.50	14.21	12.22	7.70
S	0.00	0.00	0.11	0.00	1.40
N	0.00	0.00	0.08	0.00	0.40
O	0.00	2.00	0.13	2.44	4.30
HHV/(MJ·kg ⁻¹)	46.00	40.10	–	46.40	36.80
LHV/(MJ·kg ⁻¹)	43.10	–	–	43.10	35.10

temperature range of 450–550 °C; a further increase of temperature (> 600 °C), the bio-oil yield reduces, corresponding to an increase in non-condensable gas, or biogas. Moreover, a higher temperature (530–830 °C) promotes the reduction of complex compounds (i.e., acetaldehyde, methanol, propanol, and acetone), while increasing stable compounds (benzene, naphthalene, cresols, and phenols). For the case of polymer wastes, the degradation temperature ranges generally overlap or are higher than biomass, which varies between types of polymers. According to Miandad et al. [33], PP showed a single-stage degradation, which starts at a lower temperature of 240 °C with the maximum degradation at 425 °C, PS also showed a single-stage degradation but starts at a higher temperature of 330 °C, with the maximum degradation at 470 °C. While polyethylene (PE) exhibits a two-stage degradation, the first stage starts at the temperature of 270 °C and reaches 400 °C with a conversion rate of 12%, which followed by the second stage degradation starting at 400 °C, with the maximum conversion rate of 95% at 480 °C. Hence, these differences in thermal decomposition behaviours must be considered for the co-pyrolysis of biomass and polymers. According to Salvilla et al. [35], the study studied the effect of co-pyrolysis of corn stover with different polymers, i.e., LDPE, PP, and HDPE. Thermogravimetry analysis (TGA) experiments of the biomass-plastic blends result in a two-stage decomposition. The first stage involves the degradation of hemicellulose, and cellulose of the corn stover, while the second stage degradation overlaps with the decomposition of lignin. The results from this study conclude that the biomass and plastic blends exhibit the most synergistic effect occurs at temperature near 500 °C, i.e., corn stover and PP blend (5:3), and corn stover and LDPE blend (5:3) observed the greatest decomposition rate between 8% and 10% per minute respectively between the temperature ranges of 480–505 °C.

3.2.2 Heating rate

The heating rate is another important parameter that could determine the product distribution of the biofuels. According to Akhtar and Saidina Amin [31], fast heating rates cause rapid fragmentations of biomass and produces more bio-oil yield. This is possible as at higher heating rates (1000 °C·min⁻¹), there is short amount of time for the secondary reactions (i.e., tar cracking and repolymerisation). However, once the heat and mass transfer limitations have been overcome, higher heating rates would not increase the bio-oil yield further. Besides that, heating rates also affect the quality of the bio-oil, at lower heating rates, the water content of the bio-oil increases, as it impedes the dehydration reaction. It is also observed that at low heating rates (< 15 °C·min⁻¹) the bio-oil components have a higher weight range of 500–1000 Da, while increasing the heating rate to 15 °C·min⁻¹, it

significantly reduces the weight to 200–500 Da. However, continuing to increase the heating rate does not reduce the weight further [75]. In the case of polymer waste, the study found that LDPE, PP, and PVC, the thermogravimetry or derivative thermogravimetry curves shifted to the higher temperatures when the heating rate was increased. This phenomenon was explained by the thermal lag, due to the increased thermal gradient between the furnace temperature and the sample. Hence, the lower 100 °C·min⁻¹ heating rate favoured the degradation of the plastic wastes [60].

3.2.3 Particle size

To reduce heat transfer limitations caused by the poor heat conductivity of biomass, feedstock particle size or shape is another important criterion for bio-oil production. Larger particles (> 0.5 mm) tend to have poor heat transfer to the inner surfaces of the feedstock particle, this will lead to a lower yield of volatiles associated with the great temperature differences between the inner and outer surfaces of the feedstock particle. However, it is documented further increase in particle size (> 1 mm) does not have any effect on the bio-oil yield, which indicates minor impact of the internal heat or mass transfer to the process [76]. It was also reported that larger particle size, results in lower heat transfer to the feedstock [31,75]. For the pyrolysis of bamboo biomass with particle size, 0.45–0.75 mm, the bio-oil peaked at 54.03 wt %, while for smaller particle size 0.25–0.45 mm lowers the bio-oil yield to 50.85 wt % but increases biogas yield from 18.42 to 23.46 wt % [77]. Larger particle size of 0.8–1.2 mm, on the other hand, also lowered bio-oil yield of 51.61 wt %, with increased biogas and biochar yield of 20.62 and 27.74 wt %, respectively.

3.2.4 Residence time

Likewise, since the pyrolysis vapour is susceptible to secondary reactions, it is important to note that, the vapour residence time must be kept short to maximise the bio-oil yield. However, at very short residence times, the heat transfer limitations may restrict the feedstock from undergoing complete fragmentation [32,74,75]. Hence, the parameter is restricted by the characteristic of the feedstock itself. Instead, optimisation of the vapour residence time is a more feasible direction, i.e., feedstock particle size, heating rate, and design of the reactor and heater configuration to maximise the heat transfer [31].

3.3 The role of catalysts in the pyrolysis process

Catalysts play an important role in enhancing the quality of the bio-oil. This section categorised the existing catalysts employed in the pyrolysis process into three

main groups, commercial zeolite catalysts, metal-based catalysts, and renewable waste catalysts.

3.3.1 Commercial zeolite or acid catalyst

The commercial zeolite catalysts, i.e., ZSM-5, HZSM-5, MCM-41, zeolite Y, SBA-15, and zeolite BEA are the commonly utilised catalysts for the pyrolysis of biomass [78]. These catalysts have the active sites of the catalysts and reduce the dissociation energy of C–O, C=O, and –OH functional group, which allow the ability to remove oxygen atoms from the bio-oil via dehydration, decarboxylation, decarbonylation reactions [42,79]. Besides that, according to Ratnasari et al. [80], the key attributes of the zeolite as a suitable catalyst are the micropores (0.4–1.0 nm) or mesopores (1.5–30 nm) sizes. In a study on MCM-41, a zeolite catalyst with a mesoporous structure; the bigger pores allow hydrocarbons with higher molecular weight to enter the active sites, produce less oxygenates, and yield less aromatics. While smaller pore sized zeolites, such as ZSM-5 and Y-zeolite favour the production of aromatics. However, due to its smaller pore size, it is more likely to cause coking on the surface of these zeolites, thereby deactivating them. Therefore, studies have incorporated hierarchical catalyst structure to maximise the conversion performance [78,81]. Besides that, the acidity of the zeolites refers to the Si/Al ratio of the zeolite, it is a direct representation of the Brønsted acid (–OH group) and Lewis acid (Al sources in the $\text{Al}_2\text{O}_3/\text{SiO}_2$) sites available [74]. Comparing with zeolites, the silicalite catalyst with the same pore size but without acidity produces less aromatics and increases char formation [32]. Besides that, a study on the catalytic copyrolysis of RS and B with plastic wastes concluded that HZSM-5 promoted the deoxygenation, cleavage of the aromatic rings, reforming, isomerisation and Diels–Alder reaction of the bio-oil [22]. Hence, product upgradation

was achieved, and thereby producing valuable compounds, such as aromatics (i.e., styrene, ethylbenzene, *o*-xylene, and trimethyl-benzene) and aliphatic hydrocarbons (i.e., 2,4-dimethyl heptane). Zhao et al. [82] found that, with the bamboo to PP ratio of 1:2 over HZSM-5, high bio-oil yield of 61.62 wt % can be achieved, which is higher compared to that obtained for single feedstock bamboo pyrolysis of 29.91 wt %. Besides that, the aromatic and naphthenic hydrocarbons in the bio-oil were improved, which was in agreement with the study by Suriapparao et al. [22], where with the addition of a catalyst, the biomass–plastic mixture has a lower selectivity for oxygenates, while an increase in aliphatic and aromatic hydrocarbons were observed. The findings summarising the commercial acid catalysts utilised in literature can be found in Table 4.

3.3.2 Commercial metal-based catalyst/support

The metal-based catalysts in the catalytic pyrolysis of biomass majority refers to the metal oxides, alkali earth metals, metal salts, and transition metals. Metal oxides are prominent catalysts in this case, i.e., the basic MgO, CaO, and the acidic ZnO in the study of the pyrolysis of RS. The catalytic behaviour of MgO is similar to ZSM-5, as it favours the ketonization and aldol condensation reactions, which help to reduce oxygenates from the bio-oil [75]. According to Cao et al. [83], MgO has high ionic properties, which inhibits the repolymerisation reaction, hence greatly reduces the biochar formation while increasing the bio-oil yield. Furthermore, CaO was determined to have unique properties, as it behaves differently at different mass ratio incorporated in the feedstock, at less than 0.2 mass ratios; the CaO is a reactant, that reacts with the carboxyl groups to produce ketones. Carboxyl groups are undesirable bio-oil products due to their acidity, i.e., acetic acid. At 0.2 to 0.4 mass

Table 4 Acid zeolite catalyst application in the pyrolysis process examples

Biomass	Catalyst	Bio-oil yield/(wt %)	Reactor	Scale, feed weight/g	Ref.
RS	HZSM-5	21.50	Microwave pyrolysis	200–800	[22]
Bagasse		22.40			
PP		74.20			
PS		92.30			
Baggase: PS		43.80			
B:PP		35.70			
RS:PS		31.20			
RS:PP		24.50			
RS	ZSM-5	47.40	Fixed bed reactor	10	[83]
	Y zeolite	55.20			
	Mordenite	49.10			
	SBA-15	37.30			
Rice husk and WGPF	HZSM-5/MCM41	67.90% hydrocarbon relative content	Tubular reactor	0.001	[81]
	HZSM5	60.20% hydrocarbon relative content			
Seaweed biomass	ZSM-5	51.48	Hydro-pyrolysis	10	[32]
	MCM-41	41.84			
Bamboo	HZSM-5	49.14	Bubbling fluidised bed	100 g·h ⁻¹	[77]

ratio, CaO exhibits absorbent properties, absorbing CO₂ to CaCO₃, which contributes to the mass increase in the char yield. A further increase of CaO (> 0.4 mass ratio), the catalytic effect dominates, reducing the ester content in the bio-oil into simpler hydrocarbons and H₂ [84]. Besides that, while ZnO has less deoxygenation properties compared to CaO and MgO, it does not increase biochar yield [32,75,85]. On the other hand, studies have also found that metal salts have effectively improved the bio-oil yield. In a study of metal salt catalysts, MgCl₂ produced the maximum bio-oil yield of 48.4 wt % [83], comparing to the transition metal salt FeCl₃, which has a lower bio-oil yield of 32.2 wt %. According to the study, the ionic behaviour of the alkali earth metal salt, MgCl₂ minimises the repolymerisation reaction compared to the partial covalent transition metal salts. In recent studies of the plastic pyrolysis process, the metal catalysts such as carbon-supported platinum (Pt/C), and palladium (Pd/C) were studied in the pyrolysis of PET plastic. The study aims to reduce the polycyclic compounds and biphenyls which are harmful compounds to the environment and public health. The study concludes that Pt/C aided in the reduction of polycyclic compounds such as 2-naphthalenecarboxylic acid by 102% at 800 °C, and reduction of biphenyls such as biphenyl-4-carboxylic acid by 27% at 700 °C [86]. Furthermore, metal oxides have been employed to study the co-pyrolysis process of PP with poplar wood (i.e., ZnO,

CaO, MgO, and Fe₂O₃). The researchers found that CaO has the best deoxygenation results, removing carboxylic acids and phenols from the final products. It also increases cyclopentanones and alkenes compositions, but has reduced total volatile compounds, due to its strong basicity to cause coking on the catalyst surface. ZnO has the highest alkene yield, and increased ketone and phenols yields, and reduced carboxylic acid but has the weakest deoxygenation activities among all four catalysts. MgO behaves similarly to CaO, but has weaker deoxygenation properties, as it is less basic than CaO. Moreover, in the presence of the Fe₂O₃ catalyst, formation of aromatics such as *p*-xylene and 2-methyl-1-butenylbenzene were formed [87]. Following this, the studies of metal-based catalysts are summarised in Table 5, CaO is widely utilised in many studies due to its abundance and low cost, which can be found in renewable sources such as limestone and eggshells [88], and the niche in the utilisation of metal catalysts in the co-pyrolysis process.

3.3.3 Renewable waste catalyst

Renewable waste catalysts received much attention as an economic and sustainable alternative to commercial catalysts, i.e., red mud, ash catalysts, activated carbon, biochar derived catalyst, and palm oil sludge [90–94]. Red mud has attained much research interest as it has the potential to replace commercial catalyst. It is an alkaline

Table 5 Metal based catalyst application in the pyrolysis process examples

Biomass	Catalyst	Category	Bio-oil yield/(wt %)	Reactor	Scale, feed weight/g	Ref.
EFBF	CaO	Basic metal oxide	39.90 (5 wt % CaO); 40.40 (10 wt % CaO)	Fixed bed reactor	15	[85]
	MgO	Basic metal oxide	39.30 (5 wt % MgO); 42.30 (10 wt % MgO)			
	ZnO	Acidic metal oxide	44.70 (5 wt % ZnO); 42.20 (10 wt % ZnO)			
Cotton stalk	CaO	Basic metal oxide	50.00	Fixed bed reactor	–	[84]
RS	MgCl ₂	Metal salt oxide	48.40	Fixed bed reactor	10	[83]
	FeCl ₃	Metal salt	32.20			
	CuCl ₂	Metal salt	41.50			
	MnCl ₂	Metal salt	45.30			
	CaO	Basic metal oxide	38.70			
	CaCO ₃	Basic metal oxide	30.50			
	MgO	Basic metal oxide	52.10			
	MgCO ₃	Basic metal oxide	42.40			
	CeO ₂	Acidic metal oxide	52.30			
	ZnO	Acidic metal oxide	46.20			
	ZrO ₂	Acidic metal oxide	48.30			
	TiO ₂	Acidic metal oxide	48.20			
	EFB	CaO	Basic metal oxide			
PET	Pt	Metal catalyst	–	Tube furnace	1	[86]
	Pd					
PP-poplar wood composite	ZnO	Acidic metal oxide	–	Pyrolysis-gas chromatography/mass spectrometry	0.5 mg	[87]
	CaO	Basic metal oxide				
	Fe ₂ O ₃	Acidic metal oxide				
	MgO	Basic metal oxide				

solid by-product from the Bayer process in alumina production. According to Ly et al. [77], the components within the red mud include a great amount of metal oxides, i.e., MgO, CaO, SiO₂, Fe₂O₃, Al₂O₃, and TiO₂. From the study, red mud has a comparable bio-oil yield than HZSM-5 at temperature of 475 °C and residence time of 1.8 s. Upon characterisation of the bio-oil produced from red mud, the catalyst promoted the depolymerisation of cellulose and hemicellulose to produce furan derivatives. Besides that, the formation of saturated phenols in the bio-oil indicates red mud favours the demethylation and demethoxylation reactions. Furthermore, researchers have also studied the catalytic effect of the pyrolysis biochar. According to Dong et al. [95], the experiment on the catalytic pyrolysis of bamboo waste with different ratios of biochar, concluded that, the bio-oil had been upgraded; simpler C₂–C₆ compounds have been greatly increased with reduction in the heavy C₇–C₁₁ compounds. Moreover, Chen et al. [96] proposed upgrading the biochar from the pyrolysis process such as N-doped biochar, found high yields of bio-oil (61.0–63.0 wt %) were obtainable. A study on the Fe incorporated activated carbon reduces the bio-oil yield to achieve increased phenols 60.85–86.98 wt % of the bio-oil [97]. For the pyrolysis of plastic wastes, most research utilises the low-cost fly ash and naturally occurring kaolin as renewable catalyst sources [98–100]. Furthermore, in the case of co-pyrolysis, renewable waste catalysts such as Ni-doped biochar from waste pine sawdust, and activated carbon made from coconut husks were utilized [101,102]. The summary of renewable waste catalysts is depicted in Table 6, shows that renewable waste in the literature has much lower bio-oil yields or has a higher selectivity to syngas production than commercial catalysts.

4 Kinetic analysis

Kinetic analysis is an important aspect in describing the chemical kinetics of the pyrolysis process in the form of mathematical models. Traditionally modelling the chemical kinetics of biomass pyrolysis considers cellulose, hemicellulose, and lignin, based on the TGA experimental data. These kinetic models include the iso-conversional models, the Vyazovkin method, distributed activation energy model (DAEM), and the utilisation of predictive tools, i.e., artificial neural network (ANN).

4.1 Iso-conversional models

Iso-conversional method is the simplest form of kinetic model to explain the conversion of biomass to volatiles and biochar as a one-step first-order reaction. Examples of the iso-conversional method include the Kissinger–Akahira–Sunose (KAS), Flynn–Wall–Ozawa (FWO), and Starink's method, which are integral methods ($g(a)$). In contrast, the Friedman method is an example of a differential method ($f(a)$) [104]. In this paper, Friedman and Starink's methods are chosen to demonstrate the difference between the differential and integral versions of the iso-conversional method.

4.1.1 Friedman method

Friedman method is based on the differential method as the following expression in Eq. (1). This method requires the information on the conversion rate $\frac{d\alpha}{dt}$, and T . The kinetic plots between $\ln\left(\frac{d\alpha}{dt}\right)$ and $\frac{1}{T}$ produce the slope of

Table 6 Renewable waste catalyst for pyrolysis process examples

Biomass	Catalyst	Bio-oil yield/wt %	Reactor	Scale, feed weight/g	Ref.
Bamboo	Biochar	20.20 (5 wt % biochar) 18.70 (10 wt % biochar) 16.34 (20 wt % biochar)	Microwave pyrolysis	50	[95]
Bamboo	N-doped biochar	61.00 (10 wt % biochar) 63.00 (30 wt % biochar) 62.00 (50 wt % biochar)	Fixed bed reactor	3	[96]
PKS	Fe/activated carbon	7.96	Microwave pyrolysis	10	[97]
Rice husk	Rice hull ash	–	Fixed bed reactor	0.0055	[92]
Rice husk	Coal bottom ash	–	Fixed bed reactor	0.0055	[93]
PKS	Red mud	37.37–39.95	Fixed bed reactor	2	[103]
Bamboo	Red mud	50.34	Bubbling fluidised bed	100 g·h ⁻¹	[77]
EFB	Palm oil sludge	–	Fixed bed reactor	15	[90]
LDPE	Calcinated fly ash (900 °C)	76.22–80.02	Semi batch reactor	50	[98]
	Calcinated fly ash (800 °C)	70.96–71.36			
	Natural fly ash	68.20–71.70			
HDPE (plastic tub pieces)	Fly ash (10 wt %)	50.84	Lab scale pyrolyzer unit	1 kg	[100]
LDPE	Kaolin (1350 mesh)	64.66% aliphatics, 93.91% hydrocarbons, 30.07% H ₂	Quartz furnace tube	100	[99]
Pine sawdust and PE (50 wt %)	Ni-pine sawdust biochar	70.40 wt % (gas yield)	Fixed bed reactor	1	[101]
Corn stalk-HDPE mixture	Activated carbon	–	Tubular reactor	2	[102]

$\frac{E}{R \cdot T}$ and the intercept of $\ln[Af(\alpha)^n]$. The benefit of this model is that it makes no approximations, and can be adopted in any temperature settings [105],

$$\ln\left(\frac{d\alpha}{dt}\right) = \ln[Af(\alpha)^n] - \frac{E}{R \cdot T}, \quad (1)$$

where $f(\alpha)$, T , A , R , E are the differential form of the kinetic dependence function, absolute temperature (K), exponential factor (s^{-1}), universal gas constant ($8.314 \text{ J} \cdot \text{mol}^{-1} \cdot \text{K}^{-1}$), activation energy ($\text{kJ} \cdot \text{mol}^{-1}$).

4.1.2 Starink's method

Starink's method is an extension of the Coats–Redfern equation (Eq. (2)), which is similar to the FWO method, an integral method for estimating kinetic parameters [105]. Since $2RT/E \leq 1$, and has minimal variation with T , results in Eq. (3),

$$\ln\left(\frac{\beta \cdot g(\alpha)}{T^2}\right) = \ln\left[\frac{A \cdot R}{E} \left(1 - \frac{2R \cdot T}{E}\right)\right] - \frac{E}{R \cdot T}, \quad (2)$$

$$\ln\left(\frac{\beta \cdot g(\alpha)}{T^2}\right) \cong \ln\left(\frac{A \cdot R}{E}\right) - \frac{E}{R \cdot T}, \quad (3)$$

where β , $g(\alpha)$ are the heating rate ($^{\circ}\text{C} \cdot \text{min}^{-1}$), and the integral form of the kinetic dependence function. The generalised form Eq. (4) is

$$\ln\left(\frac{\beta \cdot g(\alpha)}{T^m}\right) = B - C\left(\frac{E}{R \cdot T}\right). \quad (4)$$

Starink's equation utilises the constants, where $m = 1.92$, $B = \ln(AR/E) + 3.7545411 - 1.92 \ln E$, and $C = 1.0008$, which can be rewritten as Eq. (5),

$$\ln\left(\frac{\beta}{T^{1.92}}\right) = C_s - 1.0008\left(\frac{E}{R \cdot T}\right), \quad (5)$$

where C_s is the constant. This method is a simple direct method to obtain the expression E/R from the slopes by plotting $\ln\left(\frac{\beta}{T^{1.92}}\right)$ vs. $1/T$. Starink's method is widely employed as a comparison against other iso-conversional methods [48,106]. However, these methods are flawed, as proposed, with an addition of a secondary feedstock and the utilisation of a catalyst, the reaction mechanisms become much more complex [107]. Hence, a modified iso-conversional method is introduced, the Vyazovkin method.

4.2 Vyazovkin method

The iso-conversional methods assume a reaction ideally has a constant value of E_α . This assumption is the main source of errors, which explains the differences obtained from different iso-conversional methods [105]. Hence, to overcome these drawbacks, an advanced alternative non-linear iso-conversional Vyazovkin method is proposed. This method assumes the reaction is independent of the

heating rate, and accounts for the variation of E in the computation of the temperature integral, $I(E_\alpha, T_\alpha)$ from Eq. (6). The E_α which is the effective activation energy ($\text{kJ} \cdot \text{mol}^{-1}$) is obtained from the minimisation of the function $\varnothing(E_\alpha)$ from Eq. (7),

$$I(E_\alpha, T_\alpha) = \int_0^{T_\alpha} \left(-\frac{E_\alpha}{R \cdot T}\right) dT = \frac{E_\alpha}{R} p(x), \quad (6)$$

$$\varnothing(E_\alpha) = \sum_i^n \sum_{j=i}^n \left(\frac{I(E_\alpha, T_{\alpha,i})}{I(E_\alpha, T_{\alpha,j})} \cdot \frac{\beta_j}{\beta_i} \right), \quad (7)$$

where n , E_α , T_α are the number of heating rates in the experiment, activation energy and temperature for each α , while i and j represent the heating rates corresponding to n . For $p(x)$, it is the approximation equation obtained from using Yang equation, Eq. (8):

$$p(x) = \frac{\exp(-x)}{x} \cdot \frac{x^3 + 18x^2 + 88x + 96}{x^4 + 20x^3 + 120x^2 + 240x + 120}, \quad (8)$$

where x is the simplified expression of E/RT . Hence, due to its complex structure, this model requires a numerical approach to solve for the kinetic parameters. Recent studies have started adopting this method to compute the kinetic parameters [48,54].

4.3 Distributed activation energy model

In a complex process such as co-pyrolysis, the E_α would not be constant. Instead, it varies as an indication of a much more complex reaction in place, which is unable to explain over a single-step kinetic model. The DAEM is an accurate and versatile model to represent complex pyrolysis processes. It is the best mathematical method to show the physical and chemical heterogeneity of biomass during a devolatilisation process [34]. According to Hameed et al. [107], DAEM takes into consideration of the decomposition of species over a large number of independent parallel reactions with different activation energies, represented by a continuous distribution function (i.e., Gaussian distribution, $f(E)$), Eq. (9):

$$f(E) = \frac{1}{\sigma \sqrt{2\pi}} \exp\left[-\frac{1}{2} \left(\frac{E - E_M}{\sigma}\right)^2\right], \quad (9)$$

where σ , E_M are the standard deviation and the mean activation energy, respectively. Furthermore, studies have simplified the DAEM based on the assumption that the solid feedstock is a complex mixture of compounds. During the pyrolysis process, a great number of independent consecutive or simultaneous, irreversible reactions take place, each characterised by its corresponding activation energies and pre-exponential factor, given by Eq. (10):

$$1 - \alpha = \int_0^\infty \exp\left(-A \int_0^t \exp\left(\frac{E}{RT}\right) dt\right) \cdot f(E) dE = \varnothing, \quad (10)$$

where, according to Cano–Pleite et al. [108], $\varnothing = 0.58$,

which can be simplified as Eq. (11):

$$\ln\left(\frac{\beta}{T}\right) = \ln\left(\frac{A \cdot R}{E}\right) + 0.675 - \frac{E}{R} \cdot \frac{1}{T}. \quad (11)$$

However, this model is restricted to a constant heating rate. In the applications of DAEM, it has been utilised to estimate the behaviour of different combinations of lignocellulosic biomass (pine wood) and polymer wastes (i.e., waste tyre, polylactic acid, PS, PET, PP, and HDPE) [34]. Besides that, this method has been incorporated into an ANN model to predict the pyrolytic properties of *Staghorn sumac* [106].

4.4 Optimisation methods

Optimisation methods or often referred to as heuristic models, such as genetic algorithm (GA), and particle swarm optimisation (PSO), shuffled complex evolution (SCE) are algorithms that could solve global optimization problems, i.e., for the pyrolysis process, the optimisation of the kinetic parameters to find the best fit using the data from the TGA. These optimisation methods generally solve problems by subjecting it to an objective function to determine the fitness of the iterations [109]. The objective functions or optimisation targets for a thermal degradation problem are the mass loss \varnothing_m and the mass loss rate \varnothing_{mr} in Eqs. (12)–(14) as follows:

$$\varnothing = \varnothing_m + \varnothing_{mr}, \quad (12)$$

$$\varnothing_m = \sum_{j=1}^N \left[W_{CML,j} \frac{\sum_{k=1}^n (CML_{mod,k} - CML_{exp,k})^2}{\sum_{k=1}^n \left(CML_{exp,k} - \frac{1}{n} \sum_{p=1}^n CML_{exp,p} \right)^2} \right], \quad (13)$$

$$\varnothing_{mr} = \sum_{j=1}^N \left[W_{MLR,j} \frac{\sum_{k=1}^n (MLR_{mod,k} - MLR_{exp,k})^2}{\sum_{k=1}^n \left(MLR_{exp,k} - \frac{1}{n} \sum_{p=1}^n MLR_{exp,p} \right)^2} \right], \quad (14)$$

where CML_{mod} and CML_{exp} are the model and experimental cumulative mass loss, respectively; MLR_{mod} and MLR_{exp} are the model and experimental mass loss rate, respectively; N is the number of experiments, n is the number of data points for each experiment; and W_{CML} and W_{MLR} are the weighted value which can be defined as 1.

4.4.1 Genetic algorithm (GA)

The GA is based on an evolutionary concept to find the optimal solution to a complex problem globally. Firstly, the algorithm is initialised by carrying out a range search from a set of randomised candidate solutions referred to as a population. Each candidate solution is defined as an individual or a chromosome, containing the target

parameters to be optimised (i.e., for the pyrolysis process, A , E_α and \varnothing), where the parameters are defined as genes in the GA [109]. Following the natural survival of the fittest, the population experience evolution forming subsequent generations according to the fitness of the objective function. Besides that, the new generation is produced by the chromosomes crossing over, exchanging information, and allowing mutation, this method helps to prevent the local optimal solution. Finally, by the process of elimination of relatively “unfit” candidate solution and reproducing generations that are “fit”. The application of GA in thermal degradation experiments are quite common, it is applied to solve the hybrid pyrolysis scheme of combining both parallel and convective first order reaction. Besides that, recent studies have combined it with different algorithms to improve the performance of the model, according to Aghbashlo et al. [110], the study combines GA with Adaptive Neuro-Fuzzy Interference System (ANFIS) achieving predictions of the kinetic parameters with better fitting compared to traditional ANFIS model; GA-least squares fitting procedure [111], where GA is applied to generate the initial guess for the least square function to solve for the optimal solution. This reduces the number of iterations required for the least square.

4.4.2 Particle swarm optimization (PSO)

The PSO algorithm follows the velocity and position search model. It contains a certain number of particles, their positions, and velocity. The particles in a particular position represent a candidate of solution of space, and the velocity of this particle updates the position of these particles [112]. In addition, these particles have a memory ability which, retains its historical best position vector and its global best position found [109]. Initially, the particles are assigned a random position and velocity in a proposed range. The solution then improves with iterations via Eqs. (15) and (16):

$$v_{id}^{k+1} = \omega v_{id}^k + c_1 r_1 (p_{id} - x_{id}^k) + c_2 r_2 (p_{gd} - x_{id}^k), \quad (15)$$

$$x_{id}^{k+1} = x_{id}^k + v_{id}^{k+1}, \quad (16)$$

where k is the iteration number, i is the particle number, and d is the search direction from 1 to D , w is the inertia weight, p_{id} and p_{gd} are the local particle position and the global best position of all particles, respectively. c_1 and c_2 are the two positive acceleration constants for the local and global nature of the swarm. r_1 and r_2 are the stochastic values in the range of $[0, 1]$, respectively [113, 114].

According to Ding et al. [109], the study compares the performance between PSO and GA, and the results indicate that PSO showed closer global optimum convergence, 0.053 at the population size of 2500 compared to GA, with the best value at 0.075 at the population size of 2000. Besides that, PSO showed less

fluctuation, 0.05 to 0.08 in fitting values regardless of population size, compared to GA, which fluctuates between 0.07 and 0.29. In literature, PSO is often coupled with other algorithms, such as global sensitivity analysis, to find the parameters with the greatest effect on the prediction outcome. According to Ding et al. [112], the sensitivity order is ranked from the largest to the smallest value which are representing the activation energy of lignin, the reaction order of cellulose, and the pre-exponential factor for lignin in the pyrolysis process of pinewood. While for the co-pyrolysis of microalgae *Chlorella vulgaris* and HDPE, the activation energy of cellulose, pre-exponential factor for cellulose and the activation energy of protein, followed by the reaction order of cellulose, showed significant influence on the prediction results, indicating these parameters should be paid much attention for the pyrolysis process [115]. Besides that, Monte Carlo simulations were applied to perform uncertainty analysis, to probabilistically assess the effects of stochastic uncertainties in the predictor values ($n = 100000$) from the ANN and PSO framework [113]. In addition, a recent study proposed a neuro-evolution algorithm, progressive deep swarm evolution (PDSE), built on the PSO algorithm, to model the catalytic thermal degradation of *Chlorella vulgaris* [88]. From the validation tests, implementing the PDSE algorithm obtained a coefficient of determination (R^2) value above 0.9990, RMSE below 0.0075, and MBE below 0.0026.

4.4.3 Shuffled complex evolution (SCE)

The SCE algorithm introduced by Duan et al. [116] is effective for calibration of hydrological models. The efficacy of this algorithm, a form of differential evolution (DE), comes from its use of geometric operations to find possible optimal solutions to space parameters. The algorithm solves global optimisation problems based on four concepts: (1) probabilistic and deterministic approaches; (2) clustering; (3) systematic evolution of a complex of points spanning the space in the direction of global improvement and (4) competitive evolution. The application of SCE on the woody pyrolysis was studied with six different kinetic models, comprising of single component reactant mechanism, and multicomponent reactant mechanisms (i.e., cellulose, hemicellulose, and lignin) [117]. The optimised kinetic parameters from the results were applied to predict the pyrolysis process with different heating rates, 5 and 80 °C·min⁻¹, where the results were found better fitting of the results of the multicomponent kinetic model, which can reach R^2 values of up to 0.99 [117]. Besides that, SCE has been applied in various pyrolysis kinetic analysis, pyrolysis of beech [118], and pyrolysis of basswood waste [119].

The SCE algorithm starts with generating of a population of random points within the search space, denoted as s . Each of these points contains a vector (i.e.,

kinetic parameters) and is ranked based on their fitness function value and stored in an array D , and partitioned into p complexes, each containing m points, i.e., $D = \{A^k, k = 1, \dots, p\}$. Next, each complex evolved using the competitive complex evolution algorithm, and shuffled. All points are combined to a single population and the procedure of ranking for the function value, partition into complexes, evolution, and shuffling is repeated until convergence value is reached [116,120].

4.5 Predictive models: artificial neural network (ANN)

ANN is an intelligent learning, predictive computational technique, often employed to solve the nonlinear, and complex relationships between the input and output data. An ANN network consists of one or more hidden layers connecting the input (i) and output (o) layers. Each layer has a weight (w) matrix and an output vector [121]. The neuron of each single layer picks up the summation of the activation from the input vectors and their assigned weights and biases, the results then pass through an activation function (i.e., linear, sigmoid, and hyperbolic tangent sigmoid) to generate a new activation value to the neurons in the following layers. The weight matrix is altered to fit the learning algorithms, the learning ends when the weights of each layer achieve convergence as the final output vector (y_o) [122,123]. The ANN parameters influencing the performance are: the number of hidden layers (j), the number of neurons in each hidden layer (n), and the transfer function deployed denoted as f . The general architecture of the ANN is illustrated in Fig. 4.

Generally, the model learning process involves inputting a percentage of sample data to the network, and altering the number of neurons in the hidden layers to optimise the mean square error (MSE) [51]. Besides that, the selection is supervised by a learning algorithm. In literature, this method has been applied in predicting of the kinetic parameters of the pyrolysis process, involving the iso-conversional models, i.e., KAS and FWO shown in Table 7.

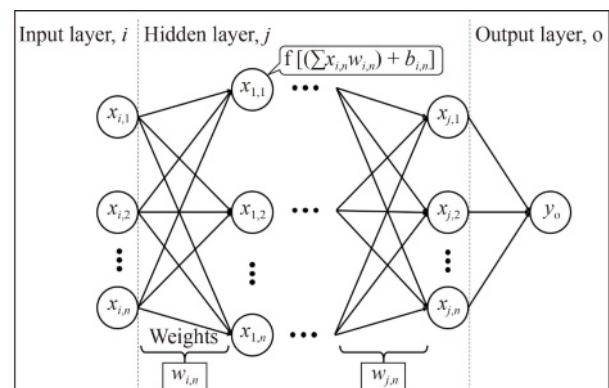


Fig. 4 General ANN architecture.

4.6 Thermodynamics relations

The thermodynamic parameters are important for the scale up and the design of the reactor, i.e., Frequency factor, A (s^{-1}), change in enthalpy, ΔH ($kJ \cdot mol^{-1}$), Gibbs free energy, ΔG ($kJ \cdot mol^{-1}$), and change in entropy, ΔS ($kJ \cdot mol^{-1} \cdot K^{-1}$). The parameters are expressed in the respective equations as Eqs. (17)–(20):

$$A = \frac{\beta \cdot E \cdot \exp\left(\frac{E}{R \cdot T_m}\right)}{R \cdot T_m^2}, \quad (17)$$

$$\Delta H = E_\alpha - R \cdot T, \quad (18)$$

$$\Delta G = E_\alpha + R \cdot T_m \cdot \ln\left(\frac{K_B \cdot T_m}{h \cdot A}\right), \quad (19)$$

$$\Delta S = \frac{\Delta H - \Delta G}{T_m}, \quad (20)$$

where T_m , K_B , h are the maximum temperature where the decomposition occurs (K), Boltzmann constant ($1.381 \times 10^{-23} J \cdot K^{-1}$), and Plank's constant ($6.626 \times 10^{-34} J \cdot s$) [30]. $A < 10^9 s^{-1}$ refers to a simpler straightforward reaction, while $A > 10^9 s^{-1}$ would mean the reaction follows a complex mechanism [129]. ΔH represents the endothermic or exothermic behaviour of the reaction mechanism; it is the amount of energy transferred during a chemical reaction. According to Gan et al. [130], the smaller the difference of ΔH with the E_α is, the more favourable for the reaction to occur. Hence, the bioenergy from the system is more likely to be attained. Moreover, ΔG is the total potential energy increased in the system, it signifies that the reactants are consumed and activated complexes are formed [21]. The ΔG also represents the suitability of the feedstock for pyrolysis, the higher the ΔG is, the more bioenergy can potentially be attained [30,51]. Furthermore, ΔS is the degree of arrangement of the carbon in the waste and biomass. It is the amount of

energy unavailable to work. For higher entropy values, it indicates that the sample has yet to achieve thermodynamic equilibrium, and is highly reactive [131]. Table 8 summarises the kinetic and thermodynamic parameters for different feedstock samples.

5 Future outlooks

Many studies have proven that the combination of feedstock, biomass with waste plastic or biomass with waste tire in co-pyrolysis, with enhancements in the pyrolysis oil through synergistic effects, is an economical way for the production of sustainable fuel as a replacement for fossil fuels. The combination of waste plastics (20 wt %) with biomass generated a higher pyrolytic liquid yield compared to the solely thermal pyrolysis of biomass. This phenomenon shows that the oil produced from co-pyrolysis process can be blended with diesel after minor upgrading or even directly applied in transportation [132]. Nonetheless, not all plastic types can be applied in the process. In this sense, PVC, which consists of about 57% chlorine by weight, is not an ideal feedstock material as it will thermally break down into a very corrosive and toxic hydrochloric acid and influence the diesel quality with the production of chlorinated hydrocarbons. A $0.0145\text{--}0.0290 \text{ mg} \cdot \text{m}^{-3}$ of total chloride level has been recorded in the fuel oil product with just merely adding 1%–3% PVC in the feedstock stream [133,134]. Besides that, Hu et al. [32] stated that more studies are needed for co-pyrolysis especially in establishing a suitable approach in selecting material and the optimum blending ratio of material with biomass [32].

Furthermore, constraints in having straightforward and efficacious characterisation strategies for co-pyrolytic oil also impede the dependence of the industrial community in the technology [135]. Despite the extensive research works on the invention of the co-pyrolysis approach using

Table 7 ANN model compilation from different studies

Biomass/catalyst	Learning algorithm/topology	Prediction result	ANN parameters	Ref.
<i>Chlorella vulgaris</i> limestone, HZSM-5	PDSE	Thermal degradation	Inputs: heating rate; heat flow; reactor temperature Outputs: remaining mass	[88]
Rice husk, sewage sludge	Levenberg–Marquardt (LM)	Thermal degradation	Inputs: reactor temperature; blend composition Outputs: mass loss	[21]
<i>Chlorella vulgaris</i> , peanut shell, microalgae ash	LM	Thermal degradation	Inputs: heating rate; reactor temperature Outputs: mass loss	[124]
Sewage sludge, peanut shell	LM	Thermal degradation	Inputs: blend compositions; heating rates; reactor temperature Outputs: remaining mass	[122]
Rice husk	Scaled conjugate gradient and LM	Thermal degradation	Inputs: heating rate; reactor temperature Outputs: remaining mass	[125]
Lignocellulosic biomass	Random forest schematic	Biochar yield	Dataset: physicochemical properties of lignocellulosic biomass	[126]
Sewage sludge	LM	HHV of syngas	Dataset: physicochemical properties of biomass	[127]
Mexican sunflower (<i>Tithonia diversifolia</i>)	LM	Bio-oil yield	Inputs: heating rate; flow rate; particle size; reactor temperature Output: bio-oil yield	[128]

Table 8 Kinetic and thermodynamic parameters of the pyrolysis process in literature

Feedstock	Catalyst	Kinetic model	$E_a/$ (kJ·mol ⁻¹)	$A/$ min ⁻¹	$\Delta H/$ (kJ·mol ⁻¹)	$\Delta S/$ (J·mol ⁻¹ ·K ⁻¹)	$\Delta G/$ (kJ·mol ⁻¹)	Ref.
<i>Pterocarpus indicus</i>	–	Coats-redfern	112.0	–	103.0	–138.0	183.00	[35]
<i>Intsia bijuga</i>	–		99.0	–	89.0	–120.0	160.00	
Corn stover	–		66.0	–	57.0	–173.0	147.00	
HDPE	–		546.0	–	533.0	420.0	226.00	
LDPE	–		487.0	–	475.0	348.0	231.00	
PP	–		423.0	–	411.0	273.0	222.00	
Rice hull	–	DAEM	175.4	2.939×10^{17}	170.2	–	–	[130]
	–	FWO	177.7	7.991×10^{16}	172.6	–	–	
	Limestone	DAEM	123.3	5.803×10^{11}	117.9	–	–	
	Limestone	FWO	132.5	4.148×10^{12}	127.1	–	–	
	Eggshell	DAEM	96.1	2.033×10^{10}	90.8	–	–	
	Eggshell	FWO	100.4	1.948×10^9	95.2	–	–	
Sewage sludge (97.5% conversion)	–	KAS	123.6	1.440×10^6	119.5	139.4	187.69	[51]
	–	FWO	132.7	1.560×10^9	128.6	138.8	196.50	
	–	Friedman	92.4	0.0103	88.3	295.4	232.80	
	–	Popescu	200.9	9.740×10^{10}	196.8	219.3	304.00	
Microalgae:microalgae ash:peanut shell 9:2:9	–	FWO	142.6	2.010×10^{14}	137.0	–	–	[124]
Garlic husk	–	KAS	154.0	–	149.4	–	150.60	[104]
	–	FWO	154.9	–	150.4	–	150.50	
	–	Starink	154.3	–	149.8	–	150.50	
<i>Staghorn sumac</i>	–	FWO	167.9	–	178.9	–	–	[106]
	–	KAS	169.4	–	167.2	–	–	
	–	Starink	169.8	–	167.6	–	–	
<i>Azadirachta indica</i>	–	FWO	–	6.288×10^{15}	188.5	–43.3	215.40	[30]
	–	Friedman	–	8.586×10^{15}	190.9	–39.4	215.40	
	–	Vyazovkin	–	2.965×10^{20}	199.7	–26.0	215.20	
<i>Phyllanthus emblica</i>	–	FWO	–	2.075×10^{14}	189.9	–40.9	215.30	[30]
	–	Friedman	–	2.864×10^{13}	181.3	–55.1	215.60	
	–	Vyazovkin	–	3.534×10^{13}	179.4	–58.3	215.60	
Rice husk	–	Friedman	–	–	186	–	–	[92]
	–	KAS	–	–	178	–	–	
	–	FWO	–	–	180	–	–	
	Rice hull ash	Friedman	–	–	148	–	–	
	Rice hull ash	KAS	–	–	148	–	–	
	Rice hull ash	FWO	–	–	146	–	–	
<i>Chlorella vulgaris</i>	–	KAS	156.2	2.898×10^{20}	151	–	–	[131]
	–	FWO	158.1	2.358×10^{20}	153	–	–	
	HZSM-5	KAS	145.3	2.790×10^{14}	140	–	–	
	HZSM-5	FWO	147.8	4.908×10^{14}	143	–	–	
	Limestone	KAS	138.8	6.360×10^{15}	133	–	–	
	Limestone	FWO	142.1	8.880×10^{15}	137	–	–	

different kinds of agricultural biomass and polymer wastes, the current heat transfer processes for co-pyrolysis, i.e., conduction, convection and radiation still impose several challenges. In conduction, solid attrition is the critical issue once there is a direct contact between fuel particles and heating agent. In convection, small fuel particles and long gas residence times are essential for gas/solid and sufficient heat transfer, respectively. Asymmetrically, the primary challenges of radiation are high concentration of radiation is required for the production of sufficient heat transfer and consideration of wall heating design in pyrolysis reactor [136,137]. Hence,

the high installation and operating costs of units with a high efficiency of heat transfer in the short gas residence time and an additional pre-treatment system for various types of biomasses are the main drawbacks of co-pyrolysis. Different studies reported that different conditions are required to blend an appropriate waste with different biomasses before co-processing. More profound fundamental studies on reaction mechanisms and kinetics of biomass with different waste materials are critical in the advancement of the co-pyrolysis process. In this sense, the properties of the co-pyrolytic oil produced with its composition can be determined from the interactivity

of the reaction intermediates. Currently, ANN and Monte Carlo serve as empirical models that are practical in the prediction of intricate input–output interrelations in a co-pyrolysis process. However, these models are only applicable to the process and fuels, which have been well-established [21]. Co-pyrolysis kinetic datasets for predicting of product formation using different reactor systems are still fairly unexplored [135].

Moreover, the commercialisation of co-pyrolysis reactors are still in the early stages since the current reactors still have the challenges of low heat efficiency, high capital and operating costs as well as complexities with biomass handling or storage [32]. Besides that, although there is plenty of extensive research on the single feedstock pyrolysis, the feasibility study of the co-pyrolysis process remains a niche area, whereby research on the techno-economic and life cycle assessment of the process is limited to single feedstock pyrolysis, such as the co-pyrolysis of biomass refineries and the DMF layers in these references [138,139]. To the best of our knowledge, these studies for the case of co-pyrolysis are scarce, existing studies focus on the microwave co-pyrolysis of food waste and LDPE [140], and the co-pyrolysis of lignite coal with single-use plastic waste [141]. Besides that, the existing research on the modelling of the co-pyrolysis of biomass with plastic waste reaction kinetics has been widely studied, but yet to have a consensus on the reaction pathway [32].

6 Conclusions

To conclude, the recent technologies and techniques of co-pyrolysis of biomass and plastic waste to produce bio-oil have been summarised in this review. The growing agriculture industry in ASEAN countries to suit the growing population of the region, has subsequently generated landfills of biomass. To exacerbate the situation, the global pandemic gives rise to the surge of the single-use plastic waste, DMFM wastes. Fortunately, the exploitation of these wastes in co-pyrolysis would positively improve the quantity and quality of the extracted bio-oil of the process, as the result of the synergistic interactions between lignocellulosic properties of biomass and the high hydrogen content of the plastic wastes. Furthermore, the advancement of the kinetic analysis of the pyrolysis process has improved as the catalytic co-pyrolysis process becomes more complex, and unable to be explained via simple iso-conversional models. Advanced conversional models such as Vyazovkin and DAEM methods have been introduced to study the pyrolysis reaction, followed by the heuristic model and predictive models, which prove to produce high-accuracy results. However, the studies of co-pyrolysis of biomass and DMFMs remain limited.

Experimental work on the binary feedstock's thermal decompositions and the bio-oil product's quantity and quality result from the co-pyrolysis has yet to be clear. The proposal of this methodology could serve as potential solution to help reduce or eliminate the pollution caused by the DMFM wastes, while producing value-added bio-oil products.

Acknowledgements The authors would like to acknowledge the technical support from Curtin University Malaysia, Swinburne University of Technology, Universiti Teknologi PETRONAS (UTP), and Manipal University Jaipur. Besides that, M.X.J. Wee would like to acknowledge the full funding support from the Curtin Malaysia Postgraduate Research Studentship (CMPRS) for the PhD study.

References

1. Adnan Z A, Saniayan V. Renewable energy outlook for ASEAN: a REmap analysis. Asean Centre for Energy & IRENA Report, 2016
2. Miranda M. Governments across Southeast Asia accelerate renewable energy investment to revive the pandemic-hit economies. Power Technology Report, 2020
3. Erdiwansyah M, Mamat R, Sani M S M, Khoerunnisa F, Kadarohman A. Target and demand for renewable energy across 10 ASEAN countries by 2040. *Electricity Journal*, 2019, 32(10): 106670
4. Sarraf M, Rismanchi B, Saidur R, Ping H W, Rahim N A. Renewable energy policies for sustainable development in Cambodia. *Renewable & Sustainable Energy Reviews*, 2013, 22: 223–229
5. Pillai I R, Banerjee R. Renewable energy in India: status and potential. *Energy*, 2009, 34(8): 970–980
6. Dani S, Wibawa A. Challenges and policy for biomass energy in Indonesia. *Journal of International Economic Law*, 2018, 15(5): 41–47
7. Mekhilef S, Barimani M, Safari A, Salam Z. Malaysia's renewable energy policies and programs with green aspects. *Renewable & Sustainable Energy Reviews*, 2014, 40: 497–504
8. Wattana S. Bioenergy development in Thailand: challenges and strategies. *Energy Procedia*, 2014, 52: 506–515
9. Truong K, Huong C, Dang Xuan T, Trung D, Khanh T. Current status and future plan of development of bioenergy crops as renewable energy sources in Vietnam. *Journal of Biology and Nature*, 2016, 5: 1–8
10. Myanmar Energy Master Plan. IEA, 2017
11. Energy policy and administration. Open Development Laos Website, 2018
12. Bangkok. East and Southeast Asia renewable energy statistics workshop. IRENA Website, 2016
13. Hirschmann R. Palm oil industry in Indonesia—statistics & facts. Statista Website, 2022
14. Malaysia palm oil production by year. Indexmundi, 2020
15. Loh S K. The potential of the Malaysian oil palm biomass as a renewable energy source. *Energy Conversion and Management*, 2017, 141: 285–298

16. Kumar N, Chhokar R S, Meena R P, Kharub A S, Gill S C, Tripathi S C, Gupta O P, Mangrauthia S K, Sundaram R M, Sawant C P, Gupta A, Naorem A, Kumar M, Singh G P. Challenges and opportunities in productivity and sustainability of rice cultivation system: a critical review in Indian perspective. *Cereal Research Communications*, 2022, 50: 573–601
17. Dai L, Wang Y, Liu Y, He C, Ruan R, Yu Z, Jiang L, Zeng Z, Wu Q. A review on selective production of value-added chemicals via catalytic pyrolysis of lignocellulosic biomass. *Science of the Total Environment*, 2020, 749: 142386
18. Kan T, Strezov V, Evans T, He J, Kumar R, Lu Q. Catalytic pyrolysis of lignocellulosic biomass: a review of variations in process factors and system structure. *Renewable & Sustainable Energy Reviews*, 2020, 134: 110305
19. Sivagurunathan P, Raj T, Mohanta C S, Semwal S, Satlewal A, Gupta R P, Puri S K, Ramakumar S S V, Kumar R. 2G waste lignin to fuel and high value-added chemicals: approaches, challenges and future outlook for sustainable development. *Chemosphere*, 2021, 268: 129326
20. Yang H, Yan R, Chen H, Lee D H, Liang D T, Zheng C. Pyrolysis of palm oil wastes for enhanced production of hydrogen rich gases. *Fuel Processing Technology*, 2006, 87(10): 935–942
21. Naqvi S R, Hameed Z, Tariq R, Taqvi S A, Ali I, Niazi M B K, Noor T, Hussain A, Iqbal N, Shahbaz M. Synergistic effect on co-pyrolysis of rice husk and sewage sludge by thermal behavior, kinetics, thermodynamic parameters and artificial neural network. *Waste Management*, 2019, 85: 131–140
22. Suriapparao D V, Vinu R, Shukla A, Haldar S. Effective deoxygenation for the production of liquid biofuels via microwave assisted co-pyrolysis of agro residues and waste plastics combined with catalytic upgradation. *Bioresource Technology*, 2020, 302: 122775
23. Geyer R, Jambeck J R, Law K L. Production, use, and fate of all plastics ever made. *Science Advances*, 2017, 3(7): e1700782
24. Jambeck J R, Geyer R, Wilcox C, Siegler T R, Perryman M, Andrady A, Narayan R, Law K L. Plastic waste inputs from land into the ocean. *Science*, 2015, 347(6223): 768–771
25. Abnisa F, Alaba P A. Recovery of liquid fuel from fossil-based solid wastes via pyrolysis technique: a review. *Journal of Environmental Chemical Engineering*, 2021, 9(6): 106593
26. Liang Y, Song Q, Wu N, Li J, Zhong Y, Zeng W. Repercussions of COVID-19 pandemic on solid waste generation and management strategies. *Frontiers of Environmental Science & Engineering*, 2021, 15(6): 115
27. Chaib F. Shortage of personal protective equipment endangering health workers worldwide. *World Health Organization Website*, 2020
28. Patrício Silva A L, Prata J C, Duarte A C, Barcelò D, Rocha-Santos T. An urgent call to think globally and act locally on landfill disposable plastics under and after Covid-19 pandemic: pollution prevention and technological (Bio) remediation solutions. *Chemical Engineering Journal*, 2021, 426: 131201
29. Patrício Silva A L, Prata J C, Mouneyrac C, Barcelò D, Duarte A C, Rocha-Santos T. Risks of Covid-19 face masks to wildlife: present and future research needs. *Science of the Total Environment*, 2021, 792: 148505
30. Mishra R K, Mohanty K. Kinetic analysis and pyrolysis behaviour of waste biomass towards its bioenergy potential. *Bioresource Technology*, 2020, 311: 123480
31. Akhtar J, Saidina Amin N. A review on operating parameters for optimum liquid oil yield in biomass pyrolysis. *Renewable & Sustainable Energy Reviews*, 2012, 16(7): 5101–5109
32. Hu X, Gholizadeh M. Biomass pyrolysis: a review of the process development and challenges from initial researches up to the commercialisation stage. *Journal of Energy Chemistry*, 2019, 39: 109–143
33. Miandad R, Barakat M A, Rehan M, Aburiazaiza A S, Ismail I M I, Nizami A S. Plastic waste to liquid oil through catalytic pyrolysis using natural and synthetic zeolite catalysts. *Waste Management*, 2017, 69: 66–78
34. Navarro M V, López J M, Veses A, Callén M S, García T. Kinetic study for the co-pyrolysis of lignocellulosic biomass and plastics using the distributed activation energy model. *Energy*, 2018, 165: 731–742
35. Salvilla J N V, Ofrasio B I G, Rollon A P, Manegdeg F G, Abarca R R M, de Luna M D G. Synergistic co-pyrolysis of polyolefin plastics with wood and agricultural wastes for biofuel production. *Applied Energy*, 2020, 279: 115668
36. Wang L, Chai M, Liu R, Cai J. Synergetic effects during co-pyrolysis of biomass and waste tire: a study on product distribution and reaction kinetics. *Bioresource Technology*, 2018, 268: 363–370
37. Ansari K B, Hassan S Z, Bhoi R, Ahmad E. Co-pyrolysis of biomass and plastic wastes: a review on reactants synergy, catalyst impact, process parameter, hydrocarbon fuel potential, COVID-19. *Journal of Environmental Chemical Engineering*, 2021, 9(6): 106436
38. Roy P, Dias G. Prospects for pyrolysis technologies in the bioenergy sector: a review. *Renewable & Sustainable Energy Reviews*, 2017, 77: 59–69
39. Bridgwater A V. Review of fast pyrolysis of biomass and product upgrading. *Biomass and Bioenergy*, 2012, 38: 68–94
40. Fahmy T Y A, Fahmy Y, Mobarak F, El-Sakhawy M, Abou-Zeid R E. Biomass pyrolysis: past, present, and future. *Environment, Development and Sustainability*, 2020, 22(1): 17–32
41. Papari S, Hawboldt K. A review on the pyrolysis of woody biomass to bio-oil: focus on kinetic models. *Renewable & Sustainable Energy Reviews*, 2015, 52: 1580–1595
42. Perkins G, Bhaskar T, Konarova M. Process development status of fast pyrolysis technologies for the manufacture of renewable transport fuels from biomass. *Renewable & Sustainable Energy Reviews*, 2018, 90: 292–315
43. Foong S Y, Liew R K, Yang Y, Cheng Y W, Yek P N Y, Wan Mahari W A, Lee X Y, Han C S, Vo D V N, Van Le Q, Aghbashlo M, Tabatabaei M, Sonne C, Peng W, Lam S S. Valorization of biomass waste to engineered activated biochar by microwave pyrolysis: progress, challenges, and future directions. *Chemical Engineering Journal*, 2020, 389: 124401
44. Tsai F M, Bui T D, Tseng M L, Lim M K, Hu J. Municipal solid waste management in a circular economy: a data-driven

- bibliometric analysis. *Journal of Cleaner Production*, 2020, 275: 124132
45. Andreo-Martínez P, Ortiz-Martínez V M, García-Martínez N, de los Ríos A P, Hernández-Fernández F J, Quesada-Medina J. Production of biodiesel under supercritical conditions: state of the art and bibliometric analysis. *Applied Energy*, 2020, 264: 114753
 46. Losse M, Geissdoerfer M. Mapping socially responsible investing: a bibliometric and citation network analysis. *Journal of Cleaner Production*, 2021, 296: 126376
 47. Murillo J, Villegas L M, Ulloa-Murillo L M, Rodríguez A R. Recent trends on omics and bioinformatics approaches to study SARS-CoV-2: a bibliometric analysis and mini-review. *Computers in Biology and Medicine*, 2021, 128: 104162
 48. Bensidhom G, Ben Hassen Trabelsi A, mahmood M A, Ceylan S. mahmood M A, Ceylan S. Insights into pyrolytic feedstock potential of date palm industry wastes: kinetic study and product characterization. *Fuel*, 2021, 285: 119096
 49. Domínguez A, Menéndez J A, Inguanzo M, Pis J J. Investigations into the characteristics of oils produced from microwave pyrolysis of sewage sludge. *Fuel Processing Technology*, 2005, 86(9): 1007–1020
 50. Ghodke P, Mandapati R N. Investigation of particle level kinetic modeling for babul wood pyrolysis. *Fuel*, 2019, 236: 1008–1017
 51. Naqvi S R, Tariq R, Hameed Z, Ali I, Taqvi S A, Naqvi M, Niazi M B K, Noor T, Farooq W. Pyrolysis of high-ash sewage sludge: thermo-kinetic study using TGA and artificial neural networks. *Fuel*, 2018, 233: 529–538
 52. Polin J P, Carr H D, Whitmer L E, Smith R G, Brown R C. Conventional and autothermal pyrolysis of corn stover: overcoming the processing challenges of high-ash agricultural residues. *Journal of Analytical and Applied Pyrolysis*, 2019, 143: 104679
 53. Singh R K, Pandey D, Patil T, Sawarkar A N. Pyrolysis of banana leaves biomass: physico-chemical characterization, thermal decomposition behavior, kinetic and thermodynamic analyses. *Bioresource Technology*, 2020, 310: 123464
 54. Tabal A, Barakat A, Aboukass A, El harfi K. Pyrolysis of ficus nitida wood: determination of kinetic and thermodynamic parameters. *Fuel*, 2021, 283: 119253
 55. Ding Z, Chen H, Liu J, Cai H, Evrendilek F, Buyukada M. Pyrolysis dynamics of two medical plastic wastes: drivers, behaviors, evolved gases, reaction mechanisms, and pathways. *Journal of Hazardous Materials*, 2021, 402: 123472
 56. Honus S, Kumagai S, Fedorko G, Molnár V, Yoshioka T. Pyrolysis gases produced from individual and mixed PE, PP, PS, PVC, and PET—Part I: Production and physical properties. *Fuel*, 2018, 221: 346–360
 57. Jeon W, Kim Y D, Lee K H. A comparative study on pyrolysis of bundle and fluffy shapes of waste packaging plastics. *Fuel*, 2021, 283: 119260
 58. Jung S, Lee S, Dou X, Kwon E E. Valorization of disposable COVID-19 mask through the thermo-chemical process. *Chemical Engineering Journal*, 2021, 405: 126658
 59. Parku G K, Collard F X, Görgens J F. Pyrolysis of waste polypropylene plastics for energy recovery: influence of heating rate and vacuum conditions on composition of fuel product. *Fuel Processing Technology*, 2020, 209: 106522
 60. Xu F, Wang B, Yang D, Hao J, Qiao Y, Tian Y. Thermal degradation of typical plastics under high heating rate conditions by TG-FTIR: pyrolysis behaviors and kinetic analysis. *Energy Conversion and Management*, 2018, 171: 1106–1115
 61. Park Y K, Ha J M, Oh S, Lee J. Bio-oil upgrading through hydrogen transfer reactions in supercritical solvents. *Chemical Engineering Journal*, 2021, 404: 126527
 62. Kwon D, Jung S, Lin K Y A, Tsang Y F, Park Y K, Kwon E E. Synergistic effects of CO₂ on complete thermal degradation of plastic waste mixture through a catalytic pyrolysis platform: a case study of disposable diaper. *Journal of Hazardous Materials*, 2021, 419: 126537
 63. Wan Mahari W A, Awang S, Zahariman N A Z, Peng W, Man M, Park Y K, Lee J, Sonne C, Lam S S. Microwave co-pyrolysis for simultaneous disposal of environmentally hazardous hospital plastic waste, lignocellulosic, and triglyceride biowaste. *Journal of Hazardous Materials*, 2022, 423: 127096
 64. Park Y K, Lee B, Lee H W, Watanabe A, Jae J, Tsang Y F, Kim Y M. Co-feeding effect of waste plastic films on the catalytic pyrolysis of *Quercus variabilis* over microporous HZSM-5 and HY catalysts. *Chemical Engineering Journal*, 2019, 378: 122151
 65. Hu Y, Yu W, Wibowo H, Xia Y, Lu Y, Yan M. Effect of catalysts on distribution of polycyclic-aromatic hydrocarbon (PAHs) in bio-oils from the pyrolysis of dewatered sewage sludge at high and low temperatures. *Science of the Total Environment*, 2019, 667: 263–270
 66. Zhang X, Lei H, Zhu L, Zhu X, Qian M, Yadavalli G, Wu J, Chen S. Thermal behavior and kinetic study for catalytic co-pyrolysis of biomass with plastics. *Bioresource Technology*, 2016, 220: 233–238
 67. Lin X, Zhang Z, Wang Q, Sun J. Interactions between biomass-derived components and polypropylene during wood-plastic composite pyrolysis. *Biomass Conversion and Biorefinery*, 2020, 12(8): 3345–3357
 68. Önal E, Uzun B B, Pütün A E. Bio-oil production via co-pyrolysis of almond shell as biomass and high density polyethylene. *Energy Conversion and Management*, 2014, 78: 704–710
 69. Sun J, Luo J, Lin J, Ma R, Sun S, Fang L, Li H. Study of co-pyrolysis endpoint and product conversion of plastic and biomass using microwave thermogravimetric technology. *Energy*, 2022, 247: 123547
 70. Yang J, Rizkiana J, Widayatno W B, Karnjanakom S, Kaewpanha M, Hao X, Abudula A, Guan G. Fast co-pyrolysis of low density polyethylene and biomass residue for oil production. *Energy Conversion and Management*, 2016, 120: 422–429
 71. Ojha D, Shukla S, Raghunath S, Sachin R S, Vinu R. Understanding the interactions between cellulose and polypropylene during fast co-pyrolysis via experiments and DFT calculations. *Chemical Engineering Transactions*, 2016, 50: 67–72
 72. Uzoejinwa B B, He X, Wang S, El-Fatah Abomohra A, Hu Y, Wang Q. Co-pyrolysis of biomass and waste plastics as a thermochemical conversion technology for high-grade biofuel

- production: recent progress and future directions elsewhere worldwide. *Energy Conversion and Management*, 2018, 163: 468–492
73. Lin X, Kong L, Ren X, Zhang D, Cai H, Lei H. Catalytic co-pyrolysis of torrefied poplar wood and high-density polyethylene over hierarchical HZSM-5 for mono-aromatics production. *Renewable Energy*, 2021, 164: 87–95
 74. Pogaku R, Hardinge B S, Vuthaluru H, Amir H A. Production of bio-oil from oil palm empty fruit bunch by catalytic fast pyrolysis: a review. *Biofuels*, 2016, 7(6): 647–660
 75. Dai L, Zhou N, Li H, Deng W, Cheng Y, Wang Y, Liu Y, Cobb K, Lei H, Chen P, Ruan R. Recent advances in improving lignocellulosic biomass-based bio-oil production. *Journal of Analytical and Applied Pyrolysis*, 2020, 149: 104845
 76. Yang H, Yan R, Chin T, Liang D T, Chen H, Zheng C. Thermogravimetric analysis-fourier transform infrared analysis of palm oil waste pyrolysis. *Energy & Fuels*, 2004, 18(6): 1814–1821
 77. Ly H V, Park J W, Kim S S, Hwang H T, Kim J, Woo H C. Catalytic pyrolysis of bamboo in a bubbling fluidized-bed reactor with two different catalysts: HZSM-5 and red mud for upgrading bio-oil. *Renewable Energy*, 2020, 149: 1434–1445
 78. Ahmed M H M, Batalha N, Mahmudul H M D, Perkins G, Konarova M. A review on advanced catalytic co-pyrolysis of biomass and hydrogen-rich feedstock: insights into synergistic effect, catalyst development and reaction mechanism. *Bioresource Technology*, 2020, 310: 123457
 79. Jin X, Lee J H, Choi J W. Catalytic co-pyrolysis of woody biomass with waste plastics: effects of HZSM-5 and pyrolysis temperature on producing high-value pyrolytic products and reducing wax formation. *Energy*, 2022, 239: 121739
 80. Ratnasari D K, Nahil M A, Williams P T. Catalytic pyrolysis of waste plastics using staged catalysis for production of gasoline range hydrocarbon oils. *Journal of Analytical and Applied Pyrolysis*, 2017, 124: 631–637
 81. Li Z, Zhong Z, Zhang B, Wang W, Seufitelli G V S, Resende F L P. Catalytic fast co-pyrolysis of waste greenhouse plastic films and rice husk using hierarchical micro-mesoporous composite molecular sieve. *Waste Management*, 2020, 102: 561–568
 82. Zhao Y, Wang Y, Duan D, Ruan R, Fan L, Zhou Y, Dai L, Lv J, Liu Y. Fast microwave-assisted ex-catalytic co-pyrolysis of bamboo and polypropylene for bio-oil production. *Bioresource Technology*, 2018, 249: 69–75
 83. Cao Z, Niu J, Gu Y, Zhang R, Liu Y, Luo L. Catalytic pyrolysis of rice straw: screening of various metal salts, metal basic oxide, acidic metal oxide and zeolite catalyst on products yield and characterization. *Journal of Cleaner Production*, 2020, 269: 122079
 84. Chen X, Chen Y, Yang H, Chen W, Wang X, Chen H. Fast pyrolysis of cotton stalk biomass using calcium oxide. *Bioresource Technology*, 2017, 233: 15–20
 85. Chong Y Y, Thangalazhy-Gopakumar S, Ng H K, Lee L Y, Gan S. Effect of oxide catalysts on the properties of bio-oil from in-situ catalytic pyrolysis of palm empty fruit bunch fiber. *Journal of Environmental Management*, 2019, 247: 38–45
 86. Kim S, Park C, Lee J. Reduction of polycyclic compounds and biphenyls generated by pyrolysis of industrial plastic waste by using supported metal catalysts: a case study of polyethylene terephthalate treatment. *Journal of Hazardous Materials*, 2020, 392: 122464
 87. Lin X, Zhang Z, Zhang Z, Sun J, Wang Q, Pittman C U. Catalytic fast pyrolysis of a wood-plastic composite with metal oxides as catalysts. *Waste Management*, 2018, 79: 38–47
 88. Teng S Y, Loy A C M, Leong W D, How B S, Chin B L F, Máša V. Catalytic thermal degradation of *Chlorella vulgaris*: evolving deep neural networks for optimization. *Bioresource Technology*, 2019, 292: 121971
 89. Thangalazhy-Gopakumar S, Wei Lee C, Gan S, Kiat Ng H, Yee Lee L. Comparison of bio-oil properties from non-catalytic and in-situ catalytic fast pyrolysis of palm empty fruit bunch. *Materials Today: Proceedings*, 2018, 5(11): 23456–23465
 90. Chow L W, Tio S A, Teoh J Y, Lim C G, Chong Y Y, Thangalazhy-Gopakumar S. Sludge as a relinquishing catalyst in co-pyrolysis with palm empty fruit bunch fiber. *Journal of Analytical and Applied Pyrolysis*, 2018, 132: 56–64
 91. Jeong J Y, Lee U D, Chang W S, Jeong S H. Production of bio-oil rich in acetic acid and phenol from fast pyrolysis of palm residues using a fluidized bed reactor: influence of activated carbons. *Bioresource Technology*, 2016, 219: 357–364
 92. Loy A C M, Gan D K W, Yusup S, Chin B L F, Lam M K, Shahbaz M, Unrean P, Acda M N, Rianawati E. Thermogravimetric kinetic modelling of *in-situ* catalytic pyrolytic conversion of rice husk to bioenergy using rice hull ash catalyst. *Bioresource Technology*, 2018, 261: 213–222
 93. Loy A C M, Yusup S, Lam M K, Chin B L F, Shahbaz M, Yamamoto A, Acda M N. The effect of industrial waste coal bottom ash as catalyst in catalytic pyrolysis of rice husk for syngas production. *Energy Conversion and Management*, 2018, 165: 541–554
 94. Santosa D M, Zhu C, Agblevor F A, Maddi B, Roberts B Q, Kutnyakov I V, Lee S J, Wang H. *In situ* catalytic fast pyrolysis using red mud catalyst: impact of catalytic fast pyrolysis temperature and biomass feedstocks. *ACS Sustainable Chemistry & Engineering*, 2020, 8(13): 5156–5164
 95. Dong Q, Li H, Niu M, Luo C, Zhang J, Qi B, Li X, Zhong W. Microwave pyrolysis of moso bamboo for syngas production and bio-oil upgrading over bamboo-based biochar catalyst. *Bioresource Technology*, 2018, 266: 284–290
 96. Chen W, Fang Y, Li K, Chen Z, Xia M, Gong M, Chen Y, Yang H, Tu X, Chen H. Bamboo wastes catalytic pyrolysis with N-doped biochar catalyst for phenols products. *Applied Energy*, 2020, 260: 114242
 97. An Y, Tahmasebi A, Zhao X, Matamba T, Yu J. Catalytic reforming of palm kernel shell microwave pyrolysis vapors over iron-loaded activated carbon: enhanced production of phenol and hydrogen. *Bioresource Technology*, 2020, 306: 123111
 98. Gaurh P, Pramanik H. Production of benzene/toluene/ethyl benzene/xylene (BTEX) via multiphase catalytic pyrolysis of hazardous waste polyethylene using low cost fly ash synthesized natural catalyst. *Waste Management*, 2018, 77: 114–130
 99. Luo W, Fan Z, Wan J, Hu Q, Dong H, Zhang X, Zhou Z. Study on the reusability of kaolin as catalysts for catalytic pyrolysis of

- low-density polyethylene. *Fuel*, 2021, 302: 121164
100. Nalluri P, Prem Kumar P, Ch Sastry M R. Experimental study on catalytic pyrolysis of plastic waste using low cost catalyst. *Materials Today: Proceedings*, 2021, 45: 7216–7221
 101. Xu D, Xiong Y, Zhang S, Su Y. The synergistic mechanism between coke depositions and gas for H₂ production from co-pyrolysis of biomass and plastic wastes via char supported catalyst. *Waste Management*, 2021, 121: 23–32
 102. Zhang D, Lin X, Zhang Q, Ren X, Yu W, Cai H. Catalytic pyrolysis of wood-plastic composite waste over activated carbon catalyst for aromatics production: effect of preparation process of activated carbon. *Energy*, 2020, 212: 118983
 103. Chang G, Shi P, Guo Y, Wang L, Wang C, Guo Q. Enhanced pyrolysis of palm kernel shell wastes to bio-based chemicals and syngas using red mud as an additive. *Journal of Cleaner Production*, 2020, 272: 122847
 104. Singh R K, Patil T, Sawarkar A N. Pyrolysis of garlic husk biomass: physico-chemical characterization, thermodynamic and kinetic analyses. *Bioresource Technology Reports*, 2020, 12: 100558
 105. Sbirrazzuoli N. Determination of pre-exponential factors and of the mathematical functions $f(\alpha)$ or $G(\alpha)$ that describe the reaction mechanism in a model-free way. *Thermochimica Acta*, 2013, 564: 59–69
 106. Sajjad Ahmad M, Liu H, Alhumade H, Hussain Tahir M, Çakman G, Yıldız A, Ceylan S, Elkamel A, Shen B. A modified DAEM: to study the bioenergy potential of invasive *Staghorn sumac* through pyrolysis, ANN, TGA, kinetic modeling, FTIR and GC-MS analysis. *Energy Conversion and Management*, 2020, 221: 113173
 107. Hameed S, Sharma A, Pareek V, Wu H, Yu Y. A review on biomass pyrolysis models: kinetic, network and mechanistic models. *Biomass and Bioenergy*, 2019, 123: 104–122
 108. Cano-Pleite E, Rubio-Rubio M, Garcia-Hernando N, Soria-Verdugo A. Microalgae pyrolysis under isothermal and non-isothermal conditions. *Algal Research*, 2020, 51: 102031
 109. Ding Y, Zhang W, Yu L, Lu K. The accuracy and efficiency of GA and PSO optimization schemes on estimating reaction kinetic parameters of biomass pyrolysis. *Energy*, 2019, 176: 582–588
 110. Aghbashlo M, Almasi F, Jafari A, Nadian M H, Soltanian S, Lam S S, Tabatabaei M. Describing biomass pyrolysis kinetics using a generic hybrid intelligent model: a critical stage in sustainable waste-oriented biorefineries. *Renewable Energy*, 2021, 170: 81–91
 111. Ferreira A I, Rabaçal M, Costa M. A combined genetic algorithm and least squares fitting procedure for the estimation of the kinetic parameters of the pyrolysis of agricultural residues. *Energy Conversion and Management*, 2016, 125: 290–300
 112. Ding Y, Zhang Y, Zhang J, Zhou R, Ren Z, Guo H. Kinetic parameters estimation of pinus sylvestris pyrolysis by Kissinger–Kai method coupled with particle swarm optimization and global sensitivity analysis. *Bioresource Technology*, 2019, 293: 122079
 113. Buyukada M. Co-combustion of peanut hull and coal blends: artificial neural networks modeling, particle swarm optimization and Monte Carlo simulation. *Bioresource Technology*, 2016, 216: 280–286
 114. Xu L, Jiang Y, Wang L. Thermal decomposition of rape straw: pyrolysis modeling and kinetic study via particle swarm optimization. *Energy Conversion and Management*, 2017, 146: 124–133
 115. Majid M, Chin B L F, Jawad Z A, Chai Y H, Lam M K, Yusup S, Cheah K W. Particle swarm optimization and global sensitivity analysis for catalytic co-pyrolysis of *Chlorella vulgaris* and plastic waste mixtures. *Bioresource Technology*, 2021, 329: 124874
 116. Duan Q Y, Gupta V K, Sorooshian S. Shuffled complex evolution approach for effective and efficient global minimization. *Journal of Optimization Theory and Applications*, 1993, 76(3): 501–521
 117. Ding Y, Zhang J, He Q, Huang B, Mao S. The application and validity of various reaction kinetic models on woody biomass pyrolysis. *Energy*, 2019, 179: 784–791
 118. Ding Y, Wang C, Chaos M, Chen R, Lu S. Estimation of beech pyrolysis kinetic parameters by Shuffled Complex Evolution. *Bioresource Technology*, 2016, 200: 658–665
 119. Liu H, Chen B, Wang C. Pyrolysis kinetics study of biomass waste using Shuffled Complex Evolution algorithm. *Fuel Processing Technology*, 2020, 208: 106509
 120. Hasalová L, Ira J, Jahoda M. Practical observations on the use of Shuffled Complex Evolution (SCE) algorithm for kinetic parameters estimation in pyrolysis modeling. *Fire Safety Journal*, 2016, 80: 71–82
 121. Al-Yaari M, Ibrahim D. Application of artificial neural networks to predict the catalytic pyrolysis of HDPE using non-isothermal TGA data. *Polymers*, 2020, 12(8): 1813
 122. Bi H, Wang C, Jiang X, Jiang C, Bao L, Lin Q. Thermodynamics, kinetics, gas emissions and artificial neural network modeling of co-pyrolysis of sewage sludge and peanut shell. *Fuel*, 2021, 284: 118988
 123. Balsora H K, S K, Dua V, Joshi J B, Kataria G, Sharma A, Chakinala A G. Machine learning approach for the prediction of biomass pyrolysis kinetics from preliminary analysis. *Journal of Environmental Chemical Engineering*, 2022, 10(3): 108025
 124. Bong J T, Loy A C M, Chin B L F, Lam M K, Tang D K H, Lim H Y, Chai Y H, Yusup S. Artificial neural network approach for co-pyrolysis of *Chlorella vulgaris* and peanut shell binary mixtures using microalgae ash catalyst. *Energy*, 2020, 207: 118289
 125. Alaba P A, Popoola S I, Abnisa F, Lee C S, Ohunakin O S, Adetiba E, Akanle M B, Abdul Patah M F, Atayero A A A, Wan Daud W M A. Thermal decomposition of rice husk: a comprehensive artificial intelligence predictive model. *Journal of Thermal Analysis and Calorimetry*, 2020, 140(4): 1811–1823
 126. Zhu X, Li Y, Wang X. Machine learning prediction of biochar yield and carbon contents in biochar based on biomass characteristics and pyrolysis conditions. *Bioresource Technology*, 2019, 288: 121527
 127. Li H, Xu Q, Xiao K, Yang J, Liang S, Hu J, Hou H, Liu B. Predicting the higher heating value of syngas pyrolyzed from

- sewage sludge using an artificial neural network. *Environmental Science and Pollution Research International*, 2020, 27(1): 785–797
128. Whiteman J K, Gueguim Kana E B. Comparative assessment of the artificial neural network and response surface modelling efficiencies for biohydrogen production on sugar cane molasses. *BioEnergy Research*, 2014, 7(1): 295–305
 129. Zhang Y, Ahmad M S, Shen B, Yuan P, Shah I A, Zhu Q, Ibrahim M, Bokhari A, Klemeš J J, Elkamel A. Co-pyrolysis of lychee and plastic waste as a source of bioenergy through kinetic study and thermodynamic analysis. *Energy*, 2022, 256: 124678
 130. Gan D K W, Loy A C M, Chin B L F, Yusup S, Unrean P, Rianawati E, Acda M N. Kinetics and thermodynamic analysis in one-pot pyrolysis of rice hull using renewable calcium oxide based catalysts. *Bioresource Technology*, 2018, 265: 180–190
 131. Fong M J B, Loy A C M, Chin B L F, Lam M K, Yusup S, Jawad Z A. Catalytic pyrolysis of *Chlorella vulgaris*: kinetic and thermodynamic analysis. *Bioresource Technology*, 2019, 289: 121689
 132. Kumar Mishra R, Mohanty K. Co-pyrolysis of waste biomass and waste plastics (polystyrene and waste nitrile gloves) into renewable fuel and value-added chemicals. *Carbon Resources Conversion*, 2020, 3: 145–155
 133. Abnisa F, Wan Daud W M A. A review on co-pyrolysis of biomass: an optional technique to obtain a high-grade pyrolysis oil. *Energy Conversion and Management*, 2014, 87: 71–85
 134. Scheirs J. *Feedstock recycling and pyrolysis of waste plastics*. Manhattan: John Wiley & Sons Inc., 2006: 381–433
 135. Gouws S M, Carrier M, Bunt J R, Neomagus H W J P. Co-pyrolysis of coal and raw/torrefied biomass: a review on chemistry, kinetics and implementation. *Renewable & Sustainable Energy Reviews*, 2021, 135: 110189
 136. Lede J. Biomass fast pyrolysis reactors: a review of a few scientific challenges and of related recommended research topics. *Oil & Gas Science and Technology*, 2013, 68(5): 801–814
 137. Venderbosch R, Prins W. Fast pyrolysis technology development. *Biofuels, Bioproducts & Biorefining*, 2010, 4(2): 178–208
 138. Yousef S, Eimontas J, Stasiulaitiene I, Zakarauskas K, Striūgas N. Pyrolysis of all layers of surgical mask waste as a mixture and its life-cycle assessment. *Sustainable Production and Consumption*, 2022, 32: 519–531
 139. Brassard P, Godbout S, Hamelin L. Framework for consequential life cycle assessment of pyrolysis biorefineries: a case study for the conversion of primary forestry residues. *Renewable & Sustainable Energy Reviews*, 2021, 138: 110549
 140. Neha S, Prasanna Kumar Ramesh K, Remya N. Techno-economic analysis and life cycle assessment of microwave co-pyrolysis of food waste and low-density polyethylene. *Sustainable Energy Technologies and Assessments*, 2022, 52: 102356
 141. Joshi V V, Swaminathan G, Prabhakaran S P S. Life cycle assessment of the co-combustion system of single-use plastic waste and lignite coal to promote circular economy. *Journal of Cleaner Production*, 2021, 329: 129579

A review on co-pyrolysis of agriculture biomass and disposable medical face mask waste for green fuel production: recent advances and thermo-kinetic models

Melvin X. J. Wee¹, Bridgid L. F. Chin (✉)^{1,2}, Agus Saptoro¹, Chung L. Yiin^{3,4}, Jiuan J. Chew⁵, Jaka Sunarso⁵, Suzana Yusup⁶, Abhishek Sharma^{7,8}

¹ Department of Chemical and Energy Engineering, Faculty of Engineering and Science, Curtin University Malaysia, CDT 250, Miri 98009, Malaysia

² Energy and Environment Research Cluster, Faculty of Engineering and Science, Curtin University Malaysia, CDT 250, Miri 98009, Malaysia

³ Department of Chemical Engineering and Energy Sustainability, Faculty of Engineering, Universiti Malaysia Sarawak (UNIMAS), Kota Samarahan 94300, Malaysia

⁴ Institute of Sustainable and Renewable Energy (ISuRE), Universiti Malaysia Sarawak (UNIMAS), Kota Samarahan 94300, Malaysia

⁵ Research Centre for Sustainable Technologies, Faculty of Engineering, Computing and Science, Swinburne University of Technology, Kuching 93350, Malaysia

⁶ Generation Unit (Fuel Technology & Combustion), Tenaga Nasional Berhad (TNB) Research Sdn Bhd, Kajang 43000, Malaysia

⁷ Department of Chemical Engineering, Manipal University Jaipur, Jaipur 303007, India

⁸ Chemical & Environmental Engineering, School of Engineering, RMIT University, Melbourne, Victoria 3000, Australia

© Higher Education Press 2023

Abstract The Association of Southeast Asian Nations is blessed with agricultural resources, and with the growing population, it will continue to prosper, which follows the abundance of agricultural biomass. Lignocellulosic biomass attracted researchers' interest in extracting bio-oil from these wastes. However, the resulting bio-oil has low heating values and undesirable physical properties. Hence, co-pyrolysis with plastic or polymer wastes is adopted to improve the yield and quality of the bio-oil. Furthermore, with the spread of the novel coronavirus, the surge of single-use plastic waste such as disposable medical face mask, can potentially set back the previous plastic waste reduction measures. Therefore, studies of existing technologies and techniques are referred in exploring the potential of disposable medical face mask waste as a candidate for co-pyrolysis with biomass. Process parameters, utilisation of catalysts and technologies are key factors in improving and optimising the process to achieve commercial standard of liquid fuel. Catalytic co-pyrolysis involves a series of complex mechanisms, which cannot be explained using simple iso-conversional models. Hence, advanced conversional models are introduced, followed by the evolutionary models and predictive models, which can solve the non-linear catalytic co-pyrolysis reaction kinetics. The outlook and challenges for

the topic are discussed in detail.

Keywords biomass, COVID-19 waste, catalyst, pyrolysis, kinetics

1 Background

1.1 Bioenergy from biomass as a crucial renewable energy source

Association of Southeast Asian Nation (ASEAN) projected its population to grow by 100 million from 2014 to 2025, with an annual growth of 5%, and 4% in energy demand per year. Hence, the association has set the goal to increase its renewable energy share from 9.4% to 23% of the primary energy supply in the ASEAN region [1]. In order to meet the target, member countries has strategise several policies, laws, and regulations [2], as summarised in Table 1, which includes ASEAN member countries and their strategies [3].

Following this, ASEAN countries are known as the top agriculture producers. Hence, there are significant prospects for bioenergy as a strategy to help realise the ASEAN renewable energy generation and consumption goals. For example, Indonesia and Malaysia are the major players in the oil palm industry, followed by Thailand as

Received April 16, 2022; accepted August 8, 2022

E-mails: bridgidchin@curtin.edu.my, bridgidchin@gmail.com

Table 1 ASEAN member countries renewable energy policies

Country	Policies/strategies	Ref.
Cambodia	<p>Energy Sector Development Policy and Rural Electrification Policy, 2007 Rural electrification fund subsidy and investment incentives are provided as support to the policy</p> <ul style="list-style-type: none"> • Providing reliable, affordable quality supply of electricity to the consumers • Promoting private-owned facilities in the renewable energy sector to instigate competition between the companies • Providing electricity to 70% of the rural households by the year 2030 	[4]
India	<p>The Electricity Act, 2003</p> <ul style="list-style-type: none"> • To encourage the co-generation of electricity with renewable sources <p>• Specify the terms and conditions for the determination of tariff, which forms the National Electricity Policy and the Tariff policy</p> <p>Tariff Policy, 2006</p> <ul style="list-style-type: none"> • States that renewable energy shall be distributed with a preferential tariff determined by the appropriate commission <ul style="list-style-type: none"> • Bidding process within suppliers offering renewable energy from the same source <p>National Rural Electrification Policies, 2006</p> <ul style="list-style-type: none"> • Provision of access of electricity to all households by the year 2009 <ul style="list-style-type: none"> • Quality and reliable power supply at affordable rates <ul style="list-style-type: none"> • Providing off grid solutions for rural areas <p>Integrated Energy Policy Report (Planning Commission), 2006 Recommends a solution to meet the energy demand of India in an integrated process up to 2031–2032</p>	[5]
Indonesia	<p>Government Rule No. 3 on Supply of Electricity, 2005 To ease the private-own power producers to set up renewable energy plants</p> <p>Blueprint of National Energy Implementation Program 2005–2025</p> <ul style="list-style-type: none"> • To outline plans for energy supply security <p>• To provide guidelines for various sectors involving renewable and non-renewable energies</p> <ul style="list-style-type: none"> • To provide subsidies to enhance energy efficiency <p>Presidential Regulation No. 5 on National Energy Policy, 2006</p> <ul style="list-style-type: none"> • To set goals to promote diversification of energy sources • To reduce energy consumption by 1% per year as target <p>Presidential Decree No. 1 on Supply and Use of Biofuels, 2006 Setting targets and guidelines for biofuels utilisation and development</p> <p>Ministerial Regulation No. 2 on Medium Scale Power Generation from Renewable Energy Sources, 2006 To set pricing guidelines for projects ranging from 1 to 10 MW</p> <p>Energy Law, 2007 Providing renewable energy developers with investment incentives</p> <p>Electricity Law, 2010 To encourage private companies to participate in energy supply To provide priority in the utilisation of renewable energy</p> <p>To promote small scaled distributed power generation from renewable sources</p> <p>Ministerial Regulation No. 4/2012, 2012 To set the Feed-in-Tariff for electricity generated from biomass</p> <p>Ministerial Regulation No. 27/2014, 2014</p> <ul style="list-style-type: none"> • To set goals to increase the renewable energy portion to 23% by the year 2025, and 31% by 2050 <ul style="list-style-type: none"> • Feed-in-tariffs for renewable energy • To encourage the government and private sectors to utilise biofuels for power generation 	[6]
Malaysia	<p>Five-Fuel Diversification Policy, 2001 To include renewable energy in the energy supply mix of power generation</p> <p>National Biofuel Policy, 2006</p> <ul style="list-style-type: none"> • To reduce dependency on fossil fuels <p>• Providing subsidies to promote the demand for alternate sources of energy</p> <p>National Renewable Energy Policy and Action Plan, 2010</p> <ul style="list-style-type: none"> • Increase the renewable energy contribution in the energy supply mix <ul style="list-style-type: none"> • Promote growth of the renewable energy sector <ul style="list-style-type: none"> • Maintaining the renewable energy at an affordable price • Instigate awareness to the community on renewable energy 	[7]
Thailand	<p>Committee on Biofuel Development and Promotion (CBDP), 2008 Government subsidies from the State Oil Fund biodiesel price reduction</p> <p>Second Alternative Energy Development Plan (2008–2022), 2008</p> <ul style="list-style-type: none"> • To increase the proportion of alternative energy to 20% of the national total energy consumption by 2022 <ul style="list-style-type: none"> • To utilise renewable energy as a substitute for imported oil <ul style="list-style-type: none"> • To increase energy security of Thailand • Promote integrated green energy utilisation in communities • Enhance the development of alternative energy industry • Research and development of efficient technology to harvest renewable energy 	[8]
Vietnam	<p>Renewable Energy Action Plan, 2001 Government intervention to promote renewable energy</p> <p>The Law of Electric, 2004 Support electricity generation from renewable sources by providing investment incentives, preferential electricity prices and taxes</p> <p>Decision 1855/QĐ-TTg: 27 Dec 2007</p> <ul style="list-style-type: none"> • National Energy Development Strategy up to 2020 with outlook to 2050 <p>• To encourage the development of new and renewable energies, bioenergy to meet the socioeconomic requirements</p> <ul style="list-style-type: none"> • To meet the target of 5% of primary commercial energy by 2020 and 11% by 2050 <p>Decision No. 177/QĐ-TTg: 20 Nov 2007</p> <ul style="list-style-type: none"> • To develop biofuel, as an alternative for fossil fuels • To build a legal framework for biofuel development <ul style="list-style-type: none"> • To develop materials for biofuel production <ul style="list-style-type: none"> • To enhance biofuel extraction <p>National Program for Biofuels Development, 2011</p> <ul style="list-style-type: none"> • Develop biofuel to partly replace fossil fuels • Create the legal framework for biofuel development • Develop relevant materials for biofuel production <ul style="list-style-type: none"> • Develop biofuel extraction technologies 	[9]

(Continued)

Country	Policies/strategies	Ref.
Myanmar	<p>Myanmar Energy Master Plan, 2015</p> <ul style="list-style-type: none"> • To study the energy demand development from 2014 to 2035 • To set a goal to achieve 15%–20% share of renewable energy in 2020 <ul style="list-style-type: none"> • To improve the rural renewable energy usage • To achieve 57% hydropower, 5% solar and wind by 2030 	[10]
Laos	<p>The Electric Law, 1997</p> <p>Setting standards for the administration, production, distribution, transmission and the import and export of electricity</p> <p>The Power Sector Policy Statement, 2001</p> <ul style="list-style-type: none"> • To increase the electricity supply rate to 90% by 2020 • Promotes the public and private partnerships in hydropower development (500 kV grid) <p>The 8th National Socio-economic Development Plan (NSEDP), 2016–2020</p> <p>Promotes sustainability and diversification of renewable energy sources</p> <p>The Renewable Energy Development Strategy</p> <p>To increase the renewable energy share to 30% and substitute 10% of the transport fuel with biofuels by 2025</p>	[11]
Philippines	<p>R. A. No. 9367: The Biofuels Act, 2006</p> <p>Encourage the utilisation of biofuel-blended transport fuels by providing fiscal incentives</p> <p>R. A. No. 9513: The Renewable Energy Act, 2008</p> <ul style="list-style-type: none"> • Enhance the renewable energy development by providing fiscal and non-fiscal incentives <ul style="list-style-type: none"> • To reduce the country's reliance of fossil fuels <p>• Adopts renewable portfolio standards, feed-in-tariffs, net-metering, and Green Energy Option policy instruments</p>	[12]

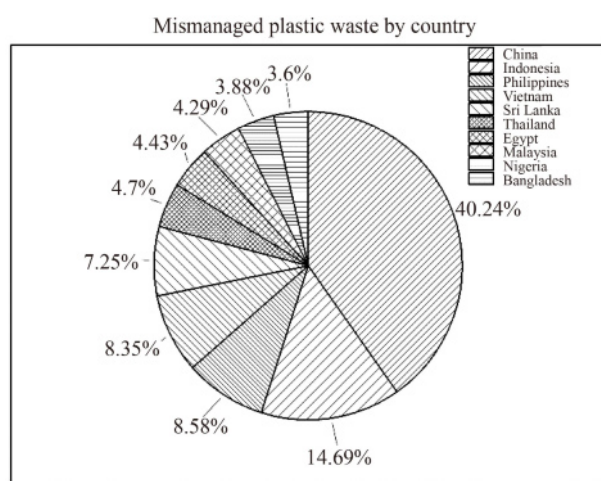


Fig. 1 Mismanaged plastic waste generated by countries. Reprinted with permission from Ref. [24], copyright 2015, American Association for the Advancement of Science.

shown in Fig. 1. In Indonesia, the production volume reached 45.86 million tonnes in 2019 [13]. Meanwhile, Malaysia produced 18.5 million tonnes in the same year [14]. However, the palm oil produced only represents 10% by weight of the total harvest; and the remainder contributed to the oil palm biomass, i.e., oil palm empty fruit bunch (EFB), palm kernel shell (PKS), palm pressed fibres (PPF), and oil palm frond [15]. To accommodate the rising population, food demand such as rice and wheat production in India has grown dramatically. In 1960, rice and wheat production was 34.6 and 11 million tonnes, respectively, and had risen to 118.9 and 107.6 million tonnes respectively in 2019 [16]. The rapid generation of biomass poses sustainability issues and waste management complications. Fortunately, this agriculture biomass is made up of lignocellulosic constituents, which include cellulose (23.3–44.9 wt %), hemicellulose (17.3–34.0 wt %),

and lignin (12–53.5 wt %) [17]. Cellulose is a complex polymer of glucose held by β -1,4-glycosidic bonds, intramolecular and intermolecular H-bonds. Hemicellulose is a heterogeneous polysaccharide, consisting of hexoses (i.e., glucose, mannose, galactose, xylose, arabinopyranose, arabinofuranose, and glucuronic acid). Lignin is made up of guaiacyl propane, syringyl propane and *p*-hydrophenyl propane [17,18]. These constituents serve as the basic precursors for the conversion into fuel, fibres, and aromatics [19]. Other properties from the proximate and ultimate analysis are depicted in Table 2, which shows that the biomass contains 50 to 70 wt % of volatile matter. In comparison, the carbon and hydrogen contents are 36–53 and 5.0–7.3 wt %, respectively.

Besides that, plastic or polymer waste generation has increased over the years. According to Geyer et al. [23], the study reports that cumulative plastic waste generation of primary and secondary plastic has reached 6300 million tonnes from 1980 to 2015. Only 12% of these plastic wastes were incinerated, while 9% were recycled. Furthermore, according to Jambeck et al. [24], ASEAN member countries such as Indonesia, Philippines, Vietnam, Thailand, and Malaysia contributed approximately 41% of the mismanaged plastic waste as illustrated in Fig. 1. Moreover, according to Abnisa and Alaba [25], the global composition of plastic wastes comprises of 26.67% low density polyethylene (LDPE), 25.33% polypropylene (PP), 18.67% high density polyethylene (HDPE), 14.67% polyethylene terephthalate (PET), 8% polystyrene (PS), and 6.67% polyvinyl chloride (PVC). Furthermore, with the rapid rise of confirmed cases of the novel coronavirus disease (COVID-19), the need for personal protective equipment (PPE) is high, resulting in the rapid generation of COVID-19 related wastes, exacerbating the current plastic waste management issue. According to Liang et al. [26], there are two categories of COVID-19 related wastes which are (1) wastes generated

Table 2 Proximate and ultimate analysis of different agriculture biomasses [20–22]

Sample	PKS	PPF	EFB	Rice husk	Rice straw (RS)	Bagasse
Proximate analysis/(wt %)						
Moisture	5.73	6.56	8.75	4.50	–	–
Ash	2.21	5.33	3.02	12.40	13.60	6.50
Volatile matter	73.74	75.99	79.67	58.60	70.10	72.70
Fixed carbon	18.37	12.39	8.65	24.40	16.30	20.80
Ultimate analysis/(wt %)						
C	53.78	50.27	48.79	43.20	37.10	36.30
H	7.20	7.07	7.33	5.00	5.20	5.80
S	0.51	0.63	0.68	0.00	0.10	0.00
N	0.00	0.42	0.00	0.30	0.50	0.30
O	36.3	36.28	40.18	51.4	43.5	51.10

from within hospitals or healthcare facilities, which are considered medical wastes and are collected and disposed of with appropriate measures (i.e., identification, collection, separation, storage, transportation, treatment, and disposal) [26], and (2) the wastes generated outside those facilities, which include disposable medical face masks (DMFM) and gloves. These wastes do not have proper waste management and are often treated as municipal solid, and plastics wastes. Besides that, according to the World Health Organisation (WHO) [27], the demand for these PPE, i.e., DMFM, and gloves, is expected to rise 20% by the year 2025. If these wastes are not managed properly, it will lead to major environmental complications. In some parts of the ASEAN region (i.e., Cambodia, Philippines, India, and Indonesia), poor waste management issues such as landfills and illegal dumping were present even before COVID-19. These uncontrollable landfills would escalate into space limitations and release toxic pollutants to the environment [28]. Moreover, the random disposal of these wastes could also lead to microplastic pollution, accumulating in the food chain, especially in aquatic life [29].

1.2 Biomass and polymer waste conversion pathways: pyrolysis

Therefore, strategies to recover energy from these wastes are keys to minimize the waste accumulation and their impacts to the environment. To convert these high-energy feedstocks into valuable fuel, there are two main pathways to convert the lignocellulosic biomass and plastic wastes into biofuels or green fuels, i.e., bio-chemical conversion and thermochemical conversion. In bio-chemical conversion, the larger and complex compounds are broken down into simpler molecules, with bacteria and enzymes. However, this method has limited feedstock options, and is not suitable to convert synthetic polymers like plastic wastes [30]. Besides that, thermochemical conversion includes low-temperature carbonisation, intermediate-temperature pyrolysis, and high-temperature gasification. Among these thermochemical

processes, pyrolysis represents a promising technology in terms of high fuel-to-feed ratios [31]. In addition, the pyrolysis process is favoured as the process that can be carried out at atmospheric pressure and faster conversion rates (<1 s) [32]. Moreover, the pyrolysis process is compatible with a wide variety of feedstocks aside from lignocellulosic biomass, i.e., plastics, and waste tires [33–36]. The pyrolysis process involves production of biofuel in the form of bio-oil, as well as producing valuable bio-chemicals such as alcohols, aldehydes, ketones, acids, furans, anhydrosugars, and phenols from biomass [37]. Fast pyrolysis yields the highest amount of bio-oil (65–75 wt %), while slow pyrolysis produces less bio-oil (20–50 wt %), with a larger proportion of bio-gas (20–50 wt %) and biochar (25–35 wt %) [38]. A detailed information on the different pyrolysis modes can be found in these references [38–43].

This paper focuses on the issues of the growing generation of biomass in ASEAN region, as well as the single-use plastics (i.e., DMFM) generated due to the COVID-19 pandemic. Following this, this review outlines the potential of co-pyrolysis of the biomass with plastic wastes as a technique to produce value-added bio-oil. Besides that, this review also looks into the technologies, (i.e., catalyst selection) and technical aspects (i.e., pyrolysis parameters) of the co-pyrolysis process. In addition, the kinetic models, and the advancements to describe the catalytic co-pyrolysis of biomass and plastic wastes are also outlined. Finally, the outlook detailing the significance and the limitations of the co-pyrolysis technique is discussed.

2 Bibliometric analysis

Bibliometric analysis is defined as the analysis of scientific publications using statistical methods to provide an outline of the research area [44]. Several publications have adopted this method in research areas of bio-diesels [45], municipal solid waste management [44], invest-

ments [46], and even COVID-19 [47]. This method of analysis provides a systematic way to sort and analyse a great number of publications, in terms of citations, co-citations, author keywords, and countries.

In this project, the bibliometric analysis of the field of pyrolysis of biomass was conducted in VOSviewer1.6.11. The utilisation of the software has been widely employed in this study, providing a visualisation of the relationships between publications in a research area or topic. The online publication database platform, Scopus, was utilised in the collection of the database for this study. The search phrase and Boolean Operators for this study were “pyrolysis AND biomass AND plastic AND bio-oil OR oil palm OR catalyst”, the publication year was limited from 2019 to 2023, and limited to journal articles only. A

total of 1448 publications were fitted into VOSviewer to analyse the co-occurrence of author keywords more than 20 times and are visualised in Fig. 2. The top-ranked link strength keywords, excluding the search phrases, include catalytic pyrolysis, co-pyrolysis, biochar, oxygen reduction reaction, and hydrogen. Based on this study, the current research trend involves around catalytic pyrolysis or co-pyrolysis, and focuses on the oxygen reduction, hydrogen and biochar formation from the process. Furthermore, another analysis of the bibliographic coupling of countries was carried out and the results were visualised in Fig. 3. The result suggests that China, United States, South Korea, Malaysia, and Australia are the active countries involved in this research area.

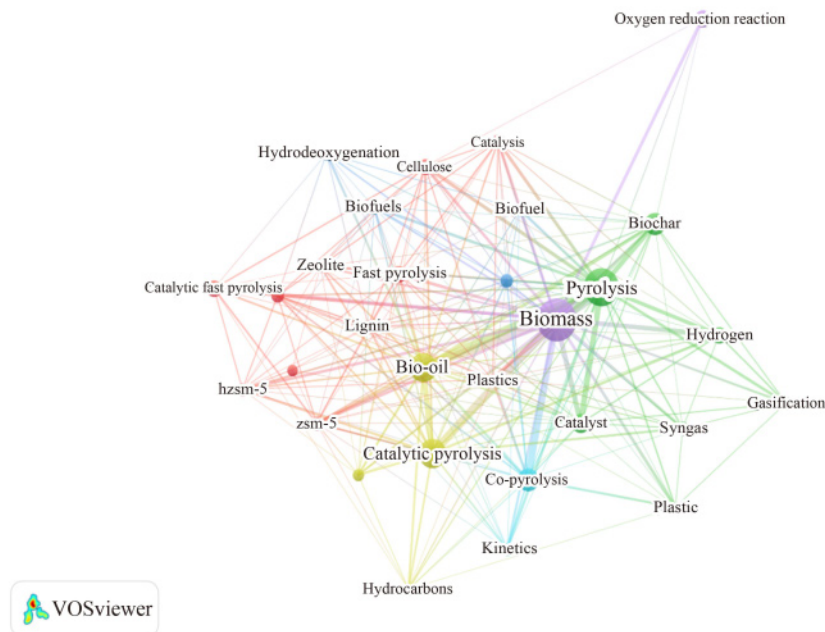


Fig. 2 Co-occurrence of author's keywords > 20 times by publication year.

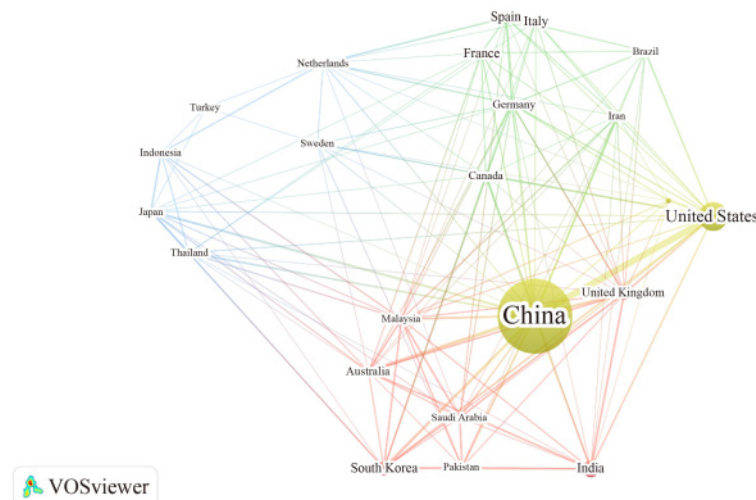


Fig. 3 Bibliographic coupling of countries by year.

3 Pyrolysis technologies/techniques for bio-oil production

Initially, most of the research studies focus on mono-component such as biomass [20,48–54] or plastic waste [55–60] in the pyrolysis process for bio-oil production. However, the pyrolysis of lignocellulosic biomass produces low quality bio-oil and yield [61]. Biomass-derived pyrolysis oil is high in oxygen content, corrosive in nature, and thermally unstable. Bio-oil generally requires upgradation using a hydrogen source and a catalyst, which makes the process complicated and expensive [37]. For plastic pyrolysis, the volatile products contain harmful compounds, i.e., polycyclic aromatic hydrocarbons (PAHs) [62–64]. PAH is a macromolecular aromatic compound with carcinogenic and mutagenic characteristics that pose health concerns upon exposure [65]. Hence, there is a growing interest in improving the pyrolysis process to produce bio-oil with enhanced properties, i.e., co-pyrolysis of two or more feedstock, and the utilisation of catalysts for product upgrading.

3.1 Mechanisms of co-pyrolysis with polymers

Hence, it is crucial to understand the reaction mechanism of co-pyrolysis of biomass and plastic wastes. Several studies have explored the co-pyrolysis of biomass with polymer wastes, i.e., RS and sugarcane bagasse with PP, and PS [34]; corn stover, ipil, and narra, with HDPE, LDPE and PP [35]; RS with waste tires [36]; sawdust with LDPE [66]. These studies show that the co-pyrolysis technique is promising in improving the bio-oil quality and calorific value, reducing energy costs by lowering the activation energy. According to Lin et al. [67], the widely accepted mechanism of co-pyrolysis of biomass with plastics can be summarised in a two-step mechanism: (1) the free radicals generated from the pyrolysis of biomass initiate the β -scission of the polymers, inhibiting the intermolecular and intramolecular H transfer, producing aliphatic hydrocarbons and reduced alkadienes; (2) the H transfers from the polymers reacting with the biomass-derived radicals to form stable compounds. This mechanism allows an increase in the decomposition rate of the biomass, greatly reducing the char yield as reported by Onal et al. [68]. The addition of a hydrogen-rich plastic waste to biomass influenced the energy recovery efficiency of bio-oil by affecting the real-time power output, reaction time, and changes in the bio-oil composition [69]. Besides that, the biomass decomposes first at a lower temperature forming free radicals, i.e., OH radicals. These radicals react with the pyrolysis products of plastic, larger molecular weight organics (C_{12}) were formed with the co-pyrolysis of biomass and LDPE [70]. According to Navarro et al. [34], this mechanism reduces the selectivity for the secondary reaction to occur,

reducing the char yield (i.e., 8.6 and 10 wt % reduction of char with the co-pyrolysis of B and PS, B and PP, respectively). Besides that, according to a study by Ojha et al. [71], the formation of C_8 – C_{20} alcohols was observed, which was explained by the reaction of hydrocarbon free radicals from PP, with water from the dehydration reaction from cellulose. According to Uzoejinwa et al. [72], synthetic polymers are derived from petroleum products with high carbon and hydrogen contents, low oxygen content, and contains high calorific values. Hence, making it suitable potential as a co-feedstock for the biomass pyrolysis. Furthermore, these polymer wastes also showed similar properties of high volatile matter, higher heating value (HHV) and lower heating value (LHV) than biomass, as observed in Table 3.

3.2 Pyrolysis reaction parameters that influence the bio-oil yield

During pyrolysis, multiple factors affect the outcome of the process, which are, reactor temperature, heating rate, feedstock particle size, and residence time. Studies on these parameters are crucial to improve the pyrolysis process in terms of bio-oil product yield and quality. Generally, the operating parameters are adjusted, to impede the secondary tar cracking reactions, which reduces the bio-oil yield.

3.2.1 Pyrolysis temperature

The role of temperature is to provide sufficient thermal energy for the decomposition of the biomass. It is important to note that for the main constituents of biomass, cellulose, hemicellulose, and lignin, their temperature degradation ranges are 225–325, 325–375, and 250–500 °C, respectively. Hence, an optimal temperature of 500 °C is sufficient to encompass these temperature ranges. Nevertheless, the optimal temperature differs with the compositions of varying feedstock [74]. Furthermore, according to Dai et al. [75], bio-oil yield peaks at the

Table 3 Proximate and ultimate analysis of polymers [22,34,60,73]

Sample	PP	PS	LDPE	HDPE	Waste tires
Proximate analysis/(wt %)					
Moisture	0.20	–	–	0.00	1.10
Ash	0.10	0.00	–	0.00	8.10
Volatile matter	99.80	99.50	99.98	100.00	62.50
Fixed carbon	0.00	0.50	0.02	0.00	28.20
Ultimate analysis/(wt %)					
C	85.40	89.50	85.47	85.34	84.60
H	14.50	8.50	14.21	12.22	7.70
S	0.00	0.00	0.11	0.00	1.40
N	0.00	0.00	0.08	0.00	0.40
O	0.00	2.00	0.13	2.44	4.30
HHV/(MJ·kg ⁻¹)	46.00	40.10	–	46.40	36.80
LHV/(MJ·kg ⁻¹)	43.10	–	–	43.10	35.10

temperature range of 450–550 °C; a further increase of temperature (> 600 °C), the bio-oil yield reduces, corresponding to an increase in non-condensable gas, or biogas. Moreover, a higher temperature (530–830 °C) promotes the reduction of complex compounds (i.e., acetaldehyde, methanol, propanol, and acetone), while increasing stable compounds (benzene, naphthalene, cresols, and phenols). For the case of polymer wastes, the degradation temperature ranges generally overlap or are higher than biomass, which varies between types of polymers. According to Miandad et al. [33], PP showed a single-stage degradation, which starts at a lower temperature of 240 °C with the maximum degradation at 425 °C, PS also showed a single-stage degradation but starts at a higher temperature of 330 °C, with the maximum degradation at 470 °C. While polyethylene (PE) exhibits a two-stage degradation, the first stage starts at the temperature of 270 °C and reaches 400 °C with a conversion rate of 12%, which followed by the second stage degradation starting at 400 °C, with the maximum conversion rate of 95% at 480 °C. Hence, these differences in thermal decomposition behaviours must be considered for the co-pyrolysis of biomass and polymers. According to Salvilla et al. [35], the study studied the effect of co-pyrolysis of corn stover with different polymers, i.e., LDPE, PP, and HDPE. Thermogravimetry analysis (TGA) experiments of the biomass-plastic blends result in a two-stage decomposition. The first stage involves the degradation of hemicellulose, and cellulose of the corn stover, while the second stage degradation overlaps with the decomposition of lignin. The results from this study conclude that the biomass and plastic blends exhibit the most synergistic effect occurs at temperature near 500 °C, i.e., corn stover and PP blend (5:3), and corn stover and LDPE blend (5:3) observed the greatest decomposition rate between 8% and 10% per minute respectively between the temperature ranges of 480–505 °C.

3.2.2 Heating rate

The heating rate is another important parameter that could determine the product distribution of the biofuels. According to Akhtar and Saidina Amin [31], fast heating rates cause rapid fragmentations of biomass and produces more bio-oil yield. This is possible as at higher heating rates (1000 °C·min⁻¹), there is short amount of time for the secondary reactions (i.e., tar cracking and repolymerisation). However, once the heat and mass transfer limitations have been overcome, higher heating rates would not increase the bio-oil yield further. Besides that, heating rates also affect the quality of the bio-oil, at lower heating rates, the water content of the bio-oil increases, as it impedes the dehydration reaction. It is also observed that at low heating rates (< 15 °C·min⁻¹) the bio-oil components have a higher weight range of 500–1000 Da, while increasing the heating rate to 15 °C·min⁻¹, it

significantly reduces the weight to 200–500 Da. However, continuing to increase the heating rate does not reduce the weight further [75]. In the case of polymer waste, the study found that LDPE, PP, and PVC, the thermogravimetry or derivative thermogravimetry curves shifted to the higher temperatures when the heating rate was increased. This phenomenon was explained by the thermal lag, due to the increased thermal gradient between the furnace temperature and the sample. Hence, the lower 100 °C·min⁻¹ heating rate favoured the degradation of the plastic wastes [60].

3.2.3 Particle size

To reduce heat transfer limitations caused by the poor heat conductivity of biomass, feedstock particle size or shape is another important criterion for bio-oil production. Larger particles (> 0.5 mm) tend to have poor heat transfer to the inner surfaces of the feedstock particle, this will lead to a lower yield of volatiles associated with the great temperature differences between the inner and outer surfaces of the feedstock particle. However, it is documented further increase in particle size (> 1 mm) does not have any effect on the bio-oil yield, which indicates minor impact of the internal heat or mass transfer to the process [76]. It was also reported that larger particle size, results in lower heat transfer to the feedstock [31,75]. For the pyrolysis of bamboo biomass with particle size, 0.45–0.75 mm, the bio-oil peaked at 54.03 wt %, while for smaller particle size 0.25–0.45 mm lowers the bio-oil yield to 50.85 wt % but increases biogas yield from 18.42 to 23.46 wt % [77]. Larger particle size of 0.8–1.2 mm, on the other hand, also lowered bio-oil yield of 51.61 wt %, with increased biogas and biochar yield of 20.62 and 27.74 wt %, respectively.

3.2.4 Residence time

Likewise, since the pyrolysis vapour is susceptible to secondary reactions, it is important to note that, the vapour residence time must be kept short to maximise the bio-oil yield. However, at very short residence times, the heat transfer limitations may restrict the feedstock from undergoing complete fragmentation [32,74,75]. Hence, the parameter is restricted by the characteristic of the feedstock itself. Instead, optimisation of the vapour residence time is a more feasible direction, i.e., feedstock particle size, heating rate, and design of the reactor and heater configuration to maximise the heat transfer [31].

3.3 The role of catalysts in the pyrolysis process

Catalysts play an important role in enhancing the quality of the bio-oil. This section categorised the existing catalysts employed in the pyrolysis process into three

main groups, commercial zeolite catalysts, metal-based catalysts, and renewable waste catalysts.

3.3.1 Commercial zeolite or acid catalyst

The commercial zeolite catalysts, i.e., ZSM-5, HZSM-5, MCM-41, zeolite Y, SBA-15, and zeolite BEA are the commonly utilised catalysts for the pyrolysis of biomass [78]. These catalysts have the active sites of the catalysts and reduce the dissociation energy of C–O, C=O, and –OH functional group, which allow the ability to remove oxygen atoms from the bio-oil via dehydration, decarboxylation, decarbonylation reactions [42,79]. Besides that, according to Ratnasari et al. [80], the key attributes of the zeolite as a suitable catalyst are the micropores (0.4–1.0 nm) or mesopores (1.5–30 nm) sizes. In a study on MCM-41, a zeolite catalyst with a mesoporous structure; the bigger pores allow hydrocarbons with higher molecular weight to enter the active sites, produce less oxygenates, and yield less aromatics. While smaller pore sized zeolites, such as ZSM-5 and Y-zeolite favour the production of aromatics. However, due to its smaller pore size, it is more likely to cause coking on the surface of these zeolites, thereby deactivating them. Therefore, studies have incorporated hierarchical catalyst structure to maximise the conversion performance [78,81]. Besides that, the acidity of the zeolites refers to the Si/Al ratio of the zeolite, it is a direct representation of the Brønsted acid (–OH group) and Lewis acid (Al sources in the Al₂O₃/SiO₂) sites available [74]. Comparing with zeolites, the silicalite catalyst with the same pore size but without acidity produces less aromatics and increases char formation [32]. Besides that, a study on the catalytic copyrolysis of RS and B with plastic wastes concluded that HZSM-5 promoted the deoxygenation, cleavage of the aromatic rings, reforming, isomerisation and Diels–Alder reaction of the bio-oil [22]. Hence, product upgradation

was achieved, and thereby producing valuable compounds, such as aromatics (i.e., styrene, ethylbenzene, *o*-xylene, and trimethyl-benzene) and aliphatic hydrocarbons (i.e., 2,4-dimethyl heptane). Zhao et al. [82] found that, with the bamboo to PP ratio of 1:2 over HZSM-5, high bio-oil yield of 61.62 wt % can be achieved, which is higher compared to that obtained for single feedstock bamboo pyrolysis of 29.91 wt %. Besides that, the aromatic and naphthenic hydrocarbons in the bio-oil were improved, which was in agreement with the study by Suriapparao et al. [22], where with the addition of a catalyst, the biomass–plastic mixture has a lower selectivity for oxygenates, while an increase in aliphatic and aromatic hydrocarbons were observed. The findings summarising the commercial acid catalysts utilised in literature can be found in Table 4.

3.3.2 Commercial metal-based catalyst/support

The metal-based catalysts in the catalytic pyrolysis of biomass majority refers to the metal oxides, alkali earth metals, metal salts, and transition metals. Metal oxides are prominent catalysts in this case, i.e., the basic MgO, CaO, and the acidic ZnO in the study of the pyrolysis of RS. The catalytic behaviour of MgO is similar to ZSM-5, as it favours the ketonization and aldol condensation reactions, which help to reduce oxygenates from the bio-oil [75]. According to Cao et al. [83], MgO has high ionic properties, which inhibits the repolymerisation reaction, hence greatly reduces the biochar formation while increasing the bio-oil yield. Furthermore, CaO was determined to have unique properties, as it behaves differently at different mass ratio incorporated in the feedstock, at less than 0.2 mass ratios; the CaO is a reactant, that reacts with the carboxyl groups to produce ketones. Carboxyl groups are undesirable bio-oil products due to their acidity, i.e., acetic acid. At 0.2 to 0.4 mass

Table 4 Acid zeolite catalyst application in the pyrolysis process examples

Biomass	Catalyst	Bio-oil yield/(wt %)	Reactor	Scale, feed weight/g	Ref.
RS	HZSM-5	21.50	Microwave pyrolysis	200–800	[22]
Bagasse		22.40			
PP		74.20			
PS		92.30			
Baggase: PS		43.80			
B:PP		35.70			
RS:PS		31.20			
RS:PP		24.50			
RS	ZSM-5	47.40	Fixed bed reactor	10	[83]
	Y zeolite	55.20			
	Mordenite	49.10			
	SBA-15	37.30			
Rice husk and WGPF	HZSM-5/MCM41	67.90% hydrocarbon relative content	Tubular reactor	0.001	[81]
	HZSM5	60.20% hydrocarbon relative content			
Seaweed biomass	ZSM-5	51.48	Hydro-pyrolysis	10	[32]
	MCM-41	41.84			
Bamboo	HZSM-5	49.14	Bubbling fluidised bed	100 g·h ⁻¹	[77]

ratio, CaO exhibits absorbent properties, absorbing CO₂ to CaCO₃, which contributes to the mass increase in the char yield. A further increase of CaO (> 0.4 mass ratio), the catalytic effect dominates, reducing the ester content in the bio-oil into simpler hydrocarbons and H₂ [84]. Besides that, while ZnO has less deoxygenation properties compared to CaO and MgO, it does not increase biochar yield [32,75,85]. On the other hand, studies have also found that metal salts have effectively improved the bio-oil yield. In a study of metal salt catalysts, MgCl₂ produced the maximum bio-oil yield of 48.4 wt % [83], comparing to the transition metal salt FeCl₃, which has a lower bio-oil yield of 32.2 wt %. According to the study, the ionic behaviour of the alkali earth metal salt, MgCl₂ minimises the repolymerisation reaction compared to the partial covalent transition metal salts. In recent studies of the plastic pyrolysis process, the metal catalysts such as carbon-supported platinum (Pt/C), and palladium (Pd/C) were studied in the pyrolysis of PET plastic. The study aims to reduce the polycyclic compounds and biphenyls which are harmful compounds to the environment and public health. The study concludes that Pt/C aided in the reduction of polycyclic compounds such as 2-naphthalenecarboxylic acid by 102% at 800 °C, and reduction of biphenyls such as biphenyl-4-carboxylic acid by 27% at 700 °C [86]. Furthermore, metal oxides have been employed to study the co-pyrolysis process of PP with poplar wood (i.e., ZnO,

CaO, MgO, and Fe₂O₃). The researchers found that CaO has the best deoxygenation results, removing carboxylic acids and phenols from the final products. It also increases cyclopentanones and alkenes compositions, but has reduced total volatile compounds, due to its strong basicity to cause coking on the catalyst surface. ZnO has the highest alkene yield, and increased ketone and phenols yields, and reduced carboxylic acid but has the weakest deoxygenation activities among all four catalysts. MgO behaves similarly to CaO, but has weaker deoxygenation properties, as it is less basic than CaO. Moreover, in the presence of the Fe₂O₃ catalyst, formation of aromatics such as *p*-xylene and 2-methyl-1-butenylbenzene were formed [87]. Following this, the studies of metal-based catalysts are summarised in Table 5, CaO is widely utilised in many studies due to its abundance and low cost, which can be found in renewable sources such as limestone and eggshells [88], and the niche in the utilisation of metal catalysts in the co-pyrolysis process.

3.3.3 Renewable waste catalyst

Renewable waste catalysts received much attention as an economic and sustainable alternative to commercial catalysts, i.e., red mud, ash catalysts, activated carbon, biochar derived catalyst, and palm oil sludge [90–94]. Red mud has attained much research interest as it has the potential to replace commercial catalyst. It is an alkaline

Table 5 Metal based catalyst application in the pyrolysis process examples

Biomass	Catalyst	Category	Bio-oil yield/(wt %)	Reactor	Scale, feed weight/g	Ref.
EFBF	CaO	Basic metal oxide	39.90 (5 wt % CaO); 40.40 (10 wt % CaO)	Fixed bed reactor	15	[85]
	MgO	Basic metal oxide	39.30 (5 wt % MgO); 42.30 (10 wt % MgO)			
	ZnO	Acidic metal oxide	44.70 (5 wt % ZnO); 42.20 (10 wt % ZnO)			
Cotton stalk	CaO	Basic metal oxide	50.00	Fixed bed reactor	–	[84]
RS	MgCl ₂	Metal salt oxide	48.40	Fixed bed reactor	10	[83]
	FeCl ₃	Metal salt	32.20			
	CuCl ₂	Metal salt	41.50			
	MnCl ₂	Metal salt	45.30			
	CaO	Basic metal oxide	38.70			
	CaCO ₃	Basic metal oxide	30.50			
	MgO	Basic metal oxide	52.10			
	MgCO ₃	Basic metal oxide	42.40			
	CeO ₂	Acidic metal oxide	52.30			
	ZnO	Acidic metal oxide	46.20			
	ZrO ₂	Acidic metal oxide	48.30			
	TiO ₂	Acidic metal oxide	48.20			
	EFB	CaO	Basic metal oxide			
PET	Pt	Metal catalyst	–	Tube furnace	1	[86]
	Pd					
PP-poplar wood composite	ZnO	Acidic metal oxide	–	Pyrolysis-gas chromatography/mass spectrometry	0.5 mg	[87]
	CaO	Basic metal oxide				
	Fe ₂ O ₃	Acidic metal oxide				
	MgO	Basic metal oxide				

solid by-product from the Bayer process in alumina production. According to Ly et al. [77], the components within the red mud include a great amount of metal oxides, i.e., MgO, CaO, SiO₂, Fe₂O₃, Al₂O₃, and TiO₂. From the study, red mud has a comparable bio-oil yield than HZSM-5 at temperature of 475 °C and residence time of 1.8 s. Upon characterisation of the bio-oil produced from red mud, the catalyst promoted the depolymerisation of cellulose and hemicellulose to produce furan derivatives. Besides that, the formation of saturated phenols in the bio-oil indicates red mud favours the demethylation and demethoxylation reactions. Furthermore, researchers have also studied the catalytic effect of the pyrolysis biochar. According to Dong et al. [95], the experiment on the catalytic pyrolysis of bamboo waste with different ratios of biochar, concluded that, the bio-oil had been upgraded; simpler C₂–C₆ compounds have been greatly increased with reduction in the heavy C₇–C₁₁ compounds. Moreover, Chen et al. [96] proposed upgrading the biochar from the pyrolysis process such as N-doped biochar, found high yields of bio-oil (61.0–63.0 wt %) were obtainable. A study on the Fe incorporated activated carbon reduces the bio-oil yield to achieve increased phenols 60.85–86.98 wt % of the bio-oil [97]. For the pyrolysis of plastic wastes, most research utilises the low-cost fly ash and naturally occurring kaolin as renewable catalyst sources [98–100]. Furthermore, in the case of co-pyrolysis, renewable waste catalysts such as Ni-doped biochar from waste pine sawdust, and activated carbon made from coconut husks were utilized [101,102]. The summary of renewable waste catalysts is depicted in Table 6, shows that renewable waste in the literature has much lower bio-oil yields or has a higher selectivity to syngas production than commercial catalysts.

4 Kinetic analysis

Kinetic analysis is an important aspect in describing the chemical kinetics of the pyrolysis process in the form of mathematical models. Traditionally modelling the chemical kinetics of biomass pyrolysis considers cellulose, hemicellulose, and lignin, based on the TGA experimental data. These kinetic models include the iso-conversional models, the Vyazovkin method, distributed activation energy model (DAEM), and the utilisation of predictive tools, i.e., artificial neural network (ANN).

4.1 Iso-conversional models

Iso-conversional method is the simplest form of kinetic model to explain the conversion of biomass to volatiles and biochar as a one-step first-order reaction. Examples of the iso-conversional method include the Kissinger–Akahira–Sunose (KAS), Flynn–Wall–Ozawa (FWO), and Starink’s method, which are integral methods ($g(a)$). In contrast, the Friedman method is an example of a differential method ($f(a)$) [104]. In this paper, Friedman and Starink’s methods are chosen to demonstrate the difference between the differential and integral versions of the iso-conversional method.

4.1.1 Friedman method

Friedman method is based on the differential method as the following expression in Eq. (1). This method requires the information on the conversion rate $\frac{d\alpha}{dt}$, and T . The kinetic plots between $\ln\left(\frac{d\alpha}{dt}\right)$ and $\frac{1}{T}$ produce the slope of

Table 6 Renewable waste catalyst for pyrolysis process examples

Biomass	Catalyst	Bio-oil yield/wt %	Reactor	Scale, feed weight/g	Ref.
Bamboo	Biochar	20.20 (5 wt % biochar) 18.70 (10 wt % biochar) 16.34 (20 wt % biochar)	Microwave pyrolysis	50	[95]
Bamboo	N-doped biochar	61.00 (10 wt % biochar) 63.00 (30 wt % biochar) 62.00 (50 wt % biochar)	Fixed bed reactor	3	[96]
PKS	Fe/activated carbon	7.96	Microwave pyrolysis	10	[97]
Rice husk	Rice hull ash	–	Fixed bed reactor	0.0055	[92]
Rice husk	Coal bottom ash	–	Fixed bed reactor	0.0055	[93]
PKS	Red mud	37.37–39.95	Fixed bed reactor	2	[103]
Bamboo	Red mud	50.34	Bubbling fluidised bed	100 g·h ⁻¹	[77]
EFB	Palm oil sludge	–	Fixed bed reactor	15	[90]
LDPE	Calcinated fly ash (900 °C)	76.22–80.02	Semi batch reactor	50	[98]
	Calcinated fly ash (800 °C)	70.96–71.36			
	Natural fly ash	68.20–71.70			
HDPE (plastic tub pieces)	Fly ash (10 wt %)	50.84	Lab scale pyrolyzer unit	1 kg	[100]
LDPE	Kaolin (1350 mesh)	64.66% aliphatics, 93.91% hydrocarbons, 30.07% H ₂	Quartz furnace tube	100	[99]
Pine sawdust and PE (50 wt %)	Ni-pine sawdust biochar	70.40 wt % (gas yield)	Fixed bed reactor	1	[101]
Corn stalk-HDPE mixture	Activated carbon	–	Tubular reactor	2	[102]

$\frac{E}{R \cdot T}$ and the intercept of $\ln[Af(\alpha)^n]$. The benefit of this model is that it makes no approximations, and can be adopted in any temperature settings [105],

$$\ln\left(\frac{d\alpha}{dt}\right) = \ln[Af(\alpha)^n] - \frac{E}{R \cdot T}, \quad (1)$$

where $f(\alpha)$, T , A , R , E are the differential form of the kinetic dependence function, absolute temperature (K), exponential factor (s^{-1}), universal gas constant ($8.314 \text{ J} \cdot \text{mol}^{-1} \cdot \text{K}^{-1}$), activation energy ($\text{kJ} \cdot \text{mol}^{-1}$).

4.1.2 Starink's method

Starink's method is an extension of the Coats–Redfern equation (Eq. (2)), which is similar to the FWO method, an integral method for estimating kinetic parameters [105]. Since $2RT/E \leq 1$, and has minimal variation with T , results in Eq. (3),

$$\ln\left(\frac{\beta \cdot g(\alpha)}{T^2}\right) = \ln\left[\frac{A \cdot R}{E} \left(1 - \frac{2R \cdot T}{E}\right)\right] - \frac{E}{R \cdot T}, \quad (2)$$

$$\ln\left(\frac{\beta \cdot g(\alpha)}{T^2}\right) \cong \ln\left(\frac{A \cdot R}{E}\right) - \frac{E}{R \cdot T}, \quad (3)$$

where β , $g(\alpha)$ are the heating rate ($^{\circ}\text{C} \cdot \text{min}^{-1}$), and the integral form of the kinetic dependence function. The generalised form Eq. (4) is

$$\ln\left(\frac{\beta \cdot g(\alpha)}{T^m}\right) = B - C\left(\frac{E}{R \cdot T}\right). \quad (4)$$

Starink's equation utilises the constants, where $m = 1.92$, $B = \ln(AR/E) + 3.7545411 - 1.92 \ln E$, and $C = 1.0008$, which can be rewritten as Eq. (5),

$$\ln\left(\frac{\beta}{T^{1.92}}\right) = C_s - 1.0008\left(\frac{E}{R \cdot T}\right), \quad (5)$$

where C_s is the constant. This method is a simple direct method to obtain the expression E/R from the slopes by plotting $\ln\left(\frac{\beta}{T^{1.92}}\right)$ vs. $1/T$. Starink's method is widely employed as a comparison against other iso-conversional methods [48,106]. However, these methods are flawed, as proposed, with an addition of a secondary feedstock and the utilisation of a catalyst, the reaction mechanisms become much more complex [107]. Hence, a modified iso-conversional method is introduced, the Vyazovkin method.

4.2 Vyazovkin method

The iso-conversional methods assume a reaction ideally has a constant value of E_α . This assumption is the main source of errors, which explains the differences obtained from different iso-conversional methods [105]. Hence, to overcome these drawbacks, an advanced alternative non-linear iso-conversional Vyazovkin method is proposed. This method assumes the reaction is independent of the

heating rate, and accounts for the variation of E in the computation of the temperature integral, $I(E_\alpha, T_\alpha)$ from Eq. (6). The E_α which is the effective activation energy ($\text{kJ} \cdot \text{mol}^{-1}$) is obtained from the minimisation of the function $\varnothing(E_\alpha)$ from Eq. (7),

$$I(E_\alpha, T_\alpha) = \int_0^{T_\alpha} \left(-\frac{E_\alpha}{R \cdot T}\right) dT = \frac{E_\alpha}{R} p(x), \quad (6)$$

$$\varnothing(E_\alpha) = \sum_i^n \sum_{j=i}^n \left(\frac{I(E_\alpha, T_{\alpha,i}) \cdot \beta_j}{I(E_\alpha, T_{\alpha,j}) \cdot \beta_i} \right), \quad (7)$$

where n , E_α , T_α are the number of heating rates in the experiment, activation energy and temperature for each α , while i and j represent the heating rates corresponding to n . For $p(x)$, it is the approximation equation obtained from using Yang equation, Eq. (8):

$$p(x) = \frac{\exp(-x)}{x} \cdot \frac{x^3 + 18x^2 + 88x + 96}{x^4 + 20x^3 + 120x^2 + 240x + 120}, \quad (8)$$

where x is the simplified expression of E/RT . Hence, due to its complex structure, this model requires a numerical approach to solve for the kinetic parameters. Recent studies have started adopting this method to compute the kinetic parameters [48,54].

4.3 Distributed activation energy model

In a complex process such as co-pyrolysis, the E_α would not be constant. Instead, it varies as an indication of a much more complex reaction in place, which is unable to explain over a single-step kinetic model. The DAEM is an accurate and versatile model to represent complex pyrolysis processes. It is the best mathematical method to show the physical and chemical heterogeneity of biomass during a devolatilisation process [34]. According to Hameed et al. [107], DAEM takes into consideration of the decomposition of species over a large number of independent parallel reactions with different activation energies, represented by a continuous distribution function (i.e., Gaussian distribution, $f(E)$), Eq. (9):

$$f(E) = \frac{1}{\sigma \sqrt{2\pi}} \exp\left[-\frac{1}{2} \left(\frac{E - E_M}{\sigma}\right)^2\right], \quad (9)$$

where σ , E_M are the standard deviation and the mean activation energy, respectively. Furthermore, studies have simplified the DAEM based on the assumption that the solid feedstock is a complex mixture of compounds. During the pyrolysis process, a great number of independent consecutive or simultaneous, irreversible reactions take place, each characterised by its corresponding activation energies and pre-exponential factor, given by Eq. (10):

$$1 - \alpha = \int_0^\infty \exp\left(-A \int_0^t \exp\left(\frac{E}{RT}\right) dt\right) \cdot f(E) dE = \varnothing, \quad (10)$$

where, according to Cano–Pleite et al. [108], $\varnothing = 0.58$,

which can be simplified as Eq. (11):

$$\ln\left(\frac{\beta}{T}\right) = \ln\left(\frac{A \cdot R}{E}\right) + 0.675 - \frac{E}{R} \cdot \frac{1}{T}. \quad (11)$$

However, this model is restricted to a constant heating rate. In the applications of DAEM, it has been utilised to estimate the behaviour of different combinations of lignocellulosic biomass (pine wood) and polymer wastes (i.e., waste tyre, polylactic acid, PS, PET, PP, and HDPE) [34]. Besides that, this method has been incorporated into an ANN model to predict the pyrolytic properties of *Staghorn sumac* [106].

4.4 Optimisation methods

Optimisation methods or often referred to as heuristic models, such as genetic algorithm (GA), and particle swarm optimisation (PSO), shuffled complex evolution (SCE) are algorithms that could solve global optimization problems, i.e., for the pyrolysis process, the optimisation of the kinetic parameters to find the best fit using the data from the TGA. These optimisation methods generally solve problems by subjecting it to an objective function to determine the fitness of the iterations [109]. The objective functions or optimisation targets for a thermal degradation problem are the mass loss \varnothing_m and the mass loss rate \varnothing_{mr} in Eqs. (12)–(14) as follows:

$$\varnothing = \varnothing_m + \varnothing_{mr}, \quad (12)$$

$$\varnothing_m = \sum_{j=1}^N \left[W_{CML,j} \frac{\sum_{k=1}^n (CML_{mod,k} - CML_{exp,k})^2}{\sum_{k=1}^n \left(CML_{exp,k} - \frac{1}{n} \sum_{p=1}^n CML_{exp,p} \right)^2} \right], \quad (13)$$

$$\varnothing_{mr} = \sum_{j=1}^N \left[W_{MLR,j} \frac{\sum_{k=1}^n (MLR_{mod,k} - MLR_{exp,k})^2}{\sum_{k=1}^n \left(MLR_{exp,k} - \frac{1}{n} \sum_{p=1}^n MLR_{exp,p} \right)^2} \right], \quad (14)$$

where CML_{mod} and CML_{exp} are the model and experimental cumulative mass loss, respectively; MLR_{mod} and MLR_{exp} are the model and experimental mass loss rate, respectively; N is the number of experiments, n is the number of data points for each experiment; and W_{CML} and W_{MLR} are the weighted value which can be defined as 1.

4.4.1 Genetic algorithm (GA)

The GA is based on an evolutionary concept to find the optimal solution to a complex problem globally. Firstly, the algorithm is initialised by carrying out a range search from a set of randomised candidate solutions referred to as a population. Each candidate solution is defined as an individual or a chromosome, containing the target

parameters to be optimised (i.e., for the pyrolysis process, A , E_α and \varnothing), where the parameters are defined as genes in the GA [109]. Following the natural survival of the fittest, the population experience evolution forming subsequent generations according to the fitness of the objective function. Besides that, the new generation is produced by the chromosomes crossing over, exchanging information, and allowing mutation, this method helps to prevent the local optimal solution. Finally, by the process of elimination of relatively “unfit” candidate solution and reproducing generations that are “fit”. The application of GA in thermal degradation experiments are quite common, it is applied to solve the hybrid pyrolysis scheme of combining both parallel and convective first order reaction. Besides that, recent studies have combined it with different algorithms to improve the performance of the model, according to Aghbashlo et al. [110], the study combines GA with Adaptive Neuro-Fuzzy Interference System (ANFIS) achieving predictions of the kinetic parameters with better fitting compared to traditional ANFIS model; GA-least squares fitting procedure [111], where GA is applied to generate the initial guess for the least square function to solve for the optimal solution. This reduces the number of iterations required for the least square.

4.4.2 Particle swarm optimization (PSO)

The PSO algorithm follows the velocity and position search model. It contains a certain number of particles, their positions, and velocity. The particles in a particular position represent a candidate of solution of space, and the velocity of this particle updates the position of these particles [112]. In addition, these particles have a memory ability which, retains its historical best position vector and its global best position found [109]. Initially, the particles are assigned a random position and velocity in a proposed range. The solution then improves with iterations via Eqs. (15) and (16):

$$v_{id}^{k+1} = \omega v_{id}^k + c_1 r_1 (p_{id} - x_{id}^k) + c_2 r_2 (p_{gd} - x_{id}^k), \quad (15)$$

$$x_{id}^{k+1} = x_{id}^k + v_{id}^{k+1}, \quad (16)$$

where k is the iteration number, i is the particle number, and d is the search direction from 1 to D , w is the inertia weight, p_{id} and p_{gd} are the local particle position and the global best position of all particles, respectively. c_1 and c_2 are the two positive acceleration constants for the local and global nature of the swarm. r_1 and r_2 are the stochastic values in the range of $[0, 1]$, respectively [113, 114].

According to Ding et al. [109], the study compares the performance between PSO and GA, and the results indicate that PSO showed closer global optimum convergence, 0.053 at the population size of 2500 compared to GA, with the best value at 0.075 at the population size of 2000. Besides that, PSO showed less

fluctuation, 0.05 to 0.08 in fitting values regardless of population size, compared to GA, which fluctuates between 0.07 and 0.29. In literature, PSO is often coupled with other algorithms, such as global sensitivity analysis, to find the parameters with the greatest effect on the prediction outcome. According to Ding et al. [112], the sensitivity order is ranked from the largest to the smallest value which are representing the activation energy of lignin, the reaction order of cellulose, and the pre-exponential factor for lignin in the pyrolysis process of pinewood. While for the co-pyrolysis of microalgae *Chlorella vulgaris* and HDPE, the activation energy of cellulose, pre-exponential factor for cellulose and the activation energy of protein, followed by the reaction order of cellulose, showed significant influence on the prediction results, indicating these parameters should be paid much attention for the pyrolysis process [115]. Besides that, Monte Carlo simulations were applied to perform uncertainty analysis, to probabilistically assess the effects of stochastic uncertainties in the predictor values ($n = 100000$) from the ANN and PSO framework [113]. In addition, a recent study proposed a neuro-evolution algorithm, progressive deep swarm evolution (PDSE), built on the PSO algorithm, to model the catalytic thermal degradation of *Chlorella vulgaris* [88]. From the validation tests, implementing the PDSE algorithm obtained a coefficient of determination (R^2) value above 0.9990, RMSE below 0.0075, and MBE below 0.0026.

4.4.3 Shuffled complex evolution (SCE)

The SCE algorithm introduced by Duan et al. [116] is effective for calibration of hydrological models. The efficacy of this algorithm, a form of differential evolution (DE), comes from its use of geometric operations to find possible optimal solutions to space parameters. The algorithm solves global optimisation problems based on four concepts: (1) probabilistic and deterministic approaches; (2) clustering; (3) systematic evolution of a complex of points spanning the space in the direction of global improvement and (4) competitive evolution. The application of SCE on the woody pyrolysis was studied with six different kinetic models, comprising of single component reactant mechanism, and multicomponent reactant mechanisms (i.e., cellulose, hemicellulose, and lignin) [117]. The optimised kinetic parameters from the results were applied to predict the pyrolysis process with different heating rates, 5 and 80 °C·min⁻¹, where the results were found better fitting of the results of the multicomponent kinetic model, which can reach R^2 values of up to 0.99 [117]. Besides that, SCE has been applied in various pyrolysis kinetic analysis, pyrolysis of beech [118], and pyrolysis of basswood waste [119].

The SCE algorithm starts with generating of a population of random points within the search space, denoted as s . Each of these points contains a vector (i.e.,

kinetic parameters) and is ranked based on their fitness function value and stored in an array D , and partitioned into p complexes, each containing m points, i.e., $D = \{A^k, k = 1, \dots, p\}$. Next, each complex evolved using the competitive complex evolution algorithm, and shuffled. All points are combined to a single population and the procedure of ranking for the function value, partition into complexes, evolution, and shuffling is repeated until convergence value is reached [116,120].

4.5 Predictive models: artificial neural network (ANN)

ANN is an intelligent learning, predictive computational technique, often employed to solve the nonlinear, and complex relationships between the input and output data. An ANN network consists of one or more hidden layers connecting the input (i) and output (o) layers. Each layer has a weight (w) matrix and an output vector [121]. The neuron of each single layer picks up the summation of the activation from the input vectors and their assigned weights and biases, the results then pass through an activation function (i.e., linear, sigmoid, and hyperbolic tangent sigmoid) to generate a new activation value to the neurons in the following layers. The weight matrix is altered to fit the learning algorithms, the learning ends when the weights of each layer achieve convergence as the final output vector (y_o) [122,123]. The ANN parameters influencing the performance are: the number of hidden layers (j), the number of neurons in each hidden layer (n), and the transfer function deployed denoted as f . The general architecture of the ANN is illustrated in Fig. 4.

Generally, the model learning process involves inputting a percentage of sample data to the network, and altering the number of neurons in the hidden layers to optimise the mean square error (MSE) [51]. Besides that, the selection is supervised by a learning algorithm. In literature, this method has been applied in predicting of the kinetic parameters of the pyrolysis process, involving the iso-conversional models, i.e., KAS and FWO shown in Table 7.

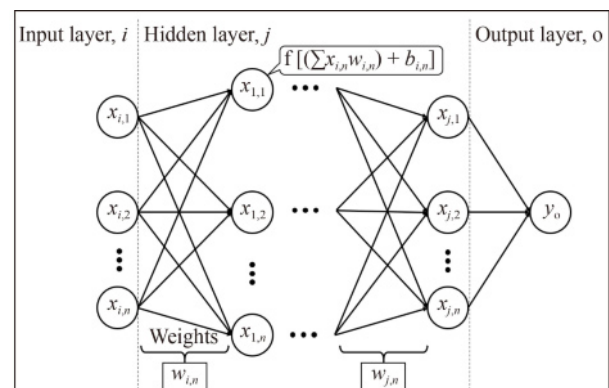


Fig. 4 General ANN architecture.

4.6 Thermodynamics relations

The thermodynamic parameters are important for the scale up and the design of the reactor, i.e., Frequency factor, A (s^{-1}), change in enthalpy, ΔH ($kJ \cdot mol^{-1}$), Gibbs free energy, ΔG ($kJ \cdot mol^{-1}$), and change in entropy, ΔS ($kJ \cdot mol^{-1} \cdot K^{-1}$). The parameters are expressed in the respective equations as Eqs. (17)–(20):

$$A = \frac{\beta \cdot E \cdot \exp\left(\frac{E}{R \cdot T_m}\right)}{R \cdot T_m^2}, \quad (17)$$

$$\Delta H = E_\alpha - R \cdot T, \quad (18)$$

$$\Delta G = E_\alpha + R \cdot T_m \cdot \ln\left(\frac{K_B \cdot T_m}{h \cdot A}\right), \quad (19)$$

$$\Delta S = \frac{\Delta H - \Delta G}{T_m}, \quad (20)$$

where T_m , K_B , h are the maximum temperature where the decomposition occurs (K), Boltzmann constant ($1.381 \times 10^{-23} \text{ J} \cdot \text{K}^{-1}$), and Planck's constant ($6.626 \times 10^{-34} \text{ J} \cdot \text{s}$) [30]. $A < 10^9 \text{ s}^{-1}$ refers to a simpler straightforward reaction, while $A > 10^9 \text{ s}^{-1}$ would mean the reaction follows a complex mechanism [129]. ΔH represents the endothermic or exothermic behaviour of the reaction mechanism; it is the amount of energy transferred during a chemical reaction. According to Gan et al. [130], the smaller the difference of ΔH with the E_α is, the more favourable for the reaction to occur. Hence, the bioenergy from the system is more likely to be attained. Moreover, ΔG is the total potential energy increased in the system, it signifies that the reactants are consumed and activated complexes are formed [21]. The ΔG also represents the suitability of the feedstock for pyrolysis, the higher the ΔG is, the more bioenergy can potentially be attained [30,51]. Furthermore, ΔS is the degree of arrangement of the carbon in the waste and biomass. It is the amount of

energy unavailable to work. For higher entropy values, it indicates that the sample has yet to achieve thermodynamic equilibrium, and is highly reactive [131]. Table 8 summarises the kinetic and thermodynamic parameters for different feedstock samples.

5 Future outlooks

Many studies have proven that the combination of feedstock, biomass with waste plastic or biomass with waste tire in co-pyrolysis, with enhancements in the pyrolysis oil through synergistic effects, is an economical way for the production of sustainable fuel as a replacement for fossil fuels. The combination of waste plastics (20 wt %) with biomass generated a higher pyrolytic liquid yield compared to the solely thermal pyrolysis of biomass. This phenomenon shows that the oil produced from co-pyrolysis process can be blended with diesel after minor upgrading or even directly applied in transportation [132]. Nonetheless, not all plastic types can be applied in the process. In this sense, PVC, which consists of about 57% chlorine by weight, is not an ideal feedstock material as it will thermally break down into a very corrosive and toxic hydrochloric acid and influence the diesel quality with the production of chlorinated hydrocarbons. A $0.0145\text{--}0.0290 \text{ mg} \cdot \text{m}^{-3}$ of total chloride level has been recorded in the fuel oil product with just merely adding 1%–3% PVC in the feedstock stream [133,134]. Besides that, Hu et al. [32] stated that more studies are needed for co-pyrolysis especially in establishing a suitable approach in selecting material and the optimum blending ratio of material with biomass [32].

Furthermore, constraints in having straightforward and efficacious characterisation strategies for co-pyrolytic oil also impede the dependence of the industrial community in the technology [135]. Despite the extensive research works on the invention of the co-pyrolysis approach using

Table 7 ANN model compilation from different studies

Biomass/catalyst	Learning algorithm/ topology	Prediction result	ANN parameters	Ref.
<i>Chlorella vulgaris</i> limestone, HZSM-5	PDSE	Thermal degradation	Inputs: heating rate; heat flow; reactor temperature Outputs: remaining mass	[88]
Rice husk, sewage sludge	Levenberg–Marquardt (LM)	Thermal degradation	Inputs: reactor temperature; blend composition Outputs: mass loss	[21]
<i>Chlorella vulgaris</i> , peanut shell, microalgae ash	LM	Thermal degradation	Inputs: heating rate; reactor temperature Outputs: mass loss	[124]
Sewage sludge, peanut shell	LM	Thermal degradation	Inputs: blend compositions; heating rates; reactor temperature Outputs: remaining mass	[122]
Rice husk	Scaled conjugate gradient and LM	Thermal degradation	Inputs: heating rate; reactor temperature Outputs: remaining mass	[125]
Lignocellulosic biomass	Random forest schematic	Biochar yield	Dataset: physicochemical properties of lignocellulosic biomass	[126]
Sewage sludge	LM	HHV of syngas	Dataset: physicochemical properties of biomass	[127]
Mexican sunflower (<i>Tithonia diversifolia</i>)	LM	Bio-oil yield	Inputs: heating rate; flow rate; particle size; reactor temperature Output: bio-oil yield	[128]

Table 8 Kinetic and thermodynamic parameters of the pyrolysis process in literature

Feedstock	Catalyst	Kinetic model	$E_a/$ (kJ·mol ⁻¹)	$A/$ min ⁻¹	$\Delta H/$ (kJ·mol ⁻¹)	$\Delta S/$ (J·mol ⁻¹ ·K ⁻¹)	$\Delta G/$ (kJ·mol ⁻¹)	Ref.
<i>Pterocarpus indicus</i>	–	Coats-redfern	112.0	–	103.0	–138.0	183.00	[35]
<i>Intsia bijuga</i>	–		99.0	–	89.0	–120.0	160.00	
Corn stover	–		66.0	–	57.0	–173.0	147.00	
HDPE	–		546.0	–	533.0	420.0	226.00	
LDPE	–		487.0	–	475.0	348.0	231.00	
PP	–		423.0	–	411.0	273.0	222.00	
Rice hull	–	DAEM	175.4	2.939×10^{17}	170.2	–	–	[130]
	–	FWO	177.7	7.991×10^{16}	172.6	–	–	
	Limestone	DAEM	123.3	5.803×10^{11}	117.9	–	–	
	Limestone	FWO	132.5	4.148×10^{12}	127.1	–	–	
	Eggshell	DAEM	96.1	2.033×10^{10}	90.8	–	–	
	Eggshell	FWO	100.4	1.948×10^9	95.2	–	–	
Sewage sludge (97.5% conversion)	–	KAS	123.6	1.440×10^6	119.5	139.4	187.69	[51]
	–	FWO	132.7	1.560×10^9	128.6	138.8	196.50	
	–	Friedman	92.4	0.0103	88.3	295.4	232.80	
	–	Popescu	200.9	9.740×10^{10}	196.8	219.3	304.00	
Microalgae:microalgae ash:peanut shell 9:2:9	–	FWO	142.6	2.010×10^{14}	137.0	–	–	[124]
Garlic husk	–	KAS	154.0	–	149.4	–	150.60	[104]
	–	FWO	154.9	–	150.4	–	150.50	
	–	Starink	154.3	–	149.8	–	150.50	
<i>Staghorn sumac</i>	–	FWO	167.9	–	178.9	–	–	[106]
	–	KAS	169.4	–	167.2	–	–	
	–	Starink	169.8	–	167.6	–	–	
<i>Azadirachta indica</i>	–	FWO	–	6.288×10^{15}	188.5	–43.3	215.40	[30]
	–	Friedman	–	8.586×10^{15}	190.9	–39.4	215.40	
	–	Vyazovkin	–	2.965×10^{20}	199.7	–26.0	215.20	
<i>Phyllanthus emblica</i>	–	FWO	–	2.075×10^{14}	189.9	–40.9	215.30	[30]
	–	Friedman	–	2.864×10^{13}	181.3	–55.1	215.60	
	–	Vyazovkin	–	3.534×10^{13}	179.4	–58.3	215.60	
Rice husk	–	Friedman	–	–	186	–	–	[92]
	–	KAS	–	–	178	–	–	
	–	FWO	–	–	180	–	–	
	Rice hull ash	Friedman	–	–	148	–	–	
	Rice hull ash	KAS	–	–	148	–	–	
	Rice hull ash	FWO	–	–	146	–	–	
<i>Chlorella vulgaris</i>	–	KAS	156.2	2.898×10^{20}	151	–	–	[131]
	–	FWO	158.1	2.358×10^{20}	153	–	–	
	HZSM-5	KAS	145.3	2.790×10^{14}	140	–	–	
	HZSM-5	FWO	147.8	4.908×10^{14}	143	–	–	
	Limestone	KAS	138.8	6.360×10^{15}	133	–	–	
	Limestone	FWO	142.1	8.880×10^{15}	137	–	–	

different kinds of agricultural biomass and polymer wastes, the current heat transfer processes for co-pyrolysis, i.e., conduction, convection and radiation still impose several challenges. In conduction, solid attrition is the critical issue once there is a direct contact between fuel particles and heating agent. In convection, small fuel particles and long gas residence times are essential for gas/solid and sufficient heat transfer, respectively. Asymmetrically, the primary challenges of radiation are high concentration of radiation is required for the production of sufficient heat transfer and consideration of wall heating design in pyrolysis reactor [136,137]. Hence,

the high installation and operating costs of units with a high efficiency of heat transfer in the short gas residence time and an additional pre-treatment system for various types of biomasses are the main drawbacks of co-pyrolysis. Different studies reported that different conditions are required to blend an appropriate waste with different biomasses before co-processing. More profound fundamental studies on reaction mechanisms and kinetics of biomass with different waste materials are critical in the advancement of the co-pyrolysis process. In this sense, the properties of the co-pyrolytic oil produced with its composition can be determined from the interactivity

of the reaction intermediates. Currently, ANN and Monte Carlo serve as empirical models that are practical in the prediction of intricate input–output interrelations in a co-pyrolysis process. However, these models are only applicable to the process and fuels, which have been well-established [21]. Co-pyrolysis kinetic datasets for predicting of product formation using different reactor systems are still fairly unexplored [135].

Moreover, the commercialisation of co-pyrolysis reactors are still in the early stages since the current reactors still have the challenges of low heat efficiency, high capital and operating costs as well as complexities with biomass handling or storage [32]. Besides that, although there is plenty of extensive research on the single feedstock pyrolysis, the feasibility study of the co-pyrolysis process remains a niche area, whereby research on the techno-economic and life cycle assessment of the process is limited to single feedstock pyrolysis, such as the co-pyrolysis of biomass refineries and the DFM layers in these references [138,139]. To the best of our knowledge, these studies for the case of co-pyrolysis are scarce, existing studies focus on the microwave co-pyrolysis of food waste and LDPE [140], and the co-pyrolysis of lignite coal with single-use plastic waste [141]. Besides that, the existing research on the modelling of the co-pyrolysis of biomass with plastic waste reaction kinetics has been widely studied, but yet to have a consensus on the reaction pathway [32].

6 Conclusions

To conclude, the recent technologies and techniques of co-pyrolysis of biomass and plastic waste to produce bio-oil have been summarised in this review. The growing agriculture industry in ASEAN countries to suit the growing population of the region, has subsequently generated landfills of biomass. To exacerbate the situation, the global pandemic gives rise to the surge of the single-use plastic waste, DMFM wastes. Fortunately, the exploitation of these wastes in co-pyrolysis would positively improve the quantity and quality of the extracted bio-oil of the process, as the result of the synergistic interactions between lignocellulosic properties of biomass and the high hydrogen content of the plastic wastes. Furthermore, the advancement of the kinetic analysis of the pyrolysis process has improved as the catalytic co-pyrolysis process becomes more complex, and unable to be explained via simple iso-conversional models. Advanced conversional models such as Vyazovkin and DAEM methods have been introduced to study the pyrolysis reaction, followed by the heuristic model and predictive models, which prove to produce high-accuracy results. However, the studies of co-pyrolysis of biomass and DMFMs remain limited.

Experimental work on the binary feedstock's thermal decompositions and the bio-oil product's quantity and quality result from the co-pyrolysis has yet to be clear. The proposal of this methodology could serve as potential solution to help reduce or eliminate the pollution caused by the DMFM wastes, while producing value-added bio-oil products.

Acknowledgements The authors would like to acknowledge the technical support from Curtin University Malaysia, Swinburne University of Technology, Universiti Teknologi PETRONAS (UTP), and Manipal University Jaipur. Besides that, M.X.J. Wee would like to acknowledge the full funding support from the Curtin Malaysia Postgraduate Research Studentship (CMPRS) for the PhD study.

References

1. Adnan Z A, Saniayan V. Renewable energy outlook for ASEAN: a REmap analysis. Asean Centre for Energy & IRENA Report, 2016
2. Miranda M. Governments across Southeast Asia accelerate renewable energy investment to revive the pandemic-hit economies. Power Technology Report, 2020
3. Erdiwansyah M, Mamat R, Sani M S M, Khoerunnisa F, Kadarohman A. Target and demand for renewable energy across 10 ASEAN countries by 2040. *Electricity Journal*, 2019, 32(10): 106670
4. Sarraf M, Rismanchi B, Saidur R, Ping H W, Rahim N A. Renewable energy policies for sustainable development in Cambodia. *Renewable & Sustainable Energy Reviews*, 2013, 22: 223–229
5. Pillai I R, Banerjee R. Renewable energy in India: status and potential. *Energy*, 2009, 34(8): 970–980
6. Dani S, Wibawa A. Challenges and policy for biomass energy in Indonesia. *Journal of International Economic Law*, 2018, 15(5): 41–47
7. Mekhilef S, Barimani M, Safari A, Salam Z. Malaysia's renewable energy policies and programs with green aspects. *Renewable & Sustainable Energy Reviews*, 2014, 40: 497–504
8. Wattana S. Bioenergy development in Thailand: challenges and strategies. *Energy Procedia*, 2014, 52: 506–515
9. Truong K, Huong C, Dang Xuan T, Trung D, Khanh T. Current status and future plan of development of bioenergy crops as renewable energy sources in Vietnam. *Journal of Biology and Nature*, 2016, 5: 1–8
10. Myanmar Energy Master Plan. IEA, 2017
11. Energy policy and administration. Open Development Laos Website, 2018
12. Bangkok. East and Southeast Asia renewable energy statistics workshop. IRENA Website, 2016
13. Hirschmann R. Palm oil industry in Indonesia—statistics & facts. Statista Website, 2022
14. Malaysia palm oil production by year. Indexmundi, 2020
15. Loh S K. The potential of the Malaysian oil palm biomass as a renewable energy source. *Energy Conversion and Management*, 2017, 141: 285–298

16. Kumar N, Chhokar R S, Meena R P, Kharub A S, Gill S C, Tripathi S C, Gupta O P, Mangrauthia S K, Sundaram R M, Sawant C P, Gupta A, Naorem A, Kumar M, Singh G P. Challenges and opportunities in productivity and sustainability of rice cultivation system: a critical review in Indian perspective. *Cereal Research Communications*, 2022, 50: 573–601
17. Dai L, Wang Y, Liu Y, He C, Ruan R, Yu Z, Jiang L, Zeng Z, Wu Q. A review on selective production of value-added chemicals via catalytic pyrolysis of lignocellulosic biomass. *Science of the Total Environment*, 2020, 749: 142386
18. Kan T, Strezov V, Evans T, He J, Kumar R, Lu Q. Catalytic pyrolysis of lignocellulosic biomass: a review of variations in process factors and system structure. *Renewable & Sustainable Energy Reviews*, 2020, 134: 110305
19. Sivagurunathan P, Raj T, Mohanta C S, Semwal S, Satlewal A, Gupta R P, Puri S K, Ramakumar S S V, Kumar R. 2G waste lignin to fuel and high value-added chemicals: approaches, challenges and future outlook for sustainable development. *Chemosphere*, 2021, 268: 129326
20. Yang H, Yan R, Chen H, Lee D H, Liang D T, Zheng C. Pyrolysis of palm oil wastes for enhanced production of hydrogen rich gases. *Fuel Processing Technology*, 2006, 87(10): 935–942
21. Naqvi S R, Hameed Z, Tariq R, Taqvi S A, Ali I, Niazi M B K, Noor T, Hussain A, Iqbal N, Shahbaz M. Synergistic effect on co-pyrolysis of rice husk and sewage sludge by thermal behavior, kinetics, thermodynamic parameters and artificial neural network. *Waste Management*, 2019, 85: 131–140
22. Suriapparao D V, Vinu R, Shukla A, Haldar S. Effective deoxygenation for the production of liquid biofuels via microwave assisted co-pyrolysis of agro residues and waste plastics combined with catalytic upgradation. *Bioresource Technology*, 2020, 302: 122775
23. Geyer R, Jambeck J R, Law K L. Production, use, and fate of all plastics ever made. *Science Advances*, 2017, 3(7): e1700782
24. Jambeck J R, Geyer R, Wilcox C, Siegler T R, Perryman M, Andrady A, Narayan R, Law K L. Plastic waste inputs from land into the ocean. *Science*, 2015, 347(6223): 768–771
25. Abnisa F, Alaba P A. Recovery of liquid fuel from fossil-based solid wastes via pyrolysis technique: a review. *Journal of Environmental Chemical Engineering*, 2021, 9(6): 106593
26. Liang Y, Song Q, Wu N, Li J, Zhong Y, Zeng W. Repercussions of COVID-19 pandemic on solid waste generation and management strategies. *Frontiers of Environmental Science & Engineering*, 2021, 15(6): 115
27. Chaib F. Shortage of personal protective equipment endangering health workers worldwide. *World Health Organization Website*, 2020
28. Patrício Silva A L, Prata J C, Duarte A C, Barcelò D, Rocha-Santos T. An urgent call to think globally and act locally on landfill disposable plastics under and after Covid-19 pandemic: pollution prevention and technological (Bio) remediation solutions. *Chemical Engineering Journal*, 2021, 426: 131201
29. Patrício Silva A L, Prata J C, Mouneyrac C, Barcelò D, Duarte A C, Rocha-Santos T. Risks of Covid-19 face masks to wildlife: present and future research needs. *Science of the Total Environment*, 2021, 792: 148505
30. Mishra R K, Mohanty K. Kinetic analysis and pyrolysis behaviour of waste biomass towards its bioenergy potential. *Bioresource Technology*, 2020, 311: 123480
31. Akhtar J, Saidina Amin N. A review on operating parameters for optimum liquid oil yield in biomass pyrolysis. *Renewable & Sustainable Energy Reviews*, 2012, 16(7): 5101–5109
32. Hu X, Gholizadeh M. Biomass pyrolysis: a review of the process development and challenges from initial researches up to the commercialisation stage. *Journal of Energy Chemistry*, 2019, 39: 109–143
33. Miandad R, Barakat M A, Rehan M, Aburizaiza A S, Ismail I M I, Nizami A S. Plastic waste to liquid oil through catalytic pyrolysis using natural and synthetic zeolite catalysts. *Waste Management*, 2017, 69: 66–78
34. Navarro M V, López J M, Veses A, Callén M S, García T. Kinetic study for the co-pyrolysis of lignocellulosic biomass and plastics using the distributed activation energy model. *Energy*, 2018, 165: 731–742
35. Salvilla J N V, Ofrasio B I G, Rollon A P, Manegdeg F G, Abarca R R M, de Luna M D G. Synergistic co-pyrolysis of polyolefin plastics with wood and agricultural wastes for biofuel production. *Applied Energy*, 2020, 279: 115668
36. Wang L, Chai M, Liu R, Cai J. Synergetic effects during co-pyrolysis of biomass and waste tire: a study on product distribution and reaction kinetics. *Bioresource Technology*, 2018, 268: 363–370
37. Ansari K B, Hassan S Z, Bhoi R, Ahmad E. Co-pyrolysis of biomass and plastic wastes: a review on reactants synergy, catalyst impact, process parameter, hydrocarbon fuel potential, COVID-19. *Journal of Environmental Chemical Engineering*, 2021, 9(6): 106436
38. Roy P, Dias G. Prospects for pyrolysis technologies in the bioenergy sector: a review. *Renewable & Sustainable Energy Reviews*, 2017, 77: 59–69
39. Bridgwater A V. Review of fast pyrolysis of biomass and product upgrading. *Biomass and Bioenergy*, 2012, 38: 68–94
40. Fahmy T Y A, Fahmy Y, Mobarak F, El-Sakhawy M, Abou-Zeid R E. Biomass pyrolysis: past, present, and future. *Environment, Development and Sustainability*, 2020, 22(1): 17–32
41. Papari S, Hawboldt K. A review on the pyrolysis of woody biomass to bio-oil: focus on kinetic models. *Renewable & Sustainable Energy Reviews*, 2015, 52: 1580–1595
42. Perkins G, Bhaskar T, Konarova M. Process development status of fast pyrolysis technologies for the manufacture of renewable transport fuels from biomass. *Renewable & Sustainable Energy Reviews*, 2018, 90: 292–315
43. Foong S Y, Liew R K, Yang Y, Cheng Y W, Yek P N Y, Wan Mahari W A, Lee X Y, Han C S, Vo D V N, Van Le Q, Aghbashlo M, Tabatabaei M, Sonne C, Peng W, Lam S S. Valorization of biomass waste to engineered activated biochar by microwave pyrolysis: progress, challenges, and future directions. *Chemical Engineering Journal*, 2020, 389: 124401
44. Tsai F M, Bui T D, Tseng M L, Lim M K, Hu J. Municipal solid waste management in a circular economy: a data-driven

- bibliometric analysis. *Journal of Cleaner Production*, 2020, 275: 124132
45. Andreo-Martínez P, Ortiz-Martínez V M, García-Martínez N, de los Ríos A P, Hernández-Fernández F J, Quesada-Medina J. Production of biodiesel under supercritical conditions: state of the art and bibliometric analysis. *Applied Energy*, 2020, 264: 114753
 46. Losse M, Geissdoerfer M. Mapping socially responsible investing: a bibliometric and citation network analysis. *Journal of Cleaner Production*, 2021, 296: 126376
 47. Murillo J, Villegas L M, Ulloa-Murillo L M, Rodríguez A R. Recent trends on omics and bioinformatics approaches to study SARS-CoV-2: a bibliometric analysis and mini-review. *Computers in Biology and Medicine*, 2021, 128: 104162
 48. Bensidhom G, Ben Hassen Trabelsi A, mahmood M A, Ceylan S. mahmood M A, Ceylan S. Insights into pyrolytic feedstock potential of date palm industry wastes: kinetic study and product characterization. *Fuel*, 2021, 285: 119096
 49. Domínguez A, Menéndez J A, Inguanzo M, Pis J J. Investigations into the characteristics of oils produced from microwave pyrolysis of sewage sludge. *Fuel Processing Technology*, 2005, 86(9): 1007–1020
 50. Ghodke P, Mandapati R N. Investigation of particle level kinetic modeling for babul wood pyrolysis. *Fuel*, 2019, 236: 1008–1017
 51. Naqvi S R, Tariq R, Hameed Z, Ali I, Taqvi S A, Naqvi M, Niazi M B K, Noor T, Farooq W. Pyrolysis of high-ash sewage sludge: thermo-kinetic study using TGA and artificial neural networks. *Fuel*, 2018, 233: 529–538
 52. Polin J P, Carr H D, Whitmer L E, Smith R G, Brown R C. Conventional and autothermal pyrolysis of corn stover: overcoming the processing challenges of high-ash agricultural residues. *Journal of Analytical and Applied Pyrolysis*, 2019, 143: 104679
 53. Singh R K, Pandey D, Patil T, Sawarkar A N. Pyrolysis of banana leaves biomass: physico-chemical characterization, thermal decomposition behavior, kinetic and thermodynamic analyses. *Bioresource Technology*, 2020, 310: 123464
 54. Tabal A, Barakat A, Aboukass A, El harfi K. Pyrolysis of ficus nitida wood: determination of kinetic and thermodynamic parameters. *Fuel*, 2021, 283: 119253
 55. Ding Z, Chen H, Liu J, Cai H, Evrendilek F, Buyukada M. Pyrolysis dynamics of two medical plastic wastes: drivers, behaviors, evolved gases, reaction mechanisms, and pathways. *Journal of Hazardous Materials*, 2021, 402: 123472
 56. Honus S, Kumagai S, Fedorko G, Molnár V, Yoshioka T. Pyrolysis gases produced from individual and mixed PE, PP, PS, PVC, and PET—Part I: Production and physical properties. *Fuel*, 2018, 221: 346–360
 57. Jeon W, Kim Y D, Lee K H. A comparative study on pyrolysis of bundle and fluffy shapes of waste packaging plastics. *Fuel*, 2021, 283: 119260
 58. Jung S, Lee S, Dou X, Kwon E E. Valorization of disposable COVID-19 mask through the thermo-chemical process. *Chemical Engineering Journal*, 2021, 405: 126658
 59. Parku G K, Collard F X, Görgens J F. Pyrolysis of waste polypropylene plastics for energy recovery: influence of heating rate and vacuum conditions on composition of fuel product. *Fuel Processing Technology*, 2020, 209: 106522
 60. Xu F, Wang B, Yang D, Hao J, Qiao Y, Tian Y. Thermal degradation of typical plastics under high heating rate conditions by TG-FTIR: pyrolysis behaviors and kinetic analysis. *Energy Conversion and Management*, 2018, 171: 1106–1115
 61. Park Y K, Ha J M, Oh S, Lee J. Bio-oil upgrading through hydrogen transfer reactions in supercritical solvents. *Chemical Engineering Journal*, 2021, 404: 126527
 62. Kwon D, Jung S, Lin K Y A, Tsang Y F, Park Y K, Kwon E E. Synergistic effects of CO₂ on complete thermal degradation of plastic waste mixture through a catalytic pyrolysis platform: a case study of disposable diaper. *Journal of Hazardous Materials*, 2021, 419: 126537
 63. Wan Mahari W A, Awang S, Zahariman N A Z, Peng W, Man M, Park Y K, Lee J, Sonne C, Lam S S. Microwave co-pyrolysis for simultaneous disposal of environmentally hazardous hospital plastic waste, lignocellulosic, and triglyceride biowaste. *Journal of Hazardous Materials*, 2022, 423: 127096
 64. Park Y K, Lee B, Lee H W, Watanabe A, Jae J, Tsang Y F, Kim Y M. Co-feeding effect of waste plastic films on the catalytic pyrolysis of *Quercus variabilis* over microporous HZSM-5 and HY catalysts. *Chemical Engineering Journal*, 2019, 378: 122151
 65. Hu Y, Yu W, Wibowo H, Xia Y, Lu Y, Yan M. Effect of catalysts on distribution of polycyclic-aromatic hydrocarbon (PAHs) in bio-oils from the pyrolysis of dewatered sewage sludge at high and low temperatures. *Science of the Total Environment*, 2019, 667: 263–270
 66. Zhang X, Lei H, Zhu L, Zhu X, Qian M, Yadavalli G, Wu J, Chen S. Thermal behavior and kinetic study for catalytic co-pyrolysis of biomass with plastics. *Bioresource Technology*, 2016, 220: 233–238
 67. Lin X, Zhang Z, Wang Q, Sun J. Interactions between biomass-derived components and polypropylene during wood-plastic composite pyrolysis. *Biomass Conversion and Biorefinery*, 2020, 12(8): 3345–3357
 68. Önal E, Uzun B B, Pütün A E. Bio-oil production via co-pyrolysis of almond shell as biomass and high density polyethylene. *Energy Conversion and Management*, 2014, 78: 704–710
 69. Sun J, Luo J, Lin J, Ma R, Sun S, Fang L, Li H. Study of co-pyrolysis endpoint and product conversion of plastic and biomass using microwave thermogravimetric technology. *Energy*, 2022, 247: 123547
 70. Yang J, Rizkiana J, Widayatno W B, Karnjanakom S, Kaewpanha M, Hao X, Abudula A, Guan G. Fast co-pyrolysis of low density polyethylene and biomass residue for oil production. *Energy Conversion and Management*, 2016, 120: 422–429
 71. Ojha D, Shukla S, Raghunath S, Sachin R S, Vinu R. Understanding the interactions between cellulose and polypropylene during fast co-pyrolysis via experiments and DFT calculations. *Chemical Engineering Transactions*, 2016, 50: 67–72
 72. Uzoejinwa B B, He X, Wang S, El-Fatah Abomohra A, Hu Y, Wang Q. Co-pyrolysis of biomass and waste plastics as a thermochemical conversion technology for high-grade biofuel

- production: recent progress and future directions elsewhere worldwide. *Energy Conversion and Management*, 2018, 163: 468–492
73. Lin X, Kong L, Ren X, Zhang D, Cai H, Lei H. Catalytic co-pyrolysis of torrefied poplar wood and high-density polyethylene over hierarchical HZSM-5 for mono-aromatics production. *Renewable Energy*, 2021, 164: 87–95
 74. Pogaku R, Hardinge B S, Vuthaluru H, Amir H A. Production of bio-oil from oil palm empty fruit bunch by catalytic fast pyrolysis: a review. *Biofuels*, 2016, 7(6): 647–660
 75. Dai L, Zhou N, Li H, Deng W, Cheng Y, Wang Y, Liu Y, Cobb K, Lei H, Chen P, Ruan R. Recent advances in improving lignocellulosic biomass-based bio-oil production. *Journal of Analytical and Applied Pyrolysis*, 2020, 149: 104845
 76. Yang H, Yan R, Chin T, Liang D T, Chen H, Zheng C. Thermogravimetric analysis-fourier transform infrared analysis of palm oil waste pyrolysis. *Energy & Fuels*, 2004, 18(6): 1814–1821
 77. Ly H V, Park J W, Kim S S, Hwang H T, Kim J, Woo H C. Catalytic pyrolysis of bamboo in a bubbling fluidized-bed reactor with two different catalysts: HZSM-5 and red mud for upgrading bio-oil. *Renewable Energy*, 2020, 149: 1434–1445
 78. Ahmed M H M, Batalha N, Mahmudul H M D, Perkins G, Konarova M. A review on advanced catalytic co-pyrolysis of biomass and hydrogen-rich feedstock: insights into synergistic effect, catalyst development and reaction mechanism. *Bioresource Technology*, 2020, 310: 123457
 79. Jin X, Lee J H, Choi J W. Catalytic co-pyrolysis of woody biomass with waste plastics: effects of HZSM-5 and pyrolysis temperature on producing high-value pyrolytic products and reducing wax formation. *Energy*, 2022, 239: 121739
 80. Ratnasari D K, Nahil M A, Williams P T. Catalytic pyrolysis of waste plastics using staged catalysis for production of gasoline range hydrocarbon oils. *Journal of Analytical and Applied Pyrolysis*, 2017, 124: 631–637
 81. Li Z, Zhong Z, Zhang B, Wang W, Seufitelli G V S, Resende F L P. Catalytic fast co-pyrolysis of waste greenhouse plastic films and rice husk using hierarchical micro-mesoporous composite molecular sieve. *Waste Management*, 2020, 102: 561–568
 82. Zhao Y, Wang Y, Duan D, Ruan R, Fan L, Zhou Y, Dai L, Lv J, Liu Y. Fast microwave-assisted ex-catalytic co-pyrolysis of bamboo and polypropylene for bio-oil production. *Bioresource Technology*, 2018, 249: 69–75
 83. Cao Z, Niu J, Gu Y, Zhang R, Liu Y, Luo L. Catalytic pyrolysis of rice straw: screening of various metal salts, metal basic oxide, acidic metal oxide and zeolite catalyst on products yield and characterization. *Journal of Cleaner Production*, 2020, 269: 122079
 84. Chen X, Chen Y, Yang H, Chen W, Wang X, Chen H. Fast pyrolysis of cotton stalk biomass using calcium oxide. *Bioresource Technology*, 2017, 233: 15–20
 85. Chong Y Y, Thangalazhy-Gopakumar S, Ng H K, Lee L Y, Gan S. Effect of oxide catalysts on the properties of bio-oil from in-situ catalytic pyrolysis of palm empty fruit bunch fiber. *Journal of Environmental Management*, 2019, 247: 38–45
 86. Kim S, Park C, Lee J. Reduction of polycyclic compounds and biphenyls generated by pyrolysis of industrial plastic waste by using supported metal catalysts: a case study of polyethylene terephthalate treatment. *Journal of Hazardous Materials*, 2020, 392: 122464
 87. Lin X, Zhang Z, Zhang Z, Sun J, Wang Q, Pittman C U. Catalytic fast pyrolysis of a wood-plastic composite with metal oxides as catalysts. *Waste Management*, 2018, 79: 38–47
 88. Teng S Y, Loy A C M, Leong W D, How B S, Chin B L F, Máša V. Catalytic thermal degradation of *Chlorella vulgaris*: evolving deep neural networks for optimization. *Bioresource Technology*, 2019, 292: 121971
 89. Thangalazhy-Gopakumar S, Wei Lee C, Gan S, Kiat Ng H, Yee Lee L. Comparison of bio-oil properties from non-catalytic and in-situ catalytic fast pyrolysis of palm empty fruit bunch. *Materials Today: Proceedings*, 2018, 5(11): 23456–23465
 90. Chow L W, Tio S A, Teoh J Y, Lim C G, Chong Y Y, Thangalazhy-Gopakumar S. Sludge as a relinquishing catalyst in co-pyrolysis with palm empty fruit bunch fiber. *Journal of Analytical and Applied Pyrolysis*, 2018, 132: 56–64
 91. Jeong J Y, Lee U D, Chang W S, Jeong S H. Production of bio-oil rich in acetic acid and phenol from fast pyrolysis of palm residues using a fluidized bed reactor: influence of activated carbons. *Bioresource Technology*, 2016, 219: 357–364
 92. Loy A C M, Gan D K W, Yusup S, Chin B L F, Lam M K, Shahbaz M, Unrean P, Acda M N, Rianawati E. Thermogravimetric kinetic modelling of *in-situ* catalytic pyrolytic conversion of rice husk to bioenergy using rice hull ash catalyst. *Bioresource Technology*, 2018, 261: 213–222
 93. Loy A C M, Yusup S, Lam M K, Chin B L F, Shahbaz M, Yamamoto A, Acda M N. The effect of industrial waste coal bottom ash as catalyst in catalytic pyrolysis of rice husk for syngas production. *Energy Conversion and Management*, 2018, 165: 541–554
 94. Santosa D M, Zhu C, Agblevor F A, Maddi B, Roberts B Q, Kutnyakov I V, Lee S J, Wang H. *In situ* catalytic fast pyrolysis using red mud catalyst: impact of catalytic fast pyrolysis temperature and biomass feedstocks. *ACS Sustainable Chemistry & Engineering*, 2020, 8(13): 5156–5164
 95. Dong Q, Li H, Niu M, Luo C, Zhang J, Qi B, Li X, Zhong W. Microwave pyrolysis of moso bamboo for syngas production and bio-oil upgrading over bamboo-based biochar catalyst. *Bioresource Technology*, 2018, 266: 284–290
 96. Chen W, Fang Y, Li K, Chen Z, Xia M, Gong M, Chen Y, Yang H, Tu X, Chen H. Bamboo wastes catalytic pyrolysis with N-doped biochar catalyst for phenols products. *Applied Energy*, 2020, 260: 114242
 97. An Y, Tahmasebi A, Zhao X, Matamba T, Yu J. Catalytic reforming of palm kernel shell microwave pyrolysis vapors over iron-loaded activated carbon: enhanced production of phenol and hydrogen. *Bioresource Technology*, 2020, 306: 123111
 98. Gaurh P, Pramanik H. Production of benzene/toluene/ethyl benzene/xylene (BTEX) via multiphase catalytic pyrolysis of hazardous waste polyethylene using low cost fly ash synthesized natural catalyst. *Waste Management*, 2018, 77: 114–130
 99. Luo W, Fan Z, Wan J, Hu Q, Dong H, Zhang X, Zhou Z. Study on the reusability of kaolin as catalysts for catalytic pyrolysis of

- low-density polyethylene. *Fuel*, 2021, 302: 121164
100. Nalluri P, Prem Kumar P, Ch Sastry M R. Experimental study on catalytic pyrolysis of plastic waste using low cost catalyst. *Materials Today: Proceedings*, 2021, 45: 7216–7221
 101. Xu D, Xiong Y, Zhang S, Su Y. The synergistic mechanism between coke depositions and gas for H₂ production from co-pyrolysis of biomass and plastic wastes via char supported catalyst. *Waste Management*, 2021, 121: 23–32
 102. Zhang D, Lin X, Zhang Q, Ren X, Yu W, Cai H. Catalytic pyrolysis of wood-plastic composite waste over activated carbon catalyst for aromatics production: effect of preparation process of activated carbon. *Energy*, 2020, 212: 118983
 103. Chang G, Shi P, Guo Y, Wang L, Wang C, Guo Q. Enhanced pyrolysis of palm kernel shell wastes to bio-based chemicals and syngas using red mud as an additive. *Journal of Cleaner Production*, 2020, 272: 122847
 104. Singh R K, Patil T, Sawarkar A N. Pyrolysis of garlic husk biomass: physico-chemical characterization, thermodynamic and kinetic analyses. *Bioresource Technology Reports*, 2020, 12: 100558
 105. Sbirrazzuoli N. Determination of pre-exponential factors and of the mathematical functions $f(\alpha)$ or $G(\alpha)$ that describe the reaction mechanism in a model-free way. *Thermochimica Acta*, 2013, 564: 59–69
 106. Sajjad Ahmad M, Liu H, Alhumade H, Hussain Tahir M, Çakman G, Yıldız A, Ceylan S, Elkamel A, Shen B. A modified DAEM: to study the bioenergy potential of invasive *Staghorn sumac* through pyrolysis, ANN, TGA, kinetic modeling, FTIR and GC-MS analysis. *Energy Conversion and Management*, 2020, 221: 113173
 107. Hameed S, Sharma A, Pareek V, Wu H, Yu Y. A review on biomass pyrolysis models: kinetic, network and mechanistic models. *Biomass and Bioenergy*, 2019, 123: 104–122
 108. Cano-Pleite E, Rubio-Rubio M, Garcia-Hernando N, Soria-Verdugo A. Microalgae pyrolysis under isothermal and non-isothermal conditions. *Algal Research*, 2020, 51: 102031
 109. Ding Y, Zhang W, Yu L, Lu K. The accuracy and efficiency of GA and PSO optimization schemes on estimating reaction kinetic parameters of biomass pyrolysis. *Energy*, 2019, 176: 582–588
 110. Aghbashlo M, Almasi F, Jafari A, Nadian M H, Soltanian S, Lam S S, Tabatabaei M. Describing biomass pyrolysis kinetics using a generic hybrid intelligent model: a critical stage in sustainable waste-oriented biorefineries. *Renewable Energy*, 2021, 170: 81–91
 111. Ferreira A I, Rabaçal M, Costa M. A combined genetic algorithm and least squares fitting procedure for the estimation of the kinetic parameters of the pyrolysis of agricultural residues. *Energy Conversion and Management*, 2016, 125: 290–300
 112. Ding Y, Zhang Y, Zhang J, Zhou R, Ren Z, Guo H. Kinetic parameters estimation of pinus sylvestris pyrolysis by Kissinger–Kai method coupled with particle swarm optimization and global sensitivity analysis. *Bioresource Technology*, 2019, 293: 122079
 113. Buyukada M. Co-combustion of peanut hull and coal blends: artificial neural networks modeling, particle swarm optimization and Monte Carlo simulation. *Bioresource Technology*, 2016, 216: 280–286
 114. Xu L, Jiang Y, Wang L. Thermal decomposition of rape straw: pyrolysis modeling and kinetic study via particle swarm optimization. *Energy Conversion and Management*, 2017, 146: 124–133
 115. Majid M, Chin B L F, Jawad Z A, Chai Y H, Lam M K, Yusup S, Cheah K W. Particle swarm optimization and global sensitivity analysis for catalytic co-pyrolysis of *Chlorella vulgaris* and plastic waste mixtures. *Bioresource Technology*, 2021, 329: 124874
 116. Duan Q Y, Gupta V K, Sorooshian S. Shuffled complex evolution approach for effective and efficient global minimization. *Journal of Optimization Theory and Applications*, 1993, 76(3): 501–521
 117. Ding Y, Zhang J, He Q, Huang B, Mao S. The application and validity of various reaction kinetic models on woody biomass pyrolysis. *Energy*, 2019, 179: 784–791
 118. Ding Y, Wang C, Chaos M, Chen R, Lu S. Estimation of beech pyrolysis kinetic parameters by Shuffled Complex Evolution. *Bioresource Technology*, 2016, 200: 658–665
 119. Liu H, Chen B, Wang C. Pyrolysis kinetics study of biomass waste using Shuffled Complex Evolution algorithm. *Fuel Processing Technology*, 2020, 208: 106509
 120. Hasalová L, Ira J, Jahoda M. Practical observations on the use of Shuffled Complex Evolution (SCE) algorithm for kinetic parameters estimation in pyrolysis modeling. *Fire Safety Journal*, 2016, 80: 71–82
 121. Al-Yaari M, Ibrahim D. Application of artificial neural networks to predict the catalytic pyrolysis of HDPE using non-isothermal TGA data. *Polymers*, 2020, 12(8): 1813
 122. Bi H, Wang C, Jiang X, Jiang C, Bao L, Lin Q. Thermodynamics, kinetics, gas emissions and artificial neural network modeling of co-pyrolysis of sewage sludge and peanut shell. *Fuel*, 2021, 284: 118988
 123. Balsora H K, S K, Dua V, Joshi J B, Kataria G, Sharma A, Chakinala A G. Machine learning approach for the prediction of biomass pyrolysis kinetics from preliminary analysis. *Journal of Environmental Chemical Engineering*, 2022, 10(3): 108025
 124. Bong J T, Loy A C M, Chin B L F, Lam M K, Tang D K H, Lim H Y, Chai Y H, Yusup S. Artificial neural network approach for co-pyrolysis of *Chlorella vulgaris* and peanut shell binary mixtures using microalgae ash catalyst. *Energy*, 2020, 207: 118289
 125. Alaba P A, Popoola S I, Abnisa F, Lee C S, Ohunakin O S, Adetiba E, Akanle M B, Abdul Patah M F, Atayero A A A, Wan Daud W M A. Thermal decomposition of rice husk: a comprehensive artificial intelligence predictive model. *Journal of Thermal Analysis and Calorimetry*, 2020, 140(4): 1811–1823
 126. Zhu X, Li Y, Wang X. Machine learning prediction of biochar yield and carbon contents in biochar based on biomass characteristics and pyrolysis conditions. *Bioresource Technology*, 2019, 288: 121527
 127. Li H, Xu Q, Xiao K, Yang J, Liang S, Hu J, Hou H, Liu B. Predicting the higher heating value of syngas pyrolyzed from

- sewage sludge using an artificial neural network. *Environmental Science and Pollution Research International*, 2020, 27(1): 785–797
128. Whiteman J K, Gueguim Kana E B. Comparative assessment of the artificial neural network and response surface modelling efficiencies for biohydrogen production on sugar cane molasses. *BioEnergy Research*, 2014, 7(1): 295–305
 129. Zhang Y, Ahmad M S, Shen B, Yuan P, Shah I A, Zhu Q, Ibrahim M, Bokhari A, Klemeš J J, Elkamel A. Co-pyrolysis of lychee and plastic waste as a source of bioenergy through kinetic study and thermodynamic analysis. *Energy*, 2022, 256: 124678
 130. Gan D K W, Loy A C M, Chin B L F, Yusup S, Unrean P, Rianawati E, Acda M N. Kinetics and thermodynamic analysis in one-pot pyrolysis of rice hull using renewable calcium oxide based catalysts. *Bioresource Technology*, 2018, 265: 180–190
 131. Fong M J B, Loy A C M, Chin B L F, Lam M K, Yusup S, Jawad Z A. Catalytic pyrolysis of *Chlorella vulgaris*: kinetic and thermodynamic analysis. *Bioresource Technology*, 2019, 289: 121689
 132. Kumar Mishra R, Mohanty K. Co-pyrolysis of waste biomass and waste plastics (polystyrene and waste nitrile gloves) into renewable fuel and value-added chemicals. *Carbon Resources Conversion*, 2020, 3: 145–155
 133. Abnisa F, Wan Daud W M A. A review on co-pyrolysis of biomass: an optional technique to obtain a high-grade pyrolysis oil. *Energy Conversion and Management*, 2014, 87: 71–85
 134. Scheirs J. *Feedstock recycling and pyrolysis of waste plastics*. Manhattan: John Wiley & Sons Inc., 2006: 381–433
 135. Gouws S M, Carrier M, Bunt J R, Neomagus H W J P. Co-pyrolysis of coal and raw/torrefied biomass: a review on chemistry, kinetics and implementation. *Renewable & Sustainable Energy Reviews*, 2021, 135: 110189
 136. Lede J. Biomass fast pyrolysis reactors: a review of a few scientific challenges and of related recommended research topics. *Oil & Gas Science and Technology*, 2013, 68(5): 801–814
 137. Venderbosch R, Prins W. Fast pyrolysis technology development. *Biofuels, Bioproducts & Biorefining*, 2010, 4(2): 178–208
 138. Yousef S, Eimontas J, Stasiulaitiene I, Zakarauskas K, Striūgas N. Pyrolysis of all layers of surgical mask waste as a mixture and its life-cycle assessment. *Sustainable Production and Consumption*, 2022, 32: 519–531
 139. Brassard P, Godbout S, Hamelin L. Framework for consequential life cycle assessment of pyrolysis biorefineries: a case study for the conversion of primary forestry residues. *Renewable & Sustainable Energy Reviews*, 2021, 138: 110549
 140. Neha S, Prasanna Kumar Ramesh K, Remya N. Techno-economic analysis and life cycle assessment of microwave co-pyrolysis of food waste and low-density polyethylene. *Sustainable Energy Technologies and Assessments*, 2022, 52: 102356
 141. Joshi V V, Swaminathan G, Prabhakaran S P S. Life cycle assessment of the co-combustion system of single-use plastic waste and lignite coal to promote circular economy. *Journal of Cleaner Production*, 2021, 329: 129579

RESEARCH ARTICLE

Efficacy evaluation of newly isolated zinc solubilizing bacteria for their potential effect on maize (*Zea mays* L.) under zinc deficient soil conditions

Aradhana Sukhwai¹ | Devendra Jain^{1,2}  | Vimal Sharma¹ | S. N. Ojha³ | Gajanand Jat⁴ | Sudhir K. Mohanty⁵  | Abhijeet Singh⁶ | Santosh Ranjan Mohanty⁷

¹Department of Molecular Biology and Biotechnology, Rajasthan College of Agriculture, Maharana Pratap University of Agriculture and Technology, Udaipur, India

²Southern Insect Management Research Unit, USDA-ARS, Stoneville, MS, USA

³Department of Extension Education, Rajasthan College of Agriculture, Maharana Pratap University of Agriculture and Technology, Udaipur, India

⁴Department of Soil Science and Agricultural Chemistry, Rajasthan College of Agriculture, Maharana Pratap University of Agriculture and Technology, Udaipur, India

⁵Department of Environmental Science, V. B. S. Purvanchal University, Jaunpur, India

⁶Department of Biosciences, Manipal University Jaipur, Jaipur, India

⁷All India Network Project on Soil Biodiversity-Biofertilizers, ICAR-Indian Institute of Soil Science, Bhopal, India

Correspondence

Devendra Jain, Department of Molecular Biology and Biotechnology, Rajasthan College of Agriculture, Maharana Pratap University of Agriculture and Technology, Udaipur-313001, India.

Email: devendrajain@mpuat.ac.in and devroshan@gmail.com

Abstract

Zinc solubilizing bacteria (ZSB) induces the conversion of fixed and unavailable soil zinc to readily available zinc contributes plant zinc nutrition and fortification. The present research intended to determine the screening of plant growth-promoting (PGP) traits of potent ZSB, biochemical and molecular characterization of ZSB, and assessment of potent ZSB for crop yield at the field level. Therefore, in the present study, molecular and functional characterization of native ZSB isolates was done to examine their response to plant growth performance and yield, mobilization of zinc, and acquisition by maize plants. Zinc solubilizing bacterial isolates namely, ZSB1, and ZSB 17 were solubilized insoluble zinc namely, ZnCO₃, ZnO, Zn₃(PO₄)₂ and significantly induced growth performance of maize crop at field conditions. A biochemical study revealed that both ZSB isolates were positive for catalase and urease production. Isolates ZSB1 & ZSB17 showed different PGP attributes like production of Indole-3-acetic acid (IAA), siderophore, NH₃, and HCN. Both isolates were solubilized phosphate, potassium, and silica and showed 1-aminocyclopropane-1-carboxylate (ACC)-deaminase activity. 16S rRNA amplification and sequence study of ZSB1 and ZSB17 revealed that both the isolates were *Cupriavidus* sp. and *Pantoea agglomerans*, respectively, and novel. The results elucidated from pot studies demonstrated that both ZSB1 & ZSB17 were the more suitable isolates than other ZSB isolates, and these isolates were further tested for field studies. *Cupriavidus* sp. and *Pantoea agglomerans* strains increased Zn-translocation toward grains and yield of Maize (cv: P3441) by 19.01% and 17.64%, respectively. We conclude that the novel indigenous ZSB strains substantially heightened zinc mobilization, the yield of maize crop, restore soil health, and can be suitable for biofortification and biofertilizers technology.

KEYWORDS

16S rDNA sequencing, field experiment, PGP attributes, zinc solubilizing bacteria, zinc translocation index

1 | INTRODUCTION

The availability of plant necessary elements has a direct impact on soil fertility and agricultural crop productivity. The availability of plant

essential elements may change as a result of the buildup of higher concentrations of metals and metalloids in contaminated soil (Alengebawey et al., 2021). A mediated metabolic pathway requires minimal metalloids and heavy metals at appropriate concentrations

for root microbiota, soil fertility, and plant growth (Barra & Terenzi, 2021; Upadhyay et al., 2022). Few metalloids and heavy metals, on the other hand, are even at low concentrations hazardous to plant development and soil fertility (Chibuiké & Obiora, 2014). Man-made activities such as mining, developing industrial zones, chemicals and pesticides, waste disposal, and so forth are increasing the prevalence of these contaminants (Alengebawey et al., 2021; Upadhyay & Edrisi, 2021).

Essential elements such as Zn (zinc), Cu (copper), Fe (iron), Mg (magnesium), and so forth are necessary to plant growth at an optimum concentration (White & Brown, 2010). Plant growth and soil fertility are also reduced by (i) a higher concentration of essential elements, and (ii) incompatible form of essential elements in the soil (Baldantoni et al., 2019), hence optimum concentration of essential micronutrients is required for soil productivity. Microbes can mobilize or solubilize trapped essential elements in contaminated soil by releasing extra-cellular enzymes; these enzymes may be facilitated by redox reactions (Garcia-Arellano et al., 2004).

Plant growth promoting rhizobacteria (PGPR) plays remarkable and promising role in phyto-stimulation by releasing plant hormones like Indole-3-acetic acid (IAA), Gibberellins and so forth (Upadhyay & Chauhan, 2022), and other solubilized trapped essential elements of soil and increasing essential element uptake in plants (Singh et al., 2022; Upadhyay et al., 2009). These procedures are known as PGPR direct mechanisms (Mahmud et al., 2021; Singh et al., 2022). The production of exo-polysaccharides (Upadhyay et al., 2011), antibiotics, antioxidants (Upadhyay & Singh, 2015), biocontrol action to reduce phytopathogens, and so forth are indirect mechanisms of PGPRs (Mahmud et al., 2021). Mobilization and solubilization of trapped essential elements by rhizobacteria can be effective sustainable approaches to improving plant growth performance and enhancing soil fertility in zinc-contaminated soil (Bhojiya et al., 2022).

The ZSB (zinc solubilizing bacteria) are renowned for their effectiveness in the solubilization of zinc when combined with plant root exudates, which function as a chemo-attractant and improve the availability of native rhizobacteria promotes plant growth (Upadhyay et al., 2022). ZSB thus facilitate native zinc for plant assimilation, leading to plant growth promotion (Shakeel et al., 2015). Previously, studies on the utilization of ZSB to enhance the Zn acquisition in crops such as wheat, mung-bean etc. and correcting Zn deficiency in soil by increasing over 50% available Zn levels in the harvest soil samples has been reported (Dinesh et al., 2018; Mumtaz et al., 2017; Sirohi et al., 2015). In more than 300 enzymes, zinc and zinc ion plays a vital biological role by maintaining protein structure & stability and is found in many metalloenzymes as essential cofactor (Sarathambal et al., 2010).

Zinc deficiency leads to biomass and fertility reduction directly reduces crop plant yield, chlorosis in leaves which negatively impact photosynthesis, increased iron accumulation causing cellular toxicity, and increased oxidative stress with reduced Cu/Zn SOD activities (Thiébaud & Hanikenne, 2022). Zinc deficiency in maize is very likely to result in stunting, acute chlorosis, reduced pollen viability, and male sterility (Brown, 2008). Due to the selective cultivation of high-yield maize varieties with synthetic fertilizers to boost cropping and quality

over the past few decades, zinc deficiency has ravaged into the soil-crop environment, making maize the most susceptible cereal crop to Zn deficiency (Fageria et al., 2002).

Fifty percent of global and Indian soils are zinc deficient which is projected to increase to an estimated 63% by 2025 leading to reductions not only in crop yield but also in food quality (Hussain et al., 2022; Shukla et al., 2021). In India, 51.2% soils from the states Andhra Pradesh, Assam, Bihar, Chhattisgarh, Goa, Gujarat, Karnataka, Madhya Pradesh, Maharashtra, Odisha, Rajasthan, Telangana, and Uttar Pradesh were deficient in available Zn (Shukla et al., 2021). Zn solubilization and mobilization by soil microbes has sustainable perspectives in comparison to chemical fertilizers. Therefore, the intent of current investigation was focused on (i) isolation and screening of potent ZSB and its plant growth-promoting (PGP) attributes, (ii) 16SrRNA characterization of potent screened bacterial isolates, (iii) Influence of potent isolates on plant growth and soil health in zinc infested soil at field level.

2 | MATERIALS AND METHODS

2.1 | Physico-chemical properties of rhizospheric soil samples

The rhizospheric soils of chickpea plant were obtained from the Durgapur (23.85° N; 73.68° E) and Pratapgarh (23.56° N; 73.74° E) districts of Rajasthan (Figure 1), both the sites were adjacent to ZAWAR mines (Latit-24.3540034; Long-73.733064). Physico-chemical properties such as EC (Electrical conductivity), OC (Organic Carbon), Av. N (available nitrogen), Av. P (available phosphorus), Av. K (available potassium), and diethylenetriaminepentaacetic acid (DTPA) extracted zinc were analyzed as per standard procedures (Jain, Kour, et al., 2020; Vance et al., 1987).

2.2 | Isolation of ZSB and screening of its zinc solubilizing potential

The ZSB isolation was done with serial dilution plate method on specific media namely, Mineral salt media (Saravanan et al., 2007) and Bunt & Rovira medium (Bunt & Rovira, 1955) supplemented with different insoluble zinc source such as ZnO, ZnCO₃, and Zn₃(PO₄)₂ to produce a clear halo zone after 48 h incubation at 28°C ± 2°C were purified and considered as ZSB. To evaluate zinc solubilization efficiency of the isolates, the halo zone forming bacterial isolates were put on Bunt and Rovira agar and MSM media plates with a 0.1% insoluble zinc-source and at 28°C ± 2°C plates were incubated for 48 h. Zn solubilization efficiency was calculated as given equation.

$$\text{Solubilization efficiency} = \frac{\text{Zone diameter}}{\text{Diameter of colony growth}} \times 100$$

Further, for quantitative estimation (broth assay) of zinc solubilizing potential of ZSB strains were determined by following Gandhi

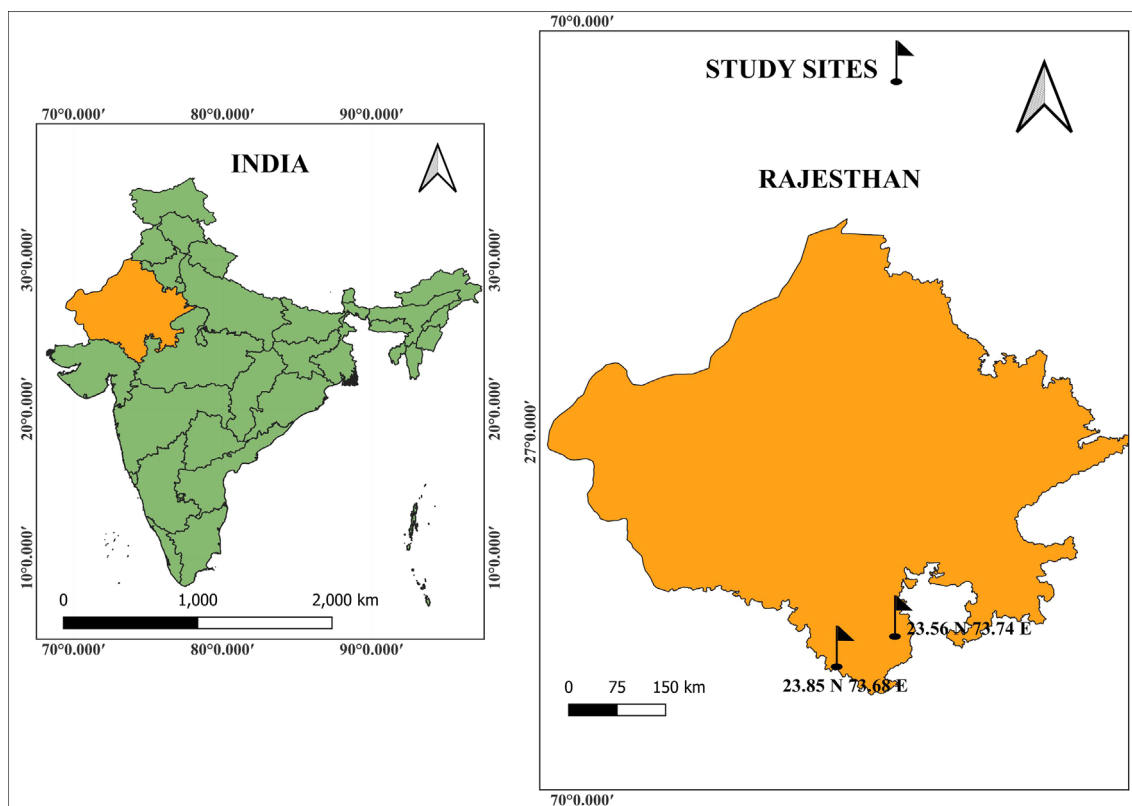


FIGURE 1 Map of the state of Rajasthan showing the geographic locations of collection of soil samples for the isolation of zinc solubilizing bacteria. [Colour figure can be viewed at wileyonlinelibrary.com]

et al. (2014). Briefly, the available zinc concentration was measured using atomic absorption spectrophotometer (AAS 4141 model, Electronics Corp. of India Ltd., India) in the culture filtrate of ZSB grown in MSM broth containing different insoluble zinc source (0.1%) at 4th, 8th, and 16th day of incubation (Gandhi et al., 2014). The pH shift of culture filtrate and uninoculated medium were also analyzed using pH meter.

2.3 | Morphological, biochemical, and molecular identification of potent ZSB

Morphological characteristics namely, form, elevation, margin, cell form, colony color, appearance colony morphology, growth, Gram staining (Gram, 1884) and basic biochemical test namely, Catalase test, Urease test, and Gelatin Liquification test were studied using the standard procedure (Blazevic & Ederer, 1975). Molecular identification of the screened ZSB isolates was carried out through 16S rRNA PCR amplification by using universal primers according to Weisburg et al. (1991) and Jain, Sanadhya, et al. (2020) and sequenced. The 16S rDNA sequences of ZSB isolates were subjected to a BLAST analysis (Altschul et al., 1990) in order to retrieve closely related sequences of type strains and further aligned using online tool CLUSTAL-W (Thompson et al., 1994). The MEGA 6.06 software was employed to construct phylogenetic tree (Tamura et al., 2013).

2.4 | HPLC and GCMS analysis for gluconic acid

The production of gluconic acid by ZSB isolates were tested by injecting the 5 days pre incubated culture filtrate in to a RP-HPLC (Agilent) having C18 column and the mobile phase acetonitrile: water (30:70 v/v) with a flow-rate @ 1.0 mL/min was used with an isocratic flow to detect gluconic acid at 210 nm through UV/Vis-detector (Jain, Kour, et al., 2020). The culture filtrates were further evaluated for the presence of various organic acids and other moieties using GCMC (GCMSQP2020, Shimadzu). Briefly, the methanol extracts (500 μ L) of lyophilized culture filtrate 100 μ L of N-Methyl-N-(trimethylsilyl) trifluoroacetamide and 100 μ L of pyridine were added and the reactions were heated (60°C for 30 min gently) in a water bath and left 12 h for stabilization. These processed samples were analyzed through GC-MS (source temperature 200°C, ionizing voltage 70 eV) and operated with scan mode (50–700 m/z) with temperature ranged 70–260°C and data was compared with NIST library.

2.5 | Physiological and PGP attributes of potent ZSB

Physiological attributes of potent ZSB isolates such as tolerance of pH (Graham, 1992), tolerance of salinity (Upadhyay et al., 2009) tolerance of temperature (Graham, 1992), tolerance of drought (Abolhasani

et al., 2010), antibiotic resistance (Li & Ramakrishna, 2011) was performed by using standard protocols. Zinc solubilizing bacterial isolates were examined for their multiple PGP traits such as production of IAA, siderophore-production, 1-aminocyclopropane-1-carboxylate (ACC) deaminase activity, phosphate-solubilization, potassium and silica solubilization, HCN, ammonia and exopolysaccharides production with standard published methodologies (Jain, Kour, et al., 2020; Naureen et al., 2015; Siddiqui et al., 2021; Upadhyay et al., 2011; Yadav et al., 2022). Hydrolytic enzymes (α amylase, cellulase, pectinase, and protease) was measured by the method of Cappuccino and Sherman (1992) & lipase (Ertugrul et al., 2007), chitinase activity (Kumar et al., 2012), and glucanase activity (Fawzy and Monaim, 2016) were screened by using standard protocols.

2.6 | Bio efficacy evaluation of potent ZSB

2.6.1 | Pot experiment

Bio efficacy and plant growth promotion ability of selected ZSB1 and ZSB17 strains as liquid microbial inoculants was evaluated under pot culture in triplicate following complete randomized design according to our previously published research (Jain et al., 2021). The maize seeds (5–10) were treated with ZSB liquid inoculants ($>8.5 \times 10^8$ cfu mL⁻¹) and placed in 4.0–5.0 cm deep in each pot. All the pots were given uniform recommended dose of fertilizers (RDF) namely, N (@ 120 kg N: P@ 60 kg P₂O₅ and K @ 40 kg K₂Oha⁻¹; Omara et al., 2016). After 30 days of sowing, plant growth parameters namely, average shoots, root-length, root-number, leaf-number, and leaf chlorophyll content (Ronen & Galun, 1984) were analyzed using standard protocols.

2.6.2 | Field experiment

The field studies were undertaken at Krishi Vigyan Kendra, Dungarpur and Instructional farm, Rajasthan College of Agriculture (RCA), (composite soil analysis reports of both experimental fields were summarized in Supplementary data sheet Table S1.1), where the DTPA extractable zinc content is low (<0.6 PPM) in 2 years of kharif seasons to differentiate the effect of two ZSB isolates on growth and yield of Maize variety P3441. The field experiment was laid out in a RBD (randomized block design) with 15 treatments in three replications including two ZSB isolates and uninoculated control (S₁: 100% RDF, T₁: ZSB1 ONLY, T₂: ZSB1+ 100% RDF, T₃: ZSB1 + 75% RDF, T₄: ZSB1 + 50% RDF, T₅: ZSB1 + 100% RDF + ZnSO₄, T₆: ZSB1 + 75% RDF + ZnSO₄, T₇: ZSB1 + 50% RDF + ZnSO₄, T₈: ZSB17 ONLY, T₉: ZSB17 + 100% RDF, T₁₀: ZSB17 + 75% RDF, T₁₁: ZSB17 + 50% RDF, T₁₂: ZSB17 + 100% RDF + ZnSO₄, T₁₃: ZSB17 + 75% RDF + ZnSO₄, T₁₄: ZSB17 + 50% RDF + ZnSO₄) as similar approach was adopted by earlier reported work of Upadhyay et al. (2019). The sowing was done by manual dibbling the seeds at a distance of 60 cm × 40 cm row to plant (Fahad et al., 2016).

ZSB liquid biofertilizer @ 5 mL kg⁻¹ treated to seed before sowing. To enhance the health of cropping over the crop season,

all recommended agronomical practices namely, sowing, weeding, manuring, harvesting, and so forth were taken. Ten plants were randomly selected from every plot at physiological maturity of the crop (106–110 days from sowing), the parameters of yield and harvest including cob length (cm); number of grains per row; number of rows per cob; weight of cobs per plot; weight of grain (g); thousand grain weight (g); biological yield per plot (g); harvest index (%) were evaluated manually (Supplementary data sheet: experimental details) (Gheith et al., 2022). Data analysis was accomplished by using the analysis of variance determining levels of significance.

2.7 | Analysis of Zn-content and Zn-translocation index (ZTI)

The powdered sample (shoot and grain) from all 15 treatments were digested using a triacid mixture (HNO₃: H₂SO₄: HClO₃ in the ratio of 9:2:1) and the Zn-content were measured using AAS to quantify the Zn translocation index (ZTI) (Rengel & Graham, 1996).

$$ZTI = \frac{\text{Zn concentration in grains}}{\text{Zn concentration in shoot}} \times 100$$

3 | RESULTS

In the present study, the physico-chemical characteristics of Dungarpur and Pratapgarh soil samples are described in Table S1.2. The soil samples textured with clay loam and sandy loam, while the soil pH ranged from acidic to neutral. The rhizospheric soils contains moderate to high range of ECe, OC, Av. N, Av. P, and Av. K. The DTPA extractable concentrations of Zn-soil (available Zn) were observed as 0.572 and 0.686 ppm.

3.1 | Isolation and assay (qualitative and quantitative) for zinc solubilization by ZSB

Microorganisms have varied solubilization response with different insoluble form of zinc hence, in the present study, ZSB isolates ZSB1 and ZSB17 were selected based on their capabilities in solubilizing multiple forms of insoluble zinc namely, ZnO, ZnPO₄, and ZnCO₃ in plate assay. Qualitative screening of zinc solubilization was carried out in MSM media and R&B media plates supplemented with different insoluble Zn compounds (Table 1). Zn solubilization zone with ZSB1 was observed in MSM media plates was 3.78 mm, 5.46 mm and 4.10 mm with ZnCO₃, ZnO, and Zn₃(PO₄)₂, respectively, and by ZSB17 was 3.09 mm, 3.79 mm, and 6.56 mm with ZnCO₃, ZnO, and Zn₃(PO₄)₂, respectively whereas in R&B media maximum zone of solubilization was observed with ZSB1 was 3.78 mm, 5.43 mm, and 4.10 mm with ZnCO₃, ZnO, and Zn₃(PO₄)₂, respectively, and by ZSB17 (3.09 mm, 2.85 mm, and 6.56 mm with ZnCO₃, ZnO, and Zn₃(PO₄)₂, respectively). Higher solubilization of Zn was observed in plates containing MSM media.

TABLE 1 Qualitative and quantitative assay for Zinc solubilization by ZSB strains on different insoluble Zn compounds.

Qualitative assay for zinc solubilization by measuring solubilizing index (SI)						
	SI ON R&B (ZNO)	SI ON R&B (ZNC)	SI ON R&B (ZNP)	SI ON MSM (ZNO)	SI ON MSM (ZNC)	SI ON MSM (ZNP)
ZSB-1	5.43 ± 0.05	3.78 ± 0.02	4.1 ± 0.02	5.46 ± 0.05	3.78 ± 0.02	4.10 ± 0.02
ZSB-17	2.85 ± 0.04	3.09 ± 0.08	6.56 ± 0.01	3.79 ± 0.02	3.09 ± 0.08	6.56 ± 0.01
Qualitative assay (broth assay) by measuring soluble Zinc (µg/mL) using AAS						
	4th day (µg/mL)	8th day (µg/mL)	16th day (µg/mL)	pH		
ZSB-1	5.1800 ± 0.0436	14.5767 ± 0.0416	17.3033 ± 0.0603	30.2		
ZSB-17	6.1100 ± 0.0201	14.2500 ± 0.0657	14.6533 ± 0.6240	40.1		

Abbreviations: MSM, mineral salt media; R&B, bunt & Rovira medium; ZNO, Zinc oxide; ZNC, Zinc carbonate; ZNP, Zinc phosphate.

Both ZSB strains were further evaluated for quantitative Zn-solubilization at different time intervals in MSM broth (broth assay). The results revealed that the amount of Zn solubilized from insoluble zinc-oxide, zinc-carbonate, and zinc-phosphate by both the ZSB isolates, and Zn solubilization rate was proportional with incubation time (Table 1). Maximum available Zn registered by ZSB1 was 5.18 µg mL⁻¹ on the fourth day, which peaked to 14.57 µg mL⁻¹ during the eighth day, followed by 17.30 µg mL⁻¹ during the 16th day whereas zinc solubilization by ZSB17 was 6.11 µg mL⁻¹ on the 4th day, which peaked to 14.25 µg mL⁻¹ during the eighth day, followed by 14.65 µg mL⁻¹ during the 16th day. Zn solubilization and reduction in pH of the culture medium showed positive correlation for both the ZSB isolates.

3.2 | Morphological, biochemical, and molecular characterization of ZSB isolates

The shape of ZSB1 and ZSB17 isolate was rod and cocci respectively, while both were gram negative. Colony characteristics as colony color, form, elevation, margin and appearance were also noted along with key biochemical tests and described in Supplementary data sheet Table S2. Biochemical analysis revealed that both ZSB isolates were negative for gelatin liquification test, while both were positive for catalase and urease production. The 16S rRNA gene sequence of isolate ZSB1 showed 95.49% homology with 16S rRNA sequence of *Cupriavidus campinensis* strain BT HNGU56 (Accession number KY010351) already submitted to GenBank data repository of the NCBI. The sequence of 16S rRNA gene of isolate ZSB17 showed 99.68% homology with 16S rRNA sequence of *Pantoea* sp. strain AS-43 (Accession number OL604306) already submitted to GenBank data repository of the NCBI [ZSB1: *Cupriavidus* sp. (Accession number: KY244144); ZSB17: *Pantoea agglomerans* strain ZSB17 (Accession number: MK773870)]. The phylogenetic position of the species is shown in Figure 2.

3.3 | Gluconic acid production by potent ZSB isolates

The reduction of pH from in broth assays was validated by measuring gluconic acid from the chosen ZSB isolates using HPLC

(Supplementary data sheet Figure S1). Both the ZSB isolates showed the secretion of gluconic acid on comparison with the standard gluconic acid and ZSB 1 and ZSB17 produced 286.14 and 102.74 mg/mL gluconic acid respectively after 5 days of incubation in Zn-supplemented MSM media. Further the culture filtrates were subjected to GCMS analysis which also revealed the secretion of different organic acids (Supplementary data sheet Figures S2 and S3).

3.4 | Physiological and PGP attributes of potent ZSB

The isolates ZSB1 and ZSB17 was screened primarily for physiological attributes that includes pH tolerance, salinity tolerance, temperature tolerance, drought tolerance, antibiotic sensitivity (Supplementary data sheet Table S3). Strain ZSB1 was able to tolerate at 1% salt concentration while ZSB17 strain were able to tolerate 2% salt concentration. Both isolates were exposed to temperature stress and ZSB1 was able to grow at various temperatures ranging from 25°C to -40°C while strain ZSB17 showed growth at temperature ranging from 20°C to -45°C. Further the drought tolerant capacities of ZSB were assessed using varying concentration of PEG on MSM-broth and ZSB1 were able to grow upto 40% PEG whereas ZSB17 were tolerated upto 10% PEG. The zinc solubilizing isolates resisted the antibiotics penicilline (µg) and ampicillin (µg) and sensitive toward kanamycin (µg), cefixime (µg), and rifampicin (µg).

Multiple PGPR activities of both ZSB isolates (Table 2) revealed that strain ZSB1 and ZSB17 were suitable plant growth promoting candidates. In the presence of L-tryptophan ZSB1 and ZSB17 produced 64.49 µg/mL IAA and 66.81 µg/mL IAA respectively. Phosphate solubilization by strain ZSB1 was 2.63 ± 0.4 and by strain ZSB17 2.97 ± 0.7 mm diameter around the colonies. Both ZSB isolates were also found positive for potassium solubilization. Both ZSB isolates were able to solubilize potash as forming clear zones in Aleksandrov agar media supplemented with mica. Zone of potash solubilization by strain ZSB1 was 2.86 ± 0.3 mm and by ZSB17 was 3.53 ± 0.02. Both isolates were also subjected for silica solubilization test. Silica solubilization by ZSB1 was 3.83 ± 0.17 and by strain ZSB17 2.64 ± 0.04 mm diameter around the colonies. These selected ZSB isolates have evaluated for different enzymes production by conducting enzyme assays. Research findings showed that both ZSB isolates

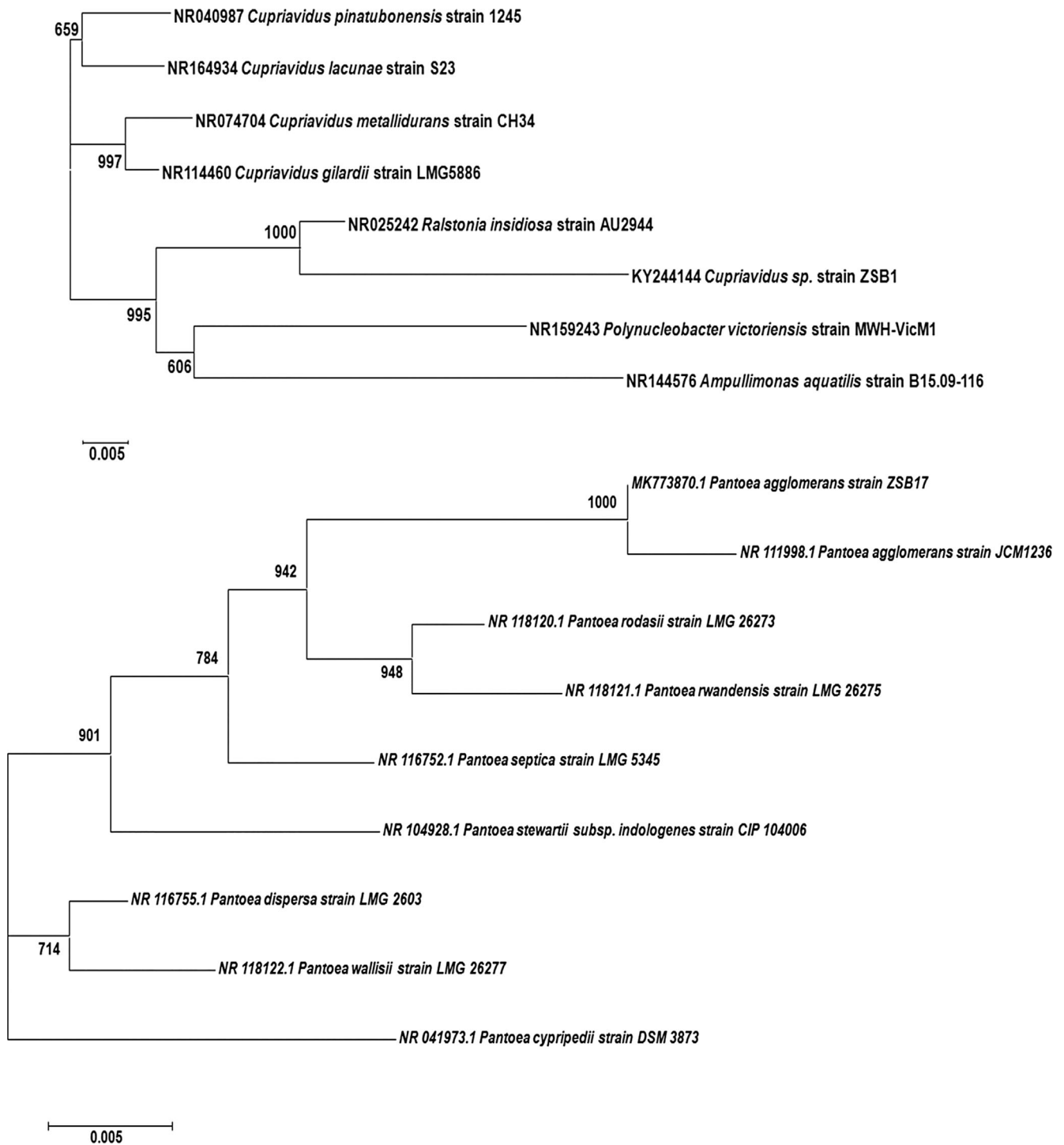


FIGURE 2 Phylogenetic analysis of potent ZSB isolates.

were positive for amylase, lipase, protease, and cellulase production and negative for chitinase and glucanase production with respect to hydrolytic enzymes.

3.5 | Bio efficacy evaluation: Pot and field study

The results from pot experiments revealed that both the ZSB isolates significantly induces maize plant growth-performance. Zinc

solubilizing isolates inoculation showed substantial growth in leaf no., leaf-length, shoots-length as compared to uninoculated control and significantly enhanced the root-length, root-number, and leaf chlorophyll content (Supplementary data sheet Table S4). The untreated control showed minimum value in all studied plant growth parameters.

Field experiment was conducted following in-vitro authentication for both selected ZSB isolates ZSB1 and ZSB17 on 13 selected growth and yield related attributes were recorded in Table 3

TABLE 2 PGP and hydrolytic enzyme production traits in ZSB isolates.

Plant growth promoting traits	ZSB1	ZSB17
ACC Deaminase	+	+
Ammonia production	+	+++
Sidero-phore	+	+
HCN	+	+
EPS	–	–
IAA ($\mu\text{g/mL}$)	640.49	668.17
P solubilization index (cm)	2.63 ± 0.04	2.97 ± 0.07
K solubilization index (cm)	2.86 ± 0.03	3.53 ± 0.02
Si solubilization index (cm)	3.8367 ± 0.17	2.6467 ± 0.04
Lipase activity	+	+++
Amylase activity	+	+
Protease activity	+	+
Cellulase activity	+	+
Chitinase activity	–	–
Glucanase activity	–	–

Note: Value (mean of triplicate) \pm standard deviation.

(Supplementary data sheet). In the present research, the preferred maize variety P3441 was used with implementing all favored SAP (standard-agronomic-practices). For field experiment 15 treatments along with control were designed with combination of RDF and ZnSO_4 . Among all the treatments, the highest biological yield (q/ha) was observed in treatment T_5 ($143.82 \pm 5.65\text{q/ha}$) which were combination of 100% RDF, ZSB1 isolates and ZnSO_4 followed by treatment T_{12} , T_6 , T_{13} , T_2 , T_{14} , T_3 , T_7 , T_9 , T_{10} , T_4 , T_{11} , T_1 , T_8 over the control. The maize plant growth and production have been significantly increased through seed bacterization with ZSB isolates. The difference was significant on yield was recorded in treated than control. Table 3 presents data on the parameters of crop growth and yield trend for maize.

The impact of ZSB isolates on the maize grain Zn content & ZTI are summarized in Table 4. In treatment T_5 (ZSB1+ 100% RDF + ZnSO_4) highest ZTI was observed (ZTI = 55.21%) followed by the maize plants treated with treatment T_{12} (ZSB17 + 100% RDF + ZnSO_4 ; ZTI = 53.4%). This clearly illustrates the role of ZSB isolates in translocating Zn toward maize grains. Zinc translocation analysis revealed that zinc acquisition in grain and shoot was significantly enhanced with strain ZSB1 than strain ZSB17 and un-inoculated control.

4 | DISCUSSION

The growth and productivity of crops were significantly impacted by a zinc shortage in the soil ultimately lead to low zinc contents in crops (Hafeez et al., 2013; Hussain et al., 2022). Following previously published studies, the ZSB isolates were obtained from rhizospheric soil

in this research (Bhatt & Maheshwari, 2020; Sunithakumari et al., 2016). *Cupriavidus* sp. and *Pantoea agglomerans* were identified as the effective ZSB strains ZSB1 and ZSB17 by 16S rRNA gene sequencing. The biochemical characterization represents the intrinsic biochemical and structural properties of the bacteria to adopt in the specific environment. In medium supplied with zinc phosphate and zinc carbonate, ZSB1 shown higher solubilization efficiency, but ZSB17 demonstrated higher solubilization in medium supplemented with zinc oxide. Ramesh et al. (2014) showed that the findings of the current investigation are supported by the ZSB strains MDSR7 and MDSR14 solubilizing all three zinc compounds (zinc, zinc-phosphate, and zinc-oxide). The current study reports that the higher Zn-solubilization zone was observed in ZnO supplemented medium compared to ZnCO_3 amended medium (Goteti et al., 2013; Mishra et al., 2017). In this work, a broth test was used to quantitatively evaluate the solubilization of zinc. As zinc solubilization increased over time, the highest amount of zinc was registered in ZSB17 on day 16 at 14.65 g mL^{-1} . Similar findings with isolated ZSB solubilized insoluble ZnO (40.81 mL^{-1} to 62.48 mL^{-1} soluble Zn) were also reported by Mishra et al. (2017). One important mechanism for the solubilization of metals and minerals is the secretion of OA (organic acids) by PGPRs, and gluconic acid is thought to be the main OA involved in the solubilization of insoluble minerals in soil (Sunithakumari et al., 2016). This will be the primary intermediary for solubilization due to the presence of 2-ketogluconic acid as a main product in cultures altered with the solubilization of insoluble zinc source (Gontia-Mishra et al., 2017) and likely as a result of increased acidity (Dinesh et al., 2018).

More or less every organism has a different active mechanism of zinc solubilization, which relies on the type of bacteria present. The ability of the ZSB strains in the current study to withstand stress, including pH, temperature, salt, and drought, is an inherent biochemical characteristic that aids in their survival in challenging rhizosphere conditions (Upadhyay et al., 2019). If a PGPR displays a variety of PGP properties, it might be a good candidate for microbial inoculants (Singh et al., 2022; Upadhyay & Chauhan, 2022). The ZSB1 and ZSB17 strains were positive for multiple PGP traits namely, ACC-deaminase-activity, siderophore-production, HCN-production, and ammonia-production. Rhizobacterial isolates are well established organisms, which may be remarkable assets for plant growth promotion through different mechanisms (Nadeem et al., 2010; Upadhyay et al., 2022; Upadhyay & Singh, 2015). ACC, a precursor for the ethylene stress hormone as the only source of nitrogen plays an important role for plant growth promotion (Mishra et al., 2017). HCN is a secondary metabolite of bacteria that inhibits growth of pathogenic microorganisms (Siddiqui, 2006). Similarly, recently Jain et al. (2020a) demonstrated that zinc tolerant PGPR produce siderophores and induced growth of plants. Ramesh et al. (2014) demonstrated that strong ammonia-producing bacterial isolates can be beneficial as a source of nitrogen for plant growth-performance.

This study, the IAA production capacities of ZSB isolates is consistent with other researchers' findings (Abaid-Ullah et al., 2015; Zhao et al., 2011). Gandhi & Muralidharan (2016) demonstrated that

TABLE 3 Effect of ZSB strains on growth and yield parameters of maize under field experiment.

Treatment	Biological yield (kg)	Cob length (cm)	Weight of cob/plot (kg)	No of cobs/plot	No of rows/cob	No of grains/row	Weight of grain/plot (kg)	Grain yield (q/ha)	Weight of fodder/plot (kg)	Stover yield (q/ha)	Biological yield (q/ha)	Harvest index (%)	1000 grain wt (g)
S ₁	60.40	20.00	40.20	24.00	14.00	40.00	20.59	54.00	30.81	79.31	133.31	40.48	210.65
T ₁	40.80	18.00	20.92	22.00	12.00	36.00	20.30	48.00	20.50	51.98	99.98	48.28	245.66
T ₂	60.10	22.00	40.10	27.00	16.00	42.00	3.12	65.00	20.98	62.06	127.06	51.26	289.82
T ₃	50.90	20.20	30.90	25.00	14.00	36.00	2.83	59.00	30.07	63.90	122.90	48.58	253.00
T ₄	50.40	19.00	30.40	24.00	14.00	36.00	20.54	53.00	20.86	59.48	112.48	47.45	254.00
T ₅	60.90	23.00	4.58	29.00	18.00	44.00	30.26	68.00	30.64	75.82	143.82	47.23	292.65
T ₆	60.40	21.50	40.30	28.00	16.00	40.00	20.98	62.00	30.42	71.31	133.31	46.62	268.00
T ₇	50.80	20.00	40.00	26.00	14.00	38.00	20.69	56.00	30.11	64.81	120.81	46.35	278.00
T ₈	40.40	17.70	20.46	20.00	12.00	34.00	2.21	46.00	20.19	45.65	91.65	50.19	269.00
T ₉	50.80	20.60	30.50	26.00	16.00	40.00	3.02	63.00	20.78	57.81	120.81	52.35	285.00
T ₁₀	50.50	19.80	30.20	24.00	14.00	38.00	20.74	57.00	20.76	57.57	114.57	50.03	269.00
T ₁₁	50.10	18.40	30.10	23.00	14.00	36.00	20.50	52.00	20.60	54.23	106.23	49.05	288.00
T ₁₂	60.60	22.00	40.30	28.00	16.00	41.58	30.07	64.00	30.53	73.48	137.48	47.11	288.51
T ₁₃	60.30	21.00	40.10	25.00	16.00	40.00	20.78	58.00	30.52	73.23	131.23	44.50	285.48
T ₁₄	60.10	20.50	30.80	23.00	14.00	38.00	20.54	53.00	30.56	74.06	127.06	41.71	255.00
SEm±	00.270	00.937	00.169	10.160	00.638	10.632	00.113	20.362	00.286	50.962	50.602	20.794	90.111
CD at 5%	00.780	20.705	00.488	30.351	10.841	40.712	00.328	60.823	00.827	17.221	16.180	80.069	26.313
CD at 1%	10.051	30.643	00.658	40.513	20.480	60.345	00.441	90.187	10.113	23.188	21.787	10.866	35.431

Note: The data express the pooled value of the triplicate data collected in two sessions.

TABLE 4 Effect of ZSB isolates on Zinc translocation from shoot to grain; Zinc Translocation Index.

Treatment	Zn in grain	Zn in Stover	Zinc translocation index (%)
S ₁	25.93	78.60	32.9
T ₁	23.20	78.37	29.62
T ₂	35.33	68.03	51.9
T ₃	33.70	70.79	47.6
T ₄	30.30	73.47	41.14
T ₅	38.20	68.77	55.21
T ₆	34.77	70.00	49.5
T ₇	32.97	70.83	46.4
T ₈	21.47	79.00	27
T ₉	34.60	71.23	48.5
T ₁₀	31.83	69.80	45.5
T ₁₁	27.50	70.33	39.11
T ₁₂	35.50	66.33	53.4
T ₁₃	31.50	65.73	47.9
T ₁₄	29.17	69.03	42.1
SEm±	0.961	1.227	
CD at 5%	2.777	3.543	
CD at 1%	3.739	4.771	

Note: The data express the pooled value of the triplicate data collected in two sessions.

phytohormone IAA (auxin) was produced by AGM3 (an isolate) at 45.61 g mL⁻¹, followed by the AGM9 37.27 g mL⁻¹ in IAA broth medium. The capability of PGP isolates to solubilize insoluble P form to a plant available P form significantly improves crop production under P limiting conditions (Majeed et al., 2015).

According to the findings of an experiment performed by Dinesh et al. (2018), *B. megaterium* (Strain CDK25) is capable of soluble and mobilized phosphate, both inorganic and organic. *Bacillus licheniformis* (BHU18) and *Pseudomonas azotoformans* (BHU21), two KSB isolates, demonstrated noticeably higher K-solubilization than the results seen in the current research, according to Saha et al. (2016). According to Naureen et al. (2015), 29 out of a total of 111 bacterial isolates can dissolve mineral silicates. Zhao et al. (2011) reported on the isolation and characterization of ZSB strains with multiple PGP traits and stated that *Bacillus* spp. exhibit numerous plant growth promoting attributes that support plant growth, including Zn and P solubilization, IAA production, oxidase activity, catalase activity, and phytohormone development. The increase in plant growth could be attributed to ZSB isolates' capacity to supply nutrients through nitrogen fixation, phosphate solubilization, siderophores synthesis, and the release of phytohormones (Mumtaz et al., 2017; Jain et al., 2017). Amylase, lipase, protease, and cellulase synthesis were found in zinc solubilizing isolates, and these enzymes indirectly aid plant growth by controlling soil-borne phytopathogens (Jha et al., 2012).

Zinc solubilizing isolates inoculation under pot conditions significantly improved the root length, root no., and leaf chlorophyll content and the results were well supported by Karnwal (2021) reported zinc solubilizing *Pseudomonas* spp. isolated from vermicompost significantly improves plant growth and maximum zinc content in Okra

fruit compared to uninoculated control. Application of ZSB substantially improves plant growth by increasing Zn bioavailability in soil to crop plants hence reduce the use of synthetic zinc fertilizers. The field experiment was conducted following in vitro authentication for ZSB1 and ZSB17 strains on 13 selected growth and yield-related attributes, among all the treatments, the highest biological yield (q/ha) was observed in treatment T5 (143.82 ± 5.65 q/ha) which were a mixture of 100% RDF, ZSB1 isolates and ZnSO₄. The maize plant growth and production have been significantly increased through seed bacterization with ZSB isolates. Hussain et al. (2015) recorded an increase in plant growth attributes primarily shoot length, root length, shoot fresh and dry biomass, and root fresh and dry biomass when Zn solubilizing *Bacillus* sp. (AZ6) was inoculated under field conditions. Sarathambal et al. (2010) have demonstrated that the dry weight of the maize is increased compared with control by the inoculation of zinc solubilizing *Gluconacetobacter diazotrophicus*. An experiment conducted by Goteti et al. (2013) in which they revealed that seed bacterization with zinc solubilizing PGP bacteria facilitates the growth of plant height (root and height of the shoot); leaf area; and dry mass.

The results of the study on the effect of ZSB isolates on zinc translocation index (ZTI) in maize plant are presented in Table 4. Zinc translocation index is used in this study as a similar notion to the translocation factor (TF) that can be viewed as the ratio of an element in a plant's shoots and roots (Upadhyay et al., 2021). The maize plant showed the highest ZTI (55.21%) in treatment T5 (ZSB1 + 100% RDF + ZnSO₄), followed by treatment T12 (ZSB17 + 100% RDF + ZnSO₄; 53.4%). This clearly shows ZSB isolates have role in translocation of Zn toward maize grains and similar finding was earlier

reported by Goteti et al. (2013) and Omara et al. (2016). In comparison to the control, the introduction of *B. aryabhatai* isolates to wheat and soybean crops dramatically boosted Zn uptake as well as shoot and seed weight (He et al., 2010). In addition to synergistic impact on plants' growth and yield, ZSBs have a strong capacity to enhance the Zn content of cereals which ultimately improves human health and immunity (Abaid-Ullah et al., 2015; Wang et al., 2014). Krithika and Balachandar (2016) reported that ZSB up-regulated the expression of Zn-regulated transporters and iron (Fe)-regulated transporter-like protein (ZIP) genes in rice suggested its important role in zinc fertilization and fortification. Uptake of micronutrients (Zn) by the plants from soil is a mutually dependent process (Bouain et al., 2014). Using microbial tools to enhance the availability of soil Zn to crop plants is one of the sustainable ways of reducing the Zn deficiency and improving Zn content of food crops grain in zinc deficient soils (Sirohi et al., 2015). Furthermore, such microbial tools will improve the zinc deficient soil and restore them to healthy soil by improving available zinc in soil. The ZSB isolates from the present study can be used for development of liquid biofertilizers to improve zinc acquisition in different crop plants cultivated in southern Rajasthan based on dedicated field studies.

5 | CONCLUSION

The primary issue that inhibits plant growth performance in degraded soil is the type of zinc that is not readily available to plants; zinc-deficient soil is frequently observed in the current research sites. Zn is a crucial micronutrient needed for healthy plant development and growth, and a deficiency does more than just harm human health and crop productivity. The findings of this research demonstrated that two distinct native bacteria, *Cupriavidus* sp. and *Pantoea agglomerans*, had the highest potential to solubilize insoluble zinc in the form of zinc that was readily available and to promote maize growth at the field level. Both isolates (*Cupriavidus* sp. and *P. agglomerans*) demonstrated a variety of PGP properties and produced catalase and urease, both of which promoted plant development. *Cupriavidus* sp. and *P. agglomerans* increased the yield of maize by 19.01% and 17.64%, respectively, and improved Zn translocation toward grains. We conclude that the *Cupriavidus* sp. and *P. agglomerans*, considerably improved soil health, maize crop production, and both unique strains could play a spectacular and promising role in bio-fertilizer technology.

AUTHOR'S CONTRIBUTION

Devendra Jain designed the research. Aradhana Sukhwil performed the experiments. Vimal Sharma interpreted the data. Gajanand Jat performed soil and AAS analysis. Aradhana Sukhwil performed HPLC and GCMS studies. Devendra Jain and Sudhir K. Udpadhyay wrote the manuscript. All authors reviewed the manuscript.

ACKNOWLEDGMENTS

The financial assistance from All India Network Project on soil biodiversity and International Zinc Association, USA are gratefully acknowledged. Dr. Devendra Jain acknowledges the financial support from

IDP, NAHEP, ICAR, New Delhi for International training. Dr. Upadhyay acknowledges to the Department of Environmental Science, VBS Purvanchal University.

CONFLICT OF INTEREST STATEMENT

No potential conflict of interest was reported by the authors.

DATA AVAILABILITY STATEMENT

The data that support the findings of this study are available on request from the corresponding author. The data are not publicly available due to privacy or ethical restrictions.

ORCID

Devendra Jain  <https://orcid.org/0000-0002-4345-1536>

Sudhir K. Mohanty  <https://orcid.org/0000-0002-2228-8063>

REFERENCES

- Abaid-Ullah, M., Hassan, M. N., Jamil, M., Brader, G., Shah, M. K. N., Sessitsch, A., & Hafeez, F. Y. (2015). Plant growth promoting rhizobacteria: An alternate way to improve yield and quality of wheat (*Triticum aestivum* L.). *International Journal of Agriculture and Biology*, 17, 51–60.
- Abolhasani, M., Lakzian, A., Tajabadipour, A., & Haghnia, G. (2010). The study salt and drought tolerance of *Sinorhizobium* bacteria to the adaptation to alkaline condition. *Australian Journal of Basic and Applied Sciences*, 4, 882–886.
- Alengebawy, A., Abdelkhalek, S. T., Qureshi, S. R., & Wang, M. Q. (2021). Heavy metals and pesticides toxicity in agricultural soil and plants: Ecological risks and human health implications. *Toxics*, 9, 42. <https://doi.org/10.3390/toxics9030042>
- Altschul, S. F., Gish, W., Miller, W., Myers, E. W., & Lipman, D. J. (1990). Basic local alignment search tool. *Journal of Molecular Biology*, 215(3), 403–410.
- Baldantoni, D., Saviello, G., & Alfani, A. (2019). Nutrients and non-essential elements in edible crops following long-term mineral and compost fertilization of a Mediterranean agricultural soil. *Environmental Science and Pollution Research*, 26(35), 35353–35364. <https://doi.org/10.1007/s11356-018-3353-8>
- Barra, C. A., & Terenzi, V. (2021). Rhizosphere microbial communities and heavy metals. *Microorganisms*, 9, 1462. <https://doi.org/10.3390/microorganisms9071462>
- Bhatt, K., & Maheshwari, D. K. (2020). Zinc solubilizing bacteria (*Bacillus megaterium*) with multifarious plant growth promoting activities alleviates growth in *Capsicum annum* L. *3 Biotech*, 10(2), 36. <https://doi.org/10.1007/s13205-019-2033-9>
- Bhojjiya, A. A., Joshi, H., Upadhyay, S. K., Srivastava, A. K., Pathak, V. V., Pandey, V. C., & Jain, D. (2022). Screening and optimization of zinc removal potential in *Pseudomonas aeruginosa*-HMR1 and its plant growth-promoting attributes. *The Bulletin of Environmental Contamination and Toxicology*, 108(3), 468–477. <https://doi.org/10.1007/s00128-021-03232-5>
- Blazevic, D. J., & Ederer, G. M. (1975). Principles of biochemical tests in diagnostic microbiology. *Wiley and Company, New York*, 2, 13–45.
- Bouain, N., Shahzad, Z., Rouached, A., Khan, G. A., Berthomieu, P., Abdelly, C., Poirier, Y., & Rouached, H. (2014). Phosphate and zinc transport and signalling in plants: Toward a better understanding of their homeostasis interaction. *The Journal of Experimental Botany*, 65, 5725–5741. <https://doi.org/10.1093/jxb/eru314>
- Brown, P. H. (2008). Micronutrient use in agriculture in the United States of America: Current practices, trends and constraints. In *Micronutrient deficiencies in global crop production, heavy metals in soils: Trace metals and metalloids in soils and their bioavailability* (Vol. 11, pp. 267–286). Springer.

- Bunt, J. S., & Rovira, A. D. (1955). Microbiological studies of some subantartic soils. *Journal of Soil Science*, 6, 119–128.
- Cappuccino, J. C., & Sherman, N. (1992). *Microbiology: A laboratory manual* (Vol. 3, third ed., pp. 125–179). Benjamin Cummings Publication company.
- Chibuikwe, G. U., & Obiora, S. C. (2014). Heavy metal polluted soils: Effect on plants and bioremediation methods. *Applied and Environmental Soil Science*, 2014, 752708 (1–12). <https://doi.org/10.1155/2014/752708>
- Dinesh, R., Srinivasan, V., Hamza, S., Sarathambal, C., Gowda, S. J. A., Ganeshamurthy, A. N., Gupta, S. B., Nair, V. A., Subila, K. P., Lijina, A., & Divya, V. C. (2018). Isolation and characterization of potential Zn solubilizing bacteria from soil and its effects on soil Zn release rates, soil available Zn and plant Zn content. *Geoderma*, 321, 173–186.
- Ertugrul, S., Donmez, G., & Takac, S. (2007). Isolation of lipase producing *Bacillus* sp. from olive mill waste water and improving its enzyme activity. *Journal of Hazardous Material*, 149, 720–724.
- Fageria, N., Baligar, V., & Clark, R. (2002). Micronutrients in crop production. *Advance Agronomy*, 77, 185–268.
- Fahad, S., Saud, S., Muhammad, H., Hassan, S., Shah, A., & Ullah, F. (2016). Effect of row spacing and methods of sowing on the performance of maize. *Austin Food Science*, 1(2), 1008.
- Fawzy, M., & Monaim, A. (2016). Efficacy of secondary metabolites and extracellular lytic enzymes of plant growth promoting rhizobacteria (PGPR) in controlling *Fusarium* wilt of chickpea. *Egyptian Journal of Agricultural Research*, 94, 573–589.
- Gandhi, A., & Muralidharan, G. (2016). Assessment of zinc solubilizing potentiality of *Acinetobacter* sp. isolated from rice rhizosphere. *European Journal of Soil Biology*, 76, 1–8.
- Gandhi, A., Muralidharan, G., Sudhakar, E., & Murugan, A. (2014). Screening for elite zinc solubilizing bacterial isolate from rice rhizosphere environment. *International Journal of Recent Scientific Research*, 5, 2201–2204.
- Garcia-Arellano, H., Alcalde, M., & Ballesteros, A. (2004). Use and improvement of microbial redox enzymes for environmental purposes. *Microbial Cell Factories*, 3, 10. <https://doi.org/10.1186/1475-2859-3-10>
- Gheith, E. M. S., El-Badry, O. Z., Lamlo, S. F., Ali, H. M., Siddiqui, M. H., Ghareeb, R. Y., El-Sheikh, M. H., Jebri, J., Abdelsalam, N. R., & Kandil, E. E. (2022). Maize (*Zea mays* L.) productivity and nitrogen use efficiency in response to nitrogen application levels and time. *Frontiers in Plant Science*, 13, 941343. <https://doi.org/10.3389/fpls.2022.941343>
- Gontia-Mishra, I., Sapre, S., & Tiwari, S. (2017). Zinc solubilizing bacteria from the rhizosphere of rice as prospective modulator of zinc biofortification in rice. *Rhizosphere*, 3, 185–190.
- Goteti, P. K., Emmanuel, L. D. A., Desai, S., & Shaik, M. H. A. (2013). Prospective zinc solubilizing bacteria for enhanced nutrient uptake and growth promotion in maize (*Zea mays* L.). *International Journal of Microbiology*, 10, 1155–1162.
- Graham, P. H. (1992). Stress tolerance in *Rhizobium* and *Bradyrhizobium* and nodulation under adverse soil conditions. *Canadian Journal of Microbiology*, 38, 475–484.
- Gram, H. C. (1884). Über die isolierte Färbung der Schizomyceten in Schnitt- und Trockenpräparaten. *Fortschritte der Medizin (in German)*, 2, 185–189.
- Hafeez, B., Khanif, Y. M., & Saleem, M. (2013). Role of zinc in plant nutrition—A review. *American Journal of Experimental Agriculture*, 3, 374–391.
- He, C. Q., Tan, G. E., Liang, X., Du, W., Chen, Y. L., Zhi, G. Y., & Zhu, Y. (2010). Effect of Zn-tolerant bacterial strains on growth and Zn accumulation in *Oryzophragmus violaceus*. *Applied Soil Ecology*, 44, 1–5.
- Hussain, A., Arshad, M., Ahmad, Z., & Asghar, M. (2015). Prospects of zinc solubilizing bacteria for enhancing growth of maize. *Pakistan Journal of Agricultural Sciences*, 52, 915–922.
- Hussain, A., Jiang, W., Wang, X., Shahid, S., Saba, N., Ahmad, M., Dar, A., Masood, S. U., Imran, M., & Mustafa, A. (2022). Mechanistic impact of zinc deficiency in human development. *Frontiers in Nutrition*, 9(1–11), 717064. <https://doi.org/10.3389/fnut.2022.717064>
- Jain, D., Kour, R., Bhojiya, A. A., Meena, R. H., Singh, A., Mohanty, S. R., Rajpurohit, D., & Ameta, K. D. (2020a). Zinc tolerant plant growth promoting bacteria alleviates phytotoxic effects of zinc on maize through zinc immobilization. *Scientific Reports*, 10, 13865. <https://doi.org/10.1038/s41598-020-70846-w>
- Jain, D., Sanadhya, S., Saheewala, H., Maheshwari, D., Shukwal, A., Singh, P. B., Meena, R. H., Choudhary, R., Mohanty, S. R., & Singh, A. (2020b). Molecular diversity analysis of plant growth promoting rhizobium isolated from groundnut and evaluation of their field efficacy. *Current Microbiology*, 77, 1550–1557. <https://doi.org/10.1007/s00284-020-01963-y>
- Jain, D., Sharma, J., Kaur, G., Bhojiya, A. A., Chauhan, S., Sharma, V., Suman, A., Mohanty, S. R., & Maharjan, E. (2021). Phenetic and molecular diversity of nitrogen fixing plant growth promoting *Azotobacter* isolated from semiarid regions of India. *BioMed Research International*, 2021, 6686283. <https://doi.org/10.1155/2021/6686283>
- Jain, D., Sunda, S. D., Sanadhya, S., Dhruva, J. N., & Khandelwal, S. K. (2017). Molecular characterization and PCR-based screening of cry genes from *Bacillus thuringiensis* strains. *3 Biotech*, 7, 4.
- Jha, B., Gontia, I., & Hartmann, A. (2012). The roots of the halophyte *Salicornia brachiata* are a source of new halotolerant diazotrophic bacteria with plant growth-promoting potential. *Plant and Soil*, 356, 265–277. <https://doi.org/10.1007/s11104-011-0877-9>
- Karnwal, A. (2021). Zinc solubilizing pseudomonas spp. from vermicompost bestowed with multifaceted plant growth promoting properties and having prospective modulation of zinc biofortification in *Abelmoschus esculentus* L. *Journal of Plant Nutrition*, 44, 1023–1038. <https://doi.org/10.1080/01904167.2020.1862199>
- Krithika, S., & Balachandrar, D. (2016). Expression of zinc transporter genes in rice as influenced by zinc-solubilizing *Enterobacter cloacae* strain ZSB14. *Frontiers in Plant Science*, 7, 446. <https://doi.org/10.3389/fpls.2016.00446>
- Kumar, P., Dubey, R. C., & Maheshwari, D. K. (2012). *Bacillus* strains isolated from rhizosphere showed plant growth promoting and antagonistic activity against phytopathogens. *Microbiology Research*, 167, 493–499.
- Li, K., & Ramakrishna, W. (2011). Effect of multiple metal resistant bacteria from contaminated lake sediments on metal accumulation and plant growth. *Journal of Hazardous Materials*, 189, 531–539.
- Mahmud, A. A., Upadhyay, S. K., Srivastava, A. K., & Bhojiya, A. A. (2021). Biofertilizers: A nexus between soil fertility and crop productivity under abiotic stress. *Current Research in Environmental Sustainability*, 3, 100063.
- Majeed, A., Abbasi, M. K., Hameed, S., Imran, A., & Rahim, N. (2015). Isolation and characterization of plant growth-promoting rhizobacteria from wheat rhizosphere and their effect on plant growth promotion. *Frontiers in Microbiology*, 6, 198.
- Mumtaz, M. Z., Ahmad, M., Jamil, M., & Hussain, T. (2017). Zinc solubilizing *Bacillus* spp. potential candidates for biofortification in maize. *Microbiological Research*, 202, 51–60.
- Nadeem, S. M., Zahir, Z. A., Naveed, M., Asghar, H. N., & Arshad, M. (2010). Rhizobacteria capable of producing ACC-deaminase may mitigate salt stress in wheat. *Soil Science Society of America Journal*, 74, 533–542. <https://doi.org/10.2136/sssaj2008.0240>
- Naureen, Z., Aqeel, M., Hassan, M. N., Gilani, S. A., Bouqellah, N., Mabood, F., Hussain, J., & Hafeez, F. Y. (2015). Isolation and screening of silicate bacteria from various habitats for biological control of phytopathogenic fungi. *American Journal of Plant Sciences*, 6, 2850–2859.
- Omara, A. A., Ghazi, A. A., & El-Akhdar, I. A. (2016). Isolation and identification of zinc dissolving bacteria and their potential on growth of *Zea mays*. *Egyptian Journal of Microbiology*, 51, 29–43.
- Ramesh, A., Sharma, S. K., Sharma, M. P., Yadav, N., & Joshi, O. P. (2014). Inoculation of zinc solubilizing *Bacillus aryabhatai* strains for improved growth, mobilization and biofortification of zinc in soybean and wheat cultivated in vertisols of central India. *Applied Soil Ecology*, 73, 87–96.

- Rengel, Z., & Graham, R. D. (1996). Uptake of zinc from chelate buffered nutrient solutions by wheat genotypes differing in Zn efficiency. *Journal of Experimental Biology*, 47, 217–226.
- Ronen, R., & Galun, M. (1984). Pigment extraction from lichens with dimethylsulfoxide (DMSO) and estimation of chlorophyll degradation. *Environmental and Experimental Botany*, 24, 239–245.
- Saha, M., Maurya, B. R., Bahadur, I., & Kumar, A. (2016). Identification and characterization of potassium solubilizing bacteria (KSB) from Indo-Gangetic Plains of India. *Biocatalysis and Agricultural Biotechnology*, 7, 202–209.
- Sarathambal, C., Thangaraju, M., Paulraj, C., & Gomathy, M. (2010). Assessing the zinc solubilization ability of *Gluconacetobacter diazotrophicus* in maize rhizosphere using labelled Zn compounds. *Indian Journal of Microbiology*, 50, 103–109.
- Saravanan, V. S., Madhaiyan, M., & Thangaraju, M. (2007). Solubilization of zinc compounds by the diazotrophic, plant growth promoting bacterium *Gluconacetobacter diazotrophicus*. *Chemosphere*, 66, 1794–1798.
- Shakeel, M., Rais, A., Hassan, M. N., & Hafeez, F. Y. (2015). Root associated *Bacillus* sp. improves growth, yield and zinc translocation for basmati rice (*Oryza sativa*) varieties. *Frontiers in Microbiology*, 6, 1286–1291.
- Shukla, A. K., Behera, S. K., Prakash, C., Tripathi, C., Patra, A. C., Dwivedi, B. S., Trivedi, V., Rao, C. S., Chaudhari, S. K., Das, S., & Singh, A. K. (2021). Deficiency of phyto-available Sulphur, zinc, boron, iron, copper and manganese in soils of India. *Scientific Reports*, 11, 19760. <https://doi.org/10.1038/s41598-021-99040-2>
- Siddiqui, A. R., Shahzad, S. M., Ashraf, M., Yasmeen, T., Kausar, R., Albasher, G., Alkahtani, S., & Shakoob, A. (2021). Development and characterization of efficient K-solubilizing rhizobacteria and mesorhizobial inoculants for chickpea. *Sustainability*, 13, 10240. <https://doi.org/10.3390/su131810240>
- Siddiqui, Z. A. (2006). PGPR: prospective bio-control agents of plant pathogens. In Z. A. Siddiqui (Ed.), *PGPR: Biocontrol and Biocontrol* (pp. 112–142). Springer.
- Singh, P., Chauhan, P. K., Upadhyay, S. K., Singh, R. K., Dwivedi, P., Wang, J., Jain, D., & Jiang, M. (2022). Mechanistic insights and potential use of siderophores producing microbes in rhizosphere for mitigation of stress in plants grown in degraded land. *Frontiers in Microbiology*, 13, 2415. <https://doi.org/10.3389/fmicb.2022.898979>
- Sirohi, G., Upadhyay, A., Srivastava, P. S., & Srivastava, S. (2015). PGPR mediated zinc biofertilization of soil and its impact on growth and productivity of wheat. *Journal of Soil Science and Plant Nutrition*, 15(1), 202–216.
- Sunithakumari, K., Devi, S. N. P., & Vasandha, S. (2016). Zinc solubilizing bacterial isolates from the agricultural fields of Coimbatore, Tamil Nadu, India. *Current Science*, 110, 196–205.
- Tamura, K., Stecher, G., Peterson, D., Filipiński, A., & Kumar, S. (2013). Molecular evolutionary genetics analysis version 6.0. *Molecular Biology and Evolution*, 30, 2725–2729.
- Thiébaud, N., & Hanikenne, M. (2022). Zinc deficiency responses: Bridging the gap between Arabidopsis and dicotyledonous crops. *Journal of Experimental Botany*, 73(6), 1699–1716. <https://doi.org/10.1093/jxb/erab491>
- Thompson, J. D., Higgins, D. G., & Gibson, J. (1994). CLUSTAL W: Improving the sensitivity of progressive multiple sequence alignment through sequence weighting, position-specific gap penalties and weight matrix choice. *Nucleic Acid Research*, 22, 4673–4680.
- Upadhyay, S. K., Saxena, A. K., Singh, J. S., & Singh, D. P. (2019). Impact of native ST-PGPR (*Bacillus pumilus*; EU927414) on PGP traits, antioxidants activities, wheat plant growth and yield under salinity. *Climate Change and Environmental Sustainability*, 7, 157–168. <https://doi.org/10.5958/2320-642X.2019.00021.8>
- Upadhyay, S. K., Ahmad, M., Srivastava, A. K., Abhilash, P. C., & Sharma, B. (2021). Optimization of eco-friendly novel amendments for sustainable utilization of Fly ash based on growth performance, hormones, antioxidant, and heavy metal translocation in chickpea (*Cicer arietinum* L.) plant. *Chemosphere*, 267, 129216. <https://doi.org/10.1016/j.chemosphere.2020.129216>
- Upadhyay, S. K., & Chauhan, P. K. (2022). Optimization of eco-friendly amendments as sustainable asset for salt-tolerant plant growth-promoting bacteria mediated maize (*Zea Mays* L.) plant growth, Na uptake reduction and saline soil restoration. *Environmental Research*, 211(113081), 1–10. <https://doi.org/10.1016/j.envres.2022.113081>
- Upadhyay, S. K., & Edrisi, S. A. (2021). Developing sustainable measures to restore fly-ash contaminated lands: Current challenges and future prospects. *Land Degradation and Development*, 32, 4817–4831. <https://doi.org/10.1002/ldr.4090>
- Upadhyay, S. K., & Singh, D. P. (2015). Effect of salt-tolerant plant growth-promoting rhizobacteria on wheat plants and soil health in a saline environment. *Plant Biology*, 17(1), 288–293. <https://doi.org/10.1111/plb.12173>
- Upadhyay, S. K., Singh, D. P., & Saikia, R. (2009). Genetic diversity of plant growth promoting rhizobacteria isolated from Rhizospheric soil of wheat under saline condition. *Current Microbiology*, 59, 489–496. <https://doi.org/10.1007/s00284-009-9464-1>
- Upadhyay, S. K., Singh, J. S., & Singh, D. P. (2011). Exopolysaccharide-producing plant growth-promoting rhizobacteria under salinity condition. *Pedosphere*, 21, 214–222. [https://doi.org/10.1016/S1002-0160\(11\)60120-3](https://doi.org/10.1016/S1002-0160(11)60120-3)
- Upadhyay, S. K., Srivastava, A. K., Rajput, V. D., Chauhan, P. K., Bhojija, A. A., Jain, D., Chaubey, G., Sharma, D. B., & Minkina, T. (2022). Root exudates: Mechanistic insight of plant growth promoting rhizobacteria for sustainable crop production. *Frontiers in Microbiology*, 13, 1–19. <https://doi.org/10.3389/fmicb.2022.916488>
- Vance, E. D., Brookes, P. C., & Jenkinson, D. S. (1987). An extraction method for measuring soil microbial biomass. *Soil Biology and Biochemistry*, 19, 703–707.
- Wang, L., Cai, Y., Zhu, L., Guo, H., & Yu, B. (2014). Major role of NAD-dependent lactate dehydrogenases in the production of L-lactic acid with high optical purity by the thermophile *Bacillus coagulans*. *Applied and Environmental Microbiology*, 80, 7134–7141.
- Weisburg, W. G., Barns, S. M., Pelletier, D. A., & Lane, D. J. (1991). 16S ribosomal DNA amplification for phylogenetic study. *Journal of Bacteriology*, 173(2), 697–703. <https://doi.org/10.1128/jb.173.2.697-703.1991>
- White, P. J., & Brown, P. H. (2010). Plant nutrition for sustainable development and global health. *Annals of Botany*, 105, 1073–1080. <https://doi.org/10.1093/aob/mcq085>
- Yadav, V. K., Bhagat, N., & Sharma, S. K. (2022). Modulation in plant growth and drought tolerance of wheat crop upon inoculation of drought-tolerant *Bacillus* species isolated from hot arid soil of India. *Journal of Pure and Applied Microbiology*, 16(1), 246–262.
- Zhao, Q., Shen, Q., Ran, W., Xiao, T., Xu, D., & Xu, Y. (2011). Inoculation of soil by *Bacillus subtilis* Y-IVI improves plant growth and colonization of the rhizosphere and interior tissues of muskmelon (*Cucumis melo* L.). *Biology and Fertility of Soils*, 47, 507–514.

SUPPORTING INFORMATION

Additional supporting information can be found online in the Supporting Information section at the end of this article.

How to cite this article: Sukhwai, A., Jain, D., Sharma, V., Ojha, S. N., Jat, G., K. Mohanty, S., Singh, A., & Mohanty, S. R. (2023). Efficacy evaluation of newly isolated zinc solubilizing bacteria for their potential effect on maize (*Zea mays* L.) under zinc deficient soil conditions. *Land Degradation & Development*, 1–12. <https://doi.org/10.1002/ldr.4818>

Research Article

Yogesh Dadhich, Reema Jain*, Karuppusamy Loganathan*, Mohamed Abbas, Kalyana Srinivasan Prabu, and Mohammed S. Alqahtani

Sisko nanofluid flow through exponential stretching sheet with swimming of motile gyrotactic microorganisms: An application to nanoengineering

<https://doi.org/10.1515/phys-2023-0132>
received July 19, 2023; accepted October 13, 2023

Abstract: The swimming of motile gyrotactic microorganism's phenomenon has recently become one of the most important topics in research due to its applicability in biotechnology, many biological systems, and numerous engineering fields. The gyrotactic microorganisms improve the stability of the nanofluids and enhance the mass/heat transmission. This research investigates the MHD fluid flow of a dissipative Sisko nanofluid containing microorganisms moving along an exponentially stretched sheet in the current framework. The mathematical model comprises equations that encompass the preservation of mass, momentum, energy, nanoparticle concentration, and microorganisms. The equations that govern are more complicated because of non-linearity, and therefore to obtain the combination of ordinary differential equations, similarity transformations are utilized.

The numerical results for the converted mathematical model are carried out with the help of the `bvp4c` solver. The resulting findings are compared to other studies that have already been published, and a high level of precision is found. The graphical explanations for velocity, temperature, and nanoparticles volume fraction distribution are shown with physical importance. Physical characteristics like Peclet number, Sisko fluid parameter, thermophoresis and Brownian motion parameter, and Hartmann number are taken into consideration for their effects. Based on the numerical outcomes, the bioconvection Peclet number enhances the density of mobile microorganisms, whereas thermal radiation contributes to an elevation in temperature. The velocity field decreases with the enhancement of magnetic parameter; however, the temperature field increases with increased magnetic parameter and thermophoresis parameter augmentation. Our numerical findings are ground breaking and distinctive, and they are used in microfluidic devices including micro instruments, sleeve electrodes, and nerve development electrodes. This study has various applications in nanoengineering, including nanomaterial synthesis, drug delivery systems, bioengineering, nanoscale heat transfer, environmental engineering.

Keywords: MHD, nanofluid, Sisko model, microorganisms, exponentially stretched sheet

* **Corresponding author: Reema Jain**, Department of Mathematics and Statistics, Manipal University Jaipur, Jaipur 303007, Rajasthan, India, e-mail: reemajain197@gmail.com

* **Corresponding author: Karuppusamy Loganathan**, Department of Mathematics and Statistics, Manipal University Jaipur, Jaipur 303007, Rajasthan, India, e-mail: loganathankaruppusamy304@gmail.com

Yogesh Dadhich: Department of Mathematics and Statistics, Manipal University Jaipur, Jaipur 303007, Rajasthan, India

Mohamed Abbas: Electrical Engineering Department, College of Engineering, King Khalid University, Abha 61421, Saudi Arabia, e-mail: mabas@kku.edu.sa

Kalyana Srinivasan Prabu: Department of Physics, Kongu Engineering College, Erode, Tamil Nadu, India, e-mail: kprabhush@kongu.edu

Mohammed S. Alqahtani: Radiological Sciences Department, College of Applied Medical Sciences, King Khalid University, Abha 61421, Saudi Arabia; BioImaging Unit, Space Research Centre, Michael Atiyah Building, University of Leicester, Leicester, LE1 7RH, United Kingdom, e-mail: mosalqhtani@kku.edu.sa

Nomenclature

A	material parameter (–)
B_0	magnetic field strength ($\text{kg s}^{-2} \text{A}^{-1}$)
C	concentration (kg m^{-3})
C_∞	ambient concentration (kg m^{-3})
C_w	sheet concentration (kg m^{-3})
c_p	specific heat ($\text{J kg}^{-1} \text{K}^{-1}$)
d	chemotaxis constant (m)
D_B	coefficient of Brownian diffusion ($\text{m}^2 \text{s}^{-1}$)

D_m	microorganism diffusion coefficient ($m^2 s^{-1}$)
D_T	coefficient of thermophoretic diffusion ($m^2 s^{-1}$)
E_c	Eckert number (–)
k	thermal conductivity ($W m^{-1} K^{-1}$)
L_b	bioconvection Lewis number (–)
L_e	Lewis parameter (–)
M	magnetic field parameter
N_b	Brownian diffusion parameter
N_t	thermophoresis parameter
Nu_x	local Nusselt number
N	concentration of microorganisms ($kg m^{-3}$)
N_w	sheet concentration of microorganisms ($kg m^{-3}$)
N_∞	ambient concentration of microorganisms ($kg m^{-3}$)
Pe	Peclet number
Pr	Prandtl number
q_r	radiative heat flux ($W m^{-2}$)
R	radiation parameter
Re_a, Re_b	local Reynolds numbers
Sh_x	Sherwood number
T	fluid temperature (K)
T_w	sheet temperature (K)
T_∞	ambient fluid temperature (K)
u, v	velocity components ($m s^{-1}$)
W_c	maximum cell swimming speed ($m s^{-1}$)
x, y	Cartesian coordinates (m)

Greek symbols

α	thermal diffusivity ($m^2 s^{-1}$)
δ	heat source/sink parameter
η	similarity parameter
θ	temperature similarity function
ϕ	concentration similarity function
χ	microorganism similarity function
λ	mixed convection parameter
ϑ	kinematic viscosity ($m^2 s^{-1}$)
ρ	density ($kg m^{-3}$)
τ	ratio of the effective heat capacity
σ	electrical conductivity (S/m)

Subscripts

∞	ambient condition
w	surface condition

1 Introduction

Numerous biological, industrial, and technical processes, such as the production of fibres, refinement of polymer, hot roll glass blasting, heat exchangers, extrusion of aerodynamics, MHD power generators, domestic refrigerator-freezers, rubber and plastic sheet manufacturing, cooling process of reactors, improving diesel generator efficiency, and cooling/drying of papers, the flow of nanofluid over stretching or shrinking sheets is extremely important [1]. Nanofluids may be useful in solar energy, nuclear reactors, medicine delivery, and cancer treatment. Nanoparticle scattering in common (base) fluids yields nanofluids. Polymer solutions can be utilized as base fluids in addition to normal fluids including oils and lubricants. Choi *et al.* [2] were the first to present the fundamental concept of such metallic nanoparticles by presenting a comprehensive model for improving the thermal characteristics of base fluid. Subsequently, Buongiorno [3] established a non-homogeneous equilibrium model by incorporating Brownian movement and thermophoresis properties to describe the slip mechanism of nanoparticles. Eastman *et al.* [4] explored the phenomena of heat transfer in the presence of copper oxide (CuO) particles made of water and Al_2O_3 particles made of ethylene glycol. Since then, Sheikholeslami *et al.* [5] have explored the properties of nanofluids. Pourfattah *et al.* [6] employed two-phase flow simulation to investigate the characteristics of microchannel heat sink. The processing methods and thermal characteristics of oil-based nanofluid were investigated by Asadi *et al.* [7]. Khan *et al.* [8] investigated the fluid flow of nanoparticles for the Jeffrey fluid. An experimental study on the effects of ultra-sonication of MWCNT- H_2O nanofluid was carried out by Asadi *et al.* [9]. Zeeshan *et al.* [10] conducted an analysis on the movement of two immiscible fluids within a lengthy, flexible tube. They formulated models for both the core and peripheral regions, making assumptions of long wavelength behaviour and creeping flow. Riaz *et al.* [11] explored the transportation of nanosized particles through a curved channel characterized by non-Darcy porous conditions. The flow in this channel is driven by a peristaltic wave. Riaz *et al.* [12] analyzed the effects of an applied magnetic field and entropy generation on Jeffrey nanofluid in the annular section between two micro non-concentric pipelines, with the inner pipe being rigid and moving at a constant speed. The researchers discovered that the magnetic field reduced the flow velocity and the rate of entropy production while increasing the temperature of the nanofluid. Following that, other researchers and technologists worked in the same field, and numerous publications have been published that

consider the existence of nanofluids and magnetic fields in addition to linear and nonlinear thermal radiation, chemical reactions, and other factors [13–15].

Bioconvection occurs when bacteria spread randomly in a single-celled and, in certain cases, colony-like pattern. Because of the gyrotactic microorganisms upstream, the buoyancy of the fluid significantly increases. The flow of microbes in nanofluids has recently drawn the attention of researchers due to wide applications in biosensors, microbial-enhanced oil recovery, engineering, biological, and chemical fields such as biofuels, cancer treatment, enzymes, biotechnological applications, production and manufacturing, industrial level, and others. Firstly, Kuznetsov [16] established the concept of nanofluid bioconvection. Later, using Navier–Stokes equations, Alloui *et al.* [17] examined the distribution of microorganisms in a cylinder. Waqas *et al.* [18] used the magnetic dipole effect to investigate the bioconvection effect that microbes produce in Jeffery nanofluid through an expanded surface. Waqas *et al.* [19] presented a computational investigation of nanofluid flow (Oldroyd-B Model) with mass and heat transport, gyrotactic microbes past a rotating disc using the MATLAB built-in function `bvp4c`. Uddin *et al.* [20] first described the blowing effect on bio-convection flow across a dynamic stretched sheet. Following that, Chamkha *et al.* [21] described the bio-convective fluid flow containing microbes through a radiating stretching plate. Using the help of a nanofluid model of Buongiorno's and the O-Boussinesq approximation, Rashad and Nabwey [22] examined the bio-convection flow containing microorganisms through a cylinder placed horizontally under convective boundaries. Alwatban *et al.* [23] investigated bioconvection using slip effects of Wu's at the surface. Aziz *et al.* [24] anticipated a bioconvective flow of microorganisms embedded in the porous medium. Shaw *et al.* [25] used a spectrum relaxation technique to derive the associated equations depicting the fluid nanoflow with microorganisms. Rashad and Nabwey [22] and Rashad *et al.* [26] recently addressed the subject of bioconvection over a vertical thin cylinder. Elboughdiri *et al.* [27] investigated radiating viscoelastic nanofluids in MHD mixed convective flows near a sucked impermeable surface with exponentially decreasing heat generation using Jeffery's model, convective mass transport, thermophoresis, and Brownian diffusion under boundary layer assumptions. The influence of nanoparticles on the thermosolutal sensitivity of non-Newtonian fluid flow is investigated by Sharma *et al.* [28], with numerical computations employing blood as the base liquid. Wakif [29] computed the two-dimensional mixed convective motion of a radiating mixture of an upper-convected Maxwell nanofluid and gyrotactic motile microorganisms along a convectively heated vertical surface with a uniform magnetic

field source, revealing the non-homogeneous appearance and dynamical properties of the system. Puneeth *et al.* [30] investigation focuses on analysing the impact of Brownian motion and thermophoresis on the flow of a tangent hyperbolic (pseudoplastic) nanofluid past a rotating cone in three-dimensional free stream conditions.

Observations from previous studies reveal the lack of evidence regarding the flow of dissipative magneto Sisko nanofluid with gyrotactic microorganisms along an exponentially stretching sheet. The goal of this study is to describe the heat transfer properties of bioconvection flow of Sisko nanofluid along an exponential stretched sheet. To obtain a simplified mathematical model, similarity transformations are employed. The computational analysis is completed using the `bvp4c` and coding MATLAB scripts. Graphical analysis is used to explore the behaviour of the relevant parameters, and results are compared with the earlier research. For designing equipment, such as electric ovens, electric heaters, microelectronics, and wind generators, the thermal industry uses these kinds of modelled problems. The study aims to analyse the behaviour of the nanofluid flow and the influence of the motile microorganisms, with potential applications in the field of nanoengineering.

2 Mathematical modelling

2.1 Rheological model

Consider a non-Newtonian fluid that is time independent and follows the Sisko rheological model; the Cauchy stress tensor for such fluids is defined as follows:

$$\mathbf{T} = -p\mathbf{I} + \mathbf{S},$$

where \mathbf{S} is the extra stress tensor and is expressed as follows:

$$\mathbf{S} = \left[\mathbf{a} + \mathbf{b} \left| \sqrt{\frac{1}{2}\text{tr}(\mathbf{A}_1^2)} \right|^{n-1} \right] \mathbf{A}_1,$$

where for “ $n > 0$ for various fluids,” a and b are the physical constants difference, $\mathbf{A}_1 = (\text{grad } V) + (\text{grad } V)^T$, V represents for the vector as velocity, and T stands for transposition and means the first Rivlin–Erickson tensor.

2.2 Governing equations and boundary conditions

The flow configuration of the current investigation is illustrated in Figure 1, which shows the movement of a two-dimensional laminar boundary layer dissipative Sisko

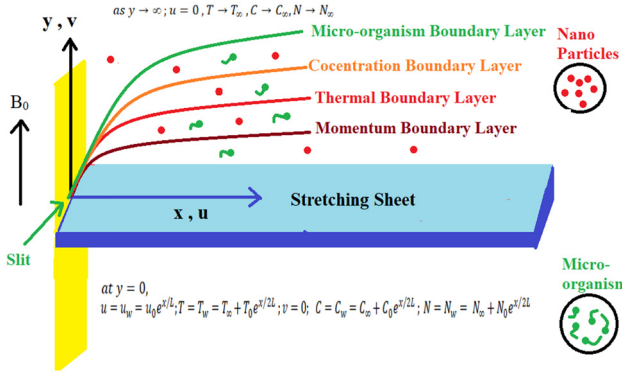


Figure 1: Physical model.

nanofluid containing microbes across an exponentially stretched surface, under steady conditions (independent of time). Here, the sheet was stretched exponentially along the x -axis with a stretching velocity $u_w(x) = u_0 e^{x/L}$ to initiate the flow of nanofluids. The effects of viscous dissipation, magnetic field, and Brownian motion are addressed in flow formulation. The x and y -axes are assumed perpendicular to each other. A fixed magnetic field, B_0 , is acted parallel to the y -direction upon. u and v represent the velocity components along the x and y axes, respectively. Furthermore, the assumption is made that the temperature, nanoparticle volume fraction, and density of motile microbes on the stretchable surface are T_w , C_w , and N_w , respectively. In addition, it is considered that these variables remain constant as T_∞ , C_∞ , and N_∞ when moving away from the stretchable surface.

Using the assumptions stated earlier, the fundamental equations for the present investigation can be addressed as follows [31]:

Continuity equation:

$$\frac{\partial u}{\partial x} + \frac{\partial v}{\partial y} = 0. \quad (1)$$

Momentum equation:

$$u \frac{\partial u}{\partial x} + v \frac{\partial u}{\partial y} = \frac{a}{\rho} \frac{\partial^2 u}{\partial y^2} - \frac{b}{\rho} \frac{\partial}{\partial y} \left(-\frac{\partial u}{\partial y} \right)^n - \frac{\sigma B_0^2 u}{\rho}. \quad (2)$$

Thermal energy equation:

$$\begin{aligned} u \frac{\partial T}{\partial x} + v \frac{\partial T}{\partial y} = & a \frac{\partial^2 T}{\partial y^2} + \tau \left[D_B \frac{\partial C}{\partial y} \frac{\partial T}{\partial y} + \frac{D_T}{T_\infty} \left(\frac{\partial T}{\partial y} \right)^2 \right] \\ & - \frac{1}{(\rho C_p)_f} \frac{\partial q_r}{\partial y} + \frac{Q}{(\rho C_p)_f} (T - T_\infty) \\ & + \frac{1}{(\rho C_p)_f} \left[a \left(\frac{\partial u}{\partial y} \right)^2 + b \left(-\frac{\partial u}{\partial y} \right)^{n+1} \right] \\ & + \frac{\sigma B_0^2 u^2}{(\rho C_p)_f}. \end{aligned} \quad (3)$$

Nanoparticle concentration equation:

$$u \frac{\partial C}{\partial x} + v \frac{\partial C}{\partial y} = D_B \frac{\partial^2 C}{\partial y^2} + \frac{D_T}{T_\infty} \frac{\partial^2 T}{\partial y^2}. \quad (4)$$

Conservation equation for microorganisms:

$$u \frac{\partial N}{\partial x} + v \frac{\partial N}{\partial y} - D_m \frac{\partial^2 N}{\partial y^2} + \frac{dW_c}{C_w - C_\infty} \left[\frac{\partial}{\partial y} \left(N \frac{\partial C}{\partial y} \right) \right] = 0. \quad (5)$$

The corresponding boundary conditions are as follows:

$$\text{at } y = 0 : u = u_w = u_0 e^{x/L}; v = 0; T = T_w; \quad (6)$$

$$C = C_w; N = N_w,$$

$$\text{at } y \rightarrow \infty; u = 0, T \rightarrow T_\infty, C \rightarrow C_\infty, N \rightarrow N_\infty. \quad (7)$$

The following transformations are used to convert the aforementioned equations into their non-dimensional forms [32]:

$$\begin{aligned} \eta &= y \sqrt{\frac{u_0}{2\vartheta L}} e^{x/2L} \\ u &= u_0 e^{x/L} f'(\eta) \\ v &= -\sqrt{\frac{u_0 \vartheta}{2L}} e^{x/2L} [f(\eta) + \eta f'(\eta)] \\ \theta(\eta) &= \frac{T - T_\infty}{T_w - T_\infty} \\ \phi(\eta) &= \frac{C - C_\infty}{C_w - C_\infty} \\ \chi(\eta) &= \frac{N - N_\infty}{N_w - N_\infty}. \end{aligned} \quad (8)$$

The radiative heat flux q_r is determined using the Rosseland diffusion approximation and is given by

$$q_r = -\frac{4\sigma^*}{3k^*} \frac{\partial T^4}{\partial y}. \quad (9)$$

The Rosseland mean absorption coefficient is denoted as k^* , and the Stefan–Boltzmann constant is represented by σ^* . Assuming minimal temperature variations within the flow, T^4 can be expressed as a linear function of temperature.

$$T^4 = 4T_\infty^3 - 3T_\infty^4. \quad (10)$$

Using Eqs. (9) and (10)

$$\frac{\partial q_r}{\partial y} = -\frac{16\sigma^* T_\infty^3}{3k^*} \frac{\partial^2 T}{\partial y^2}, \quad (11)$$

where η shows similarity parameter; $f(\eta)$ indicates dimensionless stream function; $\theta(\eta)$ represents dimensionless temperature; and $f'(\eta)$ shows the dimensionless velocity profile (the derivative of $f(\eta)$).

By utilizing the non-dimensional similarity parameters given below, Eqs. (1)–(7) can be converted into

dimensionless equations. The given equations are converted into their non-dimensional forms using the following transformations:

$$Af''' + n(-f'')^{n-1}f''' - Mf' - 2f'^2 + ff'' = 0, \quad (12)$$

$$\left(1 + \frac{4R}{3}\right)\theta'' + P_r f\theta' + \delta P_r \theta + N_b \theta' \phi' + N_t \theta'^2 + MP_r E_c f'^2 + AP_r E_c (f'')^2 + P_r E_c (-f'')^{n+1} = 0, \quad (13)$$

$$\phi'' + P_r L_e f \phi' + \left(\frac{N_t}{N_b}\right)\theta'' = 0, \quad (14)$$

$$\chi'' + L_b f \chi' - [P_e(\phi'' \chi + \phi' \chi')] = 0. \quad (15)$$

Furthermore, the boundary conditions are modified as follows: at

$$\begin{aligned} \eta = 0 : f'(\eta) = 1; f(\eta) = 0; \theta(\eta) = 1; \\ \phi(\eta) = 1; \chi(\eta) = 1, \end{aligned} \quad (16)$$

for

$$\eta \rightarrow \infty : f'(\eta) = 0; \theta(\eta) = 0; \phi(\eta) = 0; \chi(\eta) = 0. \quad (17)$$

In Eqs. (12)–(17), the prime indicates the differentiation with respect to η (similarity parameter). The following non-dimensional parameters are used:

$$\begin{aligned} L_b &= \frac{\alpha}{D_m}; P_e = \frac{dW_c}{D_m}; N_b = \frac{\tau D_B (C_w - C_\infty)}{\vartheta}; \\ N_t &= \frac{\tau D_T (T_w - T_\infty)}{\vartheta T_\infty}; L_e = \frac{\alpha_f}{D_B}; R = \frac{4\sigma^* T_\infty^3}{k^* k}; \delta = \frac{Qx}{\rho c_p u_\infty}; \\ E_c &= \frac{(u_\infty)^2}{(c_p)_f (T_w - T_\infty)}; P_r = \frac{\vartheta}{\alpha_f}; A = \frac{(Re_b)^{2/(n+1)}}{Re_a}; Re_a = \frac{\rho x u_\infty}{a}; \\ Re_b &= \frac{\rho x (u_\infty)^{(2-n)}}{b} \end{aligned}$$

2.3 Coefficients of heat and mass transport

The main objective of this analysis is to determine the factors that engineers need to take into account when addressing heat and nanoparticle mass transfer. Defining

$$\text{these as follows: local Nusselt number } Nu_x = \left(\frac{xq_w}{k(T_w - T_\infty)} \right)_{y=0}$$

$$\text{and local nanofluid Sherwood number } Sh_x = \left(\frac{xq_w}{D_B(C_w - C_\infty)} \right)_{y=0},$$

where $q_w = -k \left(\frac{\partial T}{\partial y} \right)_{y=0}$ is wall heat flux. Using the aforementioned

transformations, these parameters will reduce to $(Re_b)^{-1/(n+1)}$

$$Nu_x = -\left(1 + \frac{4R}{3}\right)\theta'(0) \text{ and } (Re_b)^{-1/(n+1)} Sh_x = -\phi'(0).$$

3 Computational procedure

The examined physical problem is addressed by a system of partial differential equations that are reduced to a system of ordinary differential equations (ODEs) using appropriate similarity transformations. Furthermore, the converted system of nonlinear ODEs (12)–(17) is solved by using the `bvp4c` function. To achieve this, the system of ODEs (18)–(23) is converted to first-order ODEs, which can be summed up as follows:

Solution by `bvp4c`:

$$f = y_1; f' = y_2; f'' = y_3; f''' = y_4; \theta = y_5; \theta' = y_6; \theta'' = y_7; \phi = y_8; \phi' = y_9; \phi'' = y_{10}; \chi = y_{11}; \chi' = y_{12}; \chi'' = y_{13}$$

$$f''' = \frac{2y_2^2 + M^2 y_2 - y_1 y_3}{A + (-1)^{n-1} n (y_3)^{n-1}}, \quad (18)$$

$$\begin{aligned} \theta'' = y_7 \\ = \frac{[P_r y_1 y_5 + \delta P_r y_4 + P_r E_c (-y_3)^{n+1} + MP_r E_c y_2^2 + N_b y_5 y_7 + N_t y_5^2 + AP_r E_c (y_3)^2]}{-\left(1 + \frac{4R}{3}\right)}, \end{aligned} \quad (19)$$

$$y_7' = \phi'' = -\left[P_r L_e y_1 y_7 + \frac{N_t}{N_b} y_5 \right] \quad (20)$$

$$y_9' = \chi'' = P_e y_7 y_9 + P_e y_8 \phi'' - L_b y_1 y_9. \quad (21)$$

Using boundary conditions

$$\begin{aligned} \text{at } \eta = 0 : y_0(1) = 0, y_0(2) - 1 = 0, y_0(4) - 1 = 0, \\ y_0(6) - 1 = 0, y_0(8) - 1 = 0, \end{aligned} \quad (22)$$

$$\begin{aligned} \text{for } \eta \rightarrow \infty : y_1(2) = 1, y_1, y_1(4) = 0, \\ y_1(6) = 0, y_1(8) = 0. \end{aligned} \quad (23)$$

The convenience with which nonlinear issues in simple domains can be dealt with is an advantage of this approach. The method is proven effective and precise in a number of boundary value problems and iteratively refined to a range of 10^{-5} and a step size of 0.05.

4 Results and discussion

In this section, we will focus on explaining the flow regime, or the conditions under which the nanofluid moves and behaves in terms of its velocity temperature, micro-organism profile, and nanoparticle concentration. The scope of variables considered in this investigation is

$$0 \leq A \leq 1.5, 0 \leq M \leq 1.5, 0 \leq P_r \leq 1.5, 0 \leq E_c \leq 1.5, 0 \leq N_b \leq 1.5, 0 \leq N_t \leq 1.5, 0 \leq L_e \leq 1.5, 0 \leq R \leq 1.5, 0 \leq \delta \leq 1.5, 0 \leq L_b \leq 1.5, 0 \leq P_e \leq 1.5.$$

4.1 Effect of A on velocity, temperature, chemical reaction, motile density profiles

Figure 2(a) shows that the fluid velocity increases as Sisko fluid parameter (material parameter) increases. Due to the fact that the relationship between the material parameter and the fluid’s viscosity is inverse. The observations from this study indicated that when the value of A was increased, the viscosity of the fluid decreased, leading to a subsequent

reduction in the resistance encountered during fluid motion. The fluid velocity rises as a result. The effect of Sisko fluid parameter A (material parameter) on fluid temperature is shown in Figure 2(b). As the material parameter A is raised, a drop in the fluid temperature is seen.

4.2 Effect of M on velocity, temperature, nanoparticle concentration, and microorganism profiles

The purpose of Figure 3(a)–(d) is to explore how the velocity, temperature, volume proportion of nanoparticles, and

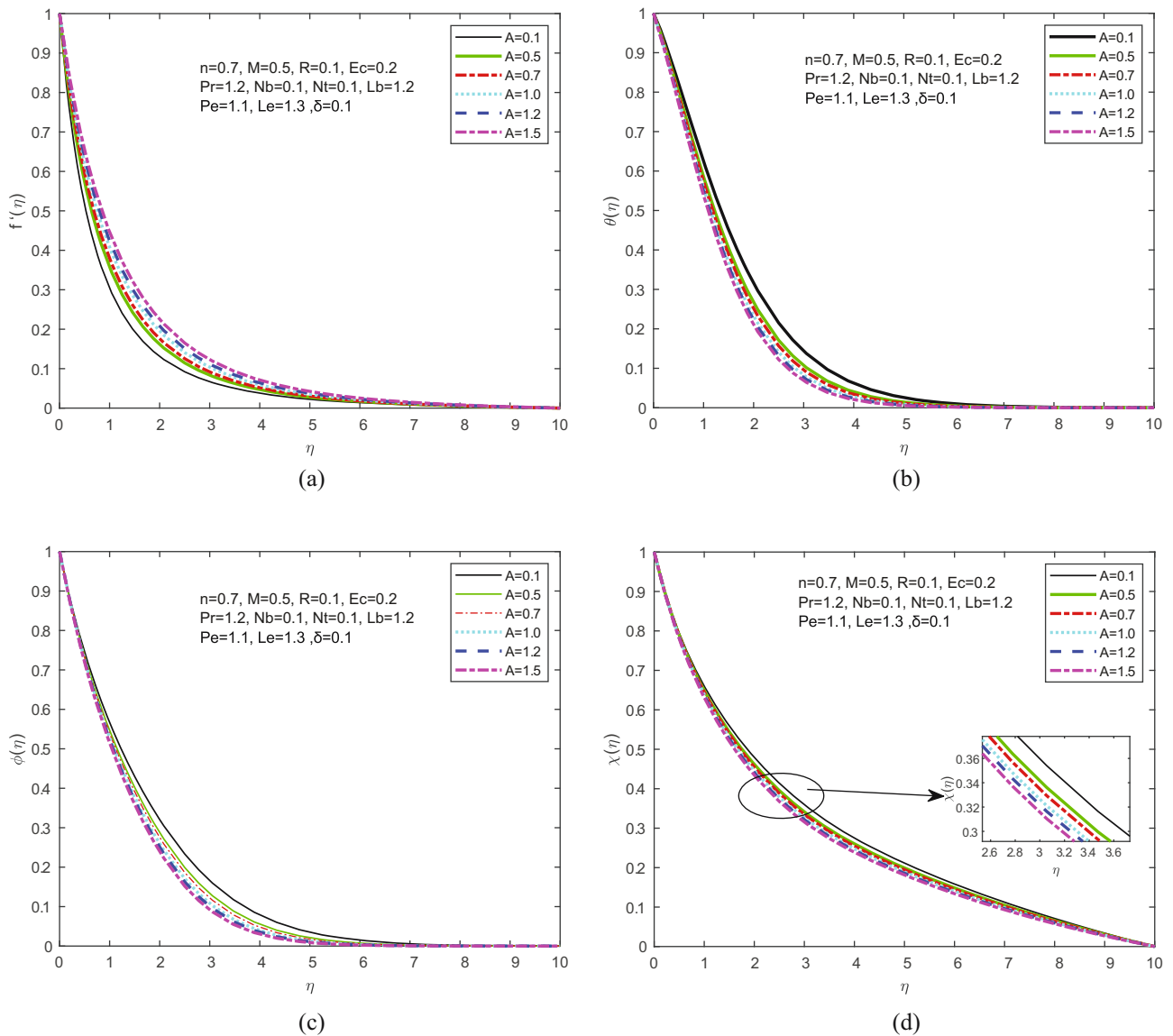


Figure 2: (a) f' vs A , (b) θ vs A , (c) ϕ vs A and (d) χ vs A .

microorganism density curves are influenced by the magnetic parameter (M). The velocity profile is observed to decrease as magnetic field strength estimates (M) increase, according to Figure 3(a), owing to the Lorentz force theorem, on which the magnetic field is established. The greater collisional impact between fluid atoms, as indicated by M , results in increased fluid flow resistance. Furthermore, the Lorentz force, which acts in opposition to the direction of flow, creates a resistance force that contributes to the thickness of the thermal boundary layer, as shown in Figure 3(b). The presence of a reversing force results in a decrease in the fluid flow, leading to a decline in the velocity field. Notably, Figure 3(c) and (d) demonstrate that the inclusion of magnetic parameters contributed to the enhancement of temperature and volume fraction

near the surface, as well as the thicknesses of the thermal and nanoparticle concentration boundary layers. These outcomes can be explained by the increased heat generation associated with higher magnetic parameter values (M), which led to the expansion of temperature, concentration, and gyrotactic microorganism boundary layers, as depicted in Figure 3(b)–(d).

4.3 Effect of P_r on temperature, nanoparticle concentration profile, and microorganism profiles

The curves for the temperature, nanoparticle volume fraction, and density of the motile microorganisms are

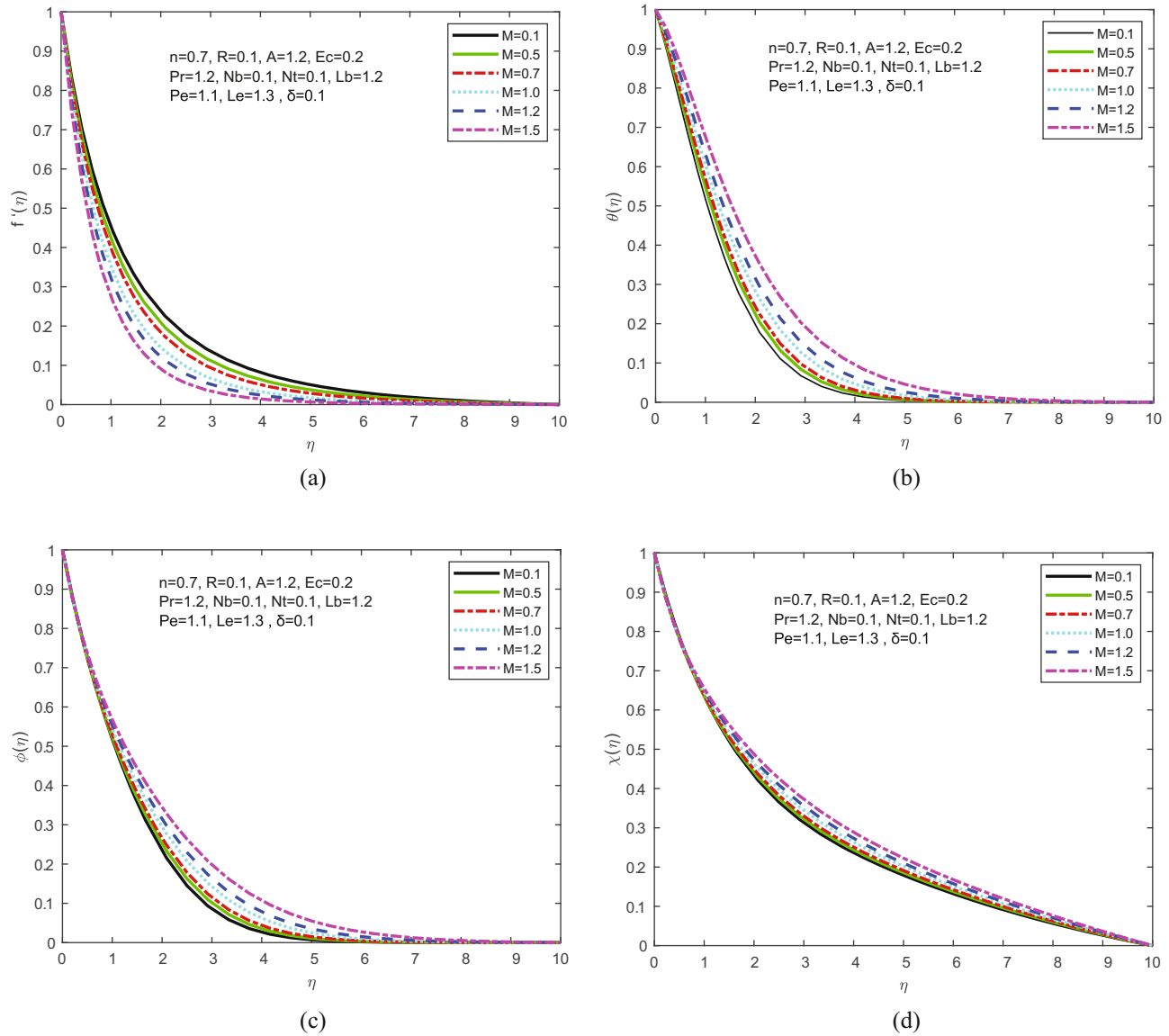


Figure 3: (a) f' vs M , (b) θ vs M , (c) ϕ vs M and χ vs M .

depicted in Figure 4(a)–(c), which illustrated the manner in which the Prandtl number P_r affected these curves. The Prandtl number had no effect on velocity, according to Eq. (9). As shown in Figure 4(a), the temperature and thickness of the thermal boundary layer decreased as P_r increased. In terms of physical significance, when P_r was raised, the thermal diffusivity dropped, leading to a reduction in the capability of energy to transfer across the thermal boundary layer. The thicknesses of the concentration boundary layer exhibited an upward trend as P_r increased as shown in Figure 4(b). The influence of the Prandtl number on the motile microorganism's density ($\chi(\eta)$) is shown in Figure 4(c), which indicates that the density of microorganisms increased with increasing

P_r . This is due to the fact that the boundary layer thicknesses of the motile microorganisms decreased with increasing P_r , causing their size to decrease. In other terms, the increase in P_r resulted in a reduction in the number of gyrotactic microbes.

4.4 Effect of E_c on temperature, nanoparticle concentration profile, and microorganism profiles

In Figure 5(a)–(c), temperature, concentration, and microorganism density variations are depicted for different

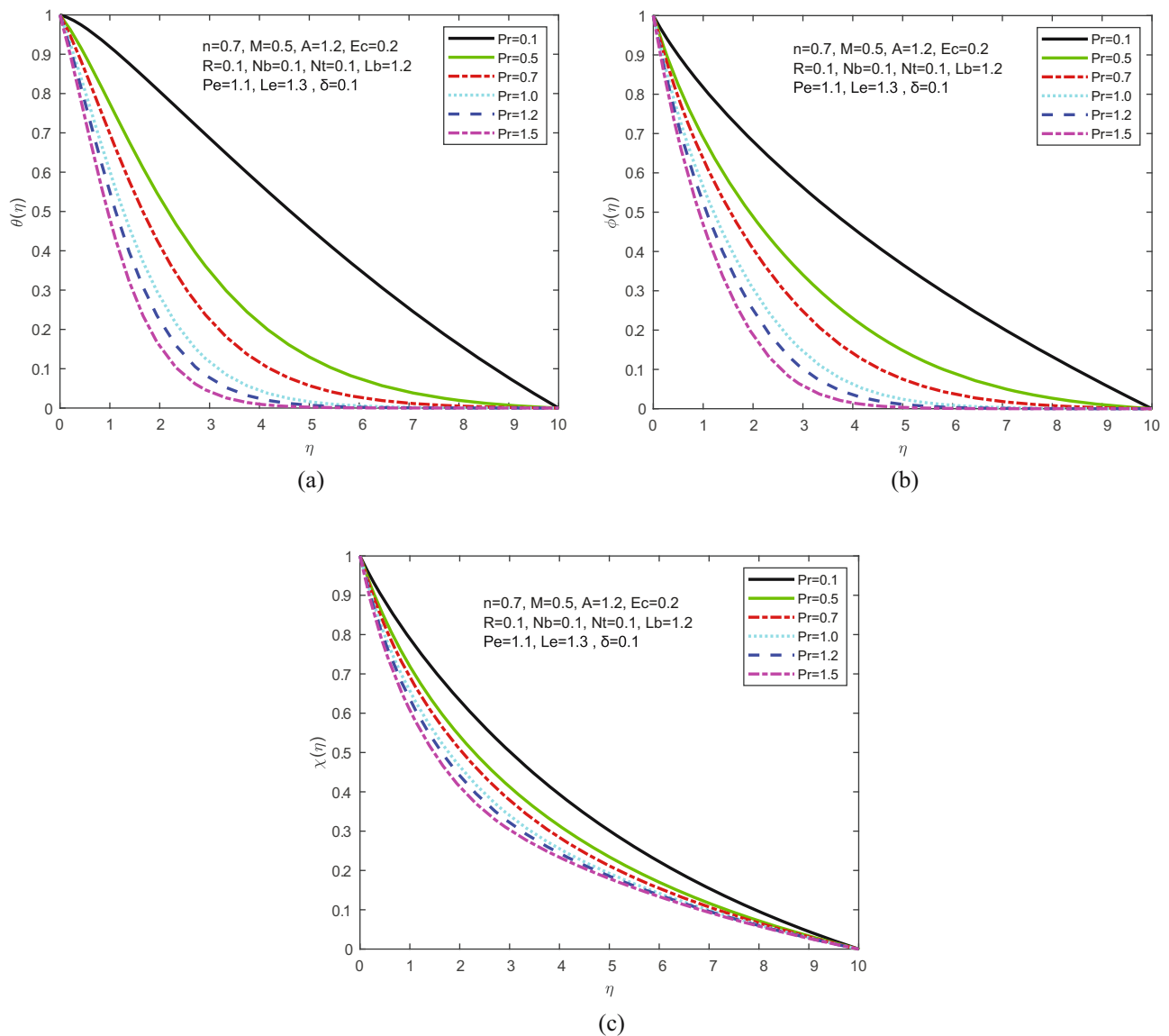


Figure 4: (a) θ vs P_r , (b) ϕ vs P_r , and (c) χ vs P_r .

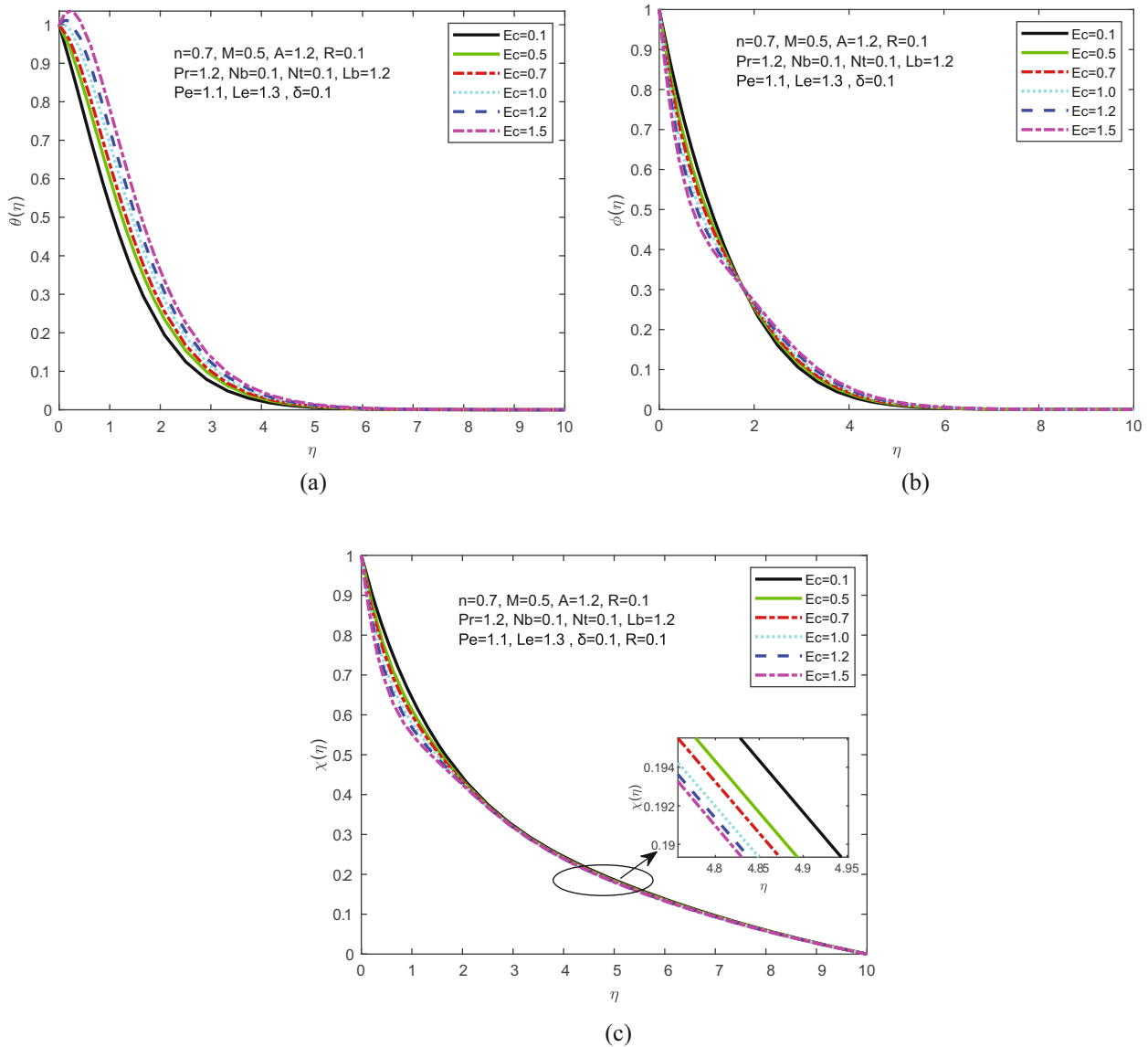


Figure 5: (a) θ vs E_c , (b) ϕ vs E_c and (c) χ vs E_c .

Eckert number (E_c) values. These figures illustrate that an elevated Eckert number leads to an increase in fluid temperature. This effect arises from the fact that E_c represents the ratio between kinetic energy and enthalpy, and as E_c increases, so does kinetic energy. Consequently, fluid particles collide more frequently, converting kinetic energy into thermal energy and resulting in higher fluid temperatures. It was observed that when E_c increased, the density of microorganism dropped. When the Eckert number increases in the fluid flow, it implies that there is a higher rate of heat transfer. Elevated temperatures resulting from increased heat transfer can be detrimental to microorganisms, leading to a drop in their density due to thermal stress.

4.5 Effect of N_b on temperature, nanoparticle concentration profile, and microorganism profiles

Figure 6(a) and (b) depict the impact of the N_b on the temperature and nanoparticle volume fraction trajectories. The temperature boundary layer was shown to be improved as N_b increased; however, the nanoparticle volume fraction boundary thickness had the reverse effect. Based on the information presented in Figure 6(b), it is evident that the Brownian motion parameter contributes to a decrease in the thickness of the concentration boundary layer, leading to a subsequent decline in the concentration. The particles travel

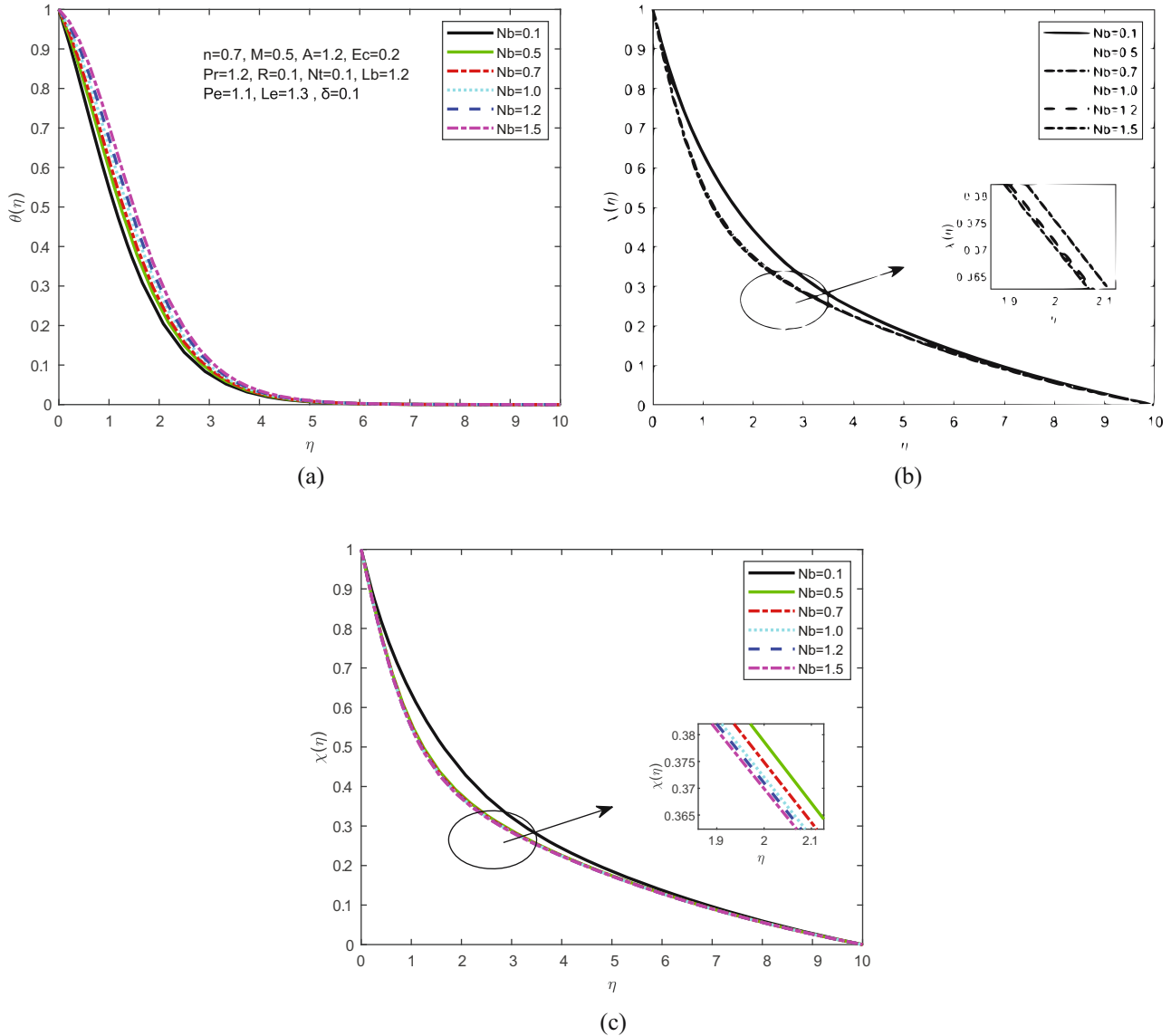


Figure 6: (a) θ vs N_b , (b) ϕ vs N_b and (c) χ vs N_b .

arbitrarily as a result of the greater Brownian motion, which is another physical explanation for the situation. This random movement results in additional heat being emitted. Hence, the formation of temperature curves was investigated. In addition, N_b has no effect on the motile microbe profiles' density and velocity.

4.6 Effect of δ on temperature, nanoparticle concentration profile, and microorganism profiles

Furthermore, the heat sink parameter (δ) represents the rate of heat removal or dissipation from a system. A higher

δ signifies more efficient cooling, leading to a lower temperature (Figure 7(a)). As shown in Figure 7(b), a higher δ indicates more efficient cooling and enhanced fluid motion, resulting in better nanoparticle dispersion and reduced concentration. An increase in the heat sink parameter (δ) leads to an increase in microorganism density profiles due to improved thermal regulation (Figure 7(c)).

4.7 Effect of L_e on nanoparticle concentration profile and microorganism profiles

By analysing Figure 8(a) and (b), it was evident that an elevated value of L_e led to a decline in concentration

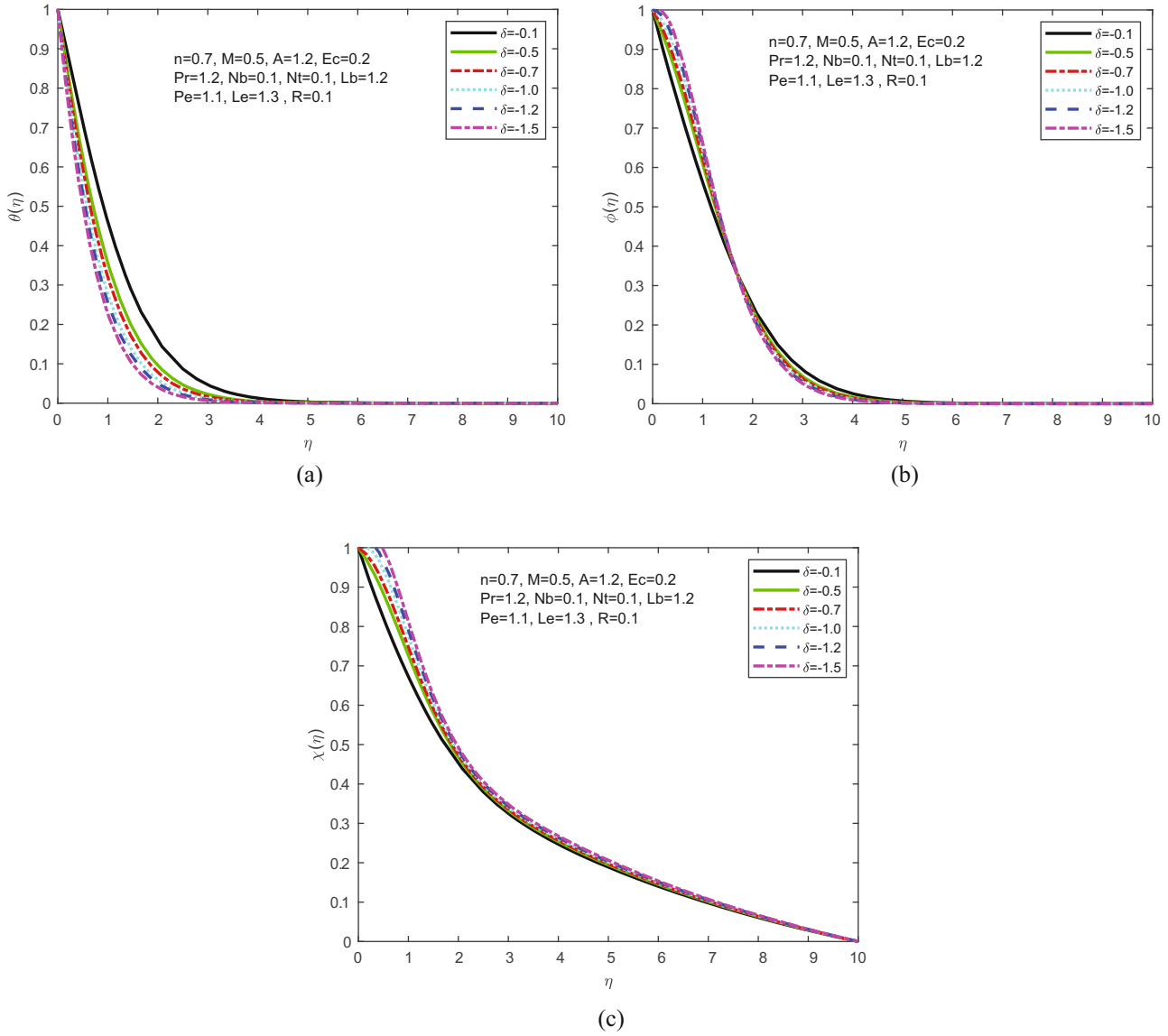


Figure 7: (a) θ vs δ , (b) ϕ vs δ , and (c) χ vs δ .

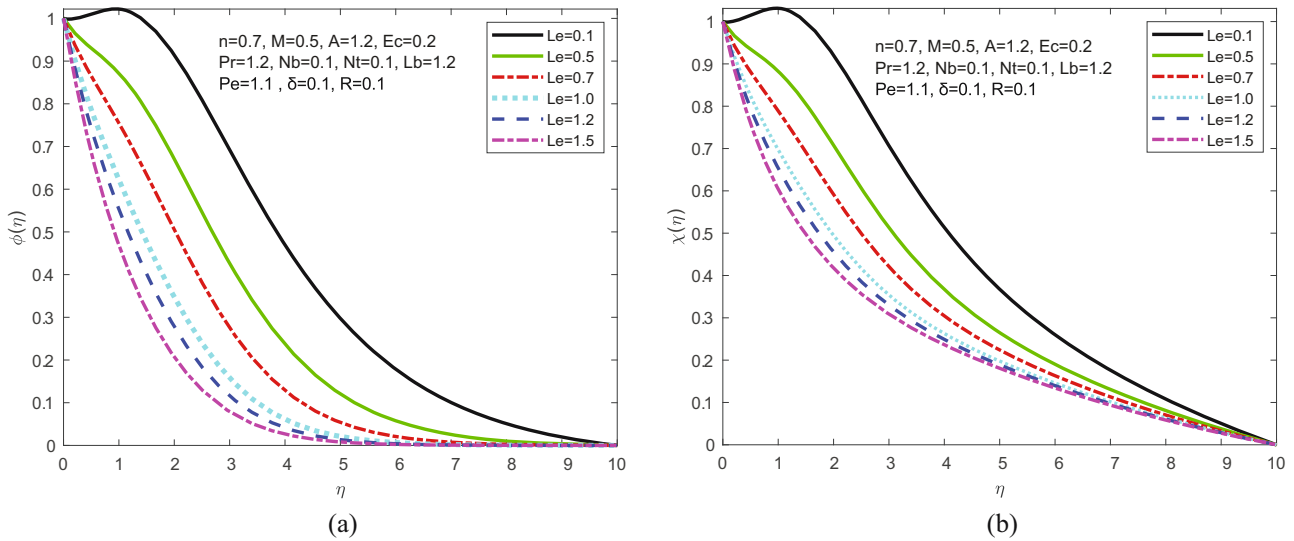


Figure 8: (a) ϕ vs Le and (b) χ vs Le .

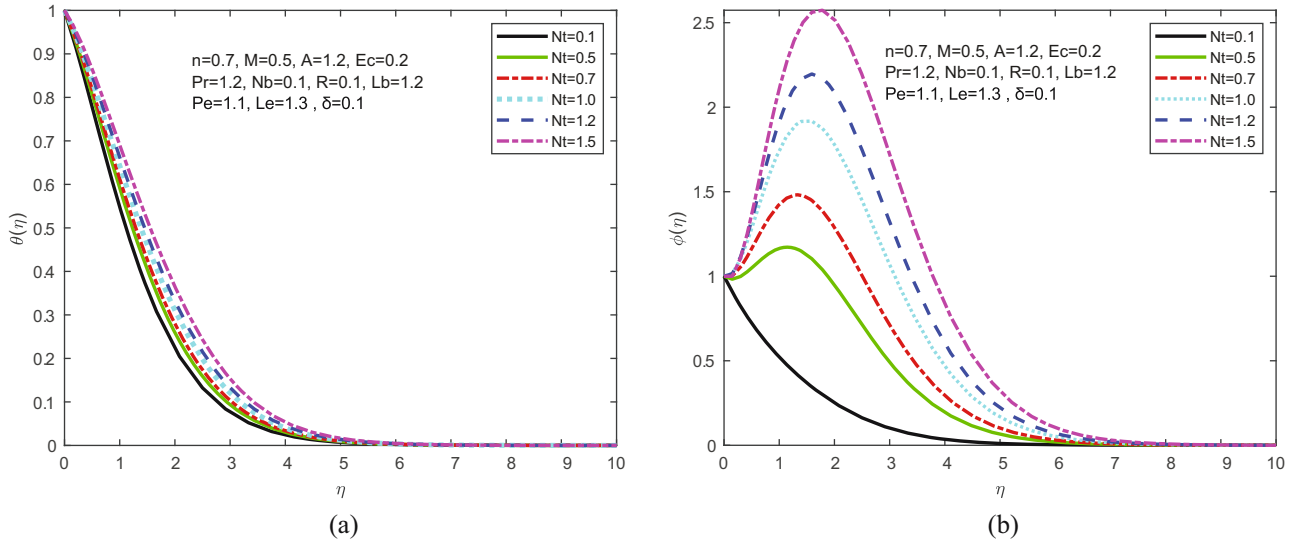


Figure 9: (a) θ vs N_t and (b) ϕ vs N_t .

profile, and on the other hand, the trend was reversed for the microorganism profile at $\eta \approx 1.2$. In the region where $\eta < 1.2$, the increase in L_e resulted in a decrease in the thickness of the microorganism boundary layers. while, for $\eta > 1.2$, the reverse trend was observed with increasing L_e . The effect of L_e on concentration is further illustrated in Figure 8(a), where it was observed that concentration decreased as L_e increased. The underlying explanation is that as L_e increases, mass diffusivity decreases, resulting in a reduction in the depth of penetration of the boundary layer.

4.8 Effect of N_t on temperature, nanoparticle concentration profile, and microorganism profiles

Variations in the thermophoresis parameter N_t are reflected in Figure 9(a) and (b), illustrating the impact on the

temperature and nanoparticle fraction curves. The results demonstrate that N_t has a significant impact on both temperature and nanoparticle fraction. This phenomenon occurs due to the increase in the thermal boundary layer density caused by the thermophoresis parameter. As observed in Figure 9(a), an increase in N_t results in an increase in temperature. The microscopic fluid particles involved in thermophoresis activities are drawn from the warm to the cold region, resulting in an improvement in temperature, thermal boundary layer, and nanoparticle volume fraction profiles. However, N_t has no impact on velocity and density curves of motile microorganism.

The local Nusselt number $[-\theta'(0)]$ for different parameters is compared with the results obtained by [15,33–35] in Table 1. It demonstrates excellent agreement between

Table 1: Comparison of local Nusselt number $-\theta'(0)$ for different values of P_r for $L_e = P_e = E_c = N_t = L_b = N_b = M = 0$

P_r	Ref. [15]	Ref. [33]	Ref. [34]	Ref. [35]	Current study
1	0.954782	0.954782	0.9547	0.954955	0.954779
1.5	1.234755				1.234823
2	1.471460		1.4714		1.471454
2.5	1.680229				1.680225
3	1.869073	1.869075	1.8691	1.869074	1.869072
5	2.500131	2.50013		2.500184	2.500139

Table 2: Comparison of Sherwood number $[-\phi'(0)]$ for different values of N_b , N_t , and P_r taking $L_e = P_e = E_c = L_b = 0$

N_b	N_t	P_r	$Sh_x \ n = 0$		$Sh_x \ n = 1$	
			Jawad <i>et al.</i> [36]	Current Study	Jawad <i>et al.</i> [36]	Current Study
0.1	0.5	1.5	-1.35820	-1.3479	-1.35938	-1.35859
0.5			-0.238811	-0.23792	-0.239002	-0.238092
1.0			-0.098888	-0.98742	-0.098954	-0.098879
1.5	0.1		0.0223188	0.022217	0.0223610	0.02228
	0.5		-1.35820	-1.35789	-1.35938	-1.35876
	1.0		-2.75366	-2.75306	-2.75610	-2.75532
	1.5		-4.14542	-4.14483	-4.14910	-4.14725
		3.0	-1.21912	-1.21754	-2.06224	-2.06212
		5.0	-1.53875	-1.53779	-2.45134	-2.45124

the current study and those obtained in the aforementioned studies.

Table 2 depicts the influence of Sherwood number due to various parameters. It is noticed that an elevation in the thermophoresis parameter causes an upward trend in local Sherwood number values, whereas an elevation in the Prandtl number results in a reduction in the Sherwood number.

5 Conclusions

In the current framework, this study investigates the MHD fluid flow of a dissipative Sisko nanofluid containing microorganisms moving along an exponentially stretched sheet. Using the *bvp4c* solver, numerical results for the converted mathematical model are calculated. The significant results are enumerated as follows:

- 1) Because of the inverse relationship between the material parameter (A) and the viscosity of the fluid. Observations from this study revealed that as the value of A increased, the fluid's viscosity decreased, resulting in a reduction in the resistance encountered during fluid motion. As a consequence, the fluid velocity increases.
- 2) Both temperature and nanoparticle fraction are significantly affected by the thermophoresis parameter (N_t). This phenomenon occurs because the increase in N_t increases the thermal boundary layer density.
- 3) When the Eckert number of a fluid increases, it indicates a higher rate of heat transfer. Microorganisms may experience a decrease in density as a consequence of thermal stress when exposed to elevated temperatures caused by increased heat transfer.
- 4) The increase in Prandtl number (P_r) resulted in a decrease in thermal diffusivity, hence causing a decline in the efficiency of energy transmission across the thermal boundary layer. The thickness of the concentration boundary layer demonstrated an increasing trend as the P_r grew.

Acknowledgments: The authors extend their appreciation to the Deanship of Scientific Research at King Khalid University (KKU) for funding this research through the Research Group Program under the grant number (R.G.P.2/453/44).

Funding information: This research is funded by the Deanship of Scientific Research at King Khalid University (KKU) for funding this research through the Research Group Program under the grant number (R.G.P.2/453/44).

Author contributions: All authors have accepted responsibility for the entire content of this manuscript and approved its submission.

Conflict of interest: The authors state no conflict of interest.

Data availability statement: All data generated or analysed during this study are included in this published article.

References

- [1] Shahid A, Huang H, Bhatti MM, Zhang L, Ellahi R. Numerical investigation on the swimming of gyrotactic microorganisms in nanofluids through porous medium over a stretched surface. *Mathematics*. 2020;8(3):380.
- [2] Choi SUS, Singer DA, Wang HP. Developments and applications of non-Newtonian flows. *ASME Fed*. 1995;66:99–105.
- [3] Buongiorno J. Convective transport in nanofluids. *J Heat Transf*. 2006;128:240–50.
- [4] Eastman JA, Choi US, Li S, Thompson LJ, Lee S. Enhanced thermal conductivity through the development of nanofluids. *MRS Proc*. 1996;457:3–11.
- [5] Sheikholeslami M, Ganji DD, Javed MY, Ellahi R. Effect of thermal radiation on magnetohydrodynamics nanofluid flow and heat transfer by means of two-phase model. *J Magn Magn Mater*. 2015;374:36–43.
- [6] Pourfattah F, Arani AAA, Babaie MR, Nguyen HM, Asadi A. On the thermal characteristics of a manifold microchannel heat sink subjected to nanofluid using two-phase flow simulation. *Int J Heat Mass Transf*. 2019;143:118518.
- [7] Asadi A, Aberoumand S, Moradikazerouni A, Pourfattah F, Żyła G, Estellé P, et al. Recent advances in preparation methods and thermophysical properties of oil-based nanofluids: A state-of-the-art review. *Powder Technol*. 2019;352:209–26.
- [8] Khan M, Shahid A, Malik MY, Salahuddin T. Thermal and concentration diffusion in Jeffery nanofluid flow over an inclined stretching sheet: A generalized Fourier's and Fick's perspective. *J Mol Liq*. 2018;251:7–14.
- [9] Asadi A, Alarifi IM, Ali V, Nguyen HM. An experimental investigation on the effects of ultrasonication time on stability and thermal conductivity of MWCNT-water nanofluid: Finding the optimum ultrasonication time. *Ultrason Sonochem*. 2019;58:104639.
- [10] Zeeshan A, Riaz A, Alzahrani F, Moqet A. Flow analysis of two-layer Nano/Johnson–Segalman fluid in a blood vessel-like tube with complex peristaltic wave. *Math Probl Eng*. 2022;2022:Article ID 5289401, 18.
- [11] Riaz A, Khan SU, Zeeshan A, Khan SU, Hassan M, Muhammad T. Thermal analysis of peristaltic flow of nanosized particles within a curved channel with second-order partial slip and porous medium. *J Therm Anal Calorim*. 2021;143:1997–2009.
- [12] Riaz A, Ellahi R, Sait SM, Muhammad T. Magnetized Jeffrey nanofluid with energy loss in between an annular part of two micro non-concentric pipes. *Energy Sources Part A: Recovery Util Environ Eff*. 2022;44(3):8314–33.
- [13] Tlili I, Nabwey HA, Ashwinkumar GP, Sandeep N. 3-D magnetohydrodynamic AA7072-AA7075/methanol hybrid nanofluid flow above an uneven thickness surface with slip effect. *Sci Rep*. 2020;10:1–13.

- [14] Chamkha AJ, Rashad AM, Alsabery AI, Abdelrahman ZMA, Nabwey HA. Impact of partial slip-on magneto-ferrofluids mixed convection flow in enclosure. *J Therm Sci Eng Appl.* 2020;12:051002.
- [15] Ferdows M, Nabwey HA, Rashad AM, Uddin MJ, Alzahrani F. Boundary layer flow of a nanofluid past a horizontal flat plate in a Darcy porous medium: A Lie group approach. *Proceedings of the Institution of Mechanical Engineers, Part C: Journal of Mechanical Engineering Science*; 2019.
- [16] Kuznetsov AV. Bio-thermal convection induced by two different species of microorganisms. *Int Commun Heat Mass Transf.* 2011;38:548–53.
- [17] Alloui Z, Nguyen TH, Bilgen E. Bioconvection of gravitactic microorganisms in a vertical cylinder. *Int Commun Heat Mass Transf.* 2005;32:739–47.
- [18] Waqas H, Hussain M, Alqarnib MS, Eid MR, Muhammad T. Numerical simulation for magnetic dipole in bioconvection flow of Jeffery nanofluid with swimming motile microorganisms. *Waves Random Complex Media.* 2021;3:1–18.
- [19] Waqas H, Imran M, Muhammad T, Salt SM, Ellahi R. Numerical investigation on bioconvection flow of Oldroyd-B nanofluid with non-linear thermal radiation and motile microorganisms over rotating disk. *J Therm Anal Calor.* 2021;145:523–39.
- [20] Uddin MJ, Kabir MN, Bég OA. Computational investigation of Stefan blowing and multiple-slip effects on buoyancy-driven bioconvection nanofluid flow with microorganisms. *Int J Heat Mass Transf.* 2016;95:116–30.
- [21] Chamkha AJ, Rashad AM, Kameswaran PK, Abdou MMM. Radiation effects on natural bioconvection flow of a nanofluid containing gyrotactic microorganisms past a vertical plate with streamwise temperature variation. *J Nanofluids.* 2017;6:587–95.
- [22] Rashad AM, Nabwey HA. Gyrotactic mixed bioconvection flow of a nanofluid past a circular cylinder with convective boundary condition. *J Taiwan Inst Chem Eng.* 2019;99:9–17.
- [23] Alwatban AM, Khan SU, Waqas H, Tlili I. Interaction of Wu's slip features in bioconvection of Eyring Powell nanoparticles with activation energy. *Process.* 2019;7:859.
- [24] Aziz A, Khan WA, Pop I. Free convection boundary layer flow past a horizontal flat plate embedded in porous medium filled by nanofluid containing gyrotactic microorganisms. *Int J Therm Sci.* 2012;56:48.
- [25] Shaw S, Sandile Motsa S, Sibanda P. Magnetic field and viscous dissipation effect on bioconvection in a permeable sphere embedded in a porous medium with a nanofluid containing gyrotactic micro-organisms. *Heat Transf – Asian Res.* 2018;47:718–34.
- [26] Rashad AM, Chamkha A, Mallikarjuna B, Abdou MMM. Mixed bioconvection flow of a nanofluid containing gyrotactic microorganisms past a vertical slender cylinder. *Front Heat Mass Transf.* 2018;10. <http://dx.doi.org/10.5098/hmt.10.21>.
- [27] Elboughdiri N, Reddy CS, Alshehri A, Eldin SM, Muhammad T, Wakif A. A passive control approach for simulating thermally enhanced Jeffery nanofluid flows nearby a sucked impermeable surface subjected to buoyancy and Lorentz forces. *Case Stud Therm Eng.* July 2023;47:103106.
- [28] Sharma J, Ahammad NA, Wakif A, Shah NA, Chung JD, Weera W. Solutal effects on thermal sensitivity of casson nanofluids with comparative investigations on Newtonian (water) and non-Newtonian (blood) base liquids. *Alex Eng J.* May 2023;71:387–400.
- [29] Wakif A. Numerical inspection of two-dimensional MHD mixed bioconvective flows of radiating Maxwell nanofluids nearby a convectively heated vertical surface. *Waves Random Complex Media.* 2023;1–22. doi: 10.1080/17455030.2023.2179853.
- [30] Puneeth V, Sarpabhusana M, Anwar MS, Aly EH, Gireesha BJ. Impact of bioconvection on the free stream flow of a pseudoplastic nanofluid past a rotating cone. *Heat Transf.* 2022;51(5):4544–61.
- [31] Jan A, Mushtaq M, Farooq U, Hussain M. Nonsimilar analysis of magnetized Sisko nanofluid flow subjected to heat generation/absorption and viscous dissipation. *J Magnetism Magnetic Mater.* 2022;564(2):170153.
- [32] Ferdows M, Zaimi K, Rashad AM, Nabwey HA. MHD bioconvection flow and heat transfer of nanofluid through an exponentially stretchable sheet. *Symmetry.* 2020;12:692.
- [33] Magyari E, Keller B. Heat and mass transfer in the boundary layers on an exponentially stretching continuous surface. *J Phys D Appl Phys.* 1999;32:577–85.
- [34] Biliana B, Nazar R. Numerical solution of the boundary layer flow over an exponentially stretching sheet with thermal radiation. *Eur J Sci Res.* 2009;33:710–7.
- [35] Loganathan P, Vimala C. MHD flow of nanofluids over an exponentially stretching sheet embedded in a stratified medium with suction and radiation effects. *J Appl Fluid Mech.* 2015;8:85–93.
- [36] Jawad M, Shah Z, Islam S, Khan W, Khan AZ. Nanofluid thin film flow of Sisko fluid and variable heat transfer over an unsteady stretching surface with external magnetic field. *J Algorithms Comput Technol.* 2019;1748301819832456.



GOVERNMENT OF INDIA
Ministry of Science & Technology
Department of Science & Technology
DST/TDT/WMT/End of life Vehicles/2021/01 (G)/2
(Technology Development Transfer)

Technology Bhawan, New Delhi

Dated: 31/05/2023

Sanction Order

Subject: Financial assistance for the project entitled “Commercial utilization of end of life tyres to produce high value chemicals and fuel using integrated technology” submitted by **Dr. Abhishek Sharma, MANIPAL UNIVERSITY JAIPUR, JAIPUR, MANIPAL UNIVERSITY JAIPUR, VPO DEHMI KALAN, JAIPUR 303007., 303007** Release of the first installment regarding

Sanction of the President is hereby accorded to the approval to the above mention project at a total cost of **Rs. 92,75,728/- (Rupees Ninety Two Lakh Seventy Five Thousand Seven Hundred Twenty Eight only)** for a duration of **3 Years Days**. The detailed breakup of the grant for General as well as Capital Components are given below:-

General Component : ₹ 76,75,728/-

Capital Component : ₹ 16,00,000/-

Total DST Contribution : ₹ 2336760.00/-

Total Host Institute/Industry/State Contribution : ₹ 0.00/-

(All Institute) Budget Summary (in Rs.)				
Items	Year-1	Year-2	Year-3	Total
1- Non-Recurring				
Carbon disper grader-for analysis of carbon dispersion - 1	0	1600000	0	1600000
Subtotal (Capital)	0	1600000	0	1600000
2- Recurring				
Project Staff	1551480	1551480	1669080	4772040
Junior Research Fellow (JRF)-1 (01 JRF @ 31,000 + 18% HRA for 2 years and SRF @ 35,000 + 18% HRA for 3rd Year)	438960	438960	495600	1373520
Junior Research Fellow (JRF)-1 (01 JRF @ 31,000 + 27% HRA for 2 years and SRF @ 35,000 + 27% HRA)	472440	472440	533400	1478280
Senior Project Associate -1 (SPA 1 no. Rs.42,000/- + 27% HRA for 3 years)	640080	640080	640080	1920240
Consumables	215000	280000	170000	665000
Contingency	80000	80000	80000	240000
Travel	100000	100000	100000	300000
Overhead	120624	165824	162240	448688
Other Cost DST-	20000	500000	500000	1020000
Other Cost DST-	80000	100000	50000	230000
Subtotal (General)	2167104	2777304	2731320	7675728
Total Contribution (Cap.+ Gen.)	0	0	0	
Total Project Cost (Cap.+ Gen.)	2167104	4377304	2731320	9275728

R. Kasilingam

Items	Budget Summary (in Rs.)			
	Year-1	Year-2	Year-3	Total
1- Non-Recurring				
Carbon disper grader-for analysis of carbon dispersion - 1	0	1600000	0	1600000
Subtotal (Capital)	0	1600000	0	1600000
2- Recurring				
Project Staff	1112520	1112520	1173480	3398520
Junior Research Fellow (JRF)-1(01 JRF @ 31,000 + 27% HRA for 2 years and SRF @ 35,000 + 27% HRA)	472440	472440	533400	1478280
Senior Project Associate -1(SPA 1 no. Rs.42,000/- + 27% HRA for 3 years)	640080	640080	640080	1920240
Consumables	100000	100000	170000	370000
Contingency	50000	50000	50000	150000
Travel	50000	50000	50000	150000
Overhead	64624	85824	100000	250448
Any Other (Other Cost DST)-	20000	500000	500000	1020000
Subtotal (General)	1397144	1898344	2043480	5338968
Total Project Cost (Cap.+ Gen.)	1397144	3498344	2043480	6938968

2 MANIPAL UNIVERSITY JAIPUR, JAIPUR (Dr. Abhishek Sharma)

Items	Budget Summary (in Rs.)			
	Year-1	Year-2	Year-3	Total
1- Non-Recurring				
Subtotal (Capital)	0	0	0	
2- Recurring				
Project Staff	438960	438960	495600	1373520
Junior Research Fellow (JRF)-1(01 JRF @ 31,000 + 18% HRA for 2 years and SRF @ 35,000 + 18% HRA for 3rd Year)	438960	438960	495600	1373520
Consumables	115000	180000	0	295000
Contingency	30000	30000	30000	90000
Travel	50000	50000	50000	150000
Overhead	56000	80000	62240	198240
Any Other (Other Cost DST)-	80000	100000	50000	230000
Subtotal (General)	769960	878960	687840	2336760
Total Project Cost (Cap.+ Gen.)	769960	878960	687840	2336760

2. The sanction of the President is also accorded to the release of Rs. 7,69,960/- (Rupees Seven Lakh Sixty Nine Thousand Nine Hundred Sixty only) to the "Director/Registrar/Principal/Controller/Comptroller, MANIPAL UNIVERSITY JAIPUR, JAIPUR" being the first installment of grant as mentioned above table under "General Component" for the above mentioned project.

3. The expenditure involved is debitable to Demand No. 89, Department of Science & Technology for the year 2023-24:

3425	Other Scientific Research(Major Head)
3425.60	Others : (Sub-Major Head)
3425.60.200	Assistance to Other Scientific Bodies(Minor Head)
3425.60.200.70	Innovation,Technology Development and Deployment

R. Khan

3425.60.200.70.00	Detailed Head
3425.60.200.70.00.31	Grants-in-aid General
	(Previous: 3425.60.200.26.01.31)

4. The amount of Rs. 7,69,960/- (Rupees Seven Lakh Sixty Nine Thousand Nine Hundred Sixty only) will be drawn by DDO, DST and disbursed to the "CNA account of Autonomous body SERB in respect of Innovation, Technology Development and Deployment Scheme".

Name of A/C Holder	Innovation Technology Development and Deployment
Bank A/C No	349902010051240
Name of the Bank & branch	Union Bank of India, Safdarjang Enclave - New Delhi
RTGS/IFSC code	UBIN0534994

5. The amount of Rs. 769960/- (Rupees Seven Lakh Sixty Nine Thousand Nine Hundred Sixty only) will be drawn by the "CNA account of Autonomous body SERB and will be disbursed to the Director/Registrar/Principal/Controller/Comptroller, MANIPAL UNIVERSITY JAIPUR, JAIPUR . The bank details for electronic transfer of funds through RTGS are given below:-

Name of A/C Holder	Manipal University Jaipur
Bank A/C No	219012010000703
Name of the Bank & branch	Union Bank of India
RTGS/IFSC code	UBIN0821900

6. As per Rule 234 of GFR 2017, the sanction has been entered at S. No 37. in the register of grants maintained in the **Technology Development Transfer** for the scheme **Waste Management Technologies** .

7. This issues with the concurrence of IFD vide their Concurrence Dy. No. **IFD/C/III/310523/31/00613** dated **31/05/2023**.

8. The GI will keep all the funds received in the Central Nodal Account only and shall not transfer the funds to any other account or not divert the same to Fixed Deposits/ Flexi-Account/ Multi-Option Deposit Account/ Corporate Liquid Term Deposit (CLTD) account etc. The funds released to GI shall not be parked in bank account of any other agency.

9. The GI will ensure the compliance of OM. No. F. No. **1/(18)/PFMS/FCD/2021** dated **March 9, 2022** of Department of Expenditure, Ministry of Finance.

10. This sanction order is subject to the **Terms & Conditions** as annexed .



Dr. Krishna Kanth Pulicherla
(Scientist - 'E')
kkpulicherla.dst@gov.in

To,
The Pay & Accounts Officer,
Department of Science & Technology,
New Delhi – 110 016.

Copy of information and necessary action to:

1. The Principal Director of Audit, Scientific Department, IIIRD floor, AGCR Building, I.P. Estate, New Delhi.
2. The Financial Advisor, Integrated Finance Division, Technology Bhavan, New Mehrauli Road, Block C, Qutab Institutional Area, New Delhi, Delhi 110016
3. The Internal Audit Wing, Department of Science & Technology, Technology Bhavan, New Mehrauli Road, Block C, Qutab Institutional Area, New Delhi, Delhi 110016
4. Drawing and Disbursing Officer, DST, Cash Section. (two copies)
5. Dr. Abhishek Sharma, Professor, Chemical Engineering, MANIPAL UNIVERSITY JAIPUR, JAIPUR, Jaipur, Jaipur, Rajasthan - 303007
6. Dr. Rajkumar Kasilingam, Director, Material Research Center, INDIAN RUBBER MANUFACTURERS RESEARCH ASSOCIATION, Thane, Thane, Maharashtra - 400604
7. The Director/Registrar/Principal/Controller/Comptroller, INDIAN RUBBER MANUFACTURERS RESEARCH ASSOCIATION, Thane, Thane, Maharashtra - 400604

8. Dr. Anees Ahmed Yunus Khan, Assistant Professor, MANIPAL UNIVERSITY JAIPUR, JAIPUR, Jaipur Rajasthan-303007
9. Dr. Debdipta Basu, Assistant Director, INDIAN RUBBER MANUFACTURERS RESEARCH ASSOCIATION, Maharashtra-400604
10. The Director/ Registrar/ Principal/ Controller/Comptroller, INDIAN RUBBER MANUFACTURERS RESEARCH ASSOCIATION, Maharashtra-400604
11. The Director/ Registrar/ Principal/ Controller/Comptroller, MANIPAL UNIVERSITY JAIPUR, JAIPUR, Jaipur Rajasthan-303007
12. Secretary, SERB, New Delhi (for allocation of limits to implementing agency)
13. Head (Technology Development Transfer) DST
14. Sanction folder (Technology Development Transfer)



Dr. Krishna Kanth Pulicherla,
Scientist-E
kkpulicherla.dst@gov.in



GOVERNMENT OF INDIA
Ministry of Science & Technology
Department of Science & Technology
DST/TDT/WMT/End of life Vehicles/2021/01 (G)/2
Terms & Conditions

1. The grantee organization will furnish to the Department of Science & Technology, financial year wise Utilization Certificate (UC) in the proforma prescribed as per GFR 2017 and audited statement of expenditure (SE) along with up to date progress report (Vis-a-Vis Target Vs-Achievement) at the end of each financial year duly reflecting the interest earned / accrued on the grant received under the project. This is also subject to the condition of submission of the final statement of expenditure, utilization certificate and project completion report within one year from the scheduled date of completion of the project.
2. The grantee organization will have to enter & upload the Utilization Certificate in the PFMS portal besides sending it in physical form to this Division. The subsequent/final installment will be released only after confirmation of the acceptance of the UC by the Division and entry of previous Utilization Certificate in the PFMS.
3. If the grant has been released under capital head through separate sanction order under the same project for purchase of equipment(s), separate SE/UC has to be furnished for the released Capital head grant.
4. The grant-in-aid being released is subject to the condition that:-
 - a) A transparent procurement procedure in line with Provisions of General Financial Rules 2017 will be followed by the Institute/Organization under the appropriate rules of grantee organization while procuring capital assets sanctioned for the above mentioned project and a certificate to this effect will be submitted by the Grantee organization immediately on receipt of the grant.
 - b) While submitting Utilization Certificate/Statement of Expenditure, the organization has to ensure submission of supporting documentary evidences with regard of the purchase of equipment/capital assets as per the provisions of GFR 2017. Subsequent release of grants under the project shall be considered only on receipt of the said documents.
5. As per the GFR 2017 Rule 230 (8) the Grantee Institute should ensure that all the interests or other earnings against Grant-in-Aid or advances (other than reimbursement) released to any Grantee institution should be mandatorily remitted to the Consolidated Fund of India immediately after finalization of the accounts. Such advances will not be allowed to be adjusted against future releases.
6. As per the GFR 2017 Rule 230 (17) "the Grantee Institute should agree to make reservations for Scheduled Castes and Scheduled Tribes or OBC in the posts or services under its control on the lines indicated by the Government of India"
7. The grantee organization will maintain separate audited account for the project and the entire amount of grant will be kept in an interest bearing bank account. For Grants released during F.Y. 2017-18 and onwards, all interests and other earnings against released Grant shall be remitted to Consolidated Fund of India (through Non-Tax Receipt Portal (NTRP), i.e. www.bharatkosh.gov.in), immediately after finalization of accounts, as it shall not be adjusted towards future release of Grant. A certificate to this effect shall have to be submitted along with Statement of Expenditure/ Utilization Certificate for considering subsequent release of Grant/ Closure of Project accounts.
8. DST reserves sole rights on the assets created out of grants. Assets acquired wholly or substantially out of government grants (except those declared as obsolete and unserviceable or condemned in accordance with the procedure laid down in GFR 2017), shall not be disposed of without obtaining the prior approval of DST.
9. The account of the grantee organization shall be open to inspection by the sanctioning authority and audit (both by C&AG of India and Internal Audit by the Principal Accounts Office of the DST), whenever the organization is called upon to do so, as laid down under Rule 236(1) of General Financial Rules 2017.
10. Due acknowledgement of technical support / financial assistance resulting from this project grant should mandatorily be highlighted by the grantee organization in bold letters in all publication / media release as well as in the opening paragraphs of their Annual Reports during and after the completion of the project.
11. Failure to comply with the terms and conditions of the Bond will entail full refund with interest in terms of Rule 231 (2) of GFR 2017.
12. It is mandatory to use EAT module in PFMS, failing which no further funds shall be released.
13. Goods (Consumable/Equipment) available in GeM portal are to be procured mandatorily online through GeM only as per the provisions of Rule 149 of GFR.
14. The Grantee Institute should follow Global Tendering Enquiry (GTE) conditions as per Department of Expenditure ID Note No:4/1/2021-PPD dated 10.09.2021.

15. If One time assistance or non-recurring grant as Grant-in-Aid for Rs. 10.00 lakhs to Rs. 50.00 lakhs, it should be included in the Annual Report of the Institute.

16. The Grantee Institute must ensure any other provisions of GFR-2017 and guidelines/amendments issued from Govt. of India from time to time.



भारत सरकार
विज्ञान और प्रौद्योगिकी मंत्रालय
विज्ञान और प्रौद्योगिकी विभाग

DST/TDT/WMT/End of life Vehicles/2021/01 (G)/2

निबंधन और शर्तें

1. अनुदानग्राही संस्थान प्रत्येक वित्त वर्ष के अंत में इस परियोजना के अंतर्गत प्राप्त अनुदान पर अर्जित/प्रोद्भूत ब्याज को विधिवत रूप से दर्शाते हुए अद्यतन प्रगति रिपोर्ट (लक्ष्य बनाम उपलब्धि) के साथ जीएफआर 2017 में विनिर्दिष्ट प्ररूप में वित्तीय वर्ष-वार उपयोग प्रमाण पत्र (यूसी) और व्यय का लेखापरीक्षित विवरण (एसई) विज्ञान और प्रौद्योगिकी विभाग को प्रस्तुत करेगा। यह परियोजना की समाप्ति की निर्धारित तारीख से एक वर्ष भीतर व्यय का अंतिम विवरण, उपयोग प्रमाण-पत्र और परियोजना समाप्ति रिपोर्ट प्रस्तुत करने की शर्त के भी अधधीन है।
2. अनुदानग्राही संस्थान को उपयोग प्रमाण-पत्र इस प्रभाग में भौतिक रूप में भेजने के साथ-साथ पीएफएमएस पोर्टल पर प्रविष्ट और अपलोड करना होगा। अनुवर्ती/अंतिम किस्त प्रभाग द्वारा यूसी की स्वीकृति की पुष्टि और पीएफएमएस में पूर्ववर्ती उपयोग प्रमाण-पत्र की प्रविष्टि के बाद ही जारी की जाएगी।
3. यदि अनुदान एक ही परियोजना के अंतर्गत उपस्कर (रों) की खरीद के लिए पृथक संस्वीकृति आदेश के माध्यम से पूंजी-शीर्ष के अंतर्गत जारी किया गया है तो जारी किया गया पूंजी-शीर्ष अनुदान के लिए पृथक एसई/यूसी प्रस्तुत करना होगा।
4. जारी किया जा रहा सहायता अनुदान निम्नलिखित शर्तों के अधधीन है-
 - क) उपर्युक्त परियोजना के लिए संस्वीकृत पूंजी आस्तियों की खरीद करते समय अनुदानग्राही संस्थान के उचित नियमों के तहत संस्थान/संगठन द्वारा सामान्य वित्तीय नियमावली 2017 के उपबंधों के अनुरूप पारदर्शी खरीद प्रक्रिया का अनुपालन किया जाए और अनुदान प्राप्ति पर तुरंत प्रभाव से अनुदानग्राही संगठन द्वारा इस आशय का प्रमाण-पत्र प्रस्तुत किया जाए।
 - ख) उपयोग प्रमाण-पत्र/ व्यय विवरण प्रस्तुत करते समय, संगठन को जीएफआर 2017 के उपबंधों के अनुसरण में उपस्कर/पूंजी आस्तियों की खरीद के संबंध में संबन्धित दस्तावेज़-साक्ष्य प्रस्तुत करना सुनिश्चित करना होता है।
5. जीएफआर नियमावली 2017 के नियम 230 (8) के अनुसार अनुदानग्राही संस्थान को सुनिश्चित करना चाहिए कि किसी भी अनुदानग्राही संस्थान को जारी किए गए सहायता अनुदान या अग्रिम (प्रतिपूर्ति से भिन्न) पर प्राप्त समस्त प्रकार के ब्याज या अन्य आय को लेखों को अंतिम रूप दिए जाने के तुरंत बाद भारतीय समेकित निधि में अनिवार्य रूप से विप्रेषित किया जाए। ऐसे अग्रिमों को भविष्य में जारी की जाने वाली निधियों में समायोजित करने की अनुमति नहीं दी जाएगी।
6. जीएफआर नियमावली 2017 के नियम 230 (17) के अनुसार, “अनुदानग्राही संस्थान को भारत सरकार के निर्देशानुसार अपने नियंत्रणाधीन पदों या सेवाओं में अनुसूचित जाति या अनुसूचित जनजाति या ओबीसी के लिए आरक्षण रखने पर सहमत होना चाहिए।”
7. अनुदानग्राही संस्थान परियोजना का पृथक परीक्षित लेखा रखेगा और अनुदान की समस्त राशि बैंक खाते में सब्याज रखी जाएगी। वित्तीय वर्ष 2017-18 के दौरान और उसके बाद जारी अनुदान के लिए, अनुदान के लिए सभी प्रकार के ब्याज या अन्य आय ऐसे लेखों को अंतिम रूप दिए जाने के तुरंत बाद भारतीय समेकित निधि में (गैर कर प्राप्ति पोर्टल (एनटीआरपी) अर्थात् www.bharatkosh.gov.in के माध्यम से) विप्रेषित की जाएगी, क्योंकि यह राशि भविष्य में जारी की जाने वाली राशि में समायोजित नहीं की जाएगी। अनुवर्ती अनुदान के निर्गम/ परियोजना खाते को बंद करने पर विचार किए जाने के लिए, व्यय विवरण/ उपयोग प्रमाण-पत्र के साथ इस आशय का प्रमाण पत्र प्रस्तुत करना होगा।
8. डीएसटी, अनुदान से सृजित परिसंपत्तियों पर एकमात्र सुरक्षित अधिकार रखता है। सरकारी अनुदानों से पूरी तरह से या पर्याप्त रूप से अर्जित संपत्ति (जीएफआर 2017 में निर्धारित प्रक्रिया के अनुसार अप्रचलित और अनुप्रयोज्य, अनुपयोगी घोषित अनुदानों से इतर), का निपटारा डीएसटी का पूर्व अनुमोदन प्राप्त किए बिना नहीं किया जाएगा।
9. जैसा कि सामान्य वित्तीय नियमावली 2017 के नियम 236 (1) के तहत निर्धारित किया गया है, अनुदानग्राही संगठन का लेखा स्वीकृति प्रदाता प्राधिकारी और लेखा परीक्षक (भारत के नियंत्रक एवं महालेखापरीक्षक और डीएसटी के प्रधान लेखा कार्यालय दोनों द्वारा आंतरिक लेखा परीक्षा) द्वारा निरीक्षण किए जाने, जब भी संगठन को ऐसा करने के लिए कहा जाता है, हेतु अभिगम्य होगा।

10. इस परियोजना अनुदान से प्राप्त तकनीकी सहायता/वित्तीय सहायता की उचित पावती को अनुदानग्राही संगठन द्वारा सभी प्रकाशनों/मिडिया प्रकाशनी में मोटे अक्षरों में और परियोजना के पूरा होने के दौरान और तदुपरांत उनकी वार्षिक रिपोर्टों के शुरुआती पैराग्राफों में अनिवार्य रूप से दिखाया किया जाना चाहिए।

11. बॉन्ड के नियमों और शर्तों का पालन करने में असफल होने पर जीएफआर 2017 के नियम 231 (2) के अनुसार पूरी राशि सब्याज वापस करनी होगी।

12. पीएफएमएस में ईएटी मॉड्यूल का उपयोग करना अनिवार्य है, ऐसा न करने पर अन्य कोई भी आगामी निधि जारी नहीं की जाएगी।

13. जीएफआर के नियम 149 के उपबंधों के अनुसार जीईएम पोर्टल पर उपलब्ध वस्तुओं (उपभोज्य वस्तु /उपस्कर) का अनिवार्यतया आनं लाइन प्रापण जैम (जीईएम) ही के माध्यम से किया जाना है।

14. अनुदान ग्राही संस्थान को व्यय विभाग के आईडी नोट संख्या: 4/1/2021-पीपीडी दिनांक 10.09.2021 के अनुसार वैश्विक निविदाकरण जांच-पड़ताल (जीटीई) नियमों का पालन करना चाहिए।

15. यदि एकबारगी सहायता या गैर-आवर्ती अनुदान 10.00 लाख रुपये से 50.00 लाख रुपये के सहायता अनुदान का हो तो इसे संस्थान की वार्षिक रिपोर्ट में दर्ज किया जाना चाहिए।

16. अनुदान ग्राही संस्थान को जीएफआर-2017 के किसी भी अन्य उपबंध और समय-समय पर भारत सरकार द्वारा जारी दिशा-निर्देश/संशोधन का अनुपालन सुनिश्चित करना चाहिए।



Research papers

Expanded waste glass/methyl palmitate/carbon nanofibers as effective shape stabilized and thermal enhanced composite phase change material for thermal energy storage

P. Singh^a, R.K. Sharma^a , Gökhan Hekimoğlu^b , Ahmet Sarı^{b,c}, Osman Gencel^d, V.V. Tyagi^e

[Show more](#) [Share](#) [Cite](#) <https://doi.org/10.1016/j.est.2023.107205> [Get rights and content](#)

Highlights

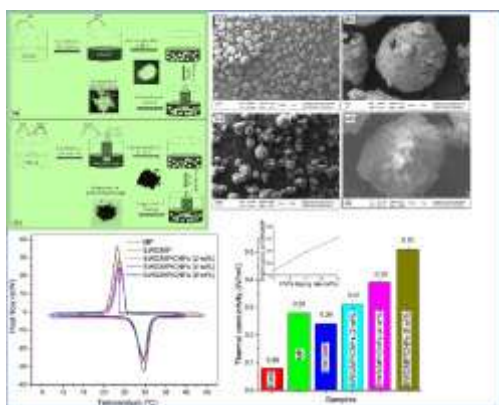
- The performance of shape stabilized PCMs with expanded waste glass and carbon nanofibers was investigated.
- Shape stabilized composites were prepared by impregnation of MP with EWG and CNFs.
- The melting temperature is in the range of 26.61-27.12°C. and melting enthalpies ranges from 96.1-96.7 J/g.
- The TGA outcomes illustrated that FSCPCM and TE-FSCPCMs had well thermal resistance.

- Thermal conductivities of FSCPCM were increased apparently especially with CNF (8 wt.%) incorporation.

Abstract

A prominent choice for phase change materials (PCMs) for passive solar thermoregulation is fatty acids because of their many beneficial characteristics for latent heat thermal energy storage (LHTES). Their low thermal conductivity and additional storage container requirements to prevent leaks during heating time, however, severely restrict their range of applications. In order to address these issues with methyl palmitate (MP) as a phase transition material, it was first doped with carbon nanofibers (CNFs) after being incorporated with expanded waste glass (EWG) using the melting/blending procedure. The SEM, XRD, FTIR, DSC, and TGA techniques were used to investigate the thermal and chemical performance of composite phase change materials (CPCMs). The leak-proof composite phase change materials (LPCPCM) and thermal enhanced shape stabilized composite phase change materials (TE-SSCPCMs) had latent energy between 96.1 and 96.7 J/g and melting temperatures between 26.61 and 27.12 °C. Doping 2, 4, and 8 wt% of CNFs into CPCMs, conductivity got enhanced by 29.2, 62.5, and 112.5% respectively, due to which, the TE-SSCPCM's charging/discharging periods were significantly shortened without changing their LHTES properties much. Further, evidence came from the thermal cycling test, TGA results, and the impressive thermal reliability, LHTES cycle performance, and chemical compatibility of all manufactured composites.

Graphical abstract



[Download: Download high-res image \(299KB\)](#)

[Download: Download full-size image](#)

Introduction

Due to the fact that about one-third of the world's total energy consumption occurs in buildings [1], the upgrade of resource efficiency has emerged as one of the energy technologist's primary concerns. In this context, thermal energy storage (TES) has emerged as a viable alternative methodology for addressing technology and environmental pollution issues within the last three decades [2]. PCMs and LPCPCMs with good thermal durability and performance have been deemed desirable TES components with energy storing and releasing capacity [3], [4]. The focus of several energy studies in recent years has shifted toward the creation of cutting-edge PCMs and LPCPCMs as well as the examination of their temperature control characteristics [5], [6], [7], [8], [9]. It has been found that fatty acids perform well for solar passive LHTES purposes as PCMs due to their desirable and readily available LHTES features [10], [11]. Nevertheless, direct functioning of these organic PCMs permits chemical interlinkage with the surroundings and also results in a leakage issue in solid to liquid state transition. They were enclosed in macro or micro configurations to avoid this complexity [12], [13]. However, PCM encapsulations are significantly more difficult and expensive, resulting in generally poor LHTES capacity. Combining porous, lightweight, and less costly building materials with LPCPCMs that are resistant to leakage is an alternative method. Moreover, fatty acids have a disadvantage of poor thermal conductivity (between 0.15 and 0.25 W/m-K), which significantly affects their rates of phase change (heat charging/discharging) [14]. Furthermore, their incorporation into stabilized clay-based porous building matrices can result in a significant decline in conductivity. Thus, doping this type of LPCPCM with a high thermal conductive material is an effective way for boosting its thermal conductivity. Materials based on carbon such as carbon nanofibers (CNFs) [15], [16], [17], carbon nanotubes (CNTs) [18], [19], expanded graphite [20], graphite nanoplatelets (GNPs) [21], and graphene oxide [22] have primarily been used to increase the thermal conductivity of organic PCMs. CNF is a material that looks and acts like graphite. It is made by carbonating and graphitizing organic fibers. At the atomic level, each CNF is made up of thousands of small fibers that are stacked on top of each other. The carbon atoms in each fiber are organized in a hexagonal pattern. CNF had nearly the same thermal conductivity, resistance to corrosion, durability, and ability to heat energy conversion as carbon nanotubes and graphene, but it was cheaper [23], [24]. So, CNF has gotten a lot of attention as an additive to improve the properties of composite materials [25], [26], [27]. The purpose of this research is to investigate the effect of CNFs on thermal outcomes of LPCPCMs. CNF is an inorganic carbon fiber compound that can have a thermal conductivity up to 900 W/m-K in the same plane. The CNF's percolating configuration worked as a filler with significant thermal conductivity [28]. Huang et al. [16] used the 5wt% CNF in cetyl alcohol/HDPE composite which increased the thermal conductivity of composite by 1.25 times as compared to original composite thermal conductivity. Liu et al. [17] reported that the thermal conductivity of PEG/SiO₂ composite was increased by 73% due to the incorporation of

3wt% CNFs. Zhang et al. [29] boosted the thermal conductivity of erythritol as about 407.8% by incorporating CNFs by 10wt% mass fraction. As distinct from the aforementioned literature, our aim is to develop a way to both alleviate the leakage issue and the poor thermal conductivity limitation of MP organic PCM without significantly diminishing its LHTES capability. EWG was chosen as an appropriate supporting material to eliminate the PCM's seepage problem due to its numerous positive qualities, such as its high absorption ratio, excellent thermal stability, good interfacial bonding, and long-term economic and ecological friendliness [30]. In the initial stage of the present research, MP, an organic PCM, was integrated into EWG by melting/blending process to create a new LPCPCM. Considering the poor thermal conductivities of the base materials of LPCPCM (0.28 and 0.08 W/m-K for MP and EWG, respectively), the thermal conductivity of LPCPCM was significantly enhanced by loading with CNFs at mass fractions of 2.0, 4.0, and 8.0wt% in the subsequent phase. Using SEM, XRD, and FT-IR, the chemical and morphological features of the produced LPCPCM and TE-SSCPCMs were characterized. The impact of CNFs loading on the thermal conductivities, LHTES characteristics, thermal compatibility, and energy charging and discharging durations of manufactured LPCPCM was studied. A comprehensive study on EWG/MP/CNFs composite has not yet been published, as far as we are aware.

Access through your organization

Check access to the full text by signing in through your organization.

Access through [Manipal University Jaipur](#)

Section snippets

Materials

Methyl palmitate (MP) was procured by Sigma-Aldrich company. Ethanol used as solvent was provided by Merck Company. Expanded waste glass (EWG) was purchased from Agrekal Company (Antalya-Turkey). Moreover, Carbon nanofibers (CNFs) in this work were purchased from Sigma-Aldrich Company. ...

Preparation of LPCPCM and TE-SSCPCM

By using the melting/blending method, the leak proof composite PCMs (LPCPCMs), EWG/MP and EWG/MP/CNFs were created in shape stabilized form. Following the procedure shown in Fig. 1, EWG/MP was prepared as a shape ...

SEM results of the prepared LPCPCM and TE-SSCPCM

Fig. 3(a-e) depicts SEM images of the EWG, FSCPCM, and TE-FSCPCM-3, which is representative of the other TE-FSCPCMs. As demonstrated in Fig. 3(a, b), the surfaces of EWG are composed of agglomerates of amorphous particles. However, these molecules have an interlinked phase picture, some of them feature holes and fissures that allow PCM molecules to be retained.

The PCM was kept uniformly within the perforations on the surface of the EWG (Fig. 3(c, d)). The CNFs with 8wt% introduced uniformly ...

Conclusions

To concurrently address the leakage problem and low thermal conductivity of MP, it was initially kept in EWG using the melting and blending technique and then loaded with CNFs. The morphology, physicochemical suitability, LHTES characteristics, conductivities, cycle TEST performances, and thermal reliabilities of LPCPCMs and TE-SSCPCMs were analyzed. The following inferences can be taken from the findings:

1. The maximum amount of MP that EWG was able to absorb was 40% by weight. Shape-stabilized ...

...

CRedit authorship contribution statement

P. Singh- Writing - Original draft, Formal analysis

R. K. Sharma- Project administration, Formal analysis

Gökhan Hekimoğlu- Validation

Ahmet Sarı- Visualization

Osman Gencel- Formal analysis

V. V. Tyagi- review & editing ...

Declaration of competing interest

The authors declare that they have no known competing financial interests or personal relationships that could have appeared to influence the work reported in this paper. ...

References (47)

K. Faraj *et al.*

[A review on phase change materials for thermal energy storage in buildings: heating and hybrid applications](#)

J. Energy Storage (2021)

R.A. Lawag *et al.*

[Phase change materials for thermal management and energy storage: a review](#)

J. Energy Storage (2022)

K. Lafdi *et al.*

[Graphite foams infiltrated with phase change materials as alternative materials for space and terrestrial thermal energy storage applications](#)

Carbon (2008)

P. Singh

[Development and characterization a novel leakage-proof form stable composite of graphitic carbon nitride and fatty alcohol for thermal energy storage](#)

J. Energy Storage (2022)

X. Zhang

[Form stable composite phase change materials from palmitic-lauric acid eutectic mixture and carbonized abandoned rice: preparation, characterization, and thermal conductivity enhancement](#)

Energy Build. (2017)

M. Jafaripour *et al.*

[Fabrication and optimization of kaolin/stearic acid composite as a form-stable phase change material for application in the thermal energy storage systems](#)

J. Energy Storage (2021)

Y. Konuklu *et al.*

[Microencapsulation of caprylic acid with different wall materials as phase change material for thermal energy storage](#)

Sol. Energy Mater. Sol. Cells (2014)

T.D. Dao *et al.*

A Pickering emulsion route to a stearic acid/graphene core–shell composite phase change material

Carbon (2016)

A. Elgafy *et al.*

Effect of carbon nanofiber additives on thermal behavior of phase change materials

Carbon (2005)

X. Huang *et al.*

Microstructure and thermal properties of cetyl alcohol/high density polyethylene composite phase change materials with carbon fiber as shape-stabilized thermal storage materials

Appl. Energy (2017)



View more references

Cited by (11)

Carbon-based porous materials for performance-enhanced composite phase change materials in thermal energy storage: Materials, fabrication and applications

2025, Journal of Materials Science and Technology

Show abstract 

Polypyrrole-modified flax fiber sponge impregnated with fatty acids as bio-based form-stable phase change materials for enhanced thermal energy storage and conversion

2024, Journal of Energy Storage

Show abstract 

3D-printed polylactic acid-microencapsulated phase change material composites for building thermal management

2024, Renewable and Sustainable Energy Reviews

Show abstract 

Heat transfer performance enhancement and mechanism analysis of thermal energy storage unit designed by using a modified transient topology optimization model

2024, Journal of Cleaner Production

[Show abstract](#) ✓

Preparation and characterization of lauric acid-stearic acid/fumed silica/expanded graphite thermally conductive enhanced composites

2023, Journal of Energy Storage

[Show abstract](#) ✓

Waste polyvinyl chloride derived latent thermal energy storage composites for waste heat recovery via packed bed system

2023, Journal of Cleaner Production

[Show abstract](#) ✓



[View all citing articles on Scopus](#) ↗

[View full text](#)

© 2023 Elsevier Ltd. All rights reserved.



All content on this site: Copyright © 2024 Elsevier B.V., its licensors, and contributors. All rights are reserved, including those for text and data mining, AI training, and similar technologies. For all open access content, the Creative Commons licensing terms apply.





Article

Molecular Structure-Based Prediction of Absorption Maxima of Dyes Using ANN Model

Neeraj Tomar ¹, Geeta Rani ^{2,*}, Vijaypal Singh Dhaka ², Praveen K. Surolia ^{1,*}, Kalpit Gupta ², Eugenio Vocaturo ^{3,4} and Ester Zumpano ^{3,4}

- ¹ Department of Chemistry, Manipal University Jaipur, Jaipur 303007, India; neerajtomar225@gmail.com
- ² Department of Computer and Communication Engineering, Manipal University Jaipur, Jaipur 303007, India; vijaypalsingh.dhaka@jaipur.manipal.edu (V.S.D.); kalpitgupta369@gmail.com (K.G.)
- ³ Department of Computer Engineering, Modeling, Electronics and Systems, University of Calabria, 87036 Rende, Italy; e.vocaturo@dimes.unical.it or eugenio.vocaturo@cnr.it (E.V.); e.zumpano@dimes.unical.it (E.Z.)
- ⁴ CNR NANOTEC, Via Pietro Bucci 33C, 87036 Arcavacata, Italy
- * Correspondence: geetachikara@gmail.com (G.R.); praveenkumar.surolia@jaipur.manipal.edu (P.K.S.)

Abstract: The exponentially growing energy requirements and, in turn, extensive depletion of non-restorable sources of energy are a major cause of concern. Restorable energy sources such as solar cells can be used as an alternative. However, their low efficiency is a barrier to their practical use. This provokes the research community to design efficient solar cells. Based on the study of efficacy, design feasibility, and cost of fabrication, DSSC shows supremacy over other photovoltaic solar cells. However, fabricating DSSC in a laboratory and then assessing their characteristics is a costly affair. The researchers applied techniques of computational chemistry such as Time-Dependent Density Functional Theory, and an ab initio method for defining the structure and electronic properties of dyes without synthesizing them. However, the inability of descriptors to provide an intuitive physical depiction of the effect of all parameters is a limitation of the proposed approaches. The proven potential of neural network models in data analysis, pattern recognition, and object detection motivated researchers to extend their applicability for predicting the absorption maxima (λ_{\max}) of dye. The objective of this research is to develop an ANN-based QSPR model for correctly predicting the value of λ_{\max} for inorganic ruthenium complex dyes used in DSSC. Furthermore, it demonstrates the impact of different activation functions, optimizers, and loss functions on the prediction accuracy of λ_{\max} . Moreover, this research showcases the impact of atomic weight, types of bonds between constituents of the dye molecule, and the molecular weight of the dye molecule on the value of λ_{\max} . The experimental results proved that the value of λ_{\max} varies with changes in constituent atoms and types of bonds in a dye molecule. In addition, the model minimizes the difference in the experimental and calculated values of absorption maxima. The comparison with the existing models proved the dominance of the proposed model.

Keywords: solar; DSSC; artificial neural network; energy; λ_{\max}



Citation: Tomar, N.; Rani, G.; Dhaka, V.S.; Surolia, P.K.; Gupta, K.; Vocaturo, E.; Zumpano, E. Molecular Structure-Based Prediction of Absorption Maxima of Dyes Using ANN Model. *Big Data Cogn. Comput.* **2023**, *7*, 115. <https://doi.org/10.3390/bdcc7020115>

Academic Editors: Domenico Ursino, Miguel-Angel Sicilia, Nik Bessis and Marcello Trovati

Received: 4 April 2023

Revised: 13 May 2023

Accepted: 26 May 2023

Published: 8 June 2023



Copyright: © 2023 by the authors. Licensee MDPI, Basel, Switzerland. This article is an open access article distributed under the terms and conditions of the Creative Commons Attribution (CC BY) license (<https://creativecommons.org/licenses/by/4.0/>).

1. Introduction

Electricity consumption is increasing proportionally with an increase in population. Mankind mainly depends on non-restorable energy sources such as coal and fossil fuels for electricity production [1]. These non-restorable sources will be exhausted in the future if depletion continues at the same rate. Furthermore, these sources cause environmental pollution. Therefore, researchers emphasize designing the devices to harness the energy from renewable sources such as biomass, wind, hydroelectric, geothermal, and solar energy [2]. Electricity production utilizing solar energy is cleaner and safer than conventional sources. In the recent era, Photovoltaics (PV) technology is considered the most encouraging technology due to its potential to convert solar energy into electrical energy [3]. The PV cells

developed so far have been categorized into three generations. The cells designed in the first generation consist of monocrystalline and polycrystalline silicon. The PV cells of the second generation consist of silicon of non-crystalline form, cadmium telluride, and copper gallium indium diselenide. Along with the advantages of the first and second generation of solar cells in their better performance, there are certain limitations. The materials used in the development of the first and second generation of solar cells are hazardous and expensive. To conquer these issues, scientists have developed third-generation solar cells, such as Dye-Sensitized Solar Cells (DSSC), quantum Dot (QDs) organic, and Perovskite Solar Cells (PSC) [4–7]. Based on the study of efficacy, design feasibility, and cost of fabrication, DSSC shows supremacy over other PV cells developed in the first and second-generation [8–10]. Furthermore, DSSC is attractive to industry and users due to its high molar absorption coefficient, and potential to perform under diffused light conditions. Moreover, DSSC has low fabrication cost, is processable at ambient temperature, easy to manufacture, and suitable for roll-to-roll production. Further, the material's ecofriendly nature, printability on a flexible substrate, and availability in a variety of colors increase the importance of DSSC in real-life [11,12].

DSSC is an integration of components viz. photoanode, with a semiconductor layer, dye sensitizer, electrolyte and counter electrode with a thin layer of catalyst [13]. Along with all components, the dye plays an important role in deciding the efficiency of a DSSC because it is responsible for the absorption of photons from the incident sunlight [14,15]. It is covalently bonded to semiconductor oxide. These dyes have been extensively tested in the fabrication of DSSC and are classified into three groups based on their source or components used for manufacturing. For example, dyes extracted from plant parts such as fruits, flowers, and leaves are considered natural dyes [16]. Dyes fabricated by using metal complexes such as ruthenium [8,17], osmium [18], platinum [19], copper [20], iridium [21], etc. are classified as metal complex dyes. Metal-based dyes are preferred in DSSC due to their advanced photo-conversion efficiency. In contrast, the metal-free organic dyes were introduced at a later stage due to their low cost, high molar extinction coefficient, and simple fabrication technique [22,23]. However, metal-free dyes still show less photovoltaic efficiency compared to metal-complex dyes. Among natural, organic and inorganic dyes, the inorganic dyes' mainly polypyridyl complex of ruthenium metal has been widely used and investigated [24]. Inorganic dyes are selected for their high stability and excellent redox properties [25]. Further, an efficient sensitizer satisfies the following five conditions.

- (i) The bond between the semiconductor oxide surface and dye must be strong enough to move the electron injection in the Conduction Band (CB) of the semiconductor oxide.
- (ii) The LUMO of the sensitizer should be greater than TiO_2 CB. It empowers the charge injection.
- (iii) The molecule of dye must be small because the bulky molecule can lead to a lower optical cross-section.
- (iv) The dye must be thermally, photochemically, and electrochemically vigorous. If the oxidation-back reduction turnover number exceeds 106, then the stability of DSSC can reach up to approximately 20 years.
- (v) The sensitizer should be effective in absorbing all light below the 920 nm wavelength strike to the surface of the semiconductor oxide [2].

The above-discussed conditions are indicative of the challenging synthesis of such an efficient and novel dye sensitizer that includes all the above-mentioned characteristics. The hit and trial experiments in the laboratory incur a high cost, require expertise in the synthesis of DSSC, and consume a lot of time. Thus, fabricating DSSC in the laboratory and then assessing their characteristics is a costly affair. Therefore, there is a strong need to find an alternative that minimizes the cost and time for trial experiments.

The researchers apply computational chemistry in defining the structure and electronic properties of dyes without actually synthesizing them. For example, the Time-Dependent Density Functional Theory (TD-DFT) [26] and an ab initio method [27] have been employed for identifying new organic dyes for synthesizing DSSC. TD-DFT is preferred for investi-

gating the properties of organic dyes in their excited state due to its higher accuracy and lower computational time than the ab initio method [28,29].

To further improve the prediction accuracy, Xu et. al. employed the QSPR model using Polak–Ribiere algorithm in HYPERCHEM for the prediction of absorption maxima (λ_{\max}) of organic dyes [30]. They employed DRAGON software to calculate three-dimensional (3-D) descriptors from the optimized molecular geometries. In the subsequent research work, Xu et.al. designed a QSPR between descriptors [31]. They represented that the molecular structures and the λ_{\max} of organic dyes used in DSSC follow the same protocols as applied by Colombo et al. in [20]. The disadvantage of the QSPR approach is that the descriptors do not always provide an intuitive physical depiction of the effect of all parameters [32].

Further, to develop a nonlinear model, researchers applied a quasi-Newton Broyden–Fletcher–Goldfarb–Shanno (BFGS) algorithm [31,33]. They applied the algorithm on the same dataset as used in the research works discussed in [30,31,34]. The details of the dataset are shown in Table S1.

In the BFGS algorithm, there is no need to specify the rate or momentum. Furthermore, it undergoes fast training. However, it is unable to determine small and medium scale minimizing functions. It requires a large amount of memory, and therefore, it involves a huge extent of numerical operations [35].

These challenges can be resolved by employing the Artificial Neural Networks (ANN) models [36,37]. Although the potential of neural network models in data analysis [38], pattern recognition [39], and object detection [40] is proven in various application areas such as healthcare [41–43], agriculture [44], and material science [45], only a few researchers employed the ANN-based models for predicting the absorption maxima (λ_{\max}) of dye [30,31]. Thus, there is a huge scope to extend their applicability. In this research, we propose an ANN-based QSPR model for correctly predicting the value of λ_{\max} for inorganic ruthenium complex dyes used in DSSC.

The major objectives of this research are as follows.

- (i) To develop an ANN-based model for predicting the absorption maxima of the dye sensitizer used in DSSC.
- (ii) To minimize the difference in the experimental and calculated values of absorption maxima.
- (iii) To showcase the impacts of the atomic weight of each atom and molecular weight on the value of λ_{\max} .
- (iv) To demonstrate the impact of different types of bonds on the value of λ_{\max} .
- (v) To justify the impact of different activation functions, optimizers, and loss functions on the prediction accuracy of λ_{\max} using the ANN model.

The structure of the article is as follows: Section 1 provides the introduction. It gives an overview of the research topic, introduces the research problem, highlights the gaps in existing knowledge, and presents the objectives of the study. Section 2 describes the data collection and methodology of the research work. Section 3 illustrates the results. It presents the findings of the study. It includes tables, figures, and statistical analyses to support the findings. Section 4 presents the discussion of the research work. It interprets and analyzes the results, relates them to the objectives, and compares them with previous research. Section 5 presents the conclusion of the work. It summarizes the main findings and their implications. It also offers insights for future investigations.

2. Materials and Methods

2.1. Data Set

To prepare the dataset, the molecular structures of 81 ruthenium dye complexes were taken from the literature. From these structures of ruthenium dye complexes, molecular weight, atomic weight, number of all types of bonds such as C-C, C=C, C-N, Ru-N, C=O, Ru-NCS, C-O, and other bonds were calculated for each dye. The prepared dataset comprises 81 rows and 15 columns. The sample dataset is shown in Table 1 and the complete dataset is shown in Table S1. As reported in the earlier works [46,47], the experimental

values of λ_{\max} are also dependent on the solvent. Therefore, to ignore the impact of solvent, the dataset is collected for a single solvent viz. Dimethylformamide (DMF). It is obvious from the sample dataset shown in Table 1 that the values of λ_{\max} lie in the range from 473 to 631 nm in the collected dataset. This large variation in the range of values is important for improving the robustness of the ANN model. It means that the performance of the model does not degrade with any change in the value of λ_{\max} . So, the model works efficiently for a wide range of dyes to correctly predict the value of λ_{\max} .

Further, the number of each type of bond was inferred from the structure of dyes. These are shown as $N^+Bu_4 = 2$, O-H=1, O-Na=1, O-H=2, C-S=4, C-S=8, C-Se=4, C-S=12, $N^+(C_4H_9)_4=1$, C-S=2, O-H=3, C-F=3, $N \equiv N=1$, C-F=6, O-H=7, $N \equiv N=2$, $TBA^+=1$, N-H=2, N-H=4, O-H=4, and $TBA^+=1$. Here, the symbol shows the type of bond, and the digit denotes the number of bonds or functional groups present in a dye molecule. For example, $N^+Bu_4 = 2$ means that the dye contains two N^+Bu_4 groups, and O-H=1 means that the dye contains one O-H bond. The other groups can be interpreted in the same way.

2.2. Experiments

2.2.1. Architecture of Model

An Artificial Neural Network (ANN) is a machine learning model that is inspired by the structure and function of biological neurons in the brain. An ANN consists of multiple interconnected nodes i.e., neurons, organized into layers. Each neuron in the network has a set of weights associated with it, which determine the strength of its connections to other neurons in the network. The input layer of an ANN receives input data, which is then passed through one or more hidden layers. Each hidden layer applies a non-linear transformation to the input. During the training phase, its neurons adjust the weights to minimize the difference (value of loss function) between the predicted output and the actual output. Finally, the output layer of the network provides the prediction.

Rather than using the ANN models available in the literature [30,31], a customized ANN-based shallow network has been designed in this research. Its architecture is shown in Figure 1.

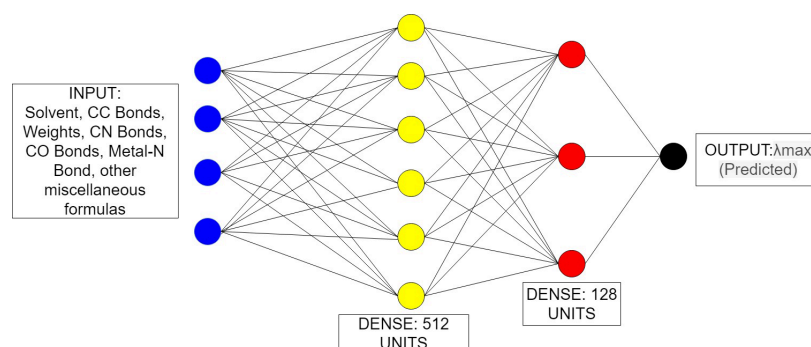
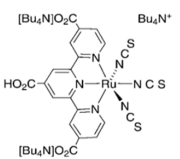
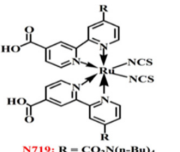
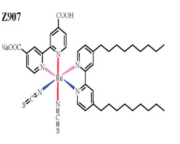
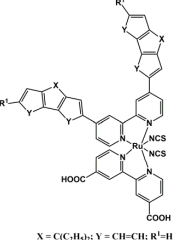
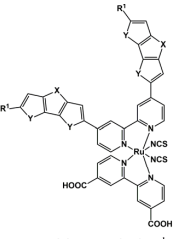


Figure 1. Sequential ANN Model.

The designed model can deal with observable outliers available in the data. Furthermore, the model requires a smaller dataset for training. Before, the final selection of the architecture, the ANN-based architectures with dense layers comprising 16, 32, 64, and 1024 Units were implemented on a trial-and-error basis. Furthermore, the experiments by employing different activation functions viz. Leaky ReLu, ReLu, Softmax, and Sigmoid; optimizers viz. Adam, AdaGrad, SGD, and RMSProp; and loss functions viz. Mean Absolute Error, Mean Square Error, Mean Squared Logarithmic Error, Binary Cross-Entropy, and Kullback Leibler Divergence Error were employed for experiments. The experimental results obtained by employing the above-mentioned parameters are shown in the subsequent Section 2.2. The impacts of these parameters on the prediction accuracy justify the selection of the 'Relu' activation function, Mean Absolute Error (MSE) loss function, and 'Adam' optimizer in the proposed ANN architecture.

Table 1. Collected and calculated data of Ruthenium dyes.

Dye	Structure	Formula	Mol. Weight	Atomic Weight	λ_{\max} (MLCT)	Solvent	C-C Bond	C=C Bond	C-N Bond	Metal-N Bond	C=O Bond	Metal-NCS Bond	C-O Bond	Other Bonds/Groups	Ref.
N749		C ₆₉ H ₁₁₆ N ₉ O ₆ RuS ₃	1364.98	C-828.74 H-116.92 N-126.06 O-96 Ru-101.07 S-96.19	600	DMF	11	6	6	3	3	3	3	N ⁺ Bu ₄ =2	[48]
N719		C ₅₈ H ₈₆ N ₈ O ₈ RuS ₂	1188.55	C-696.62 H-86.68 N-112.05 O-128.00 Ru-101.07 S-64.13	525	DMF	13	8	8	4	4	2	4	N+Bu4 =2	[49,50]
Z907		C ₄₂ H ₅₂ N ₆ O ₄ RuS ₂	870.10	C-504.45 H-52.41 N-84.04 O-64 Ru-101.07 S-64.13	520	DMF	30	8	8	4	2	2	2	O-H=1 O-Na=1	[51]
YS-1		C ₅₈ H ₄₈ N ₆ O ₄ RuS ₂	1058.24	C-696.62 H-48.38 N-84.04 O-64 Ru-101.07 S-64.13	536	DMF	40	16	8	4	2	2	2	O-H=2	[51]
YS-2		C ₇₄ H ₈₀ N ₆ O ₄ RuS ₂	1282.66	C-888.79 H-80.63 N-84.04 O-64 Ru-101.07 S-64.13	536	DMF	56	16	8	4	2	2	2	O-H=2	[51]

The proposed ANN model comprises one input layer, two dense layers, and one output layer. The first and second dense layers comprise 512 and 128 units, respectively. Further, the model contains 20,480; 65,664 parameters at the first and second dense layers, respectively. The number of trainable parameters was reduced to 129 at the output layer. This shows that the employed ANN model involves 86,273 trainable parameters. It does not involve any non-trainable parameter in its architecture. The model is trained with a batch size of 40 for 1000 epochs. Its efficacy is evaluated by using the evaluation metrics defined below.

- i **Difference λ_{\max}** : This is the difference in the predicted and experimental value of absorption maxima, as defined in Equation (1):

$$\text{Difference } \lambda_{\max} = \text{Predicted } \lambda_{\max} - \text{Experimental } \lambda_{\max} \quad (1)$$

- ii **Percentage error (Error%)**: This is the percentage of difference in the predicted and experimental value of absorption maxima, as defined in Equation (2).

$$\text{Error \%} = \frac{\text{Difference } \lambda_{\max}}{\text{Experimental } \lambda_{\max}} \times 100 \quad (2)$$

- iii **Correlation matrix**: This matrix shows the correlation between (i) λ_{\max} and all bonds in dye molecule (ii) λ_{\max} and other additional groups present in a dye structure (iii) λ_{\max} and atomic and molecular weight. The matrix represents the direct as well as inverse correlation. The value '0' denotes no correlation, '1' indicates complete and direct correlation. Whereas '-1' shows that the given parameters have a complete and inverse correlation. The values increasing from 0 to 1 show an increasing degree of direct correlation. On the other hand, values approaching from 0 to -1 indicate the increasing degree of negative correlation between the parameters.

2.2.2. Selection of Hyperparameters

In this sub-section, the experiments conducted to select the optimum parameters are demonstrated.

Selection of Activation Function

Activation functions are employed in the neural networks to introduce non-linearity and enabling them to learn complex patterns in the input data. In this research, we employed the ReLU (Rectified Linear Unit) activation function. It is a simple and computationally efficient function that sets all negative values in the input to zero and leaves positive values unchanged as defined in Equation (3).

$$f(x) = \max(0, x) \quad (3)$$

Here, x is the input to the function, and $f(x)$ is the output. The ReLU function returns the input x , if it is positive, and returns 0 otherwise. This makes the ReLU function a simple yet powerful way to introduce non-linearity into neural networks.

The selection of ReLU activation function is based on the set of experiments conducted. The performance of ANN by employing different activation functions viz. Leaky ReLU, ReLU, Sigmoid, and Softmax are demonstrated in Figure 2. The difference in the predicted and experimental values of absorption maxima was observed. Further, the percentage error was calculated by employing the above-mentioned activation functions. It is evident from the results demonstrated in Figure 2 that employing the ReLU activation function in the proposed ANN model reports the minimum, whereas the softmax activation function results in the maximum percentage error in predicting of λ_{\max} . Therefore, the ReLU activation function was employed in this research.

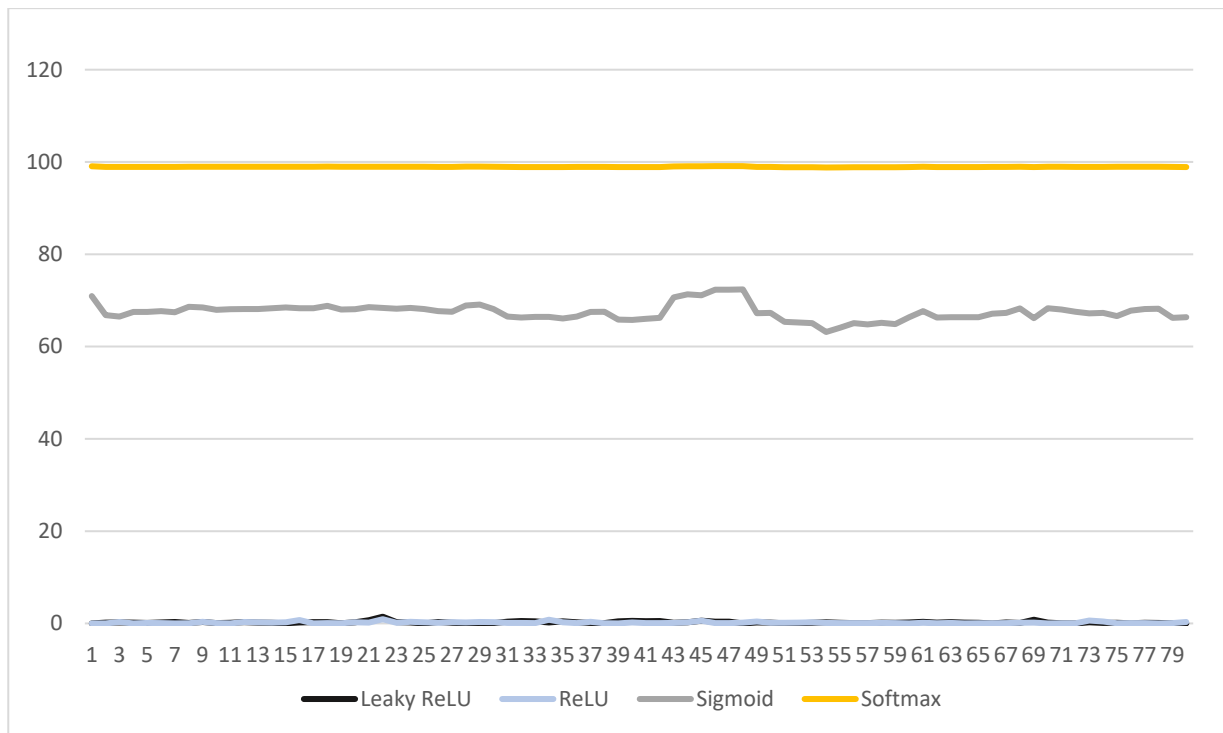


Figure 2. Comparison in percentage error reported by activation functions.

Selection of Loss Function

In this work, the selection of loss functions is accomplished strategically. Initially, the loss functions viz. mean absolute error, mean squared error, mean squared logarithmic error, categorical cross entropy and Kullback–Leibler divergence error were employed individually for predicting the value of λ_{max} . The values of percentage error in the λ_{max} obtained for each loss function were evaluated. It is evident from the results demonstrated in Figure 3 that the mean absolute error reports the minimum value of percentage error. Thus, this loss function is employed in the architecture of the proposed ANN model.

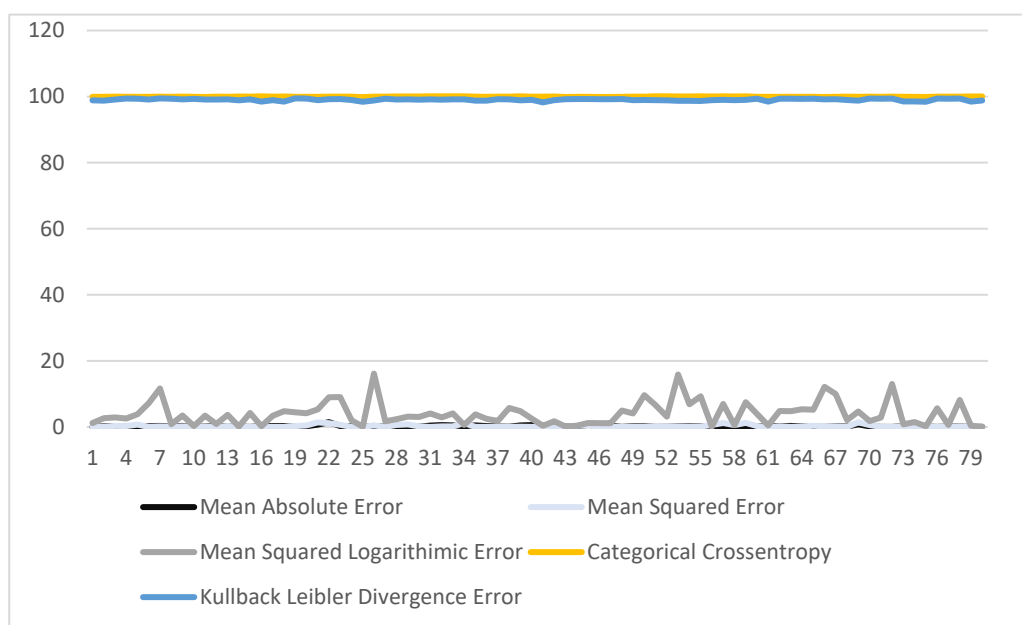


Figure 3. Percentage error comparison for loss functions.

Selection of Optimizer

Selecting the most suitable optimizer plays an important role in improving the prediction accuracy and minimizing the percentage error. For selecting the appropriate optimizer for the proposed model, a series of experiments were conducted. The optimizers, namely Adam, SGD, RMSProp, AdaGrad, were employed individually and the values of percentage error in the λ_{max} were recorded. It is clear from the results shown in Figure 4 that the Adam optimizer results in the minimum value of percentage error. Therefore, the Adam optimizer was employed with the proposed ANN model.

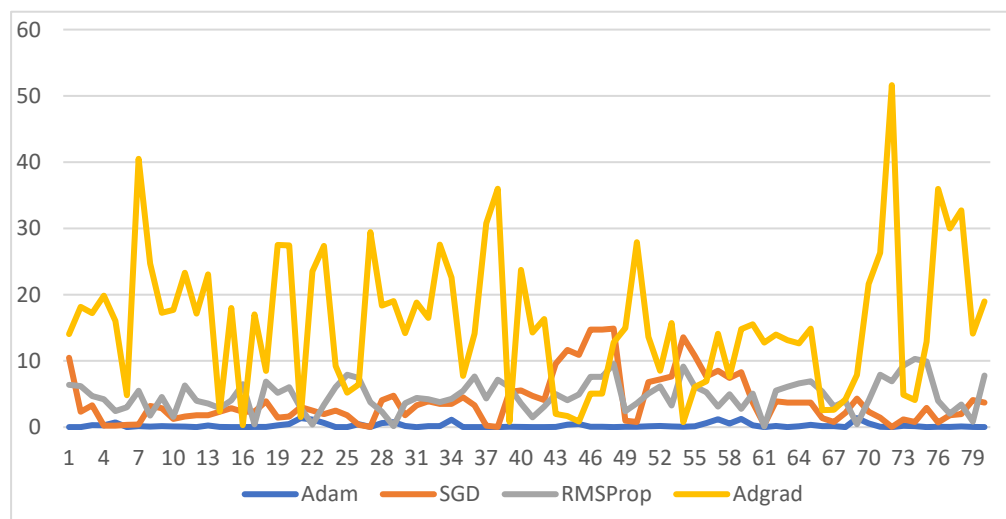


Figure 4. Percentage error comparison for optimizer functions.

3. Results

The proposed ANN model is trained for 1000 epochs. The results of the trained model were recorded on the validation and testing datasets. The predicted values of absorption maxima based on the structure of the dye molecule, numbers of bonds, molecular weight, and atomic weight are demonstrated in the correlation matrices shown in Figures 5–9. The details of the correlation obtained are discussed below. Two more machine learning algorithms ‘XGBoost’, and random forest were applied, and their performance is compared with the ANN model. The comparative analysis is demonstrated in Figures 10 and 11.

λ_{max} (MLCT)	1	-0.01	-0.049	-0.48	-0.123	0.770	0.230	-0.743	-0.019	0.019
C-C Single Bond	-0.009	1	0.542	0.376	0.254	0.178	0.110	-0.141	-0.049	0.049
C=C double bond	-0.049	0.542	1	0.470	-0.237	0.052	-0.065	-0.017	-0.023	0.023
C-N bond	-0.484	0.376	0.470	1	0.260	-0.470	0.190	0.493	0.077	-0.077
C=O bond	-0.123	0.254	-0.237	0.260	1	-0.063	0.130	0.072	0.045	-0.045
Metal-NCS bond	0.770	0.178	0.052	-0.47	-0.063	1	0.160	-0.985	-0.048	0.048
C-O bond	0.230	0.115	-0.065	-0.19	0.130	0.160	1	-0.152	0.059	-0.059
Metal-N bond	-0.743	-0.14	-0.017	0.493	0.072	-0.985	-0.150	1	0.044	-0.044
DMF	-0.019	-0.05	-0.023	0.077	0.045	-0.048	0.059	0.044	1	-1
Ethanol	0.019	0.049	0.023	-0.077	-0.045	0.048	-0.059	-0.044	-1	1
	λ_{max} (MLCT)	C-C Single Bond	C=C double bond	C-N bond	C=O bond	Metal-NCS bond	C-O bond	Metal-N bond	DMF	Ethanol

Figure 5. Correlation matrix for λ_{max} and C-C, C=C, C-N, C=O, Metal-NCS, C-O, Metal-N bonds.

λ_{\max} (MLCT)	1	0.1304	0.1	0.152	0.192	-0.0068	-0.065	0.05
N+Bu4 =2	0.13	1	-0.07	-0.06	-0.19	-0.0727	-0.053	-0.02
O-H=1	0.10	-0.073	1	0.867	-0.54	0.13646	0.068	0.24
O-Na=1	0.15	-0.063	0.87	1	-0.47	0.1	0.11	0.28
O-H=2	0.19	-0.19	-0.54	-0.47	1	0.058	0.11	-0.13
C-S=4	-0.0068	-0.073	0.14	0.105	0.058	1	-0.15	-0.05
C-S=8	-0.0651	-0.053	0.07	0.11	0.114	-0.15	1	-0.04
C-Se=4	0.045	-0.018	0.24	0.28	-0.13	-0.051	-0.037	1
λ_{\max} (MLCT)		N+Bu4 =2	O-H=1	O-Na=1	O-H=2	C-S=4	C-S=8	C-Se=4

Figure 6. Correlation matrix for λ_{\max} and N+Bu₄=2, O-H=1, O-Na=1, O-H=2 C-S=4, C-S=8, and C-Se=4.

λ_{\max} (MLCT)	1	-0.017	0.034	0.37	-0.26	-0.17	-0.11	-0.52
C-S=12	-0.017	1	-0.0178	-0.063	-0.056	-0.0527	-0.03	-0.073
N+(C4H9)4=1	0.034	-0.018	1	-0.044	-0.04	-0.037	-0.02	-0.051
C-S=2	0.37	-0.063	-0.0443	1	0.204	0.11035	0.17	0.0094
O-H=3	-0.26	-0.056	-0.0395	0.20	1	0.67	0.45	0.046
C-F=3	-0.17	-0.053	-0.037	0.11	0.67	1	0.48	-0.15
N-N=1	-0.11	-0.025	-0.0178	0.17	0.45	0.48	1	-0.073
C-F=6	-0.52	-0.073	-0.0511	0.0094	0.046	-0.15	-0.073	1
λ_{\max} (MLCT)		C-S=12	N+(C4H9)4=1	C-S=2	O-H=3	C-F=3	N-N=1	C-F=6

Figure 7. Correlation matrix for λ_{\max} and C-S, N+(C₄H₉), O-H, C-F, N≡N bonds.

λ_{\max} (MLCT)	1	-0.092	-0.36	0.66	0.00444	-0.031	-0.059	-0.081
O-H=7	-0.092	1	-0.037	-0.0344	-0.0125	-0.018	-0.013	-0.013
N-N=2	-0.36	-0.037	1	-0.1	-0.037	-0.053	-0.037	-0.037
TBA+=1	0.66	-0.034	-0.1	1	-0.0344	-0.049	-0.034	-0.034
N-H=2	0.004	-0.012	-0.037	-0.0344	1	-0.018	-0.012	-0.013
N-H=4	-0.031	-0.018	-0.0527	-0.0489	-0.0178	1	-0.018	-0.018
O-H=4	-0.059	-0.013	-0.037	-0.0344	-0.0125	-0.018	1	-0.013
TBA=1	-0.081	-0.013	-0.037	-0.0344	-0.0125	-0.018	-0.013	1
λ_{\max} (MLCT)		O-H=7	N-N=2	TBA+=1	N-H=2	N-H=4	O-H=4	TBA=1

Figure 8. Correlation matrix for λ_{\max} and O-H, N≡N, TBA⁺, N-H bonds.

λ_{\max} (MLCT)	1	0.16	0.36	-0.32	0.098	0.44	0.16	0.045	-0.58	0.17
C_Weight	0.16	1	0.75	0.37	0.14	0.26	0.03	-0.07	-0.34	0.95
H_Weight	0.36	0.75	1	0.21	0.317	0.23	-0.04	-0.05	-0.42	0.78
N_Weight	-0.32	0.37	0.21	1	0.094	-0.36	-0.01	-0.1	0.39	0.42
O_Weight	0.098	0.14	0.32	0.09	1	-0.02	0.24	-0.07	-0.03	0.27
Ru_Weight						1	0.07	-0.04	-0.53	0.33
S_Weight	0.44	0.26	0.23	-0.36	-0.02	0.07	1	-0.03	-0.15	0.05
Na_Weight	0.16	0.03	-0	-0.01	0.242	-0.04	-0.03	1	-0.06	-0
Se_Weight	0.045	-0.07	-0	-0.1	-0.07	-0.04	-0.03	-0.06	1	-0.25
F_Weight	-0.58	-0.34	-0.4	0.39	-0.03	-0.53	-0.15	-0.06	-0.25	1
Molecular Weight	0.17	0.95	0.78	0.42	0.266	0.33	0.05	-0.02	-0.25	1

Figure 9. Correlation matrix for λ_{\max} based on atomic and molecular weight.

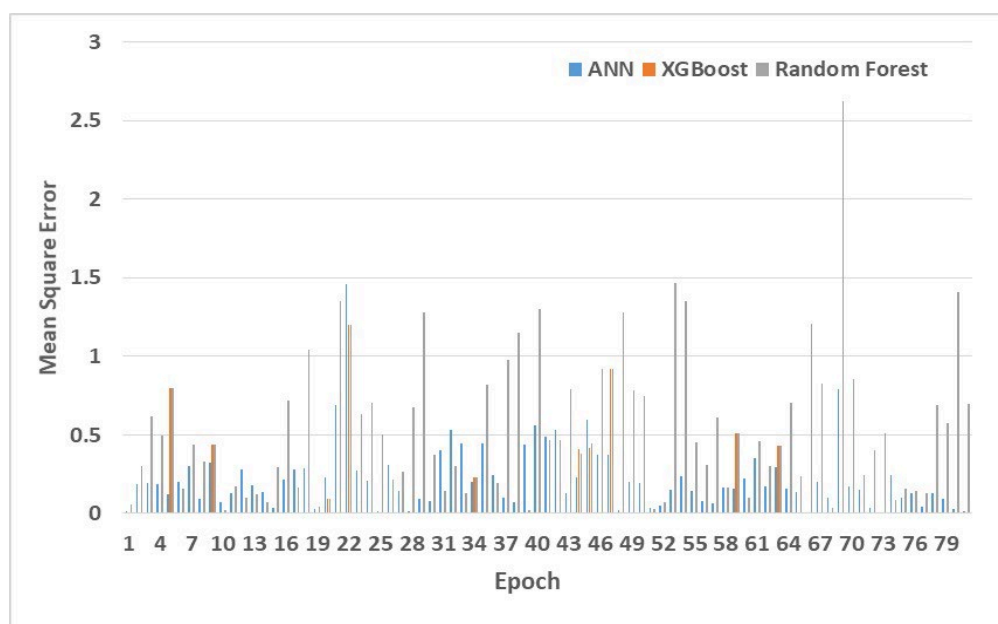


Figure 10. Comparison in MSE of ANN, XGBoost, and Random Forest Models.

3.1. Prediction of λ_{\max} Based on the C-C, C=C, C-N, C=O, Metal-NCS, C-O, Metal-N Bonds

The correlation between λ_{\max} and different types of bonds is demonstrated in Figure 5. The correlation studied from the correlation matrix is observed as linear. The range of λ_{\max} varies from 1 to -1 . Values of 1 or close to 1 indicate a higher positive correlation, whereas the value -1 or close to -1 denote a negative correlation between the considered parameters. For example, it is evident from the sixth row and first column of the correlation chart shown in Figure 5 that the metal-NCS bond reports the value 0.77 which is close to 1. It shows the highest correlation between the metal-NCS bond and the value of λ_{\max} . Furthermore, it is evident from its positive value that the increase in the metal-NCS bond leads to an increase in the value of λ_{\max} proportionally.

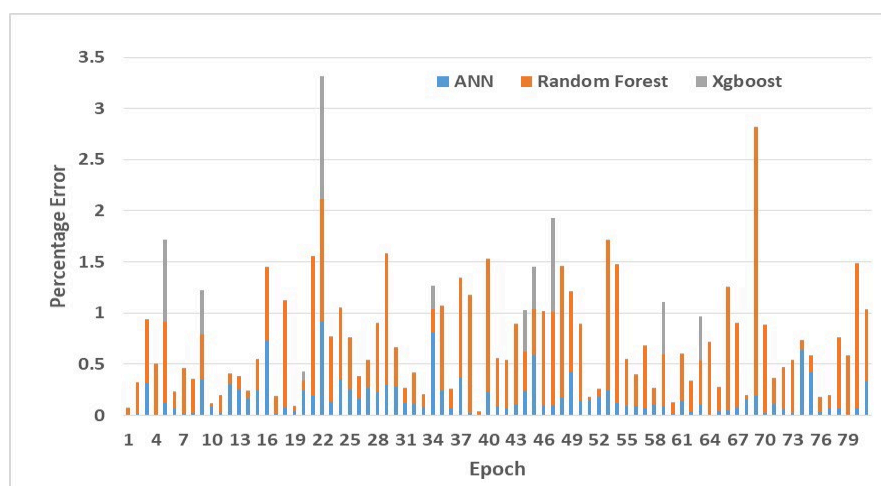


Figure 11. Comparison in percentage error reported by ANN, Xgboost, and Random Forest.

Further, the value ‘ -0.74 ’ shown in the eighth row, the first column of the correlation matrix indicates the high inverse correlation of metal-N bond with the value of λ_{\max} . This means that the increase in the number of metal-N bonds in a dye leads to a decrease in the value of λ_{\max} . Similarly, the value ‘ -0.48 ’ in the fourth row and first column shows that λ_{\max} and C-N bond are inversely correlated but the degree of correlation is lower than a metal-N bond. Next, the observation from column one of the second and ninth row shows that the C-C bond and DMF have a negligible correlation with the value of λ_{\max} .

Additionally, the correlation matrix also shows the correlation between different bonds and functional groups present in a dye. For example, the value ‘ 0.54 ’ recorded in the third column, the second row indicates that the number of C=C increases with an increase in the number of C-C single in the molecular structure of a dye. In contrast, the correlation of C-C with C-N is 0.38, C=O is 0.25, the metal-NCS bond is 0.18 and C-O is 0.11. These values are too small to have an impact on each other.

Similarly, the inter-correlation of C-N with C-C bond is 0.38, C=C bond is 0.47, C=O is 0.26, metal-NCS is -0.47 , C-O is -0.19 , and with the metal-N bond is 0.49. It reflects that the C-N bond has the highest correlation with the metal-N bond among all the above-stated bonds.

Next, the C=O bond is correlated to C-C, C=C, C-N, metal-NCS, C-O, and metal-N bonds with the values 0.25, -0.24 , 0.26, -0.063 , 0.13, and 0.072 respectively. The highest value of the Metal-N bond indicates that it has the maximum and direct correlation with C=O. In contrast, the smaller values for the other bonds mentioned above show their trivial impact on C=O.

Moreover, metal-NCS bond shows 0.18, 0.052, -0.47 , -0.063 , 0.16, with C-C bond, C=C bond, C-N bond, C=O bond, C-O bond, respectively. All the positive values are too small to impact each other. However, the value -0.99 reported in the sixth row and eighth column of fig 5 indicates the highest inverse correlation of the metal-NCS bond with the Metal-N bond. The presence of one such bond is a strong hindrance for another bond in the same dye.

Next, the C-O bond shows 0.11, -0.065 , -0.19 , 0.13, 0.16, -0.15 with C-C bond, C=C bond, C-N, C=O, metal-NCS bond, and metal-N bond respectively. This indicates the minimum impact of these bonds on the presence of a C-O bond in a dye.

Further, the Metal-N bond shows -0.14 , -0.017 , 0.49, 0.072, -0.99 , -0.15 with C-C bond, C=C bond, C-N, C=O, metal-NCS bond, C-O bond respectively. It is clear from these values that the Metal-N bond has the maximum direct correlation with the C=O bond, and the highest inverse correlation with the metal-NCS bond.

Based on the above interpretation, it is obvious that the highest direct correction value of λ_{\max} is 0.77, observed with metal-NCS bonds. Whereas the maximum inverse correlation

is -0.74 , observed with metal-N bonds. Therefore, if we want to fabricate a dye with a higher value of λ_{\max} , the dye with a greater number of metal-NCS bonds should be fabricated and vice versa.

3.2. Prediction of λ_{\max} Based on N^+Bu_4 , O-H, O-Na, C-S, and C-Se Bonds

The correlation between λ_{\max} and other bonds viz. $N^+Bu_4=2$, O-H=1, O-Na=1, O-H=2, C-S=4, C-S=8, and C-Se=4 present in a dye molecule was also studied. The correlation of these bonds with the value of λ_{\max} as well as a favor for co-existence of these bonds are shown in Figure 6. The highest correlation of λ_{\max} is 0.19 is observed in the first row and fifth column when two O-H groups are present in a dye. The positive correlation of 0.13, 0.1, 0.15, 0.19, 0.045 is observed between λ_{\max} and other bonds $N^+Bu_4=2$, O-H=1, O-Na=1, O-H=2 and C-Se=4 respectively. In contrast, a negative correlation of -0.0068 , -0.065 exists with bond C-S=4, C-S=8 respectively. So, it is evident from the results reported in Figure 6 that the above-stated bonds have a negligible impact on the value of λ_{\max} . Therefore, the study of a number of these bonds can be ignored while fabricating a dye with the desired value of λ_{\max} .

More analysis of the results given in Figure 6 shows that the maximum correlation of 0.87 is observed in the number of O-H and O-Na groups. However, these also have a negligible impact on the value of λ_{\max} .

3.3. Prediction of λ_{\max} Based on C-S, $N^+(C_4H_9)$, O-H, C-F, $N\equiv N$ Bonds

Now, the correlation of absorption maxima with the bonds such as twelve C-S groups, one $N^+(C_4H_9)$, two C-S, three O-H, three C-F, one $N\equiv N$, six C-F was also studied as shown in Figure 7. The analysis of results given in Figure 7 shows that the λ_{\max} is negatively correlated with C-S, O-H, C-F, $N\equiv N$ with a negligible impact. On the other hand, the λ_{\max} is positively correlated with $N^+(C_4H_9)$ and C-S groups with values of 0.034 and 0.37. These values indicate that the C-S group has the highest impact on the value of λ_{\max} . However, the degree of correlation is not very significant. The remaining groups have a negligible impact on the value of λ_{\max} .

Further, it is clear from the results shown in Figure 7 that C-F, O-H, and $N\equiv N$ bonds favor their coexistence in a dye. Therefore, while fabricating a dye with the desired value of λ_{\max} , the number of C-S groups should be considered. Furthermore, the number of C-F, O-H, and $N\equiv N$ bonds can be increased or decreased in proportion to each other.

3.4. Prediction of λ_{\max} Based on O-H, $N\equiv N$, TBA^+ , N-H Bond

Now, the correlation of λ_{\max} with different bonds such as O-H=7, $N\equiv N=2$, $TBA^+=1$, N-H=2, N-H=4, O-H=4, and $TBA^+=1$ was also studied. It has been observed that only the presence of one TBA^+ group in a dye have a significant and direct correlation with the value of λ_{\max} . Increasing the number of TBA^+ groups can result in the dye with a higher value of λ_{\max} . However, there is a negligible direct impact of the N-H group on the value of λ_{\max} .

Similarly, there is an insignificant inverse impact of O-H=7, $N\equiv N=2$, O-H=4 groups on the value of λ_{\max} . Furthermore, it is clear from the values reported in Figure 8 that the aforementioned bonds do not favor or hinder their co-existence.

3.5. Prediction of λ_{\max} Based on Atomic and Molecular Weight

The value of λ_{\max} is also dependent on the atomic mass of an atom present in a dye molecule. Furthermore, it is dependent on the molecular mass of a molecule present in a dye and the complete molecule of a dye. The inter-correlation of λ_{\max} with the individual atomic masses of Carbon (C), Hydrogen (H), Nitrogen (N), Oxygen (O), Ruthenium (Ru), Sulfur (S), Sodium (Na), Selenium (Se), Fluorine (F) is demonstrated in Figure 9. Furthermore, the directly or inversely correlated atoms or groups of a dye are presented in Figure 9.

The absorption maxima show a negative correlation with an atomic weight of N and F in proportion to values -0.32 and -0.58 respectively. However, it shows a positive

correlation with C, H, O, S, Na and molecular weight of the dye in proportion to the values 0.16, 0.36, 0.098, 0.44, 0.16, and 0.17 respectively. It is obvious from these values that increasing the mass of Sulfur in a dye leads to a significant increase in the value of λ_{\max} .

Increasing the mass of Fluorine may lead to a decrease in the value of λ_{\max} . Thus, it is apparent that if we want to fabricate the dye with a higher value of λ_{\max} then the number of Sulfur atoms in a dye molecule must be increased. On the other hand, if we want to fabricate a dye with a lower value of λ_{\max} , then the number of F atoms in a dye molecule must be increased. The other atoms, viz. C, H, N, O, Ru, Na, and Se, have a negligible impact on the value of λ_{\max} . Furthermore, the molecular weight of a dye has an insignificant impact on the value of λ_{\max} . The impact is in proportion to the value of 0.17 only.

Further, it is evident from the results reported in Figure 8 that the atomic weight of C shows a correlation to H, N, O, S, Na, F with values 0.75, 0.37, 0.14, 0.26, 0.26, and 0.34, respectively. The C atom is in a strong correlation of 0.95 with the molecular weight of a dye. This shows that a greater number of C atoms are present in a dye with high molecular weight and vice versa.

Similarly, the atomic weight of the H atom shows a correlation with C, N, O, S, Na, and F in proportion to values 0.75, 0.21, 0.32, 0.23, -0.043 , and -0.42 respectively. These values indicate that C and H atoms significantly favor their co-existence in a dye molecule. Whereas H and F atoms hinder the co-existence of each other. Other atoms, viz. N, O, S, and Na, have a negligible impact on the presence of H atoms in a dye molecule. Further, the H atom shows a correlation of 0.78 with the molecular weight of a dye. The higher molecular weight of a dye favors the presence of a greater number of H atoms in it.

Next, it is evident from Figure 8 that the atomic weight of N is correlated to atomic weights of C, H, O, S, Na, and F, with values 0.37, 0.21, 0.094, 0.36, -0.0066 , and 0.39, respectively. These values are too small to have any significant effect on each other. Further, it is correlated to the molecular weight of dye in proportion to the value 0.42.

Similarly, the molecular weight of the O atom is also correlated with the molecular weight of C, H, N, S, Na, Se, F in proportion to values 0.14, 0.32, 0.094, -0.021 , 0.24, -0.074 , and -0.028 , respectively. These values indicate that the O atom has minimum interference with the presence of the other atoms in a dye molecule. Moreover, the molecular weight of a dye also has a minimum correlation of 0.098 with the presence of an O atom in a dye molecule.

Further, the atomic weight of the S atom shows values 0.26, 0.23, -0.36 , -0.021 , 0.073, -0.036 , -0.53 , for the atomic weight of C, H, N, O, Na, Se, and F, respectively. Its correlation with the molecular weight of a dye is observed as 0.33. These values show that the atomic weight of S is inversely correlated with the atomic weight of N, O, Se, and F atoms but the degree of correlation is not significant. It is, however, directly correlated to atomic weights of C, H, and Na. Furthermore, the degree of direct correlation is insignificant.

The atomic weight of Na also shows a correlation with the atomic weight of C, H, N, O, Ru, Se, S, and F with values 0.16, 0.026, -0.043 , -0.0066 , 0.24, 0.073, -0.032 , -0.15 , respectively. It is apparent from these values that the direct, as well as inverse correlation of atomic weight of Na with above-stated atoms, is negligible.

Now, it has been observed from Figure 9 that the atomic weight of Se is correlated with C, H, N, O, S, Na, and F with values -0.066 , -0.046 , -0.1 , -0.074 , -0.036 , -0.032 , -0.061 , respectively. The low positive, as well as negative values, clearly show that the presence of the Se atom in a dye molecule is not determined by the presence of other atoms.

Similarly, the atomic weight of F is correlated with the atomic weights of C, H, N, O, S, Na, and Se with the values of -0.34 , -0.42 , 0.39, -0.028 , -0.53 , -0.15 , -0.061 , respectively. These values indicate that the presence of F is inversely related to all the above-mentioned atoms except N. However, the degree of correlation is not very high.

Further, the molecular weight of the dye is also correlated with absorption maxima and atomic weights of C, H, N, O, S, Na, Se, and F in proportion to the values 0.95, 0.78,

0.42, 0.27, 0.33, 0.054, −0.023, −0.25, respectively. It indicates that the molecular weight is highly dependent on the atomic weight of carbon and H.

3.6. Difference and Percentage Error

To validate the reliability and accuracy of the proposed model, we calculated the difference in the experimental values of λ_{max} reported in the literature and the predicted values [30,31]. Furthermore, we calculated the percentage error in the experimental and predicted values of λ_{max} . The values of difference and percentage error of individual dyes are demonstrated in Table 2. Its first column shows the name of the dye, the second column shows the experimental value of λ_{max} , the third column includes the predicted value of λ_{max} , the fourth column shows the difference in λ_{max} values, and the last column contains the values of percentage error.

Table 2. Comparison of experimental and predicted values of absorption maxima.

Dye	λ_{max} (Experimental)	λ_{max} (Predicted)	Difference	Percentage Error	t-Score	Ref.
N749	600	599.9605103	−0.039489746	0.006581625	2.962804	[48]
N719	525	525.081115723	0.081115723	0.015450614	2.573224	[52]
Z907	520	518.3882446	−1.611755371	0.309952945	2.554664	[51]
YS-1	536	535.9921265	−0.007873535	0.001468943	2.633939	[51]
YS-2	536	536.6464233	0.64642334	0.120601371	2.637666	[51]
YS-3	539	538.6637573	−0.336242676	0.062382687	2.65839	[51]
YS-4	535	534.9170532	−0.082946777	0.015504071	2.642976	[51]
YS-5	555	554.8757324	−0.124267578	0.022390554	2.746662	[51]
CYC-B1	553	554.9368896	1.936889648	0.350251287	2.737349	[53]
CYC-B3	544	543.5513306	−0.448669434	0.082475998	2.699216	[54]
SJW-E1	546	545.9083252	−0.091674805	0.016790258	2.713337	[54]
C101	547	545.3406372	−1.659362793	0.303357005	2.72482	[55]
C102	547	545.6287842	−1.37121582	0.250679314	2.728966	[55]
C103	550	549.0956421	−0.90435791	0.164428711	2.74789	[56]
C104	553	554.3543701	1.354370117	0.24491322	2.764281	[57]
C105	550	546.0117188	−3.98828125	0.725142062	2.759501	[58]
C106	550	549.9251099	−0.074890137	0.013616389	2.759075	[55]
C107	559	558.5645142	−0.43548584	0.07790444	2.808949	[56]
K19	545	545.203064	0.203063965	0.037259445	2.740354	[59]
K77	546	544.6682739	−1.331726074	0.243905872	2.752063	[60]
CYC-B11	554	552.9317627	−1.068237305	0.19282262	2.796931	[61]
CYC-B6L	551	545.9569702	−5.043029785	0.915250421	2.790254	[62]
CYC-B6S	548	547.302124	−0.697875977	0.12734963	2.774375	[62]
CYC-B7	551	552.8936157	1.893615723	0.343668908	2.791177	[63]
CYC-B13	547	548.375	1.375	0.251371115	2.775524	[64]
JK-55	539	538.1456909	−0.854309082	0.158498898	2.74214	[65]
JK-56	537	538.4175415	1.417541504	0.26397422	2.734822	[65]
RC-31	560	558.7681274	−1.231872559	0.219977245	2.860881	[66]
RC-32	564	562.3169556	−1.683044434	0.298412144	2.884413	[66]
RC-36	547	545.4786377	−1.521362305	0.278128386	2.798735	[66]
PRT1	520	520.6152954	0.61529541	0.118326038	2.663049	[67]
PRT2	517	517.5576172	0.557617188	0.107856326	2.652854	[67]
PRT3	519	519.3753052	0.375305176	0.072313137	2.668113	[67]
PRT4	519	514.8287964	−4.171203613	0.803700089	2.678184	[67]
PRT21	514	515.2487793	1.248779297	0.242953166	2.651222	[68]
PRT22	520	519.6818237	−0.31817627	0.061187744	2.688368	[68]
PRT23	536	537.9351196	1.935119629	0.361029774	2.774103	[68]
PRT24	537	537.1176147	0.117614746	0.021902187	2.787605	[68]
TF1	510	509.9632568	−0.036743164	0.007204542	2.653727	[69]
TF2	509	510.1255798	1.125579834	0.221135527	2.651082	[69]
TF3	513	513.4284058	0.428405762	0.083509892	2.676337	[69]
TF4	516	516.3215942	0.321594238	0.062324464	2.69655	[69]

Table 2. Cont.

Dye	λ_{\max} (Experimental)	λ_{\max} (Predicted)	Difference	Percentage Error	<i>t</i> -Score	Ref.
MJ-4	594	594.5967407	0.596740723	0.100461401	3.109695	[70]
MJ-6	608	606.5596313	−1.440368652	0.236902744	3.174494	[70]
MJ-7	603	606.5596313	3.559631348	0.590320289	3.119411	[70]
MJ-10	630	630.5605469	0.560546875	0.088975698	3.233595	[70]
MJ-11	630	630.5605469	0.560546875	0.088975698	3.149689	[70]
MJ-12	631	632.057312	1.057312012	0.167561337	3.010226	[70]
TFRS-1	532	534.241333	2.241333008	0.421303183	2.251667	[71]
TFRS-2	533	533.7162476	0.716247559	0.1343804	2.269726	[71]
TFRS-3	503	503.7233887	0.723388672	0.143814847	2.151846	[71]
TFRS-4	501	501.8835449	0.883544922	0.176356271	2.146519	[71]
TFRS-21	499	500.2005005	1.200500488	0.240581259	2.137079	[72]
TFRS-22	473	473.5461426	0.546142578	0.115463547	2.022101	[72]
TFRS-24	485	485.4335938	0.43359375	0.089400776	1.963301	[72]
TFRS-51	499	499.3976135	0.397613525	0.079682067	1.925546	[73]
TFRS-52	495	495.3208618	0.320861816	0.064820565	1.866991	[73]
TFRS-53	500	500.4888611	0.488861084	0.097772218	1.795062	[73]
TFRS-54	496	496.4121094	0.412109375	0.083086565	1.695218	[73]
CS9	518	518.0759277	0.075927734	0.014657863	1.573186	[74]
A597	539	538.2700806	−0.729919434	0.135421053	1.632301	[75]
CS27	517	517.1707764	0.170776367	0.033032179	1.590288	[76]
CS28	518	517.486084	−0.513916016	0.099211589	1.579045	[76]
CS32	518	518.0393066	0.039306641	0.007588155	1.557655	[76]
CS43	518	518.1796875	0.1796875	0.034688707	1.529054	[76]
CS17	530	529.7614136	−0.238586426	0.045016307	1.521574	[76]
CS22	533	532.6157837	−0.384216309	0.072085612	1.578218	[76]
LXJ-1	549	548.1496582	−0.850341797	0.154889211	1.686294	[56]
KW-1#	515	514.050293	−0.949707031	0.184409127	1.566551	[77]
KW-2#	550	549.9004517	−0.09954834	0.018099697	1.529517	[77]
HRD-1	543	542.3900757	−0.609924316	0.112324923	1.449902	[78]
K-73	545	545.2966309	0.296630859	0.05442768	1.48967	[79]
KC-5#	537	537.1211548	0.121154785	0.022561412	1.454641	[80]
KC-6#	531	527.5883179	−3.411682129	0.642501354	1.539624	[80]
KC-7#	533	530.7481079	−2.25189209	0.422493815	1.649544	[80]
KC-8	522	522.1340332	0.134033203	0.02567686	1.730241	[80]
MH06	541	540.6497192	−0.350280762	0.064746909	1.841917	[81]
MH11	547	546.6559448	−0.344055176	0.062898569	1.987435	[81]
MC119	548	548.0170898	0.017089844	0.003118585	1.976855	[82]
S3	516	515.6741333	−0.325866699	0.063152462	1.256043	[83]
S4	518	519.6868286	1.686828613	0.325642586	1.462133	[83]

These compounds were named after the initials of the first author of the reference cited.

It is evident from the results shown in Table 2 that the predicted values of λ_{\max} are closer to the experimental values of λ_{\max} collected from the literature. The range of difference in predicted and experimental values is -5.04 to 3.559 , which is very low. Furthermore, the percentage error observed in the experimental and predicted values lie in the range of 0.00145 to 0.915 . The low values prove the reliability of the model.

Statistical Analysis: For statistical analysis of the results shown in Table 2, we applied the *t*-test as defined in Equation (4). The value of *t* as shown in column 6 of Table 2 lies in the range of 1.25 to 3.25 . A positive absolute value of *t* indicates a moderate difference between the means of the two sets of values. It also suggests that the difference between the means is statistically significant, implying that the predicted values significantly deviate from the experimental values.

$$t - \text{score} = \frac{\text{Difference between experimental and predicted value}}{\text{standard error}} \quad (4)$$

4. Discussion

The research work proposed in this work meets the objectives of accurately predicting the absorption maxima. The ANN model designed in this research correctly predicts the value of absorption maxima of the dye sensitizer based on the structure of the dye molecule, numbers of bonds, molecular weight, and atomic weight. The model, trained with different sets of values of these parameters and their corresponding value of the compound, learns to predict the correct value of the absorption maxima. It magnificently reduced the difference and percentage error in the experimental and predicted values of λ_{\max} of a dye, reported in the literature [30,31]. Furthermore, it predicted the impact of collective atomic weights of each atom type and molecular weight of the dye molecule on the value of λ_{\max} of a dye. Moreover, the proposed research work successfully showed the impact of different bonds between constituent atoms of a dye on its absorption maxima.

To achieve the first objective ANN model is trained to predict the absorption maxima of inorganic dye mainly ruthenium complexes used in DSSC. Further, the calculated values of absorption maxima are very close to the experimental values collected from the literature as shown in Table S1. Moreover, it reported the lesser difference in experimental and calculated values of absorption maxima reported by Xu et.al. [30,31]. They reported the difference in range of -27.3 to 27.1 [30] and -16.6 to 16.2 [31]. In contrast, the difference reported in the work proposed in this manuscript lies in the range of -5.043029785 to 3.559631348 . This shows that the proposed model more accurately predicts the value of λ_{\max} . Moreover, the statistical analysis of the difference in the experimental and predicted values in terms of the t -test validates the obtained result. The t -score obtained in the range of 1.25 to 3.23 signifies the importance of the t -test.

In addition, the percentage error observed from the experimental results lies in the range of 0.01468943 to 0.915250421 , which are 96.63 and 94.35% less than the percentage error calculated in the works reported in [30,31].

To demonstrate the impacts of the atomic weight of each atom and molecular weight on the value of λ_{\max} , a correlation matrix was studied as shown in Figure 9. The atomic weight of sulfur and fluorine shows a considerable impact on λ_{\max} value. The λ_{\max} value is directly proportional to the sulfur atoms, whereas it is indirectly proportional to the fluorine atoms.

Further, the correlation matrix of λ_{\max} with different bonds was studied as shown in Figures 5–8. Initially, the correlation matrix of λ_{\max} with C-C, C=C, C-N, C=O, Metal-NCS, C-O, Metal-N bonds as demonstrated in Figure 5 shows that the λ_{\max} directly depends only on the Metal-NCS bond and inversely depends on Metal-N bonds. The next correlation matrix as shown in Figure 6 indicates the relation of λ_{\max} and N+Bu4=2, O-H=1, O-Na=1, O-H=2 C-S=4, C-S=8, and C-Se=4. It is concluded that the λ_{\max} directly depends on the bond O-H=2, whereas it inversely depends on the C-S=8 bond. Likewise, the correlation of λ_{\max} based on C-S, N⁺(C4H9), O-H, C-F, N≡N bonds were studied. It is observed that λ_{\max} directly depends on the C-S bonds and is inversely dependent on the C-F bond. Furthermore, the correlation of λ_{\max} based on O-H, N-N, TBA⁺, N-H bonds were studied. It is concluded that the impact on the λ_{\max} is observed at its maximum with the increase in the TBA⁺ group in dye structure, whereas the λ_{\max} value decreases with an increase in N≡N bonds.

The impacts of activation function 'ReLU', loss function Mean Absolute Error (MSE), and optimizer 'Adam' on the prediction accuracy of λ_{\max} using the ANN model were observed. It is concluded that the proposed model is more efficient than the methods available in the literature [30,31]. It accounts for the diminishing difference in predicted and experimental values of λ_{\max} . Furthermore, justify the relation of λ_{\max} with other bonds of dye molecule as well as the impact of atomic and molecular weight on it.

Further, the superiority of the customized ANN model over the traditional machine learning models is proved by conducting the experiments. The values of Mean Square Error (MSE), and Percentage Error reported by ANN, Xgboost, and Random Forest models were recorded for each epoch. These values are illustrated in Figures 10 and 11, respectively.

This is evident from Figure 10, that the ANN model reports the lowest value of MSE among all the three models. This proves that ANN model outperforms the Xgboost and Random Forest in predicting the value of absorption maxima.

Similarly, the results demonstrated in Figure 11 prove that the ANN model reports the lowest value of percentage error among all the above-stated three models. This justifies the efficacy of ANN model in correctly predicting the value of absorption maxima.

5. Conclusions

In this manuscript, a customized ANN model is developed for automating the prediction of the value of absorption maxima of dye without actually fabricating the dye. Further, the ANN model is fine-tuned to minimize the difference in the experimental and predicted values. The model precisely predicted values of absorption maxima. The difference reported in the proposed work is -22.3 to 23.6 values lower than the range of difference reported in [30,31]. Similarly, the difference is lower by values from 11.56 to 12.7. This proves the supremacy of the proposed work over the reported methods in the literature.

Furthermore, the research work available so far does not focus on showing the impact of the atomic weight of atoms in a dye molecule, the number, and types of bonds available in a dye molecule. The research works presented in this manuscript showcase the role of atomic weights and different types of bonds present in dye molecules on the value of their absorption maxima. Furthermore, they show the direct and inverse correlation of individual atoms present in a dye molecule on the value of absorption maxima. Moreover, they predict the inter-correlation among different atoms present in a dye molecule. The experimental results prove the efficacy of the proposed work, minimizing the requirements for hit and trial experiments. Therefore, it is a cost-saving approach for fabricating the dye of desired characteristics.

The model is purely dependent on the descriptors originated from the chemical structure of the dye molecule and valid for regular dyes of whichever chemical structure. Therefore, this model would be beneficial for the synthesis of new sensitizers with preferred absorption maxima values for DSSC.

Supplementary Materials: The following are available online at <https://www.mdpi.com/article/10.3390/bdcc7020115/s1>, Table S1: Dataset.

Author Contributions: All authors of this manuscript have equal contribution in conceptualization, methodology, software, validation, formal analysis, investigation, data curation, writing—original draft preparation, writing—review and editing, and visualization. N.T. and K.G. are involved in implementation and conducting experiments, G.R., V.S.D. and P.K.S. are also involved in supervision. E.Z. and E.V. are also involved in project administration, and funding acquisition. All authors have read and agreed to the published version of the manuscript.

Funding: This research is funded by DIMES (Department of Informatics, Modeling, Electronics and Systems)—University of Calabria with Grant/Award Number: SIMPATICO_ZUMPARNO.

Data Availability Statement: The sample dataset used in this research is submitted as Supplementary Material. The code is available with authors. They will provide the code on request.

Acknowledgments: The authors would like to acknowledge the financial support by the Science and Engineering Research Board (SERB) under Grant No. [EMR/2016/006259].

Conflicts of Interest: The authors declare no conflict of interest.

References

1. Käberger, T. Progress of renewable electricity replacing fossil fuels. *Glob. Energy Interconnect.* **2018**, *1*, 48–52.
2. Tomar, N.; Dhaka, V.S.; Suroolia, P.K. A brief review on carbon nanomaterial counter electrodes for N719 based dye-sensitized solar cells. *Mater. Today Proc.* **2021**, *43*, 2975–2978. [[CrossRef](#)]
3. Gangopadhyay, U.; Jana, S.; Das, S. State of Art of Solar Photovoltaic Technology. In *Conference Papers in Science*; Hindawi: London, UK, 2013.
4. Giribabu, L.; Sudhakar, K.; Velkannan, V. Phthalocyanines: Potential alternative sensitizers to Ru (II) polypyridyl complexes for dye-sensitized solar cells. *Curr. Sci.* **2012**, *102*, 991–1000.

5. Glunz, S.W.; Feldmann, F. SiO₂ surface passivation layers—A key technology for silicon solar cells. *Sol. Energy Mater. Sol. Cells* **2018**, *185*, 260–269. [[CrossRef](#)]
6. Lyons, C.; Dev, P.; Maji, P.; Rathi, N.; Surolia, P.K.; Byrne, O.; Xiao, X.; English, N.J.; Magner, E.; MacElroy, J.M.D.; et al. Silicon-bridged triphenylamine-based organic dyes for efficient dye-sensitized solar cells. *Sol. Energy* **2018**, *160*, 64–75. [[CrossRef](#)]
7. Meng, K.; Surolia, P.K.; Byrne, O.; Thampi, K.R. Quantum dot and quantum dot-dye co-sensitized solar cells containing organic thiolate—Disulfide redox electrolyte. *J. Power Sources* **2015**, *275*, 681–687. [[CrossRef](#)]
8. Tomar, N.; Agrawal, A.; Dhaka, V.S.; Surolia, P.K. Ruthenium complexes based dye sensitized solar cells: Fundamentals and research trends. *Sol. Energy* **2020**, *207*, 59–76. [[CrossRef](#)]
9. Brennan, L.J.; Surolia, P.K.; Rovelli, L.; Loudon, A.; Torsney, S.P.; Roche, S.; Thampi, K.R.; Gun'ko, Y.K. Electrophoretic separation and deposition of metal–graphene nanocomposites and their application as electrodes in solar cells. *RSC Adv.* **2016**, *6*, 64097–64109. [[CrossRef](#)]
10. Byrne, O.; Coughlan, A.; Surolia, P.K.; Thampi, K.R. Succinonitrile-based solid-state electrolytes for dye-sensitized solar cells. *Prog. Photovolt. Res. Appl.* **2015**, *23*, 417–427. [[CrossRef](#)]
11. Calogero, G.; Sinopoli, A.; Citro, I.; Di Marco, G.; Petrov, V.; Diniz, A.M.; Parola, A.J.; Pina, F. Synthetic analogues of anthocyanins as sensitizers for dye-sensitized solar cells. *Photochem. Photobiol. Sci.* **2013**, *12*, 883–894. [[CrossRef](#)]
12. Sheehan, S.; Surolia, P.; Byrne, O.; Garner, S.; Cimo, P.; Li, X.; Dowling, D.; Thampi, K. Flexible glass substrate based dye sensitized solar cells. *Sol. Energy Mater. Sol. Cells* **2015**, *132*, 237–244. [[CrossRef](#)]
13. Sugathan, V.; John, E.; Sudhakar, K. Recent improvements in dye sensitized solar cells: A review. *Renew. Sustain. Energy Rev.* **2015**, *52*, 54–64. [[CrossRef](#)]
14. Meyer, G.J. *Efficient Light-to-Electrical Energy Conversion: Nanocrystalline TiO₂ Films Modified with Inorganic Sensitizers*; ACS Publications: Washington, DC, USA, 1997.
15. Selvaraj, P.; Baig, H.; Mallick, T.K.; Siviter, J.; Montecucco, A.; Li, W.; Paul, M.; Sweet, T.; Gao, M.; Knox, A.R.; et al. Enhancing the efficiency of transparent dye-sensitized solar cells using concentrated light. *Sol. Energy Mater. Sol. Cells* **2018**, *175*, 29–34. [[CrossRef](#)]
16. Richhariya, G.; Kumar, A.; Tekasakul, P.; Gupta, B. Natural dyes for dye sensitized solar cell: A review. *Renew. Sustain. Energy Rev.* **2017**, *69*, 705–718. [[CrossRef](#)]
17. Jin, L.; Shi, S.; Zhao, C.; Yu, X.; Lu, J.; Wang, Q.; Wei, Y. Y-shaped organic dyes with D2–π–A configuration as efficient co-sensitizers for ruthenium-based dye sensitized solar cells. *J. Power Sources* **2021**, *481*, 228952. [[CrossRef](#)]
18. Juwita, R.; Lin, J.-Y.; Lin, S.-J.; Liu, Y.-C.; Wu, T.-Y.; Feng, Y.-M.; Chen, C.-Y.; Tsai, H.-H.G.; Wu, C.-G. Osmium sensitizer with enhanced spin–orbit coupling for panchromatic dye-sensitized solar cells. *J. Mater. Chem. A* **2020**, *8*, 12361–12369. [[CrossRef](#)]
19. Semalti, P.; Sharma, S.N. Dye sensitized solar cells (DSSCs) electrolytes and natural photo-sensitizers: A review. *J. Nanosci. Nanotechnol.* **2020**, *20*, 3647–3658. [[CrossRef](#)]
20. Colombo, A.; Dragonetti, C.; Roberto, D.; Fagnani, F. Copper Complexes as Alternative Redox Mediators in Dye-Sensitized Solar Cells. *Molecules* **2021**, *26*, 194. [[CrossRef](#)]
21. Bobo, M.V.; Paul, A.; Robb, A.J.; Arcidiacono, A.M.; Smith, M.D.; Hanson, K.; Vannucci, A.K. Bis-Cyclometalated Iridium Complexes Containing 4, 4'-Bis (phosphonomethyl)-2, 2'-bipyridine Ligands: Photophysics, Electrochemistry, and High-Voltage Dye-Sensitized Solar Cells. *Inorg. Chem.* **2020**, *59*, 6351–6358. [[CrossRef](#)]
22. Alhorani, S.; Kumar, S.; Genwa, M.; Meena, P. Review of latest efficient sensitizer in dye-sensitized solar cells. In Proceedings of the AIP Conference Proceedings, Coimbatore, India, 17–18 July 2020; AIP Publishing LLC: College Park, MD, USA, 2020; p. 030632.
23. Lyons, C.; Rathi, N.; Dev, P.; Byrne, O.; Surolia, P.K.; Maji, P.; MacElroy, J.; Yella, A.; Grätzel, M.; Magner, E. Organic dyes containing coplanar dihexyl-substituted dithienosilole groups for efficient dye-sensitized solar cells. *Int. J. Photoenergy* **2017**, *2017*, 7594869. [[CrossRef](#)]
24. Ghavre, M.; Byrne, O.; Altes, L.; Surolia, P.K.; Spulak, M.; Quilty, B.; Thampi, K.R.; Gathergood, N. Low toxicity functionalised imidazolium salts for task specific ionic liquid electrolytes in dye-sensitized solar cells: A step towards less hazardous energy production. *Green Chem.* **2014**, *16*, 2252–2265. [[CrossRef](#)]
25. Sekar, N.; Gehlot, V.Y. Metal complex dyes for dye-sensitized solar cells: Recent developments. *Resonance* **2010**, *15*, 819–831. [[CrossRef](#)]
26. Cai-Rong, Z.; Zi-Jiang, L.; Yu-Hong, C.; Hong-Shan, C.; You-Zhi, W.; Li-Hua, Y. DFT and TDDFT study on organic dye sensitizers D5, DST and DSS for solar cells. *J. Mol. Struct. THEOCHEM* **2009**, *899*, 86–93. [[CrossRef](#)]
27. Jamshidvand, A.; Keshavarzi, R.; Mirkhani, V.; Moghadam, M.; Tangestaninejad, S.; Mohammadpoor-Baltork, I.; Afzali, N.; Nematollahi, J.; Amini, M. A novel Ru (II) complex with high absorbance coefficient: Efficient sensitizer for dye-sensitized solar cells. *J. Mater. Sci. Mater. Electron.* **2021**, *32*, 9345–9356. [[CrossRef](#)]
28. El alamy, A.; Bourass, M.; Amine, A.; Hamidi, M.; Bouachrine, M. New organic dyes based on phenylenevinylene for solar cells: DFT and TD-DFT investigation. *Karbala Int. J. Mod. Sci.* **2017**, *3*, 75–82. [[CrossRef](#)]
29. Nashed, R.; Ismail, Y.; Allam, N.K. Recent advances in the use of density functional theory to design efficient solar energy-based renewable systems. *J. Renew. Sustain. Energy* **2013**, *5*, 022701. [[CrossRef](#)]
30. Xu, J.; Zhang, H.; Wang, L.; Liang, G.; Wang, L.; Shen, X.; Xu, W. QSPR study of absorption maxima of organic dyes for dye-sensitized solar cells based on 3D descriptors. *Spectrochim. Acta Part A Mol. Biomol. Spectrosc.* **2010**, *76*, 239–247. [[CrossRef](#)]

31. Xu, J.; Zhang, H.; Wang, L.; Liang, G.; Wang, L.; Shen, X. Artificial neural network-based QSPR study on absorption maxima of organic dyes for dye-sensitized solar cells. *Mol. Simul.* **2011**, *37*, 1–10. [[CrossRef](#)]
32. Schweitzer, R.C.; Morris, J.B. The development of a quantitative structure property relationship (QSPR) for the prediction of dielectric constants using neural networks. *Anal. Chim. Acta* **1999**, *384*, 285–303. [[CrossRef](#)]
33. Wessel, M.D.; Jurs, P.C. Prediction of reduced ion mobility constants from structural information using multiple linear regression analysis and computational neural networks. *Anal. Chem.* **1994**, *66*, 2480–2487. [[CrossRef](#)]
34. Asadollahi-Baboli, M.; Mani-Varnosfaderani, A. Application of computational methods to predict absorption maxima of organic dyes used in solar cells. *J. Theor. Comput. Chem.* **2013**, *12*, 1250114. [[CrossRef](#)]
35. Andrei, N. A note on memory-less SR1 and memory-less BFGS methods for large-scale unconstrained optimization. *Numer. Algorithms* **2022**, *90*, 223–240. [[CrossRef](#)]
36. Zupan, J.; Novič, M.; Ruisánchez, I. Kohonen and counterpropagation artificial neural networks in analytical chemistry. *Chemom. Intell. Lab. Syst.* **1997**, *38*, 1–23. [[CrossRef](#)]
37. Heidari, E.; Sobati, M.A.; Movahedirad, S. Accurate prediction of nanofluid viscosity using a multilayer perceptron artificial neural network (MLP-ANN). *Chemom. Intell. Lab. Syst.* **2016**, *155*, 73–85. [[CrossRef](#)]
38. Taghavi, M.; Ghareghani, A.; Nejad, F.B.; Mirsalim, M. Developing a model to predict the start of combustion in HCCI engine using ANN-GA approach. *Energy Convers. Manag.* **2019**, *195*, 57–69. [[CrossRef](#)]
39. Pradhan, N.; Singh Dhaka, V.; Rani, G.; Chaudhary, H. Machine Learning Model for Multi-View Visualization of Medical Images. *Comput. J.* **2022**, *65*, 805–817. [[CrossRef](#)]
40. Pradhan, N.; Dhaka, V.S.; Rani, G.; Chaudhary, H. Transforming view of medical images using deep learning. *Neural Comput. Appl.* **2020**, *32*, 15043–15054. [[CrossRef](#)]
41. Chaves, L.; Marques, G. Data Mining Techniques for Early Diagnosis of Diabetes: A Comparative Study. *Appl. Sci.* **2021**, *11*, 2218. [[CrossRef](#)]
42. Dhaka, V.S.; Rani, G.; Oza, M.G.; Sharma, T.; Misra, A. A deep learning model for mass screening of COVID-19. *Int. J. Imaging Syst. Technol.* **2021**, *31*, 483–498. [[CrossRef](#)]
43. Rani, G.; Oza, M.G.; Dhaka, V.S.; Pradhan, N.; Verma, S.; Rodrigues, J.J. Applying deep learning-based multi-modal for detection of coronavirus. *Multimed. Syst.* **2022**, *28*, 1251–1262. [[CrossRef](#)]
44. Sinwar, D.; Dhaka, V.S.; Sharma, M.K.; Rani, G. AI-Based Yield Prediction and Smart Irrigation. In *Internet of Things and Analytics for Agriculture*; Springer: Berlin/Heidelberg, Germany, 2020; Volume 2, pp. 155–180.
45. Dhaka, V.S.; Meena, S.V.; Rani, G.; Sinwar, D.; Ijaz, M.F.; Woźniak, M. A survey of deep convolutional neural networks applied for prediction of plant leaf diseases. *Sensors* **2021**, *21*, 4749. [[CrossRef](#)] [[PubMed](#)]
46. Ozawa, H.; Awa, M.; Ono, T.; Arakawa, H. Effects of Dye-Adsorption Solvent on the Performances of the Dye-Sensitized Solar Cells Based on Black Dye. *Chem. Asian J.* **2012**, *7*, 156–162. [[CrossRef](#)] [[PubMed](#)]
47. Gibson, E.A.; Le Pleux, L.; Fortage, J.; Pellegrin, Y.; Blart, E.; Odobel, F.; Hagfeldt, A.; Boschloo, G. Role of the Triiodide/Iodide Redox Couple in Dye Regeneration in p-Type Dye-Sensitized Solar Cells. *Langmuir* **2012**, *28*, 6485–6493. [[CrossRef](#)] [[PubMed](#)]
48. Nazeeruddin, M.K.; Pechy, P.; Renouard, T.; Zakeeruddin, S.M.; Humphry-Baker, R.; Comte, P.; Liska, P.; Cevey, L.; Costa, E.; Shklover, V. Engineering of efficient panchromatic sensitizers for nanocrystalline TiO₂-based solar cells. *J. Am. Chem. Soc.* **2001**, *123*, 1613–1624. [[CrossRef](#)] [[PubMed](#)]
49. Nazeeruddin, M.K.; De Angelis, F.; Fantacci, S.; Selloni, A.; Viscardi, G.; Liska, P.; Ito, S.; Takeru, B.; Grätzel, M. Combined experimental and DFT-TDDFT computational study of photoelectrochemical cell ruthenium sensitizers. *J. Am. Chem. Soc.* **2005**, *127*, 16835–16847. [[CrossRef](#)]
50. Wen, P.; Han, Y.; Zhao, W. Influence of TiO₂ nanocrystals fabricating dye-sensitized solar cell on the absorption spectra of N719 sensitizer. *Int. J. Photoenergy* **2012**, *2012*, 906198. [[CrossRef](#)]
51. Yen, Y.S.; Chen, Y.C.; Hsu, Y.C.; Chou, H.H.; Lin, J.T.; Yin, D.J. Heteroleptic Ruthenium Sensitizers That Contain an Ancillary Bipyridine Ligand Tethered with Hydrocarbon Chains for Efficient Dye-Sensitized Solar Cells. *Chem. A Eur. J.* **2011**, *17*, 6781–6788. [[CrossRef](#)]
52. Nazeeruddin, M.K.; Baranoff, E.; Grätzel, M. Dye-sensitized solar cells: A brief overview. *Sol. Energy* **2011**, *85*, 1172–1178. [[CrossRef](#)]
53. Chen, C.Y.; Wu, S.J.; Wu, C.G.; Chen, J.G.; Ho, K.C. A Ruthenium complex with superhigh light-harvesting capacity for dye-sensitized solar cells. *Angew. Chem.* **2006**, *118*, 5954–5957. [[CrossRef](#)]
54. Chen, C.Y.; Wu, S.J.; Li, J.Y.; Wu, C.G.; Chen, J.G.; Ho, K.C. A new route to enhance the light-harvesting capability of ruthenium complexes for dye-sensitized solar cells. *Adv. Mater.* **2007**, *19*, 3888–3891. [[CrossRef](#)]
55. Gao, F.; Wang, Y.; Shi, D.; Zhang, J.; Wang, M.; Jing, X.; Humphry-Baker, R.; Wang, P.; Zakeeruddin, S.M.; Grätzel, M. Enhance the optical absorptivity of nanocrystalline TiO₂ film with high molar extinction coefficient ruthenium sensitizers for high performance dye-sensitized solar cells. *J. Am. Chem. Soc.* **2008**, *130*, 10720–10728. [[CrossRef](#)]
56. Yu, Q.; Liu, S.; Zhang, M.; Cai, N.; Wang, Y.; Wang, P. An extremely high molar extinction coefficient ruthenium sensitizer in dye-sensitized solar cells: The effects of π -conjugation extension. *J. Phys. Chem. C* **2009**, *113*, 14559–14566. [[CrossRef](#)]
57. Gao, F.; Wang, Y.; Zhang, J.; Shi, D.; Wang, M.; Humphry-Baker, R.; Wang, P.; Zakeeruddin, S.M.; Grätzel, M. A new heteroleptic ruthenium sensitizer enhances the absorptivity of mesoporous titania film for a high efficiency dye-sensitized solar cell. *Chem. Commun.* **2008**, *59*, 2635–2637. [[CrossRef](#)]

58. Gao, F.; Cheng, Y.; Yu, Q.; Liu, S.; Shi, D.; Li, Y.; Wang, P. Conjugation of selenophene with bipyridine for a high molar extinction coefficient sensitizer in dye-sensitized solar cells. *Inorg. Chem.* **2009**, *48*, 2664–2669. [[CrossRef](#)]
59. Wang, P.; Klein, C.; Humphry-Baker, R.; Zakeeruddin, S.M.; Grätzel, M. A high molar extinction coefficient sensitizer for stable dye-sensitized solar cells. *J. Am. Chem. Soc.* **2005**, *127*, 808–809. [[CrossRef](#)]
60. Kuang, D.; Klein, C.; Ito, S.; Moser, J.E.; Humphry-Baker, R.; Evans, N.; Duriaux, F.; Graetzel, C.; Zakeeruddin, S.M.; Grätzel, M. High-efficiency and stable mesoscopic dye-sensitized solar cells based on a high molar extinction coefficient ruthenium sensitizer and nonvolatile electrolyte. *Adv. Mater.* **2007**, *19*, 1133–1137. [[CrossRef](#)]
61. Chen, C.-Y.; Wang, M.; Li, J.-Y.; Pootrakulchote, N.; Alibabaei, L.; Ngoc-le, C.-h.; Decoppet, J.-D.; Tsai, J.-H.; Grätzel, C.; Wu, C.-G. Highly efficient light-harvesting ruthenium sensitizer for thin-film dye-sensitized solar cells. *ACS Nano* **2009**, *3*, 3103–3109. [[CrossRef](#)]
62. Chen, C.Y.; Chen, J.G.; Wu, S.J.; Li, J.Y.; Wu, C.G.; Ho, K.C. Multifunctionalized ruthenium-based supersensitizers for highly efficient dye-sensitized solar cells. *Angew. Chem.* **2008**, *120*, 7452–7455. [[CrossRef](#)]
63. Li, J.-Y.; Chen, C.-Y.; Chen, J.-G.; Tan, C.-J.; Lee, K.-M.; Wu, S.-J.; Tung, Y.-L.; Tsai, H.-H.; Ho, K.-C.; Wu, C.-G. Heteroleptic ruthenium antenna-dye for high-voltage dye-sensitized solar cells. *J. Mater. Chem.* **2010**, *20*, 7158–7164. [[CrossRef](#)]
64. Chen, C.-Y.; Pootrakulchote, N.; Wu, S.-J.; Wang, M.; Li, J.-Y.; Tsai, J.-H.; Wu, C.-G.; Zakeeruddin, S.M.; Grätzel, M. New ruthenium sensitizer with carbazole antennas for efficient and stable thin-film dye-sensitized solar cells. *J. Phys. Chem. C* **2009**, *113*, 20752–20757. [[CrossRef](#)]
65. Choi, H.; Baik, C.; Kim, S.; Kang, M.-S.; Xu, X.; Kang, H.S.; Kang, S.O.; Ko, J.; Nazeeruddin, M.K.; Grätzel, M. Molecular engineering of hybrid sensitizers incorporating an organic antenna into ruthenium complex and their application in solar cells. *N. J. Chem.* **2008**, *32*, 2233–2237. [[CrossRef](#)]
66. Chen, W.-C.; Kong, F.-T.; Ghadiri, R.; Li, Z.-Q.; Guo, F.-L.; Liu, X.-P.; Huang, Y.; Yu, T.; Hayat, T.; Dai, S.-Y. Unravelling the structural-electronic impact of arylamine electron-donating antennas on the performances of efficient ruthenium sensitizers for dye-sensitized solar cells. *J. Power Sources* **2017**, *346*, 71–79. [[CrossRef](#)]
67. Chen, B.-S.; Chen, K.; Hong, Y.-H.; Liu, W.-H.; Li, T.-H.; Lai, C.-H.; Chou, P.-T.; Chi, Y.; Lee, G.-H. Neutral, panchromatic Ru (II) terpyridine sensitizers bearing pyridine pyrazolate chelates with superior DSSC performance. *Chem. Commun.* **2009**, *39*, 5844–5846. [[CrossRef](#)] [[PubMed](#)]
68. Wang, S.-W.; Chou, C.-C.; Hu, F.-C.; Wu, K.-L.; Chi, Y.; Clifford, J.N.; Palomares, E.; Liu, S.-H.; Chou, P.-T.; Wei, T.-C. Panchromatic Ru (II) sensitizers bearing single thiocyanate for high efficiency dye sensitized solar cells. *J. Mater. Chem. A* **2014**, *2*, 17618–17627. [[CrossRef](#)]
69. Chou, C.C.; Wu, K.L.; Chi, Y.; Hu, W.P.; Yu, S.J.; Lee, G.H.; Lin, C.L.; Chou, P.T. Ruthenium (II) Sensitizers with Heteroleptic Tridentate Chelates for Dye-Sensitized Solar Cells. *Angew. Chem.* **2011**, *123*, 2102–2106. [[CrossRef](#)]
70. Kimura, M.; Masuo, J.; Tohata, Y.; Obuchi, K.; Masaki, N.; Murakami, T.N.; Koumura, N.; Hara, K.; Fukui, A.; Yamanaka, R. Improvement of TiO₂/dye/electrolyte interface conditions by positional change of alkyl chains in modified panchromatic Ru complex dyes. *Chem.—A Eur. J.* **2013**, *19*, 1028–1034. [[CrossRef](#)]
71. Wu, K.-L.; Hsu, H.-C.; Chen, K.; Chi, Y.; Chung, M.-W.; Liu, W.-H.; Chou, P.-T. Development of thiocyanate-free, charge-neutral Ru (II) sensitizers for dye-sensitized solar cells. *Chem. Commun.* **2010**, *46*, 5124–5126. [[CrossRef](#)]
72. Wang, S.-W.; Wu, K.-L.; Ghadiri, E.; Lobello, M.G.; Ho, S.-T.; Chi, Y.; Moser, J.-E.; De Angelis, F.; Grätzel, M.; Nazeeruddin, M.K. Engineering of thiocyanate-free Ru (II) sensitizers for high efficiency dye-sensitized solar cells. *Chem. Sci.* **2013**, *4*, 2423–2433. [[CrossRef](#)]
73. Wu, K.-L.; Ku, W.-P.; Clifford, J.N.; Palomares, E.; Ho, S.-T.; Chi, Y.; Liu, S.-H.; Chou, P.-T.; Nazeeruddin, M.K.; Grätzel, M. Harnessing the open-circuit voltage via a new series of Ru (II) sensitizers bearing (iso-) quinolinyl pyrazolate ancillaries. *Energy Environ. Sci.* **2013**, *6*, 859–870. [[CrossRef](#)]
74. Sahin, C.; Tozlu, C.; Ocakoglu, K.; Zafer, C.; Varlikli, C.; Icli, S. Synthesis of an amphiphilic ruthenium complex with swallow-tail bipyridyl ligand and its application in nc-DSSC. *Inorg. Chim. Acta* **2008**, *361*, 671–676. [[CrossRef](#)]
75. Qin, Y.; Peng, Q. Ruthenium sensitizers and their applications in dye-sensitized solar cells. *Int. J. Photoenergy* **2012**, *2012*, 291579. [[CrossRef](#)]
76. Sahin, C.; Dittrich, T.; Varlikli, C.; Icli, S.; Lux-Steiner, M.C. Role of side groups in pyridine and bipyridine ruthenium dye complexes for modulated surface photovoltage in nanoporous TiO₂. *Sol. Energy Mater. Sol. Cells* **2010**, *94*, 686–690. [[CrossRef](#)]
77. Willinger, K.; Fischer, K.; Kisselev, R.; Thelakkat, M. Synthesis, spectral, electrochemical and photovoltaic properties of novel heteroleptic polypyridyl ruthenium (II) donor-antenna dyes. *J. Mater. Chem.* **2009**, *19*, 5364–5376. [[CrossRef](#)]
78. Giribabu, L.; Kumar, C.V.; Rao, C.S.; Reddy, V.G.; Reddy, P.Y.; Chandrasekharam, M.; Soujanya, Y. High molar extinction coefficient amphiphilic ruthenium sensitizers for efficient and stable mesoscopic dye-sensitized solar cells. *Energy Environ. Sci.* **2009**, *2*, 770–773. [[CrossRef](#)]
79. Kuang, D.; Ito, S.; Wenger, B.; Klein, C.; Moser, J.-E.; Humphry-Baker, R.; Zakeeruddin, S.M.; Grätzel, M. High molar extinction coefficient heteroleptic ruthenium complexes for thin film dye-sensitized solar cells. *J. Am. Chem. Soc.* **2006**, *128*, 4146–4154. [[CrossRef](#)]
80. Klein, C.; Nazeeruddin, M.K.; Di Censo, D.; Liska, P.; Grätzel, M. Amphiphilic ruthenium sensitizers and their applications in dye-sensitized solar cells. *Inorg. Chem.* **2004**, *43*, 4216–4226. [[CrossRef](#)]

81. Hussain, M.; El-Shafei, A.; Islam, A.; Han, L. Structure–property relationship of extended π -conjugation of ancillary ligands with and without an electron donor of heteroleptic Ru (II) bipyridyl complexes for high efficiency dye-sensitized solar cells. *Phys. Chem. Chem. Phys.* **2013**, *15*, 8401–8408. [[CrossRef](#)]
82. Chandrasekharam, M.; Suresh, T.; Singh, S.P.; Priyanka, B.; Bhanuprakash, K.; Islam, A.; Han, L.; Kantam, M.L. Functionalized styryl bipyridine as a superior chelate for a ruthenium sensitizer in dye sensitized solar cells. *Dalton Trans.* **2012**, *41*, 8770–8772. [[CrossRef](#)]
83. Sivakumar, R.; Recabarren, R.; Ramkumar, S.; Manivel, A.; Alzate-Morales, J.; Contreras, D.; Manidurai, P. Ruthenium (ii) complexes incorporating carbazole–diazfluorene based bipolar ligands for dye sensitized solar cell applications. *N. J. Chem.* **2017**, *41*, 5605–5612. [[CrossRef](#)]

Disclaimer/Publisher’s Note: The statements, opinions and data contained in all publications are solely those of the individual author(s) and contributor(s) and not of MDPI and/or the editor(s). MDPI and/or the editor(s) disclaim responsibility for any injury to people or property resulting from any ideas, methods, instructions or products referred to in the content.



Precursor-ligand induced steric control over morphology in anisotropically consistent (α -quartz) GeO_2 nanomaterials and its photocatalytic potential under direct sunlight

Lahur Mani Verma^a, Umesh Singh^a, Himanshu Arora^a, Ajay Kumar^a, Veena Dhayal^b, Pravin P. Ingole^c, Satyawati Sharma^a, Anita Raj Sanwaria^a

[Show more](#)

Share Cite

<https://doi.org/10.1016/j.matchemphys.2023.128050>

[Get rights and content](#)

Highlights

- The steric factor of Ge precursors $[\text{Ge} \{\text{OPr}^i\}_{4-n}\{\text{L}\}_n]$ controls its hydrolytic behavior.
- Ligands on Ge precursors play a defining role in the morphology of Germania NPs.
- The size of Germania NPs decreases with an increase in the ligand size of the precursor.
- The band gap affects the photocatalytic activity of Germania NPs under direct sunlight.
- The structural parameters of dye affect its degradation.

Abstract

The notable correlation between morphology and physicochemical properties of nanomaterials has called for particular attention to the synthetic methods of fine control over it. Modern theories of nucleation and crystal growth have often presented an incomplete picture of its understanding and do not apply universally. Here, we investigated a case wherein oxime-modified ligands (L)-based Ge precursors $[\text{Ge} \{\text{OPr}^i\}_{4-n}\{\text{L}\}_n]$ were synthesized from $[\text{Ge} (\text{OPr}^i)_4]$ and subjected further to hydrolysis under a sol-gel scheme. The synthesis of precursors seems to have displayed a mechanistic and thermodynamic limitation over the extent of substitution due to the steric factor of the ligands. Whereas the hydrolysis of these precursors substituted with varying sizes (steric factor) of ligand yielded spherical (20nm), sheet (16nm) and rod-shaped (14nm) nano α -quartz-like GeO_2 . These morphological variations and reduction in the size of NPs, on account of precursors, are understood to have arisen due to the changes in nucleation and Ostwald ripening processes coupled with the hydrolytic behavior of the precursors. The nanosheet structures of α -quartz-like GeO_2 with a band gap of 5.47eV have shown different degradation efficiency, indicating altered surface-interface with two dyes, viz. methylene orange and rhodamine 6G. This work extends the understanding of “Ge” coordination chemistry and the role of precursor assemblies in nano synthesis and application.

Introduction

Recently, advancements in the areas like photovoltaics, optoelectronics and photocatalysis have led to the demand for nanomaterials with tunable physicochemical

properties. This is how the range of materials like germanium dioxide (GeO_2), due to their morphology and size-dependent optoelectronic properties, have, received research attention. This has further, initiated a spurt in fundamental as well as applied investigations from across the range of disciplines [1,2]. The properties like tunable band gap and compatibility of germanium with siliconic processes have made its integration easier and economically viable. Also, the refractive index higher than SiO_2 has made it suitable for various other optical applications (wide-angle lenses, optical waveguides, photosensors, etc.). Additionally, the electrochemical properties of nano-structured GeO_2 materials have also made them useful for lithium-ion batteries [3,4]. Moreover, recent studies suggest that the direct band gap energy, surface adsorption behavior, and controlled electron (e^-) hole (h^+) pair recombination of the nanoscale GeO_2 have allowed its application in photocatalytic degradation of organic dyes too, which may help address the aggravating concern of environmental pollution [5,6]. However, the above-mentioned wide-ranging applications of nano-structured GeO_2 emerge from its suitable morphological, surficial, crystalline, and dimensional characteristics, which in turn calls for efficient methods with strong synthetic control over the material design. But the studies in this direction are very few [2,[6], [7], [8], [9]].

Advertently, unlike the energy-intensive physical methods with limited control over material design and characteristics, the wet chemical bottom-up methods (hydrothermal, precipitation and sol-gel) for nano-synthesis offer enough room for control and manipulation at the atomic level [[10], [11], [12], [13], [14]]. In addition, the control over morphology and size of inorganic nanometal oxides have been shown to be achieved by suitable choice of precursors with specific counter anion [11,12] precursor complexes with designed ligands [1,[13], [14], [15]], choice of a range of surfactants [10], precipitants, synthetic methods and other experimental conditions like temperature, concentration, pH, stirring rate, etc. [2,6,16]. As a matter of fact, there are a few important synthetic attempts of apparent but limited success in this direction. For instance, thermal vapor deposition and electrospinning methods, though efficient, are limited by the factors like one-dimensional structures, expensive precursors such as $\text{Ge}(\text{OPri})_4$, $\text{Ge}(\text{OEt})_4$, and an elevated temperature (700–1200°C). Further, the use of GeCl_4 in the aqueous phase provides a simple route to nano GeO_2 , but its fast hydrolysis limits a fine control over morphology. The reverse micelle or microemulsion system with surfactants in a non-polar system helps overcome half of the problem but remains limited by expensive hazardous $\text{Ge}(\text{OPri})_4$, $\text{Ge}(\text{OEt})_4$ type precursors [17]. As a solution, a rational design is reported for organometallic precursors to avoid salt (a by-product of GeX_4 , $\text{X}=\text{Cl}$ reduction by reducing agents) induced impurities and high thermolytic temperature due to strong $\text{Ge}-\text{Cl}$ bond [18]. This, unlike the $\text{Ge}(\text{NR}_2)_2$ and $\text{Ge}(\text{OR})_2$, (R being alkyl, aryl and silyl moieties) type tailored germanium (II) compounds along with $\text{Ge}[\text{N}(\text{SiMe}_3)_2]_2$, involves XGeZ (with $\text{Z}=\text{OMe}$, NPh_2 , and $\text{X}=\text{bi-dentate ligands}$) which brings the

thermolytic temperature down. However, the morphological control remains weak, probably due to the weak nature of bonds (Ge–N) present in these precursors. Nevertheless, there also appears an inverse correlation between Ge–X bond strength and the tenacity of the method over morphological control [18,19]. In a separate sol-gel study, the germanium alkoxide salt precursors ($\text{Ge}(\text{OR})_4$ (R=Me, Et, Pri or Bun), were employed to study their hydrolytic behavior and morphological control on nano GeO_2 but the problem remains unaddressed [20]. Moreover, a specific application like photocatalysis using nanomaterials (GeO_2) demands fine control over material properties like photostability, photo-corrosion, crystallinity, recombination rate and surface properties of the materials [5,[8], [9], [10]]. It is, therefore, the search for a suitable precursor and method is far from over.

In this study, we modified [$\text{Ge}(\text{OPr}^i)_4$] further with naturally occurring camphor and menthol-based N-oxime as a bulky ligand to assess the hitherto ignored but important role of the steric influence of the ligands on the coordination number of germanium and its subsequent effect on the hydrolytic rate and morphological control of nano GeO_2 . The study, thus, offers not only a novel route to morphologically different nano GeO_2 structures but also an understanding of the steric control over morphology and size, along with a strategy for Ge-based photocatalyst designs for advancing environmental remediation.

Access through your organization

Check access to the full text by signing in through your organization.

Access through **Manipal University Jaipur**

Section snippets

Preparation of precursors and characterization

All the reactions (except hydrolysis reactions) were carried out in anhydrous conditions due to the hygroscopic nature of the reagents and the product [21]. [$\text{Ge}(\text{OPr}^i)_4$] was synthesized by using a reported method [22]. FTIR spectra of the compounds were recorded with the help of FT-Infra rad 8400 spectrometer (SHIMADZU). NMR spectra of the compounds were recorded on JEOL FX 300 FT-NMR spectrometer at 300.4MHz and 75.45MHz frequencies. ESI-mass was noted on THERMO Finning LCQ Advantage max ion ...

Synthesis and characterization of the precursors

Compounds of the type $[\text{Ge}\{\text{OPr}^i\}_{4-n}\{\text{L}\}_n]$ were synthesized by the reactions of $[\text{Ge}(\text{OPr}^i)_4]$ with three oximes derived from acetone, camphor and citronellal in 1:1, 1:2, molar ratios as shown below [21]. These reactions yielded (~99%) white semi-solid, white solid, and thick yellow liquid for acetone, camphor, and citronellal, respectively. Synthetic details of all these complexes are shown in (Table-1). The resulting compounds were distinguished by mutually corroborative spectroscopic evidences. ...

Conclusion

In summary, this article reports the synthesis of a new class of oxime-derived compounds (2), (4) and (6), which were found to be potential precursors for the synthesis of the highly pure hexagonal phase of (α -quartz) Germania. The average particle size and morphology {spherical (2), sheets (4) and rod-like (6)} of the Germania obtained from $[\text{Ge}\{\text{ONC}(\text{CH}_3)_2\}\{\text{OPr}^i\}_2]$ (2), $[\text{Ge}\{\text{ONC}_{10}\text{H}_{16}\}_2\{\text{OPr}^i\}_2]$ (4), and $[\text{Ge}\{\text{ONC}_{10}\text{H}_{18}\}_2\{\text{OPr}^i\}_2]$ (6), are 20nm for (a), ~16nm for (b) and ~14nm for (c), range. The ...

CRedit authorship contribution statement

Lahur Mani Verma: Investigation, Conceptualization, Methodology, Writing – original draft. **Umesh Singh:** Writing – review & editing. **Himanshu Arora:** Resources. **Ajay Kumar:** Data curation. **Veena Dhayal:** Writing – review & editing. **Pravin P. Ingole:** Supervision. **Satyawati Sharma:** Conceptualization, Writing – review & editing, and, Supervision. **Anita Raj Sanwaria:** Investigation, Conceptualization, Supervision. ...

Declaration of competing interest

The authors declare that they have no known competing financial interests or personal relationships that could have appeared to influence the work reported in this paper. ...

Acknowledgment

We thank UGC for its financial assistance. We are thankful to the Physics Department & USIC of Rajasthan University for the imaging analysis. We are also grateful to the Research Medilab Therachem, Jaipur for NMR and ESI mass spectra, JNU Delhi for FT-IR & Raman Spectra and IIT Indore for C, H, N analysis and IIT Delhi for its infrastructural support. Dr. Anita Raj Sanwaria is also thankful to Prof. R. K. Bohra (Retired) from UOR for his constant motivation. ...

References (36)

K. Natarajan *et al.*

Direct sunlight driven photocatalytic activity of GeO₂/monoclinic-BiVO₄ nanoplate composites

Sol. Energy (2017)

W.J. Kim *et al.*

Room temperature synthesis of germanium dioxide nanorods and their in vitro photocatalytic application

Optik (2019)

W.J. Kim *et al.*

Room temperature synthesis of germanium dioxide nanorods and their in vitro photocatalytic application

Optik (2019)

Q. Liang *et al.*

Surfactant-assisted synthesis of photocatalysts: mechanism, synthesis, recent advances and environmental application

Chem. Eng. J. (2019)

A.Y. Shah *et al.*

Germanium tetra(tertiary butoxide): synthesis, structure and its utility as a precursor for the preparation of europium doped germanium oxide nanoparticles

Inorg. Chim. Acta. (2010)

H. Agarwal *et al.*

A review on green synthesis of zinc oxide nanoparticles – an eco-friendly approach

Resource-Efficient Technologies (2017)

A.Y. Shah *et al.*

Germanium tetra(tertiary butoxide): synthesis, structure and its utility as a precursor for the preparation of europium doped germanium oxide nanoparticles

Inorg. Chim. Acta. (2010)

C. Jing *et al.*

Morphology controls of GeO₂ particles precipitated by a facile acid-induced decomposition of germanate ions in aqueous medium

J. Cryst. Growth (2008)

A. Heuer-Jungemann *et al.*

The role of ligands in the chemical synthesis and applications of inorganic nanoparticles

Chem. Rev. (2019)

F.L. Qiu *et al.*

Synthesis of GeO₂/CeGeO₄ nanorods and photocatalytic performance for the removal of methylene blue

J. Bionanoscience (2018)



[View more references](#)

Cited by (1)

Phase controlled green synthesis of wurtzite (P63mc) ZnO nanoparticles: interplay of green ligands with precursor anions, anisotropy and photocatalysis

2023, Nanoscale Advances

[Show abstract](#) 

[View full text](#)

© 2023 Elsevier B.V. All rights reserved.



P-ROCK: A Sustainable Clustering Algorithm for Large Categorical Datasets

Ayman Altameem¹, Ramesh Chandra Poonia², Ankit Kumar³, Linesh Raja⁴ and Abdul Khader Jilani Saudagar^{5,*}

¹Department of Computer Science and Engineering, College of Applied Studies and Community Services, King Saud University, Riyadh, 11533, Saudi Arabia

²Department of Computer Science, CHRIST (Deemed to be University), Bangalore, 560029, India

³Department of Computer Engineering and Applications, GLA University, Mathura, UP, India

⁴Department of Computer Application, Manipal University Jaipur, Rajasthan, 303007, India

⁵Information Systems Department, Imam Mohammad Ibn Saud Islamic University (IMSIU), Riyadh, 11432, Saudi Arabia

*Corresponding Author: Abdul Khader Jilani Saudagar. Email: aksaudagar@imamu.edu.sa

Received: 20 January 2022; Accepted: 02 March 2022

Abstract: Data clustering is crucial when it comes to data processing and analytics. The new clustering method overcomes the challenge of evaluating and extracting data from big data. Numerical or categorical data can be grouped. Existing clustering methods favor numerical data clustering and ignore categorical data clustering. Until recently, the only way to cluster categorical data was to convert it to a numeric representation and then cluster it using current numeric clustering methods. However, these algorithms could not use the concept of categorical data for clustering. Following that, suggestions for expanding traditional categorical data processing methods were made. In addition to expansions, several new clustering methods and extensions have been proposed in recent years. ROCK is an adaptable and straightforward algorithm for calculating the similarity between data sets to cluster them. This paper aims to modify the algorithm by creating a parameterized version that takes specific algorithm parameters as input and outputs satisfactory cluster structures. The parameterized ROCK algorithm is the name given to the modified algorithm (P-ROCK). The proposed modification makes the original algorithm more flexible by using user-defined parameters. A detailed hypothesis was developed later validated with experimental results on real-world datasets using our proposed P-ROCK algorithm. A comparison with the original ROCK algorithm is also provided. Experiment results show that the proposed algorithm is on par with the original ROCK algorithm with an accuracy of 97.9%. The proposed P-ROCK algorithm has improved the runtime and is more flexible and scalable.

Keywords: ROCK; K-means algorithm; clustering approaches; unsupervised learning; K-histogram



This work is licensed under a Creative Commons Attribution 4.0 International License, which permits unrestricted use, distribution, and reproduction in any medium, provided the original work is properly cited.

1 Introduction

To group comparable data points in a cluster, data points are clustered. Numerical points are easier to cluster because several clustering methods have previously been established in this manner. There is a substantial challenge when the data has clustered numeric properties and is categorical. Categorical data must be translated into numerical data because minimal research in this field [1] represented a new promise in the research of categorical data clustering.

Recent research has concentrated on resurrecting traditional simple clustering algorithms with modifications to improve their efficiency. This serves two purposes. Traditional algorithms' scalability and ease of implementation can be preserved for starters. Second, the investment required to develop a new algorithm is significantly higher than that required to modify an existing one.

2 Literature Review

As massive data warehouses store massive amounts of data, clustering has become increasingly important in today's world. Various clustering methods have been developed over the years to cluster this massive amount of data. Clustering categorical and numerical data, on the other hand, is an entirely different challenge. Categorical data values exist on a nominal scale. Each one represents a conceptually distinct notion, they cannot be meaningfully sorted, and they cannot be handled or manipulated the same way numbers can. Blood types A, B, AB, and O, for example, indicate a person's blood type. Rocks can be classified as igneous, metamorphic, or sedimentary. Computing the similarity between data points does not require a distance similarity metric. Over the years, many clustering approaches have been created, and some of them are detailed in the following sub-section.

2.1 Categorical Clustering

The several clustering is listed in the below sub-sections.

2.1.1 K-Modes Clustering

One of the earliest attempts in this direction was the application of the widely used K-means algorithm [2] to categorical data. The authors of [3] referred to the K-modes technique because it determines the central tendency of a group of categorical variables rather than the mean or median. This K-means version worked well with categorical data by utilizing a primary matching dissimilarity method. Finally, the clustering process is updated using a frequency-based method rather than the mean value, resulting in a lower cost function. Choose a K-initial mode value and assign the item with the lowest mode value to the cluster as a starting point for clustering. Each item's dissimilarity metric is then compared to the current model. Then comes the comparison. If the object's mode value is in a different cluster than the current one, reallocate the item to a new one. The procedure is repeated until no further changes are required. However, one issue is that it selects the initial cluster centers at random for each subsequent run, resulting in non-repeatable clustering results.

2.1.2 K-Histogram

The k-means algorithm was also extended in the form of a K-Histogram [4], which required the replacement of means with the histogram to cluster categorical data efficiently. In this direction, the k-means algorithm was modified by replacing mean with histogram and applying a new similarity measure between categorical data and histogram. After the 'k' value is initialized and the cost functions are calculated, the object is assigned to a cluster whose histogram is similar. After each assignment is completed, histograms are updated, and the process is repeated until no further changes are observed.



Alexandria University
Alexandria Engineering Journal

www.elsevier.com/locate/aej
www.sciencedirect.com



Removal of congo red from water by adsorption onto activated carbon derived from waste black cardamom peels and machine learning modeling

Rameez Ahmad Aftab^a, Sadaf Zaidi^{b,*}, Aftab Aslam Parwaz Khan^{c,*},
 Mohd Arish Usman^d, Anees Y. Khan^d, Muhammad Tariq Saeed Chani^c,
 Abdullah M. Asiri^c

^a Department of Chemical Engineering, Zakir Husain College of Engineering and Technology, Aligarh Muslim University, Aligarh 202002, Uttar Pradesh, India

^b Department of Post Harvest Engineering and Technology, Faculty of Agricultural Sciences, Aligarh Muslim University, Aligarh 202002, Uttar Pradesh, India

^c Center of Excellence for Advanced Materials Research, King Abdulaziz University, Jeddah 21589, Saudi Arabia

^d Department of Chemical Engineering, Manipal University Jaipur, Dehmi Kalan, Off. Jaipur-Ajmer Expressway, Jaipur 303007, Rajasthan, India

Received 19 October 2022; revised 12 January 2023; accepted 12 March 2023

KEYWORDS

Black cardamom;
 Activated carbon;
 Machine learning modeling;
 Support vector regression;
 Langmuir isotherm

Abstract The present work utilizes waste black cardamom (BC) as an inexpensive and environmentally friendly adsorbent for sequestering the Congo Red (CR) dye from aqueous media for the first time. Following a carbonization process at 600 °C, chemical activation with KOH was carried out for waste BC and subsequent black cardamom activated carbon (BCAC) was employed as an adsorbent for CR eradication. The effect of experimental factors, including pH, adsorption time, dose and CR initial concentration, was investigated. 96.21 % of CR dye removal was achieved at pH 6 for 100 mg/L of CR concentration having 0.1 g dose at 30 °C. Maximum Langmuir adsorption capacity of BCAC was found to be 69.93 mg/g at 30 °C. The kinetic analyses showed that the CR adsorption over BCAC behaved in accordance with a pseudo-second order kinetic model as high R² values (0.997–1) were obtained. Thermodynamic parameters (ΔH° , ΔS° , and ΔG°) demonstrated that the CR adsorption over BCAC was feasible, spontaneous and exothermic in nature. In addition, the state-of-the-art machine learning (ML) approaches namely, support vector regression (SVR) and artificial neural network (ANN) were employed for modeling the BCAC adsorbent for CR removal. The statistical analysis revealed high prediction performance of SVR model with AARE value of 0.0491 and RMSE value of 0.4635 while the corresponding values for the ANN model were 0.0781 and 0.5395,

Abbreviations: BC, Black Cardamom; BCAC, Black cardamom activated carbon; CR, Congo Red; ML, Machine Learning; ANN, Artificial neural networks; SVR, Support vector regression; AARE, Average absolute relative error; R², Coefficient of determination; RMSE, Root mean square error; SEM, Scanning Electron Microscopy; FTIR, Fourier Transform Infra-Red

* Corresponding authors.

E-mail addresses: sadaf63in@yahoo.com (S. Zaidi), draapk@gmail.com (A. Aslam Parwaz Khan).

Peer review under responsibility of Faculty of Engineering, Alexandria University.

<https://doi.org/10.1016/j.aej.2023.03.055>

1110-0168 © 2023 The Authors. Published by Elsevier B.V. on behalf of Faculty of Engineering, Alexandria University
 This is an open access article under the CC BY-NC-ND license (<http://creativecommons.org/licenses/by-nc-nd/4.0/>).

Nomenclature

C_o	Initial dye concentration (mg L^{-1})	K_L	Langmuir constant (L mg^{-1})
C_e	Dye concentration at equilibrium (mg L^{-1})	qm	Maximum adsorption capacity (mg g^{-1})
q_e	Adsorption capacity at equilibrium (mg g^{-1})	R_L	Separation factor
m	Mass of Adsorbent (g)	K_F	Freundlich adsorption constant (mg g^{-1}) (L mg^{-1}) ^{1/n}
V	Volume (L)	n	Freundlich exponent (g L^{-1})
ε	Loss function	A	Temkin constant for binding energy (L/g^{-1})
w	Weight vector	B	Temkin constant for heat of adsorption (J mol^{-1})
$\lambda(c_i)$	High dimensional feature function for input vector c	χ^2	Chi-squared error
α and α^*	Lagrange multipliers	K_1	Pseudo-first-order rate constant (min^{-1})
f(c)	Regression function	K_2	Pseudo-second-order rate constant ($\text{g mg}^{-1} \text{min}^{-1}$)
b	Bias term	K_{id}	Intra particle diffusion constant ($\text{mg g}^{-1} \text{min}^{-1}$)
$K(c_i, c_j)$	Kernel function	I	Intra particle constant
L	Dual form of the Lagrangian function	K_C	Equilibrium constant
c_i	Input vector	ΔG°	Standard Free energy change (kJ mol^{-1})
d_i	Output vector	ΔH°	Standard Enthalpy change (kJ mol^{-1})
P_i	Predicted value	ΔS°	Standard Entropy change ($\text{kJ mol}^{-1} \text{K}^{-1}$)
E_i	Experimental value	T	Absolute temperature (K)
N	Total data points	t	Time (min)
R^2	Coefficient of determination		

respectively. Furthermore, the plots between experimental CR data and ML forecasted data were closely matched ($R^2 > 0.99$). Thus, it can be concluded that BC, an agro waste could be utilized for CR removal and that the adoption of ML approaches can benefit users by providing them with a tool to enhance the design and performance of wastewater treatment operations.

© 2023 The Authors. Published by Elsevier B.V. on behalf of Faculty of Engineering, Alexandria University This is an open access article under the CC BY-NC-ND license (<http://creativecommons.org/licenses/by-nc-nd/4.0/>).

1. Introduction

Water contamination is one of the main issues of our time as a result of the uncontrolled urbanization, population expansion, and industry that has occurred rapidly [1]. Although strict laws and regulations have been promulgated but proper wastewater treatment and its disposal has not been applied [2]. Particularly, a significant volume of polluted water has been released into the environment directly, harming the water resources. An important class of pollutants is synthetic dyes, which are utilized in a variety of sectors including the textile, dyeing, paper, leather tanning, cosmetics, and others [3,4]. $> 7 \times 10^5$ tons of dyes are generated yearly of which about 10% are released into the environment by the textile and associated sectors [5]. Dyes are categorised according to their chemical structures, which influence their characteristics and are divided as cationic or anionic dyes [6]. It is highly challenging to handle wastewater from the dyeing industry because dyes contain complicated molecular structures that prevent biodegradation and make them resilient to light, heat, and oxidising agents [7]. Colored dyes are aesthetically pleasing, cancer-causing, and block light from entering aquatic systems. Additionally, the hazardous and cancer-causing nature of dyeing wastewaters has an impact on both the aquatic ecology and human health [8]. Therefore, it is crucial to remove dye from wastewater or effluents before releasing them into the environment. In this study, the removal of Congo Red (CR) is considered.

Anionic CR dye is very soluble in water which causes disagreeable color changes that endanger water species [9]. CR is an azo dye that metabolizes to benzidine which poses grave risk to human health, including skin, ocular, and gastrointestinal irritation [10]. The removal of CR dye from wastewater has been accomplished using a variety of methods, including coagulation, membrane separation, adsorption, reverse osmosis and ion exchange [11]. Adsorption is rapidly rising to the forefront of treatment technologies as a means of handling dye contaminated aqueous effluent due to its affordability, procedural simplicity, efficacy, and practicality [12]. Due to its porous nature and thermal durability, activated carbon is most frequently utilized as an adsorbent on a large scale [13]. Because it is more expensive and difficult to produce, activated carbon made from non-renewable sources has fewer uses overall [14]. However, various agricultural based materials have been looked at as advantageous raw materials for the production of activated carbon, due to their abundance and non-toxic makeup [15]. Several adsorbents namely, coconut fibre [16], celery residue [7], cabbage waste [12], *Cornulaca monacantha* stem [17], Antigonon leptopus leaf [18] kenaf fibre [19], Casuarina empty fruit [20], *Teucrium polium* L.[10], Eucalyptus leaf powder [21] walnut shell [22], *Eichhornia* shoots [23], pine bark[24], Arjuna seed [25], mango leaves [26], jujube shell [27] *Phoenix dactylifera* seeds [8], apricot stone [28], powder *Bombax Buonopozense* bark [29], teak leaf [30], pineapple stem [31], litchi seed [32] have been utilized for CR removal. Thus, it is observed that efficient adsorbents have been

obtained from agricultural sources. In view of the encouraging development, an effort was made to identify some locally available, cost-effective, and novel bio-waste for scavenging of CR dye from water. It was discovered that black cardamom waste, which is usually discarded in the open or dumped in landfills, aggravates pollution and impinges upon the availability of arable land. It is estimated that nearly 400 kg of black cardamom waste is generated annually in the small Indian town of Aligarh alone. Hence, it was planned to carry out the present study by converting the BC into BCAC and estimate its performance as an adsorbent in the removal of CR dye from water by adsorption.

Modeling of any system or a process is a significant and challenging task in engineering. The challenge may be due to the physical complexity of the natural phenomenon or our limited knowledge of mathematics. Recently, ML has been found to be a very powerful tool in helping to overcome those challenges, by building basic models from the observed patterns as well as assisting decision makers in facing real world problems. Since ML is able to map causal factors and consequent outcomes from the observed patterns (experimental data), without deep knowledge of the complex physical process, these modeling techniques are becoming popular among engineers. Recently, a wide range of applications have benefited greatly from the extensive use of ML techniques for the predictive modeling of the many engineering problems in areas such as air pollution monitoring [33], heat exchanger performance analysis [34], breakthrough mechanism [35], circulation rate in thermosiphon reboiler [36], energy resources forecasting [37] and reservoir properties [38], to name a few. These computational methods accurately forecast complicated processes and quickly give an understanding of how these systems work [39]. The model eliminates the requirement for completing a pilot experiment and aids in developing adsorption apparatus [40].

The main goals of the current study were two-fold. The first was dedicated to the investigation of the efficacy of waste black cardamom based activated carbon (BCAC) to remove CR from aqueous solutions, and generate experimental data. The second was to use this data to develop ML models namely, support vector regression (SVR) and artificial neural network (ANN) for the first time to forecast the uptake capacity of the BCAC adsorbent. Study was done on the variables that affected the CR removal, including temperature, starting dye concentration and pH of the dye water. To verify the performance of the developed ML models, statistical parameters namely, coefficient of determination (R^2), average absolute relative error (AARE), root mean squared error (RMSE), and chi-square (χ^2) were employed. It was observed that the BCAC adsorbent was a promising adsorbent for CR removal from aqueous media and the novel application of ML techniques to model the dye removal efficiency of BCAC may be widely employed as a practical tool to enhance treatment procedures for the removal dyes from aqueous solutions.

2. Materials and methods

2.1. Black cardamom and reagents

Black cardamom waste was collected from local herbal medicine manufacturing plant in Aligarh. Congo Red dye was purchased from Sigma Aldrich. Salts namely, potassium

hydroxide (KOH), hydrochloric acid (HCl) and sodium hydroxide (NaOH) used in the experiments were of analytical grade. Deionized water was utilized in carrying out all the studies. One gram of CR was dissolved in one litre of deionized water to create a stock solution (1000 PPM), which was then diluted with deionized water to the precise concentrations needed.

2.2. Preparation of BCAC

The waste black cardamom pods were washed with water to eliminate dust particles and then dried in the sun for two days. Furthermore, all of these BC pods were oven dried for 24 h at 70 °C. Now the dried BC was pre-carbonised at 300 °C for 1.5 h. The pre-carbonized BC samples were then weighed and blended with a KOH solution (impregnation ratio of 1.5). The impregnated sample were dried in oven and further activated in furnace for 2 hrs at 600 °C. The obtained material was repeatedly refluxed with water. The sample material was then dried and kept before being used.

2.3. Characterization of BCAC

Scanning electron microscope (SEM) was employed for structural pattern and surface morphology of BCAC. SEM (JEOL JSM-7610 FPLUS model) was used to acquire the electron micrographs of gold-coated BCAC prior and post CR dye adsorption. The Fourier transform infra-Red (FTIR) analysis was performed using Bruker ALPHA FTIR Spectrophotometer in KBr pellets (spectroscopic grade) in the wavelength range of 500–4000 cm^{-1} . This approach could be useful in describing potential surface functional differences between feedstock and BCAC. The concentrations of CR dye were analysed by visible – spectrophotometer (Electronics India). The solid addition technique was used to determine the pH values of the adsorbent at the (pH_{pzc}). The pH of solutions was ascertained by Labman pH meter (India).

2.4. Adsorption experiments

The effect on the CR adsorption mechanism was studied by adjusting operational conditions such dose, pH (6–10), beginning CR dye concentration (50–200 mg/L), and temperature (30 °C – 50 °C) and interaction time (0–120 min) of CR dye and BCAC. The CR batch adsorption investigations were conducted using the temperature-controlled water bath shaker (REMI CIS 24). In a 250-ml conical flask, an aliquot of 0.2 g of BCAC was assorted with 20 ml of CR required concentration solution and flask was put at 150 rpm agitation speed of water bath until equilibrium was attained. The spectrophotometer (Electronics India) was used to determine the final concentration of the filtered sample. The pollutant removal percentage (% R) of CR dye and quantity of adsorption at equilibrium Q_e (mg/g), was determined at time (t) using equation (1) and (2) respectively.

$$\%R = \left(\frac{C_o - C_e}{C_o} \right) \times 100 \quad (1)$$

$$q_e = \left(\frac{C_o - C_e}{m} \right) \times V \quad (2)$$

Where, C_0 and C_e are the CR concentrations at the start and end of the experiment, respectively. The number V represents the volume of CR aqueous solution (in litres), whereas m symbolizes the BCAC adsorbent mass (in grams).

The effect of solution pH on the removal effectiveness of CR using BCAC was explored by regulating pH in the range of 6–10 for CR and utilising 0.01 M HCl and 0.01 M NaOH solution as adjusting medium. The point-of-zero charges (pH_{PZC}) is a property that establishes the pH level at which the adsorbent surface achieves net electrical neutrality and offers important details on the electrostatic interactions between the adsorbent and adsorbate. The pH_{PZC} is determined by solid addition method. At a constant temperature of 30 °C, adsorption isotherm studies were carried out with starting CR concentrations ranging from 50 to 200 mg/L. The kinetic tests were performed, with residual dye concentrations measured at specified time intervals at five different starting CR concentrations of 50, 70, 100, 150 and 200 mg/L, respectively.

2.5. Desorption studies

To conduct the reusability test, 0.1 g of CR loaded BCAC adsorbent was placed into 10 ml of 0.05 M NaOH for 24 hrs. The regenerated adsorbent was then removed and properly cleaned with deionized water before being dried at 55 °C for the subsequent cycle.

2.6. Machine learning modelling

2.6.1. Artificial neural network

The building of ANN intelligent models is based on a variety of straightforward simulations of the biological processes in the human brain that enable learning, remembering, and problem-solving [41]. The neurons of ANN are core processing units, capable of acquiring complex relationship between input and output variables [42]. The mathematical neuron's output is often represented as:

$$Y_n = F(I) = F\left(b + \sum_{n=1}^N w_n X_n\right) \quad (3)$$

In the multi layered (input, hidden and output layers) network fit the data during training, these algorithms modify the weights of the neurons based on the discrepancy between the actual output values and the desired output [43]. The best ANN architecture and training method for a particular job are discovered through a process of trial and error [44]. One of the popular ANN architecture is a first order gradient descent approach called back-propagation which is used to train an algorithm to minimise error [38]. The nodes modified their weights, and the process iterates until error is reduced to a lowest value.

2.6.2. Support vector regression (SVR)

Many literatures provides a detailed explanation of SVMs [45]. The support vector regression makes use of data sets $P = \{(c_1, d_1), (c_2, d_2), \dots, (c_n, d_n)\}$, such that each input c_i has its output d_i . The goal of epsilon SVR model is to adjust the function, $d = f(c)$, so that when it is evaluated with unknown input data $\{c_i\}$, it can predict the output values $\{d_i\}$. The regression function can be expressed as:

$$f(c, w) = (w \cdot \lambda(c) + b) \quad (4)$$

Where $\lambda(c)$ is the high dimensional input function and the dot product ($w \cdot \lambda(c)$).

The regression function represented in equation (4) can be minimized as follows:

$$\text{Minimize : } Q(f) = C \frac{1}{N} L_\epsilon(d, f(c, w)) + \frac{1}{2} \|w^2\| \quad (5)$$

The aforementioned equation has two components. The first is the empirical error, which may be assessed using the following insensitive loss function:

$$L_\epsilon(d, f(c, w)) = \begin{cases} 0 & \text{if } |d - f(c, w)| \leq \epsilon \\ |d - f(c, w)| - \epsilon & \text{otherwise} \end{cases} \quad (6)$$

The second term in the equation stands in for the function flatness. The trade-off between training error and model function flatness is provided by parameter C . With the addition of slack variables (ξ_i, ξ_i^*), the SVR problem is transformed into a dual optimization problem as follows:

$$\text{Minimize : } \frac{1}{2} \|w^2\| + C \sum_{i=1}^N \xi_i + \xi_i^* \quad (7)$$

Subjected to

$$\begin{aligned} (d_i - w \cdot \lambda(c) - b) &\leq \epsilon + \xi_i \\ (w \cdot \lambda(c) + b - d_i) &\leq \epsilon + \xi_i^*, \quad \xi_i \text{ and } \xi_i^* \geq 0 \end{aligned} \quad (8)$$

The introduction of Lagrangian multiplier α_i and α_i^* in the above convex optimization equation transforms it into dual form expressed as:

$$f(c, \alpha_i, \alpha_i^*) = \sum_{i=1}^{N_{SV}} (\alpha_i - \alpha_i^*) (\lambda(c_i) \cdot \lambda(c_j)) + b \quad (9)$$

The non-zero values of coefficients ($\alpha_i - \alpha_i^*$) and their input vectors c_i create the support vectors (SVs). The basic expression for SVR is finally got after applying the kernel function as follows:

$$f(c, \alpha_i, \alpha_i^*) = \sum_{i=1}^{N_{SV}} (\alpha_i - \alpha_i^*) k(c_i, c_j) + b \quad (10)$$

The Karush-Kuhn Tucker (KKT) conditions are used to evaluate the constant b .

2.6.3. ML Models' formulation

The computational ML models (ANN and SVR) were created with five inputs, namely starting CR concentration (50–200 mg/L), dosage (0.04–0.12 g), pH of solution (6–10), Temperature (30 °C – 50 °C) and time (2–120 mins), and adsorption capacity of CR as an output, in order to forecast the performance of BCAC for CR batch adsorption. Following the identification of independent – dependent variables, random normalised data was separated into train and test sets. In this study, the ANN toolbox component of the software package MATLAB (2019b) software was adopted. Three layers in feed forward sequence make up the ANN design, with the hidden layer and output layer each having a different transfer function of tansig and purelin respectively. For little to medium-sized data, one of the most effective back propagation methods is Levenberg-Marquardt optimization. Twelve neu-

rons at hidden layer resulted in lowest prediction error of the formulated ANN model.

The SVR model to predict CR removal over BCAC was programmed by implementing `fitsvm` in MATLAB (2019b). Since just a few settings needed to be changed and the RBF kernel has a high general efficiency, it was chosen for this study out of all the available kernels [46]. To Reduce the five-fold cross-validation loss, the optimal hyperparameter combination was determined via Bayesian optimization [47]. It is possible to compare the performance of these developed models equitably since all models are trained and evaluated using the same data sets. Statistical assessment metrics such as R^2 , AARE, RMSE and Chi-square value were used to verify the performance standard of the developed models as follows:

$$AARE = \frac{1}{N} \sum_{i=1}^N \left| \frac{p_i - E_i}{E_i} \right| \quad (11)$$

$$RMSE = \sqrt{\frac{\sum_{i=1}^N \left(\frac{E_i - p_i}{p_i} \right)^2}{N}} \quad (12)$$

$$\text{Chi-squared value, } \chi^2 = \sum \frac{(E_i - p_i)^2}{p_i} \quad (13)$$

Where, E_i and p_i represent experimental and predicted data points respectively. Whereas, N denotes total data points. The R^2 values were obtained using its command in M. S. Excel (2010).

3. Results and discussion

3.1. BCAC characterization

The SEM micrographs of BCAC and CR laden BCAC at 1 μm are depicted in Fig. 1 (a)-(b). By the pictures from the SEM examination, the structural characteristic of the BCAC adsorbent demonstrates a interconnected porous structure that provides effective CR dye adsorption. Before adsorption, empty spherical holes indicated that there was a substantial surface area available for dye uptake [48]. As from Fig. 1(b) after CR interacted with BCAC, the surface shape changes to become smoother and acquire flaky patches. These modifications show that the CR dye has effectively been loaded onto the adsorbent surface.

The FTIR spectra of BCAC can be seen in Fig. 2 indicating the existence of functional groups and bonds on the BCAC adsorbent. The band at 3438 (cm^{-1}) was shifted after CR accumulation over BCAC to 3425 (cm^{-1}) due to stretching vibrations of -OH group. The peak appear at 2886 (cm^{-1}) may be attributed to -CH stretching [49]. The alkyne group located band at 2310 (cm^{-1}) was moved to 2311 (cm^{-1}) on CR adsorption [50]. The pronounced peak at 1428 (cm^{-1}) changes to 1437 (cm^{-1}) suggest bending CH_2 and CH_3 deformation vibrations [51]. The presence of the C-N length of the aliphatic amines was confirmed by the peak at 1034 cm^{-1} which shifted to 1032 after CR treatment [26]. Following the application of

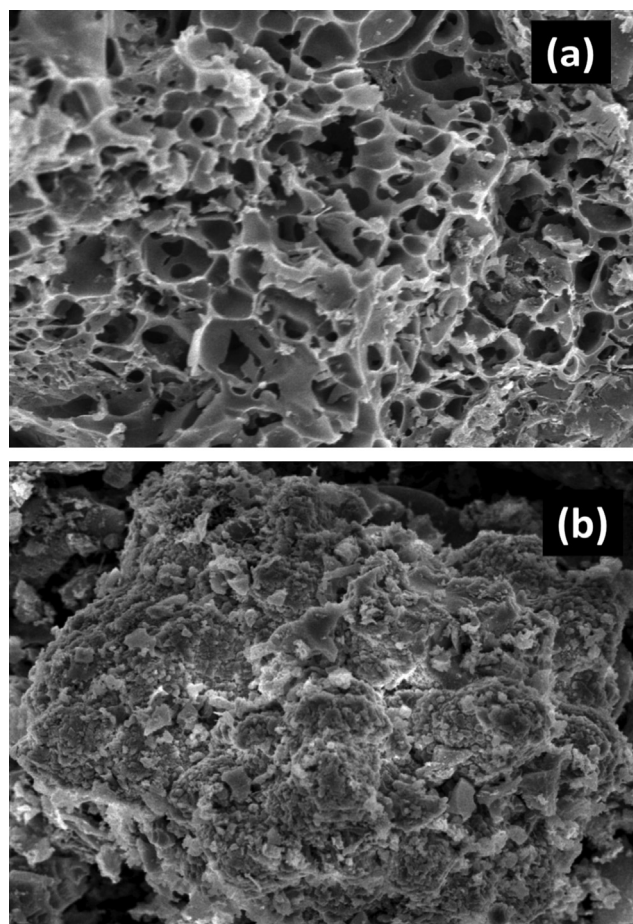


Fig. 1 SEM images of BCAC (a) Prior to CR adsorption and (b) after adsorption of CR at (Magnification: 6000 X; scale: 1 μm).

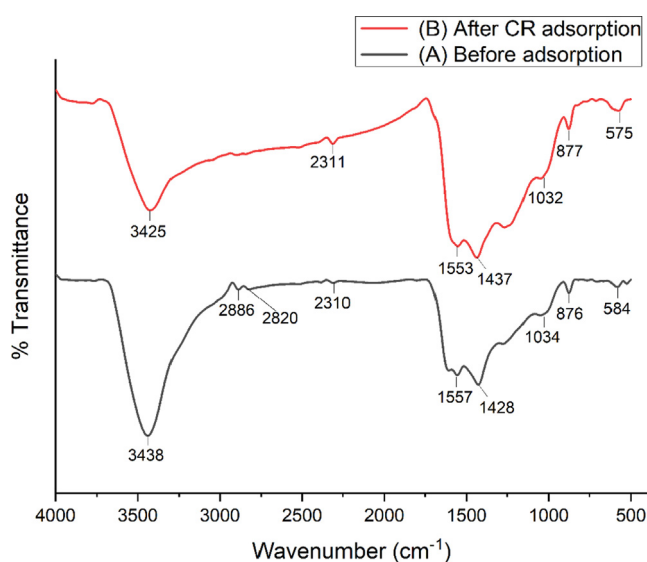


Fig. 2 FTIR spectra of BCAC.

CR dye, there were changes in peak positions, indicating that the CR dye had been successfully adhered onto the BCAC surface. The bands between 400 cm and 800 cm were due to presence of stretch vibrations of C-O and C-H.

3.2. Influence of pH

The pH exhibits a key characteristic throughout the adsorption process by regulating the adsorbent charge and ionisation level of the adsorbate in the solution. It is recognised that pH has an impact on CR's structural stability, which in turn affects the intensity of its hue. When the pH is acidic (pH 3.0–5.0), CR turns blue, whereas between pH 10.0 and 12.0, it turns to different shade of red color compared to original of CR dye [52]. It is stable in the pH range of 6 to 10. Fig. 3 illustrates the outcomes of altering the pH from 6 to 10 in order to investigate the impact of initial pH on CR adsorption. The 96.21 percent of CR dye removal was achieved at

pH 6 for 100 mg/L of CR concentration at 30 °C. Fig. 3A demonstrates that when the solution pH rose to 10, the adsorption effectiveness of BCAC for CR fell to 39.44 percent. This impact of pH change can be explained based on obtained PZC value of 7.54 (Fig. 3B). The pH_{PZC} was determined by salt addition method. The surface of the BCAC is negatively charged below this value [53]. Since CR is an azo anionic dye, removing it was facilitated by a pH value lower than pH_{PZC} because of the stronger electrostatic attraction between the anionic dye molecules and the positive adsorbent surface [40]. Thus, optimum CR uptake on BCAC was obtained at pH 6. In line with our findings, maximum adsorption of CR by bio magnetic composite was occurRed at pH 6.95 [52]; nevertheless, another published study also shows that at pH 6 maximum CR was adsorbed over coffee husk [54].

A detailed description of possible adsorption mechanisms between CR onto BCAC is proposed and described schemati-

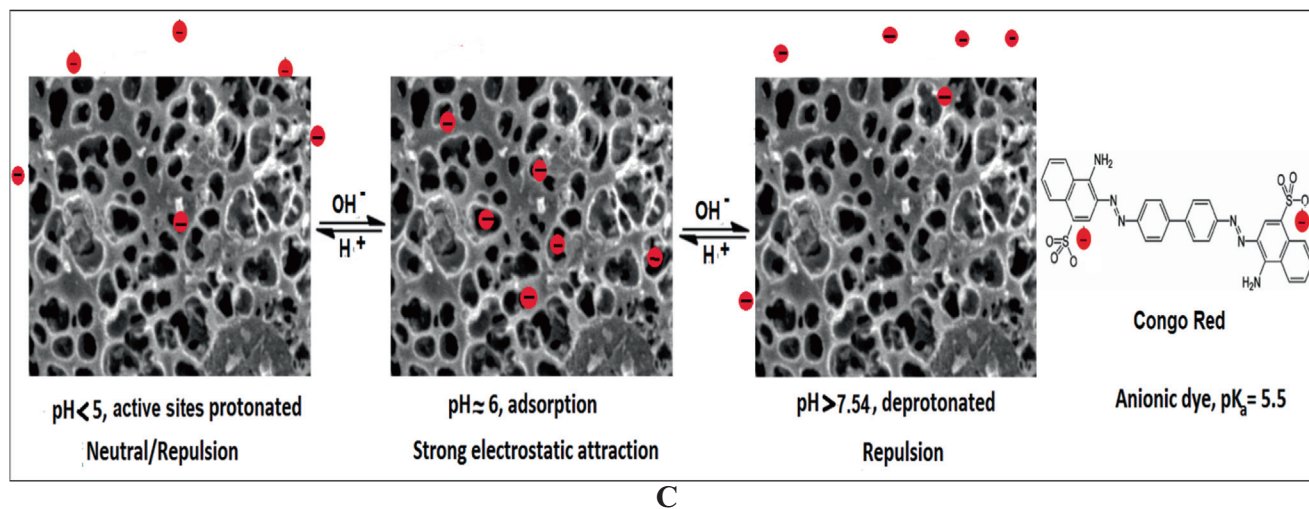
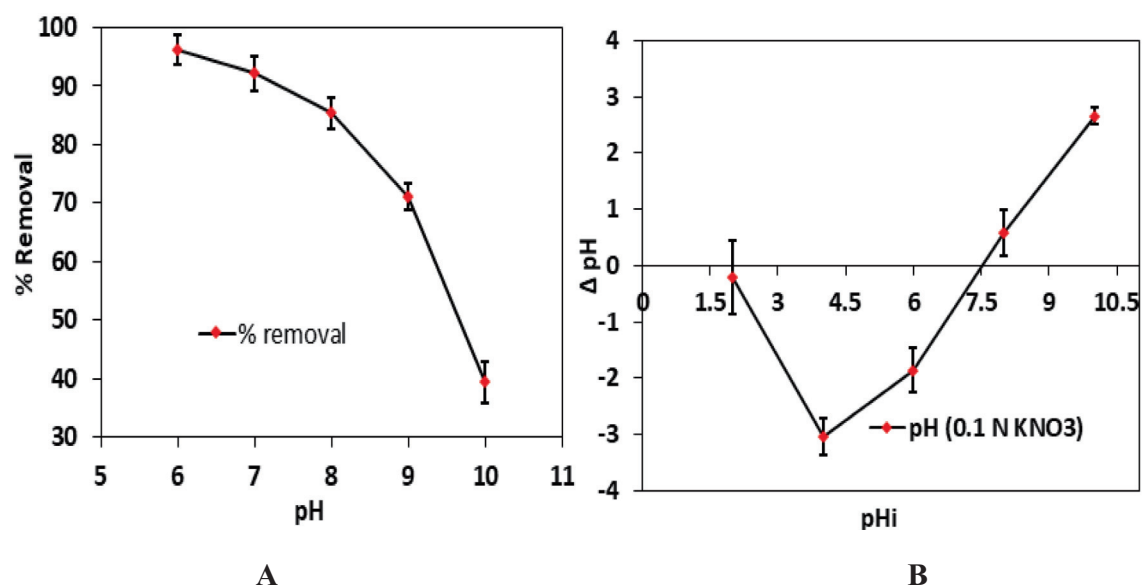


Fig. 3 (A) Outcome of pH change on CR adsorption on BCAC (B) Point of zero charge of BCAC. (C) Possible adsorption mechanism for the adsorption of CR onto BCAC.

cally in Fig. 3(C). The effect of pH on the adsorption of CR on BCAC can be explained based on the surface charges of both the sorbent and the dye in the aqueous medium and also on the basis of pK_a values of major constituents [55]. At high solution $pH > 7.54$, active sites of BCAC are completely deprotonated; at neutral $pH (\sim 7)$ active sites are primarily protonated; while at low $pH < 4$, most of the active sites are protonated [55]. Typically, CR is negatively charged when $pH > 5.5$ ($pK_a = 5.5$) [55] as can be seen in Fig. 3 (C). When the solution pH is 6 (above pK_a values of CR), dye molecules are negatively charged, while adsorbent sites of BCAC are relatively highly protonated (because of pH is much lower than 7.54). This leads to a strong electrostatic attraction between SO_3^- groups of CR and positively charged BCAC (as shown in Fig. 3(C)), thus resulting in a higher adsorption capacity for CR. However, when pH increases, the OH^- ions increase gradually, which compete with anionic dye molecules for penetrating the positively charged adsorbent. Hence adsorption capacity decreases for CR at higher pH . Therefore, based on the above-mentioned results, it is evident that the surface charge of the adsorbent surface and dye governs the adsorption behavior towards anionic dye CR.

3.3. Variation of concentration with time

Fig. 4 displays the relationship between the contact time (0–120 mins) and the CR adsorption capability of BCAC at pH 6 for initial CR concentration range (50–200 mg/L). The CR adsorption capacity increased quickly for brief time periods before settling towards equilibrium although the quantity varied for each concentration. This can be explained as at early stage of experiment many vacant spots were present and due to passage of time these active pores were get saturated [56]. The shorter equilibrium period (10, 15 and 30 mins) were attained for lower (50, 70 and 100 mg/L) initial concentration of CR. Similarly, for raised initial CR concentrations of 150 mg/L and 200 mg/L, the equilibrium times were found to be 60 and 90 mins. A similar pattern was observed in literature where equilibrium was attained within 100 mins for CR dye over pine powder adsorbent [57].

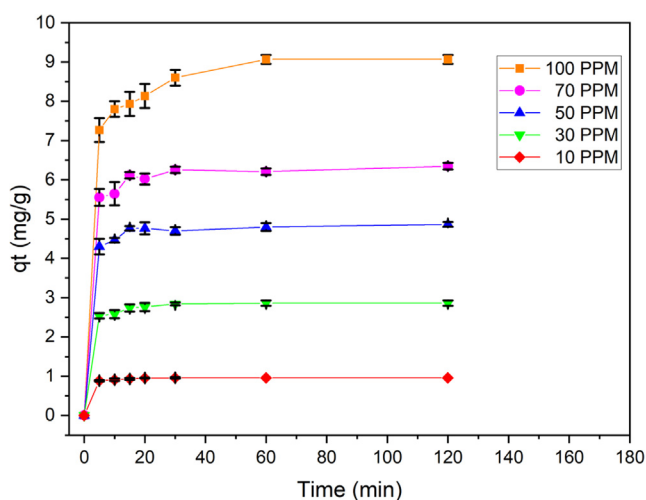


Fig. 4 The concentration vs. time graph for CR adsorption on BCAC.

3.4. Variation of dose

Fig. 5 shows how adsorbent dosage affects the amount of CR that can be adsorbed onto BCAC. Increases in BCAC dosage of 0.04, 0.06, 0.08, 0.1 and 0.12 g, respectively, resulted in increases in CR removal percentage of 84.3, 88.65, 91.33, 95.89 and 96.35 % as depicted in Fig. 5. This might be attributed to the rise in the total aggregate surface area of the BCAC particles and the number of accessible active adsorption sites [7]. At 0.1 g and 0.12 g loading of dose, there was no discernible difference in elimination of CR that may be due aggregation of adsorbent particles [8]. Thus for all experiments, BCAC of 0.1 g was discovered to be the best dosage when taking CR removal percentage values into account.

3.5. Adsorption isotherms

Adsorption isotherm investigations are crucial because they describe the distribution of the adsorbed molecules between the adsorbent and the liquid solutions at equilibrium. As it serves a useful purpose in the analysis and design of adsorption systems, it is vital to establish the most suitable correlation for equilibrium data and empirical equations. The Langmuir, Freundlich, and Temkin models were utilised to evaluate the data in order to determine which isothermal model is most appropriate for delivering the CR adsorption over BCAC. The linear forms of aforementioned isotherm models are presented in Table 1 and values of corresponding parameters were analysed from Fig. 6.

3.5.1. Langmuir isotherm

The Langmuir isotherm model, state that adsorption happens at specified homogenous sites on the adsorbent through monolayer adsorption [58]. It is also hypothesised that once a sorbate molecule fills a space, no further sorption may occur there. The adsorbate draws to all of the active vacant sites of the adsorbent using the same amount of energy [59]. In Table 1, q_e is the dye amount per unit weight of BCAC (mg/g) and C_e is remaining CR concentration at equilibrium (mg/L). The con-

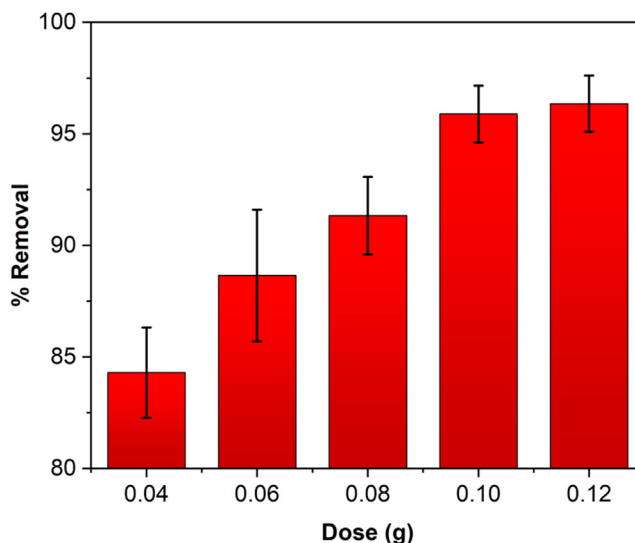
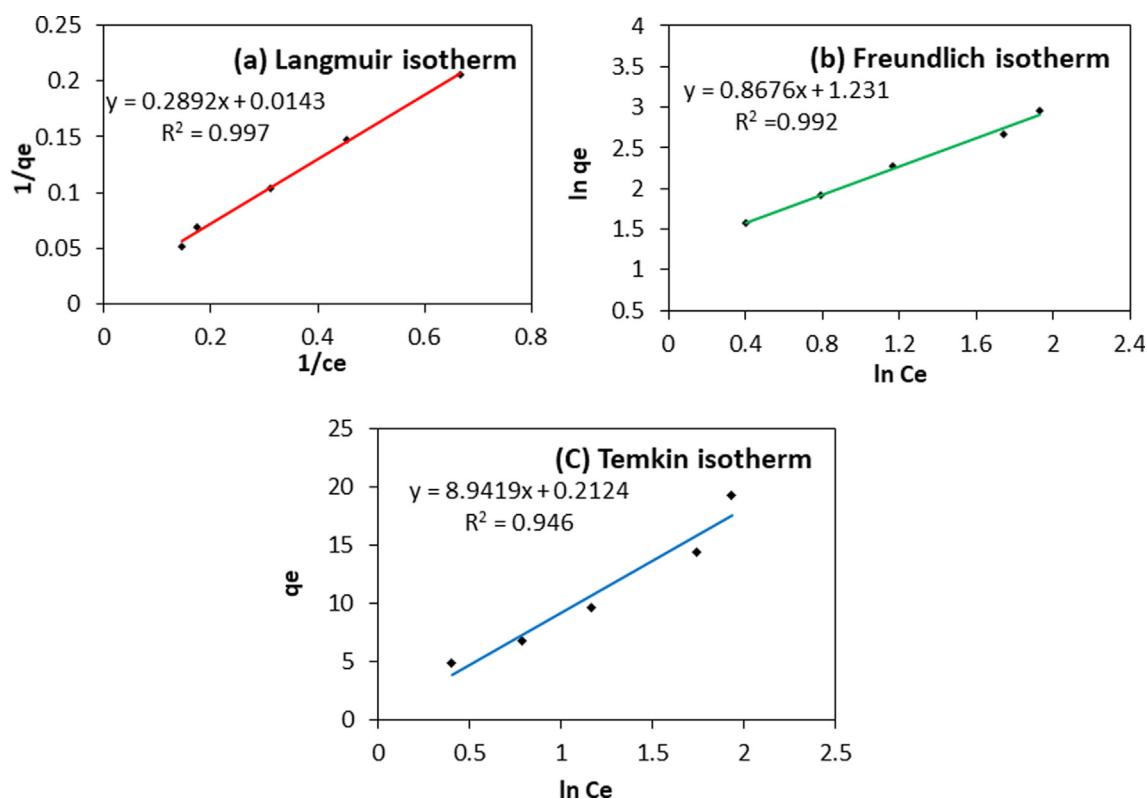


Fig. 5 Impact of changing the BCAC dose on CR adsorption.

Table 1 Isotherm's equations and constants for CR adsorption on BCAC.

Isotherms	Equations	Parameters	Values
Langmuir	$\frac{1}{q_e} = \left(\frac{1}{q_m} \times \frac{1}{b} \times \frac{1}{C_e} \right) + \frac{1}{q_m}$	q_m (mg g ⁻¹)	69.93
		b (L mg ⁻¹)	0.049
		R_L	0.091–0.287
		R^2	0.997
Freundlich	$\ln q_e = \ln K_F + \frac{1}{n} \ln C_e$	K_F (mg g ⁻¹) (L mg ⁻¹) ^{1/n}	3.424
		n	1.152
		R^2	0.992
Temkin	$q_e = B \ln A + B \ln C_e$	A (L g ⁻¹)	1.024
		B (J mol ⁻¹)	8.941
		R^2	0.946

**Fig. 6** Adsorption isotherm for CR uptake on BCAC (Temp = 30 °C, pH = 6 and contact time 120 min).

stant q_{\max} is related to the sites filled by a dye monolayer and reflects the adsorption capacity (mg/g). K_L is a constant related to adsorption energy (L/mg). Plotting the adsorption curve; $1/q_e$ vs $1/C_e$ gives the value of q_{\max} and K_L . The graph showed that the Langmuir adsorption capacity was 69.93 mg/g, and an excellent R^2 of 0.997 was observed suggesting monolayer coverage of sites by CR dye molecules (Fig. 6). Separation factor (R_L), is another dimensionless measure which provides information on how favourable is the adsorption process. The adsorption is indicated by R_L , which can be either unfavourable ($R_L > 1$), favourable ($0 < R_L < 1$), irreversible ($R_L = 0$), or linear ($R_L = 1$) [60]. The separation factor values for the present study lie in order (0.091–0.287), which ranges

from 0 to 1, indicates favourable adsorption [60]. In conformity to our results, several investigations have demonstrated that the Langmuir model best describes the sorption of CR onto agro-based adsorbent [17,32].

3.5.2. Freundlich isotherm

The Freundlich model, which is frequently used in heterogeneous systems and denotes multilayer adsorption with unstable distribution of enthalpies and affinities between adsorbent and adsorbate [61]. Freundlich sorption equilibrium constant K_F is expressed in (mg/g). (L/mg)^{1/n}, and n stands for distinctive surface heterogeneity. The linear graph $\log q_e$ vs $\log C_e$ is used to estimate the model parameters. The result of correlation

coefficient of this model is represented in Table 1. Due to lower R^2 value than Langmuir model indicate that this model does not adequately account for the variation in the experimental data.

3.5.3. Temkin isotherm

According to the above isotherm, all molecules' adsorption heat decreases in a linear manner, proving that the binding energy is homogeneous [62,63]. The constants A (g/L) and B (J/mol) corresponding to the maximal equilibrium binding energy and heat of adsorption respectively, were calculated

using the linearized Temkin equation. The obtained values of A and B are given in the following Table 1. The computed R^2 value (0.94) for Temkin isotherm in the case of CR adsorption is less than those for the Langmuir and Freundlich isotherms. This finding suggests that the Temkin model does not provided an adequate fit for the experimental data.

3.6. Adsorption kinetics

The process by which a solute bind to a sorbent can be expressed using a variety of models. Studies on adsorption rate

Table 2 Kinetic parameters for CR removal on BCAC at different initial concentration.

Kinetic models & Equations	Parameters	Concentrations (mg L ⁻¹)				
		50	70	100	150	200
Pseudo-first order $\log(q_e - q_t) = \log q_e - \left(\frac{K_1}{2.303}\right) \times t$	q_e (exp)	4.849	6.777	9.678	14.428	19.308
	q_e (calc)	0.346	0.401	1.058	2.102	3.908
	K_1	0.120	0.0778	0.094	0.066	0.041
	R^2	1	0.952	0.903	0.974	0.953
Pseudo-second order kinetics $\frac{t}{q_t} = \left(\frac{1}{K_2 q_e^2}\right) + \left(\frac{1}{q_e}\right) \times t$	q_e (exp)	4.849	6.777	9.678	14.428	19.308
	q_e (calc)	4.852	6.784	9.708	14.513	19.493
	K_2	4.045	1.633	0.392	0.108	0.038
	R^2	1	1	0.999	0.999	0.997
Intra-particle diffusion model $q_e = k_{id} \times t^{1/2} + I$	K_{id}	0.019	0.030	0.077	0.188	0.441
	I	4.699	6.534	9.025	12.753	15.271
	R^2	0.362	0.484	0.639	0.779	0.806

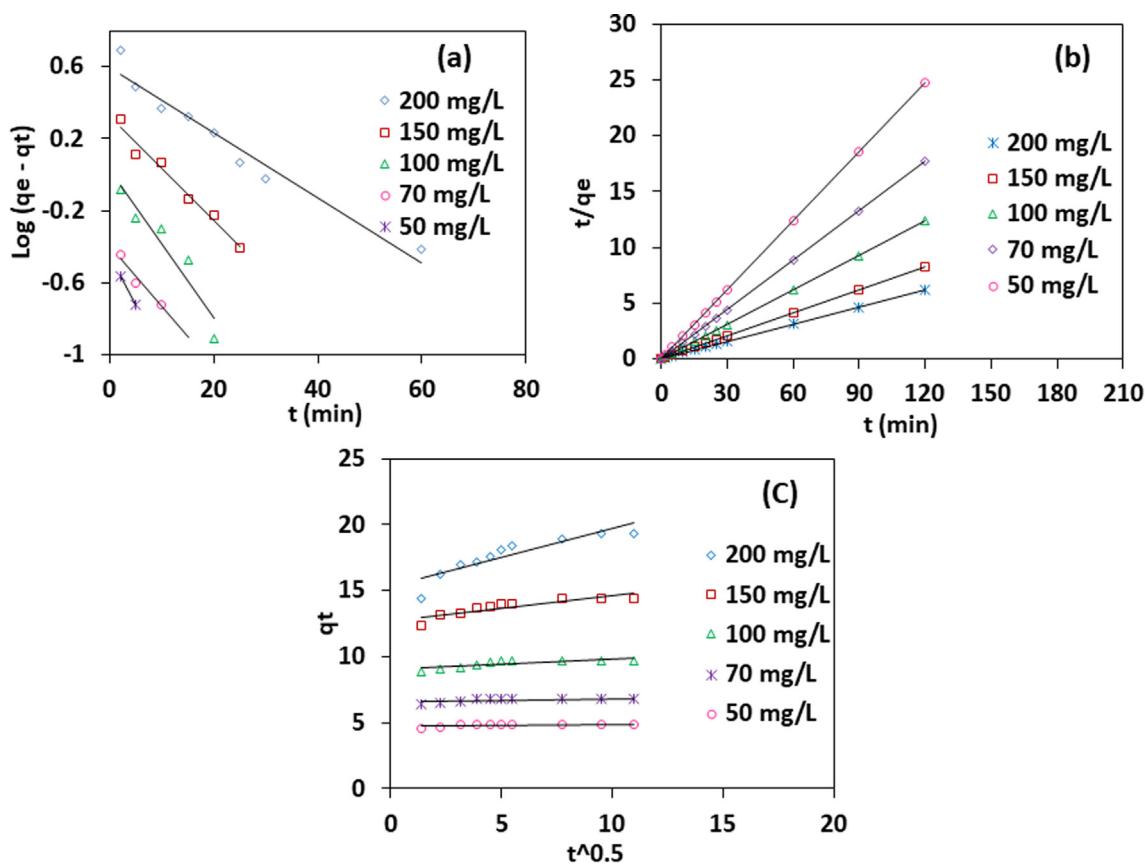
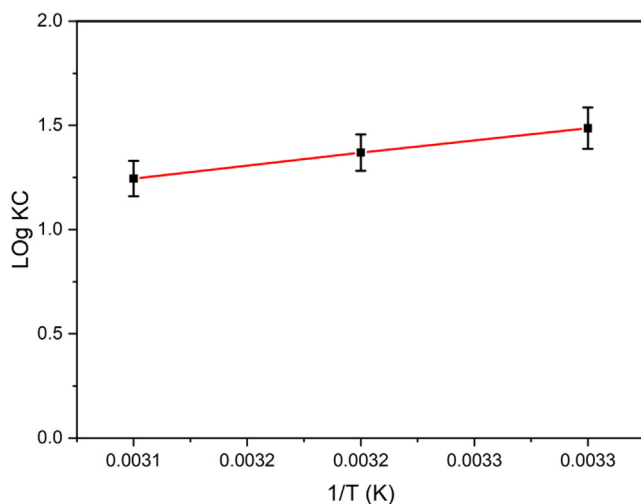


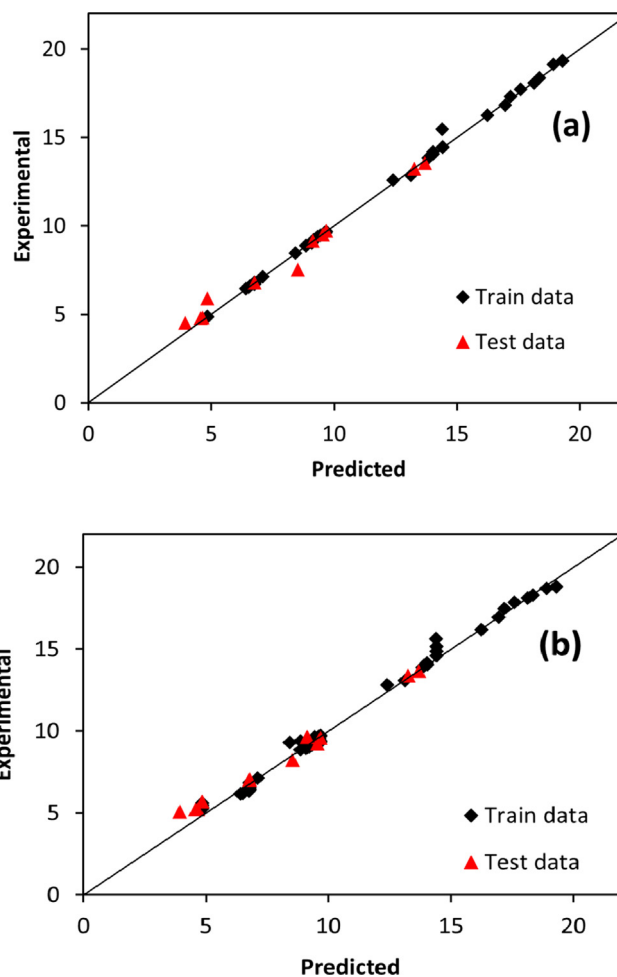
Fig. 7 Adsorption Kinetics for CR dye onto BCAC (a) pseudo-first order, (b) pseudo-second order and (c) Intra-particle diffusion (at pH = 6, temp = 30 °C and dose = 0.1 g).

Table 3 Thermodynamic variables for CR adsorptions on BCAC.

Temperature (K)	ΔG° (kJ mol ⁻¹)	ΔH° (kJ mol ⁻¹)	ΔS° (kJ mol ⁻¹ K ⁻¹)
303	-8.621	-22.697	-0.046
313	-8.202		
323	-7.696		

**Fig. 8** A graph of $\log K_c$ plotted against $1/T$ for CR adsorption on BCAC.

were conducted in order to quickly and effectively construct a model. Adsorption kinetics demonstrates how the rate of dye uptake is time-dependent and aids in calculating the residence time for the purpose of optimising the size of the adsorption device [64]. The uptake of CR over BCAC was established by fitting data into kinetic models namely, pseudo-first order, pseudo-second order and intra-particle diffusion kinetics. The linear expressions and coefficients of these kinetic models are described in Table 2. According to Fig. 7 (a-c) for adsorption of CR dye by BCAC, pseudo-second order rate kinetics had an R^2 value of 0.998, which was higher than first order rate kinetics. Additionally, the q_e values for the pseudo-first-order equation varied considerably with the experimental ones. As opposed to that, q_e values estimated by pseudo-second order rate kinetics were closely matched with experimental data. According to the intraparticle diffusion model, the value of constant (I) provides information about the boundary layer impact [3]. As qt vs $t^{1/2}$ plot show divergence from the origin pointed that the CR adsorption over BCAC comprise intra particle diffusion, in addition to the rate control step and other ways such film diffusion, surface adsorption, and pore diffusion [65]. Similar findings for the kinetics of CR uptake over kenaf activated carbon [19] and litchi seed powder [32]

**Fig. 9** ML-modelling of CR adsorption on BCAC for (a) SVR model and (b) ANN model.

that follows pseudo-second order kinetics were reported recently.

3.7. Adsorption thermodynamics

An investigation of the thermodynamics was done at three different temperatures (30 °C, 40 °C and 50 °C) for CR uptake on BCAC. The following equations (14–16) were used to compute the thermodynamic characteristics of the process, including the change in Gibbs free energy (ΔG°), change in enthalpy (ΔH°), and change in entropy (ΔS°).

$$K_c = \frac{C_{AC}}{C_e} \quad (14)$$

$$\Delta G = -RT \ln K_c \quad (15)$$

Table 4 Optimized hyperparameters for the SVR Model.

Model	Box constraint	Kernel Scale	Epsilon	Type of Kernel	Loss Function
CR-SVR Model	927.902	2.7123	0.0126	RBF	ϵ - insensitive

$$\log K_c = \frac{\Delta S^\circ}{2.303 \times R} - \frac{\Delta H^\circ}{2.303 \times R \times T} \quad (16)$$

Here, R stands for the universal gas constant ($8.314 \text{ J K}^{-1} \text{ mol}^{-1}$), and T stands for the temperature on the Kelvin scale. C_a and C_e represent the equilibrium concentrations of CR on the BCAC and in the solution, respectively. Table 3 lists the computed thermodynamic parameters obtained from Fig. 8. The process is more impulsive as ΔG° becomes more negative [66]. The CR adsorption process is spontaneous, as evidenced by the negative values of total free energy changes during the process. In light of the computed ΔG° values, which ranged between -7.696 and $-8.621 \text{ kJ mol}^{-1}$, the thermodynamic investigation came to the conclusion that the adsorption happened by a physical sorption process as $\Delta G^\circ < 20 \text{ kJ mol}^{-1}$ [67]. Since, the negative values ΔH° and ΔG° represents exothermic and spontaneous process [68]. Thus, the findings demonstrated that the negative values of ΔH° and ΔS° establish the exothermic nature of CR dye adsorption onto BCAC and Reduction in randomness. Several investigations that have been conducted for the elimination of CR reported similar thermodynamic results [23,32].

3.8. Desorption and regeneration

Regeneration of the adsorbent is a crucial consideration when evaluating the process's viability in terms of both practical use

and economics. During desorption process dye molecules are liberated from the carbon surface. Experiments with Congo Red-loaded BCAC for desorption study have been carried out by using NaOH solution. The interaction bonds between the surface sites of BCAC and adsorbed CR become weaker in an alkaline NaOH solution, making regeneration simple. According to the regeneration data, the CR percentage adsorption by BCAC was decreased in the third cycle to 84.77 % from 96.81 %. Moreover, desorption percentage was seen to diminish with an increase in the number of regeneration cycles, remaining at 88.31 % of its initial level after the first cycle and falling to 72.58% after the third. As a result, the adsorbent can be successfully employed for up to three cycles. Similar desorption studies were performed utilizing NaOH to recover Congo Red dye from jujube shell [27] and methyl orange from pumpkin seed powder adsorbent [69].

4. Simulation of machine leaning models

In order for the ML-based SVR model to function properly, the model parameters must be chosen correctly. The optimised hyperparameters are listed in Table 4. The results showed that the optimal ANN design was created using the tansig-purelin transfer functions, trainlm as the back-propagation technique, and 10 neurons in a single hidden layer. The models' output was employed, in order to create parity graphs between the

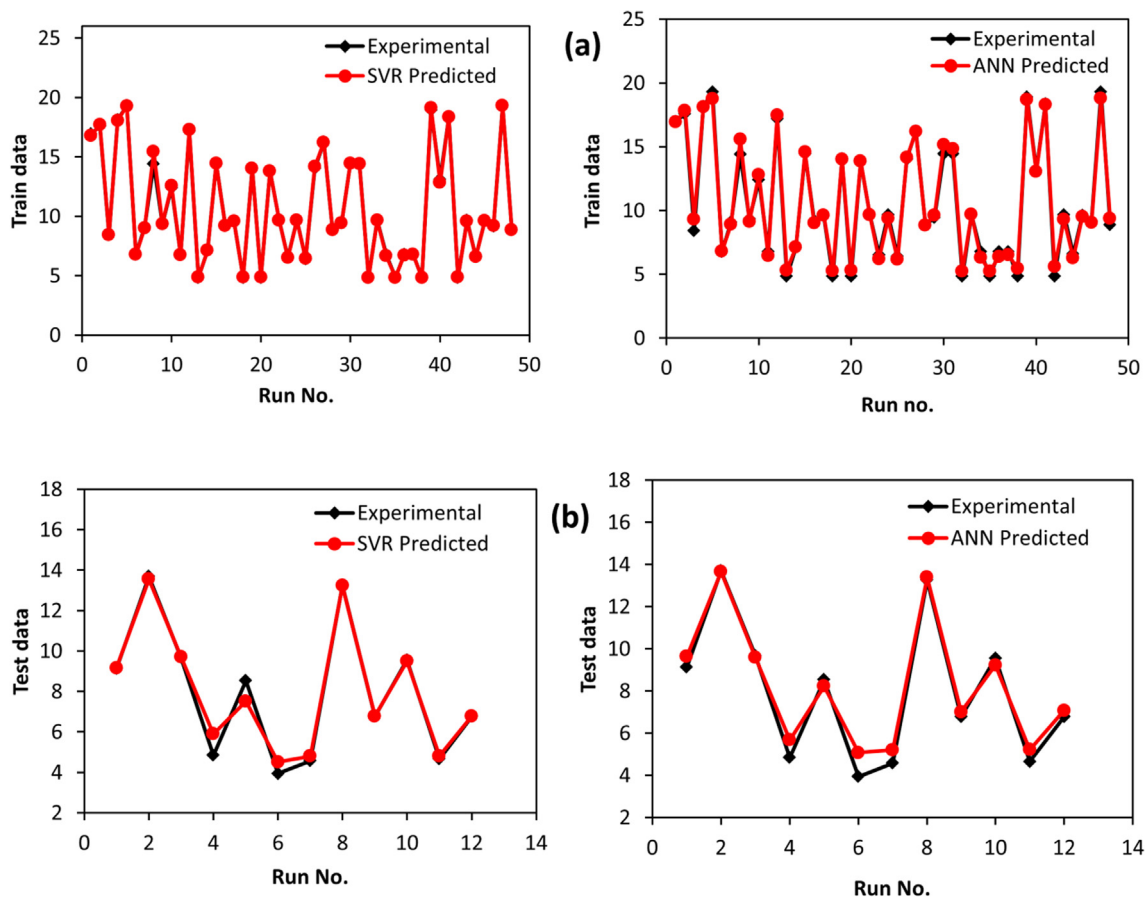


Fig. 10 Plots of Congo Red ML models during (a) training course and (b) testing course. (For interpretation of the references to color in this figure legend, the reader is referred to the web version of this article.)

Table 5 SVR model performance evaluation.

Parameter	Train data	Test data
R ²	0.9987	0.9816
AARE	0.0053	0.0491
RMSE	0.1686	0.4635
Chi-squared	0.0913	0.4165

Table 6 ANN model performance evaluation.

Parameter	Train data	Test data
R ²	0.9931	0.9884
AARE	0.0365	0.0781
RMSE	0.3855	0.5395
Chi-squared	0.8131	0.5797

actual adsorption capacity of CR over BCAC and those predicted by the ML-based models as represented in Fig. 9 (a-b). It is obvious that the anticipated train and test data both fall very near the optimum fit line, signifying that the two ML-based models performed effectively. Fig. 10 (a) - (b) demonstrates the training process and testing phase for ML-SVR and ML-ANN models respectively. It is noted that the forecasted results closely match the experimentally determined values of adsorption capacity for almost all sample runs. The two constructed ML-models produce good results, with high R² values of 0.9978 for SVR and 0.9931 for the ANN model obtained during training. These ML models were generalised since, during testing, they functioned effectively for even anonymous data, with R² for the SVR and ANN models being equivalent to 0.9816 and 0.9884, respectively. Furthermore, as depicted in Tables 5 and 6, low AARE values in ranges (0.0053–0.0491) for SVR and (0.0365–0.0781) for ANN, whereas evaluated RMSE values were found to be in ranges (0.1686–0.4635) for SVR and (0.3855 – 0.5395) for ANN were close to ideal error value of zero, confirms ML models' capacity for prediction CR removal onto BCAC. The results of the ML approach for present adsorption study were found to be consistent with previously reported literature where prediction of Chromium adsorption over Medlar seed by SVR and ANN models have R² of 0.981 and 0.958 respectively [70]. Similar

trend was also noted in ANN modelling of Basic Red 46 dye and Cu (II) with R² in between 0.98 and 0.99 [71].

5. Comparison with other adsorbents

Table 7 shows that the BCAC has a notable capacity for CR adsorption when compared to the other adsorbents that are being used. It has been determined how well various adsorbents can remove the CR dye when compared to the maximal adsorption capacity of BCAC for CR.

6. Conclusion

The herbal waste derived BCAC was discovered through this investigation to be a potential material for the elimination of harmful CR dye in water systems. Increases in initial dye concentration (50–200 mg/L), contact time (0–120 mins), and dose (0.04–0.12) were shown to enhance the amount of Congo Red dye uptake on BCAC, whereas increases in solution pH (6–10) and temperature (30–50 °C) were found to decrease it. The reported negative values for ΔH° (–22.697 kJ mol^{–1}) and ΔG° (–8.621 kJ mol^{–1}), respectively, show that adsorption is exothermic and spontaneous in nature. The provided results (R² > 0.9) demonstrate that ML models are potential forecasting techniques that can be applied successfully and have adequate accuracy for the prediction of the CR dye removal. Thus, ML prediction can help in the planning and development of a more efficient treatment for removing dye from waste effluent.

Declaration of Competing Interest

The authors declare that they have no known competing financial interests or personal relationships that could have appeared to influence the work reported in this paper.

Acknowledgements

This research work was funded by Institutional Fund Projects under grant no. (IFPIP: 1820-961-1443). The authors gratefully acknowledge technical and financial support provided by the Ministry of Education and King Abdulaziz University, DSR, Jeddah, Saudi Arabia.

Table 7 Comparison of CR adsorption over various adsorbents.

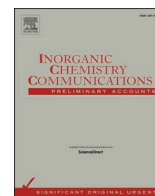
Adsorbent	Adsorption Isotherm	Adsorption Kinetic	Optimum pH	Max Adsorption (mg/g)	Reference
Mango Leaves	Freundlich	Pseudo-second order	7	21.28	[26]
Dactylifera seeds	Langmuir	Pseudo-second order	2	61.72	[8]
Kenaf-based activated carbon	Freundlich	Pseudo-second order	4	14.20	[19]
	Langmuir				
Coconut fiber based activated carbon	–	Pseudo-second order	3	22.10	[16]
Litchi seed	Freundlich	Pseudo-second order	2	20.49	[32]
	Langmuir				
<i>Acacia auriculiformis</i> biochar	Freundlich	Pseudo-second order	2	130.0	[72]
Apricote stone	Langmuir	Pseudo-second order	13	32.68	[28]
	Dubinini-Radushkevich				
Black Cardamom activated carbon	Langmuir	Pseudo-second order	6	69.93	Present study

References

- [1] M. Danish, K.B. Ansari, M. Danish, A. Khatoon, R. Ali Khan Rao, S. Zaidi, R. Ahmad Aftab, A comprehensive investigation of external mass transfer and intraparticle diffusion for batch and continuous adsorption of heavy metals using pore volume and surface diffusion model, *Sep. Purif. Technol.* 292 (2022), <https://doi.org/10.1016/j.seppur.2022.120996> 120996.
- [2] M.A. Usman, A.Y. Khan, Selective adsorption of anionic dye from wastewater using polyethyleneimine based macroporous sponge: Batch and continuous studies, *J. Hazard. Mater.* 428 (2022), <https://doi.org/10.1016/j.jhazmat.2022.128238> 128238.
- [3] M.A. Fawzy, M. Gomaa, Use of algal biorefinery waste and waste office paper in the development of xerogels: A low cost and eco-friendly biosorbent for the effective removal of congo red and Fe (II) from aqueous solutions, *J. Environ. Manage.* 262 (2020), <https://doi.org/10.1016/j.jenvman.2020.110380> 110380.
- [4] M.T. Yagub, T.K. Sen, S. Afroze, H.M. Ang, Dye and its removal from aqueous solution by adsorption: A review, *Adv. Colloid Interface Sci.* 209 (2014) 172–184, <https://doi.org/10.1016/j.cis.2014.04.002>.
- [5] S. Parvin, B.K. Biswas, A. Rahman, Chemosphere Study on adsorption of Congo red onto chemically modified egg shell membrane 236 (2019), <https://doi.org/10.1016/j.chemosphere.2019.07.057>.
- [6] Y.H. Chiu, T.F.M. Chang, C.Y. Chen, M. Sone, Y.J. Hsu, Mechanistic insights into photodegradation of organic dyes using heterostructure photocatalysts, *Catalysts*. 9 (2019), <https://doi.org/10.3390/catal9050430>.
- [7] S. Mohebbi, D. Bastani, H. Shayesteh, Equilibrium, kinetic and thermodynamic studies of a low-cost biosorbent for the removal of Congo red dye: acid and CTAB-acid modified celery (*Apium graveolens*), *J. Mol. Struct.* 1176 (2018) 181–193, <https://doi.org/10.1016/j.molstruc.2018.08.068>.
- [8] D. Pathania, A. Sharma, Z. Siddiqi, Removal of congo red dye from aqueous system using *Phoenix dactylifera* seeds, *J. Mol. Liq.* 219 (2016) 359–367, <https://doi.org/10.1016/j.molliq.2016.03.020>.
- [9] M.A. Adebayo, J.M. Jabar, J.S. Amoko, E.O. Openiyi, O.O. Shodiya, Coconut husk-raw clay-Fe composite: preparation, characteristics and mechanisms of Congo red adsorption, *Sci. Rep.* 12 (2022) 1–12, <https://doi.org/10.1038/s41598-022-18763-y>.
- [10] N.A. Alamrani, Elimination of Congo Red Dye from Industrial Wastewater Using *Teucrium polium L.* as a Low-Cost Local Adsorbent, *Adsorpt. Sci. Technol.* (2021) 12.
- [11] S. Mishra, L. Cheng, A. Maiti, The utilization of agro-biomass/byproducts for effective bio-removal of dyes from dyeing wastewater: A comprehensive review, *J. Environ. Chem. Eng.* 9 (2021), <https://doi.org/10.1016/j.jece.2020.104901> 104901.
- [12] J.N. Wekoye, W.C. Wanyonyi, P.T. Wangila, M.K. Tonui, Kinetic and equilibrium studies of Congo red dye adsorption on cabbage waste powder, *Environ. Chem. Ecotoxicol.* 2 (2020) 24–31, <https://doi.org/10.1016/j.enceco.2020.01.004>.
- [13] A. Kumar, H.M. Jena, Removal of methylene blue and phenol onto prepared activated carbon from Fox nutshell by chemical activation in batch and fixed-bed column, *J. Clean. Prod.* 137 (2016) 1246–1259, <https://doi.org/10.1016/j.jclepro.2016.07.177>.
- [14] A. Sharma, G. Sharma, M. Naushad, A.A. Ghfar, D. Pathania, Remediation of anionic dye from aqueous system using bio-adsorbent prepared by microwave activation, *Environ. Technol. (United Kingdom)* 39 (2018) 917–930, <https://doi.org/10.1080/09593330.2017.1317293>.
- [15] R.A.K. Rao, U. Khan, Adsorption of Ni(II) on alkali treated pineapple residue (*Ananas comosus L.*): Batch and column studies, *Groundw. Sustain. Dev.* 5 (2017) 244–252, <https://doi.org/10.1016/j.gsd.2017.08.002>.
- [16] L. Zhang, L.Y. Tu, Y. Liang, Q. Chen, Z.S. Li, C.H. Li, Z.H. Wang, W. Li, Coconut-based activated carbon fibers for efficient adsorption of various organic dyes, *RSC Adv.* 8 (2018) 42280–42291, <https://doi.org/10.1039/c8ra08990f>.
- [17] A. Sharma, Z.M. Siddiqui, S. Dhar, P. Mehta, D. Pathania, Adsorptive removal of congo red dye (CR) from aqueous solution by *Cornulaca monacantha* stem and biomass-based activated carbon: isotherm, kinetics and thermodynamics, *Sep. Sci. Technol.* 54 (2019) 916–929, <https://doi.org/10.1080/01496395.2018.1524908>.
- [18] V.S. Devi, B. Sudhakar, K. Prasad, P. Jeremiah Sunadh, M. Krishna, Adsorption of Congo red from aqueous solution onto *Antigonon leptopus* leaf powder: Equilibrium and kinetic modeling, *Mater. Today Proc.* 26 (2019) 3197–3206, <https://doi.org/10.1016/j.matpr.2020.02.715>.
- [19] S. Mandal, J. Calderon, S.B. Marpu, M.A. Omary, S.Q. Shi, Mesoporous activated carbon as a green adsorbent for the removal of heavy metals and Congo red: Characterization, adsorption kinetics, and isotherm studies, *J. Contam. Hydrol.* 243 (2021), <https://doi.org/10.1016/j.jconhyd.2021.103869> 103869.
- [20] F. Amran, M.A.A. Zaini, Sodium hydroxide-activated Casuarina empty fruit: Isotherm, kinetics and thermodynamics of methylene blue and congo red adsorption, *Environ. Technol. Innov.* 23 (2021), <https://doi.org/10.1016/j.eti.2021.101727> 101727.
- [21] R. Kumari, J. Mohanta, B. Dey, S. Dey, Eucalyptus leaf powder as an efficient scavenger for Congo red from water: Comprehensive batch and column investigation, *Sep. Sci. Technol.* 55 (2020) 3047–3059, <https://doi.org/10.1080/01496395.2019.1670208>.
- [22] Z. Li, H. Hanafy, L. Zhang, L. Sellaoui, M. Schadeck Netto, M. L.S. Oliveira, M.K. Seliem, G. Luiz Dotto, A. Bonilla-Petriciolet, Q. Li, Adsorption of congo red and methylene blue dyes on an ashitaba waste and a walnut shell-based activated carbon from aqueous solutions: Experiments, characterization and physical interpretations, *Chem. Eng. J.* 388 (2020), <https://doi.org/10.1016/j.cej.2020.124263> 124263.
- [23] T.K. Roy, N.K. Mondal, Potentiality of *Eichhornia* shoots ash towards removal of Congo red from aqueous solution: Isotherms, kinetics, thermodynamics and optimization studies, *Groundw. Sustain. Dev.* 9 (2019), <https://doi.org/10.1016/j.gsd.2019.100269> 100269.
- [24] K. Litefti, M.S. Freire, M. Stitou, J. González-Álvarez, Adsorption of an anionic dye (Congo red) from aqueous solutions by pine bark, *Sci. Rep.* 9 (2019) 1–11, <https://doi.org/10.1038/s41598-019-53046-z>.
- [25] M. Goswami, P. Chaturvedi, R. Kumar Sonwani, A. Dutta Gupta, R. Rani Singhania, B. Shekher Giri, B. Nath Rai, H. Singh, S. Yadav, R. Sharan Singh, Application of *Arjuna* (*Terminalia arjuna*) seed biochar in hybrid treatment system for the bioremediation of Congo red dye, *Bioresour. Technol.* 307 (2020), <https://doi.org/10.1016/j.biortech.2020.123203> 123203.
- [26] O.A. Adelaja, A.C. Bankole, M.E. Oladipo, D.B. Lene, Biosorption of Hg(II) ions, Congo red and their binary mixture using raw and chemically activated mango leaves, *Int. J. Energy Water Resour.* 3 (2019) 1–12, <https://doi.org/10.1007/s42108-019-00012-0>.
- [27] N. El messaoudi, M. Elkhomri, A. Dbik, S. Bentahar, A. Lacherai, B. Bakiz, Biosorption of Congo red in a fixed-bed column from aqueous solution using jujube shell: Experimental and mathematical modeling, *J. Environ. Chem. Eng.* 4 (2016) 3848–3855, <https://doi.org/10.1016/j.jece.2016.08.027>.
- [28] M. Abbas, M. Trari, Kinetic, equilibrium and thermodynamic study on the removal of Congo Red from aqueous solutions by adsorption onto apricot stone, *Process Saf. Environ. Prot.* 98 (2015) 424–436, <https://doi.org/10.1016/j.psep.2015.09.015>.

- [29] Y. Achour, L. Bahsis, E.H. Ablouh, H. Yazid, M.R. Laamari, M. El Haddad, Insight into adsorption mechanism of Congo red dye onto Bombax Buonopozense bark Activated-carbon using Central composite design and DFT studies, *Surfaces and Interfaces*. 23 (2021), <https://doi.org/10.1016/j.surfin.2021.100977>.
- [30] V.V. Gedam, P. Raut, A. Chahande, P. Pathak, Kinetic, thermodynamics and equilibrium studies on the removal of Congo red dye using activated teak leaf powder, *Appl. Water Sci.* 9 (2019) 1–13, <https://doi.org/10.1007/s13201-019-0933-9>.
- [31] S.L. Chan, Y.P. Tan, A.H. Abdullah, S.T. Ong, Equilibrium, kinetic and thermodynamic studies of a new potential biosorbent for the removal of Basic Blue 3 and Congo Red dyes: Pineapple (*Ananas comosus*) plant stem, *J. Taiwan Inst. Chem. Eng.* 61 (2016) 306–315, <https://doi.org/10.1016/j.jtice.2016.01.010>.
- [32] J.N. Edokpayi, E. Makete, Removal of Congo red dye from aqueous media using Litchi seeds powder: Equilibrium, kinetics and thermodynamics, *Phys. Chem. Earth*. 123 (2021), <https://doi.org/10.1016/j.pce.2021.103007>.
- [33] W.C. Leong, R.O. Kelani, Z. Ahmad, Prediction of air pollution index (API) using support vector machine (SVM), *J. Environ. Chem. Eng.* 8 (2020), <https://doi.org/10.1016/j.jece.2019.103208>.
- [34] J. Huang, T. Jin, M. Liang, H. Chen, Prediction of heat exchanger performance in cryogenic oscillating flow conditions by support vector machine, *Appl. Therm. Eng.* 182 (2021), <https://doi.org/10.1016/j.applthermaleng.2020.116053>.
- [35] R.A. Aftab, S. Zaidi, M. Danish, K.B. Ansari, M. Danish, Novel Machine Learning (ML) Models for Predicting the Performance of Multi-Metal Binding Green Adsorbent for the Removal of Cd (II), Cu (II), Pb (II) and Zn (II) ions, *Environ. Adv.* 9 (2022), <https://doi.org/10.1016/j.envadv.2022.100256>.
- [36] S. Zaidi, Development of support vector regression (SVR)-based model for prediction of circulation rate in a vertical tube thermosiphon reboiler, *Chem. Eng. Sci.* 69 (2012) 514–521, <https://doi.org/10.1016/j.ces.2011.11.005>.
- [37] A. Zendejboudi, M.A. Baseer, R. Saidur, Application of support vector machine models for forecasting solar and wind energy resources: A review, *J. Clean. Prod.* 199 (2018) 272–285, <https://doi.org/10.1016/j.jclepro.2018.07.164>.
- [38] D.A. Otchere, T.O.A. Ganat, R. Gholami, S. Ridha, Application of supervised machine learning paradigms in the prediction of petroleum reservoir properties: Comparative analysis of ANN and SVM models, *J. Pet. Sci. Eng.* 200 (2020), <https://doi.org/10.1016/j.petrol.2020.108182>.
- [39] M. Danish, K.B. Ansari, R.A. Aftab, M. Danish, S. Zaidi, Q.T. Trinh, gPROMS-driven modeling and simulation of fixed bed adsorption of heavy metals on a biosorbent: benchmarking and case study, *Environ. Sci. Pollut. Res.* (2021), <https://doi.org/10.1007/s11356-021-13207-y>.
- [40] M.A. Usman, R.A. Aftab, S. Zaidi, S.M. Adnan, R.A.K. Rao, Adsorption of aniline blue dye on activated pomegranate peel: equilibrium, kinetics, thermodynamics and support vector regression modelling, *Int. J. Environ. Sci. Technol.* (2021), <https://doi.org/10.1007/s13762-021-03571-0>.
- [41] A.M. Ghaedi, A. Vafaei, Applications of artificial neural networks for adsorption removal of dyes from aqueous solution: A review, *Adv. Colloid Interface Sci.* 245 (2017) 20–39, <https://doi.org/10.1016/j.cis.2017.04.015>.
- [42] R.A. Aftab, S. Zaidi, M. Danish, S.M. Adnan, K.B. Ansari, M. Danish, Support vector regression-based model for phenol adsorption in rotating packed bed adsorber, *Environ. Sci. Pollut. Res.* (2021), <https://doi.org/10.1007/s11356-021-14953-9>.
- [43] P.R. Souza, G.L. Dotto, N.P.G. Salau, Artificial neural network (ANN) and adaptive neuro-fuzzy interference system (ANFIS) modelling for nickel adsorption onto agro-wastes and commercial activated carbon, *J. Environ. Chem. Eng.* 6 (2018) 7152–7160, <https://doi.org/10.1016/j.jece.2018.11.013>.
- [44] S. Ullah, M.A. Assiri, A.G. Al-Sehemi, M.A. Bustam, M. Sagir, F.A. Abdulkareem, M.R. Raza, M. Ayoub, A. Irfan, Characteristically Insights, Artificial Neural Network (ANN), Equilibrium, and Kinetic Studies of Pb(II) Ion Adsorption on Rice Husks Treated with Nitric Acid, *Int. J. Environ. Res.* 14 (2020) 43–60, <https://doi.org/10.1007/s41742-019-00235-3>.
- [45] A.J. Smola, B. Scholkopf, A tutorial on support vector regression, *Stat. Comput.* 14 (2004) 199–222, <https://doi.org/10.1023/B:STCO.0000035301.49549.88>.
- [46] H. Peng, X. Ling, Predicting thermal – hydraulic performances in compact heat exchangers by support vector regression, *Int. J. Heat Mass Transf.* 84 (2015) 203–213, <https://doi.org/10.1016/j.ijheatmasstransfer.2015.01.017>.
- [47] I. Olanrewaju, M. Amiruddin, A. Rahman, T.A. Saleh, An approach to predict the isobaric specific heat capacity of nitrides / ethylene glycol-based nanofluids using support vector regression, *J. Energy Storage*. 29 (2020) 1–10.
- [48] M.K. Uddin, A. Nasar, Walnut shell powder as a low-cost adsorbent for methylene blue dye: isotherm, kinetics, thermodynamic, desorption and response surface methodology examinations, *Sci. Rep.* 10 (2020) 1–13, <https://doi.org/10.1038/s41598-020-64745-3>.
- [49] R. Ahmad, R. Kumar, Adsorptive removal of congo red dye from aqueous solution using bael shell carbon, *Appl. Surf. Sci.* 257 (2010) 1628–1633, <https://doi.org/10.1016/j.apsusc.2010.08.111>.
- [50] N. Hoc Thang, D. Sy Khang, T. Duy Hai, D. Thi Nga, P. Dinh Tuan, Methylene blue adsorption mechanism of activated carbon synthesised from cashew nut shells, *RSC Adv.* 11 (2021) 26563–26570, <https://doi.org/10.1039/d1ra04672a>.
- [51] Q. Du, J. Sun, Y. Li, X. Yang, X. Wang, Z. Wang, L. Xia, Highly enhanced adsorption of congo red onto graphene oxide/chitosan fibers by wet-chemical etching off silica nanoparticles, *Chem. Eng. J.* 245 (2014) 99–106, <https://doi.org/10.1016/j.ccej.2014.02.006>.
- [52] G. Akkaya Saygılı, Synthesis, characterization and adsorption properties of a novel biomagnetic composite for the removal of Congo red from aqueous medium, *J. Mol. Liq.* 211 (2015) 515–526, <https://doi.org/10.1016/j.molliq.2015.07.048>.
- [53] F. Gündüz, B. Bayrak, Biosorption of malachite green from an aqueous solution using pomegranate peel: Equilibrium modelling, kinetic and thermodynamic studies, *J. Mol. Liq.* 243 (2017) 790–798, <https://doi.org/10.1016/j.molliq.2017.08.095>.
- [54] P. Vairavel, N. Rampal, G. Jeppu, Adsorption of toxic Congo red dye from aqueous solution using untreated coffee husks: kinetics, equilibrium, thermodynamics and desorption study, *Int. J. Environ. Anal. Chem.* 00 (2021) 1–20, <https://doi.org/10.1080/03067319.2021.1897982>.
- [55] B. Huang, Y. Liu, B. Li, H. Wang, G. Zeng, Adsorption mechanism of polyethyleneimine modified magnetic core-shell Fe₃O₄@SiO₂ nanoparticles for anionic dye removal, *RSC Adv.* 9 (2019) 32462–32471, <https://doi.org/10.1039/c9ra06299h>.
- [56] O. Paşka, R. Ianoş, C. Păcurariu, A. Brădeanu, Magnetic nanopowder as effective adsorbent for the removal of Congo Red from aqueous solution, *Water Sci. Technol.* 69 (2014) 1234–1240, <https://doi.org/10.2166/wst.2013.827>.
- [57] S. Dawood, T.K. Sen, Removal of anionic dye Congo red from aqueous solution by raw pine and acid-treated pine cone powder as adsorbent: Equilibrium, thermodynamic, kinetics, mechanism and process design, *Water Res.* 46 (2012) 1933–1946, <https://doi.org/10.1016/j.watres.2012.01.009>.
- [58] P.C. Bhomick, A. Supong, M. Baruah, C. Pongener, D. Sinha, Pine Cone biomass as an efficient precursor for the synthesis of activated biocarbon for adsorption of anionic dye from aqueous solution: Isotherm, kinetic, thermodynamic and regeneration

- studies, *Sustain. Chem. Pharm.* 10 (2018) 41–49, <https://doi.org/10.1016/j.scp.2018.09.001>.
- [59] I. Langmuir, The adsorption of gases on plane surfaces of glass, mica and platinum, *J. Am. Chem. Soc.* 40 (1918) 1361–1403, <https://doi.org/10.1021/ja02242a004>.
- [60] M. Dirbaz, A. Roosta, Adsorption, kinetic and thermodynamic studies for the biosorption of cadmium onto microalgae *Parachlorella sp.*, *J. Environ. Chem. Eng.* 6 (2018) 2302–2309, <https://doi.org/10.1016/j.jece.2018.03.039>.
- [61] H.M.F. Freundlich, Over the adsorption in solution, *J. Phys. Chem.* 57 (1906) 385–471, <https://doi.org/10.4161/epi.6.7.16250>.
- [62] S.J. Allen, G. Mckay, J.F. Porter, Adsorption isotherm models for basic dye adsorption by peat in single and binary component systems, *J. Colloid Interface Sci.* 280 (2004) 322–333, <https://doi.org/10.1016/j.jcis.2004.08.078>.
- [63] H. Shayesteh, A. Rahbar-kelishami, R. Norouzbeigi, Treatment Adsorption of malachite green and crystal violet cationic dyes from aqueous solution using pumice stone as a low-cost adsorbent : kinetic, equilibrium, and thermodynamic studies, *Desalin. Water Treat.* (2015) 12822–12831, <https://doi.org/10.1080/19443994.2015.1054315>.
- [64] A. Dutta, Y. Diao, R. Jain, E.R. Rene, S. Dutta, Adsorption of Cadmium from Aqueous Solutions onto Coffee Grounds and Wheat Straw : Equilibrium and Kinetic Study, *J. Environ. Eng.* 142 (2016) 1–6, [https://doi.org/10.1061/\(ASCE\)EE.1943-7870.0001015](https://doi.org/10.1061/(ASCE)EE.1943-7870.0001015).
- [65] F. Zhang, B. Ma, X. Jiang, Y. Ji, Dual function magnetic hydroxyapatite nanopowder for removal of malachite green and Congo red from aqueous solution, *Powder Technol.* 302 (2016) 207–214, <https://doi.org/10.1016/j.powtec.2016.08.044>.
- [66] H.S. AL-Shehri, E. Almudaifer, A.Q. Alorabi, H.S. Alanazi, A. S. Alkorbi, F.A. Alharthi, Effective adsorption of crystal violet from aqueous solutions with effective adsorbent: equilibrium, mechanism studies and modeling analysis, *Environ. Pollut.* Bioavailab. 33 (2021) 214–226, <https://doi.org/10.1080/26395940.2021.1960199>.
- [67] M.A. Ahmad, N.A. Ahmad Puad, O.S. Bello, Kinetic, equilibrium and thermodynamic studies of synthetic dye removal using pomegranate peel activated carbon prepared by microwave-induced KOH activation, *Water Resour. Ind.* 6 (2014) 18–35, <https://doi.org/10.1016/j.wri.2014.06.002>.
- [68] A.T. Ojedokun, O.S. Bello, Kinetic modeling of liquid-phase adsorption of Congo red dye using guava leaf-based activated carbon, *Appl. Water Sci.* 7 (2017) 1965–1977, <https://doi.org/10.1007/s13201-015-0375-y>.
- [69] M.V. Subbaiah, D.S. Kim, Adsorption of methyl orange from aqueous solution by aminated pumpkin seed powder: Kinetics, isotherms, and thermodynamic studies, *Ecotoxicol. Environ. Saf.* 128 (2016) 109–117, <https://doi.org/10.1016/j.ecoenv.2016.02.016>.
- [70] M. Solgi, T. Najib, S. Ahmadnejad, B. Nasernejad, Synthesis and characterization of novel activated carbon from Medlar seed for chromium removal: Experimental analysis and modeling with artificial neural network and support vector regression, *Resour. Technol.* 3 (2017) 236–248, <https://doi.org/10.1016/j.refit.2017.08.003>.
- [71] M. Dolatabadi, M. Mehrabpour, M. Esfandyari, H. Alidadi, M. Davoudi, Modeling of simultaneous adsorption of dye and metal ion by sawdust from aqueous solution using of ANN and ANFIS, *Chemom. Intell. Lab. Syst.* 181 (2018) 72–78, <https://doi.org/10.1016/j.chemolab.2018.07.012>.
- [72] D.L.T. Nguyen, Q.A. Binh, X.C. Nguyen, T.T. Huyen Nguyen, Q.N. Vo, T.D. Nguyen, T.C. Phuong Tran, T.A. Hang Nguyen, S.Y. Kim, T.P. Nguyen, J. Bae, I.T. Kim, Q. Van Le, Metal salt-modified biochars derived from agro-waste for effective congo red dye removal, *Environ. Res.* 200 (2021), <https://doi.org/10.1016/j.envres.2021.111492>



Short communication

Role of Ag and g-C₃N₄ over CaTiO₃ for effective photocatalytic degradation of nitrobenzene

Akshima Soni^a, Saurav Mishra^b, Dipti Vaya^{a,*}, Praveen K. Surolia^{b,*}^a Department of Chemistry, Amity School of Applied Sciences, Gurugram, Haryana, India^b Solar Energy Conversion and Nanomaterials Laboratory, Department of Chemistry, Manipal University Jaipur, Jaipur 303007, Rajasthan, India

ARTICLE INFO

Keywords:

Photocatalysis
Degradation
Ag/g-C₃N₄/CaTiO₃
CaTiO₃, g-C₃N₄
Nitrobenzene

ABSTRACT

In the present study, g-C₃N₄/CaTiO₃ (GCT) heterostructure with various Ag contents have been synthesized via simple hydrothermal method and characterized using various instrumental techniques. Stability of synthesized samples was measured by thermogravimetric analysis (TGA) and zeta potential measurement. The photocatalytic activity of all the synthesized was evaluated by the degradation of nitrobenzene (NB) in aqueous media. The photocatalytic activity of heterostructure AGCT was observed enhanced under the light irradiation. This would be attributed to the suitable band structure, resulting in the efficient charge separation and transfer of photo-generated charge carriers. The final percentage of degradation was observed 70% with AGCT5 and 64% with AGCT1 which were highest among other catalysts applied after 2 h. The Ag doping in CT catalyst led to antagonist performance, and to better degradation of NB. The multivalency of Ag leads to prevent agglomeration and recombination of electrons and holes and transferring them from Ag to Ca. The reaction rate ($2.36 \times 10^{-3} \text{ molL}^{-1} \text{ min}^{-1}$ at 20 °C) and percentage degradation (~70%) were observed to get increased with the increase in the temperature with the apparent activation energy of 40.3 kJ/mol. The enhanced performance at increased temperature was attributed to overcome the energy of activation and high mobility of charge carriers.

1. Introduction

Exponential increase in water pollution has attracted the attention all over the world. For the sack of development, ample quantity of wastewater is released from industries without proper pre-treatment. Thus, a balance in clean water supply and management is a must requirement in current scenario. Various inorganic and organic materials are released from industries such as dyes, pesticides, antibiotics, phenol, nitrobenzene etc. The regular exposure to nitrobenzene can reduce the oxygen carrying capacity of blood to body organs and tissues. This can cause many serious health problems, from dizziness to respiratory distress, called methemoglobinemia. The change in skin colour to blue is a key indicator of this disease [1–5]. Many water treatment technologies have been adopted to treat the wastewater and photocatalysis is one of the prominent fields to handle this situation [6,7].

CaTiO₃ (CT) is a member of perovskite material and one of the conventional photocatalyst. It offers combinations of high ionic conductivity, good ferroelectric, excellent photoluminescent, and unique dielectric polarization [8]. CT belong to metal titanate compounds with a perovskite structure that has attracted attention in fundamental and

applied research fields [9]. The novel structure of these functional materials makes them a suitable candidate for a wide range of optical and electrical applications [10]. Similarly, graphitic carbon nitride (g-C₃N₄) is also utilized not only as photocatalyst but also as supporting material [11]. It is a two-dimensional polymeric semiconductor with a bandgap of around 2.7 eV, which is considered as a prominent photocatalyst for the degradation of organic pollutant. g-C₃N₄ exhibit good chemical stability and unique optical and electronic properties. In addition, it can be prepared from the low-cost nitrogen-rich compound by simple heat treatment process [12]. It was observed that conventional photocatalysts such as TiO₂, ZnO, Fe₂O₃, SnO₂ CaTiO₃ etc. were modified and make heterostructure with another semiconductor to enhance their photocatalytic performance [13–16]. Further, it was found that CT and g-C₃N₄ have well-matched overlapping band structures, suitable for the construction of heterostructures which favour high photocatalytic performance [17]. Owing to the polymeric nature of g-C₃N₄, its surface chemistry can be modified by surface engineering without obviously altering the theoretical composition [18]. The composite of the g-C₃N₄ with a semiconductor such as CaTiO₃ could reduce the bandgap of the semiconductor which may shift the activity of the photocatalyst in

* Corresponding authors.

E-mail addresses: diptivaya08@gmail.com (D. Vaya), praveenkumar.surolia@jaipur.manipal.edu (P.K. Surolia).<https://doi.org/10.1016/j.inoche.2023.111862>

Received 11 October 2023; Received in revised form 28 November 2023; Accepted 8 December 2023

Available online 12 December 2023

1387-7003/© 2023 Elsevier B.V. All rights reserved.

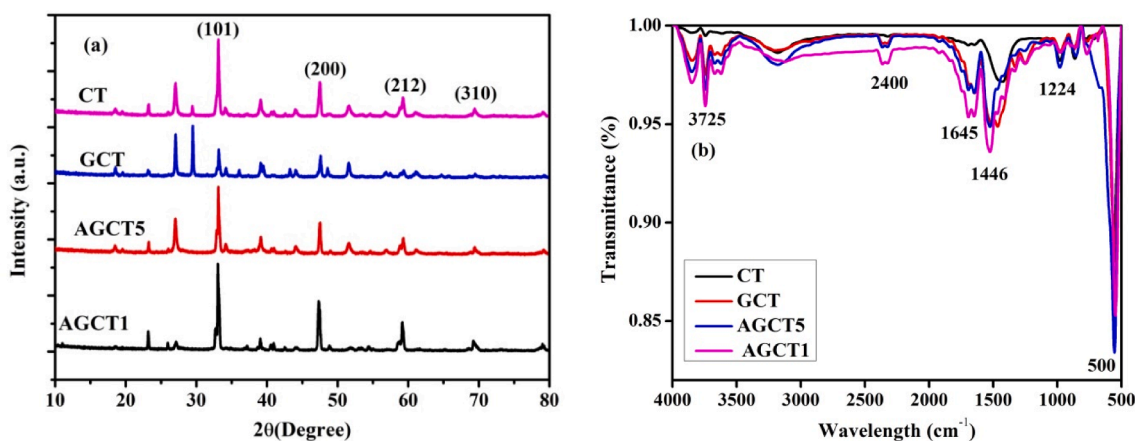


Fig. 1. (a) P-XRD and (b) FTIR spectra of the synthesized photocatalysts.

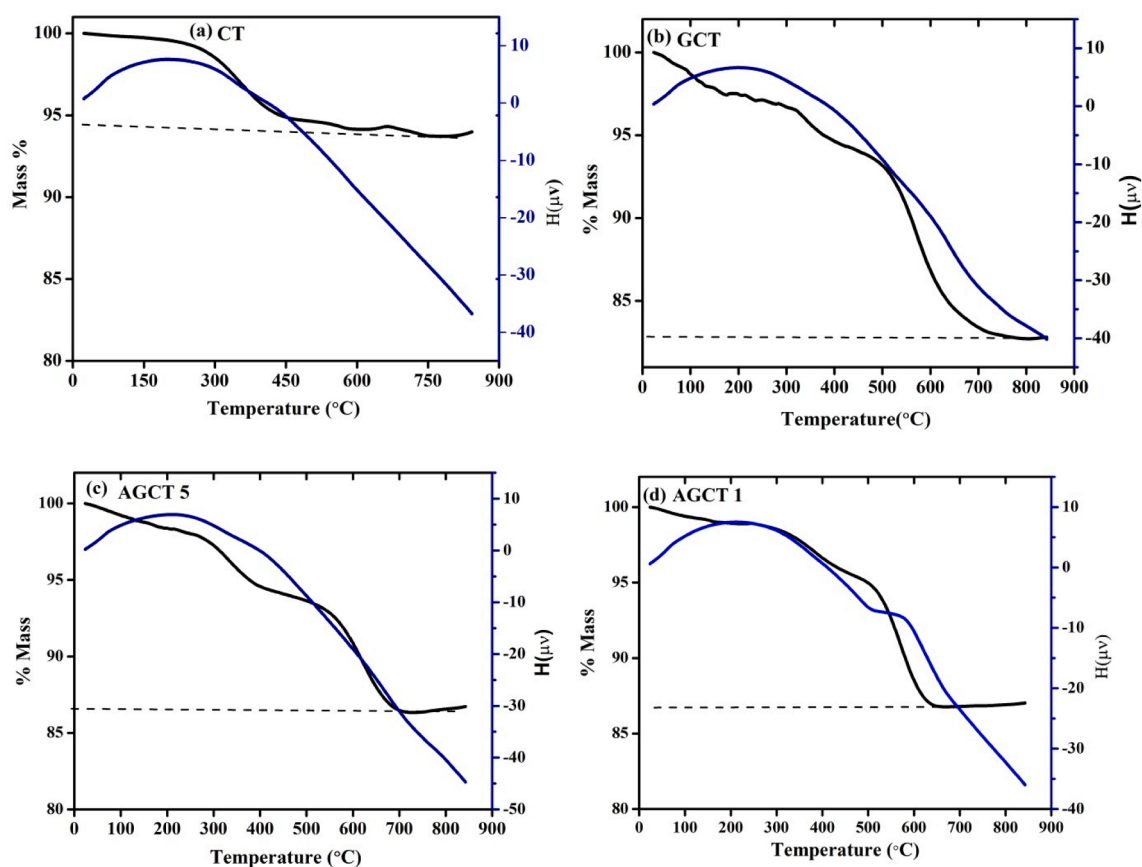


Fig. 2. TGA and DTA spectra of the synthesized photocatalysts.

visible region [11]. Different studies conducted with the combination of $g\text{-C}_3\text{N}_4/\text{CT}$ (GCT) revealed that nanocomposite exhibit superior activity as compared to its counterpart [19,20]. To increase further performance of these nanocomposites, metal and non-metal doping were reported in literature [8,21,22]. Several authors have reported that introduction of Ag^+ ions in semiconductor can generate the intrinsic defects in the host that usefully modify the photocatalytic properties of semiconductor [13,23,24]. Ag leads to a red-shift and increases its photocatalytic efficiency in the visible-light region. Since Ag metal is a good conductor, it can act as a sink for free electrons and increases the separation rates of photo-induced electron-hole pairs.

In this work, we have synthesized ternary $\text{Ag}/g\text{C}_3\text{N}_4/\text{CaTiO}_3$

nanocomposites and their photocatalytic activity was studied for the degradation of model organic pollutant nitrobenzene (NB). A kinetic study was applied to all the reaction performed and results were analysed in terms of final degradation, initial rate of reaction and rate constant. The results demonstrated that the photocatalytic activity of ternary composite was superior to the other combination tried. Further, thermodynamic study was also conducted with the best performing ternary nanocomposite. As per our best knowledge, Ag incorporated $\text{Ag}/g\text{C}_3\text{N}_4/\text{CaTiO}_3$ nanocomposites has not been reported so far for the photocatalytic degradation to remove organic pollutants in water.

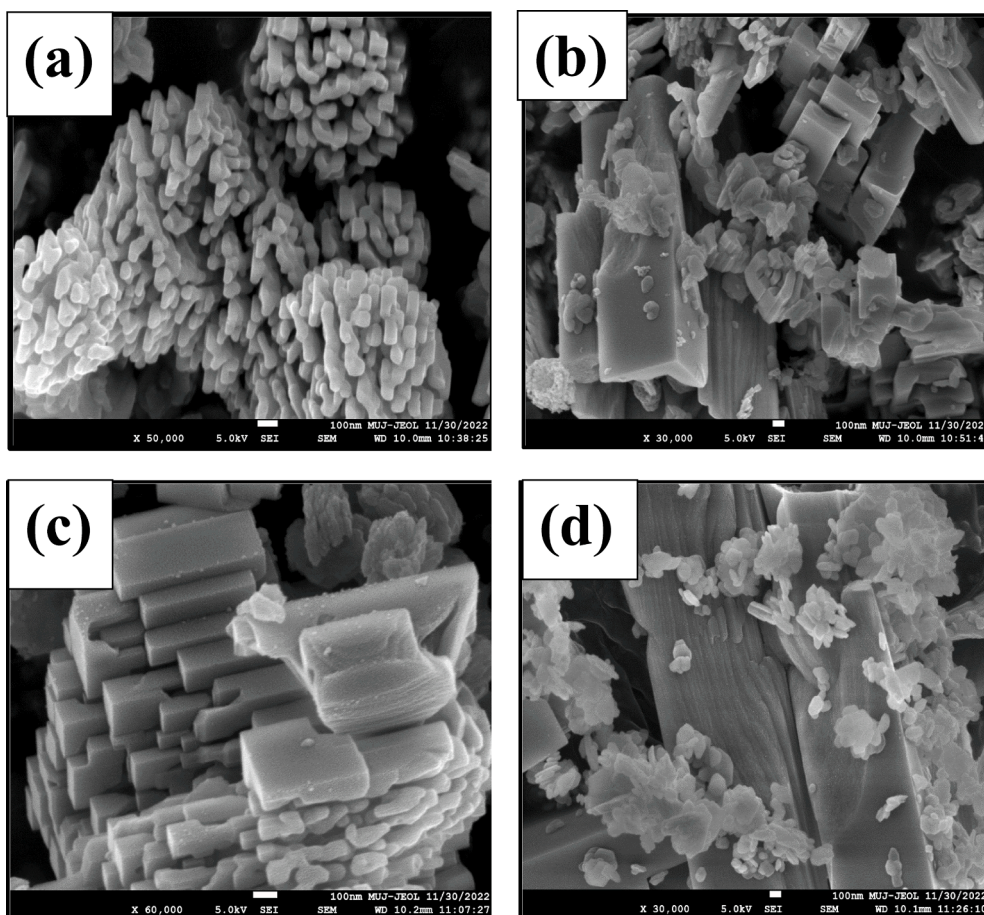


Fig. 3. SEM Images of (a) CT, (b) GCT, (c) AGCT5, (d) AGCT1 samples.

2. Experimental

2.1. Materials and synthesis of the catalysts

CaTiO_3 (CT), $\text{g-C}_3\text{N}_4/\text{CaTiO}_3$ (GCT) heterostructure and $\text{Ag/g-C}_3\text{N}_4/\text{CaTiO}_3$ (AGCT) nanocomposite were synthesized and applied as photocatalysts. The detailed synthesis method and materials used are reported in the [supporting information S.1–S.4](#).

2.2. Catalyst characterization

The prepared catalysts were characterized using different analysis techniques such as XRD, FESEM, DRS, FT-IR, TGA, and UV-Visible analysis was done to measure the progress of degradation reaction. The details are provided in [supporting information \(Section S.5\)](#).

2.3. Photocatalytic activity set-up

The photocatalytic reactor equipped with 500 mL reaction vessel and a 450-Watt power mercury lamp manufactured and supplied by the 'Lelesil Innovation Systems, India' was used to investigate photocatalytic properties of all synthesized samples. The reactor was consisting of two parts. The inner part was made of double-wall jacket quartz with the facility to place the lamp at the centre of it and a water inlet–outlet facility to maintain the temperature throughout the reaction progress [25]. The outer part was made of 500 mL capacity borosilicate glass. The 50 mg photocatalyst was spread in 500 mL of 25 ppm NB solution. Afterwards, the samples were magnetically stirred for 30 min in the dark condition to determine the adsorption–desorption equilibrium. After that 5 mL of sample was taken at every 10 min for first hour,

and finally one sample at 90 min. All the reactions were performed with similar conditions.

3. Results and discussion

3.1. X-ray diffraction analysis

Fig. 1 depicts powder X-ray diffraction (PXRD) patterns for all prepared samples. The PXRD pattern showed a single-phase orthorhombic structure of CT. The corresponding planes were (101), (200), (212) and (310), confirmed with JCPDS card No. 78-2480 with having unit cell parameters as $a = 5.377$, $b = 5.358$ and $c = 7.586$ Å and that were calculated using the formula $d = a/(\frac{1}{h^2} + \frac{1}{k^2} + \frac{1}{l^2})$ [26].

Addition of $\text{g-C}_3\text{N}_4$ caused in the shift in the composite peaks. Diffraction peak was not seen due to the low amount of $\text{g-C}_3\text{N}_4$. After silver doping no additional plane could be seen that might be due to its low concentration. The crystallite size of nanoparticles was calculated using Debye Scherrer Equation (1).

$$D = \frac{k\lambda}{\beta \cos\theta} \quad (1)$$

where D = crystalline size (nm), $K = 0.9$ (Scherrer constant), $\lambda = 0.15406$ nm (wavelength of the X-ray source), β = FWHM (radians), θ = Peak position (radian).

The crystalline size of CT, GCT, AGCT5 and AGCT1 was calculated as 26.31, 47.03, 23.63, 24.87 nm, respectively. It was observed that the particle size decreased with increase in the dopant concentration [27].

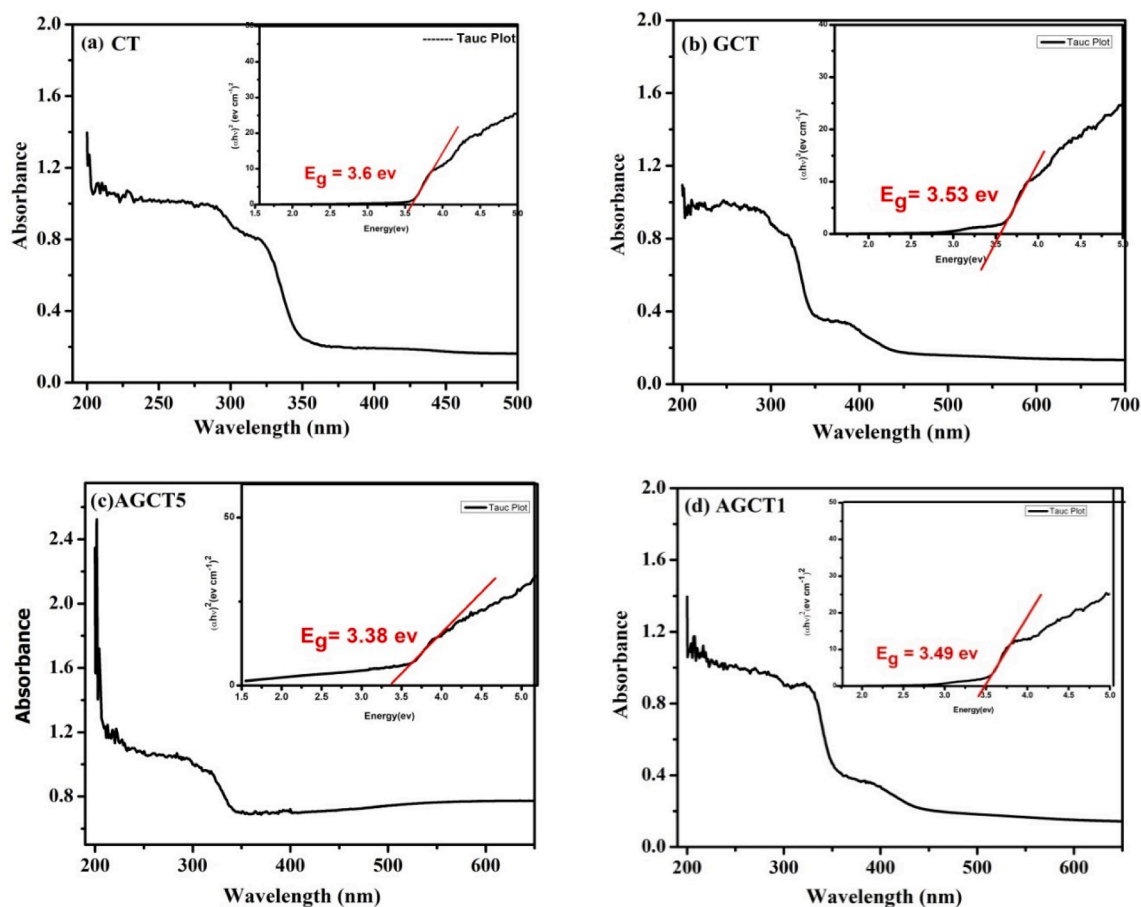


Fig. 4. Tauc plot and bandgap energy of (a) CT, (b) GCT, (c) AGCT5 (d) AGCT1.

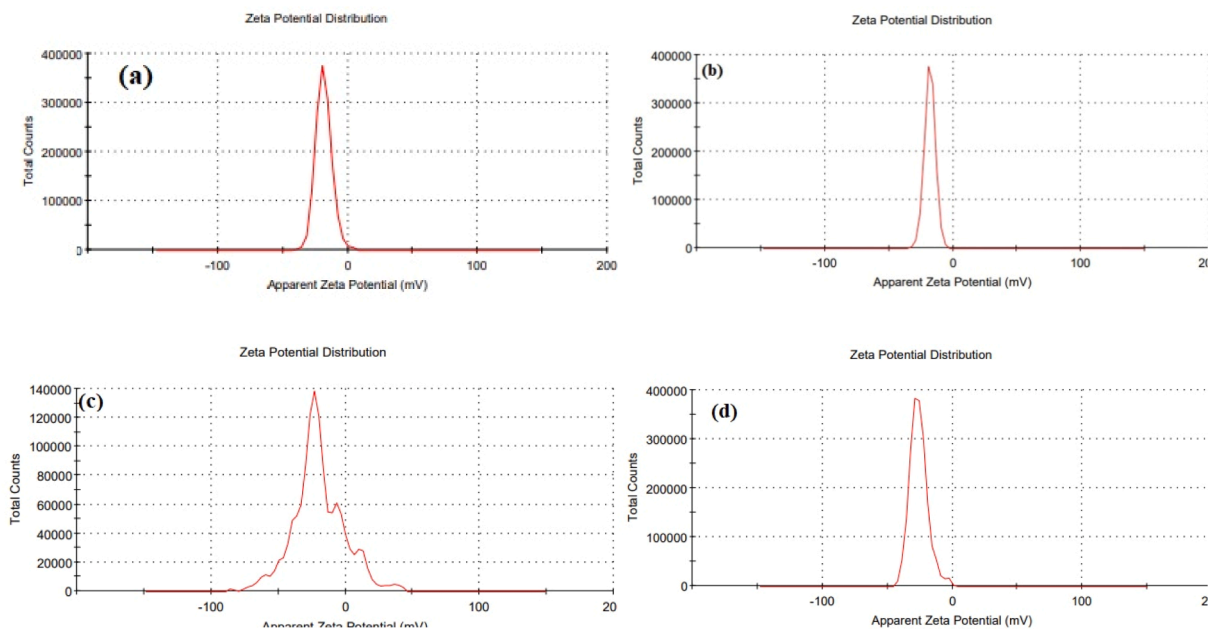


Fig. 5. Zeta potential of (a) CT, (b) GCT, (c) AGCT5 and (d) AGCT1 photocatalysts.

3.2. Fourier transform infrared spectra (FTIR) analysis

Fig. 1 (b) displays the FTIR spectra of CT, GCT, and AGCT heterostructures. The characteristic bands of $g\text{-C}_3\text{N}_4$ and CT were found in the

FTIR spectra of GCT [28]. The strong peak at 1446 cm^{-1} is assigned to the bending vibration of the O–H bond (OH), due to the formation of the Ca–Ti–O–H layer. The peak at 3725 cm^{-1} is ascribed in GCT and AGCT whereas it is not observed in CT due to N–H or NH_2 stretching. The peak

Table 1

Electronic and kinetic properties of all the photocatalytic materials for NB degradation.

Catalyst	Bandgap (eV)	% degradation	Initial rate $\times 10^{-3}$ [mol/L min ⁻¹]	Rate constant $\times 10^{-3}$ [min ⁻¹]	R ²
Blank	–	38.8	1.10	2.6	0.97
CT	3.6	60.9	2.62	5.0	0.95
GCT	3.53	55.7	2.56	4.4	0.95
AGCT5	3.38	70.0	2.36	5.6	0.99
AGCT1	3.49	64.3	2.36	5.3	0.98

at 1224 cm⁻¹ is ascribed in CT, GCT and AGCT due to C–OH stretching. The peak at 1645 cm⁻¹ is not observed in CT while GCT shows a bit broader peak as compared to silver doped sample due to C=N stretching [29]. The prominent peak at 500 cm⁻¹ is present in all samples due to Ti–O stretching vibration.

3.3. Thermogravimetric analysis (TGA) and differential thermal analysis (DTA)

The spectra of all samples CT, GCT, AGCT5 and AGCT1 are displayed in Fig. 2. Three steps of weight loss in TGA were observed in all samples except CT. First weight loss from 50 to 350 °C was due to the moisture loss and removal of water content, second weight loss from 350 to 600 °C was due to the degradation of functional groups such as hydroxyl, nitride etc and then finally in third stage weight loss represent degradation of carbon chain in smaller fragments from 600 to 850 °C [26]. Two steps degradation was observed with CT. First step is removal of moisture, and second stage is removal of functional groups. However, total weight loss % in CT was 6%, GCT 18% while AGCT 5 and AGCT1 13%. This data favour that thermal stability increases by addition of silver doping in GCT. Different concentration of silver doping show nearly same thermal stability.

3.4. Scanning electron microscopy (SEM) analysis

The particle size and surface morphology of all the synthesized samples were studied using SEM as shown in Fig. 3 (a–d). The agglomeration was seen due to the smaller particle size of CT in Fig. 3 (a). With addition of g-C₃N₄, rod like morphology was seen, which is clearly visible in 4 (b) and in this case CT is scattered over surface. In Fig. 3 (c) and 3 (d), there is no visible difference in the images. Silver nanoparticles have spherical morphology and distribute over the complete surface. AGCT1 and AGCT5 nanoparticles were agglomerated and

there was high interconnectivity among grains [30].

3.5. UV – Vis spectroscopy (DRS) analysis

The Optical properties of the samples were analysed using UV–Vis diffuse reflectance spectroscopy, and the bandgap of the samples were determined from the Tauc plots (Fig. 4) [31]. The DRS of CT showed an absorption edge at around 300–330 nm and second absorption edge at around 330–350 nm respectively and the band gap (E_g) calculated of CT was 3.6 eV. The absorption edge of GCT heterostructures was observed to be in between 330–350 nm and the bandgap calculated was 3.53 eV, g-C₃N₄ might be act as a sensitizer, thus the CT heterostructures showed absorption ability towards red end of spectrum. Similarly, bandgaps of AGCT5, AGCT1 calculated were 3.38, 3.49 eV respectively (see Fig. 4).

3.6. Zeta potential study

Zeta potential was measured to check stability of nanomaterials in dispersion (see Fig. 5). In this work, water was used as dispersing solvent. The values of zeta potential measured were –18.4, –18, –19.2, –25.8 mV for CT, GCT, AGCT5 and AGCT1 respectively. The zeta potential from +30 to –30 mV showed stability in the dispersed systems [32]. It can be clearly seen that silver doped samples AGCT5 and AGCT1 showed higher dispersion stability in water and that can be seen in their effective photocatalytic performance as well.

4. Photocatalytic activity and kinetics of nitrobenzene degradation

The photocatalytic degradation study of the synthesized catalysts was conducted for the degradation of NB solution and results are provided in Table 1. A 500 mL 25 ppm solution of NB was taken in the photochemical reactor and a catalyst dose of 50 mg was used in all the performed experiments. The initial rate of degradation was calculated at a time 10 min of the reaction and the final degradation was reported at

Table 2

Electronic and kinetic properties of Ag/g-C₃N₄/CaTiO₃ for NB degradation at different temperature.

Temperature	% Degradation	Initial rate $\times 10^{-3}$ [molL ⁻¹ min ⁻¹]	Rate constant $\times 10^{-3}$ [min ⁻¹]	R ²
5 °C	39.4	0.85	2.3	0.99
10 °C	51.1	1.25	3.6	0.99
15 °C	63.9	2.21	5.2	0.97
20 °C	70.4	2.36	5.6	0.98

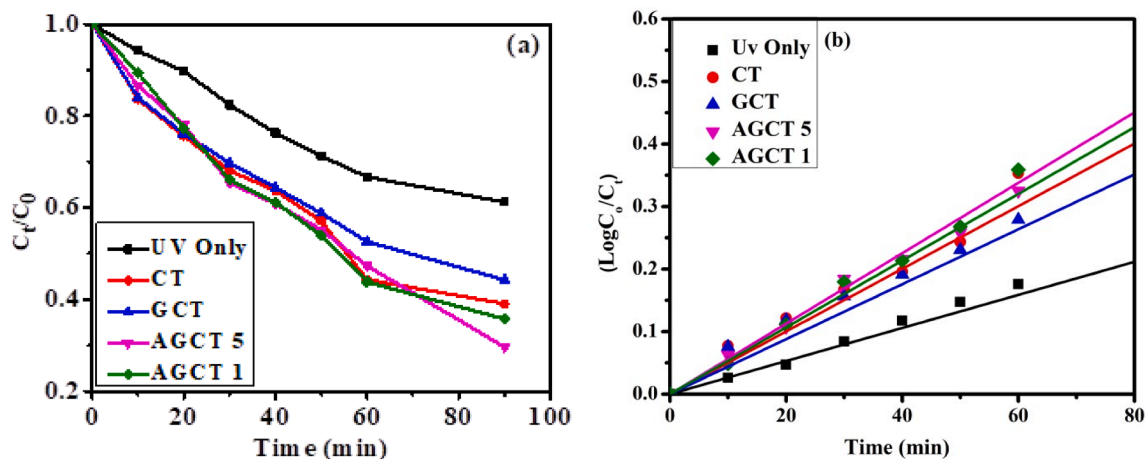


Fig. 6. (a) Increase in % degradation of nitrobenzene as a function of irradiation time, and (b) kinetics of nitrobenzene degradation [NB = 500 mL, 25 ppm; Catalyst: 50 mg; Reaction time: 90 min].

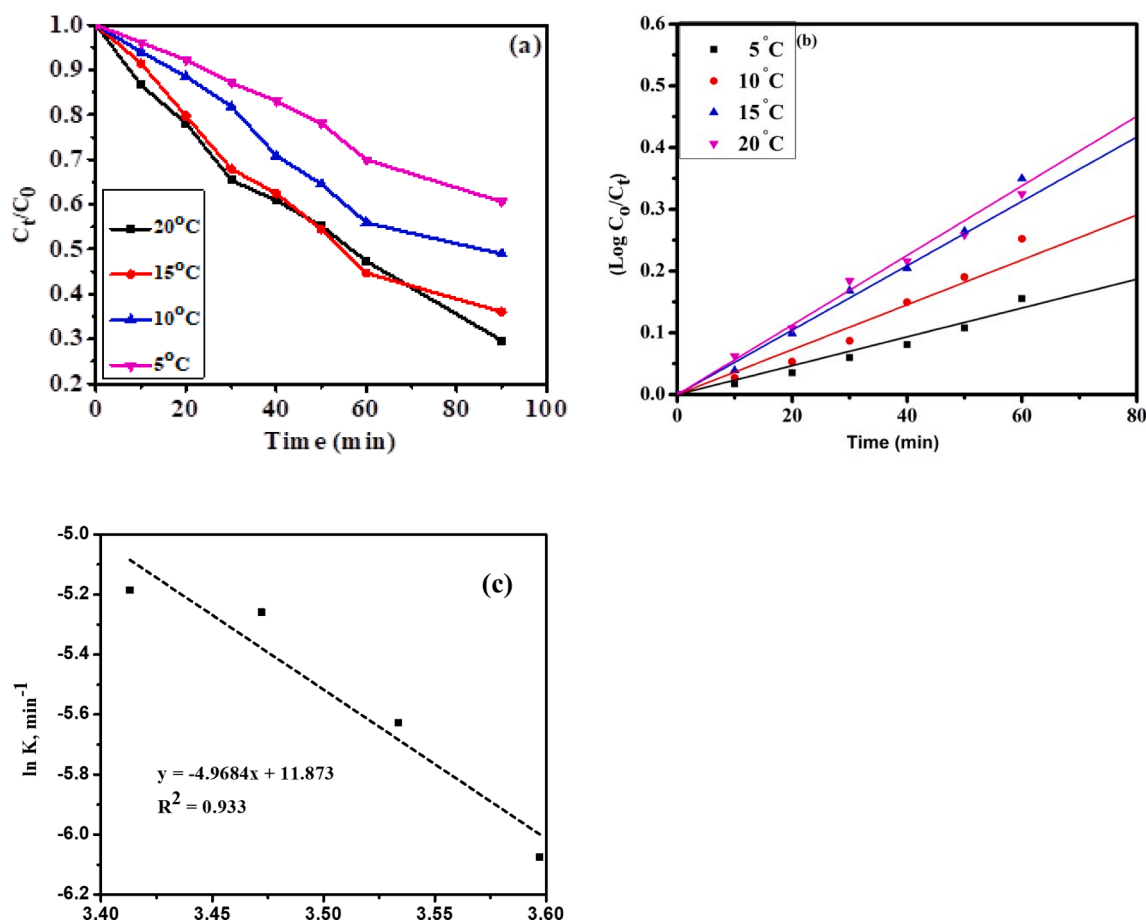


Fig. 7. Kinetics of nitrobenzene degradation with AGCT5 (a) Increase in % degradation of as a function of irradiation time at different temperature, (b) kinetics of Nitrobenzene degradation at different temperature (c) the plot of natural logarithm of rate constant, $\ln(k)$ as a function of reciprocal temperature ($1/T$).

Table 3

Comparison of synthesized Ag/g- C_3N_4 /CaTiO₃ nanocomposite catalyst with other similar kind of photocatalysts.

S. No	Photocatalyst	Application	Efficiency	Ref.
1.	Silver decorated ZnO nanocomposite with sulfurized graphitic carbon nitride	Photodegradation of MB	98%	[35]
2.	C_3N_4 @porphyrin nanorods hybrid material	Photodegradation of MB	100%	[36]
3.	g- C_3N_4 /SrTiO ₃	Photocatalytic degradation of reactive blue 198 (RB 198), reactive black 5 (RB 5) and reactive yellow 145 (RY 145)	50%	[12]
4.	CaTiO ₃ /g- C_3N_4 /AgBr	Degradation of RhB	99.6%	[20]
5.	TiO ₂ /ZrO ₂ /g- C_3N_4	Degradation of berberine hydrochloride	86%	[37]
6.	Ag/g- C_3N_4 /NaTaO ₃	Degradation of tetracycline	95.47%	[38]
7.	Ag/g- C_3N_4 /CaTiO ₃ nanocomposite	Photodegradation of nitrobenzene	70%	This Work

90 min. The final percentage of degradation was observed 70% with AGCT5 and 64.2% with AGCT1 which were highest among other catalyst applied after 90 min. Pristine CT showed 60.9% and GCT 55.7% degradation in the similar time. For a comparison, a blank study was also conducted without any catalyst and 34.7% degradation was observed

after 90 min. This clearly shows the role of catalyst in the photocatalytic degradation process. The final percentage degradation was observed in the range of 34 to 70% for all the reaction performed. The initial rate of reactions was almost in similar range of 2.36×10^{-3} to $2.62 \times 10^{-3} \text{ molL}^{-1}\text{min}^{-1}$. These values were very high compared to blank reaction without any catalyst ($1.10 \times 10^{-3} \text{ molL}^{-1}\text{min}^{-1}$). Comparison of photocatalytic performance of CT, GCT, AGCT5, AGCT1 validates that the AGCT5 expressed the higher extent of photocatalytic performance compared to other applied photocatalysts. Further, it could be seen that the addition of Ag content increased the photocatalytic performance. The Ag dopant possesses the multivalency which leads to prevent agglomeration and recombination of electrons and holes and transferring them from Ag to Ca. Thus, we may conclude that the Ag doping in CT catalyst leads to antagonist performance, and to better degradation of NB (Table 1). Kinetics in Fig. 6 (a) shows that the degradation pattern of NB follow pseudo-first order kinetics, where the rate of degradation reaction “r” is proportional to the concentration C_t at time “t” (Eq. (2)) [33].

$$r = kK C_t \div 1 + K C_t \quad (2)$$

where k is the reaction rate constant, and K is the reactant adsorption constant. The apparent first order linear expression is expressed in Fig. 6. The calculated apparent R^2 values of linearity are specified in Table 1. Further, the best performing catalyst AGCT5 was tested at four different reaction temperatures viz. 5, 10, 15 and 20 °C. The results are shown in Table 2. The reaction rate and percentage degradation were observed to get increased with the increase in the temperature. The minimum degradation was just 39.4% at 5 °C and highest 70.4% at 20 °C. The initial rate of reaction and rate constant values also followed the similar

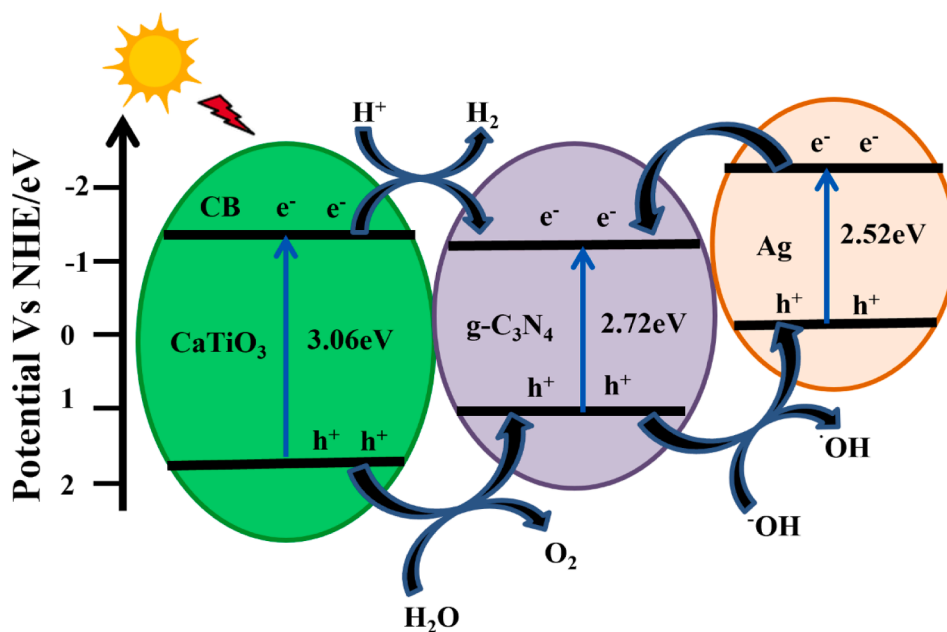


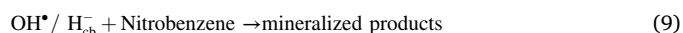
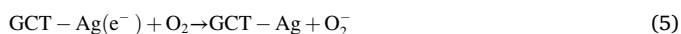
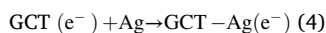
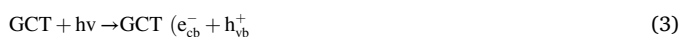
Fig. 8. Proposed process of charge separation in Ag/g-C₃N₄/CaTiO₃ photocatalyst.

trend. The minimum initial rate of reaction was observed $0.85 \times 10^{-3} \text{ molL}^{-1} \text{ min}^{-1}$ at 5 °C and highest 2.36×10^{-3} at 20 °C $\text{molL}^{-1} \text{ min}^{-1}$.

The temperature influences primarily to the energy of activation and helps to overcome that. Thus, the oxidation of organic pollutants occurs at higher rate at high reaction temperature conditions [34]. Further, at increased temperature, charge carrier species become more active and shows higher mobility. Photogenerated charged species e^- and h^+ react with adsorbed oxygen and OH^- at greater speed and improve the degradation capacity of the catalyst. However, previous studies reported that photocatalytic activity may get reduced if the temperature is increased after an optimum level. That happens due to more recombination of charge carriers. In this study, we observed an increasing pattern of performance with increase in temperature as reaction temperature applied was 20 °C and below. Fig. 7 (C) demonstrates the plot of natural logarithm of rate constant $\ln(k)$ as a function of reciprocal temperature ($1/T$). The slope of the plot relates to the apparent activation energy (E_a) of the overall reaction, expressed in kilojoules per mole (kJ mol^{-1}). The calculated value for the overall apparent activation energy of the NB degradation process from the data of Table 2 was found to be 41.3 kJ/mol. This value is much higher than the previously reported studies where the activation energy of photocatalytic degradation of NB with P25 was to be around 22 kJ/mol [34]. The Comparative literature of synthesized Ag/g-C₃N₄/CaTiO₃ nanocomposite photocatalyst with other similar kind of catalysts is given in Table 3.

5. Mechanism approach nitrobenzene degradation

Photocatalytic degradation of organic materials in water can be explained by bandgap model of semiconductors. Semiconductors are composed by band framework, where valence band (VB) and conduction band (CB) are separated with an energy gap (E_g). Based on experimental data received, the photocatalytic process and its mechanistic approaches are proposed. The proposed mechanism of NB degradation using metal doped CT is given from Eqs. (3)–(9).



Firstly, synthesized GCT photocatalyst take a photon with energy higher or equal to its band gap and generate e^-/h^+ charge carrier in CB and VB respectively as Eq. (3). These e^- transfer from GCT to Ag. Further, these e^- and h^+ react with the reactive oxygen species O_2 and H_2O to generate superoxide anion (O_2^-), hydroxyl radical (OH^\bullet) and H_2O_2 as shown in Equation 5–7. These strong oxidative species that is reactive oxygen species (ROS) further oxidize NB and other organic fragments adsorbed on the photocatalyst, finally convert to the mineralized product CO_2 , H_2O and NH_4^+ as in Eq. (9) [39,40]. The involvement of these major reactive species can be confirmed by application of suitable scavengers during the process [41]. As shown by Fig. 8, bandgap of all CT, g-C₃N₄ and Ag are suitable for electron and hole transport, and this leads to minimise electron hole recombination which is more suitable for photocatalysis of pollutants.

6. Conclusion

In summary, Ag/g-C₃N₄/CaTiO₃ (AGCT) heterostructure photocatalysts were synthesized. Compared with bare CT nanoparticles, the photocatalytic activity of AGCT heterostructures was improved for the degradation of nitrobenzene under sunlight irradiation. The enhanced photocatalytic activity of AGCT heterostructure photocatalysts could be ascribed to the formation of heterojunction between CT and g-C₃N₄. The Final percentage of degradation was observed 70 % with AGCT5 and 64 % with AGCT1 which were highest among other catalyst applied after 2 h. The final percentage degradation was observed in the range of 34–70 % for all the reaction performed because silver nanoparticle has proven to exhibit excellent electrical conductivity, chemical stability, and catalytic properties. The presence of silver nanoparticles on the surface of GCT can facilitate catalytic reaction by providing active sites for adsorption and reaction. This enhanced catalytic activity makes silver-doped GCT potentially useful for the application such as catalytic

converter for water purification. From the result it was concluded that the doped material increased the efficiency of the catalyst as compared to the without doped material.

Consent to participate

Not applicable.

Consent to publish

Not applicable.

Ethical approval

Not applicable for this work.

CRedit authorship contribution statement

Akshima Soni: Data curation, Investigation, Writing – original draft.
Saurav Mishra: Formal analysis. **Dipti Vaya:** . **Praveen K. Surolia:** .

Declaration of Competing Interest

The authors declare that they have no known competing financial interests or personal relationships that could have appeared to influence the work reported in this paper.

Data availability

The data used and/or analysed during the present study are available from the corresponding author on request.

Acknowledgements

All Authors are thankful to Amity university, Haryana, 'Central Analytical Facilities (CAF)' and 'Sophisticated Analytical Instrument Facility (SAIF)' at Manipal University Jaipur for providing the materials characterization facility and support. DV acknowledges the support provided under the DST-FIST Grant No. SR/FST/PS-I/2018/48 of Govt. of India. PKS acknowledge funding support from Science and Engineering Research Board (SERB), India, under the Grant No. [CRG/2021/002477-G].

Appendix A. Supplementary material

Supplementary data to this article can be found online at <https://doi.org/10.1016/j.inoche.2023.111862>.

References

- [1] P.K. Arora, H. Bae, Toxicity and microbial degradation of nitrobenzene, monochloronitrobenzenes, polynitrobenzenes, and pentachloronitrobenzene, *J. Chem.* 2014 (2014), 265140, <https://doi.org/10.1155/2014/265140>.
- [2] R. Emmanuel, C. Karupiah, S.-M. Chen, S. Palanisamy, S. Padmavathy, P. Prakash, Green synthesis of gold nanoparticles for trace level detection of a hazardous pollutant (nitrobenzene) causing Methemoglobinemia, *J. Hazard. Mater.* 279 (2014) 117–124, <https://doi.org/10.1016/j.jhazmat.2014.06.066>.
- [3] S. Majeed, H.M. Junaid, M.T. Waseem, T. Mahmood, U. Farooq, S.A. Shahzad, Receptor free fluorescent and colorimetric sensors for solution and vapor phase detection of hazardous pollutant nitrobenzene; a new structural approach to design AIEE active and piezofluorochromic sensors, *J. Photochem. Photobiol. A Chem.* 431 (2022), 114022, <https://doi.org/10.1016/j.jphotochem.2022.114022>.
- [4] S. Mishra, N. Chakinala, A.G. Chakinala, P.K. Surolia, Photocatalytic performance of Bi/Zn co-doped sol-gel synthesized TiO₂ nanoparticles, *J. Chem. Technol. Biotechnol. n/a (n.d.)*. <<https://doi.org/https://doi.org/10.1002/jctb.7555>>.
- [5] S. Mishra, N. Chakinala, A.G. Chakinala, P.K. Surolia, Photocatalytic degradation of methylene blue using monometallic and bimetallic Bi-Fe doped TiO₂, *Catal. Commun.* 171 (2022), 106518, <https://doi.org/10.1016/j.catcom.2022.106518>.
- [6] N. Verma, T.S. Chundawat, H. Chandra, D. Vaya, An efficient time reductive photocatalytic degradation of carcinogenic dyes by TiO₂-GO nanocomposite, *Mater. Res. Bull.* 158 (2023), 112043, <https://doi.org/10.1016/j.materresbull.2022.112043>.
- [7] R. Yadav, T.S. Chundawat, P.K. Surolia, D. Vaya, Photocatalytic degradation of ortho-nitrophenol using ZnO-β-CD nanocomposite, *ChemistrySelect* 7 (2022) e202200394.
- [8] H. Zhang, G. Chen, Y. Li, Y. Teng, Electronic structure and photocatalytic properties of copper-doped CaTiO₃, *Int. J. Hydrogen Energy.* 35 (2010) 2713–2716, <https://doi.org/10.1016/j.ijhydene.2009.04.050>.
- [9] H. Wang, Q. Zhang, M. Qiu, B. Hu, Synthesis and application of perovskite-based photocatalysts in environmental remediation: a review, *J. Mol. Liq.* 334 (2021), 116029, <https://doi.org/10.1016/j.molliq.2021.116029>.
- [10] P. Kanhere, Z. Chen, A review on visible light active perovskite-based photocatalysts, *Molecules* 19 (2014) 19995–20022, <https://doi.org/10.3390/molecules191219995>.
- [11] D. Vaya, B. Kaushik, P.K. Surolia, Recent advances in graphitic carbon nitride semiconductor: structure, synthesis and applications, *Mater. Sci. Semicond. Process.* 137 (2022), 106181, <https://doi.org/10.1016/j.mssp.2021.106181>.
- [12] T. Sureshkumar, S. Thiripuranthagan, S.M.K. Paskalis, S. Kumaravel, K. Kannan, A. Devarajan, Synthesis, characterization and photodegradation activity of graphitic C₃N₄-SrTiO₃ nanocomposites, *J. Photochem. Photobiol. A Chem.* 356 (2018) 425–439, <https://doi.org/10.1016/j.jphotochem.2018.01.027>.
- [13] D. Gogoi, A. Namdeo, A.K. Golder, N.R. Peela, Ag-doped TiO₂ photocatalysts with effective charge transfer for highly efficient hydrogen production through water splitting, *Int. J. Hydrogen Energy.* 45 (2020) 2729–2744, <https://doi.org/10.1016/j.ijhydene.2019.11.127>.
- [14] J. Tao, M. Zhang, X. Gao, H. Zhao, Z. Ren, D. Li, J. Li, R. Zhang, Y. Liu, Y. Zhai, Photocatalyst Co₃O₄/red phosphorus for efficient degradation of malachite green under visible light irradiation, *Mater. Chem. Phys.* 240 (2020), 122185, <https://doi.org/10.1016/j.matchemphys.2019.122185>.
- [15] X.J. Huang, X. Yan, H.Y. Wu, Y. Fang, Y.H. Min, W.S. Li, S.Y. Wang, Z.J. Wu, Preparation of Zr-doped CaTiO₃ with enhanced charge separation efficiency and photocatalytic activity, *Trans. Nonferr. Metals Soc. China (English Ed.)*. 26 (2016) 464–471, [https://doi.org/10.1016/S1003-6326\(16\)64097-9](https://doi.org/10.1016/S1003-6326(16)64097-9).
- [16] Y. Zhang, M. Sillanpää, Chapter 5 – modification of photocatalyst with enhanced photocatalytic activity for water treatment, in: M. Sillanpää (Ed.), *Advanced Water Treatment*, Elsevier, 2020, pp. 289–366. <<https://doi.org/https://doi.org/10.1016/B978-0-12-819225-2.00005-3>>.
- [17] A. Kumar, C. Schuerings, S. Kumar, A. Kumar, V. Krishnan, Perovskite-structured CaTiO₃ coupled with g-C₃N₄ as a heterojunction photocatalyst for organic pollutant degradation, *Beilstein J. Nanotechnol.* 9 (2018) 671–685, <https://doi.org/10.3762/bjnano.9.62>.
- [18] W. Zhang, J. Zhang, F. Dong, Y. Zhang, Facile synthesis of in situ phosphorus-doped g-C₃N₄ with enhanced visible light photocatalytic property for NO purification, *RSC Adv.* 6 (2016) 88085–88089, <https://doi.org/10.1039/C6RA18349B>.
- [19] J. Zhao, X. Cao, Y. Bai, J. Chen, C. Zhang, Simple synthesis of CaTiO₃/g-C₃N₄ heterojunction for efficient photodegradation of methylene blue and levofloxacin, *Opt. Mater. (Amst.)* 135 (2023), 113239, <https://doi.org/10.1016/j.optmat.2022.113239>.
- [20] Y. Yan, H. Yang, Z. Yi, R. Li, T. Xian, Design of ternary CaTiO₃/g-C₃N₄/AgBr Z-scheme heterostructured photocatalysts and their application for dye photodegradation, *Solid State Sci.* 100 (2020), 106102, <https://doi.org/10.1016/j.solidstatesciences.2019.106102>.
- [21] C.W. Chang, C. Hu, Graphene oxide-derived carbon-doped SrTiO₃ for highly efficient photocatalytic degradation of organic pollutants under visible light irradiation, *Chem. Eng. J.* 383 (2020), 123116, <https://doi.org/10.1016/j.cej.2019.123116>.
- [22] P. Akhter, A. Arshad, A. Saleem, M. Hussain, Recent development in non-metal-doped titanium dioxide photocatalysts for different dyes degradation and the study of their strategic factors: a review, *Catalysts* 12 (2022) 1331, <https://doi.org/10.3390/catal12111331>.
- [23] S. Krejčíková, L. Matějová, K. Kočí, L. Obalová, Z. Matěj, L. Čapek, O. Šolcová, Preparation and characterization of Ag-doped crystalline titania for photocatalysis applications, *Appl. Catal. B.* 111–112 (2012) 119–125, <https://doi.org/10.1016/j.apcatb.2011.09.024>.
- [24] S.P. Onkani, P.N. Diagboya, F.M. Mtunzi, M.J. Klink, B.I. Olu-Owolabi, V. Pakade, Comparative study of the photocatalytic degradation of 2-chlorophenol under UV irradiation using pristine and Ag-doped species of TiO₂, ZnO and ZnS photocatalysts, *J. Environ. Manage.* 260 (2020), 110145, <https://doi.org/10.1016/j.jenvman.2020.110145>.
- [25] S. Preeti, N. Mishra, A.G. Chakinala, P.K. Chakinala, Surolia, Bimetallic Bi/Zn decorated hydrothermally synthesized TiO₂ for efficient photocatalytic degradation of nitrobenzene, *Catal. Commun.* 172 (2022), 106538, <https://doi.org/10.1016/j.catcom.2022.106538>.
- [26] V. Lalan, V.P.M. Pillai, K.G. Gopchandran, Enhanced electron transfer due to rGO makes Ag e CaTiO₃ @ rGO a promising plasmonic photocatalyst, *J. Sci.: Adv. Mater. Devices* 7 (2022), 100468, <https://doi.org/10.1016/j.jsamd.2022.100468>.
- [27] M. Karimipour, S. Khazraei, B.J. Kim, G. Boschloo, E.M.J. Johansson, Efficient and bending durable flexible perovskite solar cells via interface modification using a combination of thin MoS₂ nanosheets and molecules binding to the perovskite, *Nano Energy* 95 (2022), 107044, <https://doi.org/10.1016/j.nanoen.2022.107044>.
- [28] S. Kappadan, S. Thomas, N. Kalarikkal, Enhanced photocatalytic performance of BaTiO₃/g-C₃N₄ heterojunction for the degradation of organic pollutants, *Chem. Phys. Lett.* 771 (2021), 138513, <https://doi.org/10.1016/j.cplett.2021.138513>.

- [29] T. Xian, H. Yang, L.J. Di, J.F. Dai, Enhanced photocatalytic activity of BaTiO₃@g-C₃N₄ for the degradation of methyl orange under simulated sunlight irradiation 622 (2015) 1098–1104. <<https://doi.org/10.1016/j.jallcom.2014.11.051>>.
- [30] B. Yang, C. Wu, J. Wang, J. Bian, L. Wang, M. Liu, Y. Du, When C₃N₄ meets BaTiO₃: ferroelectric polarization plays a critical role in building a better photocatalyst, *Ceram. Int.* 46 (2020) 4248–4255, <https://doi.org/10.1016/j.ceramint.2019.10.145>.
- [31] S.K.K. Aung, A. Vijayan, M. Karimipour, T. Seetawan, G. Boschloo, Reduced hysteresis and enhanced air stability of low-temperature processed carbon-based perovskite solar cells by surface modification, *Electrochim. Acta.* 443 (2023), 141935, <https://doi.org/10.1016/j.electacta.2023.141935>.
- [32] R.P. Singh, K. Sharma, K. Mausam, Dispersion and stability of metal oxide nanoparticles in aqueous suspension: a review, *Mater Today Proc.* 26 (2020) 2021–2025, <https://doi.org/10.1016/j.matpr.2020.02.439>.
- [33] P.K. Surolia, R.V. Jasra, Photocatalytic degradation of p-nitrotoluene (PNT) using TiO₂-modified silver-exchanged NaY zeolite: kinetic study and identification of mineralization pathway, *Desal. Water Treat.* 57 (2016) 22081–22098, <https://doi.org/10.1080/19443994.2015.1125798>.
- [34] X. Shen, L. Zhu, N. Wang, T. Zhang, H. Tang, Selective photocatalytic degradation of nitrobenzene facilitated by molecular imprinting with a transition state analog, *Catal. Today.* 225 (2014) 164–170, <https://doi.org/10.1016/j.cattod.2013.07.011>.
- [35] S. Iqbal, A. Bahadur, S. Ali, Z. Ahmad, M. Javed, R.M. Irfan, N. Ahmad, M. A. Qamar, G. Liu, M.B. Akbar, M. Nawaz, Critical role of the heterojunction interface of silver decorated ZnO nanocomposite with sulfurized graphitic carbon nitride heterostructure materials for photocatalytic applications, *J. Alloys Compd.* 858 (2021), 158338, <https://doi.org/10.1016/j.jallcom.2020.158338>.
- [36] Q.D. Ho, T.T. Le, G.T. Nguyen, D.H. Nguyen, H.H. Nguyen, H.T.T. Le, L.T.T. Chu, C. Van Tran, P.T.H. Nguyen, M.-J. Um, T.T. Nguyen, D.D. Nguyen, D.D. La, Fabrication of g-C₃N₄@porphyrin nanorods hybrid material via CTAB surfactant-assisted self-assembly for photocatalytic degradation of Cr(VI) and methylene blue, *Nano-Struct. Nano-Obj.* 36 (2023), 101063, <https://doi.org/10.1016/j.nanos.2023.101063>.
- [37] P. Ding, H. Ji, P. Li, Q. Liu, Y. Wu, M. Guo, Z. Zhou, S. Gao, W. Xu, W. Liu, Q. Wang, S. Chen, Visible-light degradation of antibiotics catalyzed by titania/zirconia/graphitic carbon nitride ternary nanocomposites: a combined experimental and theoretical study, *Appl. Catal. B.* 300 (2022), 120633, <https://doi.org/10.1016/j.apcatb.2021.120633>.
- [38] L. Tang, C. Feng, Y. Deng, G. Zeng, J. Wang, Y. Liu, H. Feng, J. Wang, Enhanced photocatalytic activity of ternary Ag/g-C₃N₄/NaTaO₃ photocatalysts under wide spectrum light radiation: the high potential band protection mechanism, *Appl. Catal. B.* 230 (2018) 102–114, <https://doi.org/10.1016/j.apcatb.2018.02.031>.
- [39] P.K. Surolia, R.J. Tayade, R.V. Jasra, Photocatalytic degradation of nitrobenzene in an aqueous system by transition-metal-exchanged ETS-10 zeolites, *Ind. Eng. Chem. Res.* 49 (2010) 3961–3966, <https://doi.org/10.1021/ie901603k>.
- [40] P.K. Surolia, R.V. Jasra, Degradation and mineralization of aqueous nitrobenzene using ETS-4 photocatalysis, *Desalination, Water Treat.* 57 (2016) 15989–15998, <https://doi.org/10.1080/19443994.2015.1079801>.
- [41] R. Yadav, T.S. Chundawat, P.K. Surolia, D. Vaya, Photocatalytic degradation of textile dyes using β-CD-CuO/ZnO nanocomposite, *J. Phys. Chem. Solid* 165 (2022), 110691, <https://doi.org/10.1016/j.jpcs.2022.110691>.